FACULTY OF BIOLOGICAL SCIENCES

Doctoral Program in Biomedicine and Biotechnology

POLYMER THERAPEUTICS LABORATORY

DESIGN OF NOVEL TARGETED POLYMER THERAPEUTICS AS COMBINATION THERAPY FOR THE TREATMENT OF BRAIN METASTASIS - OVERCOMING THE BLOOD-BRAIN BARRIER

FERNANDA DAYANA RODRÍGUEZ OTORMIN

Doctoral Thesis – University of Valencia

January 2022

Thesis directors: **Dr. María J. Vicent Docón** and **Dr. Aroa Duro Castaño**

1

Dr. María J. Vicent Docón, Ph.D. in Chemistry and Head of the Polymer Therapeutics Laboratory at the Centro de Investigación Príncipe Felipe (Valencia, Spain), and Dr. Aroa Duro Castaño, Ph.D. in Biochemistry and Biomedicine and Head of the Research and Development Department in Polypeptide Therapeutic Solutions S.L. (Valencia, Spain)

CERTIFY, that the work

"DESIGN OF NOVEL TARGETED POLYMER THERAPEUTICS AS COMBINATION THERAPY FOR THE TREATMENT OF BRAIN METASTASIS - OVERCOMING THE BLOOD-BRAIN BARRIER"

has been developed by Fernanda Dayana Rodríguez Otormin under their supervision in the Centro de Investigación Príncipe Felipe in Valencia, as a thesis project to obtain a Ph.D. degree in Biomedicine and Biotechnology from the University of Valencia, Faculty of Biological Sciences.

A mis padres

INDEX

10

13

CHAPTER 4. RATIONAL DESIGN OF BRAIN-TARGETED COMBINATION CONJUGATES FOR THE TREATMENT OF BREAST CANCER BRAIN METASTASIS……………………… 371

15

16

AKNOWLEDGEMENTS

Soy de esas personas que creen que todos los que se cruzan contigo en la vida te aportan algo, te enseñan cosas, te van moldeando como persona. Que cada experiencia que vives te cambia. Yo no soy la misma persona que era cuando empecé la tesis. Pero tampoco voy a echarle la culpa de eso solo a la tesis. Muchas cosas han pasado en estos últimos 5 años y no habría sobrevivido, ni mucho menos terminado esta tesis, sin el apoyo de muchas personas. Me gustaría agradecer en los siguientes párrafos a esas personas y dedicarles alguna frase que creo se ajusta a su papel en esta tesis y que a mí me han valido de inspiración.

Para lograr grandes cosas, se necesita un plan y poco tiempo.

Leonard Bernstein

Un plan y poco tiempo para llevarlo a cabo es lo que tenía al empezar la tesis, aunque yo no lo supiera entonces… Este plan no se habría llevado a cabo sin la colaboración de muchas personas. Por supuesto, tengo que empezar por mis directoras de tesis, María Jesús y Aroa. María Jesús, gracias por darme la oportunidad de hacer la tesis en tu laboratorio. Siempre has creído en mí y en mis capacidades y me has dado tu apoyo, sobre todo a nivel personal y cuando más lo necesitaba. Nunca olvidaré eso. ¡Aroa! ¡Mi directora en la distancia! Si ya es difícil ser directora de tesis, ¡imaginaros desde otro país y huso horario! Gracias por estar ahí a pesar de la distancia y por apoyarme tanto, por enseñarme lo que sé de química (si alguien tiene alguna queja, hablad con ella), y por ayudarme a tener perspectiva. Admiro tu forma de sacarle el lado bueno a todos los resultados. A TODOS. Me ha venido muy bien tener esa visión positiva cerca.

A ambas también tengo que agradeceros la oportunidad de trabajar con tan buenos colaboradores. Empezando por el Prof. Giuseppe Battaglia, a quien agradezco la oportunidad de hacer una estancia en su laboratorio. Quiero agradecer también a todo su equipo, en especial a Diana por enseñarme y hacer los experimentos *in vitro*. Finalmente, agradecer al Dr. Manuel Valiente y a su equipo por realizar el experimento *in vivo* de metástasis cerebral, en especial a Mariam por dedicarle su tiempo y esfuerzo y ayudarme con la redacción de los métodos. Ha sido un placer colaborar con vosotros y espero que el siguiente experimento nos dé más alegrías.

Una constante a lo largo de estos años ha sido el apoyo de la Junta Provincial de Valencia de la Asociación Española Contra el Cáncer, quienes financiaron mi contrato predoctoral. Pero más allá de eso, agradezco que nos halláis brindado a mí y a mis compañeros becarios tantas oportunidades de difundir nuestro trabajo fuera del ámbito académico. Compartir mi trabajo con colaboradores de las juntas provinciales, pacientes y familiares de pacientes ha resultado ser una de mis principales fuentes de motivación a lo largo de estos años. Quiero agradecer especialmente a la asociación de Sollana por invitarnos a mí y a mi familia a su cena vecinal; es uno de los mejores recuerdos que me llevo de la tesis.

Sin embargo, lo mejor que me ha dado la beca es a mis compañeros becarios, Elena, Gabriela, Mireia y David. Hemos hecho piña, nos hemos apoyado mutuamente. Esta experiencia no habría sido lo mismo sin vosotros. Espero que esta amistad dure para siempre. Lo que ha unido la AECC que no lo separe el hombre, ¿no? Gracias por todo.

Pon tu corazón, mente y alma incluso en tus actos más pequeños.
Este es el secreto del éxito.

Swami Sivananda

Como he dicho arriba, todas las personas que se cruzan en tu vida te aportan algo. Así que tengo que dar las gracias a mucha gente.

Voy a empezar por mis compañeros, presentes y pasados, del Laboratorio de Polímeros Terapéuticos. Os agradezco a todos vuestro apoyo y ayuda a lo largo de estos años. Realmente, somos como una gran familia. Siempre puedes contar con que alguien te levante cuando te caes, y eso tiene un valor infinito.

Voy a empezar por los clásicos.

Ana, gracias por toda tu ayuda con los experimentos bio, por tener paciencia conmigo en el animalario y, en lo personal, por mostrarme tu apoyo siempre.

Esther "No ha sido nadie" Masiá, ya he dicho muchas veces que soy tu fan así que solo te voy a decir que gracias por ser como eres, por aportar esa energía inagotable al laboratorio, por todo.

Inma, no sé por dónde empezar contigo. Aprecio infinitamente tu amistad. Siempre estás ahí, para alegrarte de lo bueno, para llorar con lo malo y para animar y dar consejo. Has sido un gran apoyo para mí durante estos años y nunca podré agradecerte lo suficiente. Te mereces todo lo bueno que pueda darte la vida. GRACIAS.

Ahora, los más nuevos.

María, me encantaría ser más como tú, tan tranquila y productiva a la vez. Gracias por aportar esa tranquilidad y por tus palabras de ánimo y apoyo. Eres única.

María Helena, como los tramoyistas en el teatro, eres crucial para que el trabajo salga bien, aunque nunca te lleves los aplausos. ¡Gracias por todo!

¡Compañeros Predocs! Toni, Paz, Snex, Camilla, Tetiana, Paula, Inés. Me llevo muy buen recuerdo de vosotros, y de Snex me llevo también algún que otro conocimiento de química analítica. Mucho ánimo para el trayecto que os queda.

Ahora, las "viejas glorias".

Sonia, mi compañera de escritorio durante gran parte de este viaje. La de cosas que hemos vivido juntas. Hemos reído. Hemos llorado. Nos hemos quedado hasta horas intempestivas en el laboratorio. Me alegra haberte tenido ahí todos estos años. Gracias por tener siempre palabras de ánimo para mí y por creer en mí.

¡Irene! Una de las mejores cosas que me llevo de la tesis es tu amistad y todas las anécdotas que hemos ido recopilando estos años; desde nuestro intento de cultivar aguacates, hasta nuestra particular forma de abrir latas de reactivos o mis intentos de enseñarte a calcular diluciones. Muchas gracias por estar ahí, por tu amistad, por las risas, por… todo.

Juanjo, creo que todo lo que tengo que decirte, ya lo sabes. Aquí sólo quiero recalcar que esta tesis no habría salido adelante sin ti. Gracias por preocuparte por mí e intentar aconsejarme (siento no haberme dejado).

David, nunca sabré cómo has conseguido convertirte en uno de mis mejores amigos. Gracias por todo, por las charlas de cinco horas y las de cinco minutos, por las conversaciones tontas y las profundas, y por intentar arrancarme una sonrisa siempre.

¡Elena! Perdón, *Élena*. Me siento muy afortunada de tenerte como amiga. Eres como parte de mi familia. Gracias por todos los buenos momentos, dentro y fuera del laboratorio. Eres una de las mejores personas que conozco y te mereces lo mejor en la vida.

Luz, lo siento, pero voy a desvelar tu secreto. Luz, aunque pretenda mantener una fachada de "chunga", es un ser adorable, amable y

considerado. Te quiero agradecer en concreto dos cosas. Primero, abrirme las puertas de tu casa en Alcublas (bueno, ese agradecimiento va para tu madre también); sólo guardo buenos recuerdos de ello. Segundo, que me compraras un kit de supervivencia cuando ingresaron a mi padre en el hospital; no por el kit en sí sino por el pensamiento. Eso son solo ejemplos que demuestran que lo que digo es cierto, eres una persona alucinante. Gracias por ser mi amiga.

Alessio, pasar el rato contigo siempre es garantía de diversión. Gracias por ser mi amigo, por animarme y apoyarme siempre, por creer en mí, por preocuparte por mí y por ayudarme siempre que has podido. Gracias.

Silvia, mi estudiante favorita. Aunque creo que tú me has enseñado más de lo que yo te enseñé a ti. Gracias por ser como eres, porque por eso eres de las personas que más me entienden. Además, no todos los días encuentras a alguien con un sentido del humor similar y que te siga el rollo. Espero que te vaya genial en tu tesis. Sabes que me tienes aquí para lo que necesites.

Han sido muchas las personas con las que he coincidido en el laboratorio estos años. Casi todos han dejado alguna anécdota para contar o algún post-it en la nevera. Soy consciente de que me he dejado personas en el tintero. Por eso quiero dar un GRACIAS general, porque si echo la vista atrás, una sonrisa se dibuja en mi cara gracias a todos vosotros, y eso no tiene precio.

I find writing really, really hard and painful.

Phoebe Waller-Bridge

This one is all for you, Stuart! Thank you for all your input during the writing part of the thesis, and for all the office talks during these years, the funny comments on the word documents, your messages to check if I was all right. I am happy to have you as a friend. Thank you for everything.

Desearía que hubiera una forma de saber que estás en los buenos tiempos antes de que los dejes.

The Office, S9 E19, Finale.

Ahora, retrocedamos en el tiempo un poco (bastante) a mis años universitarios. María José, Natalia, Laura (a Raquel me la dejo para más adelante) gracias por estar ahí. A María José en concreto por haberme servido de guía para el depósito de la tesis. Aunque cada una esté haciendo su vida, alguna a muchos kilómetros de distancia, sé que siempre puedo contar con vosotras y que vais a estar ahí en lo bueno y en lo malo, como siempre habéis estado. María José, te deseo lo mejor en tu nueva etapa profesional y personal; espero que la vida te de tranquilidad y felicidad, que te lo mereces. Natalia, protagonista indiscutible de nuestras anécdotas, gracias por ser como eres y por enviarme corazones por WhatsApp cuando más lo necesitaba; eres única y te mereces lo mejor. Laura, mi primera compañera de laboratorio y una de las personas más buenas que conozco (a ver si el universo nos vuelve a sentar juntas en una bancada); gracias por tu amistad, por estar ahí.

Retrocediendo un poco más, Ali, Marcelo, Maritza y Asun, mis amigos del colegio e instituto. A algunos hace mucho que no os veo. La pandemia no ha ayudado mucho. Pero siempre os tengo presentes y sé que cuento con vosotros. Gracias por todos estos años de amistad.

Todo lo que hagas en la vida será insignificante, pero es muy importante que lo hagas.

Mahatma Ghandi

Los siguientes párrafos están llenos de nombres de personas que probablemente no sepan lo importante que fue lo que hicieron por mí. Pero es necesario que lo sepan.

Tengo que empezar por Raquel. Sólo cogiste el teléfono. Qué insignificante, ¿no? Pues me atrevo a decir que no habría tesis ni tesista si no fuera por ti. Pero ese es tu superpoder, estar ahí cuando alguien te necesita. Has estado ahí para mí desde el momento en que nos conocimos en el pasillo antes de entrar a clase y estuviste para mí esa tarde, cuando yo solo necesitaba hablar con alguien para que no se me viniera el mundo encima. Quiero que sepas que eres una persona maravillosa, que tu amistad para mí es un tesoro y que vales mucho. Que nunca se te olvide.

Unas veces son llamadas, otras veces son charlas durante la comida. Dra. Laura Rodriguez-Arco, espero que leas esto. Siempre es un placer hablar contigo y, no sé cómo, has estado ahí en momentos en los que necesitaba palabras de confort. En uno de esos momentos, me llamaste "valiente". Yo nunca me había considerado una persona valiente hasta ese día. Y era lo que necesitaba oír y lo que me repito ahora casi a diario. Gracias por ser como eres.

Todos vamos a morir. El objetivo no es ser inmortales, sino crear algo que lo sea.

Chuck Palahniuk

Hay mucha gente que me gustaría que estuviera aquí en este momento y por desgracia ya no está. Mi abuela, mi tío Jorge, mi padrino, mi padre… Pero me siento muy afortunada de haberlos tenido en mi vida y de tener aún a mucha gente que me quiere a mi lado.

He dejado para el final a las dos personas más importantes del mundo para mí, José Manuel Rodríguez y Myriam Otormin, mis padres.

Papá, me voy a tomar la licencia de escribirte en presente en estas líneas porque, realmente, te siento conmigo cada día, aunque ya no estés. Daría todo lo que tengo porque estuvieras aquí viéndome cruzar la línea de meta. Sé que estás orgulloso de mí, pero también sé que lo estarías incluso si hubiera dejado la tesis alguna de las millones de veces que en estos 5 años dije que la dejaba. Gracias por apoyarme siempre, por creer en mí siempre, por quererme incondicionalmente y decírmelo siempre. Me duele inmensamente que ya no estés, pero me alegra incluso más haberte tenido como padre.

Mamá, tengo la suerte infinita de seguir teniéndote a mi lado. No hay en el mundo persona a la que admire más. Sé que no lo crees, pero eres fuerte y valiente. Eres mi punto de referencia, mi roca y mi mejor amiga. Te agradezco todo, cada cosa que haces por mí a diario. Te agradezco tu infinita paciencia, tu apoyo, tus ánimos, tus intentos de entender lo que hago en el laboratorio. Todo. Sé que tú también estás orgullosa de mí. Pero quiero que sepas que yo estoy orgullosa de ti por salir adelante a pesar de todo. Date crédito, porque no todos consiguen aguantar tanto peso sobre sus espaldas. Te quiero.

Sé que cada decisión habéis tomado papá y tú en estos últimos 28 años se ha basado en que yo tuviera una vida feliz, que hiciera aquello que me hacía feliz. Esta tesis, mi aportación inmortal al mundo, es tan mía como vuestra. Esta tesis nos hace a los tres, de alguna forma, inmortales.

ABBREVIATIONS

% mol	Mole percent
% wt	Weight percent
ABC	ATP-binding cassette
ADP-ribose	Adenosine diphosphate-ribose
AF4	Asymmetric flow field-flow fractionation
AGM	Aminoglutethimide
AMM	Activated monomer mechanism
AMT	Adsorption-mediated transcytosis
ANG	Angiopep-2
AR	Androgen receptor
ATP	Adenosine triphosphate
BBB	Blood-brain barrier
BCRP	Breast cancer resistant protein
BEC	Brain endothelial cell
BL1	Basal-like 1 (TNBC subtype)
BL2	Basal-like 2 (TNBC subtype)
BMP	Bone morphogenetic protein
BrdU	Bromodeoxyuridine
BSA	Bovine serum albumin
BTB	Blood-tumor barrier
CAC	Critical aggregation concentration
cat.	Catalytic amounts
CD	Circular dichroism
CDK	Cyclin-dependent kinase
CE	Conjugation efficacy
CED	Convection-enhanced delivery
CL	Crosslinked
CMT	Carrier-mediated transcytosis
CNS	Central nervous system

COX2	Cyclooxygenase-2
CTC	Circulating tumor cell
CuAAC	Copper-catalyzed azide-alkyne cycloaddition
Cy	Cyanine
Das	Dasatinib
DCIS	Ductal carcinoma in situ
DDS	Drug delivery system
Dh	Hydrodynamic diameter
DIC	N,N'-Diisopropyl carbodiimide
DIEA	N,N-Diisopropylethylamine
DLS	Dynamic Light Scattering
DMAP	4-Dimethylaminopyridine
DMF	N,N'-Dimethylformamide
DMSO	Dimethylsulfoxide
DMTMM	4-(4,6-Dimethoxy-1,3,5-triazin-2-yl)-4-methylmorpholinium
Dox	Doxorubicin
DPBS	Dulbecco's phosphate-buffered saline
DTT	Dithiothreitol
EDC	1-Ethyl-3-(3-dimethylaminopropyl)carbodiimide
EDTA	Ethylenediaminetetraacetic acid
ELS	Electrophoretic light scattering
EMCH	N-ε-maleimidocaproic acid hydrazide
EMT	Epithelial-to-mesenchymal transition
EPR	Enhanced permeability and retention
eq.	equivalents
ER	Estrogen receptor
FBS	Fetal bovine serum
FDA	USA Food and Drug Administration
FRET	Förster Resonance Energy Transfer
FUS	Focused ultrasound

G-CSF	Granulocyte colony-stimulating factor
GFP	Green fluorescent protein
GLUT1	Glucose transporter 1
GnRH	Gonadotropin-releasing hormone
GSH	Glutathione
GSSG	Glutathione disulfide
HA	Hyaluronic acid
HBEGF	Heparin-binding epidermal growth factor-like growth factor
HER2	Human epidermal growth factor receptor 2
HPMA	N-(2-hydroxypropyl)methacrylamide
HR	Homologous recombination
HRD	Homologous recombination repair deficiency
hyd	Hydrazone
i.v.	Intravenous
ID	Injected dose
IHC	Immunohistochemical
IM	Immunomodulatory (TNBC subtype)
LAR	Luminal androgen (TNBC subtype)
LCIS	Lobular carcinoma in situ
LfR	Lactoferrin receptor
Malei	N-(2-Aminoethyl)maleimide
MALS	Multi-angle light scattering
MCR	Mean count rate
MET	Mesenchymal-to-epithelial transition
MMP	Matrix metalloproteinase
MSC	Mesenchymal stem cells
MSL	Mesenchymal stem-like (TNBC subtype)
MSN	Mesoporous silica nanoparticles
mTOR	Mammalian target of rapamycin

MTS	3-(4,5-dimethylthiazol-2-yl)-5-(3-carboxymethoxyphenyl)-2-(4-sulfophenyl)-2H-tetrazolium salt
MWCO	Molecular weight cut-off
NAC	N-acetyl-L-cysteine
NAD	Nicotinamide adenine dinucleotide
NADH	Reduced nicotinamide adenine dinucleotide
NADP	Nicotinamide adenine dinucleotide phosphate
NADPH	Reduced nicotinamide adenine dinucleotide phosphate
NAM	Normal amine mechanism
NCA	α-N-carboxyanhydride
NCS	Neocarzinostatin
NETs	Neutrophil extracellular traps
NGS	Normal goat serum
NK	Natural killer
NMR	Nuclear magnetic resonance
NSC	Neural stem cells
PARP	Poly(adenosine diphosphate-ribose) polymerase
PB	Phosphate buffer
PBS	Phosphate buffer saline
pCR	Pathological complete response
PD	Pyridyl dithiol cysteamine
PD-1	Programmed cell death protein 1
PDEM	Pyridyl disulfide ethyl methacrylate
PD-L1	Programmed cell death protein 1 ligand
PEG	Poly(ethylene glycol)
PEGMA	Poly(ethylene glycol) methacrylate
PES	Polyethersulfone
PG	Polyglycerol
PGA	Poly-L-glutamic acid
P-gp	P-glycoprotein

pHLIP	pH (low) insertion peptide
PMS	Phenazine methyl sulfate
PR	Progesterone receptor
PTX	Paclitaxel
PVP	Poly(vinylpyrrolidone)
r.o.	Retro-orbital
RC	Regenerated cellulose
RES	Reticuloendothelial system
R_f	Retention factor
RI	Refractive index
RMT	Receptor-mediated transcytosis
ROP	Ring-opening polymerization
RP-HPLC	Reverse-phase high-performance liquid chromatography
SANS	Small-angle neutron scattering
SD	Standard deviation
SEC	Size exclusion chromatography
SEM	Standard error of the mean
SMA	Styrene-co-maleic anhydride
SPPS	Solid-phase peptide synthesis
STORM	Stochastic Optical Reconstruction Microscopy
St-PGA	Star-shaped polyglutamic acid
TBC	Tert-butyl carbazate
TBS	Tris-buffered saline
TCEP	Tris(2-carboxyethyl)phosphine
T-DM1	Trastuzumab emtansine
TFA	Trifluoroacetic acid
TfR	Transferrin receptor
TGF-β	Transforming growth factor-β
THF	Tetrahydrofuran
TLC	Thin layer chromatography

TRAIL	Tumor necrosis factor-related apoptosis-inducing ligand
TrMA	Methacrylate-functionalized trehalose
TSP-1	Thrombospondin-1
UV-VIS	Ultraviolet-visible
WBRT	Whole-brain radiation therapy
λ	Wavelength
λ_{em}	Emission wavelength
λ_{exc}	Excitation wavelength

ABSTRACT

Breast cancer represents the second most common cause of brain metastasis after lung cancer, with HER2-positive and triple negative breast cancer (TNBC) displaying the highest incidence. Although the development of brain metastasis represents a late event in disease progression, the incidence of breast cancer-associated brain metastasis has increased over the last decade. Overall, 25-46% of metastatic TNBC patients will develop brain metastasis, with a survival time between four and eight months after diagnosis.

The clinical management of breast cancer brain metastasis has traditionally relied on local approaches as the blood-brain barrier/blood-tumor barrier hinders the accumulation of systemically administered therapies to therapeutically relevant concentrations in the brain. In this context, polymer therapeutics, especially polypeptide-drug conjugates, can provide significant advantages, including an increase in drug solubility, long circulation times, the development of combination therapies, controlled drug release, and active targeting.

In this thesis, we pursued the development of novel biodegradable and biocompatible targeted polypeptide-drug combination conjugates for the treatment of brain metastasis via intravenous administration with a focus on TNBC.

Following a rational design approach, we first developed a polypeptide-drug combination conjugate with optimized drug loading and linking chemistries to treat TNBC (primary tumors and lung metastasis). We employed star-shaped poly-L-glutamic acid (St-PGA) as our biodegradable and biocompatible polypeptidic carrier. We synthesized the St-PGA unimer by controlled polymerization techniques via ring-opening polymerization of N-carboxy anhydrides and the St-PGA-based single and combination conjugates using various drug ratios and pH-labile linkers. The characterization and biological evaluation of our conjugate family using state-of-the-art physico-chemical characterization techniques and well-

established *in vitro* and *in vivo* disease models allowed the identification of the optimal combination of drug ratio and linking chemistry to obtain a St-PGA-based combination conjugate with robust anti-tumor and anti-metastatic activity.

To further improve treatment efficacy, we pursued the development of a bottom-up strategy for the synthesis of St-PGA-based combination conjugates by exploiting carrier self-assembly in water and reversible stimuli-responsive bonds for nanosystem stabilization. During the synthesis of the building blocks for this strategy, we discovered the influence of hydrophobic moieties in the self- and co-assembly behavior of St-PGA conjugates. This altered behavior hampered the development of an efficient redox responsive stabilization strategy.

Therefore, we developed a brain-targeted combination conjugate using the St-PGA unimer as a polypeptidic carrier and the previously identified optimal drug ratio and linking chemistries as the final step in the development of a novel therapeutic approach to TNBC brain metastasis. We employed the peptide Angiopep-2, a ligand of the low-density lipoprotein receptor-related protein 1 (expressed by brain endothelial cells), as a targeting moiety to promote blood-brain barrier crossing by receptor-mediated transcytosis. We developed an efficient and reproducible protocol for Angiopep-2 conjugation to St-PGA conjugates in aqueous media. The targeted St-PGA conjugate accumulated in the brain of healthy mice, supplying a 1.4-fold accumulation compared to an untargeted counterpart. The orthogonal chemistries employed for drug and Angiopep-2 conjugation allowed the synthesis of a St-PGA-Angiopep-2 combination conjugate and the evaluation of anti-metastatic activity in a relevant TNBC brain metastasis mouse model, which provided promising therapeutic outcomes.

Overall, this thesis provides evidence to support the use of St-PGA unimer as polypeptidic carriers in the development of combination conjugates as novel therapeutic strategies for solid tumors and paves the

way for the development of rationally-designed treatments for brain metastasis.

OBJECTIVES OF THE RESEARCH

The clinical management of breast cancer brain metastasis has traditionally relied on local approaches since the blood-brain barrier/blood-tumor barrier hinders the penetration and accumulation of systemically administered small drugs and biological agents in the brain. We hypothesized targeted polypeptide-based polymer-drug conjugates as an efficient therapeutic alternative for brain metastasis systemic treatment.

The main objective of this thesis involves the design and development of a targeted polyglutamate-based combination conjugate with enhanced anti-tumor activity and brain accumulation for the treatment of breast cancer brain metastasis. Reiterative design cycles employing well-established *in vitro* and *in vivo* models and state-of-the-art physico-chemical characterization techniques supported the optimization of drug ratio and linking chemistries to achieve anticancer drug synergism and adequate drug(s) release kinetics, respectively. Furthermore, the conjugation of a targeting moiety sought to take advantage of receptor-mediated transcytosis transport mechanisms in brain endothelial cells to enhance brain accumulation.

Following a rational design approach, we divided this main objective into the following sub-objectives:

I. Design, synthesis, and exhaustive physico-chemical characterization of star-shaped poly L-glutamic acid combination conjugates and the assessment of anti-tumor and anti-metastatic activity in clinically relevant *in vitro* and *in vivo* triple-negative breast cancer models (*Chapter 2*).

II. Development of a bottom-up strategy for the synthesis of star-shaped poly L-glutamic acid-based combination conjugates by exploiting self-assembly in water and reversible stimuli-responsive bonds for nanosystem stabilization (*Chapter 3*).

III. Development of a brain-targeted version of a lead candidate (selected from *Chapter 2* or *3*), including a complete physico-chemical

characterization, *in vivo* biodistribution to assess brain targeting, and pharmacological evaluation of proof-of-concept in relevant *in vivo* breast cancer brain metastasis models (*Chapter 4*).

CHAPTER 1. INTRODUCTION AND BACKGROUND

1.1. Breast Cancer

1.1.1. Basic Facts: Definition, Histological Heterogeneity, and Staging

Breast cancer refers to malignant tumors that develop in the mammary glands (1), which themselves contain milk-producing cell glands or lobules and the tubular passages that drain milk to the nipple or ducts (2,3) (**Figure 1.1**). Three main cell types (ductal, alveolar, and myoepithelial) form these structures. Ductal cells form the ductal passage, while alveolar cells produce and secrete milk after pregnancy. Both cells surround the central lumen (**Figure 1.1**), where the milk is secreted and transported to the nipple. The highly elongated myoepithelial cells locate to the basal epithelium, adjacent to the basement membrane (composed of type IV collagen and laminin) (4) (**Figure 1.1**), and contract in response to oxytocin to aid milk transport. The gland is embedded in the breast stromal tissue, which comprises adipocytes, fibroblasts, mast cells, capillaries, nerves, and type I collagen (5). Most breast tumors originate in the ducts; however, disease can also arise from lobules and, much less commonly, the stromal tissue (1,2).

Breast tumor classification employs histological grading, which evaluates how closely cancer cells resemble their normal cell of origin. To determine the histological grade, specialists analyze tumor tissue and evaluate the mitotic count, nuclear pleomorphisms, and the degree of gland formation observed in a microscope field, giving a score from 1 to 3 to each parameter (**Figure 1.2**). Score addition provides a final score that defines tumor grade, with higher histological grades associated with higher aggressiveness and, thus, poorer prognosis (6,7).
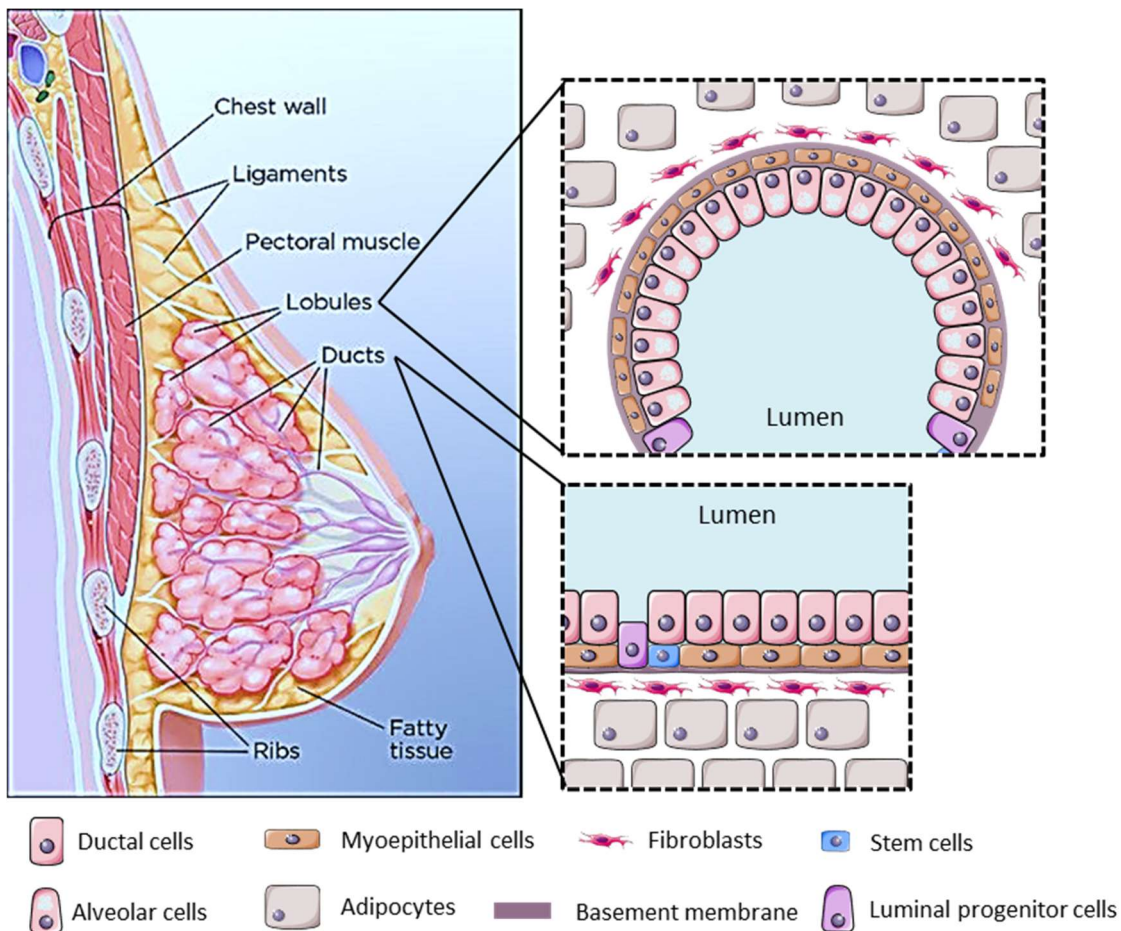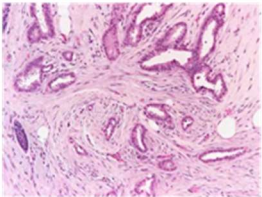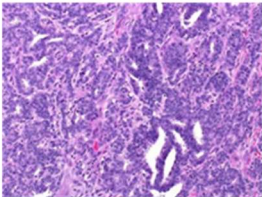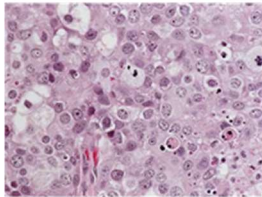
Figure 1.1. Mammary Gland Anatomy and Histology. Diagram depicting breast tissue (adapted from www.mskcc.org (3)). The mammary gland is embedded in stromal tissue formed by adipocytes, fibroblasts, mast cells, capillaries, nerves, and type I collagen. The diagram indicates the main anatomical structures and depicts sections of the mammary gland showing ductal passage and lobular histology (drawn with smart.servier.com (8)).

Breast tumors can be described as *in situ* (non-invasive) or invasive. Ductal carcinoma *in situ* (DCIS) and lobular carcinoma *in situ* (LCIS) represent the two main types of *in situ* breast cancer. DCIS can develop into breast cancer and represents a risk factor for developing a new *in situ* or invasive breast tumor. While considered a benign condition, LCIS also associates with a higher risk of developing DCIS or invasive breast cancer. Most breast tumors possess an invasive nature, in which the cancer cells breach the basement membrane and grow into the stromal tissue (9). The extent of this invasion determines the tumor stage at diagnosis (1,2). Graded

from 0 to 4, tumor stages reflect disease severity and prognosis (7,10) (**Table 1.1**).

Grade	1	2	3
Global score	3-5	6-7	8-9

Score	Glandular formation	Nuclear pleomorphism	Mitotic count*
1	>75% of tumor forms glands	Uniform cells with small nuclei, similar in size to normal cells	<7 mitoses per 10 high power fields
2	10-75% of tumor forms glands	Cells larger than normal with open vesicular nuclei, visible nucleoli, and moderate variability in size and shape	8-15 mitoses per 10 high power fields
3	<10% of tumor forms glands	Cells with vesicular nuclei, prominent nucleoli, marked variation in size and shape	>16 mitoses per 10 high power fields

Figure 1.2. Histological grade determination. Classification depends on tumor tissue analysis by a pathologist. *The mitotic count score criteria vary depending on the microscope field diameter used. A pathologist counts the mitotic events observed in ten high power fields (i.e., the tissue area observed at a microscope's highest magnification). The criteria above use a high-power field diameter of 0.52 mm. Adapted from www.pathology.jhu.edu (6).

Table 1.1. Description of Breast Cancer Stages.

Stage 0	
	Tumor cells have not invaded neighboring tissue
Stage 1	
Stage 1A	Cancer cells have invaded neighboring tissue, but the tumor measures < 2 cm and has not reached lymph nodes
Stage 1B	Lymph node invasion
Stage 2	
Stage 2A	No breast tumor, but cancer cells found in one to three axillary or breastbone-neighboring lymph nodes or Tumor measures < 2 cm and has spread to axillary lymph nodes or Tumor is > 2 and < 5 cm and has not spread to axillary lymph nodes
Stage 2B	Tumor is > 2 and < 5 cm and has spread to lymph nodes (axillary and breastbone-neighboring) or Tumor > 5 cm without affecting lymph nodes
Stage 3	
Stage 3A	Tumor > 5 cm and has spread to lymph nodes (including axillary and breastbone) or No tumor but four to nine axillary or breastbone-neighboring lymph nodes affected
Stage 3B	Tumor has spread to the chest wall and/or skin of the breast and may have spread to axillary (up to nine) or breastbone-neighboring lymph nodes
Stage 3C	Tumor (if any) has spread to the chest wall and/or skin of the breast, with up to ten or more axillary lymph nodes affected or Lymph nodes above or below the collarbone and breastbone affected
Stage 4	
	Metastatic disease. Breast cancer has spread to organs beyond the lymph nodes

1.1.2. Statistics: Incidence, Mortality, and Survival Rate

Breast cancer represents the most frequently diagnosed cancer worldwide, accounting for 11.7% of new cancer cases in 2020 (11). The year 2021 will see the diagnosis of an estimated 33,375 new breast cancer cases in Spain, representing the third most frequent tumor in the total population and the most frequent tumor among women (12). Other similar high-income countries will likely suffer the same unfortunate trend. For example, 2021 will see the diagnosis of an estimated 281,550 new cases of invasive breast cancer and 49,290 *in situ* breast cancer in the USA, accounting for 30% of female cancers. From these new cases, an estimated 43,600 women will succumb to the disease (13). Breast cancer also affects men but to a much lower extent; overall, the year 2021 will see the diagnosis of an estimated 2,650 breast cancer cases in men in the US, with 530 men expected to succumb to the disease (13).

Incidence reflects the effect of risk factors and improvements in diagnosis. Between 1980 and the late 1990s, breast cancer incidence in Western countries increased, most probably due to menopausal hormone therapy and mammography screening (14,15). Furthermore, a reduction in the use of menopausal hormones may have prompted a decrease in breast cancer incidence since the year 2000 (9,14,15); however, the incidence of invasive breast cancer has been slowly increasing since 2004, likely due to the increased body mass index of patients and a reduction in the average number of births per woman (6,13,15).

Mortality reflects disease incidence and the availability of early detection and treatment. For this reason, low-to-medium income countries suffer from higher mortality rates than high-income countries. Since 1990, breast cancer mortality rates have decreased in high-income countries due to early diagnosis via mammography screening, which allows clinical intervention at early stages when treatment approaches have a higher

probability of succeeding (14). For instance, the breast cancer death rate in the USA decreased by 40% from 1990 to 2017 (15).

Survival rates are also higher in high-income countries than in low-to-medium income countries due to early diagnosis and treatment availability (14). While the mortality rate refers to deaths caused by breast cancer in the country's total population, the survival rate describes the percentage of patients surviving after a certain amount of time after diagnosis. Thus, this parameter depends on the tumor subtype and stage at diagnosis (16). For instance, the overall five-year survival rate for patients diagnosed between 2009 to 2015 was 98% for stage I breast cancers, 92% for stage II, 75% for stage III, and 27% for stage IV in the USA (15), thus highlighting the severity of metastatic disease and the need to develop novel treatment strategies for advanced breast cancer.

1.1.3. Intertumoral Heterogeneity: Defining Molecular Subtypes

Cancer is a heterogeneous disease – this manifests as genetic heterogeneity between tumors (intertumoral heterogeneity) and heterogeneity within the same tumor (intratumoral heterogeneity) (17). Intertumoral heterogeneity defines cancer subtypes, with various tumor aspects employed in breast tumor classification. Clinical prognosis and treatment selection routinely employ the immunohistochemical (IHC) analysis of estrogen receptor (ER), progesterone receptor (PR), and human epidermal growth factor receptor 2 (HER2) expression status (7,18). ER and PR expression occur in ~75% of all breast cancers, indicating responsiveness to hormonal therapy. Tumors that express both receptors are usually low-grade and less aggressive. The small percentage (~18%) of breast tumors that express only one hormone receptor (ER or PR) are more aggressive and less responsive to hormone therapy (7,19,20). Overexpression of HER2 occurs in ~15% of cases; these tumors display greater aggressivity and suffer from a poor prognosis; however, HER2-

positive tumors display good responsiveness to anti-HER2 therapies. The 10 to 15% of cases that fail to express ER, PR, and HER2 are classified as triple-negative breast cancer (TNBC); these cases are usually high-grade, suffer from a poor prognosis, and fail to respond to hormonal or HER2-targeted therapies (7).

The ER, PR, and HER2 expression status combined with Ki67 cell proliferation marker expression help to define four breast cancer subtypes (21).

Luminal A - ER-positive, PR-positive, HER2-negative, Ki67 low.

Luminal B - includes ER-positive tumors that are HER2-negative and PR-positive or HER2-negative with elevated levels of Ki67, and ER-positive tumors that are also HER2-positive but PR-negative with low levels of Ki67.

HER2-positive - ER-negative, PR-negative, HER2-positive.

TNBC - ER-negative, PR-negative, HER2-negative.

The staining and analysis of tumor tissue samples help to establish molecular status. According to current American Society of Clinical Oncology (ASCO) guidelines, an immunoreactivity of ≥1% of tumor cell nuclei for ER and/or PR is a positive result. (22). HER2 assessment remains more complex - >10% of cell membranes showing complete and intense staining (IHC 3+) is considered HER2-positive, moderate staining in >10% of cells is considered equivocal and requires confirmation by DNA hybridization techniques, while incomplete or faint staining in >10% of cells (IHC 1+) or ≤ 10% stained cells (IHC 0) is considered HER2-negative (23). Of note, we currently lack a consensus regarding a Ki67 expression threshold (7,21).

Breast tumors classification can also take advantage of gene expression profiling, which defines five intrinsic subtypes - (i) luminal A, (ii) luminal B, (iii) HER2-overexpressing, (iv) basal-like, and (v) normal-like.

Overall, these subtypes correlate well with the subtypes defined by IHC classification (**Table 1.2**) (7).

i. The **Luminal A subtype** represents the most common molecular subtype (7,24). Gene expression- and IHC-based classifications correlate well, with an observed overexpression of ER- and PR- but not HER2-related genes (24). For this reason, the luminal A subtype benefits from hormonal therapy. Luminal A cancers are typically low-grade and have the best prognosis among intrinsic subtypes (7).

ii. The **Luminal B subtype** displays a high expression of ER-related genes, as with the luminal A subtype; however, the luminal B subtype has lower expression of PR-related genes and higher expression of proliferation-related genes (18,24). The expression of HER2-related genes varies, although one subgroup overexpresses HER2 (18), thereby resembling the luminal B subtype defined by IHC markers (18,24). Luminal B tumors are higher grade than luminal A and suffer from a worse prognosis. Luminal B cancers also benefit from hormonal therapy, but additional chemotherapy may also be used (7,24).

iii. The **HER2-overexpressing subtype** overexpresses HER2-related genes but fails to express ER and PR, which correlates with the HER2-positive IHC subtype (7). These tumors are usually aggressive and high-grade but respond well to anti-HER2 therapies (7,17,24).

iv. The **Basal-like subtype** fails to express ER, PR, and HER2 but overexpresses proliferation-related genes. Basal-like tumors are usually high-grade with a poor prognosis (7,24). Basal-like tumors account for 60 to 90% of TNBC (an IHC subtype) cases, depending on the gene set employed during profiling (24).

v. The **Normal-like subtype** remains controversial, given that its gene expression profile is similar to normal breast epithelium. Studies have

suggested that the normal-like subtype may derive from contamination with healthy breast epithelium (7).

Table 1.2. Breast cancer molecular subtypes.

IHC subtypes	Luminal A	Luminal B	HER2 positive	TNBC
IHC markers	ER+, PR+, HER2-, Ki67 low	ER+, PR+, HER2- and Ki67 high, or HER2+, PR-, and Ki67 low	ER-, PR-, HER2+	ER-, PR-, HER2-
% of breast cancers	≈ 75 %		15 %	10-15 %
Intrinsic subtype correspondence	Luminal A	Luminal B	HER2-overexpressing	Basal-like
Histological grade	Low → High			
Prognosis	Good → Poor			

Definition by IHC markers, prevalence, correspondence with genetically defined intrinsic subtypes, histological grade, and prognosis

The subtypes mentioned above have been confirmed by several studies using various gene sets (25,26), which prompted the development of a standardized method for gene expression profiling using fifty classifier genes plus five reference genes - the so-called PAM50 (Prediction Analysis of Microarray 50) (7,27,28). Unfortunately, high costs and technical complexity have hindered the application of PAM50 in the clinic, where breast cancer classification still relies on ER, PR, HER2, and Ki67 expression (7). Of note, comparisons between PAM50 and IHC classifications demonstrated a discordance rate of 31% (18), implying that one-third of patients analyzed by IHC will be classified in a non-concordant intrinsic subtype.

Gene expression profiling initially described a claudin-low subtype as a sixth intrinsic subtype; however, this subtype is usually excluded in classifications as the most complete study performed in breast cancer, led by The Cancer Genome Atlas project (TCGA), failed to identify this group as an intrinsic subtype (18).

This thesis focuses its attention on the development of new treatments for advanced (metastatic, stage 4) TNBC, with a particular interest in targeting brain metastasis. Both TNBC and brain metastasis will be described in detail in upcoming sections (*1.2.Triple-Negative Breast Cancer* and *1.3.Brain Metastasis in Breast Cancer: The Rising Challenge*).

1.1.4. Intratumoral Heterogeneity: The Next Step

Generating a robust classification for breast cancer tumors reflects the need to improve treatment selection, moving towards personalized medicine. The classifications mentioned above have helped this approach; however, intratumoral heterogeneity prompts varying responses to the same treatment strategy. Intratumoral heterogeneity in breast cancer results from genetic and epigenetic differences between tumor cells (17,29). During the division of cancer cells, genetic material can undergo alterations, giving rise to subclones with differing proliferative capacities. As a result, cells with different phenotypes co-exist within the same tumor (30). Thus, a tumor comprises phenotypically different cell populations with different proliferation, migration, and invasive capacities and, hence, treatment responses.

Intratumor heterogeneity has important implications in cancer treatment. Cell subpopulations with resistance to a targeted treatment may remain unnoticed during molecular diagnosis and subtype identification due to their low number or the sampling method employed. Thus, a selected treatment may only eradicate those cancer cells belonging to the identified

subtype, while other subpopulations could survive and divide, leading to disease relapse (17,29). Following the same rationale as for tumor subtyping, the identification and classification of different cellular subpopulations may guide the selection of optimal treatment approaches. For instance, a combination of drugs routinely used for different tumor subtypes may function synergistically to eradicate different subpopulations, eventually reducing the possibilities of relapse. This approach requires the implementation of single-cell diagnostics, which currently remain unfeasible for common use in the clinic (29,30).

1.1.5. Breast Cancer Metastasis

Breast cancer can spread to lymph nodes (axillary, breastbone, and supraclavicular), bone, liver, lungs, brain, peritoneum, and the contralateral breast (31), with bone the most common site for distant metastasis (32,33). This site-specific incidence depends on the breast cancer subtype - hormone receptor-positive tumors exhibit a greater tendency to metastasize to the bone (32,33) while TNBC and HER2-positive display an increased incidence of visceral metastasis (liver, lungs, and brain) (24,32,34). Cell survival in the circulation and adherence to the endothelium and the metastatic site's vascular architecture and microenvironment also influence the tropism of metastatic breast cancer cells (35).

Breast cancer can metastasize through the lymphatic or the venous route (36), with the metastatic process subdivided into five steps - (i) invasion, (ii) intravasation into lymphatic and/or blood vessels, (iii) circulation, (iv) extravasation, and (v) colonization of distant organs (**Figure 1.3**).
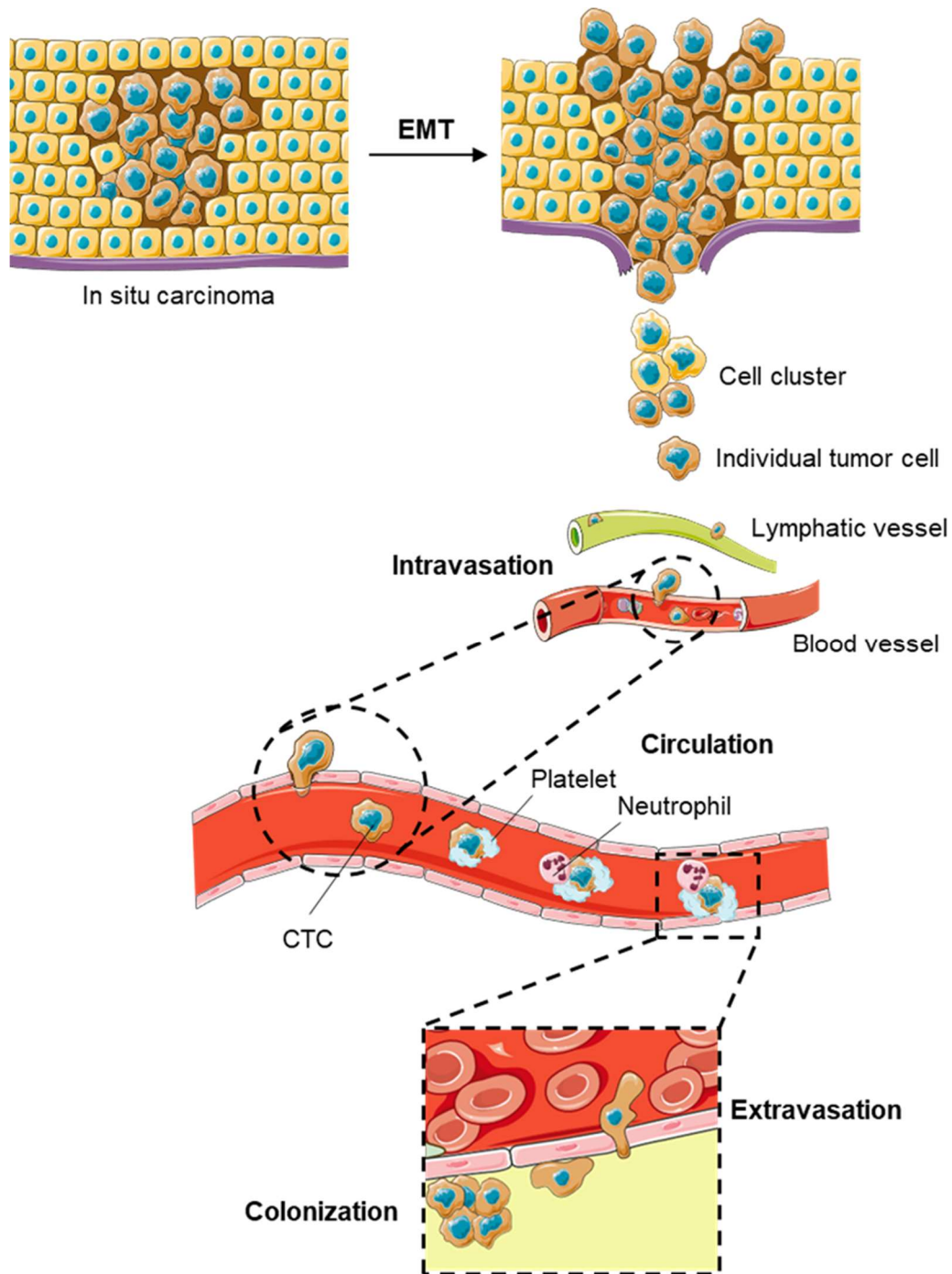
Figure 1.3. The Metastatic Process. Tumor cells undergo an epithelial-mesenchymal transition (EMT) and acquire invasive capacities. Tumor cells invade the stroma as single cells or cell clusters, which breach the lymphatic or blood vessel walls to reach the lumen. Tumor cells reach the bloodstream via the major thoracic duct via the lymphatic route. When in circulation, circulating tumor cells (CTCs) or cell clusters can associate with platelets and neutrophils, which protect against immune responses (T and natural killer cells). Tumor cells then move across the endothelium to access the target organ, forming the secondary tumor. Drawn with smart.servier.com (8).

1.1.5.1. Invasion

This first step comprises those processes that allow tumor cells to escape the primary tumor site and travel to distant organs (37). The epithelial-mesenchymal transition (EMT) of tumor cells represents a crucial component of this first step. EMT is a reversible cellular program that normally occurs during embryogenesis and adult wound healing (36–38). The expression of EMT-inducing transcriptional factors in healthy epithelial cells provokes the loss of cell polarization and cell-cell adhesion, basement membrane degradation, extracellular matrix reorganization, and the acquisition of motile and invasive capacities; i.e., epithelial cells acquire mesenchymal features (37,38). Breast cancer cells use EMT to detach from the epithelium, invade surrounding tissue, intravasate blood or lymphatic vessels, and acquire tumor-initiating capabilities (36,37). The appearance of cell subpopulations with tumor-initiating capabilities (cancer stem cells or CSCs) during EMT has been documented for various carcinoma types apart from breast cancer; however, the molecular mechanisms underlying this process remain elusive. CSCs overexpress ATP-binding cassette transport pumps that mediate drug efflux, inducing drug resistance (38). Additionally, EMT confers drug resistance by other mechanisms, e.g., the dysregulation of genes involved in cell death (38).

Paracrine signaling from the tumor microenvironment triggers EMT activation in breast cancer cells (37,38). Stromal cells secrete cytokines and chemokines (such as transforming growth factor-β, TGF-β) that activate signaling pathways in the tumor cell, thereby inducing EMT programs and promoting tumor progression/metastasis (38). Notably, the activation of EMT fails to completely transform epithelial tumor cells into a mesenchymal state; instead, tumor cells exhibit an intermediate phenotype (37,38).

Initial stromal invasion of tumor cells involves the collective migration of cell clusters formed by a leading edge and a cohort of follower cells. The leading edge comprises invading cells displaying a mesenchymal-like

phenotype that pave the way for follower cells, which possess an epithelial-like phenotype, that remain attached to the leading edge and each other by cell-cell interactions (37,38). This collective migration of cell clusters is commonly seen at tumor borders (37).

1.1.5.2. Intravasation Into Lymphatic and/or Blood Vessels

The second step of the metastatic cascade comprises the invasion of individual tumor cells and invasive cell clusters into lymphatic and/or blood vessels (37). This process frequently occurs through the hematogenous route, where tumor cells intravasate into the blood vessels located on the adjacent normal tissue or the tumor neovasculature (37,39). Hematogenous intravasation represents an inefficient process, as the shear stress of blood flow alone destroys many intravasating tumor cells (39). The survivors, so-called circulating tumor cells (CTCs), employ the blood vessel network to travel to distant sites and promote metastasis (37).

The presence of lymph nodes and lymphatic vasculature in the neighboring tissue support the frequent lymphatic intravasation associated with breast tumors. Importantly, lymphatic intravasation occurs via a different process to hematogenous intravasation, as the lymphatic system lacks the tight endothelial junctions that seal blood vessels and possesses a lower flow rate than blood, which reduces shear stress and improves the survival rate of intravasating cells. Lymph vessels eventually drain into the blood through the major thoracic duct, allowing tumor cells to access blood circulation; however, tumor cells encounter a series of lymph nodes before reaching blood vessels, where they may seed and raise a metastatic tumor. The closest lymph nodes to the primary tumor are the so-called sentinel lymph nodes (39), a biopsy of which is used in the clinic to diagnose axillary lymph node metastasis (40).

1.1.5.3. Circulation

CTCs can circulate as single cells or clusters after reaching the bloodstream (37), with clusters less frequent but displaying higher viability and metastatic potential (41,42). Typically, CTCs become entrapped in the low-flow environment in the first capillary bed they encounter (35), which supports their interaction with the endothelium (43). Breast cancer cells travel through the heart to the lungs, where they become trapped; however, some CTCs pass through the lungs, enter the systemic circulation, and disseminate to distant organs (35).

CTCs and clusters encounter several obstacles that hinder their viability in the circulation, including mechanical injuries due to shear stress and attack by the immune system (37,42). The formation of clusters may protect against these insults, explaining their enhanced viability in the bloodstream (42). Association with platelets also protects against the immune system, specifically from natural killer (NK) cell activity. Platelets protect CTCs by physically shielding them from the recognition of NK cells and by secreting factors (such as TGF-β) that inhibit NK cell activity (35,37,42). Additionally, secretion of TGF-β by platelets helps to maintain EMT program activity (37).

Platelets also secrete chemokines that recruit neutrophils to positively impact the metastatic process (37). Neutrophils form extracellular traps (NETs) to entrap pathogens in response to inflammatory cues; however, NETs also capture and protect CTCs and enhance endothelial adhesion, thus facilitating extravasation as the next step of the metastatic process (35,37,42). Additionally, neutrophils exert immunosuppressive effects against T and NK cells, thereby protecting CTCs from the immune system (37). Nevertheless, neutrophils can also inhibit metastasis; for instance, neutrophils generate hydrogen peroxide (H_2O_2) in response to chemokine ligand 2 (CCL2) secretion by tumor cells, which inhibits metastatic cell seeding (35).

1.1.5.4. Extravasation

CTCs must exit the circulation and enter the parenchyma of a distant organ to form a secondary tumor (37). After CTCs or cell clusters become trapped in the host organ's small capillaries, they adhere to the endothelium by weak and intermittent interactions mediated by selectins (44). Selectin-ligand interactions mediate the leukocyte-endothelial interactions during physiological inflammatory processes that result in leukocyte rolling on the endothelial surface before immobilization and transendothelial migration (42). A similar process occurs during cancer cell extravasation, with CTCs expressing the selectin ligands that support endothelial adhesion. Endothelial cells express selectins in response to pro-inflammatory cytokines secreted by cancer cells or cancer-associated leukocytes. Cytokines also provoke the translocation of selectins to the surface of platelets, allowing them to serve as a bridge between tumor cells and endothelial cells. These selectin-mediated weak interactions become replaced by high-affinity interactions mediated by integrins and their ligands, which play a crucial role in cell-cell and cell-extracellular matrix interactions. The expression of adhesion proteins by CTCs represents a critical mechanism supporting tumor cell-endothelium interactions (44).

Following stable adhesion, tumor cells move across the endothelium between adjacent endothelial cells using dynamic protrusions called invadopodia in a process known as transendothelial migration (42). These structures secrete matrix metalloproteinases (MMPs) such as MMP9 and MMP2 that degrade the extracellular matrix to enhance tumor cell invasion and transendothelial migration (44). Many mechanisms induce vascular permeability to facilitate transendothelial migration; for instance, tumor cells induce ATP release by platelets, which provokes the retraction of endothelial cells, thus increasing vasculature permeability (37). Cancer cells also induce endothelial necroptosis (programmed necrosis) in endothelial cells to disrupt

endothelial integrity (37,44). Additionally, endothelial cells undergoing necroptosis release damage-associated molecular patterns that trigger endothelial opening, thereby facilitating transendothelial migration (44). Neutrophils also secrete MMPs that increase vascular permeability and CTC extravasation (37,42).

CTCs can also migrate across the endothelium through a mechanism known as angiopellosis, which relies on active endothelial remodeling to cover cancer cells and direct them to the abluminal side (the host tissue parenchyma). While angiopellosis appears to represent a more straightforward route of extravasation for cell clusters, the molecular mechanisms governing this process remain elusive (44).

The requirements for successful extravasation depend on the characteristics of the host tissue vasculature. For example, metastasis in bone and liver do not require many of the above-described mechanisms due to the vasculature's fenestrated nature (37). Meanwhile, CTC extravasation in the brain requires the expression of a specific profile of genes that facilitate the process. Consequently, studies into the metastatic process have identified characteristic cancer cell gene expression profiles or signatures for each metastatic site (35). For example, the lung metastasis signature includes angiopoietin-like 4 (ANGPTL4) (45), a protein that enhances lung vasculature permeability and promotes the transendothelial migration of cancer cells (37).

CTCs can also give rise to intraluminal metastasis instead of migrating across the endothelium. In those cases, CTCs and/or clusters become trapped in the lumen of capillary beds together with platelets and neutrophils and form a tumor colony that eventually breaks through the endothelium to access the surrounding tissue (37,42).

1.1.5.5. Colonization of Distant Organs

Colony formation in the host tissue represents the last step in the metastatic process. Successful colonization relies on the ability of cancer cells to adapt to the environment and form a new tumor (i.e., tumor-initiating capacity). Based on experimental data, only 0.01% of intravenously injected tumor cells form metastases, highlighting the low efficacy of this process (37,42).

Immediately after crossing the endothelium, cancer cells remain attached to the abluminal side of pre-existing capillaries in a process known as vascular co-option. This interaction depends on cell-adhesion molecules, such as integrins, which allow tumor cells to survive without switching on pro-angiogenic programs (37,46). In breast cancer, single disseminated tumor cells and cell clusters typically enter a dormant state that inhibits metastatic progression (37,47). Three types of dormancy have been described: cellular, angiogenic, and immune-mediated (47,48). Cellular dormancy results from cancer cells entering into a quiescent status due to the presence of anti-proliferative signals or the lack of proliferative signals in the host tissue (37,42). For example, bone morphogenetic proteins (BMPs) such as BMP4 induce breast cancer cell quiescence in the lung (35,37). Additionally, co-opted endothelial cells secrete thrombospondin-1 (TSP-1) in the abluminal side to induce quiescence (37,46). Angiogenic and immune-mediated dormancy generate an equilibrium between dividing and apoptosing cells, resulting in the maintenance of metastatic cluster size (37,47,48). Angiogenic dormancy occurs in response to the inability of cancer cells to form new blood vessels, while immune-mediated dormancy results from the elimination of cancer cells by the immune system (47,48).

Disseminated tumor cells can remain in a dormant state for weeks to years (depending on the cancer type) before beginning to proliferate again. This cellular "awakening" depends on the acquisition of genetic programs that allow tumor cells to proliferate (37). For example, breast cancer

disseminated tumor cells maintained in a quiescent state by BMPs in the lungs can acquire the ability to express molecules such as N-acetyl-galactosaminyltransferase and Coco (both inhibitors of BMP signaling) that neutralize BMP activity, prompting metastatic tumor growth (35). The acquisition of these genetic programs may represent an evolutionary process in which low-level tumor cell proliferation occurring during the dormancy period provokes the selection of those clones expressing relevant genetic programs (37).

Cells undergoing an EMT also gain stem cell traits, including tumor-initiating abilities. Only those dormant disseminated tumor cells that have tumor-initiating capacity will give rise to a metastatic tumor (37); however, to efficiently form a new tumor in the host tissue, cancer cells usually undergo a mesenchymal-to-epithelial transition (MET), the reverse mechanism to EMT, to give rise to metastatic tumors that resemble the hierarchical cell organization present in the primary tumor (37,38).

1.1.6. Clinical Management of Breast Cancer

The choice of breast cancer treatment requires the differentiation of cases into non-metastatic from metastatic subgroups. For non-metastatic breast cancer (stages 1 to 3, **Table 1.1**), therapeutic goals include tumor eradication from the breast and regional lymph nodes and metastasis prevention. Treatment consists of either total mastectomy or the surgical resection of the primary tumor (lumpectomy) plus postoperative local radiation together with the removal or sampling of axillary lymph nodes (49). At early stages, there exists no significant difference in the overall survival rate between lumpectomy plus radiotherapy and mastectomy (50). Systemic therapy may be prescribed before (neoadjuvant) or after (adjuvant) the surgery or both (49). The prescription of neoadjuvant therapy reduces tumor size before surgery or if the pathological complete response (pCR, i.e., absence of cancer cells in the surgical specimen after neoadjuvant

treatment) has prognostic value. In contrast, the prescription of adjuvant therapy occurs when the surgical results or other biomarkers suggest a high risk of recurrence (31).

Therapeutic goals for metastatic breast cancer (stage 4, see **Table 1.1**) include prolonging life through systemic therapy and symptom palliation via surgery and radiation (49); however, metastatic disease remains incurable and represents the leading cause of death in breast cancer patients, with a median overall survival of two to three years (31).

The stratification of breast cancer tumors and our increasing knowledge regarding each subtype have fostered the development of targeted systemic therapies that have improved therapeutic outcomes. ER and HER2 represent the two main molecular targets in breast cancer treatment (49).

Patients with ER-positive and/or PR-positive breast cancer (luminal subtypes) benefit from endocrine therapies that inhibit the activation of estrogen-dependent signaling pathways that induce proliferation (49,51). Standard treatment consists of adjuvant endocrine therapy for at least five years after surgery (31). Tamoxifen, a competitive inhibitor of ER, represents the first-line treatment in pre- and post-menopausal women; however, a "switch strategy" consisting of two-to-three years of tamoxifen treatment followed by two-to-three years of aromatase inhibitor treatment to reduce estrogen levels helps to diminish the toxicities of both therapies in post-menopausal women (49). In pre-menopausal women with high-risk disease, standard treatments usually involve ovarian suppression (induced menopause) with a gonadotropin-releasing hormone (GnRH) analog to reduce the production of sex hormones in combination with tamoxifen (31) or an aromatase inhibitor (40,49). Common side effects of tamoxifen and aromatase inhibitors include hot flushes, vaginal dryness, arthralgia (joint pain), and myalgia (muscle pain). Tamoxifen also increases the risk of

venous thromboembolism and uterine cancer, while aromatase inhibitors can accelerate osteopenia and osteoporosis (40).

The treatment of metastatic disease follows a similar approach, i.e., ovarian suppression in pre-menopausal women and endocrine therapy until the development of resistance (31). Non-steroidal aromatase inhibitors (letrozole and anastrozole) represent the first-line treatment, with steroidal aromatase inhibitors (exemestane) in the second line. Additional second-line treatments include mammalian target of rapamycin (mTOR) inhibitors (everolimus) with exemestane or cyclin-dependent kinase 4 and 6 (CDK4/6) inhibitors (palbociclib, ribociclib, and abemaciclib) with fulvestrant (inhibitor of ER dimerization). The combination of aromatase inhibitors with CDK4/6 inhibitors has been included as a first-line treatment to delay endocrine resistance (51). Single-agent chemotherapy treatment follows after the exhaustion of endocrine-targeted options and a lack of observed responses, leaving combination chemotherapy for patients with visceral crisis (i.e., organ disfunction due to rapid disease progression) (31,49,51,52).

In HER2-positive breast cancer cases, HER2-targeted therapies have dramatically improved treatment outcomes for both early and metastatic disease (49,53). The standard of care for patients is trastuzumab, a recombinant humanized monoclonal antibody that binds to the extracellular domain of HER2 (54,55), combined with chemotherapy (taxanes) as adjuvant or neoadjuvant treatment (21). Cardiac dysfunction represents the major limitation associated with trastuzumab treatment, although these side effects are treatable and reversible (21,53).

Metastatic HER2-positive breast cancer also employs trastuzumab combined with taxanes as first-line treatment (53); however, dual blockade of HER2 with trastuzumab and pertuzumab (a humanized monoclonal antibody targeting HER2 dimerization domain) plus chemotherapy can be applied in patients not previously treated with trastuzumab. Second-line treatments include trastuzumab emtansine (T-DM1) - an antibody-drug

conjugate composed of trastuzumab and an analog of maytansine (a potent inhibitor of microtubule polymerization) conjugated through a thioether linker (55) - and combinations of trastuzumab plus chemotherapy (different than taxanes) or trastuzumab plus lapatinib (a tyrosine kinase inhibitor targeting HER2 and epidermal growth factor pathways) (31).

In the case of luminal B breast cancer (ER-positive, HER2 variable), HER2 expression levels define treatment choice. Luminal B HER2-high patients receive chemotherapy, endocrine therapy, and HER2-targeted therapy, while Luminal B HER2-low tumors receive endocrine therapy with or without chemotherapy (21). Endocrine therapy represents the preferred treatment option for metastatic disease regardless of HER2 status; however, endocrine therapy combined with HER2-targeted therapies are often employed for luminal B HER2-high tumors (31,56).

In the case of TNBC, the lack of ER, PR, and HER2 expression impedes the use of endocrine or HER2-targeted therapies, leaving chemotherapy as the only viable treatment option (17,49,57,58). In upcoming sections, systemic therapies for TNBC will be discussed in detail (see *1.1.6.Clinical Management of TNBC*).

1.2. Triple-Negative Breast Cancer

1.2.1. Basic Facts: IHC Definition, Histology, Stage, and Statistics

TNBC presents with the highest aggressiveness and the worst patient prognosis (18,24). TNBC tumors do not express ER, PR, and HER2, the IHC subtype that best correlates with its intrinsic counterpart, with 86% of cases falling into basal-like subtypes (18). Accounting for ~15% of all breast tumors (49), TNBC usually affects young women (< 50 years old) (57) and displays more prevalence in the African-American population (14). Most TNBC tumors (95%) are invasive and originate in the ducts (59). TNBC tumors are usually diagnosed at histological grade III (low glandular formation rate, high

nuclear pleomorphism, and mitotic activity) (57) and stage 2B or 3A (tumor size > 2 cm and lymph node involvement, **Table 1.1**) (60), thus having a poor prognosis (61).

Earlier and higher rates of disease recurrences and distant metastasis also characterize TNBC (17,61). The development of visceral metastasis associates with low survival rates, with a 12-18 month median survival time for metastatic TNBC patients (61). TNBC tumors usually metastasize to the brain and lungs, with a lower prevalence of bone metastasis (24,60).

1.2.2. Intertumoral Heterogeneity: TNBC Subtypes

TNBC represents a heterogeneous subtype with different reported gene expression-based classifications (62–64). A commonly used classification proposed by Lehmann and colleagues in 2011 (62) divides TNBC into six subtypes - basal-like 1 (BL1), basal-like 2 (BL2), mesenchymal (M), mesenchymal stem-like (MSL), immunomodulatory (IM), and luminal androgen subtype (LAR).

The BL1 subtype overexpresses genes involved in the cell cycle, cell division and proliferation, and DNA damage responses, while the BL2 subtype overexpresses factors related to growth factor signaling pathways, glycolysis, and gluconeogenesis. The M and MSL subtypes overexpress genes involved in cell motility, extracellular matrix receptor interactions, and cell differentiation pathways; however, the MSL subtype also displays the specific upregulated expression of genes involved in cell growth, EMT, angiogenesis, and immune signaling. The IM subtype gene expression profile reflects the dysregulation of pathways related to the immune system (e.g., B and T cell receptor signaling pathway), which overlaps with the signature for medullary breast cancer, a rare form of TNBC associated with a good prognosis despite its high histological grade. The LAR subtype expresses genes from hormonally regulated pathways such as steroid

synthesis, porphyrin metabolism, and androgen/estrogen metabolism; furthermore, this subtype overexpresses the androgen receptor (AR) and various downstream effectors and genes belonging to the luminal subtypes profiles (62).

While IHC analysis classifies LAR tumors as TNBC, gene expression profiling suggests that the LAR subtype comprises luminal A or B tumors (82%), and no LAR-classified tumors were classified as basal-like (62). A subsequent study by Lehmann et al. (65) confirmed this observation. Except for LAR, all TNBC subtypes comprise basal-like tumors (BL1 (99%), BL2 (95%), M (97%), MSL (50%), and IM (84%)). PAM50 classified LAR tumors as HER2-overexpressing (74%) and luminal B (14%). Of note, the MSL subtype comprised only 50% basal-like tumors, followed by 28% normal-like and 14% luminal B (65).

Around 10% of TNBC tumors also harbor germline mutations in the BRCA1 and BRCA2 DNA repair associated genes (*BRCA1/2*) (59,66), the highest prevalence among the different breast cancer subtypes (61). The *BRCA1* and *BRCA2* tumor-suppressor genes encode proteins required for DNA double-strand break repair by homologous recombination (HR), a crucial mechanism for the maintenance of genomic stability. Thus, alterations to genes encoding proteins taking part in this process prompt the development of HR repair deficiency (HRD), genomic instability, and an increased risk of cancer development. *BRCA1* and *BRCA2* mutations increase the lifetime risk of developing breast cancer in women to approximately 65% and 45%, respectively. Mutations in *BRCA1* also associate with the basal-like breast cancer phenotype, with 80% of tumors developed by patients with *BRCA1* germline mutations classified as TNBC with a basal-like profile (67). Thus, *BRCA1* germline mutations entail a higher risk of developing breast cancer and a higher probability of diagnosis with a high-grade invasive tumor.

Somatic mutations in *BRCA1/2* and germline/somatic mutations in genes encoding related proteins involved in the HR pathway can also lead to HRD. These alterations define the term "BRCAness," i.e., genetic alterations leading to HRD other than germline *BRCA1/2* mutations (50,60,61,67). Overall, ~35% of TNBC tumors display HRD; therefore, HRD may represent a biomarker for treatment selection (67). Such tumors generally display heightened responsiveness to HR-targeted therapies (e.g., poly(adenosine diphosphate-ribose) polymerase [PARP] inhibitors) and DNA-damaging agents (e.g., platinum salts) since they exhibit increased sensitivity to DNA damage (see *1.1.6.Clinical Management of Breast Cancer*).

In summary, breast cancers display significant heterogeneity, with intertumoral and intratumoral heterogeneity resulting in different disease progression and therapeutic responsiveness (17). This status has prompted the use of drug combinations as adjuvant and neoadjuvant therapy. Overall, the simultaneous targeting of several pathways using drug combinations aims to increase treatment efficacy and improve patient outcomes. For this reason, in this thesis, we studied a drug combination used at an optimized ratio as a potentially efficient treatment for TNBC and associated brain metastasis.

1.2.3. Clinical Management of TNBC

We currently lack specific recommendations for local therapy (surgery and radiation) for TNBC treatment (61); as for the other breast cancer subtypes, overall survival rates remain similar after lumpectomy plus radiotherapy than after mastectomy. Nevertheless, special consideration should be given to patients with family histories of breast cancer or pathogenic genetic mutations associated with TNBC, such as *BRCA1*. Prophylactic mastectomy may be recommended for these patients to prevent local recurrence (50).

Due to the lack of ER, PR, and HER2 expression, we currently lack targeted systemically administered therapies for TNBC, leaving chemotherapy as the standard of care (17,24,49,57,58,68). Neoadjuvant chemotherapy prescribed to patients diagnosed with high-risk early-stage TNBC (60,68) aims to reduce tumor size before lumpectomy, assure complete tumor resection, and reduce the extent of tissue resection (50). Neoadjuvant chemotherapy is also employed when surgery is contraindicated (60). Patients that show a partial complete response (pCR) to neoadjuvant therapy display increased long-term survival rates, whereas those with residual or progressive disease (non-pCR) suffer from an increased risk of recurrence (50,61,68). Most guidelines recommend anthracycline plus taxane-based chemotherapy (61); however, these chemotherapeutic treatments result in severe side effects such as leukopenia, neutropenia, anemia, and thrombocytopenia (69). Treatment with adjuvant capecitabine is recommended in patients not achieving pCR after neoadjuvant chemotherapy (21); however, side effects include diarrhea, nausea, stomatitis, hand-foot syndrome, and vomiting (70).

Fortunately, TNBC tumors exhibit higher chemotherapy responses than other subtypes (59,68). BL1 and BL2 subtypes overexpress the proliferation marker Ki-67, suggesting responsiveness to antimitotic agents such as taxanes (e.g., paclitaxel and docetaxel) (62); however, over 50% of patients treated with chemotherapy after early diagnosis suffers from disease recurrence, with 37% of these patients succumbing to the disease within the first five years (17). The high response to chemotherapy and high recurrence associated with TNBC is known as "the triple-negative paradox."

Treatments for patients with metastatic disease, which are generally considered palliative rather than therapeutic (50), include multiple single chemotherapeutic agents (sequentially used until maximal response/maximal tolerance achieved) with treatment breaks considered on a patient-specific basis (50,59). Rapid disease progression can prompt the

application of combination-based chemotherapeutic approaches in a patient-specific manner (52,56). With no standard treatment established, chemotherapeutics employed include taxanes, anthracyclines, vinca alkaloids, and antimetabolites (50,52,56). Thus, the clinical management of TNBC metastatic disease remains a significant unmet clinical need. This thesis aims to generate new knowledge towards developing efficient treatments for metastatic TNBC.

1.2.4. Recent Advances in the Systemic Treatment of TNBC

Recent breakthroughs in our understanding of TNBC development and progression and the mechanisms underlying disease heterogeneity have prompted research into the development of targeted therapies.

1.2.4.1. Platinum Salts

Platinum salts (carboplatin, cisplatin) induce DNA strand breaks by crosslinking, which subsequently promotes apoptosis (59,67). Adding a platinum salt to neoadjuvant chemotherapy improves treatment outcome (pCR rates) in non-metastatic TNBC (71), which correlates with the high prevalence of *BRCA1/2* mutations (67,71). *BRCA1/2* mutations provoke HRD, increasing the sensitivity to platinum compounds and other drugs that induce genetic damage; however, these drugs exhibit significant toxicity. Patients treated with a platinum-based regimen frequently suffer from anemia, neutropenia, thrombocytopenia, and nausea, with side effect severity usually prompting dose reduction or discontinuation of treatment (71).

1.2.4.2. Immune Checkpoint Inhibitors

Immunotherapy as a cancer treatment has dramatically progressed in recent years, yielding encouraging results in a wide range of tumors (59,67). Immunotherapy stimulates the host immune system to recognize and eliminate tumor cells via multiple approaches (72).

Checkpoint inhibitor therapy represents one of the most advanced immunotherapeutic approaches. T-cell activation occurs after antigen recognition and presentation by antigen-presenting cells. To allow self-tolerance, the immune system emits inhibitory signals, or immune checkpoints, to inhibit T-cell responses; however, overexpression of inhibitory signals in the tumor microenvironment leads to tumor cell immune evasion. Checkpoint inhibitor therapies target this immune checkpoint to restore immune responses against tumor cells (72).

Compared to other breast cancer subtypes, TNBC (and especially the IM subtype (17)) represents an excellent candidate for checkpoint inhibitor therapies for three main reasons; i) the high number of tumor-infiltrating lymphocytes (including T-cells and B-cells), ii) higher genomic instability, which increases the generation of tumor-specific neoantigens recognized by the immune system to activate an immune response that checkpoint inhibitors can further improve, and iii) the elevated expression of programmed cell death protein 1 ligand (PD-L1) (59,73). PD-L1, as part of an immune checkpoint pathway, interacts with programmed cell death protein 1 (PD-1) expressed by T-cells to induce their inhibition (68). PD-L1 overexpression by tumor cells and in the tumor microenvironment, combined with the increased number of tumor-infiltrating lymphocytes, provides targets for checkpoint inhibition (73).

Multiple clinical trials have evaluated the efficacy and safety of PD-1/PD-L1 inhibitors as a single-agent or combination therapy (73). These efforts prompted the approval of atezolizumab (a humanized monoclonal antibody against PD-L1) in combination with nab-paclitaxel (a paclitaxel-

albumin conjugate) for the treatment of PD-L1-positive locally-advanced or metastatic TNBC in 2019 (the first immunotherapy approval for breast cancer). Common reported side effects include alopecia, peripheral neuropathy, fatigue, and nausea (74).

1.2.4.3. PARP Inhibitors

PARP catalyzes the transfer of adenosine diphosphate-ribose (ADP-ribose) from NAD+ to proteins and participates in DNA repair processes. PARP inhibition results in double-strand breaks that can be repaired by HR; however, PARP inhibition induces lethality in cells with HRD (75). For this reason, PARP inhibitors (PARPi) have been studied as a treatment for *BRCA1/2*-mutated breast cancer tumors such as TNBC.

The PARPi olaparib represents an effective monotherapy against metastatic HER2-negative *BRCA1*-mutated breast cancer and has gained approval to treat *BRCA1/2* mutated breast cancer tumors (67). The PARPi talazoparib has proven an efficient monotherapy in the neoadjuvant setting in early breast cancer cases with germline *BRCA1/2* mutations. Encouragingly, both drugs suffer from clinically manageable hematological alterations as the main side effects (e.g., anemia) (75).

1.2.4.4. Androgen Receptor Pathway Inhibitors

The AR is a nuclear steroid hormone receptor that binds androgens, such as testosterone and dihydrotestosterone (76). Following androgen-mediated activation, the AR functions as a transcriptional factor and can activate multiple signaling pathways (77).

The role of the AR in TNBC and its prognostic value remains unclear (76); however, AR overexpression does occur in the LAR subtype of TNBC (17,62). As this subtype displayed sensitivity to AR antagonists in preclinical

studies (59,67), several phase II clinical trials have been carried out to assess effectiveness against AR-positive TNBC (76). The results of phase II clinical trials suggested that AR inhibitors bicalutamide and enzalutamide (clinically approved for the treatment of metastatic prostate cancer) display promising if limited results (78,79). AR-positive TNBC patients tolerated both drugs well, with fatigue the most prevalent adverse effect.

Several clinical trials evaluating the safety and efficacy of AR pathway inhibitors, alone or in combination, are currently ongoing (76). A combination therapy with phosphoinositide-3 kinase (PI3K) inhibitors is of particular interest, as the LAR subtype displays an enrichment for activating PI3K gene mutations (59,62).

1.2.4.5. Phosphoinositide-3 Kinase/Protein Kinase B/Mammalian Target of Rapamycin Pathway Inhibition

The PI3K pathway plays a crucial role in cell proliferation, angiogenesis, invasion, and metastasis. Following membrane receptor tyrosine kinase (RTK) activation by ligand binding (e.g., growth factors or cytokines), the induced signaling cascade prompts the activation of PI3K, which phosphorylates phosphoinositide-2 (PIP2) to generate phosphoinositide-3 (PIP3), which acts as a second messenger activating protein kinase B (AKT). AKT then phosphorylates downstream effector proteins, eventually promoting angiogenesis, cell survival, extracellular matrix degradation, and other mechanisms related to cell invasion and metastasis. The mammalian target of rapamycin (mTOR), whose activation promotes cell growth and division (80), represents one such effector protein.

Mutations that provoke PI3K/AKT/mTOR pathway hyperactivation occur in ~25% of TNBC (68), making these proteins potential therapeutic targets. Several clinical trials have evaluated the efficacy and safety of PI3K, AKT, and mTOR inhibitors for breast cancer treatment alone or in

combination; however, only a few have focused on TNBC. The combination of paclitaxel with the AKT inhibitors ipatasertib or capivasertib improved therapeutic responses compared to paclitaxel alone in phase II clinical trials in metastatic TNBC. The most common side effects included diarrhea, fatigue, and rash (81,82).

1.3. Brain Metastasis in Breast Cancer: The Rising Challenge

1.3.1. Basic Facts: Incidence and Prognosis

Breast cancer is the second most common cause of brain metastasis after lung cancer. Patients with brain metastases suffer from a poor prognosis and neurological impairments, resulting in a reduced quality of life (83–85). Although the development of brain metastasis represents a late event in disease progress (35,86), 30-50% of patients with metastatic breast cancer develop brain metastasis (87) with incidence depending on the subtype and risk factors such as the presence of lung or liver metastasis (88). The incidence of breast cancer-associated brain metastasis has increased over time, most probably due to the improved treatment of the primary disease, which has increased patient life expectancy and, thus, the probability of developing brain metastasis (83,84,87). The HER2-positive and TNBC subtypes possess a higher risk of developing brain metastasis, with TNBC suffering from the worst prognosis (83–85,88,89). Overall, 25-46% of metastatic TNBC patients will develop brain metastasis (89), displaying a survival time between four and eight months after diagnosis (88).

1.3.2. The Blood-Brain Barrier as the Guardian of the Brain

The brain represents a highly protected organ and is guarded by various barriers: the blood-brain barrier (or the BBB), the blood-

cerebrospinal fluid barrier, and the arachnoid epithelial membrane barrier/meningeal barrier (90). Such barriers (i) control the highly selective and specific uptake/efflux mechanisms and the metabolism of endogenous/exogenous molecules, (ii) contribute to ion homeostasis, (iii) preserve neural connectivity in the central nervous system (CNS), (iv) separate central and peripheral neurotransmitters pools to reduce cross-talk and allow non-synaptic signaling in the CNS, and (v) allow immune surveillance and response with minimal inflammation and cell damage (91).

With 12 to 18 m^2 of surface, the physical and metabolic barrier formed by the BBB represents the most significant interface between blood and brain (90). The BBB comprises the brain vasculature whose endothelial cells (BECs) closely connect to each other by intercellular tight junctions to form a continuous (non-fenestrated) endothelium surrounded on its abluminal side by a pericyte-embedded basement membrane tightly associated with the endfeet of astrocytes (**Figure 1.4**). To complete the so-called neurovascular unit, neurons and microglial cells (and, optionally, peripheral immune cells) provide functional and structural support to the BBB (92,93). BECs possess location-specific features, which include (i) a lower number of endocytic vesicles compared to other endothelial cells, which limits transcellular transport, (ii) a lack of fenestrations, (iii) high electrical resistance provided by tight junctions, which restricts paracellular flux, (iv) specialized transport systems, and (v) a higher volume of mitochondria, suggesting higher metabolism (94).
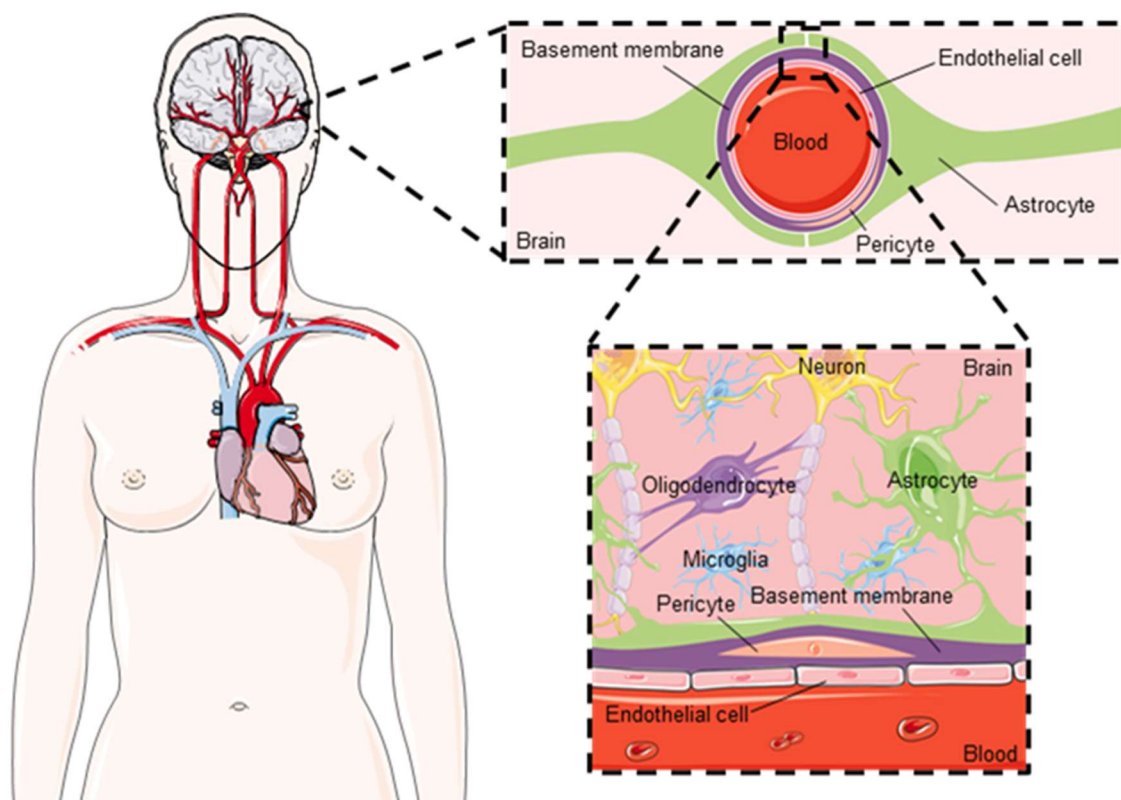
Figure 1.4. Schematic representation of the blood-brain barrier. Drawn with smart.servier.com (8).

The BBB protects the brain from external insults and impedes the penetration of 98% of small drugs and ~100% of biological agents from the blood to the brain (87,95,96) (**Figure 1.5**). The tight junctions between BECs hamper the exchange of molecules via paracellular diffusion (93), a passive process where molecules travel through the intercellular space of the endothelial cells following electrochemical, hydrostatic, osmotic, or concentration gradients (94). Only water and a limited number of small water-soluble molecules and lipophilic solutes cross the BBB by paracellular diffusion; therefore, the paracellular pathway plays a limited role in brain drug delivery (94). In the transcellular pathway, molecules travel across endothelial cells using passive or active mechanisms. Small lipophilic molecules (<500 Da) and gases (e.g., O_2 and CO_2) can cross the BBB by passive transcellular diffusion through the endothelial cell membrane (97). Indeed, most CNS drugs follow this mechanism (98). Some small hydrophilic

molecules are transported by carrier-mediated transport (CMT) using specific energy-dependent or independent membrane transporters (99). These transporters mediate the uptake of glucose, amino acids, fatty acids, and vitamins, among other molecules (93). Hormones, growth factors, lipoproteins, and other macromolecules cross the BBB by receptor-mediated transcytosis (RMT). In this active transcellular pathway, a specific receptor recognizes a molecule and prompts endocytosis, intracellular transport within a vesicle, and exocytosis on the abluminal side (100,101). The two-way nature of this route can prompt the extrusion of the transported molecule from the brain given the appropriate concentration gradient (102). Finally, positively charged compounds, such as plasma macromolecules (albumin), can be transported by adsorptive-mediated transcytosis (AMT) (94).
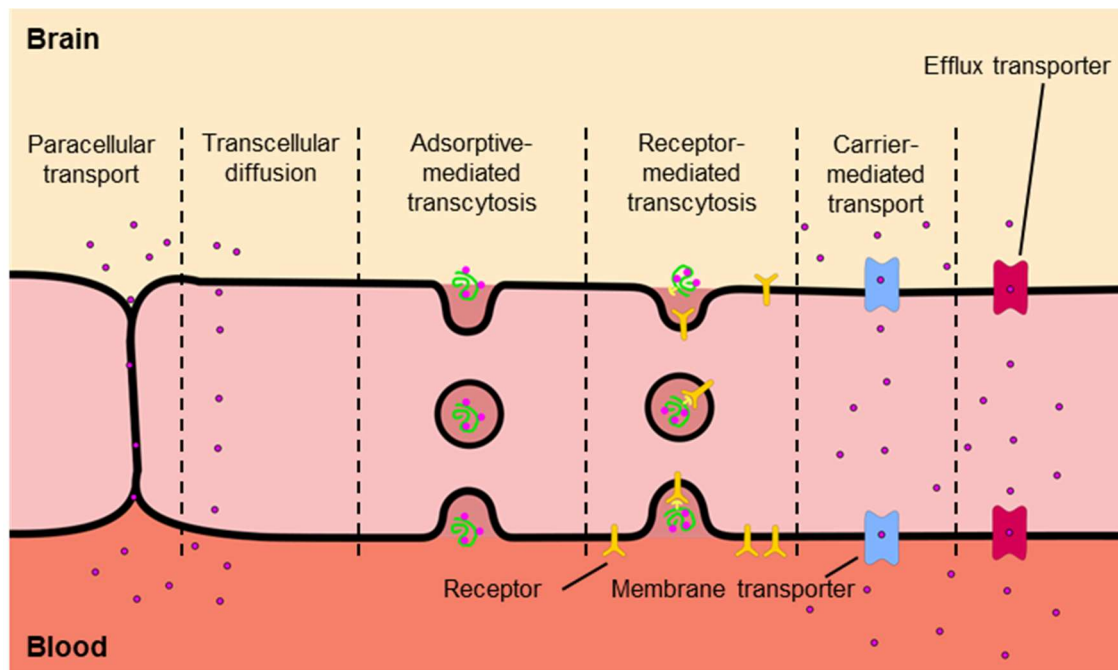
Figure 1.5. Transport mechanisms across the BBB. Redrawn from Duro-Castano et al. 2020 (93) with smart.servier.com (8).

Efflux transport systems in the BBB and blood-cerebrospinal fluid barrier hinder the accumulation of many lipophilic compounds in the CNS (99), which impedes their accumulation at therapeutically relevant

concentrations in the brain. The P-glycoprotein (P-gp), a member of the ATP-binding cassette (ABC) transporters (94,99), represents one of the best-understood efflux transporters and forms part of the multidrug resistance receptors (MDRs). Of note, tumor cells overexpress efflux transporters as a mechanism of chemoresistance (103,104). Additionally, the activation of EMT programs as one of the first events in the metastatic process (see *1.1.5.Breast Cancer Metastasis*) associates with the overexpression of ABC transporters to induce drug resistance (38). When disseminated tumor cells enter the brain (see *1.3.3.The Metastatic Process in the Brain*), their interaction with astrocytes favors the development of chemoresistance (85,105,106). Therefore, these transporters imply a double hurdle to surpass when treating brain metastasis.

1.3.3. The Metastatic Process in the Brain

To form a tumor in the brain, breast cancer tumor cells must reach the brain parenchyma and establish a metastatic colony. Since CTCs spread through blood circulation, the BBB represents the most significant hurdle to the successful metastatic colonization of the brain parenchyma (107).

Given the specific characteristics of the BBB, tumor cells require specific traits to breach the barrier and access the brain. The study of the metastatic process in the brain has led to the identification of a brain metastasis gene expression signature, which includes common mediators for extravasation of non-fenestrated capillaries (included in, for example, the lung metastasis signature), complemented with specific enhancers of BBB crossing and brain colonization (35,86). For instance, heparin-binding epidermal growth factor-like growth factor (HBEGF) and cyclooxygenase-2 (COX2) as general extravasation mediators increase vascular permeability and induce cell motility and invasiveness, respectively. Both genes form part of the lung and brain metastasis signatures from breast cancer. ST6 N-acetylglucosamine alpha-2,6-sialyltransferase (ST6GalNAcV) represents a

specific mediator of TNBC-associated brain metastasis and acts by inducing a specific glycosylation pattern to the cancer cell surface to enhance cell adhesion to the BBB endothelium (35,85,86,105).

Tumor cell extravasation in the BBB occurs mainly by transendothelial migration, i.e., movement between adjacent endothelial cells (35,84,107). Studies performed using *in vivo* brain metastasis models (obtained by inoculating cancer cells into the bloodstream) have demonstrated the extended time required for CTCs to cross the BBB compared to other organs. For instance, a CTC takes three to seven days to extravasate through the BBB, while extravasation into the lungs takes only twelve hours (105). The arrival of CTCs at the abluminal side of the brain endothelium leads to the activation of astrocytes (105). Reactive astrocytes secrete paracrine mediators that stimulate tumor cell proliferation (e.g., interleukin 1β, IL-1β) (85,105). Disseminated tumor cells also secrete IL-1β to activate a signaling pathway that induces the expression of proliferative signals in reactive astrocytes, which subsequently activates tumor cell proliferation (105). Reactive astrocytes also secrete MMP2 and MMP9, which degrade the extracellular matrix to favor cell migration and invasion of brain parenchyma. Extracellular matrix degradation also results in the release of vascular endothelial growth factor (VEGF), which activates angiogenesis (105) and increases endothelial permeability (85). Reactive astrocytes also directly interact with tumor cells via gap junctions, which allow the transport of secondary messengers such as 2',3'-cyclic guanosine monophosphate-adenosine monophosphate (cGAMP) from tumor cells to astrocytes, which then secrete cytokines that favors the development of chemoresistance in tumor cells (85,105,106). Reactive astrocytes also display anti-metastatic activity, including plasminogen activator (PA) secretion, which converts the neuron-derived plasminogen to plasmin. While this molecule displays lethality in non-adapted cancer cells, some metastatic cells express serpins to block astrocyte-derived PA and protect cancer cells from plasmin-mediated death (105).

Once cells have extravasated into the brain, they remain in a dormant state within the perivascular area (i.e., the microenvironment surrounding the vasculature), where they interact with pre-existing capillaries (46,84,105). Interactions with endothelial cells rely on cell adhesion molecules, thanks to the upregulation of integrins in tumor cells (85). In the perivascular area, cancer cells have preferential access to oxygen, nutrients, and factors produced by BECs, which influence the growth, dormancy, and immune evasion of cancer cells (37,105). For instance, the stable expression of TSP-1 by non-angiogenic BECs induces cell quiescence and tumor dormancy (46,105). While several programs have been linked to the regulation of disseminated tumor cell dormancy in the brain, the process remains incompletely understood.

When disseminated tumor cells switch to a proliferative state, metastatic tumor growth occurs within the perivascular area (i.e., vascular co-option) thanks to the expression of integrins and L1 cell adhesion molecule (L1CAM) in cancer cells. These molecules mediate the interaction of tumor cells with the endothelial basement membrane and induce proliferation (46). The general influence of angiogenesis in metastatic tumor growth depends on the tumor type. For instance, melanoma brain metastases rely only on vascular co-option, while non-small cell lung cancer and breast cancer require the formation of new vessels to evolve from micrometastasis to macrometastasis (105). The expression of VEGF by tumor cells remains crucial to activating the angiogenic program in BECs. Once activated, these cells express TGF-β1 and periostin instead of TSP-1, which favors tumor growth (105).

Metastatic tumor growth within the perivascular area provokes alterations in the structure and function of the BBB to such an extent that the formation of a blood-tumor barrier (BTB) has been proposed (108). During brain metastasis, the molecular (e.g., junctional proteins) and cellular components of the BBB become disrupted. BECs appear swollen, the

basement membrane composition and the pericytes become altered, and astrocytes lack endfeet polarization (85,109). Additionally, the BTB displays differences according to tumor nature (109); for instance, while the BTB in HER2-positive-derived metastases expresses high levels of glucose transporter 1 (GLUT1) and breast cancer resistant protein (BCRP), TNBC metastases display the opposite profile (110). While the BTB exhibits a leakier nature than the BBB, permeability remains heterogeneous and generally impedes the accumulation of most bioactive molecules to a therapeutically relevant concentration within tumor tissue (85).

1.3.4. Clinical Management of Breast Cancer Brain Metastasis

The clinical management of breast cancer brain metastasis has traditionally relied on local approaches since the BBB/BTB hinders the penetration and accumulation of small drugs and biological agents in the brain (87,95,96). The therapeutic approach also depends significantly on the extent of the disease. Breast cancer brain metastasis patients with a single or limited number of metastatic foci usually receive surgical resection or stereotactic radiosurgery, with the latter approach recommended when tumor location impedes surgical resection. Both interventions can be followed by whole-brain radiation therapy (WBRT), but this decision should be discussed with the patient, considering both the risks (i.e., neurological impairment) and benefits (i.e., intracranial disease control) (52).

Surgical resection improves patient survival and can immediately reduce symptoms associated with metastasis, relieve intracranial hypertension, and allow for histological diagnosis (83,111). Surgical resection is recommended in the cases of absent/controlled systemic disease, active extracranial disease with available systemic treatments, or radioresistant primary tumors (111); however, metastatic location can entail a significant limitation to this treatment (83,111). Stereotactic radiosurgery is used instead of surgical resection in those patients whose lesions locate to

anatomical locations with difficult access and those deemed poor candidates for surgical resection (111). This approach delivers high-precision photon radiation to a small target volume inside the brain without affecting normal tissue to avoid neurocognitive degeneration (83); however, cases of micrometastases remain unaddressed (112). WBRT addresses both macroscopic and microscopic metastasis (112) and represents the treatment of choice in patients with multiple (>10) metastatic foci (96,112,113). While WBRT can increase overall survival from one to seven months, irradiation can cause adverse effects such as alopecia, nausea, decreased appetite, fatigue, and neurocognitive degeneration (112).

1.3.5. Recent Advances in the Systemic Treatment of Breast Cancer Brain Metastasis

As few prospective studies have focused on systemic treatments for brain metastasis, efficacy data mainly derives from retrospective subgroup analysis (87,113). Consistent with the lack of evidence of clinical benefit, systemic therapies are not currently considered standard of care for breast cancer brain metastasis patients (52).

Even fewer prospective clinical trials have evaluated treatments for TNBC-related brain metastasis (113); furthermore, there exists a general lack of representation of TNBC in studies considering all breast cancer subtypes, making any results insignificant. The sparse number of patients enrolled in these studies may result from the rapid progression of primary and metastatic TNBC; in these cases, local therapy (surgery or radiotherapy) represents the preferred treatment choice and provides rapid symptom alleviation. Unfortunately, very few prospective clinical trials are currently evaluating treatments for TNBC brain metastasis (**Table 1.3**).

In conclusion, increased efforts to develop personalized approaches for breast cancer treatment have prompted the identification of different

breast cancer subtypes; however, the treatment of metastatic brain disease currently benefits little from this classification. Since metastatic spread in the brain can occur with the progression of extracranial metastatic lesions, the development of a subtype-specific treatment that displays efficacy for extracranial and intracranial disease may represent a turning point in treating brain metastasis.

Table 1.3. Current prospective clinical trials for TNBC-related brain metastasis treatment including systemic therapies.

NCT Number	Title	Status	Conditions	Interventions	Phase	Study Type
NCT04711824	Study of Stereotactic Radiosurgery with Olaparib Followed by Durvalumab and Physician's Choice Systemic Therapy in Subjects with Breast Cancer Brain Metastases	Not yet recruiting	TNBC and/or BRCA-mutated brain metastasis	Olaparib (oral) + stereotactic radiosurgery followed by durvalumab (intravenous) vs. physician's best choice	1/2	Interventional
NCT04789668	Bintrafusp Alfa and Pimasertib for the Treatment of Patients with Brain Metastases	Recruiting	Various, including TNBC	Bintrafusp alfa (intravenous) + pimasertib (oral)	1/2	Interventional
NCT03483012	Atezolizumab + Stereotactic Radiation in Triple-negative Breast Cancer and Brain Metastasis	Active, not recruiting	TNBC brain metastasis	Stereotactic radiosurgery + atezolizumab (intravenous)	2	Interventional
NCT04348747	Dendritic Cell Vaccines Against Her2/Her3, Cytokine Modulation Regimen, and Pembrolizumab for the Treatment of Brain Metastasis from Triple Negative Breast Cancer or HER2-positive Breast Cancer	Not yet recruiting	TNBC brain metastasis	Anti-HER2/3 dendritic cell vaccine (intradermal) + celecoxib (oral) + INF-α2b (intravenous) + rintatolimod (intravenous) followed by pembrolizumab (intravenous)	2	Interventional

NCT04303988	A Multi-cohort Phase II Study of HER2-positive and Triple-negative Breast Cancer Brain Metastases	Not yet recruiting	TNBC or HER2-positive brain metastasis	In TNBC subgroup: SHR1316 (intravenous) + bevacizumab (intravenous) + cisplatin or carboplatin (intravenous)	2	Interventional
NCT02595905	Cisplatin with or Without Veliparib in Treating Patients with Recurrent or Metastatic Triple-Negative and/or BRCA Mutation-Associated Breast Cancer with or Without Brain Metastases	Active, not recruiting	TNBC and/or BRCA-mutated with or without brain metastasis	Cisplatin + placebo vs. cisplatin + veliparib (intravenous)	2	Interventional
NCT05064280	Phase II Study of Pembrolizumab in Combination with Lenvatinib in Patients With TNBC, NSCLC, and Other Tumor Types and Brain Metastases	Not yet recruiting	TNBC and other solid tumors with brain metastasis	Pembrolizumab (intravenous) + lenvatinib (oral)	2	Interventional
NCT03613181	ANG1005 in Leptomeningeal Disease from Breast Cancer (ANGLeD)	Not yet recruiting	HER2-negative brain and leptomeningeal metastasis	ANG1005 vs. physician's best choice	3	Interventional

Data obtained from clinicaltrials.gov (114).

1.4. Polymer Therapeutics for Triple Negative Breast Cancer Treatment

1.4.1. Polymer Therapeutics: Definition and Classification

The term "polymer therapeutics," coined by Prof. Ruth Duncan, designates a family of new chemical entities formed by rationally designed macromolecular drugs considered the first polymeric nanomedicines with demonstrated clinical benefit (115,116).

Polymer therapeutics include five groups (**Figure 1.6**) (115,117,118):

i.   **Polymeric drugs** – polymers with inherent activity

ii. **Polymer-drug conjugates** – small drug(s) covalently bound to a water-soluble polymer

iii. **Polymer-protein conjugates** – therapeutic protein(s)/peptide(s) covalently bound to a water-soluble polymer

iv. **Polymeric micelles** – with the bioactive molecule covalently bound to the polymer forming the micelle

v.   **Polyplexes** – multi-component systems developed as non-viral vectors for gene/small interfering ribonucleic acid (siRNA) delivery.

This thesis focuses on developing polymer-drug conjugates, which will be described in-depth in the following sections (see *1.4.3.Polymer-Drug Conjugates for Cancer Treatment* and *1.4.3.1.Rational Design of Polymer-Drug Conjugates for Cancer Treatment*).
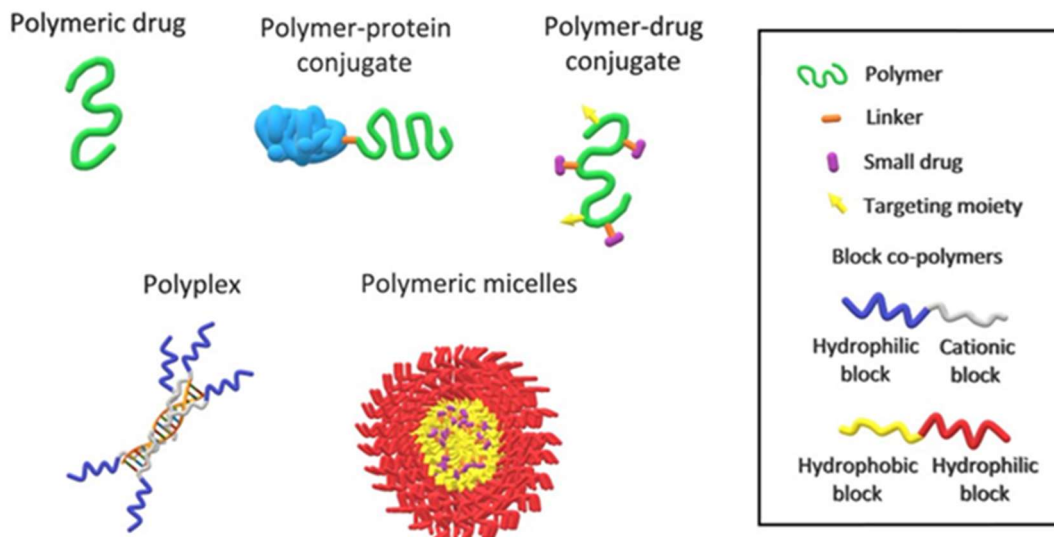
Figure 1.6. Schematic representation of Polymer Therapeutics major categories. Redrawn from (117).

1.4.2. A Brief History of Polymer Therapeutics

The first recorded use of synthetic polymers as therapeutics date to the 1940s, when polymers were studied in the clinics as plasma expanders (e.g., poly(vinylpyrrolidone) – PVP), wound dressing materials, and antiseptics (e.g., PVP-iodine or Povidone) (116). 1958 saw the first clinical application of polymer therapeutics when the USA Food and Drug Administration (FDA) approved sodium polystyrene sulfonate, a potassium-binding resin, to treat hyperkalemia (119,120).

The marketing of the polymer-protein conjugate SMANCS for the treatment of hepatocellular carcinoma followed in 1990 (121). SMANCs comprises two polymer chains of styrene-co-maleic anhydride (SMA) covalently bound to the antitumor protein neocarzinostatin (NCS) (121). More than two decades after the approval of SMANCS, two polymer therapeutics entered the USA Top 10 selling drugs in 2013 – the polymeric drug Copaxone®, and the polymer-protein conjugate Neulasta® (120,122).

Copaxone®, a synthetic polypeptide approved in 1995 for the treatment of relapsing-remitting multiple sclerosis (122), comprises a heterogeneous mixture of random copolymers of the amino acids L-alanine, L-lysine, L-glutamic acid, and L-tyrosine (in a fixed molar ratio of 0.43:0.14:0.34:0.09) present as single molecules or as aggregates forming a colloidal suspension (122,123). Given the random polypeptidic sequence, this strategy requires strict control over the manufacturing process to assure reproducibility, which has even greater importance now as a generic drug (123). The mechanism of action underlying the activity of Copaxone® remains unclear (122,123); however, studies have provided evidence for immunomodulatory, anti-inflammatory, and neuroprotective capabilities (123).

Neulasta®, a poly(ethylene glycol) (PEG) conjugate of recombinant granulocyte colony-stimulating factor (G-CSF), was FDA-approved in 2002 for the treatment of chemotherapy-induced neutropenia (122). The formulation of Neulasta® allows for a prolonged circulation time compared to the unconjugated "free" form of G-CSF ($t_{1/2}$ = 33 h vs. 3.5 h) (124), thereby allowing a single subcutaneous injection per chemotherapy cycle (122). In this case, site-specific PEGylation helps to maintain G-CSF's tertiary structure and supports G-CSF-receptor interactions (125).

The exponential increase in the number of polymer therapeutics on the market for different medical applications reflects the enormous potential of these nanomedicines (**Table 1.4**). The development of novel methods for controlled polymer synthesis, optimized biodegradable carriers, and highly accurate analytical techniques combined with a growing biomolecular understanding of disease (120,126) will support the development of disease-specific rationally-designed therapeutics for a range of indications.

Table 1.4. Clinically approved polymer therapeutics

Product name	Description	Indication	First Approval Year	References
Sodium Polystyrene Sulfonate	Potassium chelator	Hyperkalemia	1958	(120,127)
Adagen	PEGylated adenosine deaminase derived from bovine intestine	Severe combined immunodeficiency	1990	(120,127)
SMANCS (Japan)	Styrene-co-maleic anhydride-neocarzinostatin conjugate	Hepatocellular carcinoma	1993	(120,127)
Oncaspar	PEGylated recombinant L-asparagine amidohydrolase	Acute leukemia	1994	(120,127,128)
Copaxone	Random polypeptides of L-glutamic acid, L-alanine, L-tyrosine, and L-lysine	Relapsing-remitting multiple sclerosis	1996	(120,127,128)
Synvisc	Hyaluronic acid	Joint pain	1997*	(127,129)
Renagel	Phosphate binding drug	Serum phosphorus in patients with chronic kidney disease	1998	(120,127)
PegIntron	PEGylated recombinant human interferon alfa-2b	Chronic hepatitis C	2001	(120,127,128)
Neulasta	PEGylated recombinant human granulocyte colony stimulating factor	Chemotherapy-induced neutropenia	2002	(120,127,128)
Pegasys	PEGylated recombinant human interferon alfa-2a	Chronic hepatitis C	2002	(120,127,128)
Somavert	PEGylated growth hormone receptor agonist	Acromegaly	2003	(120,127)
Macugen	PEGylated aptamer that acts as a selective vascular endothelial growth factor antagonist	Neovascular form of age-related macular degeneration	2004	(120,127,128)

Mircera	PEGylated epoetin beta	Anemia in chronic renal diseases	2007	(120,127,128)
Cimzia	PEGylated monoclonal antibody against tumor necrosis factor-alpha	Crohn's disease	2008	(120,127,128)
Cholestagel	Bile acid sequestrant	Primary hypercholesterolemia	2009	(120,127)
Krystexxa	PEGylated recombinant uricase	Chronic gout	2010	(120,127,128)
Lonquex	Site-specific PEGylated recombinant granulocyte colony-stimulating factor	Chemotherapy-induced neutropenia	2012	(120,127)
Lymphoseek	Diethylenetriaminepentaacetic acid (a chelating agent for Tc-99m) and mannose covalently bound to 10 kDa dextran	Diagnostic imaging agent	2013	(120,127)
Plegridy	PEGylated recombinant interferon beta-1a	Relapsing forms of multiple sclerosis	2014	(120,127,128)
Movantik	PEGylated naloxol	Opioid-induced constipation	2014	(120,127)
Adynovate	PEGylated recombinant human coagulation factor VIII	Hemophilia A	2015	(120,127,128)
Veltassa	Cation-exchange polymer	Hyperkalemia	2015	(120,127)
Rebinyn	Glyco-PEGylated coagulation factor IX	Hemophilia B	2017	(128)
Palynziq	PEGylated recombinant phenylalanine ammonia lyase	Phenylketonuria	2018	(127,130)
Revcovi	PEGylated recombinant adenosine deaminase	Severe combined immunodeficiency	2018	(127,131)
Jivi	Site-specific PEGylated coagulation factor VIII	Hemophilia A	2018	(127,130)
Givosiran	GalNAc-siRNA conjugate	Acute hepatic porphyria	2019	(128)

*Approved as a device

1.4.3. Polymer-Drug Conjugates for Cancer Treatment

Despite considerable improvements in recent decades, conventional cancer treatments (i.e., surgery, radiotherapy, and chemotherapy) still entail significant limitations (124). Specifically, systemic treatment with non-targeted small drugs suffer from important limitations that include (i) reduced water solubility of the therapeutic agent (124,132); (ii) side effects in healthy tissues due to poor selectivity/lack of targeting (133); (iii) short circulation half-life due to early degradation and high renal excretion (thereby requiring higher dosing, which increases the incidence of side effects) (124,133); and (iv) development of drug resistance (133).

Polymer therapeutics and polymer-drug conjugates, in particular, can help to overcome some of these limitations and provide additional advantages. The conjugation of a small drug to a water-soluble polymer offers a wide variety of advantages, which include (i) an increment in the solubility of the drug (118,120,134–136), (ii) the improvement of drug pharmacokinetic and pharmacodynamic profiles by rational polymer selection (137), (iii) passive targeting via the enhanced permeability and retention (EPR) effect (138), (iv) the development of combination therapies, theranostics, and active targeting strategies due to polymer polyvalence and versatility (139,140), (v) the reduction of immunogenicity and increment of plasma stability of the drug, (vi) enhanced passage through biological barriers and resistance to chemoresistant mechanisms (141,142), and (vii) controlled release via the rational selection of linking and polymeric components, which allow the release of the drug under specific physiological conditions or in response to a specific stimulus (118,143). The overall objective is to specifically release the drug at a desired site of action and maintain a therapeutically relevant concentration of the said drug for the desired duration (118).

The possibility of the optimized delivery of drug combinations represents perhaps the most encouraging advantage of polymer-drug

conjugates. Given the previously described heterogeneous nature of tumors, treatment with synergistic drug combinations that target different signaling pathways or different aspects of the same pathway represents an exciting means of improving therapeutic outcomes in cancer (144–146). The conjugation of drug combinations to the same polymeric backbone can ensure the delivery to the desired target and support optimal therapeutic activity (147–151). Moreover, optimized drug ratios combined with the rational choice of linking moieties can strictly control drug release and bioavailability to improve therapeutic outcomes (126).

In this thesis, we pursued the optimization of drug ratios and linking chemistries to develop an efficient polymer-drug combination conjugate for the treatment of metastatic TNBC (*Chapter 2*).

1.4.3.1. Rational Design of Polymer-Drug Conjugates for Cancer Treatment

As first described by Ringsdorf in 1975 (152), polymer-drug conjugates minimally comprise (i) a water-soluble polymeric carrier, (ii) the therapeutic agent, and (iii) the cleavable linker, with targeting moieties a fourth optional component. The rational choice of each component, based on the biological barriers specific to the indication, supports overall therapeutic potential. Said barriers depend primarily on the administration route; intravenous administration represents the preferred route for polymer-drug conjugates, allowing for safe, repeated administrations and avoiding the first-pass effect that reduces the bioavailability of orally administered drugs due to extensive metabolism in the liver before entering the systemic circulation (126,153,154). Alternative administration routes for polymer-drug conjugates, each with their specific advantages/disadvantages, include intranasal (155), oral (156), subcutaneous (157), and transdermal (158,159).

This thesis focuses on developing polymer-drug combination conjugates for the treatment of TNBC brain metastasis by intravenous administration; therefore, in the upcoming section, we will discuss how rational design can help overcome the biological barriers associated with intravenous administration and exploit specific tumor characteristics to yield efficient treatment outcomes.

1.4.3.1.1.   Circulation Time and Clearance

In the case of intravenous administration of polymer-drug conjugates, blood represents the first significant biological barrier. Effective polymer-drug conjugates must display stability in blood circulation to assure adequate delivery to target tissues (137,160). The polymeric carrier must lack toxicity and immunogenicity (i.e., must avoid recognition as a foreign object by the immune system) and display hemocompatibility (i.e., lack coagulation cascade activating capacities) (158,160,161).

Non-biodegradable polymeric carriers must display a size below the renal filtration threshold (6-8 nm) to assure elimination by glomerular filtration (162). Polymer-drug conjugates with sizes above this threshold exhibit prolonged circulation times (148,163), permitting more amenable dosing schedules. Polymers that break down into smaller excretable subunits and/or biocompatible degradation products are preferred, as large non-biodegradable polymers can accumulate in the body and cause toxicity (158,162).

The reticuloendothelial system (RES) represents another critical biological barrier encountered after the intravenous administration of polymer-drug conjugates. The RES comprises tissue-resident phagocytic cells that remove foreign particles from circulation; specifically, liver-resident Kupffer cells sequester and remove nanoparticles from the circulation (164,165) when they present a size larger than 200 nm (137). As positively

charged systems readily bind to negatively charged cell surfaces resulting in rapid clearance from circulation, negatively charged systems support extended circulation times of polymer-drug conjugates (138). In general, implementing polymer-drug conjugates with a slightly negative to neutral charge avoids opsonization (i.e., adsorption of opsonins promoting phagocytosis) and RES uptake (137), thereby supporting optimal therapeutic outcomes.

1.4.3.1.2.   Protein Corona

The interaction of polymer-drug conjugates with blood leads to the adsorption of circulating proteins, forming the so-called "protein corona" (160,166). The corona comprises proteins such as albumin, immunoglobulin G, transferrin, fibrinogen, and apolipoproteins; however, the final composition alters according to the polymer employed, physiological environments encountered, exposure time, and patient characteristics (e.g., genetic background, sex, and disease status) (160). The adsorbed proteins distribute around the conjugate forming two layers known as the "hard" and "soft" coronas. The hard corona comprises an inner layer of proteins tightly bound to the conjugate, while the soft corona makes up an outer layer of rapidly-exchanging weakly-bound proteins. Some models propose that only hard corona proteins interact directly with the carrier, and the soft protein corona associates with the hard corona via weak protein-protein interactions (166,167).

The protein corona can affect conjugate biological performance in several distinct manners. Protein adsorption typically increases conjugate size, which increases conjugate circulation time; however, the adsorption of factors known as "opsonins" (e.g., immunoglobulins, coagulation factors, and complement proteins) can provoke immune-mediated conjugate clearance. The protein corona can also impact the targeting ligands conjugated to the nanosystem and hamper receptor recognition;

furthermore, this mode of "steric" interference can also influence drug release kinetics. Corona proteins also interact with their specific receptors, which can redirect conjugates to undesired cells/organs, thereby impacting therapeutic outcomes and increasing unwanted side effects (168).

Given these problems, researchers initially searched for strategies that inhibited protein corona formation (166), which gave rise to design rules to reduce protein adsorption. For instance, larger particles adsorb a higher amount of protein due to their large surface area and low curvature degree (which improves the interaction with large proteins) (168). Furthermore, spherical morphologies display lower levels of protein absorption than rod-like morphologies (167,168). A neutral charge supports a lower level of protein absorption than strong surface charges, while a positive surface charge prompts the formation of a thicker protein corona compared to a negative surface charge since negatively charged proteins have a greater abundance in plasma. Finally, hydrophobic particles support higher protein adsorption than hydrophilic particles as hydrophobic surfaces interact robustly with the hydrophobic domains of proteins such as apolipoproteins (168). Recent studies show that polymeric nanocarriers with dense hydrophilic surface coatings display neglectable protein corona formation (169,170).

As an alternative approach, researchers aim to exploit the protein corona to target specific cells (171) and increase circulation times (165); however, we require a complete understanding of those mechanisms controlling protein corona formation to take full advantage of this strategy.

1.4.3.1.3.   Enhanced Permeability and Retention effect

The increased size of polymer-drug conjugates allows for enhanced passive tumor accumulation via the EPR effect, which also reduces undesired side effects (138,143,172,173). The EPR effect, first described by

Maeda and collaborators during their evaluation of SMANCS as a treatment for hepatocarcinoma (172), relies on hyperpermeable or fenestrated vasculature irrigating solid tumors, which allows for the passage of large particles such as polymer-drug conjugates. This phenomenon, together with impaired tumor tissue lymphatic drainage (which hinders polymer clearance), results in conjugate accumulation in the tumor (138,143,173) (**Figure 1.7**); however, the EPR effect remains a heterogeneous and dynamic process (138). Small solid tumors during early disease progression accumulate and retain macromolecular systems to a greater degree through the influence of the EPR effect; however, larger tumors tend to develop necrotic and avascular areas where the lack of irrigation impedes accumulation via the EPR effect (138,174,175). Additionally, rapid tumor growth, high tumor interstitial fluid pressure, and occlusion of tumor blood vessels also impair the EPR-mediated accumulation of macromolecules (138). Importantly, research in pre-clinical animal models has provided data that reflect heterogeneity at this level (175), which has promoted the assessment of EPR "power" to evaluate the suitability of a model to examine the efficacy of macromolecular drug delivery systems.
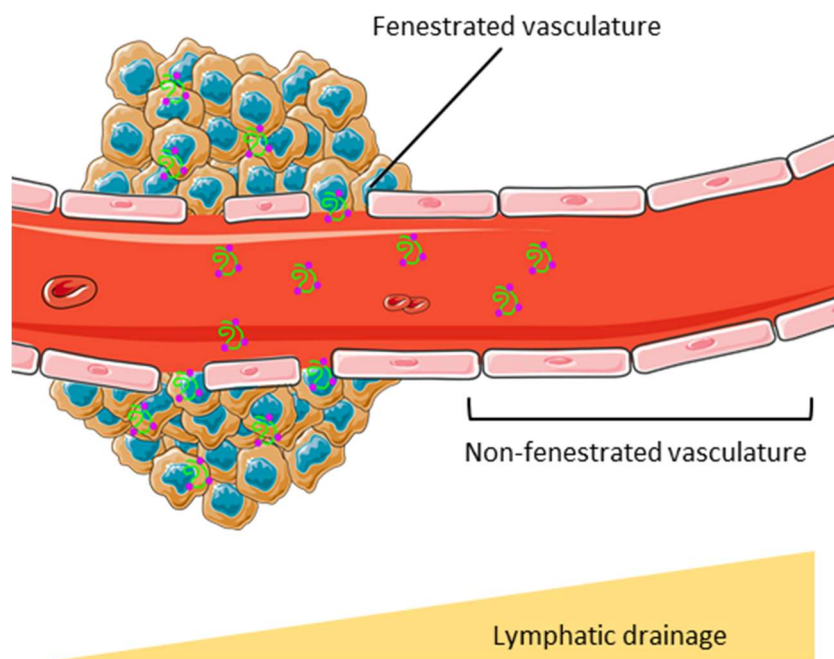
Figure 1.7. Passive targeting via the EPR effect. Hyperpermeable or fenestrated vasculature irrigating solid tumors allows for the passage of large particles, such as polymer-drug conjugates. Impaired tumor tissue lymphatic drainage also hinders polymer clearance, with both mechanisms resulting in conjugate accumulation in the tumor. Redrawn from Jhaveri et al. (176) with smart.servier.com (8).

1.4.3.1.4. Endogenous Triggers within the Tumor Site

An ideal polymer-drug conjugate requires overall stability in the bloodstream but drug release from the conjugate within the desired target tissue/cell/organelle in response to a tissue-specific stimulus (177). Polymer-drug conjugates used as cancer treatments often employ pH-responsive drug linkers, including ester, hydrazone, imine, ketal/acetal, and carbamate/carbonate bonds (126). Metabolic alterations in tumors cells (including the well-known Warburg effect (178)) provoke an increase in the acidity of the microenvironment (pH 6.3 to 7.0) compared to healthy tissue (pH 7.35 to 7.45) (179). The use of linkers that cleave at pH 6.3-7.0 but remain stable at pH 7.4 allows for controlled drug release in tumor tissue, thereby increasing drug bioavailability and reducing side effects. For instance, the acid-cleavable hydrazone bond (extensively used to conjugate the chemotherapeutic drug doxorubicin [Dox]) displays relative stability at

physiological pH values and drug release under mildly acidic conditions (pH ≤ 6) (149,180–182). The implementation of acid-degradable polymeric carriers (e.g., polyacetals (126)) or pH-responsive polymers that change their structure in mild acidic media (183) represent additional means of exploiting the acidic tumor microenvironment. For example, the water-soluble pH (low) insertion peptides (pHLIPs) become inserted into lipid bilayers under acidic conditions (pH <6.5) via conformational changes (α-helix transitions) (184). In this study, the attachment of a photosensitizer yielded a pH-driven membrane-anchoring photosensitizer construct (pHMAPS) that effectively targeted tumor cells and, upon laser irradiation, produced reactive oxygen species that eliminated tumor cells, which significantly reduced tumor volume.

Large sizes and their hydrophilic nature limit the cellular uptake of polymer-drug conjugates via endocytosis, phagocytosis, or micropinocytosis and subsequent delivery to lysosomes (177,185,186) (**Figure 1.8**), which can help to avoid drug resistance mechanisms (136,177). Interactions with the cell surface prompt the engulfment of polymer-drug conjugates within fluid-filled vesicles (186), which retain a pH value similar to the extracellular space. Within minutes, these vesicles fuse with early endosomes (185,186) with a pH of ~6.3 (185) (**Figure 1.8**), which act as a sorting hub, directing cargo to the endoplasmic reticulum, the trans-Golgi network, or back to the membrane (endosomal recycling network) (186). Early endosomes can undergo maturation, forming multivesicular late endosomes with lower pH (~5.5) that eventually fuse with lysosomes, an organelle with pH ~4.7 that permits the activity of a myriad of proteases, nucleases, esterases, and lipases (**Figure 1.8**) (185,186).
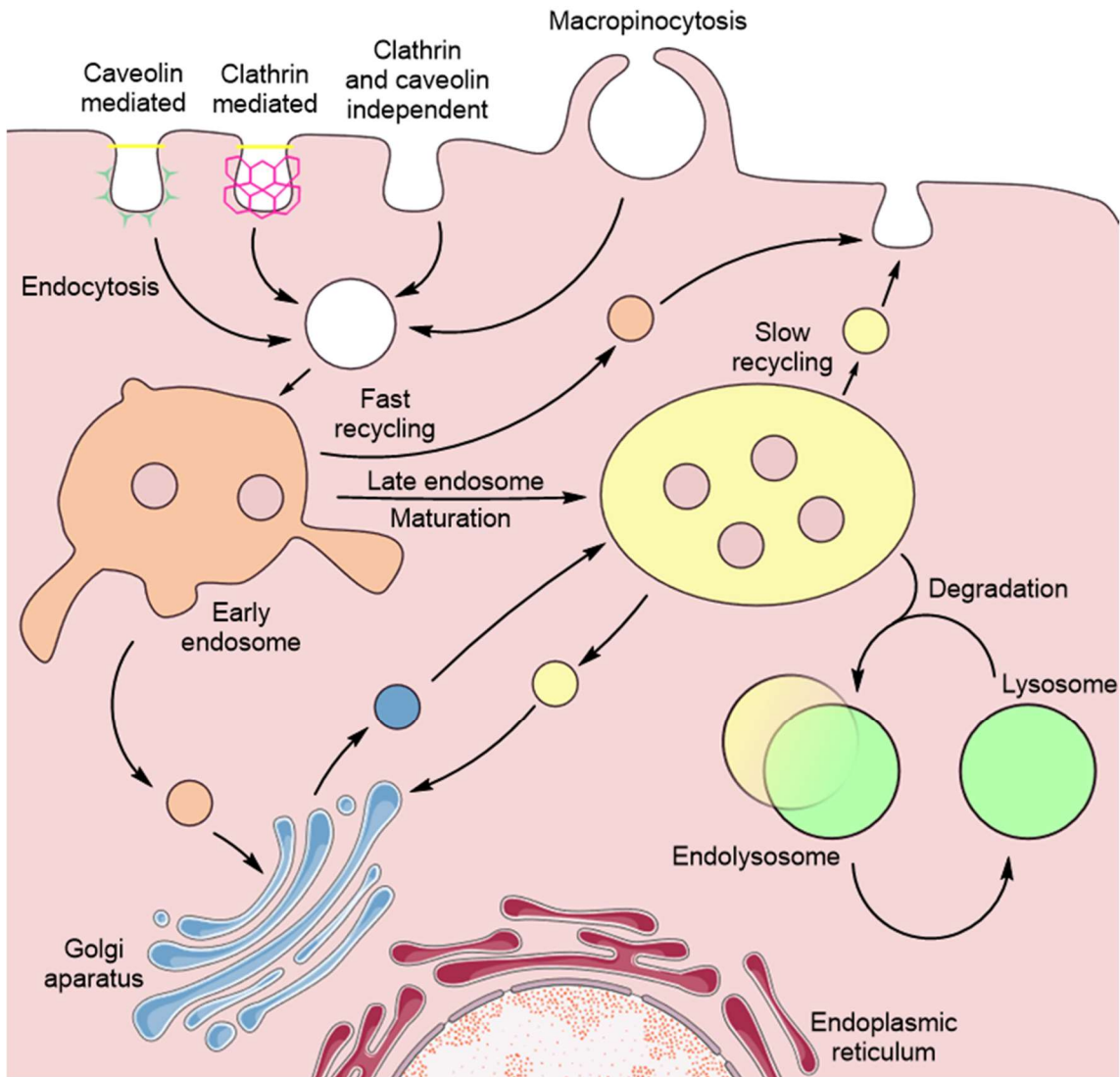
Figure 1.8. Cellular uptake and trafficking. Polymer-drug conjugates enter the cell by caveolin-mediated, clathrin-mediated, clathrin- and caveolin-independent, or macropinocytic endocytosis. Endocytic vesicles then fuse with early endosomes (pH~6.3), which undergo maturation to form multivesicular late endosomes with lower pH (~5.5) that eventually fuse with lysosomes, an organelle with pH ~4.7 that permits the activity of a myriad of proteases, nucleases, esterases, and lipases. Adapted from Patel et al. 2019 (186) with smart.servier.com (8).

The acidic pH and hydrolases present within lysosomes can serve as a stimulus to prompt drug release/polymer degradation inside the cell, with the serine-protease cathepsin B representing a prime example due to its tumor overexpression(187). For instance, an N-(2-hydroxypropyl)methacrylamide (HPMA) copolymer conjugated with doxorubicin (Dox) using a cathepsin B cleavable peptide (GFLG) reached

phase II clinical trials for the treatment of breast, colorectal, and lung cancer (163,188–190). The GLFG peptide also allowed the synthesis of dual sensitive polymeric micelles formed by a nifuroxazide-loaded HPMA-oligo-(ethylene glycol) methacrylate co-polymer bearing Dox conjugated via a pH-responsive hydrazone linker (191). The presence of the GFLG peptide between the HPMA and oligo-(ethylene glycol) blocks permitted prolonged circulation of the micelle in the bloodstream and EPR-mediated tumor accumulation, where the associated acidic pH prompted the release of Dox. After tumor cell internalization, cathepsin B prompted GFLG peptide hydrolysis, co-polymer cleavage into small excretable subunits, micelle disassembly, and nifuroxazide release. Importantly, Cathepsin B also degrades polypeptides such as poly-L-glutamic acid (PGA) (192). Studies of the clinical candidate PGA-paclitaxel conjugate (Xyotax^{TM} or PPX) demonstrated that drug release relied on the combined effect of cathepsin B-mediated carrier degradation and acid hydrolysis of the ester bond between PTX and the polypeptidic carrier (193).

Cancer cells also display higher reductive potential (194,195), with the glutathione/glutathione disulfide ratio (GSH/GSSG) responsible for the redox status of a given media. Cytosolic GSH occurs at a concentration in the millimolar range (0.5-10 mM); however, the extracellular concentration of GSH is generally 1000 times less (2-20 μM in plasma) (196). Cancer cells generally display a higher level of GSH, although the exact level depends on factors such as tumor type and stage. For instance, studies have linked metastatic spread to increased GSH levels (194,197); therefore, the use of redox-responsive linkers represents a crucial design feature of many polymer-drug conjugates (126,160,198). Disulfide bonds represent the most commonly employed redox-responsive linkers for drug conjugation (199,200) and/or structure stabilization (201,202). For example, Sun et al. developed a poly(oligo(ethylene glycol)methacrylate) conjugate of dasatinib (Das) using a disulfide bond, which self-assembled into micelles of ~160 nm thanks to drug-drug interactions to allow doxorubicin (Dox) loading (203).

While remaining stable in conditions that mimic the extracellular microenvironment (10 µM GSH), micelles disassembled and released both drugs in the presence of a highly reductive environment (10 mM GSH) comparable to that of the cell cytosol. The large size and stability of these micelles under extracellular microenvironmental conditions permitted an increase in the circulation time of Dox after administration to a murine model of TNBC (when compared to free Dox), which supported increased Dox accumulation in the tumor, reduced tumor growth, and improved survival. Importantly, treatment of Das-conjugated Dox-loaded micelles that employed non-redox-responsive linkers failed to display similar anti-tumor activities, thereby highlighting the importance of the linking chemistry employed (203).

The use of pH-labile linkers (hydrazone and ester bond, specifically) for drug conjugation and redox-responsive disulfide bonds for nanosystem stabilization will be further discussed in *Chapters 2* and *3*, respectively.

1.4.3.1.5.   Combination Therapy

Delivering combinations of drugs that target different signaling pathways or various aspects of the same pathway remains a potentially exciting approach for cancer treatment, considering the myriad genetic mutations and dysregulated pathways of a cancer cell. Indeed, treatment of metastatic TNBC often relies on administering drug combinations (see *1.2.3.Clinical Management of TNBC*). Rationally designed polymer-drug conjugates may help to support the development of safer and more effective combination therapies for TNBC treatment.

In this regard, four types of combinatorial scenarios can be supported (204):

Type I: Polymer-drug conjugate plus free drug. This approach comprises the co-administration of a polymer-drug conjugate bearing one

therapeutic agent with another type of treatment (e.g., small drug chemotherapeutics, radiotherapy).

Type II: Polymer-drug conjugate plus polymer-drug conjugate. This approach employs the co-administration of two polymer-drug conjugates bearing single but different therapeutic agents.

Type III: A single polymeric carrier bearing a drug combination. This approach employs the conjugation of two or more drugs to the same polymeric carrier.

Type IV: Polymer-directed enzyme prodrug therapy (PDEPT) and polymer enzyme liposome therapy (PELT). This approach employs the administration of a polymer-drug conjugate with a polymer-enzyme conjugate (PDEPT) or the administration of a liposomal system together with a polymer-phospholipase conjugate (PELT). The polymer-enzyme conjugate functions to trigger drug release by cleaving the drug-polymer linker (PDEPT) or by disrupting the liposomal system (PELT).

Of note, only type III systems ensure the simultaneous co-delivery of drug combinations to the same cell (204). Markovsky and co-workers showed that co-conjugation of paclitaxel (PTX) and Dox to the same linear PGA carrier increased therapeutic efficacy compared to treatment with the combination of free drugs *in vitro* and *in vivo* in a human MDA-MB-231 TNBC mouse model (182). Notably, integrating the conjugation of drug combinations with the rational design of polymer-drug linkers allows the fine-tuning of drug release kinetics to enhance drug combination synergism (204). For instance, Arroyo-Crespo et al. developed a family of PGA-based combination conjugates with Dox and aminoglutethimide (AGM) using different drug linkers and loadings for AGM, which provoked alterations to conjugate conformation, yielding different drug release profiles and, consequently, different biological outputs (148). In this study, the small flexible glycine (G) residue used as a linker for AGM conjugation induced drug synergism in mouse 4T1 TNBC cells regardless of AGM loading.

103

Cathepsin B-mediated drug release experiments demonstrated that high AGM loading translated to a higher release of Dox than AGM. The conjugate with low AGM loading displayed the best anti-tumor activity in an orthotopic spontaneously metastatic 4T1 TNBC model; furthermore, this combination conjugate performed significantly better than a combined treatment of the PGA-Dox *and* PGA-G-AGM single-agent conjugates, underscoring the importance of having both drugs in the same polymeric carrier to assure co-delivery (148). A follow-up study evaluated Dox linkers and loadings while maintaining a constant AGM loading (149). The pH-labile linkers employed in this second study included a simple hydrazine moiety and a longer, flexible, and hydrophobic N-ε-maleimidocaproic acid hydrazide (EMCH) moiety. Conjugates with low Dox loading displayed stability at pH 7.4 but released the drug at pH 5.0; however, conjugates with high Dox loading failed to release the drug at either pH, which translated into poor cytotoxic activity in 4T1 cells. Furthermore, low-loaded conjugates exhibited optimal performance with regard to tumor growth inhibition and metastatic spread reduction *in vivo*; however, treatment with the low-loaded combination conjugate possessing the longer EMCH spacer prompted reduced overall survival and hepatotoxicity compared to the other combination conjugates and free Dox. Overall, these results highlight the importance of linking chemistry and drug loading optimization (149).

This thesis aims to develop a type III polymer-drug combination conjugate for the treatment of TNBC primary and secondary tumors employing a synergistic drug combination with optimal drug ratios and linking chemistries.

1.4.3.1.6. Targeting Moieties

The versatility of polymer-drug conjugate design also permits the conjugation of additional non-drug moieties such as targeting ligands (205,206) to further improve treatment selectivity to tumor cells or cell

organelles (207). Ligand-mediated active targeting in combination with passive targeting of polymer-drug conjugates can prompt significant tumor accumulation and induce receptor-mediated endocytosis (208). Antigens employed for targeting breast cancer include ER ligands and HER2 ligands for luminal subtypes and HER2-positive tumors, respectively. Additional antigens include the epidermal growth factor receptor, the folate receptor, CD44, the transferrin receptor (TfR), $\alpha_v\beta_3$ integrin, the biotin receptor, and the GnRH receptor (208). Interestingly, the polymer compound hyaluronic acid (HA) binds to CD44; therefore, HA possesses inherent passive and active targeting capabilities in the case of CD44-overexpressing cancer cells (147,209,210). The conjugation of targeting moieties also fosters passage through critical biological barriers, such as the previously discussed BBB. Since this biological barrier is of particular interest to this thesis, this example will be discussed at length in an upcoming section *1.5.Drug Delivery Strategies to Cross/Bypass the Blood-Brain Barrier*.

In summary, the rational design of each component of a polymer-drug conjugate will optimize drug bioavailability at the desired site of action and reduce unwanted off-target side-effects, which will improve both patient compliance and therapeutic outcomes. Polymer-drug conjugates also ensure the co-delivery of synergistic drug combinations to the same cell, with optimized linking chemistries and drug ratios further supporting any synergism. Furthermore, targeting moieties can synergize with passive targeting to promote the accumulation of any therapeutic agents within the tumor tissues and support passage through critical biological barriers.

1.4.3.2. Polypeptides as Polymeric Carriers: A Focus on Polyglutamic Acid

1.4.3.2.1. Why Polypeptides?

Rational polymer selection represents perhaps the most critical choice in polymer-drug conjugate design due to the influence on the pharmacokinetic and pharmacodynamic profile of the conjugate. Overall, a polymeric carrier must be non-toxic, non-immunogenic, hemocompatible, biodegradable (158,161,162), and of a size that supports passive accumulation (138,158,164).

Given these requirements, *polypeptides* have emerged as leading candidates for the polymeric component of polymer-drug conjugates due to their similarities to native proteins and their safe, non-immunogenic, biocompatible, and biodegradable nature (126,211). These characteristics support the use of high molecular weight polypeptides as carriers, which supports increased circulation times and passive tumor accumulation (138,158) and permits repeated parenteral administrations (126).

The marketing of two polypeptide-based materials provides evidence of their clinical potential – the previously described polymeric drug Copaxone® and Vivagel®, an intravaginal-administered polylysine dendrimer that functions as an anti-viral and anti-bacterial treatment for sexually transmitted infections (126). PGA, polylysine, and polyaspartic acid represent the most commonly employed components in the synthesis of polypeptide-drug conjugates used for various approaches (including cancer treatment) (126) as their side-chain functionalities (amine groups of lysine and carboxylic acid groups of glutamic and aspartic acid) allow for facile chemical modification (211). This thesis employs a branched PGA-based architecture as a polymeric carrier to synthesize combination conjugates.

1.4.3.2.2.   Synthesis of Polypeptides

Polypeptide synthesis must exhibit reproducibility, cost-effectiveness, and easy large-scale production control to allow their use as polymeric carriers. Three synthetic techniques have been typically employed for polypeptide synthesis - solid-phase peptide synthesis (SPPS), recombinant peptide synthesis, and ring-opening polymerization (ROP) of N-carboxyanhydrides derived from α-amino acids (NCA) (211–213).

SPPS begins by immobilizing the first amino acid to a resin and then creating the target peptide by repeating deprotection and amide coupling cycles before release (214). This technique allows for the synthesis of monodisperse peptides with precise sequence control (212); however, SPPS remains limited to the synthesis of peptides of 30 to 40 amino acids. Short peptide coupling can form larger polypeptides to bypass this limitation (214). SPPS also requires several isolation/purification steps that dramatically reduce yield, increase cost, and hamper application to large-scale synthesis (126,211,212).

Recombinant peptide synthesis comprises the expression of proteins by biological hosts (i.e., eukaryotic or prokaryotic cell cultures) via transfection of an expression plasmid/vector (93). Recombinant peptide synthesis generates high molecular weight polypeptides with precise control over their sequence; however, this approach remains limited to natural amino acids and requires specialized equipment for large-scale peptide synthesis, isolation, and purification. This process remains time- and cost-intensive (93,211,212), thereby hampering large-scale synthesis.

ROP of NCA allows for the efficient and economical synthesis of large quantities of high molecular weight (> 50 amino acids) polypeptides made of single or randomly distributed amino acids with precise control over molecular mass, architecture, polydispersity, and end-group presence (93,126,211,213,215). With more than 200 NCA monomers described in the literature (211), this method offers a high level of chemical complexity,

allowing the incorporation of non-natural residues into the peptide sequence (213). While the ROP of NCA offers high yields and scalable synthesis, extreme sensitivity to heat and moisture (which reduces NCA stability) represents a significant limitation; however, advances in NCA storage have made ROP of NCA the most commonly employed polypeptide synthesis technique in both academia and industry (93).

Traditionally, the initiation of ROP of NCA employs primary amines and less nucleophilic hydrochloride and tetrafluoroborate salt derivatives. Other initiators include tertiary and secondary amines, thiols, and transition metal initiators. The development of synthetic alternatives has increased the versatility of ROP of NCA, allowing the creation of a wide variety of polypeptide-based architectures that suit biomedical applications ranging from tumor treatment to tissue engineering (211). In this thesis, we employed the ROP of NCA to synthesize the branched PGA-based polymeric carrier (*Chapter 2* will fully describe the ROP of NCA and associated initiators).

1.4.3.2.3. Poly-L-glutamic Acid

A range of varied studies has provided evidence for the overall versatility of PGA with regards to conjugation of a wide variety of moieties (148,149,159,216–224), which represents a crucial aspect of combination therapy design. PGA supports the conjugation of drug combinations with different chemical characteristics, the control of drug ratio, and the use of myriad orthogonal linkers that support the controlled release of therapeutic agents (148,149,182,225). The serine-protease cathepsin B present in the lysosome and overexpressed in breast cancer cells (187) represents the major factor degrading PGA; overall, this biodegradability permits the use of larger PGA-based structures that support enhanced passive accumulation and become degraded into small non-toxic subunits.

The development of controlled ROP of NCA techniques has fostered the controlled and straightforward synthesis of PGA-based nanosystems with different topologies at a large scale (226–228). Duro-Castano et al. reported that 1,3,5-(benzenetricarbonyltris(azanediyl))-initiated three-arm star-shaped PGAs (St-PGA) displayed increased cellular uptake and prolonged circulation times compared to linear PGAs with a similar molecular weight (227). Interestingly, this polymer displays self-assembly behavior in non-salty aqueous solutions - driven by ionic interactions, St-PGA forms large spherical structures in a concentration-dependent fashion. These same structures subsequently disassemble in response to increased ionic strength. Covalent capture of self-assembled structures yielded large (~200 nm diameter) stable spheric structures that further increased cellular uptake and circulation time when compared to the St-PGA unimer (222). Despite the increasing complexity, St-PGA and the covalently captured assembly (St-PGA-Click) maintained a lack of toxicity, cathepsin B-mediated degradation, and renal excretion profiles (222,227). Interestingly, only St-PGA-Click accumulated in axillary and cervical lymph nodes after administration in mice (222,227).

The encouraging results from these studies prompted the exploration of St-PGA-Click-based approaches to the treatment of acute kidney injury (219), alcohol-induced neuroinflammation (217), and Alzheimer's disease (229). The latter two studies will be discussed below (*1.5.5.3.Receptor-mediated - 1.5.5.3.3.Low-density Lipoprotein Receptor-related Proteins 1 and 2*).

1.5. Drug Delivery Strategies to Cross/Bypass the Blood-Brain Barrier

During brain metastasis, CTCs cross the BBB and then remain associated with brain vasculature in a dormant state. The activation of proliferation programs (46,84,105) then prompts secondary tumor growth in

the perivascular area, activating angiogenesis as the tumor develops (105). Both vascular co-option and angiogenesis affect the BBB, forming a heterogeneous BTB that, despite possessing areas of increased permeability, retains most BBB features and impedes the accumulation of systemically administered small drugs and biological agents in the brain tumor tissue (85). Therefore, nanomedicines (including polymer therapeutics) have employed alternative delivery strategies, including local delivery and BBB/BTB disruption; however, current nanomedicine research for CNS delivery focuses on delivering therapeutics using non-invasive administration routes, including intravenous and intranasal administration.

In the upcoming sections, we will discuss relevant strategies for brain delivery with a focus on brain tumor/metastasis treatment via polymer therapeutics; however, the widespread exploration of such strategies remains unreported in the realm of polymer therapeutics. In these cases, relevant examples of related nanomedicines will be provided.

1.5.1. Local Delivery

Alternate strategies developed to overcome or bypass the BBB include local delivery via implantation of wafers, gels, or microchips (109) or by intracerebroventricular, intrathecal, or stereotactic injection into the tumor tissue (93). Despite the invasiveness of local delivery, the FDA approval of the Gliadel® wafer (Arbor Pharmaceuticals LLC., Atlanta, GA, USA) (a 1,3-bis(p-carboxyphenoxy)propane and sebacic acid copolymer wafer impregnated with the anticancer agent carmustine (230)) for the treatment of glioma in 1997 highlighted the safety and efficacy of this approach and underscored the relevance of polymeric systems in CNS-targeted treatments (93).

1.5.2. Disruption of the Blood-brain Barrier/Blood-tumor Barrier

Convection-enhanced delivery (CED), another invasive strategy to overcome the BBB, employs the direct intraparenchymal infusion of a therapeutic agent via a cannula to promote the bulk convective flow of the agent in the interstitial space. CED reached phase III clinical trials, where it induced modest improvements in the survival rates of glioblastoma patients (109). CED has also been employed in preclinical studies to deliver PEG-poly(aspartic acid)-Dox conjugated micelles to gliosarcoma tumors in rats (93), where it supported the extensive distribution of Dox throughout the tumor and improved anti-tumor activity when compared to the free drug (231).

Related strategies rely on BBB disruption to enhance the paracellular diffusion of small and large therapeutic agents. Hyperosmotic shock, where the intraarterial injection of a hyperosmotic solution (e.g., mannitol) produces the shrinkage of BECs and disruption of intercellular tight junctions, supports the passage of therapeutic agents via the paracellular pathway (232); however, this method is highly invasive and requires general anesthesia. Furthermore, patients suffer from side effects such as focal seizures (an epileptic crisis that starts on one side of the brain), bradycardia, and hypotension (232).

Ultrasound can also increase BBB permeability (233). Focused ultrasound (FUS) pulses combined with circulating microbubbles can efficiently disrupt the BBB/BTB to increase permeability in a transient, targeted, minimally-invasive, and repeatable fashion (109,232). Circulating microbubbles consist of gas-encapsulated semi-rigid lipid or albumin shells that reduce the FUS exposure levels needed for BBB disruption by concentrating ultrasound's effects at blood vessel walls, thereby avoiding significant skull heating upon FUS application (232). Although the mechanism of action remains incompletely understood, BBB disruption occurs almost immediately after applying ultrasound and then decays exponentially, providing a window of six hours to one day of permeability.

Besides physical disruption of the brain endothelium, FUS also increases transcytosis (232). Examples of FUS in the delivery of nanomedicines include liposomal Dox in treating a rat glioblastoma model (234). In this case, three weekly administrations of liposomal Dox by FUS with microbubbles significantly reduced tumor volume and improved survival by 72% compared with intravenous administration. Of note, animals suffered from side effects such as neurological impairment and skin alterations, which the authors attributed to Dox activity, thus suggesting the need to tune the dose and/or FUS parameters.

1.5.3. Cell-mediated Delivery

Another interesting strategy to induce passage across the BBB/BTB employs cells as a delivery system. Neural stem cells (NSCs) and mesenchymal stem cells (MSCs) display strong tropism to the brain and tumors and an ability to cross the BBB/BTB. The genetic modification of MSCs and NSCs allows the forced expression of anti-tumor proteins, anti-angiogenic and immunostimulatory factors, or enzymes that convert a non-toxic prodrug into a cytotoxic drug. Alternatively, MSCs and NSCs can be loaded with cytotoxic agents as free drugs or drug-containing nanosystems (109). As an example, Cheng et al. locally and contralaterally administered an FDA-approved NSC line (HB1.F3.CD) loaded with Dox-conjugated mesoporous silica nanoparticles in a human glioma xenograft mouse model (235). The delayed toxicity provided by the pH-labile hydrazone bond supported Dox delivery by NSCs and release after contralateral migration to the tumor. The intratumoral and contralateral administration of mesoporous silica nanoparticle-loaded NSCs displayed a similar increase in survival compared to vehicle control (235). In a related study, Mooney et al. intravenously administered NSCs bearing ~800 nm wide polystyrene nanoparticles loaded with Nile-red as a model molecule in a human glioma xenograft intracranial tumor in mice (236). The nanoparticles were bound to

the cell surface by streptavidin-biotin coupling (biotinylated NSCs with streptavidin-conjugated nanoparticles). The study detected 0.9% of the initially administered engineered NSCs in the tumor tissue, a value that represented a 46-fold increase compared to the administration of the polystyrene nanoparticles alone (236).

1.5.4. Intranasal Administration

With numerous advantages over oral or parenteral administration, intranasal administration has emerged as an alternative route for the delivery of therapeutics to the CNS. The intranasal approach takes advantage of direct nose-to-brain routes through the trigeminal and olfactory pathways that avoid the BBB (153,237,238). Other than its non-invasive nature, intranasal administration also offers (i) facile self-administration, (ii) rapid drug absorption via the highly vascularized mucosa, (iii) improved drug bioavailability and avoidance of the gastrointestinal tract and first-pass metabolism, (iv) and rapid onset of action with lower side effects (117).

Intranasal administration generally allows for elevated brain targeting (about a ten-fold increase) compared with intravenous administration and, therefore, requires lower drug doses to achieve successful clinical outcomes with reduced off-target effects (117). Nevertheless, intranasal administration suffers from several limitations. The nasal microenvironment is the primary barrier for nasal permeation due to low membrane permeability, rapid mucociliary clearance mechanisms, possible enzymatic degradation in the nasal cavity, and the slightly acidic pH in adults (5.5–6.5) (239). Not all drugs/biologicals can bypass nasal barriers; furthermore, only around 1% of the total dose of amenable administered therapeutics reach the brain, thus highlighting a need for strategies that increase this percentage (240,241). Additionally, the nasal cavity size limits the administration volume (25–200 µL in humans), which requires highly concentrated solutions (242) or highly potent therapeutic agents (153). Most preclinical studies for intranasal

delivery to the CNS employ rodent models who possess an olfactory epithelial area ten times larger than humans, which therefore hampers clinical translation (153).

The evaluation of monoterpene perillyl alcohol to treat recurrent glioblastoma (NCT02704858) and modified temozolomide to treat glioma, gliosarcoma, and astrocytoma (NCT04091503) provide evidence for the feasibility of brain tumor treatment via the intranasal route. Unfortunately, the use of intranasal administration for the treatment of brain tumors/metastasis via polymer therapeutics remains relatively explored.

1.5.5. Intravenous Administration: Crossing the Blood-brain Barrier

Intravenous administration of therapeutics represents the clinically preferable route, as it allows for rapid, safe, and relatively non-invasive single/repeated administration and is the most widely used route for polymer therapeutics. Using the intravenous route, therapeutic agents bypass first-pass metabolism and reach vascularized tissues (153); however, the therapeutic agent must first cross the BBB/BTB to exert biological activity in the brain.

Unspecific BEC transport by AMT and targeted delivery by CMT or RMT represent the three main strategies employed for polymer therapeutics to cross the BBB/BTB.

1.5.5.1. Adsorption-mediated transcytosis

Liposomal formulations (neutral or cationic), colloidal nanoparticles (neutral or cationic), and solid lipid nanoparticles all employ AMT (117,243,244). In this transport mechanism, the interaction of cationic systems with the anionic surface of BECs triggers endocytosis, intracellular transport within a vesicle, and exocytosis on the abluminal side (245). Few

114

examples of polymer therapeutics exploiting AMT to cross the BBB have been described, with Pluronic® block copolymers the notable exception. Composed of hydrophilic poly(ethylene oxide) and hydrophobic poly(propylene oxide) blocks, Pluronic® block copolymers act as polymeric drugs alone or as micellar agents for imaging probes and/or drug delivery (246) and have reached the clinics in the form of Pluronic® 407 gel (LeGoo®, Pluromed Inc., Woburn, MA, USA) for vessel occlusion in coronary bypass surgery (247). Pluronic® block copolymers have been extensively explored for CNS delivery due to their inherent ability to interact with hydrophobic surfaces and cross biological barriers. Moreover, pluronics inhibit drug efflux transporters (248) (especially P-gp) present in the BBB (249). Pluronics technology has also been applied to the delivery of peptides and proteins to the CNS (104,250–255), small drugs (e.g., digoxin) (256), and other P-gp efflux transporter substrates (e.g., Rho123) (257). Nevertheless, AMT lacks specificity and, for this reason, is not a preferred strategy for crossing the BBB (258).

1.5.5.2. Carrier-mediated Transport

Differential expression of CMT transporters at BECs compared to other tissues prompted their use as targets for brain delivery (93). Their normal function involved binding a substrate, transporting the substrate across the cell membrane, and releasing the substrate thanks to a conformational change; however, substrate conjugation to a nanomedicine entails an alternative transport process. The macromolecular nature of nanomedicines impedes regular transport, and interaction with the receptor instead provokes membrane invagination and then internalization, which displays broad similarities to crossing the BBB via AMT/RMT (259).

Targets for CMT-mediated transport through the BBB include glucose transporter 1 (GLUT1), acetylcholine receptor (AChR), and GSH transporters. GSH-tagged PEGylated liposomal Dox has reached phase I/II

clinical trials to treat brain metastasis and recurrent high-grade gliomas (260,261). As choline derivatives target AChR, Li and co-workers employed a dendrigraft poly-L-lysine decorated with a choline derivative to deliver a tumor necrosis factor-related apoptosis-inducing ligand (TRAIL) expression plasmid and Dox (intercalated in the plasmid) to a U87 glioma murine model (which also overexpress AChR, thereby allowing tumor targeting) (262). The authors demonstrated increased tumor accumulation for the targeted nanomedicine, which induced increased levels of apoptosis and improved animal survival.

1.5.5.3. Receptor-mediated Transcytosis

RMT represents a highly investigated strategy for brain delivery of polymer therapeutics (100,101,103,117). RMT uses the "trojan horse" strategy, which comprises the conjugation of ligands for specific BBB receptors to a nanocarrier to promote intact barrier crossing. RMT starts with ligand binding to its receptor, which triggers receptor-ligand complex endocytosis with the surrounding fluid and cell membrane. The resulting vesicle travels across the cell to the abluminal side, where it fuses with the cell membrane to release content in the extracellular media (93,101,102). The strength of ligand-receptor interactions decides the vesicular fate and, therefore, the nanocarrier's capacity to cross the BBB and accumulate in the brain. Low avidity results in poor receptor binding on the luminal side, hindering transcytosis; however, high avidity allows for strong receptor binding but drives the vesicle towards the lysosomes for degradation instead of transcytosis. Intermediate avidity results in BBB crossing following a pathway independent of lysosomal sorting (100–102).

Differential expression of BBB receptors compared to other tissues and different pathological conditions provides high selectivity; however, the "both-ways" nature of this route allows for the extrusion of polymer therapeutics from the brain given a concentration gradient change. Although

the RMT pathway displays neither size limitations nor lipophilic-dependence, some studies have highlighted more efficient transcytosis for particle sizes between 50 and 60 nm (102).

The most employed receptors for RMT-mediated delivery of polymer therapeutics to the brain include the TfR, the lactoferrin receptor (LfR), and the low-density lipoprotein receptor-related proteins 1 and 2 (LRP-1 and 2).

1.5.5.3.1. Transferrin Receptor

The TfR mediates blood-to-brain iron delivery by binding and intracellular trafficking of the iron-binding protein transferrin (263). Transferrin itself has served as a targeting moiety for many nanomedicines; however, endogenous transferrin reduces efficacy due to competition for TfR binding. Thus, studies developed antibodies targeting epitopes distal to the transferrin binding site to overcome this limitation (99), which include OX26 (264,265) and 8D3 (266). Advances in genetic engineering have also fostered the development of fusion proteins and chimeric antibodies to optimize antibody-receptor affinity and improve BBB transport (267–270). In addition, several peptides have been identified as TfR ligands and employed in targeting, including the CRT, THR, and T7 peptides (93).

Importantly, TfR displays certain limitations as a target for RMT in delivering polymer therapeutics. While studies have highlighted the brain region-specific expression of TfR, the elevated expression of TfR by hepatocytes and Kupffer cells in the liver and red pulp cells/resident macrophages in the spleen may lead to unwanted accumulation in non-target tissues (263)

Research groups have explored the TfR to induce RMT of various nanomedicines despite these limitations. Poly-β-L-malic acid-based polymer therapeutics developed to treat glioma have combined anti-TfR antibodies to target the BBB/BTB, trileucine units to disrupt endosomes, and antisense

oligonucleotides against laminin-411 to inhibit tumorigenesis (271,272). Liu et al. employed the T7 peptide to target a Dox-conjugated (via a pH-labile hydrazone linker) dendrigraft poly-L-lysine polyplex with a TRAIL expression plasmid to treat an orthotopic U87 glioma mouse model (273). The peptide served a dual purpose in this case, as the U87 cells also overexpress TfR. When administered intravenously, the targeted complex efficiently accumulated in the tumor tissue as early as one hour after injection; furthermore, repeated administration significantly prolonged animal survival (273).

1.5.5.3.2.   Lactoferrin Receptor

The iron-binding glycoprotein lactoferrin, whose receptor (LfR) is highly expressed by BECs, has also been used as a targeting moiety for brain delivery (274,275). To treat glioma, Yin et al. developed a lactoferrin-tagged HA-Dox (Lf-HA-Dox) conjugate (258). In this case, the glioma cells (C6) overexpressed the CD44 receptor (bound by HA) and LfR (bound by lactoferrin); therefore, lactoferrin can induce improvement in both BBB crossing and tumor targeting. In the glioma mouse model, Lf-HA-Dox displayed progressive and sustained accumulation in the tumor tissue up to 24 hours after intravenous administration.

Importantly, lactoferrin not only binds to the LfR; for instance, lactoferrin also binds to the TfR, LRP-1, and LRP-2 (276), which decreases control over targeting and may lead to off-target effects. Additionally, lactoferrin displays inherent biological activity, including anti-tumor activity by apoptosis induction (276).

1.5.5.3.3.   Low-density Lipoprotein Receptor-related Proteins 1 and 2

The expression of LRP-1 and -2 by BECs (277,278) serves to mediate the transport of lipoproteins and other ligands, such as apolipoprotein E (279). Studies have explored the use of the low-density lipoprotein receptor (LDLR) and LRP-1/2 ligands and peptide-ligand mimics as targeting moieties for brain delivery. Angiopep-2 (ANG), a nineteen-amino acid peptide, reported as an LRP-1 ligand (280), represents the most relevant example and has been used to deliver genes, peptides, proteins, antibodies, and enzymes (281–284). Angiochem Inc. (Montreal, Canada) has developed several ANG-drug conjugates to treat brain tumors (285,286), with ANG1005 reaching phase III clinical trials for metastatic breast cancer with brain metastases (NCT03613181).

ANG has also been used to transport polymer therapeutics and related nanomedicines across the BBB. For instance, an ANG-modified poly-(L-lysine)-grafted polyethyleneimine non-viral vector developed by Gao and co-workers as a treatment for glioblastoma multiforme displayed enhanced brain accumulation compared with an untargeted vector and greater transfection efficiency in an orthotopic *in vivo* glioblastoma mouse model (287). Alternative non-viral vectors, including polyamidoamine (PAMAM) dendrimers, have also used ANG as a targeting moiety. Huang et al. employed ANG-modified PEGylated PAMAM dendrimers modified to deliver a TRAIL expression plasmid to glioma cells (288). This approach permitted increased brain permeation and significantly prolonged survival in a C6 glioma mouse model. Meanwhile, An et al. developed an ANG-modified T-shaped succinoyl tetraethylenepentamine-based redox-responsive polyplex carrying a siRNA targeting the BAG3 cochaperone transcript (289). Intravenous administration of the polyplex to a U87 orthotopic glioma *in* vivo mouse model provided evidence of enhanced targeting and improved target gene downregulation compared to non-targeted polyplexes. Importantly,

ANG also provided tumor-targeting since glial cells express LRP-1 (287–289).

As RMT represents a two-way route, nanomedicines can be transported from the brain to the blood following the same mechanism; however, complex peptides can overcome this hurdle. Khan et al. employed a fusion peptide comprising a HER2-targeting peptide linked to ANG through an MMP1-sensitive peptide linker as a targeting moiety to deliver chemotherapy to HER2-overexpressing MDA-MB-231 brain metastatic tumors in mice (290,291). This strategy employs LRP-1 to promote the passage of a poly(lactic-co-glycolic acid)-poly(ε-carbobenzoxy-L-lysine) nanoparticle encapsulating Dox and lapatinib from blood to the brain, where the specific overexpression of MMP1 in the brain metastasis microenvironment cleaves the linker and exposes the HER2-targeting peptide, which allows for metastatic cell targeting and impedes LRP-1-mediated brain extrusion. Data from *in vivo* biodistribution and anti-metastatic activity supported their hypothesis, demonstrating a five-fold accumulation of the targeted nanoparticle in the brain of metastasis-bearing mice compared to a non-targeted counterpart, the sustained reduction of brain metastasis, and a significant increase in animal survival (291).

Our laboratory recently developed a brain-targeted St-PGA-Click platform using ANG as a targeting moiety (229). ANG-conjugated St-PGA-Click supported increased brain accumulation compared to a non-targeted counterpart with good diffusion in the brain parenchyma. Overall, we observed the accumulation of 1.5% of the injected dose in the brain three hours after intravenous administration in healthy mice. Confocal microscopy revealed that ANG-conjugated St-PGA-Click remained attached to the brain vasculature where it acted as a drug "depot." The additional conjugation of bisdemethoxycurcumin using an ester linkage allowed ANG-conjugated St-PGA-Click to safely ameliorate the classic symptoms of early-onset Alzheimer's disease in a mouse model, such as olfactory dysfunction and

loss of recognition memory and hippocampal learning (229). Bisdemethoxycurcumin- and ANG-conjugated St-PGA-Click also induced promising therapeutic outcomes in a mouse model of alcohol-induced neuroinflammation (217).

The promising results obtained for the ANG-conjugated St-PGA-Click platform encouraged us to employ ANG-conjugated St-PGA-based nanosystems to treat brain metastasis. In this thesis, we aimed to develop a St-PGA combination conjugate with optimized drug ratios and pH-responsive linkers to treat metastatic TNBC (*Chapter 2*). We also pursued the development of a bottom-up strategy for the synthesis of larger crosslinked St-PGA self-assembly-based combination conjugates employing reversible stimuli-responsive bonds for assembly stabilization (*Chapter 3*). Finally, we aimed to develop the brain-targeted version of the candidate with the best anti-tumor and anti-metastatic activity from the combination conjugates obtained by both strategies (*Chapter 4*).

1.6. Bibliography

1. What Is Breast Cancer? | Breastcancer.org [Internet]. [cited 2021 Jul 31]. Available from: https://www.breastcancer.org/symptoms/understand_bc/what_is_bc

2. What is breast cancer? | Cancer Research UK [Internet]. [cited 2021 Jul 31]. Available from: https://www.cancerresearchuk.org/about-cancer/breast-cancer/about

3. Anatomy of the Breast | Memorial Sloan Kettering Cancer Center [Internet]. [cited 2021 Jul 31]. Available from: https://www.mskcc.org/cancer-care/types/breast/anatomy-breast

4. Visvader JE, Stingl J. Mammary stem cells and the differentiation hierarchy: current status and perspectives. Genes Dev. 2014 Jun 1;28(11):1143–58.

5. Nerger BA, Nelson CM. 3D culture models for studying branching morphogenesis in the mammary gland and mammalian lung. Biomaterials. 2019 Apr 1;198:135–45.

6. Staging & Grade - Breast Pathology | Johns Hopkins Pathology [Internet]. [cited 2021 Jul 31]. Available from: https://pathology.jhu.edu/breast/staging-grade/

7. Tsang JYS, Tse GM. Molecular Classification of Breast Cancer. Adv Anat Pathol. 2020 Jan;27(1):27–35.

8. SMART - Servier Medical ART [Internet]. [cited 2022 Jan 12]. Available from: https://smart.servier.com/

9. American Cancer Society. Breast Cancer Facts & Figures 2019-2020. Atlanta; 2019.

10. Breast Cancer Stages: 0 Through IV [Internet]. [cited 2021 Jul 31]. Available from: https://www.breastcancer.org/symptoms/diagnosis/staging

11. Sung H, Ferlay J, Siegel RL, Laversanne M, Soerjomataram I, Jemal A, et al. Global Cancer Statistics 2020: GLOBOCAN Estimates of Incidence and Mortality Worldwide for 36 Cancers in 185 Countries. CA Cancer J Clin. 2021 May 4;71(3):209–49.

12. Red Española de Registros de Cáncer (REDECAN). Estimaciones de la incidencia del cáncer en España, 2021. 2021.

13. Siegel RL, Miller KD, Fuchs HE, Jemal A. Cancer Statistics, 2021. CA Cancer J Clin. 2021 Jan 12;71(1):7–33.

14. Torre LA, Islami F, Siegel RL, Ward EM, Jemal A. Global Cancer in Women: Burden and Trends. Cancer Epidemiol Biomarkers Prev. 2017 Apr;26(4):444–57.

15. DeSantis CE, Ma J, Gaudet MM, Newman LA, Miller KD, Goding Sauer A, et al. Breast cancer statistics, 2019. CA Cancer J Clin. 2019 Nov 2;69(6):438–51.

16. Breast cancer survival statistics | Cancer Research UK [Internet]. [cited 2021 Feb 6]. Available from: https://www.cancerresearchuk.org/health-professional/cancer-statistics/statistics-by-cancer-type/breast-cancer/survival#heading-Zero

17. Januškevičienė I, Petrikaitė V. Heterogeneity of breast cancer: The importance of interaction between different tumor cell populations. Life Sci. 2019 Dec 15;239:117009.

18. Prat A, Pineda E, Adamo B, Galván P, Fernández A, Gaba L, et al. Clinical implications of the intrinsic molecular subtypes of breast cancer. The Breast. 2015 Nov 1;24:S26–35.

19. Ethier JL, Ocaña A, Rodríguez Lescure A, Ruíz A, Alba E, Calvo L, et al. Outcomes of single versus double hormone receptor–positive breast cancer. A GEICAM/9906 sub-study. Eur J Cancer. 2018 May;94:199–205.

20. Rakha EA, El-Sayed ME, Green AR, Paish EC, Powe DG, Gee J, et al. Biologic and Clinical Characteristics of Breast Cancer With Single Hormone Receptor–Positive Phenotype. J Clin Oncol. 2007 Oct 20;25(30):4772–8.

21. Cardoso F, Kyriakides S, Ohno S, Penault-Llorca F, Poortmans P, Rubio IT, et al. Early breast cancer: ESMO Clinical Practice Guidelines for diagnosis, treatment and follow-up. Ann Oncol. 2019;30(8):1194–220.

22. Allison KH, Hammond MEH, Dowsett M, McKernin SE, Carey LA, Fitzgibbons PL, et al. Estrogen and progesterone receptor testing in breast cancer: ASCO/CAP guideline update. J Clin Oncol. 2020 Apr 20;38(12):1346–66.

23. Wolff AC, Elizabeth Hale Hammond M, Allison KH, Harvey BE, Mangu PB, Bartlett JMS, et al. Human epidermal growth factor receptor 2 testing in breast cancer: American society of clinical oncology/ college of American pathologists clinical practice guideline focused update. J Clin Oncol. 2018 Jul 10;36(20):2105–22.

24. Dai X, Li T, Bai Z, Yang Y, Liu X, Zhan J, et al. Breast cancer intrinsic subtype classification, clinical use and future trends. Am J Cancer Res. 2015;5(10):2929–43.

25. Hu Z, Fan C, Oh DS, Marron JS, He X, Qaqish BF, et al. The molecular portraits of breast tumors are conserved across microarray platforms. BMC Genomics. 2006 Apr 27;7(1):1–12.

26. Calza S, Hall P, Auer G, Björhle J, Klaar S, Kronenwett U, et al. Intrinsic molecular signature of breast cancer in a population-based cohort of 412 patients. Breast Cancer Res. 2006 Jul 17;8(4):1–9.

27. Parker JS, Mullins M, Cheang MCU, Leung S, Voduc D, Vickery T, et al. Supervised Risk Predictor of Breast Cancer Based on Intrinsic Subtypes. J Clin Oncol. 2009 Mar 10;27(8):1160–7.

28. Gnant M, Filipits M, Greil R, Stoeger H, Rudas M, Bago-Horvath Z, et al. Predicting distant recurrence in receptor-positive breast cancer patients with limited clinicopathological risk: using the PAM50 Risk of Recurrence score in 1478 postmenopausal patients of the ABCSG-8 trial treated with adjuvant endocrine therapy alone. Ann Oncol. 2014 Feb;25(2):339–45.

29. Ng CK, Pemberton HN, Reis-Filho JS. Breast cancer intratumor genetic heterogeneity: causes and implications. Expert Rev Anticancer Ther. 2012 Aug 10;12(8):1021–32.

30. Yeo SK, Guan JL. Breast Cancer: Multiple Subtypes within a Tumor? Trends in Cancer. 2017 Nov 1;3(11):753–60.

31. Harbeck N, Penault-Llorca F, Cortes J, Gnant M, Houssami N, Poortmans P, et al. Breast cancer. Nat Rev Dis Prim. 2019 Dec 23;5(1):66.

32. Savci-Heijink CD, Halfwerk H, Hooijer GKJ, Horlings HM, Wesseling J, van de Vijver MJ. Retrospective analysis of metastatic behaviour of breast cancer subtypes. Breast Cancer Res Treat. 2015 Apr 29;150(3):547–57.

33. Buonomo OC, Caredda E, Portarena I, Vanni G, Orlandi A, Bagni C, et al. New insights into the metastatic behavior after breast cancer surgery, according to well-established clinicopathological variables and molecular subtypes. Coleman WB, editor. PLoS One. 2017 Sep 18;12(9):e0184680.

34. Van Mechelen M, Van Herck A, Punie K, Nevelsteen I, Smeets A, Neven P, et al. Behavior of metastatic breast cancer according to subtype. Breast Cancer Res Treat. 2020 May 19;181(1):115–25.

35. Chen W, Hoffmann AD, Liu H, Liu X. Organotropism: new insights into molecular mechanisms of breast cancer metastasis. npj Precis Oncol. 2018 Dec 16;2(1):4.

36. Sflomos G, Brisken C. Breast Cancer Microenvironment and the Metastatic Process. In: Breast Cancer. Cham: Springer International Publishing; 2017. p. 39–48.

37. Lambert AW, Pattabiraman DR, Weinberg RA. Emerging Biological Principles of Metastasis. Cell. 2017 Feb;168(4):670–91.

38. Dongre A, Weinberg RA. New insights into the mechanisms of epithelial–mesenchymal transition and implications for cancer. Nat Rev Mol Cell Biol. 2019 Feb 20;20(2):69–84.

39. Chiang SPH, Cabrera RM, Segall JE. Tumor cell intravasation. Am J Physiol Physiol. 2016 Jul 1;311(1):C1–14.

40. Moo T-A, Sanford R, Dang C, Morrow M. Overview of Breast Cancer Therapy. PET Clin. 2018 Jul;13(3):339–54.

41. Menyailo ME, Tretyakova MS, Denisov E V. Heterogeneity of Circulating Tumor Cells in Breast Cancer: Identifying Metastatic Seeds. Int J Mol Sci. 2020 Mar 2;21(5):1696.

42. Riggi N, Aguet M, Stamenkovic I. Cancer Metastasis: A Reappraisal of Its Underlying Mechanisms and Their Relevance to Treatment. Annu Rev Pathol Mech

Dis. 2018 Jan 24;13(1):117–40.

43. Follain G, Osmani N, Azevedo AS, Allio G, Mercier L, Karreman MA, et al. Hemodynamic Forces Tune the Arrest, Adhesion, and Extravasation of Circulating Tumor Cells. Dev Cell. 2018 Apr 9;45(1):33-52.e12.

44. Cheng X, Cheng K. Visualizing cancer extravasation: from mechanistic studies to drug development. Cancer Metastasis Rev. 2021 Mar 6;40(1):71–88.

45. Minn AJ, Gupta GP, Siegel PM, Bos PD, Shu W, Giri DD, et al. Genes that mediate breast cancer metastasis to lung. Nature. 2005 Jul 28;436(7050):518–24.

46. García-Gómez P, Valiente M. Vascular co-option. In: Tumor Vascularization. Elsevier; 2020. p. 33–47.

47. Fares J, Fares MY, Khachfe HH, Salhab HA, Fares Y. Molecular principles of metastasis: a hallmark of cancer revisited. Signal Transduct Target Ther. 2020 Dec 12;5(1):28.

48. Fouad YA, Aanei C. Revisiting the hallmarks of cancer. Am J Cancer Res. 2017;7(5):1016–36.

49. Waks AG, Winer EP. Breast Cancer Treatment. JAMA. 2019 Jan 22;321(3):288.

50. Gadi VK, Davidson NE. Practical Approach to Triple-Negative Breast Cancer. J Oncol Pr. 2017;13(5):293–300.

51. Aggelis V, Johnston SRD. Advances in Endocrine-Based Therapies for Estrogen Receptor-Positive Metastatic Breast Cancer. Drugs. 2019;79(17):1849–66.

52. Cardoso F, Paluch-Shimon S, Senkus E, Curigliano G, Aapro MS, André F, et al. 5th ESO-ESMO international consensus guidelines for advanced breast cancer (ABC 5). Ann Oncol. 2020 Dec;31(12):1623–49.

53. Tesch ME, Gelmon KA. Targeting HER2 in Breast Cancer: Latest Developments on Treatment Sequencing and the Introduction of Biosimilars. Drugs. 2020 Nov 6;80(17):1811–30.

54. Vu T, Claret FX. Trastuzumab: updated mechanisms of action and resistance in breast cancer. Front Oncol. 2012;2:62.

55. Poon KA, Flagella K, Beyer J, Tibbitts J, Kaur S, Saad O, et al. Preclinical safety profile of trastuzumab emtansine (T-DM1): Mechanism of action of its cytotoxic component retained with improved tolerability. Toxicol Appl Pharmacol. 2013 Dec 1;273(2):298–313.

56. Cardoso F, Harbeck N, Fallowfield L, Kyriakides S, Senkus E. Locally recurrent or metastatic breast cancer: ESMO Clinical Practice Guidelines for diagnosis, treatment and follow-up. Ann Oncol. 2012 Oct;23(SUPPL. 7):vii11–9.

57. Jitariu AA, Cimpean AM, Ribatti D, Raica M. Triple negative breast cancer: the kiss of death. Oncotarget. 2017;8(28):46652–62.

58. Denkert C, Liedtke C, Tutt A, von Minckwitz G. Molecular alterations in triple-negative breast cancer-the road to new treatment strategies. Lancet. 2017;389(10087):2430–42.

59. Bianchini G, Balko JM, Mayer IA, Sanders ME, Gianni L. Triple-negative breast cancer: challenges and opportunities of a heterogeneous disease. Nat Rev Clin Oncol. 2016;13(11):674–90.

60. Lebert JM, Lester R, Powell E, Seal M, McCarthy J. Advances in the Systemic Treatment of Triple-Negative Breast Cancer. Curr Oncol. 2018 Jun 1;25(11):142–50.

61. Sharma P. Biology and Management of Patients With Triple-Negative Breast Cancer. Oncologist. 2016;21(9):1050–62.

62. Lehmann BD, Bauer JA, Chen X, Sanders ME, Chakravarthy AB, Shyr Y, et al. Identification of human triple-negative breast cancer subtypes and preclinical models for selection of targeted therapies. J Clin Invest. 2011;121(7):2750–67.

63. Lehmann BD, Jovanović B, Chen X, Estrada M V, Johnson KN, Shyr Y, et al. Refinement of Triple-Negative Breast Cancer Molecular Subtypes: Implications for Neoadjuvant Chemotherapy Selection. PLoS One. 2016 Jun 16;11(6):e0157368.

64. Burstein MD, Tsimelzon A, Poage GM, Covington KR, Contreras A, Fuqua SA, et al. Comprehensive genomic analysis identifies novel subtypes and targets of triple-negative breast cancer. Clin Cancer Res. 2015;21(7):1688–98.

65. Lehmann BD, Pietenpol JA. Identification and use of biomarkers in treatment strategies for triple-negative breast cancer subtypes. J Pathol. 2014;232(2):142–50.

66. Garrido-Castro AC, Lin NU, Polyak K. Insights into Molecular Classifications of Triple-Negative Breast Cancer: Improving Patient Selection for Treatment. Cancer Discov. 2019;9(2):176–98.

67. Vagia E, Mahalingam D, Cristofanilli M. The Landscape of Targeted Therapies in TNBC. Cancers (Basel). 2020 Apr 8;12(4):916.

68. Gupta GK, Collier AL, Lee D, Hoefer RA, Zheleva V, Siewertsz van Reesema LL, et al. Perspectives on Triple-Negative Breast Cancer: Current Treatment Strategies, Unmet Needs, and Potential Targets for Future Therapies. Cancers (Basel). 2020 Aug 24;12(9):2392.

69. Zheng R, Han S, Duan C, Chen K, You Z, Jia J, et al. Role of Taxane and Anthracycline Combination Regimens in the Management of Advanced Breast Cancer. Medicine (Baltimore). 2015 May;94(17):e803.

70. Saif MW, Katirtzoglou NA, Syrigos KN. Capecitabine: an overview of the side effects and their management. Anticancer Drugs. 2008 Jun;19(5):447–64.

71. Pandy JGP, Balolong-Garcia JC, Cruz-Ordinario MVB, Que FVF. Triple negative breast cancer and platinum-based systemic treatment: a meta-analysis and systematic review. BMC Cancer. 2019 Dec 8;19(1):1065.

72. García-Aranda M, Redondo M. Immunotherapy: A Challenge of Breast Cancer Treatment. Cancers (Basel). 2019 Nov 20;11(12):1822.

73. Keenan TE, Tolaney SM. Role of immunotherapy in triple-negative breast cancer. JNCCN J Natl Compr Cancer Netw. 2020 Apr;18(4):479–89.

74. Narayan P, Wahby S, Gao JJ, Amiri-Kordestani L, Ibrahim A, Bloomquist E, et al. FDA Approval Summary: Atezolizumab Plus Paclitaxel Protein-bound for the Treatment of Patients with Advanced or Metastatic TNBC Whose Tumors Express PD-L1. Clin Cancer Res. 2020 May 15;26(10):2284–9.

75. Gonçalves A, Bertucci A, Bertucci F. PARP Inhibitors in the Treatment of Early Breast Cancer: The Step Beyond? Cancers (Basel). 2020 May 27;12(6):1378.

76. Rampurwala M, Wisinski KB, O'Regan R. Role of the androgen receptor in triple-negative breast cancer. Clin Adv Hematol Oncol. 2016;14(3):186–93.

77. Davey RA, Grossmann M. Androgen Receptor Structure, Function and Biology: From Bench to Bedside. Clin Biochem Rev. 2016;37(1):3–15.

78. Gucalp A, Tolaney S, Isakoff SJ, Ingle JN, Liu MC, Carey LA, et al. Phase II trial of bicalutamide in patients with androgen receptor-positive, estrogen receptor-

negative metastatic breast cancer. Clin Cancer Res. 2013 Oct 1;19(19):5505–12.

79. Traina TA, Miller K, Yardley DA, O'Shaughnessy J, Cortes J, Awada A, et al. Results from a phase 2 study of enzalutamide (ENZA), an androgen receptor (AR) inhibitor, in advanced AR+ triple-negative breast cancer (TNBC). J Clin Oncol. 2015 May 20;33(15_suppl):1003–1003.

80. Xu F, Na L, Li Y, Chen L. RETRACTED ARTICLE: Roles of the PI3K/AKT/mTOR signalling pathways in neurodegenerative diseases and tumours. Cell Biosci. 2020 Dec 1;10(1):54.

81. Oliveira M, Saura C, Nuciforo P, Calvo I, Andersen J, Passos-Coelho JL, et al. FAIRLANE, a double-blind placebo-controlled randomized phase II trial of neoadjuvant ipatasertib plus paclitaxel for early triple-negative breast cancer. Ann Oncol. 2019 Aug;30(8):1289–97.

82. Pascual J, Turner NC. Targeting the PI3-kinase pathway in triple-negative breast cancer. Ann Oncol. 2019 Jul;30(7):1051–60.

83. Leone JP, Leone BA. Breast cancer brain metastases: the last frontier. Exp Hematol Oncol. 2015/11/24. 2015 Dec 24;4(1):33.

84. Witzel I, Oliveira-Ferrer L, Pantel K, Müller V, Wikman H. Breast cancer brain metastases: biology and new clinical perspectives. Breast Cancer Res. 2016 Dec 19;18(1):8.

85. Achrol AS, Rennert RC, Anders C, Soffietti R, Ahluwalia MS, Nayak L, et al. Brain metastases. Nat Rev Dis Prim. 2019 Dec 17;5(1):5.

86. Bos PD, Zhang XHF, Nadal C, Shu W, Gomis RR, Nguyen DX, et al. Genes that mediate breast cancer metastasis to the brain. Nature. 2009 Jun 6;459(7249):1005–9.

87. Witzel I, Oliveira-Ferrer L, Müller V. Brain Metastasis in Breast Cancer Patients—Need for Improvement. Cancers (Basel). 2020 Oct 30;12(11):3190.

88. Kim Y-J, Kim J-S, Kim IA. Molecular subtype predicts incidence and prognosis of brain metastasis from breast cancer in SEER database. J Cancer Res Clin Oncol. 2018 Sep 3;144(9):1803–16.

89. Soffietti R, Ahluwalia M, Lin N, Rudà R. Management of brain metastases according to molecular subtypes. Nat Rev Neurol. 2020 Oct 1;16(10):557–74.

90. Abbott NJ, Patabendige AAK, Dolman DEM, Yusof SR, Begley DJ. Structure and function of the blood–brain barrier. Neurobiol Dis. 2009/08/05. 2010 Jan;37(1):13–25.

91. Abbott NJ. Blood–brain barrier structure and function and the challenges for CNS drug delivery. J Inherit Metab Dis. 2013 May 23;36(3):437–49.

92. Oller-Salvia B, Sánchez-Navarro M, Giralt E, Teixidó M. Blood–brain barrier shuttle peptides: an emerging paradigm for brain delivery. Chem Soc Rev. 2016;45(17):4690–707.

93. Duro-Castano A, Moreira Leite D, Forth J, Deng Y, Matias D, Noble Jesus C, et al. Designing peptide nanoparticles for efficient brain delivery. Adv Drug Deliv Rev. 2020 May;160:52–77.

94. Theodorakis PE, Müller EA, Craster R V., Matar OK. Physical insights into the blood–brain barrier translocation mechanisms. Phys Biol. 2017 Jun 6;14(4):041001.

95. Cerna T, Stiborova M, Adam V, Kizek R, Eckschlager T. Nanocarrier drugs in the treatment of brain tumors. J Cancer Metastasis Treat. 2016;2(10):407–16.

96. Mills MN, Figura NB, Arrington JA, Yu H-HM, Etame AB, Vogelbaum MA, et al. Management of brain metastases in breast cancer: a review of current practices and emerging treatments. Breast Cancer Res Treat. 2020 Apr 6;180(2):279–300.

97. Obermeier B, Daneman R, Ransohoff RM. Development, maintenance and disruption of the blood-brain barrier. Nat Med. 2013 Dec 5;19(12):1584–96.

98. Alam MI, Beg S, Samad A, Baboota S, Kohli K, Ali J, et al. Strategy for effective brain drug delivery. Eur J Pharm Sci. 2010/05/26. 2010 Aug;40(5):385–403.

99. Lajoie JM, Shusta E V. Targeting Receptor-Mediated Transport for Delivery of Biologics Across the Blood-Brain Barrier. Annu Rev Pharmacol Toxicol. 2015 Jan 6;55(1):613–31.

100. Tian X, Nyberg S, Sharp PS, Madsen J, Daneshpour N, Armes SP, et al. LRP-1-mediated intracellular antibody delivery to the Central Nervous System. Sci Rep. 2015 Dec 20;5(1):11990.

101. Tian X, Leite DM, Scarpa E, Nyberg S, Fullstone G, Forth J, et al. On the shuttling across the blood-brain barrier via tubule formation: Mechanism and cargo avidity bias. Sci Adv. 2020 Nov 27;6(48):eabc4397.

102. Fullstone G, Nyberg S, Tian X, Battaglia G. From the Blood to the Central Nervous System. In: International Review of Neurobiology. 2016. p. 41–72.

103. England RM, Conejos–sánchez I, Vicent* MJ. Chapter 8.2. Drug Delivery Strategies: Polymer Therapeutics. In 2012. p. 456–82.

104. Yi X, Yuan D, Farr SA, Banks WA, Poon C-D, Kabanov A V. Pluronic modified leptin with increased systemic circulation, brain uptake and efficacy for treatment of obesity. J Control Release. 2014 Oct;191:34–46.

105. García-Gómez P, Priego N, Álvaro-Espinosa L, Valiente M. Brain Metastases Cell Partners and Tumor Microenvironment. In: Central Nervous System Metastases. Cham: Springer International Publishing; 2020. p. 59–71.

106. Hosonaga M, Saya H, Arima Y. Molecular and cellular mechanisms underlying brain metastasis of breast cancer. Cancer Metastasis Rev. 2020 Sep 13;39(3):711–20.

107. Pedrosa RMSM, Mustafa DA, Soffietti R, Kros JM. Breast cancer brain metastasis: molecular mechanisms and directions for treatment. Neuro Oncol. 2018 Oct 9;20(11):1439–49.

108. Er EE, Boire A. Molecular Mechanisms in Brain Metastasis. In: Central Nervous System Metastases. Cham: Springer International Publishing; 2020. p. 31–41.

109. Arvanitis CD, Ferraro GB, Jain RK. The blood–brain barrier and blood–tumour barrier in brain tumours and metastases. Nat Rev Cancer. 2020 Jan 10;20(1):26–41.

110. Yonemori K, Tsuta K, Ono M, Shimizu C, Hirakawa A, Hasegawa T, et al. Disruption of the blood brain barrier by brain metastases of triple-negative and basal-type breast cancer but not HER2/neu -positive breast cancer. Cancer. 2010 Jan 15;116(2):302–8.

111. Soffietti R, Abacioglu U, Baumert B, Combs SE, Kinhult S, Kros JM, et al. Diagnosis and treatment of brain metastases from solid tumors: guidelines from the European Association of Neuro-Oncology (EANO). Neuro Oncol. 2017 Feb 1;19(2):162–74.

112. McTyre E, Scott J, Chinnaiyan P. Whole brain radiotherapy for brain metastasis. Surg Neurol Int. 2013/05/02. 2013;4(5):236.

113. Bailleux C, Eberst L, Bachelot T. Treatment strategies for breast cancer brain metastases. Br J Cancer. 2021 Jan 5;124(1):142–55.

114. Search of: triple negative breast cancer | Recruiting, Not yet recruiting, Active, not recruiting, Enrolling by invitation Studies | Brain Metastases - List Results - ClinicalTrials.gov [Internet]. [cited 2022 Jan 13]. Available from: https://clinicaltrials.gov/ct2/results?cond=Brain+Metastases&term=triple+negative+breast+cancer&cntry=&state=&city=&dist=&Search=Search&recrs=a&recrs=b&recrs=d&recrs=f

115. Canal F, Sanchis J, Vicent MJ. Polymer–drug conjugates as nano-sized medicines. Curr Opin Biotechnol. 2011 Dec;22(6):894–900.

116. Duncan R, Vicent MJ. Polymer therapeutics-prospects for 21st century: The end of the beginning. Adv Drug Deliv Rev. 2013 Jan;65(1):60–70.

117. Rodriguez-Otormin F, Duro-Castano A, Conejos-Sánchez I, Vicent MJ. Envisioning the future of polymer therapeutics for brain disorders. WIREs Nanomedicine and Nanobiotechnology. 2019 Jan 14;11(1).

118. Duro-Castano A, Conejos-Sanchez I, Vicent MJ. Peptide-Based Polymer Therapeutics. Polymers (Basel). 2014;6(2):515–51.

119. Batterink J, Lin J, Au-Yeung SHM, Cessford T. Effectiveness of Sodium Polystyrene Sulfonate for Short-Term Treatment of Hyperkalemia. Can J Hosp Pharm. 2015 Aug 25;68(4).

120. Duncan R. Polymer therapeutics at a crossroads? Finding the path for improved translation in the twenty-first century. J Drug Target. 2017 Nov 26;25(9–10):759–80.

121. Vicent MJ, Duncan R. Polymer conjugates: nanosized medicines for treating cancer. Trends Biotechnol. 2006 Jan;24(1):39–47.

122. Duncan R. Polymer therapeutics: Top 10 selling pharmaceuticals — What next? J Control Release. 2014 Sep;190:371–80.

123. Weinstein V, Schwartz R, Grossman I, Zeskind B, Nicholas JM. Glatiramoids. In: AAPS Advances in the Pharmaceutical Sciences Series. 2015. p. 107–48.

124. Alphandéry E, Grand-Dewyse P, Lefèvre R, Mandawala C, Durand-Dubief M. Cancer therapy using nanoformulated substances: scientific, regulatory and financial aspects. Expert Rev Anticancer Ther. 2015 Oct 3;15(10):1233–55.

125. Molineux G. The design and development of pegfilgrastim (PEG-rmetHuG-CSF, Neulasta). Curr Pharm Des. 2004;10(11):1235–44.

126. Melnyk T, Đorđević S, Conejos-Sánchez I, Vicent MJ. Therapeutic potential of polypeptide-based conjugates: Rational design and analytical tools that can boost clinical translation. Adv Drug Deliv Rev. 2020 May;160:136–69.

127. DrugBank Online | Database for Drug and Drug Target Info [Internet]. [cited 2022 Jan 12]. Available from: https://go.drugbank.com/

128. Younis MA, Tawfeek HM, Abdellatif AAH, Abdel-Aleem JA, Harashima H. Clinical translation of nanomedicines: Challenges, opportunities, and keys. Adv Drug Deliv Rev. 2022 Feb 1;181:114083.

129. Premarket Approval (PMA) [Internet]. [cited 2022 Jan 12]. Available from: https://www.accessdata.fda.gov/scripts/cdrh/cfdocs/cfpma/pma.cfm?id=P940015

130. Ekladious I, Colson YL, Grinstaff MW. Polymer–drug conjugate therapeutics: advances, insights and prospects. Nat Rev Drug Discov 2018 184. 2018 Dec 12;18(4):273–94.

131. Drugs@FDA: FDA-Approved Drugs [Internet]. [cited 2022 Jan 12]. Available from: https://www.accessdata.fda.gov/scripts/cder/daf/index.cfm?event=overview.proces

s&varApplNo=761092

132. Thakor P, Bhavana V, Sharma R, Srivastava S, Singh SB, Mehra NK. Polymer–drug conjugates: recent advances and future perspectives. Drug Discov Today. 2020 Sep;25(9):1718–26.

133. Alven S, Nqoro X, Buyana B, Aderibigbe BA. Polymer-Drug Conjugate, a Potential Therapeutic to Combat Breast and Lung Cancer. Pharmaceutics. 2020 Apr 29;12(5):406.

134. Meerum Terwogt JM, ten Bokkel Huinink WW, Schellens JHM, Schot M, Mandjes IAM, Zurlo MG, et al. Phase I clinical and pharmacokinetic study of PNU166945, a novel water-soluble polymer-conjugated prodrug of paclitaxel. Anticancer Drugs. 2001 Apr;12(4):315–23.

135. Piao X, Yin H, Guo S, Wang H, Guo P. RNA Nanotechnology to Solubilize Hydrophobic Antitumor Drug for Targeted Delivery. Adv Sci. 2019 Nov 30;6(22):1900951.

136. Zhou H, Lv S, Zhang D, Deng M, Zhang X, Tang Z, et al. A polypeptide based podophyllotoxin conjugate for the treatment of multi drug resistant breast cancer with enhanced efficiency and minimal toxicity. Acta Biomater. 2018 Jun;73:388–99.

137. Zagorodko O, Arroyo-Crespo JJ, Nebot VJ, Vicent MJ. Polypeptide-Based Conjugates as Therapeutics: Opportunities and Challenges. Macromol Biosci. 2017 Jan;17(1):1600316.

138. Fang J, Islam W, Maeda H. Exploiting the dynamics of the EPR effect and strategies to improve the therapeutic effects of nanomedicines by using EPR effect enhancers. Adv Drug Deliv Rev. 2020 Jan 1;157:142–60.

139. Theek B, Rizzo LY, Ehling J, Kiessling F, Lammers T. The theranostic path to personalized nanomedicine. Clin Transl Imaging. 2014 Feb 19;2(1):67–76.

140. Vicent MJ, Greco F, Nicholson RI, Paul A, Griffiths PC, Duncan R. Polymer therapeutics designed for a combination therapy of hormone-dependent cancer. Angew Chemie - Int Ed. 2005 Jun 27;44(26):4061–6.

141. Prat A, Perou CM. Deconstructing the molecular portraits of breast cancer. Mol Oncol. 2011 Feb;5(1):5–23.

142. Markman JL, Rekechenetskiy A, Holler E, Ljubimova JY. Nanomedicine therapeutic approaches to overcome cancer drug resistance. Adv Drug Deliv Rev. 2013 Nov;65(13–14):1866–79.

143. Kobayashi H, Turkbey B, Watanabe R, Choyke PL. Cancer Drug Delivery: Considerations in the Rational Design of Nanosized Bioconjugates. Bioconjug Chem. 2014 Dec 17;25(12):2093–100.

144. Narayan RS, Molenaar P, Teng J, Cornelissen FMG, Roelofs I, Menezes R, et al. A cancer drug atlas enables synergistic targeting of independent drug vulnerabilities. Nat Commun. 2020 Dec 10;11(1):2935.

145. Ayoub N, Al-Shami K, Alqudah MAY, Mhaidat N. Crizotinib, a MET inhibitor, inhibits growth, migration, and invasion of breast cancer cells in vitro and synergizes with chemotherapeutic agents. Onco Targets Ther. 2017 Oct;10:4869–83.

146. Nan X, Wang J, Cheng H, Yin Z, Sheng J, Qiu B, et al. Imatinib revives the therapeutic potential of metformin on ewing sarcoma by attenuating tumor hypoxic response and inhibiting convergent signaling pathways. Cancer Lett. 2020 Jan 28;469:195–206.

147. Vogus DR, Evans MA, Pusuluri A, Barajas A, Zhang M, Krishnan V, et al. A

hyaluronic acid conjugate engineered to synergistically and sequentially deliver gemcitabine and doxorubicin to treat triple negative breast cancer. J Control Release. 2017 Dec 10;267:191–202.

148. Arroyo-Crespo JJ, Deladriere C, Nebot VJ, Charbonnier D, Masiá E, Paul A, et al. Anticancer Activity Driven by Drug Linker Modification in a Polyglutamic Acid-Based Combination-Drug Conjugate. Adv Funct Mater. 2018 May 16;28(22):1800931.

149. Arroyo-Crespo JJ, Armiñán A, Charbonnier D, Balzano-Nogueira L, Huertas-López F, Martí C, et al. Tumor microenvironment-targeted poly-L-glutamic acid-based combination conjugate for enhanced triple negative breast cancer treatment. Biomaterials. 2018 Dec;186:8–21.

150. Sun H, Yan L, Chang MYZ, Carter KA, Zhang R, Slyker L, et al. A multifunctional biodegradable brush polymer-drug conjugate for paclitaxel/gemcitabine co-delivery and tumor imaging. Nanoscale Adv. 2019;1(7):2761–71.

151. Dong S, Sun Y, Liu J, Li L, He J, Zhang M, et al. Multifunctional Polymeric Prodrug with Simultaneous Conjugating Camptothecin and Doxorubicin for pH/Reduction Dual-Responsive Drug Delivery. ACS Appl Mater Interfaces. 2019 Mar 6;11(9):8740–8.

152. Ringsdorf H. STRUCTURE AND PROPERTIES OF PHARMACOLOGICALLY ACTIVE POLYMERS. In: J Polym Sci Polym Symp. 1975. p. 135–53.

153. Spencer AP, Torrado M, Custódio B, Silva-Reis SC, Santos SD, Leiro V, et al. Breaking Barriers: Bioinspired Strategies for Targeted Neuronal Delivery to the Central Nervous System. Pharmaceutics. 2020 Feb 23;12(2):192.

154. Maheshwari R, Kuche K, Mane A, Chourasiya Y, Tekade M, Tekade RK. Manipulation of Physiological Processes for Pharmaceutical Product Development. In: Dosage Form Design Considerations. Elsevier; 2018. p. 701–29.

155. de Oliveira Junior ER, Truzzi E, Ferraro L, Fogagnolo M, Pavan B, Beggiato S, et al. Nasal administration of nanoencapsulated geraniol/ursodeoxycholic acid conjugate: Towards a new approach for the management of Parkinson's disease. J Control Release. 2020 May;321:540–52.

156. Al-Hilal TA, Alam F, Byun Y. Oral drug delivery systems using chemical conjugates or physical complexes. Adv Drug Deliv Rev. 2013 Jun;65(6):845–64.

157. Vong LB, Ibayashi Y, Lee Y, Ngo D-N, Nishikawa Y, Nagasaki Y. Poly(ornithine)-based self-assembling drug for recovery of hyperammonemia and damage in acute liver injury. J Control Release. 2019 Sep;310:74–81.

158. Pang X, Yang X, Zhai G. Polymer-drug conjugates: recent progress on administration routes. Expert Opin Drug Deliv. 2014 Jul 23;11(7):1075–86.

159. Dolz-Pérez I, Sallam MA, Masiá E, Morelló-Bolumar D, Pérez del Caz MD, Graff P, et al. Polypeptide-corticosteroid conjugates as a topical treatment approach to psoriasis. J Control Release. 2020 Feb;318:210–22.

160. Atkinson S, Andreu Z, Vicent M. Polymer Therapeutics: Biomarkers and New Approaches for Personalized Cancer Treatment. J Pers Med. 2018 Jan 23;8(1):6.

161. Mulinti P, Brooks JE, Lervick B, Pullan JE, Brooks AE. Strategies to improve the hemocompatibility of biodegradable biomaterials. In: Hemocompatibility of Biomaterials for Clinical Applications. Elsevier; 2018. p. 253–78.

162. Kopeček J, Yang J. Polymer nanomedicines. Adv Drug Deliv Rev. 2020 Jul;156:40–64.

163. Vasey PA, Kaye SB, Morrison R, Twelves C, Wilson P, Duncan R, et al. Phase I

clinical and pharmacokinetic study of PK1 [N-(2-hydroxypropyl)methacrylamide copolymer doxorubicin]: first member of a new class of chemotherapeutic agents-drug-polymer conjugates. Cancer Research Campaign Phase I/II Committee. Clin Cancer Res. 1999 Jan;5(1):83–94.

164. Poon W, Kingston BR, Ouyang B, Ngo W, Chan WCW. A framework for designing delivery systems. Nat Nanotechnol. 2020 Oct 7;15(10):819–29.

165. Abbina S, Takeuchi LE, Anilkumar P, Yu K, Rogalski JC, Shenoi RA, et al. Blood circulation of soft nanomaterials is governed by dynamic remodeling of protein opsonins at nano-biointerface. Nat Commun 2020 111. 2020 Jun 16;11(1):1–12.

166. Hadjidemetriou M, Kostarelos K. Evolution of the nanoparticle corona. Nat Nanotechnol. 2017 Apr 6;12(4):288–90.

167. Nguyen VH, Lee B-J. Protein corona: a new approach for nanomedicine design. Int J Nanomedicine. 2017 Apr;Volume 12:3137–51.

168. Berrecoso G, Crecente-Campo J, Alonso MJ. Unveiling the pitfalls of the protein corona of polymeric drug nanocarriers. Drug Deliv Transl Res 2020 103. 2020 Mar 9;10(3):730–50.

169. Alberg I, Kramer S, Schinnerer M, Hu Q, Seidl C, Leps C, et al. Polymeric Nanoparticles with Neglectable Protein Corona. Small. 2020 May 6;16(18):1907574.

170. Richtering W, Alberg I, Zentel R, Richtering W, Alberg I, Zentel R. Nanoparticles in the Biological Context: Surface Morphology and Protein Corona Formation. Small. 2020 Oct 1;16(39):2002162.

171. Zhang Z, Wang C, Zha Y, Hu W, Gao Z, Zang Y, et al. Corona-Directed Nucleic Acid Delivery into Hepatic Stellate Cells for Liver Fibrosis Therapy. ACS Nano. 2015 Mar 24;9(3):2405–19.

172. Matsumura Y, Maeda H. A new concept for macromolecular therapeutics in cancer chemotherapy: mechanism of tumoritropic accumulation of proteins and the antitumor agent smancs. Cancer Res. 1986 Dec;46(12 Pt 1):6387–92.

173. Nichols JW, Bae YH. EPR: Evidence and fallacy. J Control Release. 2014 Sep;190:451–64.

174. Duncan R, Sat-Klopsch Y-N, Burger AM, Bibby MC, Fiebig HH, Sausville EA. Validation of tumour models for use in anticancer nanomedicine evaluation: the EPR effect and cathepsin B-mediated drug release rate. Cancer Chemother Pharmacol. 2013 Aug 25;72(2):417–27.

175. Arroyo-Crespo JJ, Armiñán A, Charbonnier D, Deladriere C, Palomino-Schätzlein M, Lamas-Domingo R, et al. Characterization of triple-negative breast cancer preclinical models provides functional evidence of metastatic progression. Int J Cancer. 2019 Oct 15;145(8):2267–81.

176. Jhaveri AM, Torchilin VP. Multifunctional polymeric micelles for delivery of drugs and siRNA. Front Pharmacol. 2014 Apr 25;5:77.

177. Duncan R. Designing polymer conjugates as lysosomotropic nanomedicines. Biochem Soc Trans. 2007 Feb 1;35(1):56–60.

178. DeBerardinis RJ, Chandel NS. We need to talk about the Warburg effect. Nat Metab. 2020 Feb 3;2(2):127–9.

179. Lee S-H, Griffiths JR. How and Why Are Cancers Acidic? Carbonic Anhydrase IX and the Homeostatic Control of Tumour Extracellular pH. Cancers (Basel). 2020 Jun 18;12(6):1616.

180. Kostka L, Kotrchová L, Šubr V, Libánská A, Ferreira CA, Malátová I, et al. HPMA-based star polymer biomaterials with tuneable structure and biodegradability tailored for advanced drug delivery to solid tumours. Biomaterials. 2020 Mar 1;235:119728.

181. Heinrich AK, Lucas H, Schindler L, Chytil P, Etrych T, Mäder K, et al. Improved tumor-specific drug accumulation by polymer therapeutics with pH-sensitive drug release overcomes chemotherapy resistance. Mol Cancer Ther. 2016 May 1;15(5):998–1007.

182. Markovsky E, Baabur-Cohen H, Satchi-Fainaro R. Anticancer polymeric nanomedicine bearing synergistic drug combination is superior to a mixture of individually-conjugated drugs. J Control Release. 2014 Aug 10;187:145–57.

183. Li K, Liu C-J, Zhang X-Z. Multifunctional peptides for tumor therapy. Adv Drug Deliv Rev. 2020 Jan 1;160:36–51.

184. Luo G-F, Chen W-H, Hong S, Cheng Q, Qiu W-X, Zhang X-Z. A Self-Transformable pH-Driven Membrane-Anchoring Photosensitizer for Effective Photodynamic Therapy to Inhibit Tumor Growth and Metastasis. Adv Funct Mater. 2017 Sep;27(36):1702122.

185. Selby LI, Cortez-Jugo CM, Such GK, Johnston APR. Nanoescapology: progress toward understanding the endosomal escape of polymeric nanoparticles. WIREs Nanomedicine and Nanobiotechnology. 2017 Sep 3;9(5).

186. Patel S, Kim J, Herrera M, Mukherjee A, Kabanov A V., Sahay G. Brief update on endocytosis of nanomedicines. Adv Drug Deliv Rev. 2019 Apr;144:90–111.

187. Berquin IM, Sloane BF. Cathepsin B Expression in Human Tumors. In: Advances in Experimental Medicine and Biology. 1996. p. 281–94.

188. Thomson AH, Vasey PA, Murray LS, Cassidy J, Fraier D, Frigerio E, et al. Population pharmacokinetics in phase I drug development: a phase I study of PK1 in patients with solid tumours. Br J Cancer. 1999 Sep 13;81(1):99–107.

189. Seymour. Phase II studies of polymer-doxorubicin (PK1, FCE28068) in the treatment of breast, lung and colorectal cancer. Int J Oncol. 2009 May 7;34(6):1629–36.

190. Seymour LW, Ferry DR, Anderson D, Hesslewood S, Julyan PJ, Poyner R, et al. Hepatic Drug Targeting: Phase I Evaluation of Polymer-Bound Doxorubicin. J Clin Oncol. 2002 Mar 15;20(6):1668–76.

191. Luo L, Xu F, Peng H, Luo Y, Tian X, Battaglia G, et al. Stimuli-responsive polymeric prodrug-based nanomedicine delivering nifuroxazide and doxorubicin against primary breast cancer and pulmonary metastasis. J Control Release. 2020 Feb;318:124–35.

192. Shaffer SA, Baker-Lee C, Kennedy J, Lai MS, de Vries P, Buhler K, et al. In vitro and in vivo metabolism of paclitaxel poliglumex: identification of metabolites and active proteases. Cancer Chemother Pharmacol. 2007 Mar 19;59(4):537–48.

193. Singer JW, Baker B, de Vries P, Kumar A, Shaffer S, Vawter E, et al. Poly-(L)-Glutamic Acid-Paclitaxel (CT-2103) [XYOTAXTM], a Biodegradable Polymeric Drug Conjugate. In: Advances in experimental medicine and biology. Adv Exp Med Biol; 2004. p. 81–99.

194. Bansal A, Simon MC. Glutathione metabolism in cancer progression and treatment resistance. J Cell Biol. 2018;217(7):2291–8.

195. Lv H, Zhen C, Liu J, Yang P, Hu L, Shang P. Unraveling the Potential Role of Glutathione in Multiple Forms of Cell Death in Cancer Therapy. Oxid Med Cell

Longev. 2019 Jun 10;2019:1–16.

196. Wu G, Fang Y-Z, Yang S, Lupton JR, Turner ND. Glutathione Metabolism and Its Implications for Health. J Nutr. 2004;134(3):489–92.

197. Estrela JM, Ortega A, Obrador E. Glutathione in Cancer Biology and Therapy. Crit Rev Clin Lab Sci. 2006 Jan 10;43(2):143–81.

198. Taresco V, Alexander C, Singh N, Pearce AK. Stimuli-Responsive Prodrug Chemistries for Drug Delivery. Adv Ther. 2018 Aug;1(4):1800030.

199. Mi P, Yanagie H, Dewi N, Yen H-C, Liu X, Suzuki M, et al. Block copolymer-boron cluster conjugate for effective boron neutron capture therapy of solid tumors. J Control Release. 2017 May 28;254:1–9.

200. Liu J, Ai X, Zhang H, Zhuo W, Mi P. Polymeric Micelles with Endosome Escape and Redox-Responsive Functions for Enhanced Intracellular Drug Delivery. J Biomed Nanotechnol. 2019 Feb 1;15(2):373–81.

201. Wei JR, Sun J, Yang X, Ji SF, Wei YH, Li ZB. Self-crosslinking assemblies with tunable nanostructures from photoresponsive polypeptoid-based block copolymers. Polym Chem. 2020;11(2):337–43.

202. Cai K, Yen J, Yin Q, Liu Y, Song Z, Lezmi S, et al. Redox-responsive self-assembled chain-shattering polymeric therapeutics. Biomater Sci. 2015 Jun 16;3(7):1061–5.

203. Sun J, Liu Y, Chen Y, Zhao W, Zhai Q, Rathod S, et al. Doxorubicin delivered by a redox-responsive dasatinib-containing polymeric prodrug carrier for combination therapy. J Control Release. 2017 Jul;258:43–55.

204. Greco F, Vicent MJ. Combination therapy: Opportunities and challenges for polymer–drug conjugates as anticancer nanomedicines. Adv Drug Deliv Rev. 2009 Nov;61(13):1203–13.

205. Yuan X, Liu L, Wang W, Gao Y, Zhang D, Jia T, et al. Development of (G3-C12)-mediated camptothecin polymeric prodrug targeting to Galectin-3 receptor against androgen-independent prostate cancer. Int J Pharm. 2020 Apr 30;580:119123.

206. Peng M, Qin S, Jia H, Zheng D, Rong L, Zhang X. Self-delivery of a peptide-based prodrug for tumor-targeting therapy. Nano Res. 2016 Mar 1;9(3):663–73.

207. Han K, Zhang W-Y, Zhang J, Lei Q, Wang S-B, Liu J-W, et al. Acidity-Triggered Tumor-Targeted Chimeric Peptide for Enhanced Intra-Nuclear Photodynamic Therapy. Adv Funct Mater. 2016 Jun;26(24):4351–61.

208. Jahan S, Karim ME, Chowdhury EH. Nanoparticles Targeting Receptors on Breast Cancer for Efficient Delivery of Chemotherapeutics. Biomed 2021, Vol 9, Page 114. 2021 Jan 26;9(2):114.

209. Zhong Y, Goltsche K, Cheng L, Xie F, Meng F, Deng C, et al. Hyaluronic acid-shelled acid-activatable paclitaxel prodrug micelles effectively target and treat CD44-overexpressing human breast tumor xenografts in vivo. Biomaterials. 2016 Apr;84:250–61.

210. Li J, Li M, Tian L, Qiu Y, Yu Q, Wang X, et al. Facile strategy by hyaluronic acid functional carbon dot-doxorubicin nanoparticles for CD44 targeted drug delivery and enhanced breast cancer therapy. Int J Pharm. 2020 Mar;578:119122.

211. Rasines Mazo A, Allison-Logan S, Karimi F, Chan NJ-A, Qiu W, Duan W, et al. Ring opening polymerization of α-amino acids: advances in synthesis, architecture and applications of polypeptides and their hybrids. Chem Soc Rev. 2020;49(14):4737–834.

212. Song Z, Han Z, Lv S, Chen C, Chen L, Yin L, et al. Synthetic polypeptides: from

polymer design to supramolecular assembly and biomedical application. Chem Soc Rev. 2017;46(21):6570–99.

213. Song Z, Tan Z, Cheng J. Recent Advances and Future Perspectives of Synthetic Polypeptides from N -Carboxyanhydrides. Macromolecules. 2019 Nov 26;52(22):8521–39.

214. Jaradat DMM. Thirteen decades of peptide synthesis: key developments in solid phase peptide synthesis and amide bond formation utilized in peptide ligation. Amino Acids. 2018 Jan 28;50(1):39–68.

215. Mandal BM. Ring-Opening Polymerization and Ring-Opening Metathesis Polymerization. In: Fundamentals of Polymerization. WORLD SCIENTIFIC; 2013. p. 323–71.

216. Conejos-Sánchez I, Cardoso I, Oteo-Vives M, Romero-Sanz E, Paul A, Sauri AR, et al. Polymer-doxycycline conjugates as fibril disrupters: An approach towards the treatment of a rare amyloidotic disease. J Control Release. 2015 Jan 28;198:80–90.

217. Cuesta CM, Ibañez F, Lopez-Hidalgo R, Ureña J, Duro-Castano A, Armiñán A, et al. A targeted polypeptide-based nanoconjugate as a nanotherapeutic for alcohol-induced neuroinflammation. Nanomedicine Nanotechnology, Biol Med. 2021 Jun 1;34:102376.

218. Barz M, Duro-Castano A, Vicent MJ. A versatile post-polymerization modification method for polyglutamic acid: synthesis of orthogonal reactive polyglutamates and their use in "click chemistry." Polym Chem. 2013 Apr 24;4(10):2989.

219. Córdoba-David G, Duro-Castano A, Castelo-Branco RC, González-Guerrero C, Cannata P, Sanz AB, et al. Effective Nephroprotection Against Acute Kidney Injury with a Star-Shaped Polyglutamate-Curcuminoid Conjugate. Sci Rep. 2020 Dec 1;10(1):1–15.

220. Duro-Castano A, Lim NH, Tranchant I, Amoura M, Beau F, Wieland H, et al. In Vivo Imaging of MMP-13 Activity Using a Specific Polymer-FRET Peptide Conjugate Detects Early Osteoarthritis and Inhibitor Efficacy. Adv Funct Mater. 2018 Sep 12;28(37):1802738.

221. Cheah HY, Gallon E, Dumoulin F, Hoe SZ, Japundžić-Žigon N, Glumac S, et al. Near-Infrared Activatable Phthalocyanine-Poly-L-Glutamic Acid Conjugate: Enhanced in Vivo Safety and Antitumor Efficacy toward an Effective Photodynamic Cancer Therapy. Mol Pharm. 2018 Jul 2;15(7):2594–605.

222. Duro-Castano A, Nebot VJ, Niño-Pariente A, Armiñán A, Arroyo-Crespo JJ, Paul A, et al. Capturing "Extraordinary" Soft-Assembled Charge-Like Polypeptides as a Strategy for Nanocarrier Design. Adv Mater. 2017 Oct;29(39):1702888.

223. Niño-Pariente A, Armiñán A, Reinhard S, Scholz C, Wagner E, Vicent MJ. Design of Poly- <scp>l</scp> -Glutamate-Based Complexes for pDNA Delivery. Macromol Biosci. 2017 Oct 1;17(10):1700029.

224. Kiew LV, Cheah HY, Voon SH, Gallon E, Movellan J, Ng KH, et al. Near-infrared activatable phthalocyanine-poly-L-glutamic acid conjugate: increased cellular uptake and light–dark toxicity ratio toward an effective photodynamic cancer therapy. Nanomedicine Nanotechnology, Biol Med. 2017 May 1;13(4):1447–58.

225. Arroyo Crespo JJ. Polymer-based combination conjugates for the treatment of triple negative breast cancer : From rational design to preclinical evaluation. University of Valencia; 2018.

226. Conejos-Sánchez I, Duro-Castano A, Birke A, Barz M, Vicent MJ. A controlled and

versatile NCA polymerization method for the synthesis of polypeptides. Polym Chem. 2013;4(11):3182.

227. Duro-Castano A, England RM, Razola D, Romero E, Oteo-Vives M, Morcillo MA, et al. Well-defined star-shaped polyglutamates with improved pharmacokinetic profiles as excellent candidates for biomedical applications. Mol Pharm. 2015 Oct 5;12(10):3639–49.

228. Zagorodko O, Nebot VJ, Vicent MJ. The generation of stabilized supramolecular nanorods from star-shaped polyglutamates. Polym Chem. 2020 Feb 11;11(6):1220–9.

229. Duro-Castano A, Borrás C, Herranz-Pérez V, Blanco-Gandía MC, Conejos-Sánchez I, Armiñán A, et al. Targeting Alzheimer's disease with multimodal polypeptide-based nanoconjugates. Sci Adv. 2021 Mar 26;7(13):eabf9180.

230. Dang W, Daviau T, Ying P, Zhao Y, Nowotnik D, Clow CS, et al. Effects of GLIADEL® wafer initial molecular weight on the erosion of wafer and release of BCNU. J Control Release. 1996 Oct 1;42(1):83–92.

231. Inoue T, Yamashita Y, Nishihara M, Sugiyama S, Sonoda Y, Kumabe T, et al. Therapeutic efficacy of a polymeric micellar doxorubicin infused by convection-enhanced delivery against intracranial 9L brain tumor models. Neuro Oncol. 2009 Apr 1;11(2):151–7.

232. Aryal M, Arvanitis CD, Alexander PM, McDannold N. Ultrasound-mediated blood–brain barrier disruption for targeted drug delivery in the central nervous system. Adv Drug Deliv Rev. 2014 Jun 15;72:94–109.

233. Parodi A, Rudzińska M, Deviatkin A, Soond S, Baldin A, Zamyatnin A. Established and Emerging Strategies for Drug Delivery Across the Blood-Brain Barrier in Brain Cancer. Pharmaceutics. 2019 May 24;11(5):245.

234. Aryal M, Vykhodtseva N, Zhang Y-Z, Park J, McDannold N. Multiple treatments with liposomal doxorubicin and ultrasound-induced disruption of blood–tumor and blood–brain barriers improve outcomes in a rat glioma model. J Control Release. 2013 Jul;169(1–2):103–11.

235. Cheng Y, Morshed R, Cheng S-H, Tobias A, Auffinger B, Wainwright DA, et al. Nanoparticle-Programmed Self-Destructive Neural Stem Cells for Glioblastoma Targeting and Therapy. Small. 2013 Dec 20;9(24):4123–9.

236. Mooney R, Weng Y, Tirughana-Sambandan R, Valenzuela V, Aramburo S, Garcia E, et al. Neural stem cells improve intracranial nanoparticle retention and tumor-selective distribution. Futur Oncol. 2014 Feb;10(3):401–15.

237. Chapman CD, Frey WH, Craft S, Danielyan L, Hallschmid M, Schiöth HB, et al. Intranasal Treatment of Central Nervous System Dysfunction in Humans. Pharm Res. 2013 Oct 8;30(10):2475–84.

238. Khan AR, Liu M, Khan MW, Zhai G. Progress in brain targeting drug delivery system by nasal route. J Control Release. 2017 Dec;268:364–89.

239. Misra A, Kher G. Drug Delivery Systems from Nose to Brain. Curr Pharm Biotechnol. 2012 Oct 1;13(12):2355–79.

240. Illum L. Is nose-to-brain transport of drugs in man a reality? J Pharm Pharmacol. 2010 Feb 18;56(1):3–17.

241. Mistry A, Stolnik S, Illum L. Nose-to-Brain Delivery: Investigation of the Transport of Nanoparticles with Different Surface Characteristics and Sizes in Excised Porcine Olfactory Epithelium. Mol Pharm. 2015 Aug 3;12(8):2755–66.

242. Van Woensel M, Wauthoz N, Rosière R, Mathieu V, Kiss R, Lefranc F, et al. Development of siRNA-loaded chitosan nanoparticles targeting Galectin-1 for the treatment of glioblastoma multiforme via intranasal administration. J Control Release. 2016 Apr;227:71–81.

243. Tajes M, Ramos-Fernandez E, Weng-Jiang X, Bosch-Morato M, Guivernau B, Eraso-Pichot A, et al. The blood-brain barrier: structure, function and therapeutic approaches to cross it. Mol Membr Biol. 2014;31(5):152–67.

244. Vlieghe P, Khrestchatisky M. Medicinal Chemistry Based Approaches and Nanotechnology-Based Systems to Improve CNS Drug Targeting and Delivery. Med Res Rev. 2013 May;33(3):457–516.

245. Gao X, Li C. Nanoprobes Visualizing Gliomas by Crossing the Blood Brain Tumor Barrier. Small. 2014 Feb 1;10(3):426–40.

246. Batrakova E V., Kabanov A V. Pluronic block copolymers: Evolution of drug delivery concept from inert nanocarriers to biological response modifiers. J Control Release. 2008 Sep;130(2):98–106.

247. Pitto-Barry A, Barry NPE. Pluronic® block-copolymers in medicine: from chemical and biological versatility to rationalisation and clinical advances. Polym Chem. 2014 Mar 24;5(10):3291–7.

248. Kabanov A V., Batrakova E V., Alakhov VY. Pluronic® block copolymers for overcoming drug resistance in cancer. Adv Drug Deliv Rev. 2002 Sep;54(5):759–79.

249. Alakhova DY, Kabanov A V. Pluronics and MDR Reversal: An Update. Mol Pharm. 2014;11(8):2566–78.

250. Witt KA, Huber JD, Egleton RD, Davis TP. Pluronic P85 Block Copolymer Enhances Opioid Peptide Analgesia. J Pharmacol Exp Ther. 2002 Nov 1;303(2):760–7.

251. Batrakova E V., Vinogradov S V., Robinson SM, Niehoff ML, Banks WA, Kabanov A V. Polypeptide Point Modifications with Fatty Acid and Amphiphilic Block Copolymers for Enhanced Brain Delivery. Bioconjug Chem. 2005 Jul 1;16(4):793–802.

252. Banks WA, Gertler A, Solomon G, Niv-Spector L, Shpilman M, Yi X, et al. Principles of strategic drug delivery to the brain (SDDB): Development of anorectic and orexigenic analogs of leptin. Physiol Behav. 2011 Nov;105(1):145–9.

253. Price TO, Farr SA, Yi X, Vinogradov S, Batrakova E, Banks WA, et al. Transport across the Blood-Brain Barrier of Pluronic Leptin. J Pharmacol Exp Ther. 2010 Apr;333(1):253–63.

254. Yuan D, Yi X, Zhao Y, Poon C-D, Bullock KM, Hansen KM, et al. Intranasal delivery of N-terminal modified leptin-pluronic conjugate for treatment of obesity. J Control Release. 2017 Oct;263:172–84.

255. Yi X, Zimmerman MC, Yang R, Tong J, Vinogradov S, Kabanov A V. Pluronic-modified superoxide dismutase 1 attenuates angiotensin II-induced increase in intracellular superoxide in neurons. Free Radic Biol Med. 2010 Aug 15;49(4):548–58.

256. Batrakova E V., Miller DW, Li S, Alakhov VY, Kabanov A V., Elmquist WF. Pluronic P85 enhances the delivery of digoxin to the brain: in vitro and in vivo studies. J Pharmacol Exp Ther. 2001 Feb;296(2):551–7.

257. Meng X, Liu J, Yu X, Li J, Lu X, Shen T. Pluronic F127 and D-α-Tocopheryl Polyethylene Glycol Succinate (TPGS) Mixed Micelles for Targeting Drug Delivery across The Blood Brain Barrier. Sci Rep. 2017 Dec 7;7(1):2964.

258. Yin Y, Fu C, Li M, Li X, Wang M, He L, et al. A pH-sensitive hyaluronic acid prodrug modified with lactoferrin for glioma dual-targeted treatment. Mater Sci Eng C. 2016 Oct;67:159–69.

259. Kou L, Bhutia YD, Yao Q, He Z, Sun J, Ganapathy V. Transporter-Guided Delivery of Nanoparticles to Improve Drug Permeation across Cellular Barriers and Drug Exposure to Selective Cell Types. Front Pharmacol. 2018 Jan 26;9(JAN):27.

260. Aftimos PG, Milojkovic-Kerklaan B, Diéras V, Altintas S, Anders C, Arnedos M, et al. Abstract P6-16-04: Phase 1/2a study of glutathione PEGylated liposomal doxorubicin (2B3-101) in breast cancer patients with brain metastases. In: Poster Session Abstracts. American Association for Cancer Research; 2015. p. P6-16-04-P6-16–04.

261. Kerklaan BM, Jager A, Aftimos P, Dieras V, Altintas S, Anders C, et al. NT-23 * PHASE 1/2A STUDY OF GLUTATHIONE PEGYLATED LIPOSOMAL DOXORUBICIN (2B3-101) IN BREAST CANCER PATIENTS WITH BRAIN METASTASES (BCBM) OR RECURRENT HIGH GRADE GLIOMAS (HGG). Neuro Oncol. 2014 Nov 1;16(suppl 5):v163–v163.

262. Li J, Guo Y, Kuang Y, An S, Ma H, Jiang C. Choline transporter-targeting and co-delivery system for glioma therapy. Biomaterials. 2013 Dec;34(36):9142–8.

263. Johnsen KB, Burkhart A, Thomsen LB, Andresen TL, Moos T. Targeting the transferrin receptor for brain drug delivery. Prog Neurobiol. 2019 Oct;181:101665.

264. Johnsen KB, Burkhart A, Melander F, Kempen PJ, Vejlebo JB, Siupka P, et al. Targeting transferrin receptors at the blood-brain barrier improves the uptake of immunoliposomes and subsequent cargo transport into the brain parenchyma. Sci Rep. 2017 Dec 4;7(1):10396.

265. Loureiro J, Andrade S, Duarte A, Neves A, Queiroz J, Nunes C, et al. Resveratrol and Grape Extract-loaded Solid Lipid Nanoparticles for the Treatment of Alzheimer's Disease. Molecules. 2017 Feb 13;22(2):277.

266. Cabezón I, Manich G, Martín-Venegas R, Camins A, Pelegrí C, Vilaplana J. Trafficking of Gold Nanoparticles Coated with the 8D3 Anti-Transferrin Receptor Antibody at the Mouse Blood–Brain Barrier. Mol Pharm. 2015 Nov 2;12(11):4137–45.

267. Chang R, Knox J, Chang J, Derbedrossian A, Vasilevko V, Cribbs D, et al. Blood–Brain Barrier Penetrating Biologic TNF-α Inhibitor for Alzheimer's Disease. Mol Pharm. 2017 Jul 3;14(7):2340–9.

268. Sehlin D, Fang XT, Meier SR, Jansson M, Syvänen S. Pharmacokinetics, biodistribution and brain retention of a bispecific antibody-based PET radioligand for imaging of amyloid-β. Sci Rep. 2017 Dec 8;7(1):17254.

269. Syvänen S, Fang XT, Hultqvist G, Meier SR, Lannfelt L, Sehlin D. A bispecific Tribody PET radioligand for visualization of amyloid-beta protofibrils – a new concept for neuroimaging. Neuroimage. 2017 Mar;148:55–63.

270. Hultqvist G, Syvänen S, Fang XT, Lannfelt L, Sehlin D. Bivalent Brain Shuttle Increases Antibody Uptake by Monovalent Binding to the Transferrin Receptor. Theranostics. 2017;7(2):308–18.

271. Ding H, Inoue S, Ljubimov A V., Patil R, Portilla-Arias J, Hu J, et al. Inhibition of brain tumor growth by intravenous poly(-L-malic acid) nanobioconjugate with pH-dependent drug release. Proc Natl Acad Sci. 2010 Oct 19;107(42):18143–8.

272. Fujita M, Lee B-S, Khazenzon NM, Penichet ML, Wawrowsky KA, Patil R, et al. Brain tumor tandem targeting using a combination of monoclonal antibodies

attached to biopoly(β-l-malic acid). J Control Release. 2007 Oct;122(3):356–63.

273.   Liu S, Guo Y, Huang R, Li J, Huang S, Kuang Y, et al. Gene and doxorubicin co-delivery system for targeting therapy of glioma. Biomaterials. 2012 Jun 1;33(19):4907–16.

274.   Song M-M, Xu H-L, Liang J-X, Xiang H-H, Liu R, Shen Y-X. Lactoferrin modified graphene oxide iron oxide nanocomposite for glioma-targeted drug delivery. Mater Sci Eng C. 2017 Aug;77:904–11.

275.   Xu Y, Asghar S, Yang L, Li H, Wang Z, Ping Q, et al. Lactoferrin-coated polysaccharide nanoparticles based on chitosan hydrochloride/hyaluronic acid/PEG for treating brain glioma. Carbohydr Polym. 2017 Feb;157:419–28.

276.   Elzoghby AO, Abdelmoneem MA, Hassanin IA, Abd Elwakil MM, Elnaggar MA, Mokhtar S, et al. Lactoferrin, a multi-functional glycoprotein: Active therapeutic, drug nanocarrier & targeting ligand. Biomaterials. 2020 Dec 1;263:120355.

277.   Uchida Y, Ohtsuki S, Katsukura Y, Ikeda C, Suzuki T, Kamiie J, et al. Quantitative targeted absolute proteomics of human blood-brain barrier transporters and receptors. J Neurochem. 2011 Apr;117(2):333–45.

278.   Daneman R, Zhou L, Agalliu D, Cahoy JD, Kaushal A, Barres BA. The Mouse Blood-Brain Barrier Transcriptome: A New Resource for Understanding the Development and Function of Brain Endothelial Cells. Ikezu T, editor. PLoS One. 2010 Oct 29;5(10):e13741.

279.   Candela P, Saint-Pol J, Kuntz M, Boucau M-C, Lamartiniere Y, Gosselet F, et al. In vitro discrimination of the role of LRP1 at the BBB cellular level: Focus on brain capillary endothelial cells and brain pericytes. Brain Res. 2015 Jan 12;1594:15–26.

280.   Demeule M, Currie J-C, Bertrand Y, Ché C, Nguyen T, Régina A, et al. Involvement of the low-density lipoprotein receptor-related protein in the transcytosis of the brain delivery vector Angiopep-2. J Neurochem. 2008 Aug;106(4):1534–44.

281.   Demeule M, Beaudet N, Régina A, Besserer-Offroy É, Murza A, Tétreault P, et al. Conjugation of a brain-penetrant peptide with neurotensin provides antinociceptive properties. J Clin Invest. 2014 Mar 3;124(3):1199–213.

282.   Ke W, Shao K, Huang R, Han L, Liu Y, Li J, et al. Gene delivery targeted to the brain using an Angiopep-conjugated polyethyleneglycol-modified polyamidoamine dendrimer. Biomaterials. 2009 Dec;30(36):6976–85.

283.   Lachowicz J, Demeule M, Regina A, Boivin D, Larocque A, Tripathy S, et al. Brain-penetrant lysosomal enzymes constructed by fusion with Angiopep-2, a unique LRP-1 binding peptide. Mol Genet Metab. 2013 Feb 1;108(2):S57.

284.   Regina A, Demeule M, Tripathy S, Lord-Dufour S, Currie JC, Iddir M, et al. ANG4043, a novel brain-penetrant peptide-mAb conjugate, is efficacious against HER2-positive intracranial tumors in mice. Mol Cancer Ther. 2015 Jan 1;14(1):129–40.

285.   Ché C, Yang G, Thiot C, Lacoste MC, Currie JC, Demeule M, et al. New angiopep-modified doxorubicin (ANG1007) and etoposide (ANG1009) chemotherapeutics with increased brain penetration. J Med Chem. 2010 Apr 8;53(7):2814–24.

286.   Régina A, Demeule M, Ché C, Lavallée I, Poirier J, Gabathuler R, et al. Antitumour activity of ANG1005, a conjugate between paclitaxel and the new brain delivery vector Angiopep-2. Br J Pharmacol. 2008 Sep;155(2):185–97.

287.   Gao S, Tian H, Xing Z, Zhang D, Guo Y, Guo Z, et al. A non-viral suicide gene delivery system traversing the blood brain barrier for non-invasive glioma targeting treatment. J Control Release. 2016 Dec 10;243:357–69.

288. Huang S, Li J, Han L, Liu S, Ma H, Huang R, et al. Dual targeting effect of Angiopep-2-modified, DNA-loaded nanoparticles for glioma. Biomaterials. 2011 Oct;32(28):6832–8.

289. An S, He D, Wagner E, Jiang C. Peptide-like Polymers Exerting Effective Glioma-Targeted siRNA Delivery and Release for Therapeutic Application. Small. 2015 Oct;11(38):5142–50.

290. Palmieri D, Bronder JL, Herring JM, Yoneda T, Weil RJ, Stark AM, et al. Her-2 Overexpression Increases the Metastatic Outgrowth of Breast Cancer Cells in the Brain. Cancer Res. 2007 May 1;67(9):4190–8.

291. Khan NU, Ni J, Ju X, Miao T, Chen H, Han L. Escape from abluminal LRP1-mediated clearance for boosted nanoparticle brain delivery and brain metastasis treatment. Acta Pharm Sin B. 2021 May 1;11(5):1341–54.

CHAPTER 2. STAR-SHAPED POLYGLUTAMATE-BASED COMBINATION CONJUGATES FOR METASTATIC TRIPLE NEGATIVE BREAST CANCER TREATMENT

2.1. Introduction and Background

Breast cancer represents the most frequently diagnosed cancer worldwide (1). Accounting for approximately 15% of all breast tumors (2,3), triple negative breast cancer (TNBC) is the most aggressive breast cancer molecular subtype. Overall, TNBC suffers from the worst prognosis (4) and an earlier and higher rate of recurrence and distant metastasis (3,5). At the molecular level, the lack of expression of estrogen receptor (ER), progesterone receptor (PR), and human epidermal growth factor receptor 2 (HER2) characterizes TNBC (4,6,7). For this reason, TNBC patients have not benefited from advances in endocrine and HER2-targeted therapies that have increased survival rates in other subtypes (5,8,9). Even given huge research/clinical efforts devoted to the development of new therapies, the treatment of TNBC still relies on the administration of chemotherapeutics that induce severe side effects (10,11).

TNBC commonly metastasizes to the lungs and brain (12), with affected patients displaying a median survival rate of 12-18 months (3). The treatment for metastatic TNBC is considered palliative rather than therapeutic and usually comprises the sequential administration of chemotherapeutics (often in combination) until the patient displays maximal response or maximal tolerance (13–15). Thus, the clinical management of metastatic TNBC remains a critical unmet clinical need. To this end, we synthesized, characterized, and biologically evaluated a new family of polymer-drug combination conjugates for the treatment of metastatic TNBC.

Polymer-drug conjugates as drug delivery systems (DDSs) are obtained through the conjugation of a bioactive therapeutic agent (i.e., a drug) to a polymeric carrier (16,17). As proposed by Ringsdorf in 1975 (18), polymer-drug conjugates minimally comprise a water-soluble polymeric carrier with a therapeutic agent attached through a cleavable linker; however, they can optionally carry an active targeting moiety. The nanoscale size of conjugates combined with the rational design of the covalent drug

linkage offers unique advantages, such as (i) an increment in the water solubility of the drug (19,20), (ii) passive targeting in solid tumors due to the enhanced permeability and retention (EPR) effect (21), (iii) the ability to cross biological barriers and overcome chemoresistance (22,23), (iv) improved pharmacokinetics due to the controlled release of the drugs achieved by rational selection of a stimuli-responsive linker and polymer (19,24), and (v) the capacity to accommodate several therapeutic agents, probes, and/or targeting moieties, allowing for combination therapy, theranostics, and active targeting, respectively (25,26).

Using polypeptides as the polymeric carrier provides additional advantages, including their inherent biocompatibility and biodegradability mediated by the amide bonds forming the polypeptide backbone (27). Together with their high versatility, these advantages have prompted a dramatic increase in the application of polypeptides in DDSs (28). As a prime example, poly L-glutamic acid (PGA) has a proven versatility that allows for the conjugation of a wide variety of molecules (29–40), a trait of crucial importance when designing combination therapies. PGA supports the conjugation of combinations of drugs of differing chemical characteristics at controlled ratios (34,37,41). The versatility of PGA also allows for the use of myriad stimuli-responsive orthogonal linkers, thereby supporting the specific release of conjugated drug combinations in response to distinct stimuli. This strategy enables the optimization of drug release, a key aspect in the design of combination therapies (37).

The development of controlled polymerization techniques has allowed the large-scale synthesis of PGA-based nanosystems with different topologies in a controlled and straightforward manner (42). Previous research has demonstrated that a three-armed star-shaped PGA (St-PGA) as the starting material for combination conjugate design supports increased cell uptake, prolonged half-lives, and more significant organ accumulation in mice compared to linear PGA (of a similar molecular weight) (43). Overall,

144

together with the inherent biodegradability, safety, and versatility of PGA, the advantages of the star-shaped architecture make St-PGA an excellent nanocarrier for advanced DDSs for TNBC treatment.

In this work, we focused on the synergistic combination of doxorubicin (Dox) and dasatinib (Das) previously described in the human MDA-MB-231 TNBC cell line (44). The anthracycline drug Dox, one of the most potent chemotherapeutic agents in routine clinical use, intercalates DNA to inhibit topoisomerase I and II and induce programmed cell death. Dox has been employed to treat multiple cancer types, including cervical cancer, prostate cancer, lung cancer, and breast cancer (45). Das is an inhibitor of SRC and SRC-family tyrosine kinases, which are critical regulators in cell proliferation, growth, migration, differentiation, and death. Das has been approved to treat chronic myeloid leukemia and Philadelphia chromosome-positive acute lymphoblastic leukemia (46).

Previous work performed by our group (41) with MDA-MB-231-Luc cell line (an MDA-MB-231 cell line stably expressing luciferase) revealed that a combination of Dox with Das at ratio 1:5 with a 24 h delay in Das administration provided for the most significant synergistic therapeutic effect. Therefore, we aimed to optimize the linking chemistry used for Das conjugation to a linear PGA (100 glutamic acid units, 12900 Da); overall, we found that conjugation through an ester bond with a valine (Val) spacer reduced Das release sufficiently. The creation of a combination conjugate by additionally binding Dox through a pH-labile hydrazone (hyd) linker to the same polymeric backbone (1:1 ratio) demonstrated robust *in vitro* antitumor activity and effectively reduced the primary tumor and lung metastasis in an orthotopic *in vivo* mouse model of metastatic TNBC (41).

In the hope of further improving this strategy, we synthesized St-PGA analogs of the previously described conjugates using a hydrazone linker to conjugate Dox and an ester bond (with and without the Val spacer) for Das. We hypothesized that the increased circulation time observed for St-PGA

145

compared to linear PGA (43) would improve the anti-tumor and anti-metastatic activity observed for the linear combination conjugate. We performed exhaustive physico-chemical and biological characterization steps to choose the optimal combination of drug ratio and linker, with the final aim to develop an efficient treatment for metastatic TNBC.

2.2. Results and Discussion

2.2.1. Synthesis and Characterization of St-PGA

2.2.1.1. St-PGA Synthesis

The synthesis of a well-defined water-soluble polypeptide macromolecule represents the first and perhaps most crucial step in developing polypeptide-drug conjugates. The most common methods for the generation of synthetic polypeptides include solid-phase peptide synthesis (SPPS), recombinant peptide synthesis, and ring-opening polymerization (ROP) of α-N-carboxyanhydrides (NCA) (27,47). SPPS and recombinant peptide synthesis yield monodisperse polypeptides with precise sequence control (47); however, these approaches suffer from several limitations that hinder their application at a large/industrial scale. SPPS is limited to the generation of short peptides (typically < 50 amino acids) and requires several isolation and purification steps that dramatically reduce the yield. Meanwhile, recombinant peptide synthesis generates high molecular weight polypeptides; however, this approach is limited to natural amino acids and requires specialized equipment for large-scale synthesis (both time- and cost-intensive) (27,47). ROP of NCA supports the synthesis of large quantities of high molecular weight (> 50 amino acids) homo- and block- co-polymers with precise control over molecular weight, architecture, polydispersity, and end-group in a straightforward and economical manner (27,48). With more than 200 associated monomers described in the literature (27), ROP of NCA offers an additional level of chemical complexity that

supports the incorporation of non-natural residues into the peptide sequence (47). Altogether, these advantages make the ROP of NCA an invaluable tool for the synthesis of polypeptides for DDS development.

Traditionally, the initiation of ROP of NCA has employed primary amines (27). The classic amine-initiated ROP of NCA can proceed via two mechanisms – the normal amine mechanism (NAM) and the activated monomer mechanism (AMM) (27,42,49). In NAM, polymerization commences with the nucleophilic attack of the amine initiator, which will form part of the final polymer. In AMM, the initiator acts as a base, deprotonating the monomer from which the polymer will grow, which precludes the initiator from the final product (27,49). These mechanisms can coincide and compete, which reduces control over molecular weight and molecular weight distribution of the final product (27,42).

We used amine tetrafluoroborate salt initiators to aid control over the amine-initiated polymerization process. These initiators increase control over the polymerization process to reduce the undesirable AMM in two ways. First, the equilibrium between the dormant protonated amine salt and the active amine site diminishes the activation of the monomer by deprotonation (27,49) (**Scheme 2.1**). Second, the non-nucleophilic nature of the tetrafluoroborate anion avoids activated monomer re-protonation during polymerization (42). This increased control over the polymerization process enables the synthesis of well-defined high molecular weight polypeptides.

We synthesized a three-armed St-PGA (our starting material) by ROP of NCA using the 1,3,5-(benzenetricarbonyltris(azanediyl))-triethanammonium BF_4 non-nucleophilic salt as initiator, following a protocol previously described by our group (42). The synthesis of the three-armed initiator consists of two synthetic steps (**Scheme 2.2**). We introduced three amino groups using a coupling reaction of N-Boc-ethylenediamine and 1,2,3-benzenetricarbonyl chloride in the first reaction. We evaluated the identity of the Boc-protected initiator by ^{1}H-NMR (**Supplementary Figure 2.1**).

Integration of the signals corresponding to the benzene tricarbonyl core (8.43 ppm, three protons), the ethyl arms (3.43-3.01 ppm, 12 protons), and the Boc protecting groups (1.40 ppm, 27 protons) confirmed the success of the reaction.
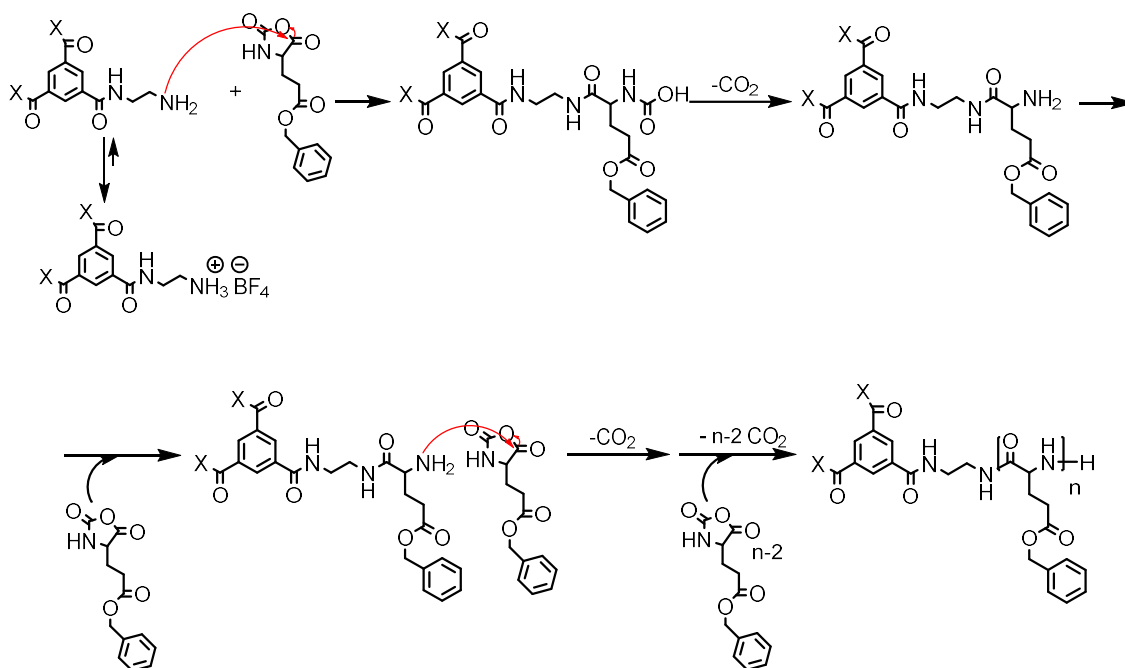
Scheme 2.1. Ring-opening polymerization (ROP) of α-N-carboxyanhydrides (NCA) mechanism for 1,3,5-(benzenetricarbonyltris(azanediyl))-triethanammonium BF$_4$ salt initiator and y-benzyl L-glutamate N-carboxyanhydride monomer.
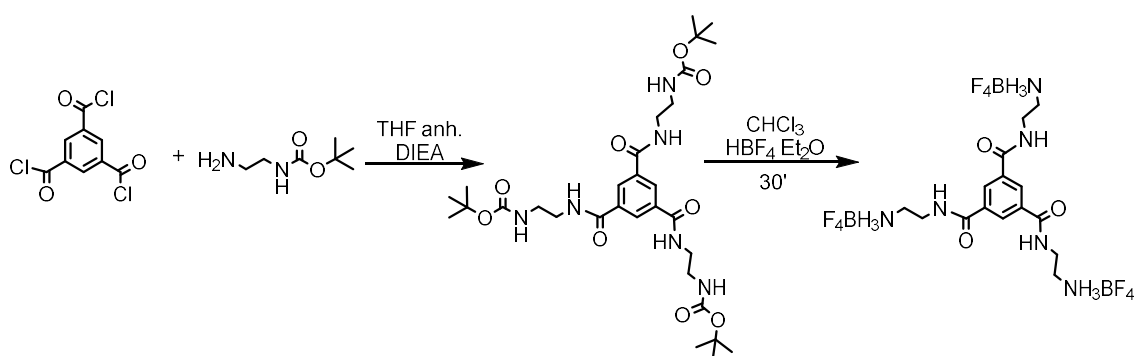
Scheme 2.2. Synthesis of the three-arm ethyl-based ammonium tetrafluoroborate initiator 1,3,5-(benzenetricarbonyltris(azanediyl))-triethanammonium BF$_4$ salt. HBF$_4$·Et$_2$O: tetrafluoroboric acid diethyl ether. THF: tetrahydrofuran. DIEA: N,N-diisopropylethylamine.

In the second reaction, we removed the Boc protecting groups to obtain the tetrafluoroborate (BF_4) salt in the same step (**Scheme 2.2**). The absence of the signal at 1.50 ppm in the ^{1}H-NMR spectrum confirmed the complete deprotection of the initiator exposing the amino group (**Supplementary Figure 2.2A**). The presence of one single signal in the ^{19}F-NMR spectrum confirmed the obtention of the tetrafluoroborate salt (**Supplementary Figure 2.2B**).

Using the three-armed 1,3,5-(benzenetricarbonyltris(azanediyl))-triethanammonium BF_4 initiator, we synthesized star-poly(γ-benzyl L-glutamate) (St-PBLG) by polymerizing the γ-benzyl protected NCA of glutamic acid. We determined the degree of polymerization (DP) by ^{1}H-NMR by comparing the signal of the benzene tricarbonyl initiator at 8.73 ppm with the α-carbon proton in the polypeptide backbone at 4.7 ppm (**Figure 2.1**). The obtained value of 171 indicated the presence of 57 glutamic acid units per arm. We then deprotected St-PBLG in an HBr/TFA mixture to yield St-PGA. The disappearance of the peak of the benzyl groups at 7.3 ppm confirmed complete polymer deprotection (**Figure 2.2**).
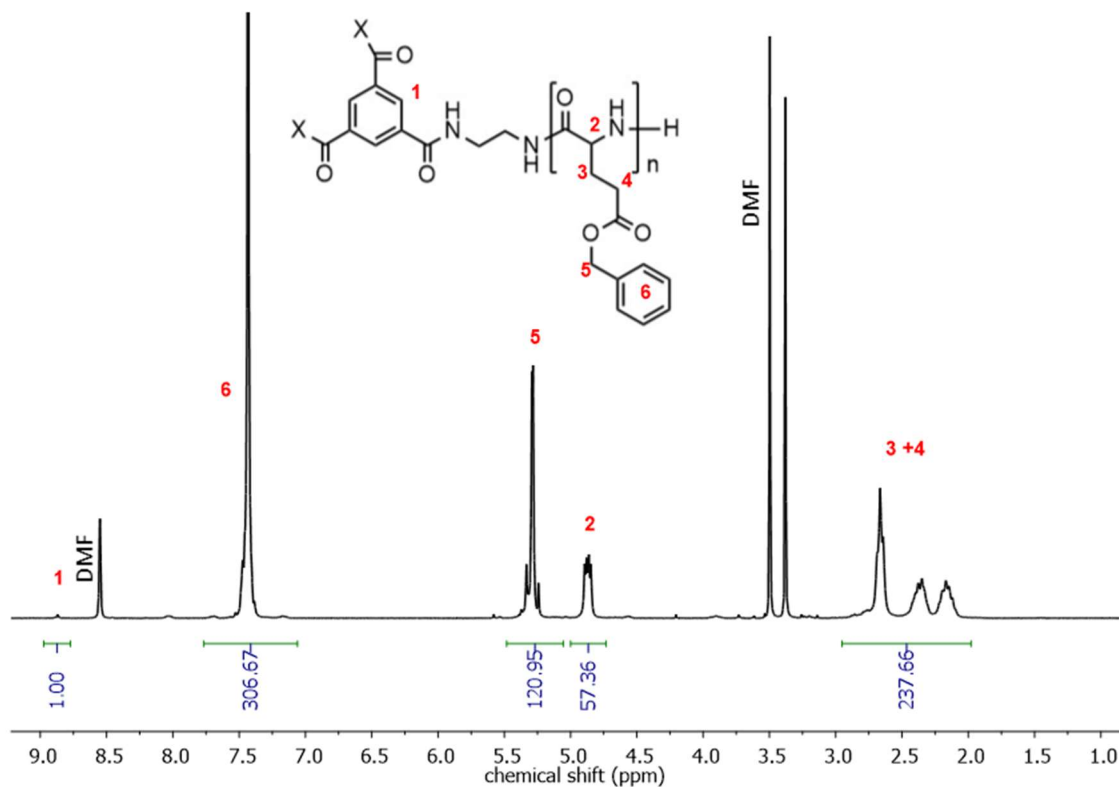
Figure 2.1. ^{1}H-NMR (TFA-d) spectrum of star-poly(γ-benzyl L-glutamate) (St-PBLG). Signals from the benzenetricarbonyl initiator (1) and the α-carbon proton in the polypeptide backbone (2) were used to determine the DP of the polypeptide, obtaining 171 units (57 glutamic acid units per arm).
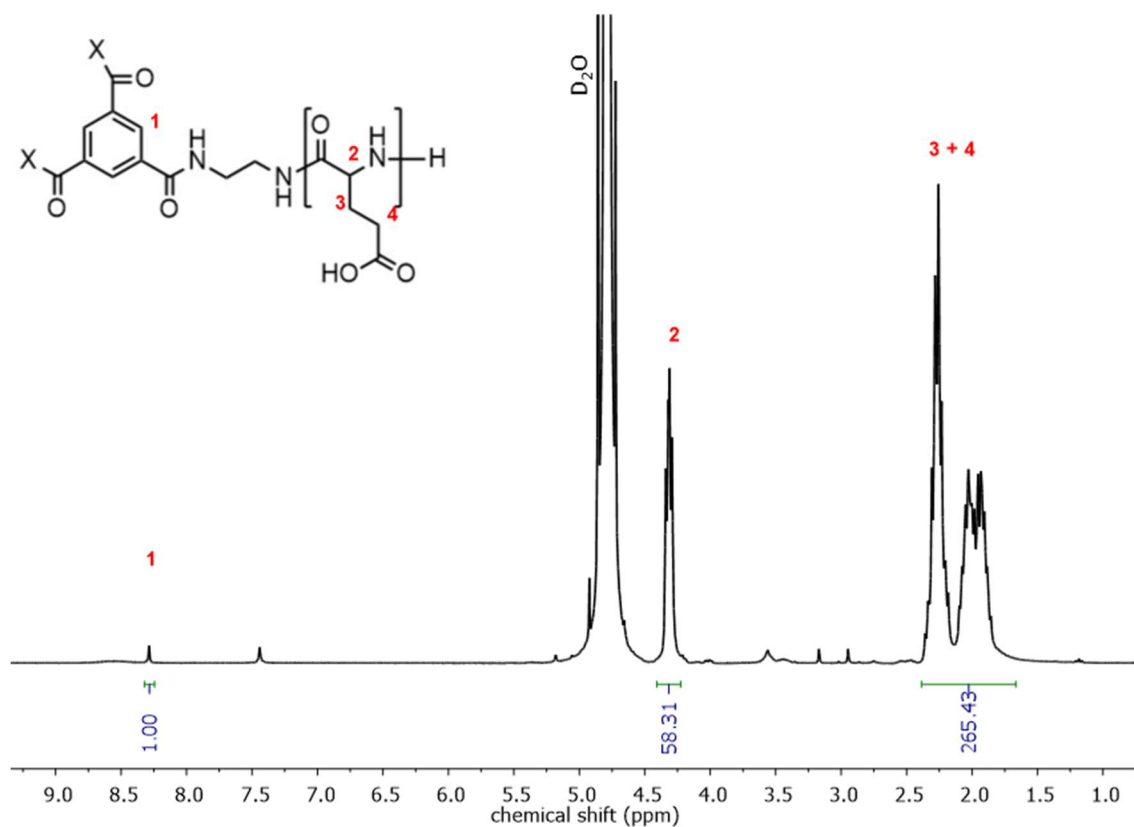
Figure 2.2. ^{1}H-NMR (D_2O) spectrum of star-poly glutamic acid (St-PGA). The spectrum confirms the complete removal of the benzyl protecting groups.

2.2.1.2. Physico-chemical Characterization of St-PGA

We obtained St-PGA's water-soluble sodium salt form by adding sodium bicarbonate in water and subsequent desalting by ultrafiltration. We used the salt form of St-PGA for basic polymer characterization before moving to drug conjugation. Size exclusion chromatography (SEC) studies performed using 10 mM phosphate buffer (PB) as the mobile phase displayed a single homogeneous molecular weight distribution of the polymer as shown by the multi-angle light scattering (MALS) and refractive index (RI) detectors (**Figure 2.3A**). The RI detector can also detect the presence of the sodium counterion eluting at 21 min (**Figure 2.3A**).

151
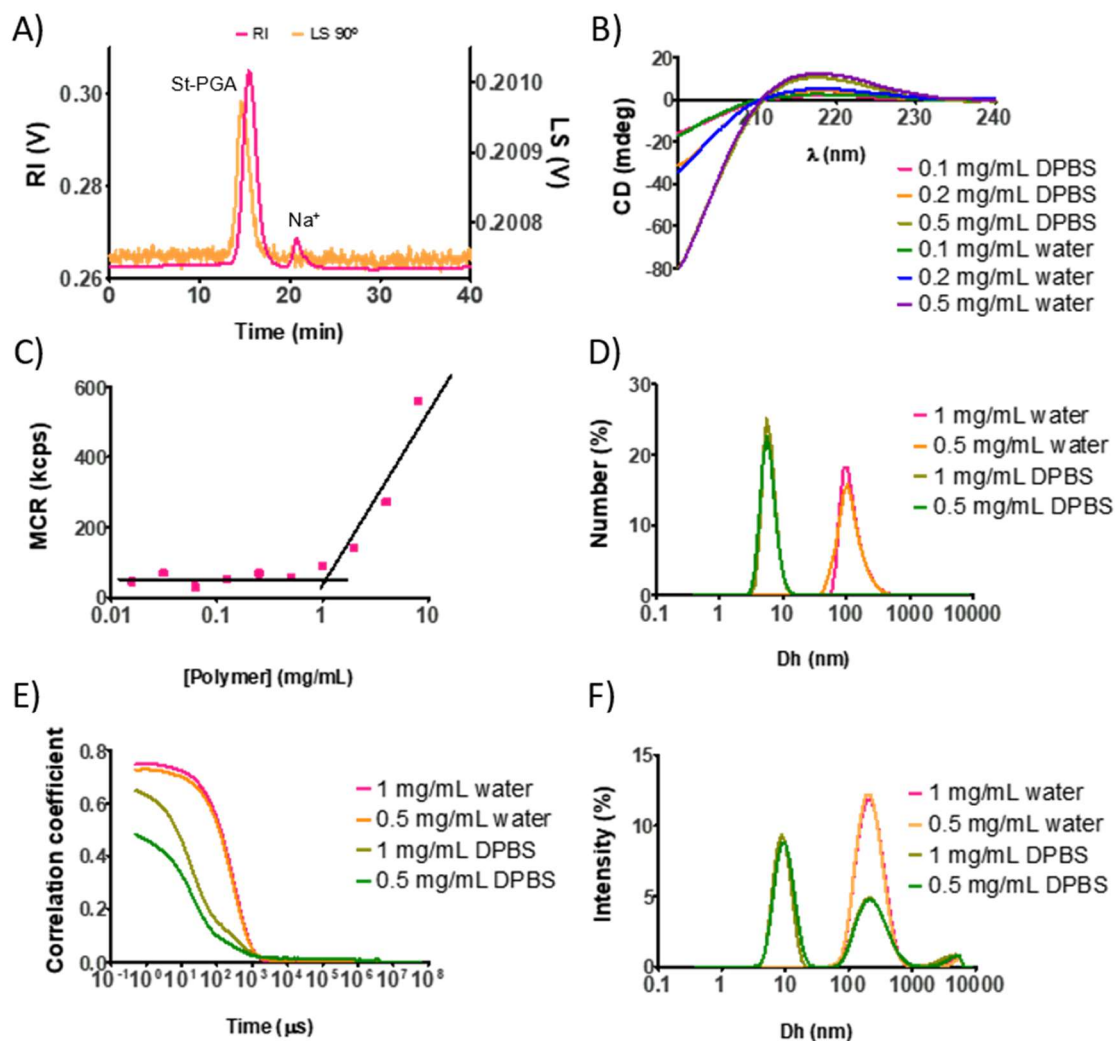
Figure 2.3. Characterization of St-PGA. (**A**) Representative SEC chromatogram - refractive index (RI) and light scattering detector at 90º (LS 90º). The peak at 21 min by RI corresponds to sodium counter-cation of PGA. (**B**) Circular dichroism (CD) profile obtained in relevant aqueous media - DPBS (Dulbecco's phosphate-buffered saline) and MilliQ water, at 0.1, 0.2, and 0.5 mg/mL St-PGA. Average results with three accumulated measurements displayed. (**C**) Graphical determination of the critical aggregation concentration (CAC) by dynamic light scattering (DLS). Data represented as average mean count rate (MCR) of two measurements vs. St-PGA concentration (logarithmic scale). (**D**) Size distribution by number in MilliQ water and DPBS obtained by DLS at 0.5 and 1 mg/mL St-PGA. (**E**) The correlation functions of DLS measurements. (**F**) Size distribution by intensity in MilliQ water and DPBS obtained by DLS at 0.5 and 1 mg/mL St-PGA. Average result obtained from at least five measurements displayed for each condition.

Circular dichroism (CD) provides valuable information regarding the spatial conformation of polypeptides in solution. Peptide bonds absorb light in the region below 240 nm due to n → π (220 nm) and π → π* (190 nm) transitions providing information regarding the secondary structure of the

polypeptide (50). The water-soluble salt form of PGA typically displays a random coil conformation characterized by a negative band at 200 nm in the CD spectrum (38,42,43,51,52). St-PGA displayed a similar profile in MilliQ water and DPBS at 0.1, 0.2, and 0.5 mg/mL, thereby providing evidence of random coil conformation in aqueous media (**Figure 2.3B**).

Zeta potential analysis of polypeptides provides information regarding the surface charge, a parameter of crucial relevance for DDSs. Electrophoretic light scattering (ELS) determines the zeta potential by applying an electric field to a polypeptide solution and measuring the velocity of the moving particles by light scattering (53). We determined the zeta potential of St-PGA by ELS, finding a value of -42.6 mV at 1 mg/mL of polymer in 1 mM KCl, in agreement with previously reported data (38).

St-PGA molecules self-assemble into large spherical structures in non-salty aqueous solutions in a concentration-dependent manner (200 nm diameter for the self-assembled structure vs. 10 nm for the unimer). Structures can then disassemble upon an increase in the solution's ionic strength (38). Ionic interactions drive this self-assembly behavior (38,54–56). In non-salty aqueous solutions, highly-charged polyelectrolytes induce electrostatic attraction and counterion binding to the polyelectrolyte backbone (counterion condensation) (54). Counterion adsorption to the polyelectrolyte leads to the formation of a strong transient dipole that interacts with a parallel or antiparallel dipole attractively, forming transient crosslinking points that support the self-assembly/aggregation of polyelectrolyte chains (St-PGA in our case). The critical aggregation concentration (CAC) acts as a transition point; for concentrations above the CAC, the aggregation process takes place, and the aggregate number and size increase with polymer concentration. This behavior disappears upon an increment in the solution's salt content, which prompts aggregate disruption (56).

We determined the CAC of St-PGA to confirm that our starting material also holds the capacity to form self-assembled structures in water as a means to prove its identity and purity (e.g., salt content). We prepared samples of St-PGA in MilliQ water at increasing polymer concentrations (0.02 to 8 mg/mL) and measured the scattered light by mean count rate (MCR) using dynamic light scattering (DLS) with fixed measurement parameters, then plotted the MCR values in kilo counts per second (kcps) versus the logarithm of sample concentration. The first part of the graph, representing lower polymer concentrations, corresponded to the presence of St-PGA unimers (thereby providing lower MCR values), which fitted to a linear equation with a low slope. The second part of the graph, representing higher polymer concentrations, corresponded to the formation of aggregates (thereby providing higher MCR values), which fitted to a linear equation with a higher slope. We graphically obtained the CAC value from the intersections of the linear fittings. With this method, we obtained a CAC value of ~1 mg/mL (**Figure 2.3C**), higher than the previously reported CAC value for St-PGA with similar DP (i.e., 0.5 mg/mL) (38).

We measured St-PGA hydrodynamic diameter by DLS in high ionic strength media (i.e., DPBS) and MilliQ water, using two polymer concentrations (i.e., 0.5 and 1 mg/mL). In MilliQ water, we observed a hydrodynamic diameter of ~125 nm for both concentrations evaluated according to the number-weighted size distribution (**Figure 2.3D**), similar to that reported in the literature for St-PGAs of similar molecular weight under the same conditions (38). The subsequent analysis in DPBS revealed a significantly smaller diameter (~6 nm) at both concentrations (**Figure 2.3D**), a similar size compared to values reported in the literature for St-PGAs of a similar molecular weight in high ionic strength media (43). Considering the CAC, we expected St-PGA to appear in a non-aggregated state in concentrations below 1 mg/mL; thus, we attribute the observation of a larger size in MilliQ water than in DPBS to the effect of high salt concentration in the buffer, which neutralizes the negatively charged carboxyl groups,

reduces the repulsion between glutamic acid units, and allows PGA chains to contract (57). The correlation functions of both measurements in MilliQ water possessed acceptable quality with an intercept of ~0.8 and exponential decay; however, the measurements in DPBS possessed lower intercepts and a non-pure exponential decay (**Figure 2.3E**), reflecting the poor quality of the measurement, probably due to the presence of more than one particle population in the sample and/or a suboptimal particle concentration (considering the small particle size obtained in DPBS) (58). When evaluating the hydrodynamic diameter of St-PGA by intensity, we observed two populations in DPBS - one population with a small diameter (~9 nm) and a second with a much larger diameter of ~240 nm (**Figure 2.3F**). In MilliQ water, we observed only the second larger population (**Figure 2.3F**). These results suggest that a small percentage of the St-PGA molecules aggregate in DPBS despite the high ionic strength of the media, therefore showing the second population by intensity.

In summary, we successfully obtained the St-PGA polypeptide material for our subsequent combination conjugates. Characterization confirmed the physico-chemical characteristics of St-PGA, i.e., random coil conformation and self-assembly capacity in aqueous media, negative zeta potential, and monomodal molecular weight distribution. With this information, we can evaluate the effect of drug loading and linking chemistry in St-PGA by comparing the characterization of the single-drug and combination conjugates described in the following sections.

2.2.2. Synthesis and Characterization of Star-poly(glutamic acid)-based Combination Conjugates and Single-drug Counterparts

We synthesized three St-PGA-based combination conjugates (**Table 2.1**) with Dox and Das using pH-labile linking moieties to support the controlled release of the drugs under acidic conditions (the tumor microenvironment and lysosomes). We conjugated Dox to St-PGA using a simple hydrazone linker. For Das, we explored two alternatives; (i) direct conjugation through an ester bond and (ii) the use of a Val spacer between the PGA backbone and the ester bond (based on prior work from our group (41)). We also synthesized single polymer-drug conjugates for comparative purposes (**Table 2.1**, **Scheme 2.3** for Das single-drug conjugates, **Scheme 2.4** for Dox single-drug conjugates, and **Scheme 2.5** for combination conjugates).

Table 2.1. Summary of the St-PGA-based single-drug and combination conjugates and their basic characteristics.

Compound	Dox linker	Das linker	Desired Dox loading (% mol)	Desired Das loading (% mol)	Desired Drug Ratio
St-PGA-Das	-	Ester	-	5	-
St-PGA-Val-Das	-	Valine-ester	-	5	-
St-PGA-hyd-Dox	Hydrazone	-	5	-	-
St-PGA-hyd-Dox_1-Val-Das_1	Hydrazone	Valine-ester	5	5	1:1
St-PGA-hyd-Dox_1-Das_1	Hydrazone	Ester	5	5	1:1
St-PGA-hyd-Dox_1-Das_{10}	Hydrazone	Ester	0.5	5	1:10
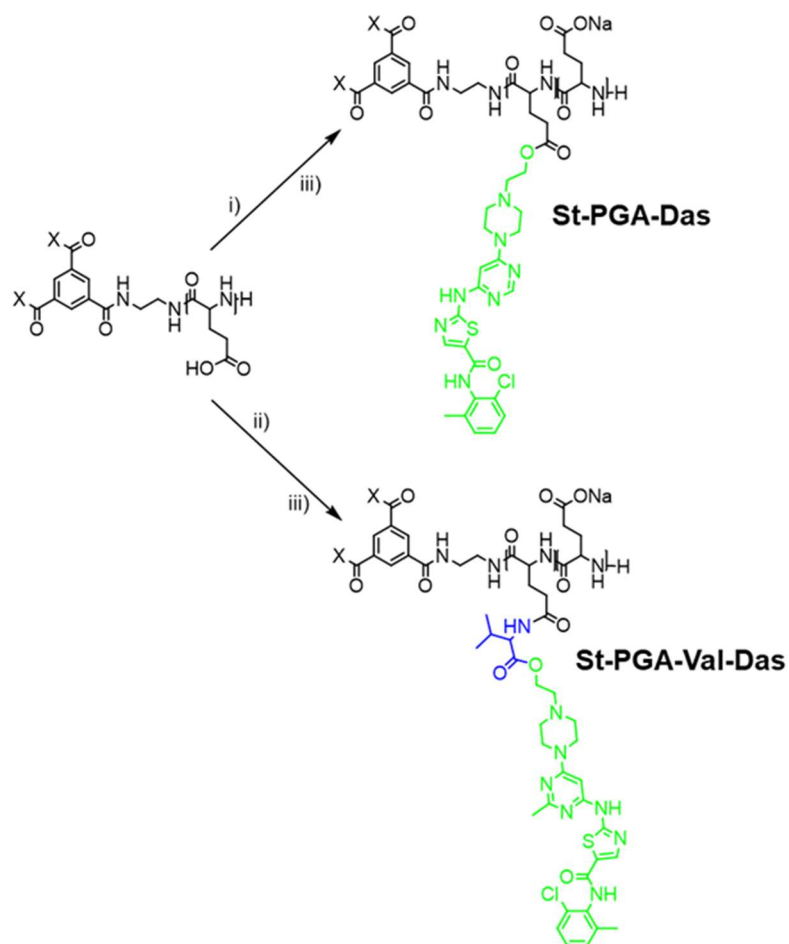
Scheme 2.3. Synthesis of Das conjugates. i) N,N'-Dimethylformamide (DMF) anhydrous, 4-dimethylaminopyridine (DMAP), 1-Ethyl-3-(3-dimethyl aminopropyl) carbodiimide (EDC), Das, DIEA, pH 8, 72 h. ii) DMF anh., 4-(4,6-Dimethoxy-1,3,5-triazin-2-yl)-4-methylmorpholinium (DMTMM) BF_4, H_2N-valine-dasatinib, DIEA, pH 8, 48 h. iii) sodium bicarbonate, MilliQ water.
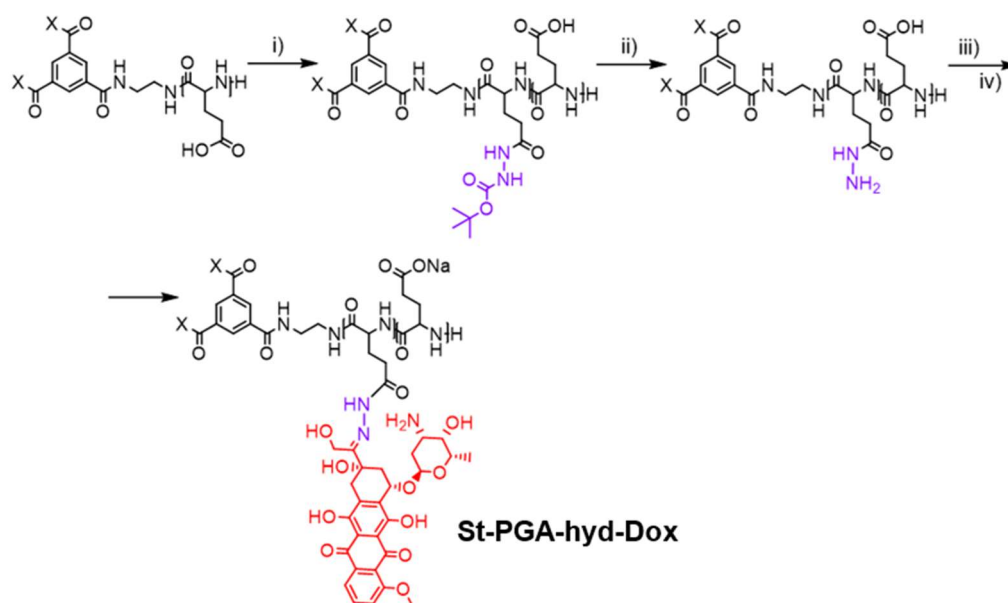
Scheme 2.4. Synthesis of Dox conjugates. i) DMF anh., DMTMM BF$_4$, tert-butyl carbazate (TBC), DIEA, pH 8, 48 h. ii) trifluoroacetic acid (TFA), 45 min. iii) dimethylsulfoxide (DMSO) anh., Dox, acetic acid (cat.). iv) sodium bicarbonate, MilliQ water.
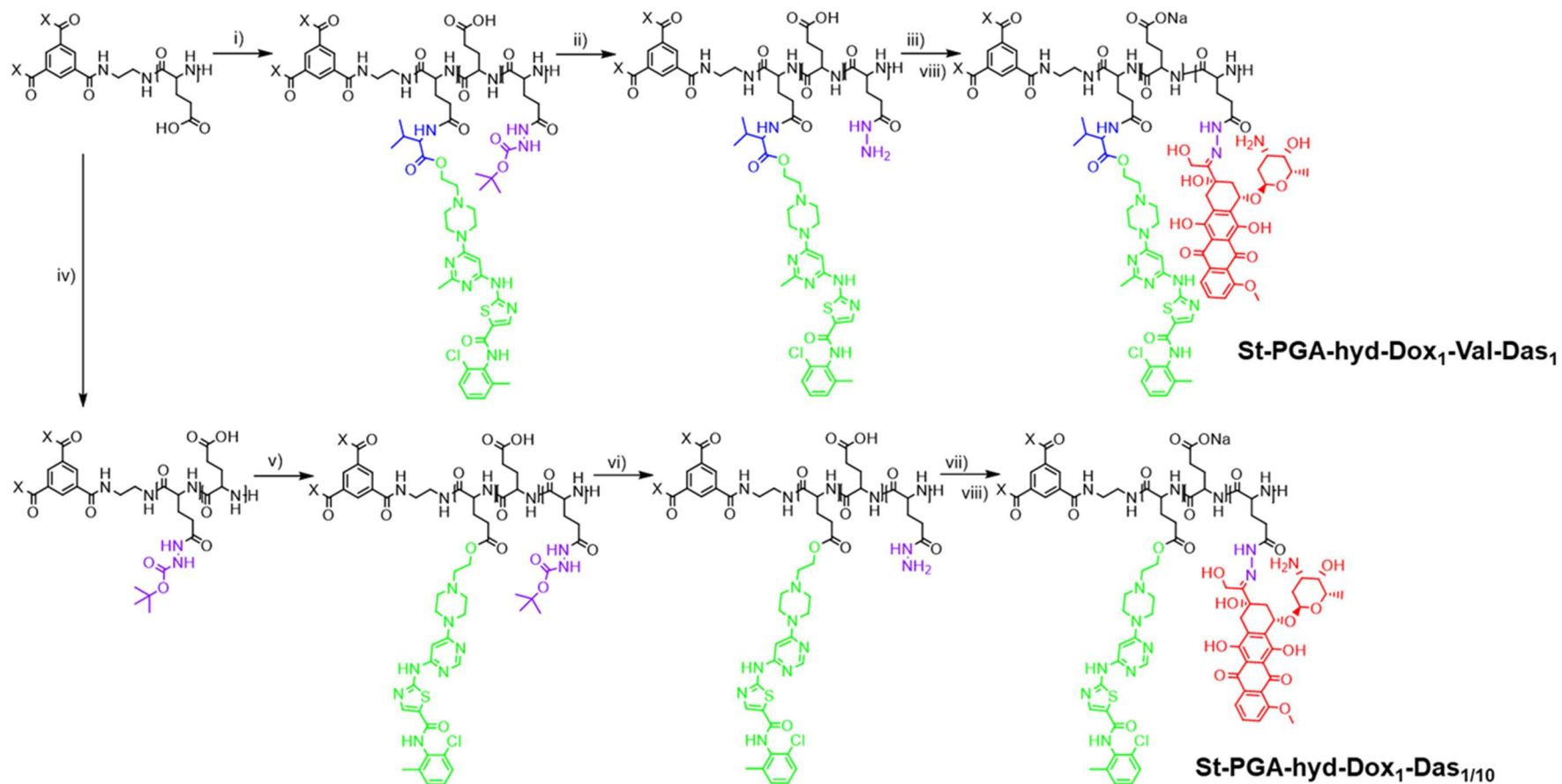
Scheme 2.5. Synthesis of Dox-Das combination conjugates. i) DMF anh., DMTMM BF$_4$, TBC, H$_2$N-valine-dasatinib, DIEA, pH 8, 48 h. ii) TFA, 45 min. iii) DMSO anh., Dox, acetic acid (catalytic), 72 h. iv) DMF anh., DMTMM BF$_4$, TBC, DIEA, pH 8, 48 h. v) DMF anh., DMAP, EDC, Das, DIEA, pH 8, 72 h. vi) TFA, 45 min. vii) DMSO anh., Dox, acetic acid (cat.), 72 h. viii) sodium bicarbonate, MilliQ water.

2.2.2.1.   Synthesis of St-PGA-Das and St-PGA-Val-Das

A wide range of studies supports using ester bonds for drug conjugation (28,59). These carboxylic acid derivatives can be hydrolyzed by acids, bases, metal ions, or enzymes such as esterases (59,60); however, ester hydrolysis represents a slow process, and bonds are deemed stable under physiological conditions (60) with drug release attributed to cell uptake and intracellular linker hydrolysis. Following cell internalization, conjugates pass through the endocytic pathway to the lysosomes, where the acidic milieu and presence of numerous enzymes prompt ester hydrolysis and drug release, allowing the drug to exert its intracellular biological activity (59).

Related studies on paclitaxel polyglumex (Xyotax^{TM}) metabolism support this mechanism (61,62). This PGA-based paclitaxel (PGA-PTX) conjugate, which reached phase III clinical trials (28), employs an ester bond for drug conjugation (61,62). A first study demonstrated PGA-PTX stability in circulation but revealed the presence of metabolites such as paclitaxel-2'-ɣ-glutamic acid ester in tumor tissues (of varied nature) as well as in the liver and spleen. The presence of this metabolite (together with free PTX) in these tissues suggested that conjugate metabolism began with the proteolytic degradation of the carrier (PGA) followed by ester bond hydrolysis to yield free PTX (62). Subsequent studies identified the lysosomal serine-protease cathepsin B as the main factor mediating carrier degradation (61); however, other enzymes (such as esterase) also contribute to ester degradation (63).

In this study, we explored the modulation of ester bond hydrolysis by incorporating a Val spacer between Das and St-PGA. Our group previously evaluated the effect of incorporating various amino acids as spacers on Das release as part of the optimization of a linear PGA Dox-Das combination conjugate (41). As explained in the introduction, Das's delayed administration increased the Das-Dox combination's synergism in MDA-MB-231 cell cultures. This earlier work demonstrated that Das conjugation using a Val spacer (PGA-Val-Das) reduced drug release at pH 5.0 and 7.4.

Accordingly, the combination conjugate PGA-hyd-Dox-Val-Das displayed a delayed release of Das compared to Dox in the presence of cathepsin B in a pH 5.0 buffer that mimicked the lysosomal milieu, which resulted in enhanced anti-tumor activity *in vivo*. Overall, PGA-hyd-Dox-Val-Das efficiently reduced tumor growth and metastasis progression without signs of associated toxicity in a spontaneously metastatic MDA-MB-231-Luc TNBC model. In this present work, we aimed to obtain a St-PGA counterpart as a part of the optimization process for developing effective treatments against metastatic TNBC.

Conjugation of Das through a simple ester bond (St-PGA-Das) requires only one reaction in organic media using carbodiimides as coupling agents (**Scheme 2.3**). In this reaction (**Scheme 2.6**), the carbodiimide **2** reacts with the carboxylic groups of St-PGA **1,** forming the O-acylisourea intermediate **3** that reacts with the alcohol of Das, yielding the desired ester bond **4** and the urea by-product **5**. We used 1-ethyl-3-(3-dimethylaminopropyl)carbodiimide (EDC), given the water solubility of the molecule itself **2** and its urea by-product **5**, making them easy to remove by workup in aqueous media. The O-acylisourea intermediate **3** can undergo other side reactions – it can react with another carboxylic group to form the symmetric anhydride **6**, which reacts with the hydroxyl group of Das forming the ester bond **4**, or it can undergo intramolecular rearrangement to form the undesirable N-acyl urea byproduct **7**. To avoid the formation of N-acyl urea, we added catalytic amounts of 4-dimethylaminopyridine (DMAP) **8** to the reaction, which reacts with the O-acylisourea forming an intermediate specie **9** that cannot undergo intermolecular rearrangement (64).
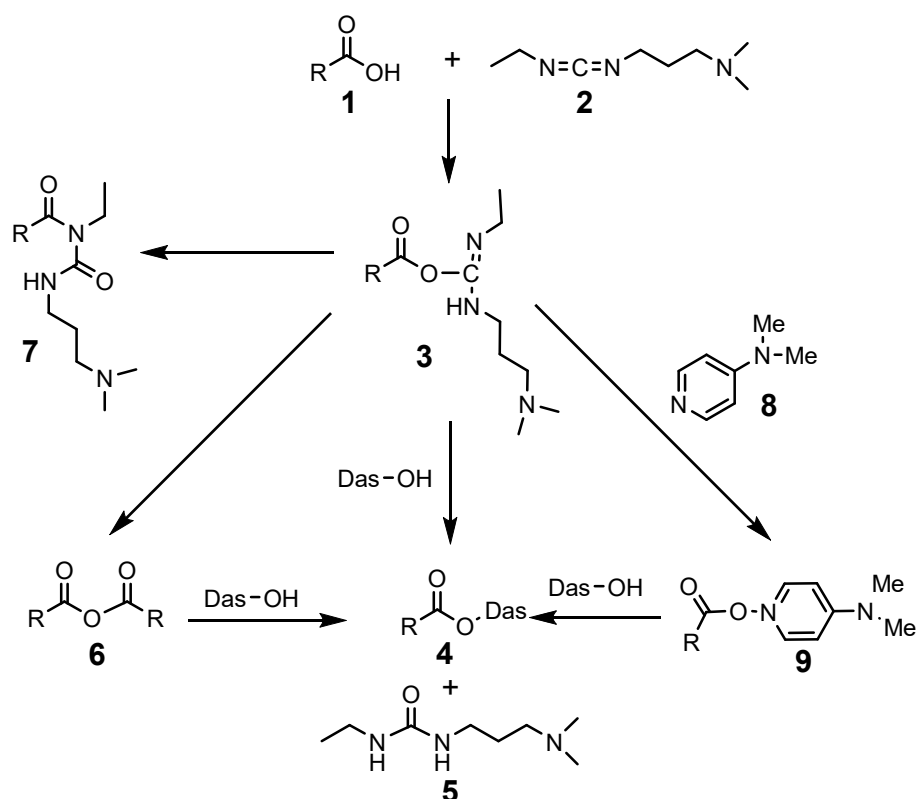
Scheme 2.6. Mechanism of EDC/DMAP ester coupling. Modified from Tsakos et al. 2015 (64).

We evaluated the identity and purity of the final compound, St-PGA-Das, in its water-soluble sodium salt form by ^{1}H-NMR and ultraviolet-visible (UV-VIS) spectroscopy. In the aromatic region of the ^{1}H-NMR (8.7-7.0 ppm) spectra of St-PGA-Das, we identified signals corresponding to Das protons (**Figure 2.4**); however, their low definition (as a consequence of drug conjugation) plus the interference of the proton of the benzene tricarbonyl initiator impeded the quantification of drug loading by ^{1}H-NMR. Thus, we used the absorbance of Das in the UV-VIS spectrum to quantify drug loading. The UV-VIS spectrum of St-PGA-Das in DMSO:water (1:1 v/v) displayed a peak at 324 nm, which confirmed the presence of Das in the sample (**Supplementary Figure 2.3A**). We prepared a calibration curve of free Das in DMSO:water (1:1 v/v) at 324 nm (**Supplementary Figure 2.3B**) and used the absorbance value at 324 nm in the St-PGA-Das sample to

determine Das loading, obtaining a value of 9.9% wt Das (3.4% mol), i.e., 68% of conjugation efficacy (CE).
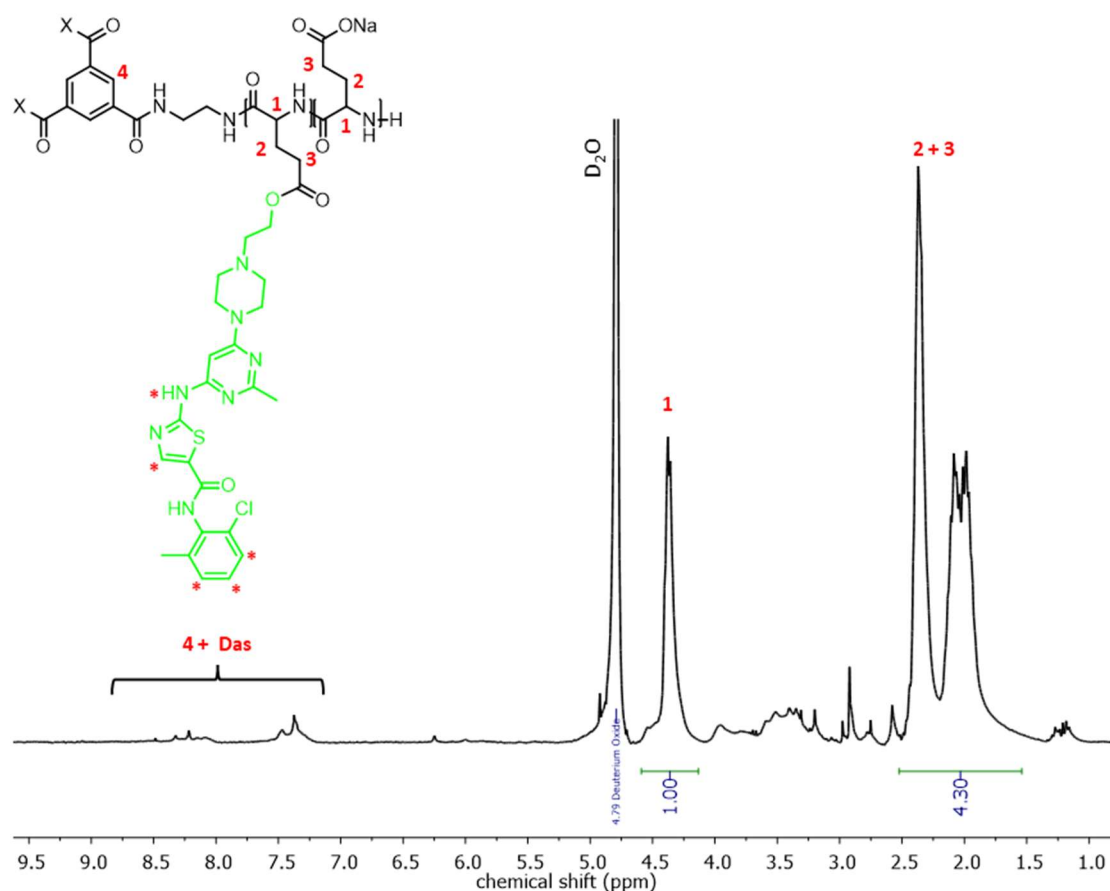
Figure 2.4. ^{1}H-NMR (D$_2$O) spectrum of St-PGA-Das. The spectrum confirms Das conjugation. *Identified Das protons.

For the synthesis of St-PGA-Val-Das (**Scheme 2.3**) (the single-drug conjugate with Das and the spacer Val), we modified Das to form an ester bond between the drug alcohol and the amino acid's carboxylic acid (H$_2$N-Val-Das). The synthesis of H$_2$N-Val-Das required two reactions. First, we conjugated Val with its amino group protected by a tert-butyloxycarbonyl group (Boc-valine-OH) to Das in a reaction mediated by EDC/DMAP that followed the same mechanism as for St-PGA-Das ester coupling (**Scheme 2.6**, where Boc-valine-OH is **1**). From that reaction, we obtained the precursor Boc-Val-Das. We evaluated the identity and purity of the product by ^{1}H-NMR (**Figure 2.5**), where we integrated the signals of the six protons

of the isopropyl group of Val (1.06-0.85 ppm) as a reference. We confirmed the coupling of Boc-valine-OH to Das by integrating all identifiable signals of Das and the Boc protecting group of Val. Then, we deprotected the Val amino group by eliminating Boc in acidic conditions, obtaining H_2N-Val-Das. We confirmed the complete removal of the Boc group (the absence of the signal of its nine protons at 1.5 ppm) by ^{1}H-NMR (**Figure 2.6**).

We conjugated H_2N-Val-Das to St-PGA by DMTMM (4-(4,6-dimethoxy-1,3,5-triazin-2-yl)-4-methylmorpholinium) chemistry in organic media (**Scheme 2.3**). In this reaction (**Scheme 2.7**), DMTMM **2** forms an activated ester **3** with the carboxylic groups of St-PGA that is then displaced by the amine **4**, forming the amide bond (65).

We evaluated the identity and purity of St-PGA-Val-Das in its water-soluble sodium salt form by ^{1}H-NMR and UV-VIS spectroscopy. The ^{1}H-NMR spectrum of St-PGA-Val-Das displayed broad peaks in the aromatic region (8.7-7.0 ppm), corresponding to Das protons, and a broad peak at 1.06-0.85 ppm, corresponding to the isopropyl group of Val, thereby confirming the conjugation of Val-Das to St-PGA (**Figure 2.7**). The ^{1}H-NMR spectra also confirmed the absence of DMTMM, which appears as a multiplet at ~3.1 ppm (**Figure 2.7**). As in St-PGA-Das, the UV-VIS spectrum of St-PGA-Val-Das in DMSO:water (1:1 v/v) displayed a peak at 324 nm, confirming the presence of Das in the sample (**Supplementary Figure 2.3A**), which we used to quantify Das loading, obtaining a value of 10.8% wt (3.1% mol, 62% CE).
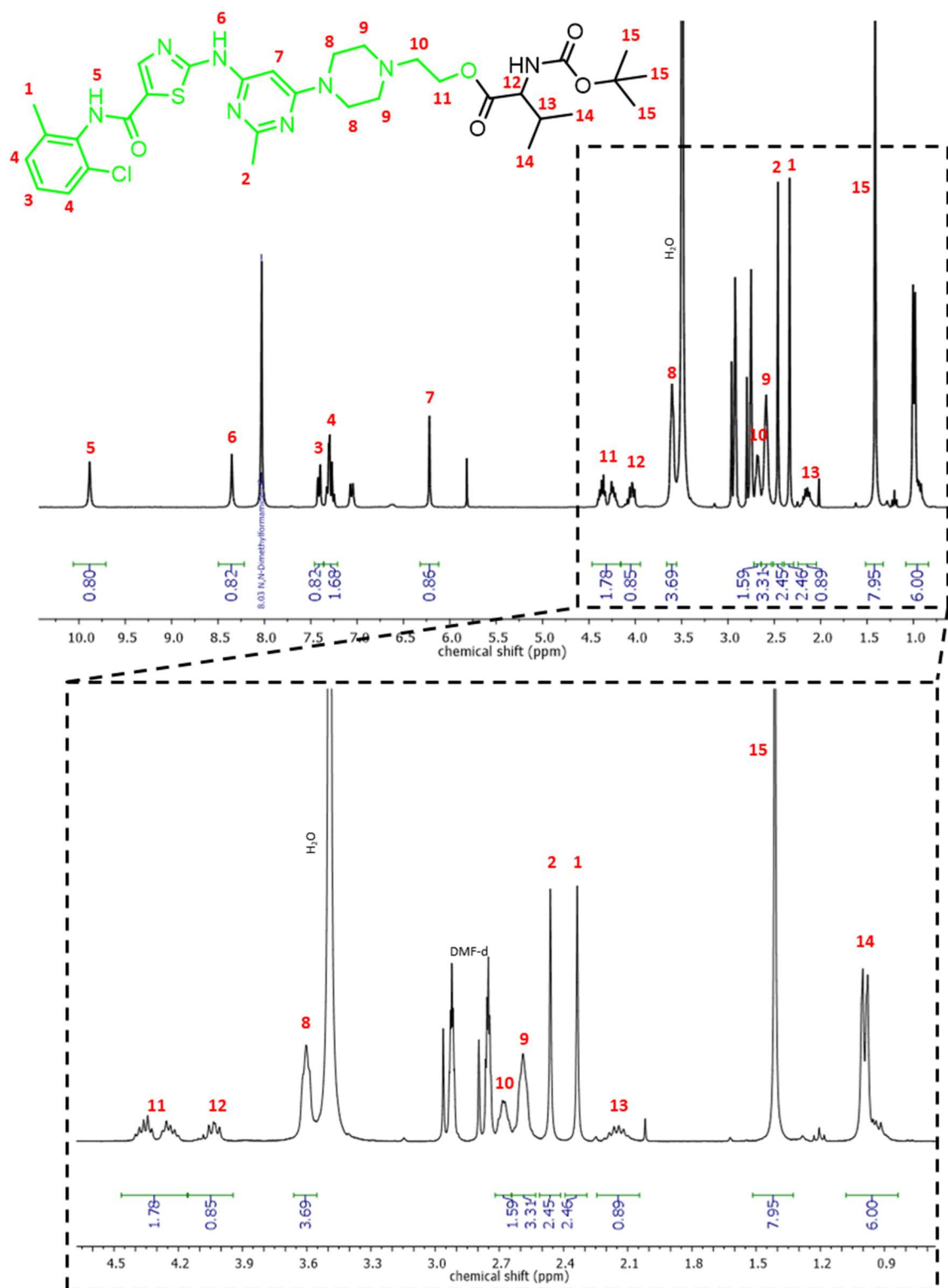
Figure 2.5. ^{1}H-NMR (DMF-d) spectrum of Boc-Val-Das. The spectrum confirms the identity of the product. The signal of the six protons of the isopropyl group of Val (14) was used as a reference (six protons) to integrate the remaining signals.
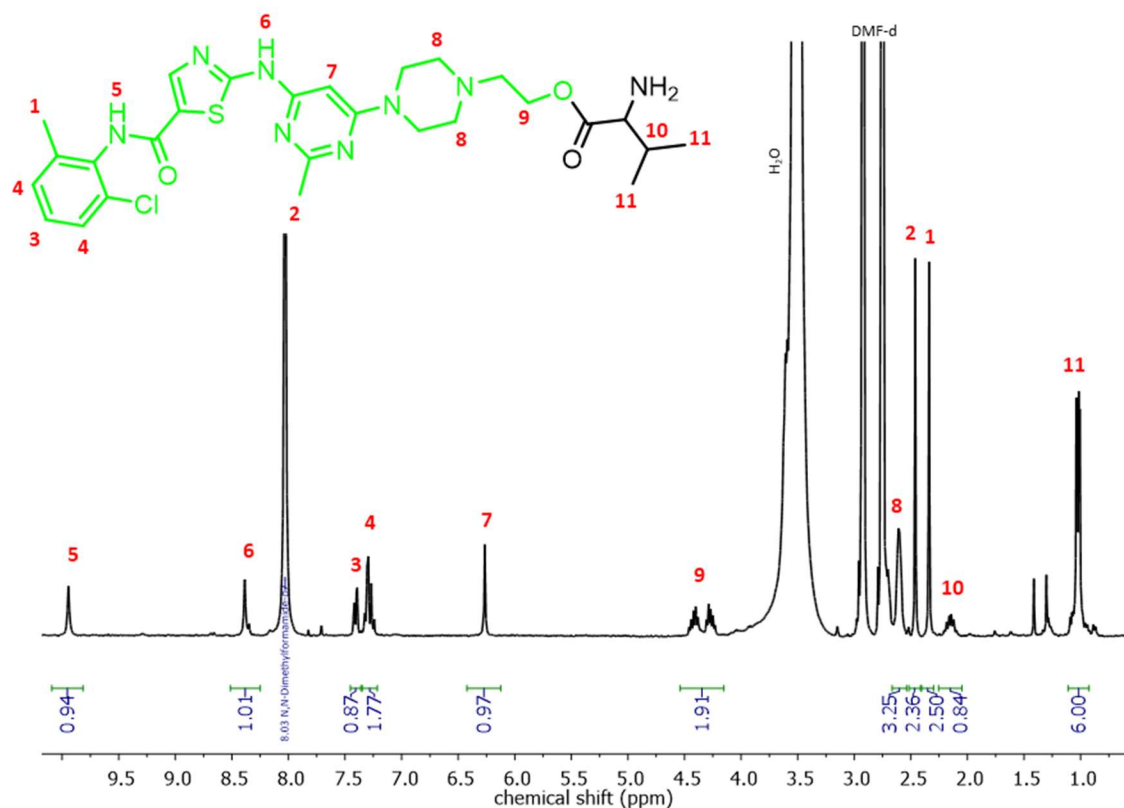
Figure 2.6. ^{1}H-NMR (DMF-d) spectrum of H_2N-Val-Das. The spectrum confirms the complete removal of the Boc protecting group (absence of the signal at 1.5 ppm) and compound identity. The signal of the six protons of the isopropyl group of Val (14) was used as reference (six protons) to integrate the remaining signals.
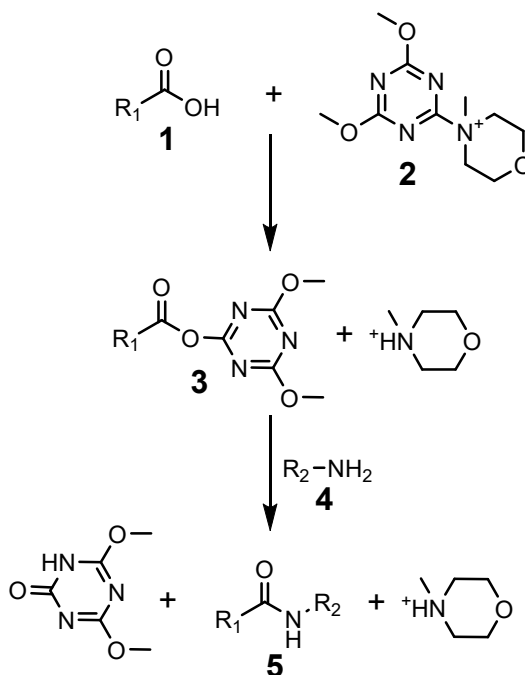
Scheme 2.7. Mechanism of DMTMM mediated amide coupling. Modified from Montalbetti and Falque 2005 (65).
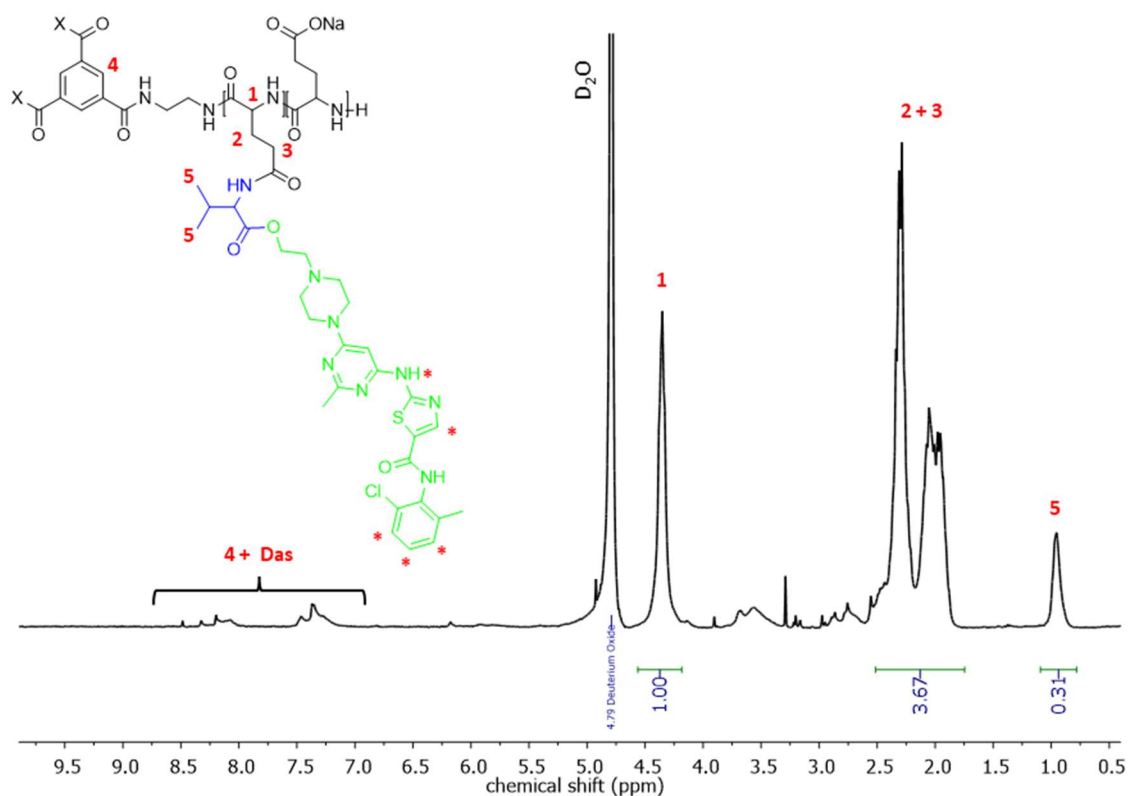
Figure 2.7. ^{1}H-NMR (D$_2$O) spectrum of St-PGA-Val-Das. The spectrum confirms drug's conjugation (5 – six protons – and Das – five protons). *Identified Das protons.

2.2.2.2.　Synthesis of St-PGA-hyd-Dox

We used a hydrazone bond to conjugate Dox to St-PGA (**Scheme 2.4**), a linking moiety that has been widely used for drug conjugation with various polymers. This linker has particular relevance for Dox due to the rapid hydrolysis of the hydrazone moiety in acidic media compared to physiological pH (60,66). Generally, hydrazone bonds form between hydrazide groups introduced in the polymeric carrier and aldehydes or ketones in the bioactive molecule in question (66,67). For instance, Vogus and co-workers explored the use of hydrazone bonds to conjugate Dox to hyaluronic acid (HA) and compared its performance with direct amide coupling (HA-hyd-Dox vs. HA-amide-Dox) with the final aim of synthesizing an efficient combination conjugate with gemcitabine (68). Their study of pH-dependent release kinetics of Dox demonstrated that HA-hyd-Dox released

50% of the drug after 100 h at pH 5.0, while HA-amide-Dox released less than 10% under the same conditions. The higher availability of Dox in HA-hyd-Dox compared to HA-amide-Dox translated into more significant cytotoxic activity in MDA-MB-231 cell cultures.

The hydrazone bond has also been extensively used for conjugation to the N-(2-hydroxypropyl)methacrylamide (HPMA) copolymer (69,70). For instance, Etrych et al. developed an HPMA-Dox conjugate using a hydrazone bond with a cathepsin B hydrolyzable peptide spacer (GFLG) (HPMA-GFLG-hyd-Dox) (69). This study represented the evolution of previously described and clinically-evaluated HPMA-Dox conjugates that used the GFLG linker without the hydrazone linker (71–74). The HPMA-GFLG-hyd-Dox conjugate remained stable (< 10% of drug release at 100 h) at normal blood pH (7.4) but released Dox at late endosomal pH values (5.0) (> 70% of drug release at 100 h). Furthermore, the GFLG peptide linker allowed an even higher release of the drug in the presence of the lysosomal enzyme cathepsin B. Overall, the HPMA-GFLG-hyd-Dox conjugate allowed an increment in the administrated dose of Dox in a mouse model of EL-4 T-cell lymphoma, which prompted a significant increase in treatment efficacy in terms of tumor growth and survival (69). Aiming for prolonged circulation times and increased tumor accumulation via the EPR effect, subsequent studies reported the development of HPMA-based architectures with increased molecular weight and size (75,76). Star-shaped HPMA-based Dox conjugates using a hydrazone bond (without the GFLG linker) remained stable at pH 7.4 (< 10% of drug release at 36 h) but released the drug at pH 5.0 more rapidly than the linear HPMA copolymer with the GFLG spacer (77). These new conjugates efficiently inhibited subcutaneous EL-4 T-cell tumor growth and significantly increased animal survival compared to free Dox administration at an equivalent dose. The authors also reported cytotoxic activity of the star-shaped HPMA conjugate of Dox in the 4T1 murine breast cancer cell line *in vitro*.

Recent work performed by our laboratory compared the efficacy of two linking moieties for hydrazone-mediated Dox conjugation in a PGA combination conjugate with aminoglutethimide (AGM) (34). The approach directly conjugated Dox through a hydrazine moiety or a long, flexible, and hydrophobic N-ε-maleimidocaproic acid hydrazide (EMCH) moiety and employed a constant loading of AGM (10% mol) while altering Dox loading (1% for low loading and 3% mol for high loading). Conjugates with low Dox loading displayed stability at pH 7.4 but released Dox at pH 5.0, while conjugates with high Dox loading failed to release the drug at either pH. *In vitro* cytotoxic activity of conjugates in the 4T1 cell line reflected the drug release profiles, with low-loaded conjugates performing better (lower IC50 values) than high-loaded conjugates. *In vivo* data obtained in a spontaneously metastatic orthotopic 4T1 breast cancer mouse model agreed with *in vitro* data, with low-loaded conjugates displaying optimal performance in terms of tumor growth and metastatic spread reduction. Treatment with low-loaded conjugates containing the longer EMCH spacer led to lower overall survival and more significant hepatotoxicity than combination conjugates with direct hydrazone conjugation or free Dox. Notably, the conjugate with the short hydrazone linker and low Dox loading displayed antitumor activity against the primary tumor and achieved a 90% reduction in lung metastasis compared to non-treated control (without impacting safety) thus highlighting the importance of linking chemistry and drug loading.

In this study, we conjugated Dox to St-PGA using the same short hydrazone linker. This linking chemistry requires three synthetic steps (**Scheme 2.4**). First, we conjugated tert-butyl carbazate (TBC) to St-PGA through an amide bond by DMTMM chemistry in organic media. This moiety consists of a hydrazine molecule protected by a Boc group. The second reaction consisted of TBC deprotection (elimination of Boc protecting group) under acidic conditions (i.e., TFA). Finally, we conjugated Dox to the

hydrazide moieties in organic media (DMSO anhydrous) with catalytic amounts of acid (i.e., acetic acid).

To obtain a conjugate with hydrazone-Dox (St-PGA-hyd-Dox), we modified St-PGA with TBC. We evaluated the identity of the precursor St-PGA-TBC by ^{1}H-NMR. To quantify the percentage of modification, we compared the signal at 1.5 ppm corresponding to the three methyl groups of TBC with the α-carbon proton of PGA (4.3 ppm), obtaining 6% mol (100% CE) (**Figure 2.8**). After deprotection of the hydrazide groups in TFA, we confirmed the complete removal of Boc and the purity of the compound by ^{1}H-NMR (**Figure 2.9A**). In this step, the purity of the material (St-PGA-HYD) is of crucial importance, as traces of DMTMM from earlier reactions can lead to the conjugation of Dox through its amino group, forming an amide bond insensitive to acidic pH. The ^{1}H-NMR spectra confirmed the absence of DMTMM, which appears as a multiplet at ~3.1 ppm.
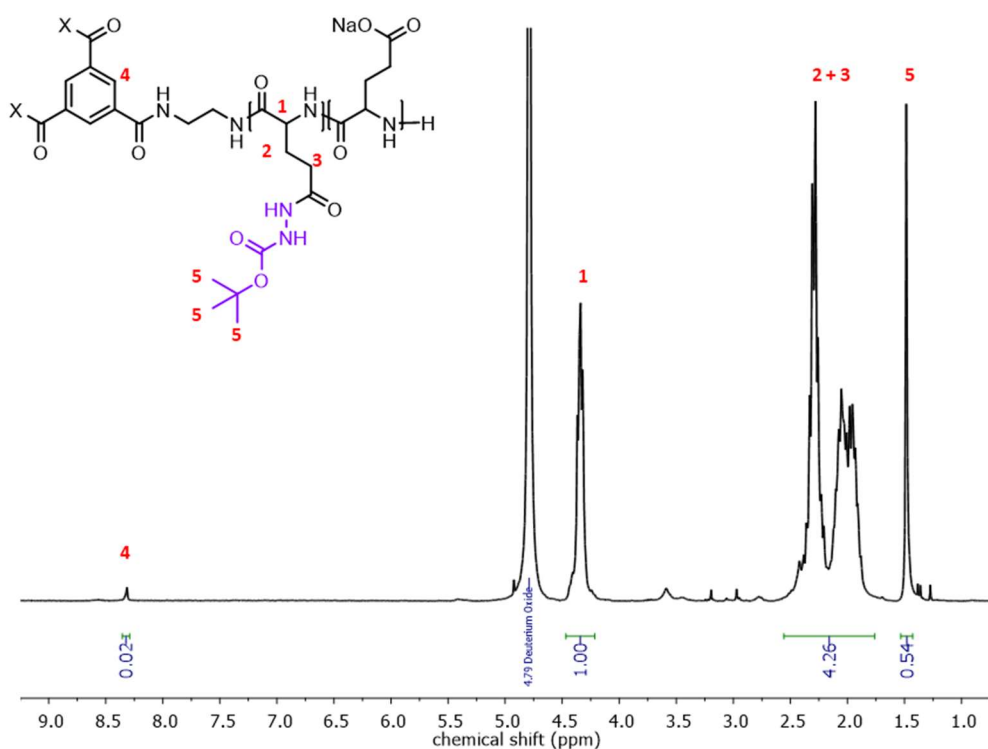
Figure 2.8. Representative ^{1}H-NMR (D$_2$O) spectrum of St-PGA-TBC. The spectrum confirms TBC conjugation. Signals from the Boc protecting group (5 – nine protons) and PGA α-carbon proton (1 – one proton) were used to calculate TBC loading (% mol).

Dox can then be conjugated to the hydrazide groups in organic media with catalytic amounts of acid (**Scheme 2.8**). The acid allows for the nucleophilic attack of the hydrazide **1** to the carbonyl carbon of the ketone (i.e., Dox) **2**. A tetrahedral intermediate **4** is formed upon proton transfer, which can undergo dehydration by protonation of the hydroxyl group and elimination of a water molecule, obtaining a protonated intermediate **5**. Finally, deprotonation yields hydrazone **6** (67).
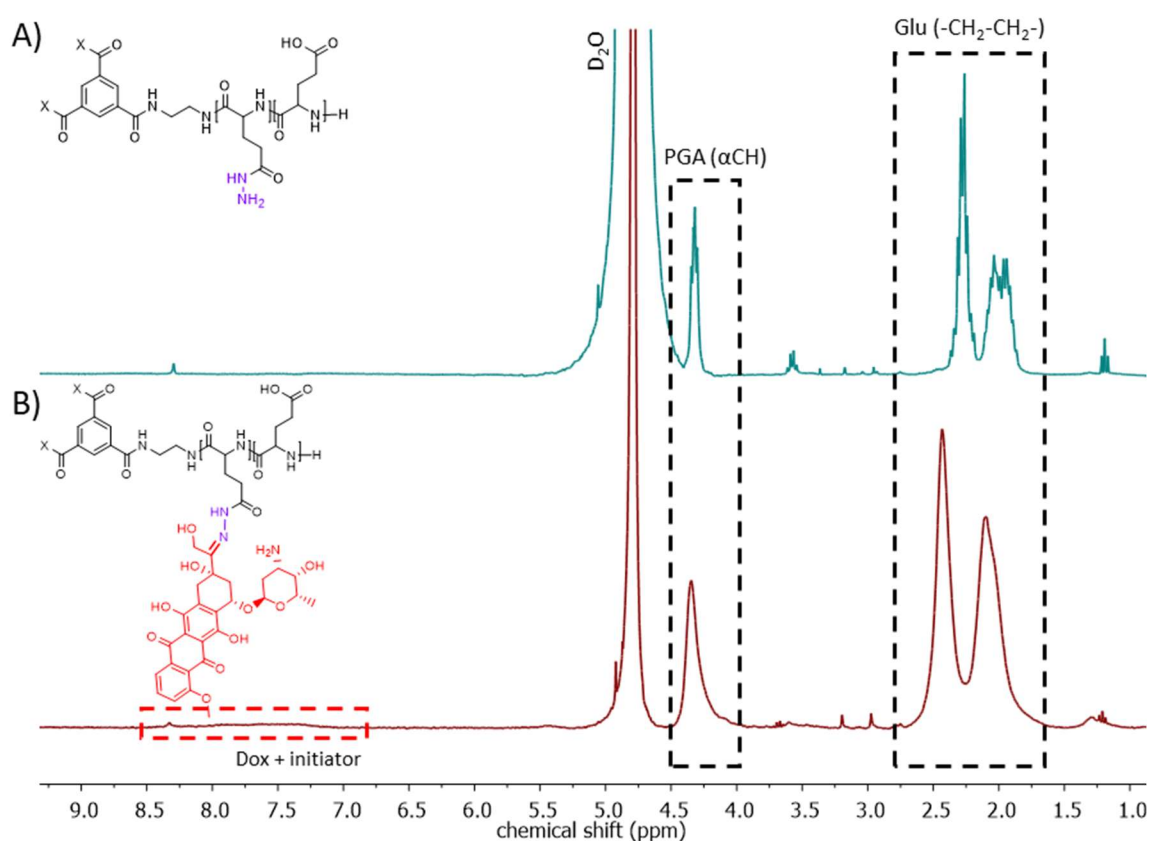
Figure 2.9. (**A**) ^{1}H-NMR (D$_2$O) spectrum of St-PGA-HYD. The absence of Boc signal at 1.5 ppm confirms complete deprotection of the hydrazide groups. (**B**) ^{1}H-NMR (D$_2$O) spectrum of St-PGA-hyd-Dox. The spectrum confirms Dox conjugation (6.7-8.5 ppm – three protons).
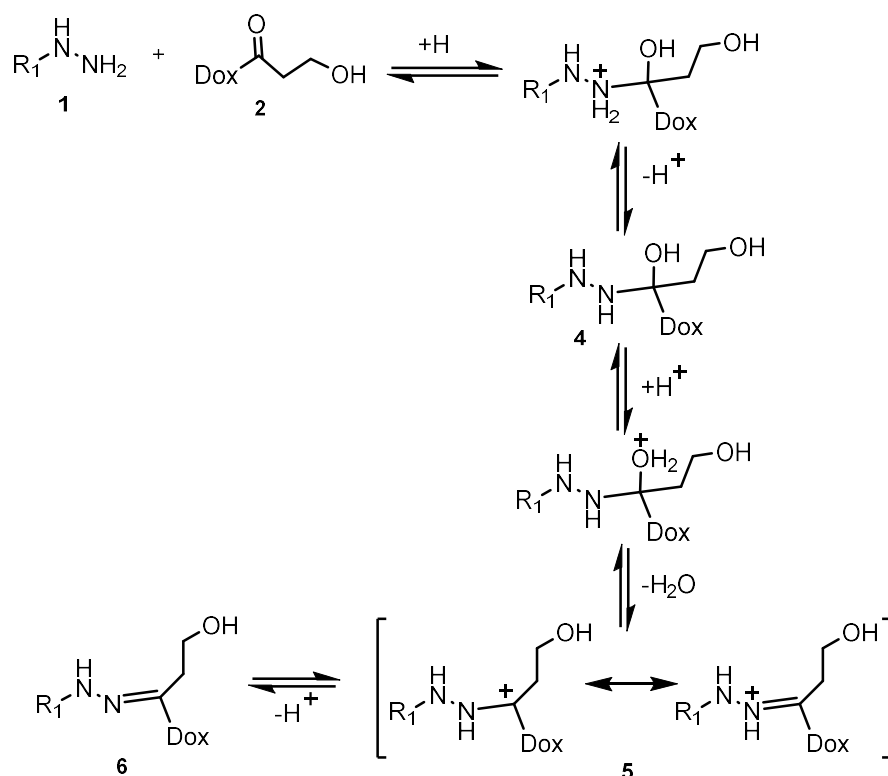
Scheme 2.8. Mechanism of acid-catalyzed hydrazone formation. Adapted from Kölmel and Kool 2017 (67).

We evaluated the identity and purity of St-PGA-hyd-Dox in its water-soluble sodium salt form by ^{1}H-NMR and UV-VIS spectroscopy. In the ^{1}H-NMR spectra of St-PGA-hyd-Dox, we identified broad signals in the aromatic region (6.7-8.5 ppm) that we attribute to Dox conjugation (**Figure 2.9B**); however, as for Das conjugates, the low definition of the peaks (as a consequence of drug conjugation) and the interference of the proton of the benzene tricarbonyl initiator impeded the quantification of the drug loading by ^{1}H-NMR. Thus, we used the absorbance of Dox in the UV-VIS spectrum to quantify drug loading. The UV-VIS spectrum of St-PGA-hyd-Dox in DMSO:water (1:1 v/v) displayed a maximum at 480 nm, which confirmed the presence of Dox in the sample (**Supplementary Figure 2.3A**) and allowed for drug loading quantification by interpolation of the absorbance value at 480 nm in a calibration curve of Dox in DMSO:water (1:1 v/v) at 480 nm (**Supplementary Figure 2.3C**). Following this method, we obtained a value of 9.4% wt (2.9% mol) Dox (58% CE).

2.2.2.3. Synthesis of Dox-Das St-PGA-based Combination Conjugates

We synthesized three St-PGA-based combination conjugates using both linking chemistries explored for Das (i.e., direct ester conjugation and the use of the Val spacer), the hydrazone bond for Dox conjugation, and two drug ratios (i.e., 1:1 and 1:10) (**Table 2.1**).

i) St-PGA-hyd-Dox$_1$-Val-Das$_1$ (a 1:1 ratio of Dox:Das)

ii) St-PGA-hyd-Dox$_1$-Das$_1$ (a 1:1 ratio of Dox:Das)

iii) St-PGA-hyd-Dox$_1$-Das$_{10}$ (a 1:10 ratio of Dox:Das)

The synthesis of all the combination conjugates followed a similar scheme (**Scheme 2.5**), comprising amide conjugation followed by ester coupling of Das (in those conjugates with direct conjugation of Das), deprotection of TBC, and the conjugation of Dox.

For the synthesis of St-PGA-hyd-Dox$_1$-Val-Das$_1$, we conjugated TBC and H$_2$N-Val-Das in a one-pot reaction using DMTMM as carboxyl group activator, obtaining St-PGA-TBC-Val-Das. We evaluated the identity of the compound by ^{1}H-NMR. The ^{1}H-NMR spectrum of St-PGA-TBC-Val-Das displayed broad signals in the aromatic region (8.7-7.0 ppm) corresponding to Das protons and the broad peak at 1.06-0.85 ppm corresponding to the isopropyl group of Val, thereby confirming the conjugation of Val-Das to St-PGA (**Figure 2.10A**). As explained above, we used the peak at 1.50 ppm in the ^{1}H-NMR spectrum of St-PGA-TBC-Val-Das precursor, corresponding to the nine protons of the Boc protecting group, to quantify TBC loading, obtaining a value of 3.6% mol (60% CE) (**Figure 2.10A**).
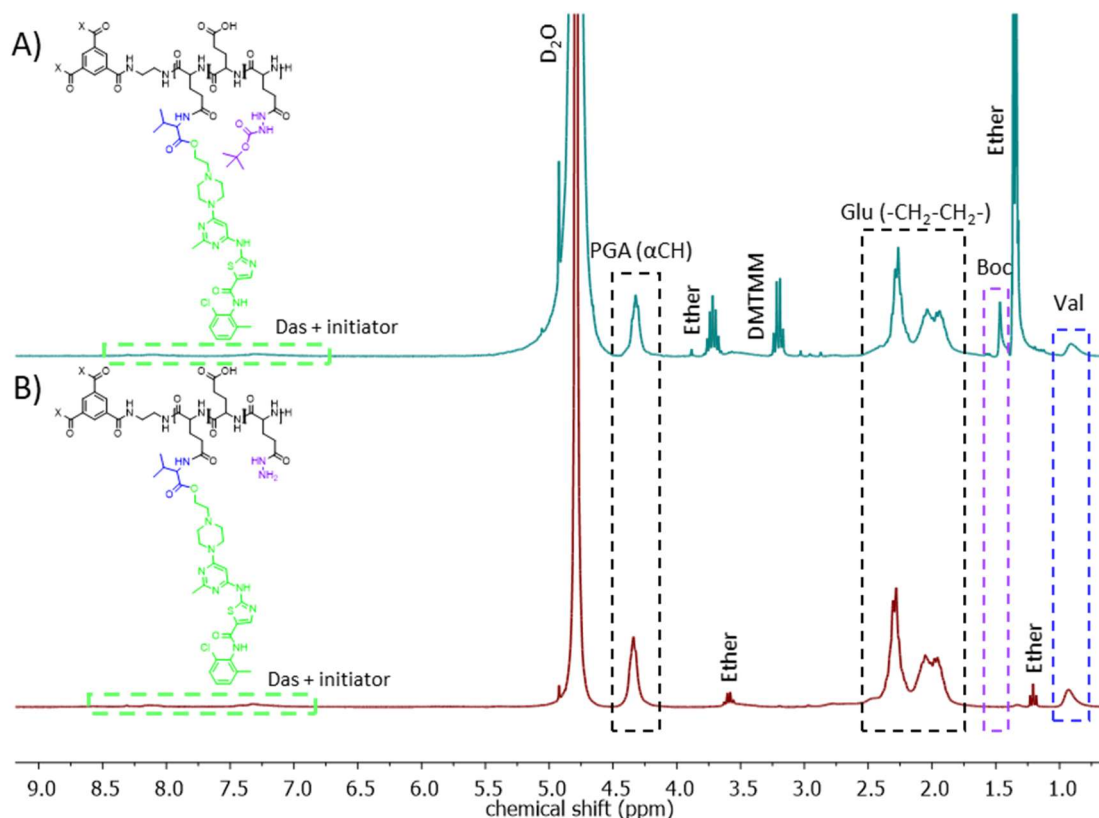
Figure 2.10. (**A**)^{1}H-NMR (D$_2$O) spectrum of St-PGA-TBC-Val-Das. The spectrum confirms Val-Das (Das – five protons – and Val – six protons) and TBC (Boc – nine protons) conjugation. Signals from the Boc protecting group and PGA α-carbon proton (αCH – one proton) were used to calculate TBC loading (% mol). (**B**) ^{1}H-NMR (D$_2$O) spectrum of St-PGA-(HYD)-Val-Das. The absence of the signal at 1.5 ppm confirms complete removal of Boc protecting group. The spectrum confirms the presence of Val-Das (Das – five protons – and Val – six protons).

After confirming the conjugation of TBC and Val-Das, we deprotected TBC (St-PGA-Val-Das-HYD). The absence of the signal at 1.50 ppm corresponding to the nine protons of the Boc protecting group in the ^{1}H-NMR spectrum of St-PGA-Val-Das-HYD confirmed the complete deprotection of the hydrazide moieties (**Figure 2.10B**). The ^{1}H-NMR spectrum of St-PGA-Val-Das-HYD also confirmed the presence of Val-Das as indicated by the peaks in the aromatic region (8.7-7.0 ppm), corresponding to Das, and the peak in the aliphatic region (1.06-0.85 ppm), corresponding to the isopropyl group of Val (**Figure 2.10B**).

Finally, we conjugated Dox to the hydrazide groups, obtaining the final combination conjugate St-PGA-hyd-Dox$_1$-Val-Das$_1$. We evaluated the

identity of the final compound on its water-soluble salt form by ^{1}H-NMR (**Figure 2.11**) and UV-VIS spectroscopy (**Supplementary Figure 2.3A**). The ^{1}H-NMR spectrum of the conjugate revealed broad peaks in the aromatic region (8.5-7.0 ppm) that we attribute to the conjugation of Dox and Das to St-PGA; however, the low definition of the peaks impeded drug loading determination by ^{1}H-NMR (**Figure 2.11**). We evaluated drug loading by UV-VIS spectroscopy using calibration curves of Dox and Das in DMSO:water (1:1 v/v) (**Supplementary Figure 2.3B** and **C**), obtaining a value of 7.8% wt Dox (2.6% mol, 52% CE) by direct interpolation of the absorbance of the sample at 480 nm in the corresponding calibration curve. Due to the co-existence of both drugs in the same carrier and the interference of Dox absorbance spectrum in the peak absorption of Das, we performed a calibration curve of Dox in DMSO:water (1:1 v/v) at 324 nm (**Supplementary Figure 2.3D**). We used Dox loading to calculate the absorbance of Dox at 324 nm in the sample and subtracted this value from the total absorbance at 324 nm. Employing this method to quantify Das loading we obtained a value of 9.7% wt Das (3.0% mol, 60% CE), thereby providing a ratio Dox:Das of 1:1.2.

For the synthesis of the combination conjugates with Das conjugated to St-PGA with a direct ester bond (St-PGA-hyd-Dox$_1$-Das$_1$ and St-PGA-hyd-Dox$_1$-Das$_{10}$), we followed a similar synthetic scheme to St-PGA-hyd-Dox$_1$-Val-Das$_1$ (**Scheme 2.5**) - TBC conjugation, Das conjugation by EDC/DMAP chemistry, deprotection of TBC to expose the hydrazide moieties, and then Dox conjugation. After each reaction, we evaluated the identity and purity of the intermediates by ^{1}H-NMR before moving to the next synthetic step (**Figure 2.12A-C**). The ^{1}H-NMR spectrum of St-PGA-TBC revealed a loading of 5.6 % mol hydrazide moiety according to the signal at 1.50 ppm corresponding to Boc protecting group (nine protons) and the signal of the α-carbon proton of PGA at 4.3 ppm (**Figure 2.12A**). The appearance of broad signals in the aromatic region (8.7 - 6.7 ppm) of the ^{1}H-NMR spectrum of St-PGA-TBC-Das confirmed the conjugation of Das (**Figure 2.12B**).

Finally, the absence of the signal at 1.50 ppm in the ^{1}H-NMR spectrum of St-PGA-Das-HYD confirmed the complete removal of the Boc protecting group exposing the hydrazide moiety for Dox conjugation (**Figure 2.12C**). The spectrum also showed the broad peaks in the aromatic region (8.7-6.7 ppm) that we attributed to Das protons (**Figure 2.12C**).
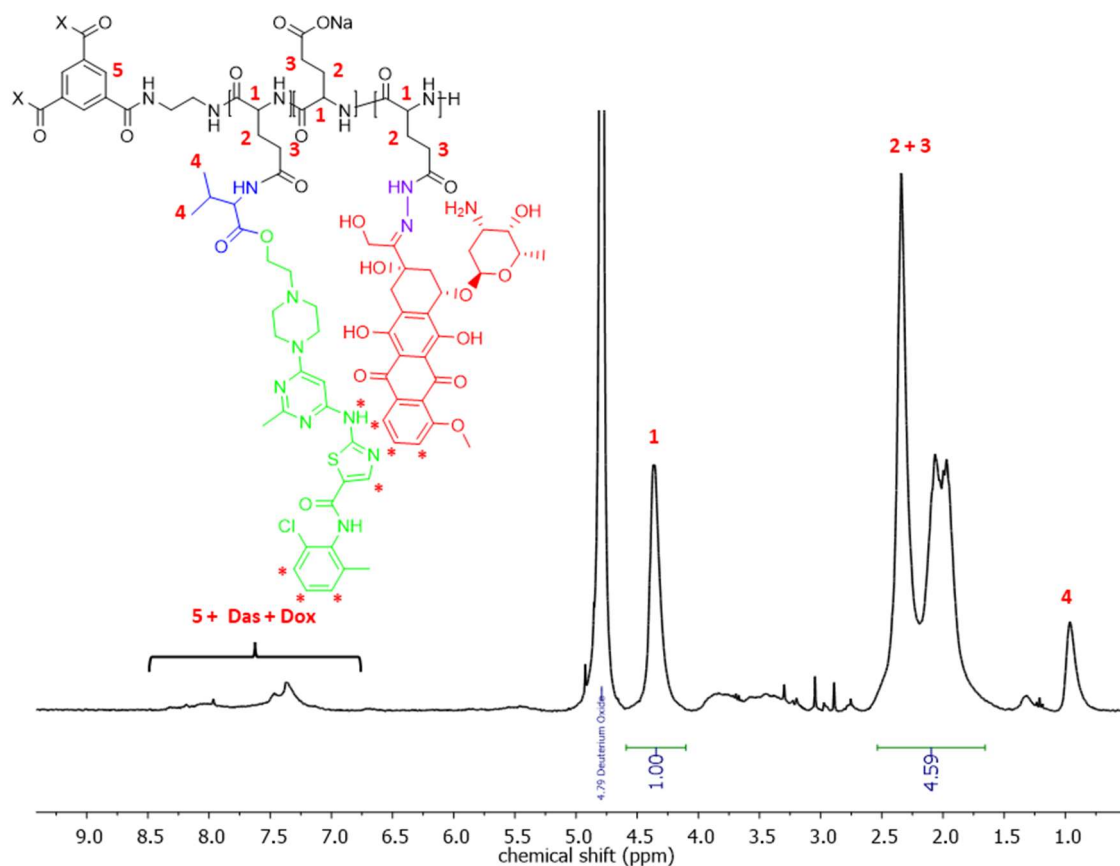
Figure 2.11. ^{1}H-NMR (D$_2$O) spectrum of St-PGA-hyd-Dox$_1$-Val-Das$_1$. The spectrum confirms the conjugation of Val-Das (Das – five protons – and Val – six protons) and Dox (Dox – three protons). *Aromatic Das and Dox signals.
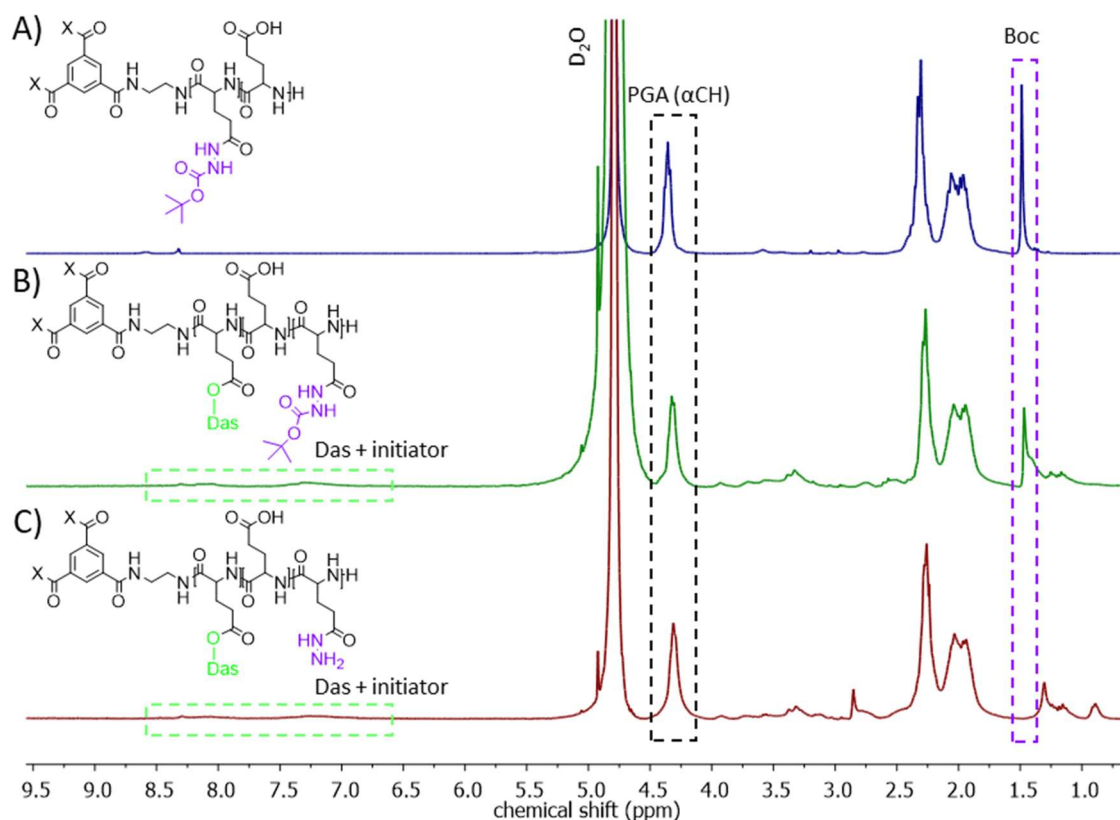
Figure 2.12. Representative ^{1}H-NMR (D$_2$O) spectra of the precursors of St-PGA-hyd-Dox$_1$-Das$_{1/10}$ combination conjugates. (**A**) The spectrum of St-PGA-TBC confirms TBC conjugation. Signals from the Boc protecting group (Boc – nine protons) and PGA α-carbon proton (αCH – one proton) were used to calculate TBC loading (% mol). (**B**) The spectrum of St-PGA-TBC-Das confirms Das conjugation (Das – five protons). (**C**) The spectrum of St-PGA-Das-HYD confirms complete removal of Boc protecting group (absence of the signal at 1.5 ppm) while keeping Das (Das – five protons).

In the final reaction (Dox conjugation to the hydrazide moieties), we tuned Dox loading by changing Dox equivalents. We assessed the identity and purity of the final compounds by ^{1}H-NMR and UV-VIS spectroscopy. The ^{1}H-NMR spectra of St-PGA-hyd-Dox$_1$-Das$_1$ (**Figure 2.13A**) and St-PGA-hyd-Dox$_1$-Das$_{10}$ (**Figure 2.13B**) displayed broad signals in the aromatic region (8.7-7.0 ppm) that we attributed to the successful conjugation of Dox and Das. The UV-VIS spectra of both conjugates also confirmed the presence of Dox (maximum at 480 nm) and Das (maximum at 324 nm) (**Supplementary Figure 2.3A**) and allowed for drug loading quantification following the same procedure as for St-PGA-hyd-Dox$_1$-Val-Das$_1$ obtaining a value of 5.3% wt Dox (1.7% mol, 34% CE) and 7.8% wt Das (2.8% mol, 56% CE) for St-PGA-

hyd-Dox$_1$-Das$_1$, and 1.0% wt Dox (0.3% mol, 60% CE) and 8.5% wt Das (2.9% mol, 58% CE) for St-PGA-hyd-Dox$_1$-Das$_{10}$.
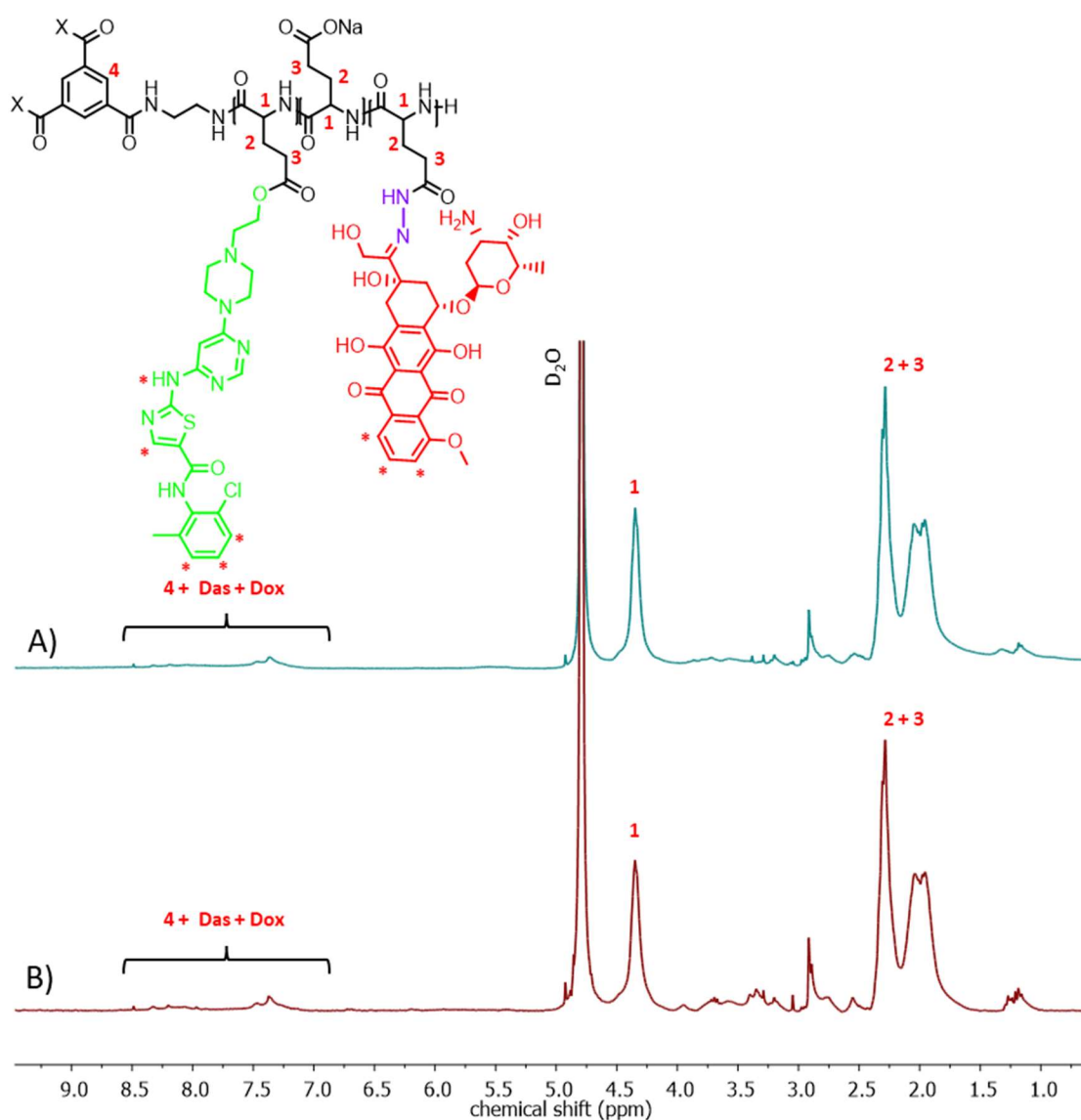
Figure 2.13. ^{1}H-NMR (D$_2$O) spectra of (**A**) St-PGA-hyd-Dox$_1$-Das$_1$ and (**B**) St-PGA-hyd-Dox$_1$-Das$_{10}$. The spectra confirm the presence of Dox and Das (8.7-7.0 ppm). * Aromatic Das and Dox signals.

To evaluate the possible biological activity of spare hydrazide moieties (HYD) in St-PGA-hyd-Dox$_1$-Das$_{10}$, we isolated St-PGA-HYD and St-PGA-Das-HYD intermediates. We used ^{1}H-NMR to calculate the loading of hydrazide moieties of the precursor St-PGA-TBC (6% mol, 100% CE, **Supplementary Figure 2.4A**) before deprotection and confirm the complete

removal of the Boc protecting group after deprotection (St-PGA-HYD, **Supplementary Figure 2.4B**), as explained previously. We conjugated Das to St-PGA-TBC to obtain St-PGA-TBC-Das (**Supplementary Figure 2.4C**) and St-PGA-Das-HYD after hydrazide deprotection (**Supplementary Figure 2.4D**) following the protocols described for St-PGA-hyd-Dox$_1$-Das$_{10}$ synthesis. We calculated Das loading by UV-VIS spectroscopy under the same conditions described above (**Supplementary Figure 2.3A** and **B**), obtaining a value of 11.8% wt (4.1% mol, 82% CE) for St-PGA-Das-HYD.

We synthesized a family of St-PGA-based conjugates composed of three combination conjugates (St-PGA-hyd-Dox$_1$-Val-Das$_1$, St-PGA-hyd-Dox$_1$-Das$_1$, and St-PGA-hyd-Dox$_1$-Das$_{10}$) and their respective single-drug counterparts (St-PGA-Das, St-PGA-Val-Das, and St-PGA-hyd-Dox) with high conjugation efficacies. We also isolated relevant intermediates for their cytotoxic activity evaluation *in vitro*. **Table 2.2** summarizes the synthesized St-PGA-based single-drug and combination conjugates and intermediates. The following section describes the complete physico-chemical characterization of conjugates and intermediates.

Table 2.2. Summary of the synthesized single-drug and combination conjugates.

	% mol HYD[A]	% wt Dox[B]	% mol Dox[C]	% wt Das[B]	% mol Das[C]	Ratio Dox:Das	CE Dox (%)	CE Das (%)	Yield[D] (%)
St-PGA	-	-	-	-	-	-	-	-	89
St-PGA-Das	-	-	-	9.9	3.4	-	-	68	75
St-PGA-Val-Das	-	-	-	10.8	3.1	-	-	62	71
St-PGA-hyd-Dox	6.0	9.4	2.9	-	-	-	58	-	30
St-PGA-hyd-Dox$_1$-Val-Das$_1$	3.6	7.8	2.6	9.7	3.0	1:1.2	52	60	64
St-PGA-hyd-Dox$_1$-Das$_1$	5.6	5.3	1.7	7.8	2.8	1:1.6	34	56	25
St-PGA-hyd-Dox$_1$-Das$_{10}$	5.6	1.0	0.3	8.5	2.9	1:9	60	58	39
St-PGA-HYD	6.0	-	-	-	-	-	-	-	82
St-PGA-Das-HYD	6.0	-	-	11.8	4.1	-	-	82	59

(**A**) Obtained by ^{1}H-NMR (D$_2$O). (**B**) Obtained by UV-VIS spectroscopy. (**C**) Obtained by iterative calculation from the loading in %wt. (**D**) Global yield, calculated considering the starting material and the final mass obtained or the yields of each reaction plus purification, except for St-PGA, which considers only the deprotection step. CE = conjugation efficacy.

2.2.2.4. Physico-chemical Characterization of St-PGA-based Single-drug and Combination Conjugates

Complete physico-chemical characterization is crucial for the development of polypeptide-based combination conjugates, as the integration of this information with biological activity assessments can provide for the delineation of structure-activity relationships, which are highly useful tools for rational design (78). For this reason, we performed an exhaustive physico-chemical characterization of all the polypeptide-based single-drug and combination conjugates detailed in **Table 2.2.**

SEC chromatograms demonstrate a single homogeneous molecular weight distribution by RI for all conjugates, where we also identified the sodium counterion eluting at 21.7 min (**Figure 2.14A**). Additionally, we followed conjugate elution using the fluorescent properties of Das and Dox and obtained single homogeneous distributions (**Figure 2.14B**). Both SEC profiles suggest a homogeneous distribution of the drug and moiety content throughout the conjugate population. Of note, we failed to observe any signs of the free drug by any of the detectors.
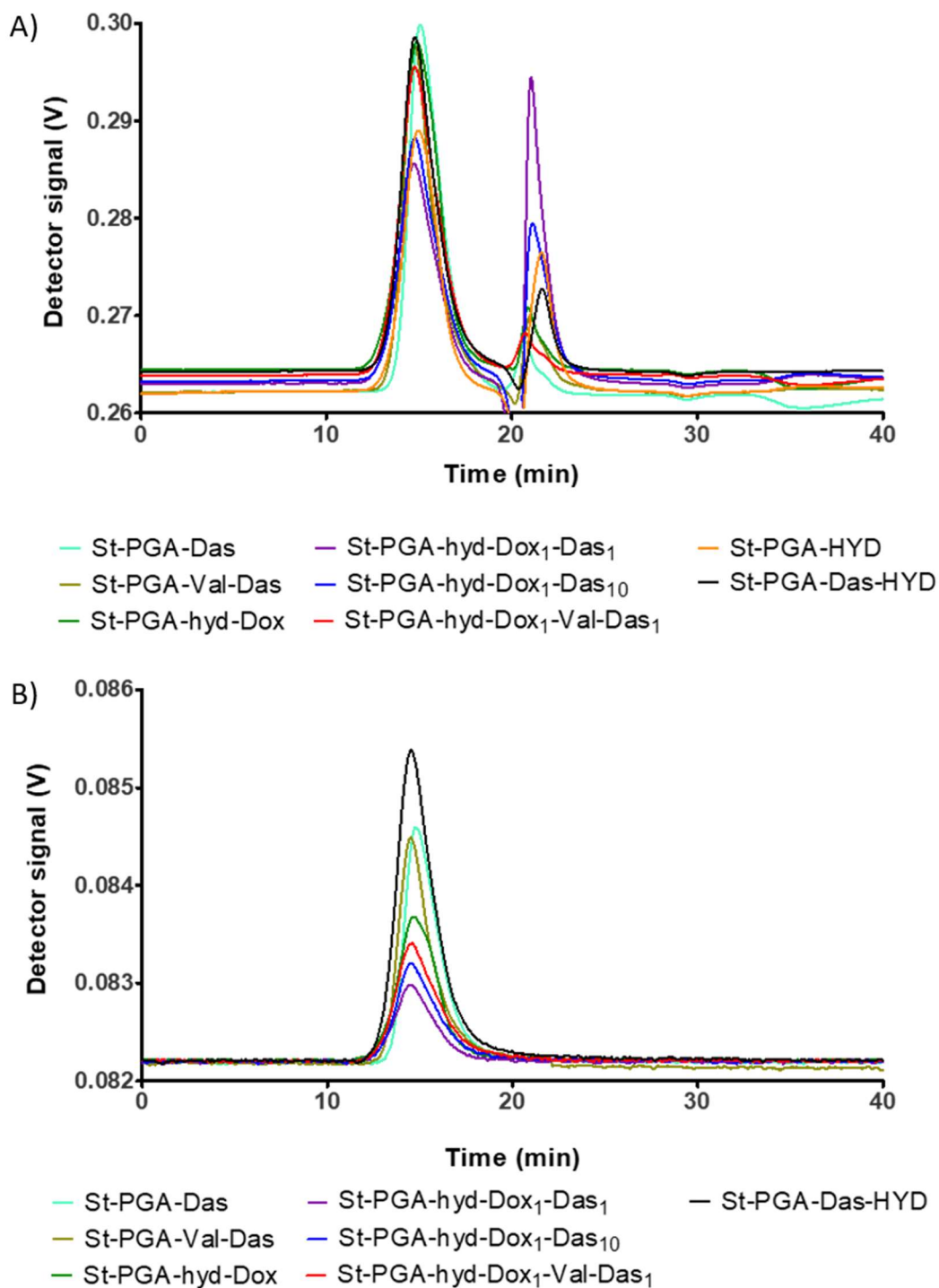
Figure 2.14. Representative SEC chromatograms of the St-PGA-based single-drug and combination conjugates. (**A**) RI detector. The peak at 21 min corresponds to the sodium counter-cation of PGA. (**B**) Fluorescence detector configured to detect Das (λ_{exc} = 340 nm, λ_{em} = 374 nm) for all conjugates except St-PGA-hyd-Dox, whose elution was monitored with Dox fluorescence (λ_{exc} = 480 nm, λ_{em} = 495 nm). Data obtained by injecting 20 µL of a 2 mg/mL polymer solution using 10 mM PB pH 7.4 NaN$_3$ 0.005% as the mobile phase.

As depicted in previous sections (see *2.2.1.2.Physico-chemical Characterization of St-PGA*), St-PGA molecules can self-assemble in aqueous solutions in a concentration-dependent manner (38). For this reason, we evaluated the CAC values of our St-PGA-based single-drug and combination conjugates using DLS, as described previously (see *2.2.1.2.Physico-chemical Characterization of St-PGA*). All conjugates aggregated in a concentration-dependent manner as expected for St-PGA; however, we did observe differential behavior (**Figure 2.15** and **Table 2.3**). St-PGA-Das possessed the higher CAC value (0.8 mg/mL), followed by St-PGA-HYD (0.7 mg/mL), St-PGA-hyd-Dox_1-Das_{10} (0.5 mg/mL), St-PGA-hyd-Dox and St-PGA-hyd-Dox_1-Das_1 (0.4 mg/mL) and St-PGA-Val-Das and St-PGA-hyd-Dox_1-Val-Das_1 (0.2 mg/mL). Das and Dox drive self-assembly in polymeric micelles (79), and both drugs can interact via π-π stacking (80), perhaps explaining the low CAC of Dox containing-conjugates. However, in our case, Das alone did not enhance polymer aggregation unless conjugated through the Val spacer. Interestingly, the conjugate with free hydrazides plus Das (St-PGA-Das-HYD) possessed a lower CAC than without Das (St-PGA-HYD), suggesting that Das enhances aggregation in this case. We further evaluated the influence of drug-drug interactions in the solution conformation of St-PGA-based conjugates by CD; we describe these results later in this section.
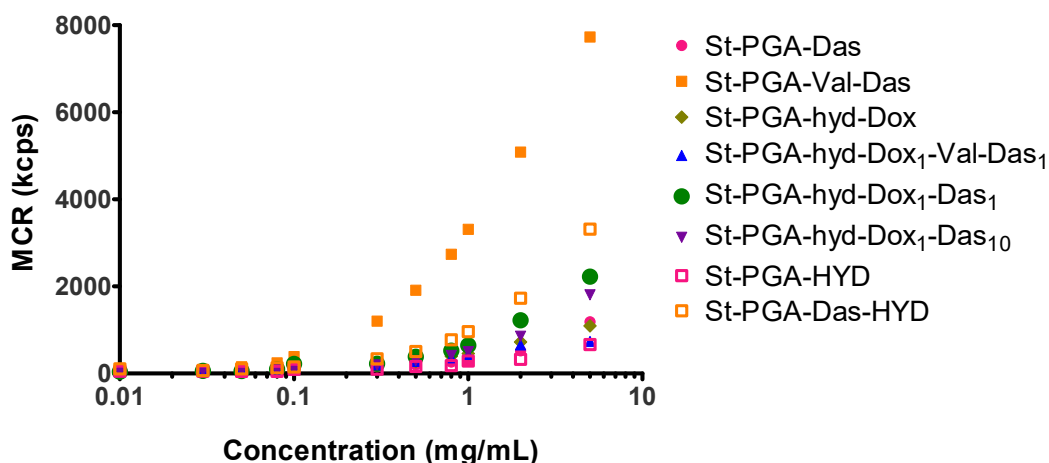
Figure 2.15. CAC determination graph of St-PGA-based single-drug and combination conjugates. Data represented as average MCR of two measurements vs. conjugate concentration (logarithmic scale). These data were employed for the graphical determination of CAC.

Table 2.3. Summary of the synthesized compounds and their CAC values.

	% mol HYD[A]	% mol Dox[B]	% mol Das[B]	CAC[C] (mg/mL)
St-PGA	-	-	-	1.0
St-PGA-Das	-	-	3.4	0.8
St-PGA-Val-Das	-	-	3.1	0.2
St-PGA-hyd-Dox	6.0	2.9	-	0.4
St-PGA-hyd-Dox$_1$-Val-Das$_1$	3.6	2.6	3.0	0.2
St-PGA-hyd-Dox$_1$-Das$_1$	5.6	1.7	2.8	0.4
St-PGA-hyd-Dox$_1$-Das$_{10}$	5.6	0.3	2.9	0.5
St-PGA-HYD	6.0	-	-	0.7
St-PGA-Das-HYD	6.0	-	4.1	0.3

(**A**) Obtained by ^{1}H-NMR (D$_2$O) of the Boc-protected precursor. (**B**) Obtained by iterative calculation from the loading in % wt. (**C**) Graphically calculated from Figure 2.15.

Considering the CAC study results, we next evaluated conjugate size by DLS in MilliQ water (**Supplementary Figure 2.5**) and DPBS (**Supplementary Figure 2.6**) at three different concentrations - above the CAC (1 mg/mL), below the CAC (0.1 mg/mL), and an intermediate concentration (0.5 mg/mL). In general, measurements made in MilliQ water displayed greater heterogeneity, with more than one peak by number (**Supplementary Figure 2.5A, D, G, J, M, P, S,** and **V**) and intensity (**Supplementary Figure 2.5B, E, H, K, N, Q, T,** and **W**), suggesting the existence of an equilibrium between St-PGA aggregates and unimers even at 0.1 mg/mL, below the CAC value of all the conjugates (see **Table 2.2**). Nevertheless, the correlation function of the measurements performed in MilliQ water at 0.1 mg/mL possessed low intercepts (<0.8), reflecting a poor quality of the measurement due to a poor signal-noise ratio (**Supplementary Figure 2.5C, F, I, L, O, R,** and **X**). Thus, considering the data obtained at 0.5 and 1 mg/mL, the heterogeneity we observed in the size distribution by number and intensity for all St-PGA-based conjugates agrees with the aggregation behavior observed in the CAC experiment performed earlier (**Figure 2.15** and **Table 2.3**).

Interestingly, measurements made in DPBS provided a single population by number for all St-PGA-based conjugates (**Supplementary Figure 2.6A, G, J, M, P, S,** and **V**) except for St-PGA-Val-Das, which showed two populations at 0.1 and 1 mg/mL (**Supplementary Figure 2.6D**). The size distribution by intensity in DPBS suggests the presence of aggregates for all St-PGA-based conjugates, showing multiple populations in the samples (**Supplementary Figure 2.6B, E, H, K, N, Q, T,** and **W**); thereby suggesting the coexistence of unimers with a small number of aggregates for all conjugates. As in MilliQ water, the correlation function of the measurements performed in DPBS generally showed exponential decay; however, the measurements performed at 0.1 mg/mL tended to possess lower intercepts (<0.8), reflecting a poor quality of the measurement (**Supplementary Figure 2.6 F, I, L, R, O,** and **U**), with the following

exceptions. St-PGA-Das displayed a high noise level at long delay times (**Supplementary Figure 2.6**C). St-PGA-Das-HYD measurement performed at 1 mg/mL in DPBS possessed a lower intercept (<0.5) than the sample at 0.1 mg/mL, which can be a consequence of a high particle concentration (**Supplementary Figure 2.6X**).

As explained above, St-PGA self-assembles in non-salty aqueous media in a concentration-dependent manner; however, high salt content disrupts the interactions driving self-assembly (38). In agreement, sizes obtained in DPBS at 0.5 and 1 mg/mL displayed no significant differences for all the conjugates except St-PGA-hyd-Dox, which exhibits a hydrodynamic diameter of 3.4 nm at 0.5 mg/mL and 8.2 nm at 1 mg/mL, suggesting that St-PGA-hyd-Dox still aggregates in high ionic strength media. The study of the secondary structure of St-PGA-hyd-Dox and the remaining St-PGA-based conjugates will shed more light on this regard.

We designed our conjugates with intravenous administration in a DPBS solution in mind; thus, conjugate dilution in blood after administration will eventually provoke aggregate disassembly. Considering the data provided by the size study and the quality of the measurements, we assumed size by number in DPBS at 0.5 mg/mL as the hydrodynamic diameter of the unimers, as the correlation function obtained for the measurements in this condition displays acceptable quality (**Supplementary Figure 2.6C, F, I, L, O, R, U,** and **X**) for all the St-PGA-based conjugates and St-PGA-hyd-Dox displayed aggregation at 1 mg/mL. Under the noted conditions, all conjugates displayed hydrodynamic diameters similar to the "parental" St-PGA unimer (**Figure 2.3**), ranging from 3 to 18 nm (**Figure 2.16A**). This size range agrees with data reported for linear PGA Dox-Das conjugates (41) and St-PGAs generated with different initiators (43). Our conjugates exhibit sizes above the limit for renal clearance (6-8 nm) (21), except St-PGA-hyd-Dox (3.4 ± 1.3 nm), thus meeting one of our design requirements.
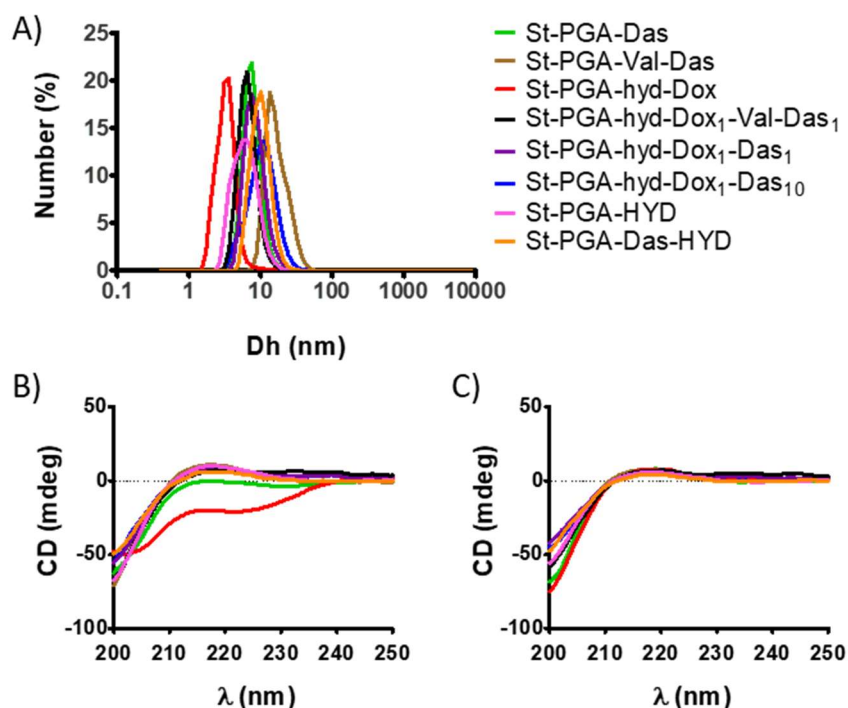
Figure 2.16. Characterization of single-drug and combination conjugates size and secondary structure. (**A**) Hydrodynamic diameter distribution graphs by number obtained by DLS in DPBS at 0.5 mg/mL. Data obtained from the average result of at least four measurements. (**B-C**) CD data in (**B**) water and (**C**) DPBS at 0.5 mg/mL. The results with three accumulated measurements are displayed.

To study conjugate conformation and the associated intramolecular interactions involved, we evaluated secondary structure by CD. PGAs display water solubility in their random coil state (27); however, they undergo coil-to-helix transitions at low pH (51,81,82) in a process that depends on polymer and salt concentrations (83). Additionally, the presence of drugs, drug loadings, and linker nature alter conformational transitions (37). Thus, we studied conjugate secondary structure in various media (MilliQ water and DPBS) and concentrations (0.1, 0.2, and 0.5 mg/mL). Although we aimed to understand these interactions in concentrations above and below the CAC for each conjugate, instrumental limitations allowed 0.5 mg/mL as a maximal concentration. Thus, the secondary structures of St-PGA-Das, St-PGA-hyd-Dox_1-Das_{10}, and St-PGA-HYD above their CAC remain unassessed.

All single-drug and combination conjugates evaluated exhibited a random coil conformation (with a typical negative band at 200 nm) in all evaluated conditions except for St-PGA-hyd-Dox (**Figure 2.16B** and **C**, and **Supplementary Figure 2.7**). In MilliQ water, St-PGA-hyd-Dox exhibited a double minimum at 208 and 222 nm typical of an α-helix conformation (51) at all concentrations evaluated (**Figure 2.16B**, and **Supplementary Figure 2.7E**), representing a more rigid conformation with a lower solubility in aqueous media than random coil (27). As St-PGA-HYD displays a random coil conformation under all evaluated conditions (**Figure 2.16B** and **C**, and **Supplementary Figure 2.7M** and **N**), we attribute the α-helix conformation switch in water to the presence of Dox. Of note, this phenomenon did not occur in DPBS, where St-PGA-hyd-Dox exhibited a random coil conformation at all evaluated concentrations (**Figure 2.16C**, and **Supplementary Figure 2.7F**). We attribute this behavior to a reduction in the repulsion between carboxyl groups provoked by the high concentration of NaCl in DPBS (84).

CD spectra above 250 nm, where the peptide bond absorption contributes negligibly, provide information regarding other chromophores (85). We identified alterations in this regard compared to the spectrum of the parental St-PGA. At ~335 nm, we observed a positive band for conjugates bearing Val-Das (St-PGA-Val-Das and St-PGA-hyd-Dox$_1$-Val-Das$_1$) in MilliQ water and DPBS (**Figure 2.17**). These findings suggest that the Val linker alters the arrangement of Das molecules compared to the direct ester bond. St-PGA-hyd-Dox$_1$-Val-Das$_1$ CD spectra in MilliQ water and DPBS also exhibited a negative band at ~ 300 nm, thus a negative first Cotton effect at a longer wavelength and a positive second Cotton effect at a shorter wavelength, centered in ~ 324 nm, the maximum of absorbance for Das, suggesting the stacking of Das molecules (86). This different arrangement of Das molecules in St-PGA-Val-Das and St-PGA-hyd-Dox$_1$-Val-Das$_1$ may explain the low CAC value observed during our evaluation of conjugate aggregation (**Table 2.3**).

When we studied Dox-bearing conjugates, we failed to identify any evidence of Dox dimerization under any condition (**Figure 2.17**) as revealed by the absence of a negative band at 540 nm, a typical sign of Dox dimerization (87,88). Therefore, the low CAC observed for Dox-bearing conjugates does not rely on the π-π stacking of Dox molecules, as we suggested earlier. Dox-Dox interactions cannot explain the change to α-helix conformation in St-PGA-hyd-Dox either.
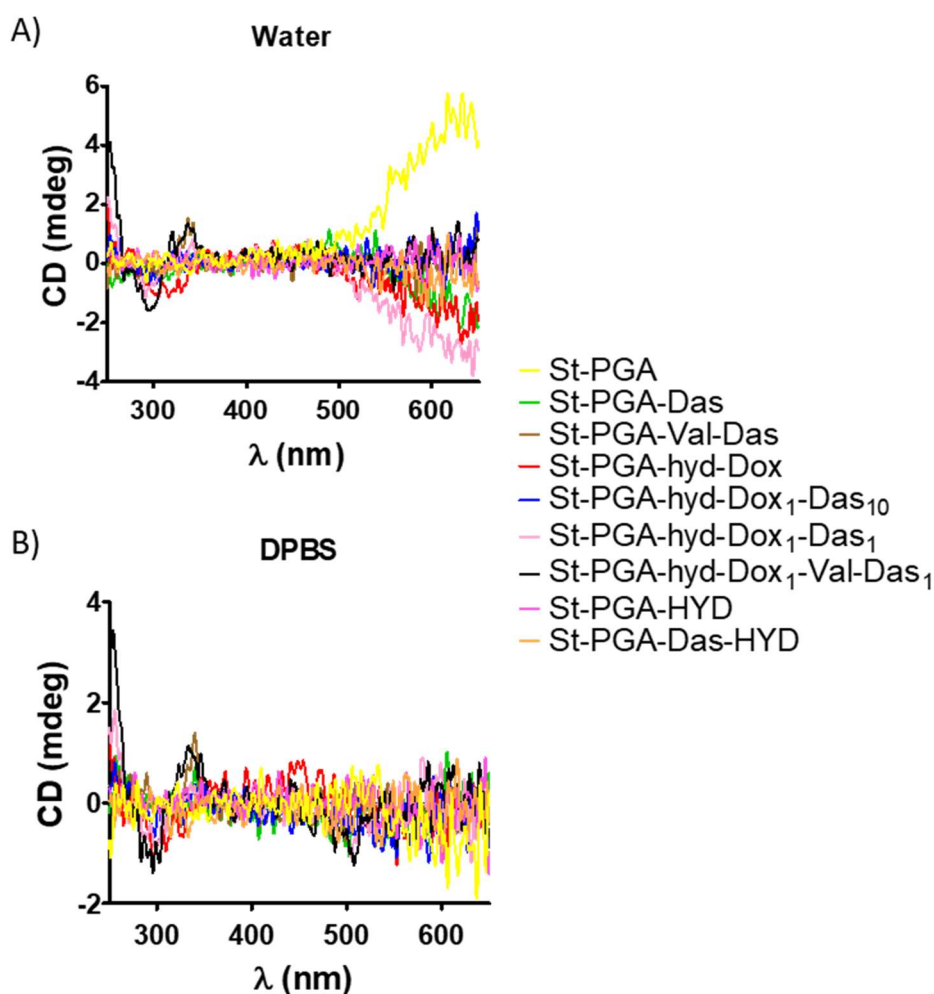
Figure 2.17. Characterization of Dox and Das dimerization in single-drug and combination conjugates in (A) MilliQ water and (B) DPBS. Data obtained by CD. Average results with three accumulated measurements are displayed.

Finally, we studied the zeta potential of conjugates by ELS. As expected for PGAs (33,37,38,43), all conjugates exhibited negative zeta potential ranging from -49 to -28 mV with little to no variation between the two concentrations evaluated (values noted as part of **Table 2.4**). These results do not agree with previously reported data where St-PGA displayed increased negative zeta potential upon aggregation (38), which may suggest an alteration in the aggregation behavior of the polymers.

In summary, we successfully synthesized a family of St-PGA-based drug conjugates that display solubility in aqueous media following a strategy that allows for precise control over drug loading and drug ratio. **Table 2.4** summarizes the main physico-chemical traits of our St-PGA-based conjugate family.

Table 2.4. Summary of the primary physico-chemical descriptors for St-PGA and single-drug and combination conjugates.

	% mol HYD[A]	% wt Dox[B]	% mol Dox[C]	% wt Das[B]	% mol Das[C]	Ratio Dox:Das[D]	CAC[E] (mg/mL)	Dh[F] (nm)	Z-Pot$^{1\ mg/mL}$ (mV)	Z-Pot$^{0.5\ mg/mL}$ (mV)
St-PGA	-	-	-	-	-	-	1.0	6.1 ± 1.7	-42.6 ± 3.7	-50.7 ± 1.3
St-PGA-Das	-	-	-	9.9	3.4	-	0.8	7.8 ± 2.4	-28.5 ± 3.7	-36.3 ± 4.0
St-PGA-Val-Das	-	-	-	10.8	3.1	-	0.2	17.6 ± 6.7	-48.9 ± 0.4	-45.5 ± 0.8
St-PGA-hyd-Dox	6.0	9.4	2.9	-	-	-	0.4	3.4 ± 1.3	-39.2 ± 1.8	-38.3 ± 3.4
St-PGA-hyd-Dox$_1$-Val-Das$_1$	3.6	7.8	2.6	9.7	3.0	1:1.2	0.2	6.8 ± 2.4	-43.1 ± 1.3	-43.4 ± 1.5
St-PGA-hyd-Dox$_1$-Das$_1$	5.6	5.3	1.7	7.8	2.8	1:1.6	0.4	8.7 ± 3.3	-44.7 ± 0.1	-44.9 ± 0.6
St-PGA-hyd-Dox$_1$-Das$_{10}$	5.6	1.0	0.3	8.5	2.9	1:9	0.5	11.3 ± 5.1	-41.2 ± 2.7	-40.5 ± 1.7
St-PGA-HYD	6.0	-	-	-	-	-	0.7	6.5 ± 2.8	-54.2 ± 0.9	-49.8 ± 2.7
St-PGA-Das-HYD	6.0	-	-	11.8	4.1	-	0.3	10.4 ± 3.5	-46.2 ± 1.8	-46.9 ± 0.9

(**A**) Total loading of hydrazide (HYD) obtained by ^{1}H-NMR (D$_2$O). (**B**) Obtained by UV-VIS spectroscopy. (**C**) Obtained by iterative calculation from the loading in weight percent. (**D**) Obtained using the loadings in mol percent. (**E**) CAC value obtained graphically following a DLS method. (**F**) Hydrodynamic diameter (Dh) measured in DPBS at 0.5 mg/mL of the conjugate. Data obtained from the distributions presented in Figure 2.16A and expressed as mean ± SD. Z-Pot measured in in KCl 1 mM. Data expressed as mean ± SD of three measurements.

2.2.3. In vitro Evaluation of Anti-tumor Activity

We evaluated the anti-tumor activity of our family of St-PGA-based conjugates *in vitro* in the human breast cancer cell line MDA-MB-231-Luc using the MTS (3-(4,5-dimethylthiazol-2-yl)-5-(3-carboxymethoxyphenyl)-2-(4-sulfophenyl)-2H-tetrazolium salt) assay. The MTS assay takes advantage of the ability of metabolically active cells to reduce weakly colored tetrazolium salts to yield a brightly colored formazan derivative, which can be measured by UV-VIS spectroscopy at $\lambda = 490$ nm (89,90). The coenzyme NAD(P)H (reduced nicotinamide adenine dinucleotide (phosphate)) present within metabolically active cells is the main factor mediating the reduction of tetrazolium salts (91); however, the hydrophilicity of MTS hinders permeation across the cellular membrane, making necessary the use of an intermediate electron acceptor such as phenazine methyl sulfate (PMS) that permeates inside viable cells, becomes reduced and exits the cell to convert MTS to its formazan derivative (**Scheme 2.9**) (92). Overall, the amount of formazan derivative produced in culture is proportional to the number of viable cells (91), thereby providing information regarding cell viability.

Data from cell viability assays are typically employed to obtain dose-response curves that fit in a logistic sigmoid function to evaluate and compare anti-tumor activity (**Figure 2.18**). From this function, we can extract information regarding drug efficacy and potency. Data analysis primarily seeks the IC50 value - the drug concentration that reduces cell viability by 50% - which measures drug potency (93,94); however, other dose-response parameters provide complementary information. The maximum effect observed for a drug (E_{max}) serves as a measure of efficacy, while the slope of the curve informs on the benefit of increasing the drug dose (a higher slope means more significant benefit) and can be helpful in a translational scenario (94).
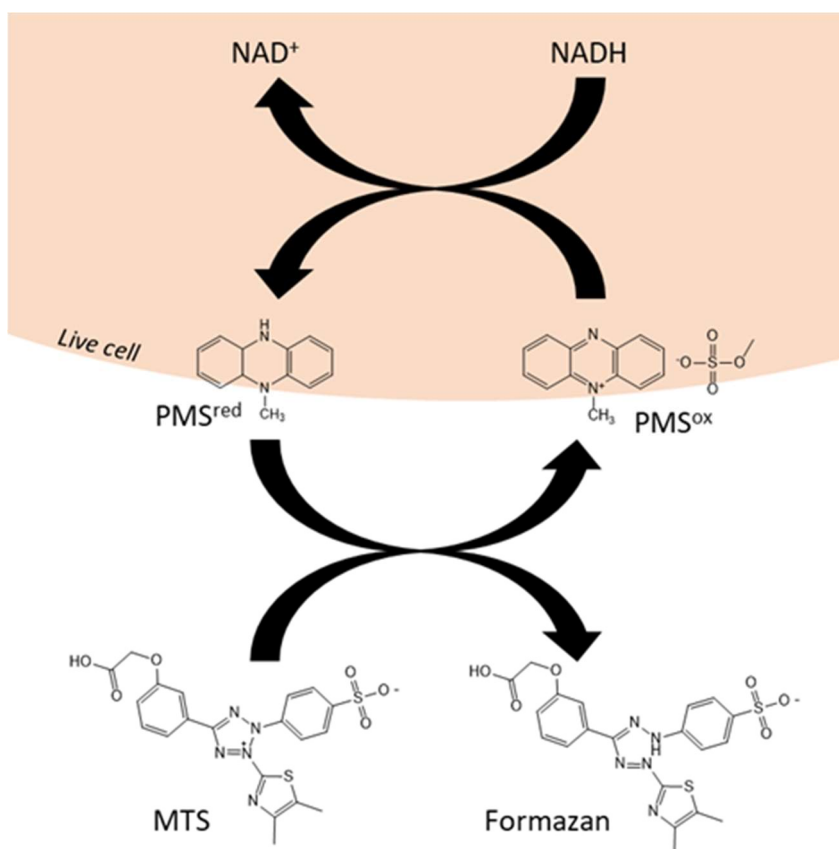
Scheme 2.9. MTS assay scheme. The intermediate electron acceptor PMS transfers the electron from NAD(P)H in the cytoplasm of metabolically active cells to MTS, producing its reduction to the brightly colored formazan derivative.
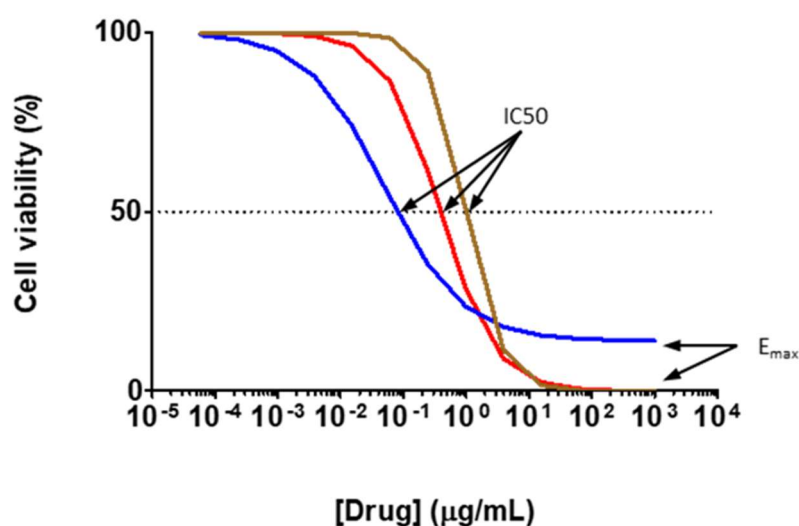
Figure 2.18. Example of dose-response curves. The "blue" drug displays lower efficiency (higher E_{max}) but greater potency (lower IC50) than the "brown" or "red" drugs. The brown and red drugs possess equal efficiency (same E_{max}), but the red drug possesses greater potency (lower IC50). As the brown drug exhibits the steepest slope, increasing the administered dose will provide a more significant benefit compared to the red and blue drugs.

We used MDA-MB-231-Luc cells (obtained by the stable transfection of MDA-MB-231 cells with a luciferase expression plasmid (95)) as an *in vitro* model for TNBC. MDA-MB-231 cells lack HER2, PR, and ER expression, and this line is commonly employed as an *in vitro* model of TNBC (95,96). The MDA-MB-231 cell line was initially isolated from a single sample of a pleural infusion from a metastatic breast cancer patient (97). Stable luciferase expression allows non-invasive monitoring of tumor growth and metastatic spread *in vivo* by the simple parenteral administration of luciferin and bioluminescence detection (98,99). Our laboratory has employed the MDA-MB-231-Luc cell line to establish a metastatic TNBC murine model (95), which we also used as an *in vivo* model in this study (see *2.2.5.In vivo Evaluation of Anti-tumor and Anti-metastatic Activity*).

We administered conjugates to the cell culture dissolved in cell media and measured cell viability after seventy-two hours by MTS assay. St-PGA failed to induce any cytotoxic activity in MDA-MB-231-Luc cells up to 0.5 mg/mL (**Figure 2.19**), which confirms the safety of our starting material and agrees with previously reported data for St-PGA in the SHSY5Y neuroblastoma cell line (38,43).
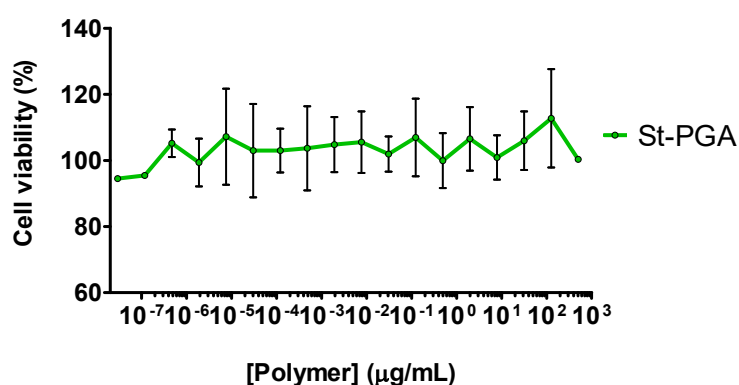
Figure 2.19. Cytotoxic activity of St-PGA in MDA-MB-231-Luc cells. Cell viability measured by MTS assay after 72 h of treatment with St-PGA. Data expressed as the percentage of cell viability normalized to the untreated control (mean ± SEM, n=2).

From the statistical comparison of the cell viability curves and the IC50 values calculated (in brackets and **Table 2.5**), we discovered that the single-drug conjugate St-PGA-hyd-Dox (18.62 ng/mL) displayed more significant cytotoxic activity (p=0.0008) than free Dox (76.42 ng/mL) (**Figure 2.20A**). Thus, Dox conjugation to St-PGA using a pH-labile hydrazone linker enhances the cytotoxic activity of Dox. Of note, previous studies performed in our laboratory failed to discover a similar finding for linear counterparts (41), suggesting an advantage of St-PGA architectures.

Table 2.5. IC50 values obtained for St-PGA-based single-drug and combination conjugates, selected intermediates, and the free drugs as single agents and in combination at specific drug ratios.

	Treatment	Ratio Dox:Das	IC50 (ng Dox/mL)	IC50 (ng Das/mL)
Dox	St-PGA-hyd-Dox	-	18.62	-
	St-PGA-HYD + Dox	1:9*	355.06	
	Dox	-	76.42	-
Das	St-PGA-Das	-	-	30.73
	St-PGA-Val-Das	-	-	102.80
	St-PGA-Das-HYD	-	-	85.63
	Das	-	-	0.82
Combinations	St-PGA-hyd-Dox$_1$-Val-Das$_1$	1:1.2	4.15	5.16
	Dox + Das	1:1.2	0.83	1.03
	St-PGA-hyd-Dox$_1$-Das$_1$	1:1.6	1.39	2.04
	Dox + Das	1:1.6	0.29	0.42
	St-PGA-hyd-Dox$_1$-Das$_{10}$	1:9	0.21	1.75
	St-PGA-Das-HYD + Dox	1:9	0.03	0.22
	Dox + Das	1:9	0.05	0.46

*This ratio corresponds to the Dox loading of St-PGA-hyd-Dox$_1$-Das$_{10}$.
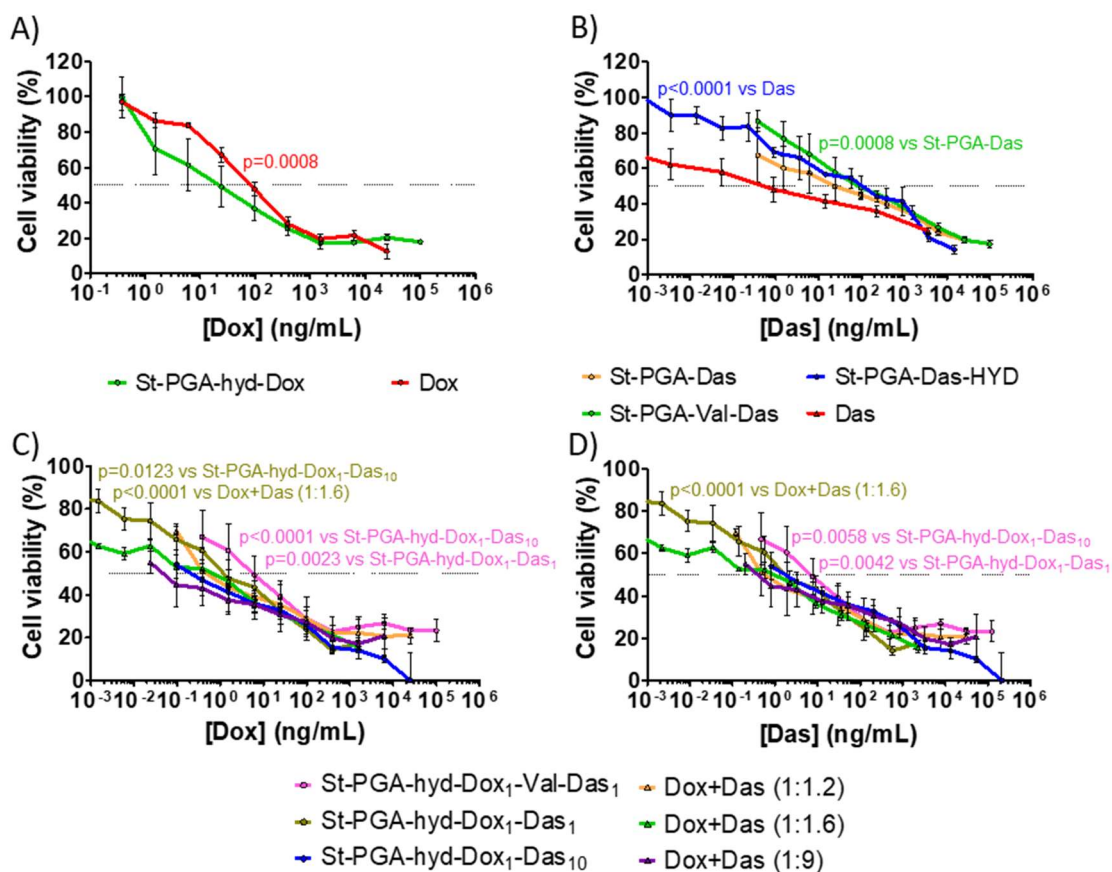
Figure 2.20. Cytotoxic activity of St-PGA-based single-drug and combination conjugates in MDA-MB-231-Luc cells. Cell viability measured by MTS assay after 72 h of treatment with (**A**) St-PGA-hyd-Dox or free Dox, (**B**) St-PGA-Das, St-PGA-Val-Das, or free Das, (**C** and **D**) St-PGA-hyd-Dox_1-Val-Das_1, St-PGA-hyd-Dox_1-Das_1, St-PGA-hyd-Dox_1-Das_{10}, or the combination of the free drugs at the equivalent ratio for each conjugate. (**C**) Data represented in Dox equivalents. (**D**) Data represented in Das equivalents. Data expressed as the percentage of cell viability normalized to the untreated control (mean ± SEM, n≥3). Statistical analysis conducted via extra sum-of-squares F test fit comparison.

The evaluation of the St-PGA-Das and St-PGA-Val-Das single-drug conjugates failed to provide proof of improved cytotoxic activity compared to free Das (**Figure 2.20B**). In agreement with findings from the evaluation of linear PGA counterparts (41), St-PGA-Das (30.73 ng/mL) possessed significantly increased cytotoxic activity (p=0.0249) compared to St-PGA-Val-Das (102.80 ng/mL).

We next evaluated combination conjugates with a 1:1 drug ratio in a comparable manner (**Figure 2.20C** and **D**). Considering the results reported for a PGA-hyd-Dox-Val-Das linear combination conjugate (41), we expected

St-PGA-hyd-Dox$_1$-Val-Das$_1$ to display improved cytotoxic activity compared to St-PGA-hyd-Dox$_1$-Das$_1$; however, our results provided evidence for an opposite trend. St-PGA-hyd-Dox$_1$-Das$_1$ (1.39 ng/mL of Dox and 2.04 ng/mL of Das) displayed greater cytotoxic activity (p=0.0023 in Dox equivalents, p=0.042 in Das equivalents) compared to St-PGA-hyd-Dox$_1$-Val-Das$_1$ (4.15 mg/mL of Dox and 5.16 ng/mL of Das). Together with the higher IC50 value of St-PGA-Val-Das compared to St-PGA-Das, these results suggest that the Val spacer fails to provide any advantage over direct ester conjugation of Das in St-PGA-based conjugates.

The administration of low doses of Dox with higher doses of Das leads to enhanced synergism (41); therefore, we expected improved cytotoxic activity from St-PGA-hyd-Dox$_1$-Das$_{10}$ compared to St-PGA-hyd-Dox$_1$-Das$_1$. Accordingly, St-PGA-hyd-Dox$_1$-Das$_{10}$ (0.21 ng/mL of Dox and 1.75 ng/mL of Das) displayed more significant cytotoxic activity compared to St-PGA-hyd-Dox$_1$-Das$_1$ when comparing cell viability curves in Dox equivalents (p=0.0123) but not Das equivalents (p=0.1087, **Figure 2.20C** and **D**). St-PGA-hyd-Dox$_1$-Das$_{10}$ also exhibited more significant cytotoxic activity than St-PGA-hyd-Dox$_1$-Val-Das$_1$ (p<0.0001 in Dox equivalents and p=0.0058 in Das equivalents, **Figure 2.20C** and **D**), providing additional proof of the lack of benefit of the Val-mediated Das conjugation in St-PGA-based conjugates.

The combination of free Dox and Das at 1:1.6 (Dox:Das) ratio exhibited significantly greater cytotoxic activity than St-PGA-hyd-Dox$_1$-Das$_1$ (with the same Dox:Das ratio) (p<0.001 for both drug equivalents) while St-PGA-hyd-Dox$_1$-Das$_{10}$ and St-PGA-hyd-Dox$_1$-Val-Das$_1$ displayed comparable cytotoxic activities compared to the combination of free Dox and Das at a 1:9 (p=0.183 for both drugs) and 1:1.2 ratio (p=0.1321 for both drugs), respectively (**Figure 2.20C** and **D**). Therefore, St-PGA-hyd-Dox$_1$-Das$_1$, St-PGA-hyd-Dox$_1$-Das$_{10}$, and St-PGA-hyd-Dox$_1$-Val-Das$_1$ failed to provide a significant benefit over the treatment with the combination of free Dox and Das; however, we did expect to observe benefits to polypeptide-

conjugation in the *in vivo* scenario due to passive tumor targeting provided by the EPR effect.

The synthetic protocol for St-PGA-hyd-Dox$_1$-Das$_1$ and St-PGA-hyd-Dox$_1$-Das$_{10}$ conjugates changes only at the last step, which involves differing amounts of Dox according to the drug ratio required. Therefore, St-PGA-hyd-Dox$_1$-Das$_{10}$ possesses a significant amount of free hydrazide moieties compared to St-PGA-hyd-Dox$_1$-Das$_1$. The toxicity of hydrazide as a component of small drugs has been previously reported in breast cancer cell lines (100). To ensure that the improved cytotoxic activity of St-PGA-hyd-Dox$_1$-Das$_{10}$ compared to St-PGA-hyd-Dox$_1$-Das$_1$ derives from Dox and Das loading alone, we verified the potential biological activity of the free hydrazide moieties in St-PGA-based conjugates. Thus, we evaluated the cytotoxic activity of the St-PGA-HYD and St-PGA-Das-HYD precursors (**Figure 2.21A**-**C**).

We failed to observe cytotoxic activity for St-PGA-HYD in MDA-MB-231-Luc cells up to a concentration of 0.5 mg/mL (**Figure 2.21A**). Moreover, St-PGA-Das-HYD (85.63 ng/mL Das) displayed a similar cytotoxic activity to St-PGA-Das (p=0.0767, **Figure 2.21B**). Additionally, the administration of St-PGA-HYD with free Dox at an equivalent Dox content of St-PGA-hyd-Dox$_1$-Das$_{10}$ (**Figure 2.21C**) exhibited a lower cytotoxic activity (355.06 µg/mL Dox) than free Dox alone (p=0.0002) and St-PGA-hyd-Dox (p<0.0001). These results suggest that hydrazide moieties do not exert any biological activity in MDA-MB-231-Luc cells.

Nevertheless, the treatment with St-PGA-Das-HYD in combination with free Dox at the same Dox:Das ratio of St-PGA-hyd-Dox$_1$-Das$_{10}$ (**Figure 2.21B** and **C**, 0.03 ng/mL Dox and 0.22 ng/mL Das) induced a more significant cytotoxic activity than St-PGA-hyd-Dox$_1$-Das$_{10}$ (p=0.0236 for both drugs) and similar to that of the combination of free Dox and Das at the same ratio (1:9, p=0.2985 for both drugs). Therefore, we hypothesize that the improved cytotoxic activity of St-PGA-Das-HYD + Dox compared to St-PGA-

hyd-Dox$_1$-Das$_{10}$ derives from the different bioavailability of Dox that arises from drug conjugation and release. A study of the drug release profile of St-PGA-hyd-Dox$_1$-Das$_{10}$ and remaining conjugates will provide further insight in this regard (see *2.2.4.pH and Cathepsin B-mediated Drug Release*).
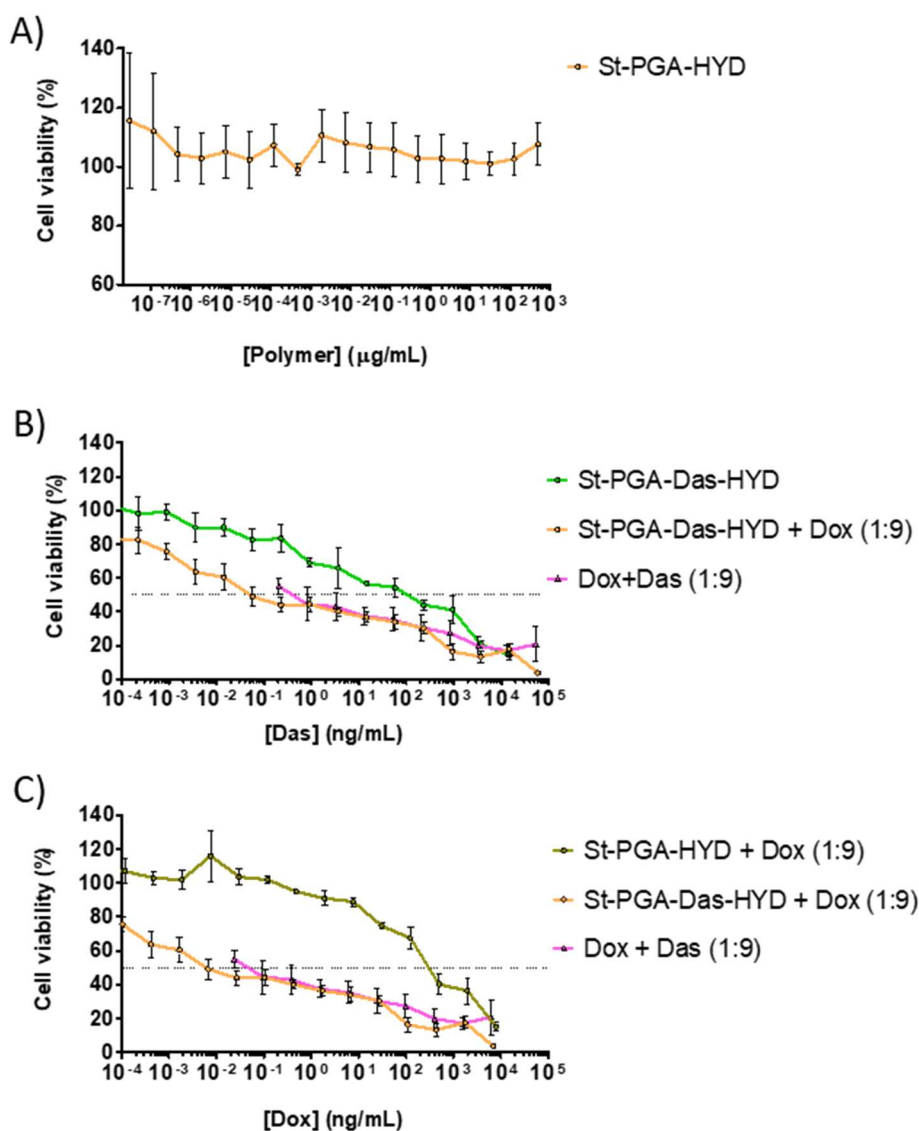
Figure 2.21. Evaluation of the cytotoxic activity of hydrazide moieties. Cell viability measured by MTS assay after 72 h of treatment with (**A**) St-PGA-HYD - graph in polymer concentration, (**B**) St-PGA-Das-HYD, St-PGA-Das-HYD plus Dox (equivalent to St-PGA-hyd-Dox$_1$-Das$_{10}$ Dox loading), and Dox plus Das (1:9 ratio) - graph in Dox equivalents, (**C**) St-PGA-HYD plus Dox (equivalent to St-PGA-hyd-Dox$_1$-Das$_{10}$ Dox loading), St-PGA-Das-HYD plus Dox (equivalent to St-PGA-hyd-Dox$_1$-Das$_{10}$ Dox loading), and Dox plus Das (1:9 ratio) - graph in Das equivalents. Data expressed as the percentage of cell viability normalized to untreated control (mean ± SEM, n=3). Statistical analysis was conducted via extra sum-of-squares F test fit comparison.

Overall, our data suggest that our family of combination conjugates display robust *in vitro* anti-tumor activities. The comparison between the conjugates with the Val spacer and direct ester Das conjugation suggests that the use of Val fails to provide any benefit to our St-PGA-based conjugates. The study of drug release profiles of single-drug and combination St-PGA-based conjugates will provide additional information regarding the different *in vitro* cytotoxic activities (see *2.2.4.pH and Cathepsin B-mediated Drug Release*).

2.2.4. pH and Cathepsin B-mediated Drug Release

The drug release profile represents an essential aspect of single-drug and combination polypeptide-drug conjugates. While a conjugate must display stability under normal physiological conditions, it must also allow for specific drug release within target tissues/organelles to improve drug bioavailability, enhance treatment efficacy, and reduce side effects. The conjugation of drugs to the polypeptide backbone via stimuli-responsive linkers represents one means to ensure controlled release. Given the known acidity of the tumor microenvironment (101,102) compared to the neutral pH of blood/healthy tissues (101), acidic pH-labile linkers have been widely explored in the field of oncological nanomedicine (37,41,68,69,77,103).

Furthermore, polypeptide-drug conjugates become internalized via endocytosis, whereafter they are delivered to the lysosome (43), which possesses an acidic pH and contains a myriad of active hydrolases (104). Hydrolases include cathepsin B, a cysteine protease overexpressed in many cancers, including breast cancer (105). Cathepsin B degrades PGA (linear and star-shaped) by cleavage of the peptidic backbone (i.e., hydrolysis of the amide bonds) (43,61), which can also mediate drug release (34). As described in earlier sections, ester bonds can undergo hydrolysis in response to exposure to acids, bases, metal ions, or enzymes (e.g., esterases) (59,60); meanwhile, the hydrazone bond undergoes hydrolysis in

acidic environments following the inverse path of the conjugation reaction (**Scheme 2.8**) (67).

Therefore, we evaluated Dox and Das release from single-drug and combination conjugates at physiological pH (7.4) and tumor microenvironment/lysosomal pH (5.0); furthermore, we evaluated Dox and Das release from St-PGA-hyd-Dox$_1$-Das$_1$ and St-PGA-hyd-Dox$_1$-Das$_{10}$ in the presence of cathepsin B.

2.2.4.1.   Protocol Optimization

Based on procedures optimized for linear PGA-based conjugates (41), we performed the release studies by dissolving conjugates in relevant buffers and extracting the released Dox and Das at fixed time points. We improved the protocol for the liquid-liquid extraction of free Dox and Das from release buffers by using a mixture of chloroform:isopropanol (7:3 v/v) as an extraction solvent and reducing the amount of solvent for the extraction procedure (from 5 mL to 1 mL). These procedures allowed a reduction in the time for solvent evaporation and, thus, the overall time needed for sample processing.

We studied drug recovery from the buffers used for release studies; 10 mM PB with 150 mM NaCl (PBS) at pH 7.4 or 5.0 for pH-dependent drug release, and 20 mM sodium acetate pH 5.0 with 5 mM dithiothreitol (DTT) and 2 mM disodium ethylenediaminetetraacetic acid (EDTA) for cathepsin B mediated drug release. We prepared mixtures of Dox, Das, and St-PGA in PBS pH 7.4, PBS pH 5.0, and cathepsin B buffer (without the enzyme) at three drug concentrations: low (0.012 mg/mL Dox, 0.012 mg/mL Das), medium (0.025 mg/mL Dox, 0.025 mg/mL Das), and high (0.1 mg/mL Dox, 0.1 mg/mL Das). We took 100 µL of each mixture (adding 5 µL of NaOH 0.2 M to the samples at pH 5.0 to neutralize the pH) and immediately extracted drugs with 1 mL of chloroform:isopropanol (7:3).

We isolated and dried the organic phase and then reconstituted it with methanol for analysis by reverse-phase high-performance liquid chromatography (RP-HPLC). We used inherent fluorescent properties to detect and quantify drugs, using λ_{exc} = 340 nm and λ_{em} = 374 nm for Das detection, and λ_{exc} = 480 nm and λ_{em} = 495 nm for Dox detection (**Figure 2.22A**).
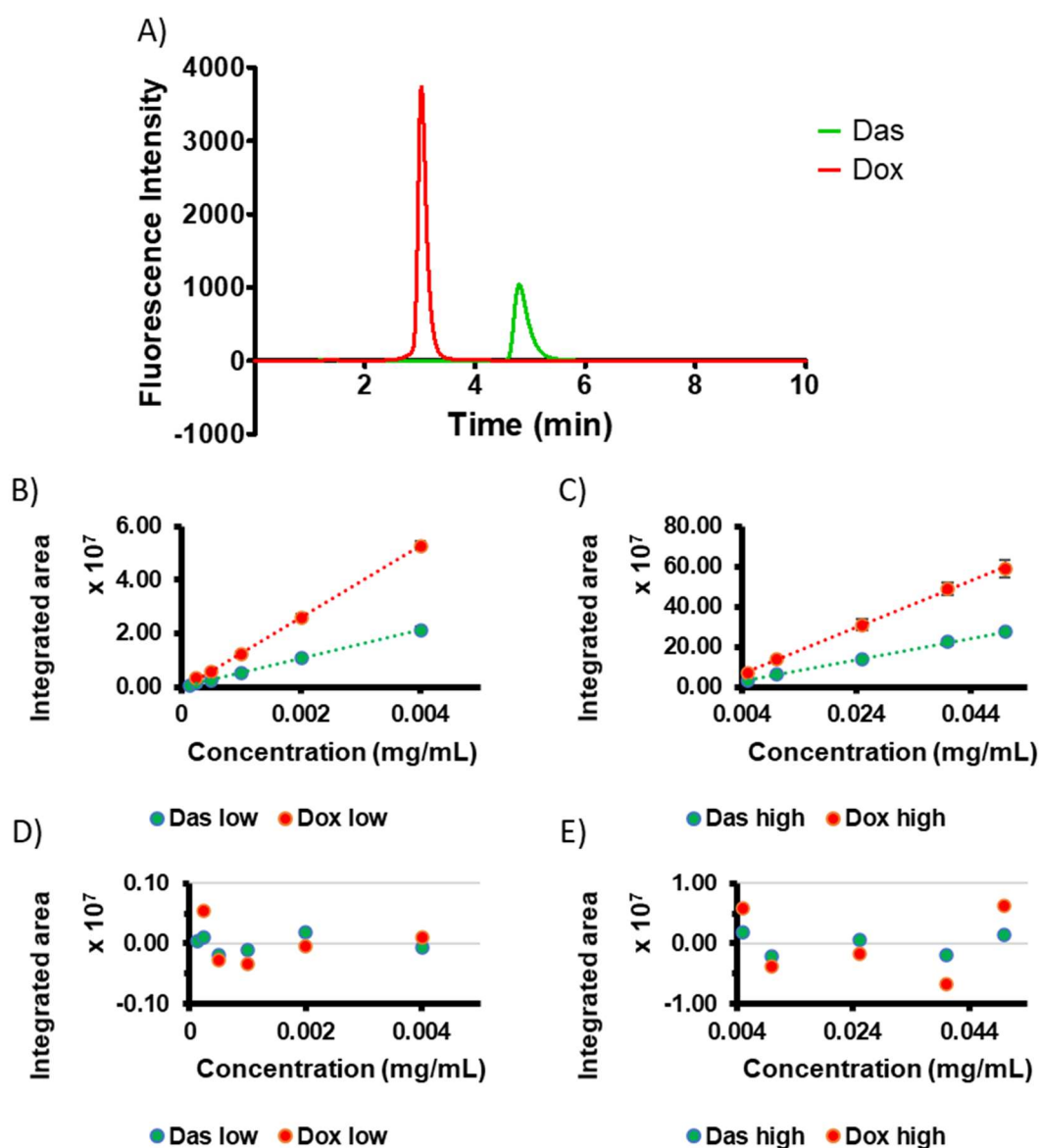
Figure 2.22. Validation of the analytical method used for the simultaneous detection of Dox and Das. (**A**) Representative chromatograms of calibration solutions, showing proper separation of Dox and Das elution peaks. (**B** and **C**) Proof of linearity. (**B**) Calibration curves for low concentrations of Dox (0.0005 to 0.004 mg/mL) and Das (0.000125 to 0.004 mg/mL). (**C**) Calibration curves for high concentrations of Dox (0.005 to 0.05 mg/mL) and

Das (0.005 to 0.05 mg/mL). Data represented as integrated area versus drug concentration (mean ± SD; n=3). (**D** and **E**) Residuals distribution graphs.

Considering the wide range of drug loadings in the conjugates, we prepared two calibration curves for accurate drug quantification (0.000125 to 0.004 mg/mL for Das low, 0.0005 to 0.004 mg/mL for Dox low, 0.005 to 0.05 mg/mL for Das high and Dox high, **Figure 2.22B** and **C**). Using this strategy, we achieved a limit of quantification (LOQ - the lowest concentration of drug quantitatively determined with suitable precision and accuracy (106)) of 0.16 µg/mL for Das and 0.21 µg/mL for Dox (**Table 2.6**). All calibration curves met the criteria for linearity (106) with randomly distributed residuals (**Figure 2.22D** and **E**).

Table 2.6. Main calibration curves' parameters.

	Dox low	Dox high	Das low	Das high
Slope	13302190326	11516500711	5362104243	5362687470
Intercept	-572825	19814185	-2811	7466654
R^2	0.99970	0.99931	0.99970	0.99968
LOD (mg/mL)	0.00007	0.00156	0.00005	0.00107
LOQ (mg/mL)	0.00021	0.00473	0.00016	0.00324

R^2: Coefficient of determination. LOD: Limit of detection. LOQ: Limit of quantification.

Using this protocol, we obtained percentages of drug recovery close to 70% with PBS buffers (even at low pH and drug concentrations), ranging from 66 to 88% for Dox (**Figure 2.23A**) and from 72 to 95% for Das (**Figure 2.23B**); however, extraction from the cathepsin B release buffer yielded lower percentages of recovery, with a maximum recovery of 63% for Dox (**Figure 2.24A**) and 77% for Das (**Figure 2.24B**). Thus, we explored a modification of the extraction protocol, performing two sequential extractions with 0.5 mL of fresh solvent for the cathepsin B buffer. This alteration to the protocol increased the recovery percentage to 74% for Dox (**Figure 2.24A**)

and 88% for Das (**Figure 2.24B**). The attainment of similar values to those obtained for drug recovery in PBS pH 5.0 buffer (**Figure 2.23A and B**) allows a comparison between the release in these two media and to discern the effect of cathepsin B from that of the pH.
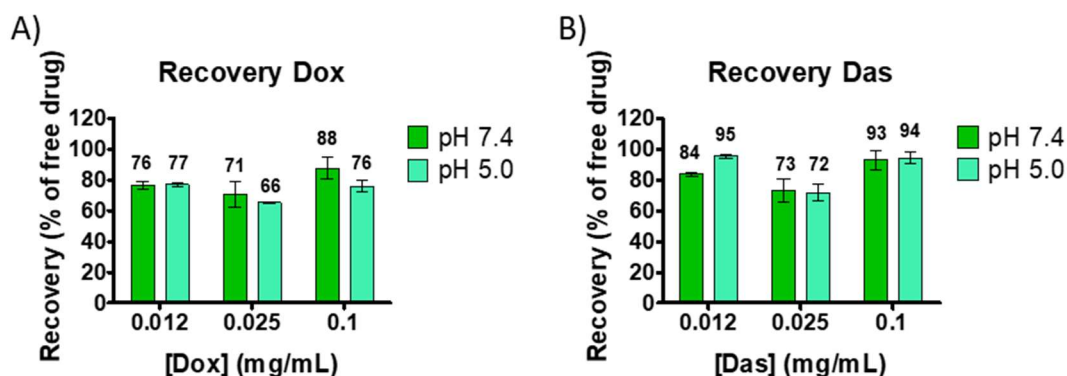
Figure 2.23. Drug recovery study in PBS pH 7.4 and 5.0 buffers. Data represented as the percentage of drug detected after the extraction procedure in samples of St-PGA in PBS pH 5.0 and pH 7.4 with known concentrations of Dox and Das (0.012, 0.025, and 0.1 mg/mL) (mean ± SEM, n=3).
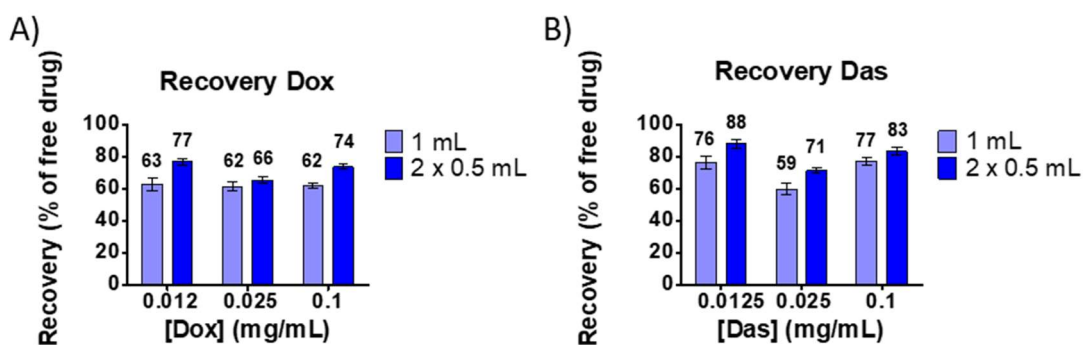
Figure 2.24. Recovery study in cathepsin B buffer. Comparison of two extraction procedures: one extraction with 1 mL of solvent or two sequential extractions with 0.5 mL of solvent. Data represented as the percentage of the detected drug after liquid-liquid extraction in samples of St-PGA with known concentrations of Dox and Das (0.012, 0.025, and 0.1 mg/mL) (mean ± SEM, n=3).

2.2.4.2. pH-dependent Drug Release

We studied pH-dependent Das and Dox release for our family of single-drug conjugates using the above-described buffers and procedures.

As reported for linear PGA conjugates (41), the Val spacer used with ester-Das conjugation in St-PGA-Val-Das reduced drug release compared to St-PGA-Das at pH 7.4 and 5.0 (**Figure 2.25**). At pH 7.4, we observed significant differences from early time points, with 10% Das release after 15 min for St-PGA-Das versus 6% for St-PGA-Val-Das over the same time ($p<0.01$) – a difference that increased over time until 24 h, when we observed a 73% Das release from St-PGA-Das but only 41% release from St-PGA-Val-Das ($p<0.001$, **Figure 2.25**). We observed a similar trend at pH 5.0, with 11% Das release after 15 min for St-PGA-Das versus 6% for St-PGA-Val-Das over the same time ($p<0.001$), and 15% Das release from St-PGA-Das at 5 h and 7% Das release from St-PGA-Val-Das over the same time ($p<0.05$, **Figure 2.25**); however, at longer time points the difference lacked statistical significance. The reduced Das release observed for St-PGA-Val-Das compared to St-PGA-Das may explain the different cytotoxic activity of these conjugates, with St-PGA-Das inducing more significant cytotoxic activity than St-PGA-Val-Das (**Figure 2.20B** and **Table 2.5**).

We also observed a significantly higher Das release at physiological pH than at pH 5.0 for both linking moieties, starting at 1.5 h for St-PGA-Das ($p<0.05$, $p<0.001$ from 3h to 24h) and at 24 h for St-PGA-Val-Das ($p<0.05$) (**Figure 2.25**), which agrees with findings using linear PGA-based conjugates (41).
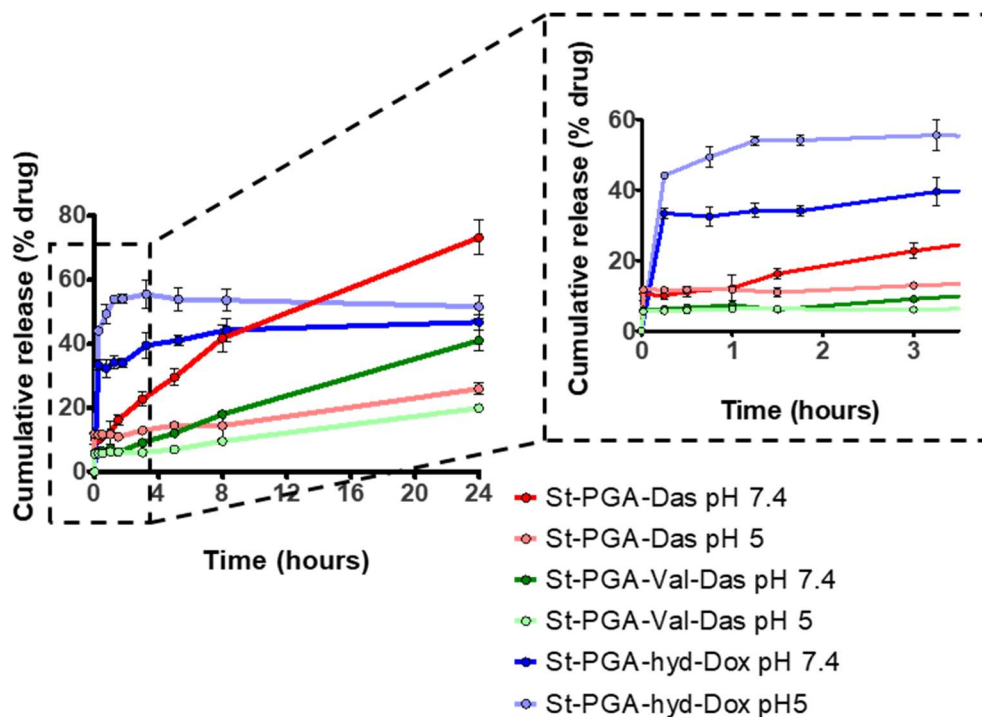
Figure 2.25. pH-dependent drug release of St-PGA-based single-drug conjugates. Data represented as the percentage of the free drugs normalized to the total drug loading (mean ± SEM, n=2 for St-PGA-hyd-Dox, n=3 for St-PGA-Das and St-PGA-Val-Das). Statistical analysis performed by one-way ANOVA and Tukey's test for multiple comparisons. Statistical significance of the data is not displayed for reasons of clarity.

We observed rapid Dox release from St-PGA-hyd-Dox at pH 5.0 and 7.4 (**Figure 2.25**). In agreement with previous reports of hydrazone-mediated Dox conjugation (34,68,77), we observed a more rapid release of Dox from St-PGA-hyd-Dox at pH 5.0 than 7.4, reaching a plateau (56% of the drug loading at pH 5.0, 40% at pH 7.4, p<0.05) after 1.5 h (**Figure 2.25**). At longer time points, we failed to find significant differences between pH 7.4 and 5.0.

We next evaluated the pH-dependent release of Das and Dox from our family of combination conjugates. St-PGA-hyd-Dox$_1$-Val-Das$_1$ displayed higher Das release at physiological pH than at pH 5.0, with 26% Das release after 24 h at pH 7.4 versus 7% Das release at pH 5.0 over the same time (p<0.05, **Figure 2.26A**). At 24 h, St-PGA-hyd-Dox$_1$-Val-Das$_1$ displayed lower Das release compared to St-PGA-hyd-Dox$_1$-Das$_1$ (p<0.01 for pH 5.0, p<0.001 for pH 7.4, **Figure 2.26B**) and St-PGA-hyd-Dox$_1$-Das$_{10}$ (p<0.001 for

both pH, **Figure 2.26C**) at pH 7.4 and 5.0. These results agree with low Das release from St-PGA-Val-Das compared to St-PGA-Das (**Figure 2.25**). Compared to St-PGA-Val-Das, St-PGA-hyd-Dox$_1$-Val-Das$_1$ displayed lower Das release at early time points (p<0.001 at 15 and 30 min for pH 5 and 7); however, this did not translate into a significantly lower release at longer time points.

When evaluating Dox release from St-PGA-hyd-Dox$_1$-Val-Das$_1$, we observed burst release of Dox at early time points at pH 7.4 and 5.0, with 100% drug release occurring during the first 15 min (**Figure 2.26A**). These findings suggest that most drug release occurs before the conjugate reaches and enters the target cell.

Interestingly, St-PGA-hyd-Dox$_1$-Das$_1$ (**Figure 2.26B**) and St-PGA-hyd-Dox$_1$-Das$_{10}$ (**Figure 2.26C**) exhibited a significantly different drug release profile compared to St-PGA-hyd-Dox$_1$-Val-Das$_1$, but similar to each other and St-PGA-hyd-Dox (lack of statistically significant differences up to 8 h). St-PGA-hyd-Dox$_1$-Das$_1$ and St-PGA-hyd-Dox$_1$-Das$_{10}$ displayed a rapid but lower Dox release compared to St-PGA-hyd-Dox$_1$-Val-Das$_1$, reaching a plateau at 5 h with 37% Dox release at pH 7.4 (p<0.001 vs. St-PGA-hyd-Dox$_1$-Val-Das$_1$) and 70% at pH 5.0 (p<0.001 vs. St-PGA-hyd-Dox$_1$-Val-Das$_1$) for St-PGA-hyd-Dox$_1$-Das$_1$, and 33% Dox release at pH 7.4 (p<0.001 vs. St-PGA-hyd-Dox$_1$-Val-Das$_1$) and 63% at pH 5.0 (p<0.001 vs. St-PGA-hyd-Dox$_1$-Val-Das$_1$) for St-PGA-hyd-Dox$_1$-Das$_{10}$. We found a higher Dox release at pH 5.0 compared to pH 7.4 for St-PGA-hyd-Dox$_1$-Das$_1$ (p<0.01 at 5h) and St-PGA-hyd-Dox$_1$-Das$_{10}$ (p<0.05 at 5h) (**Figure 2.26B** and **C**), meeting one of the requirements of our rational design.
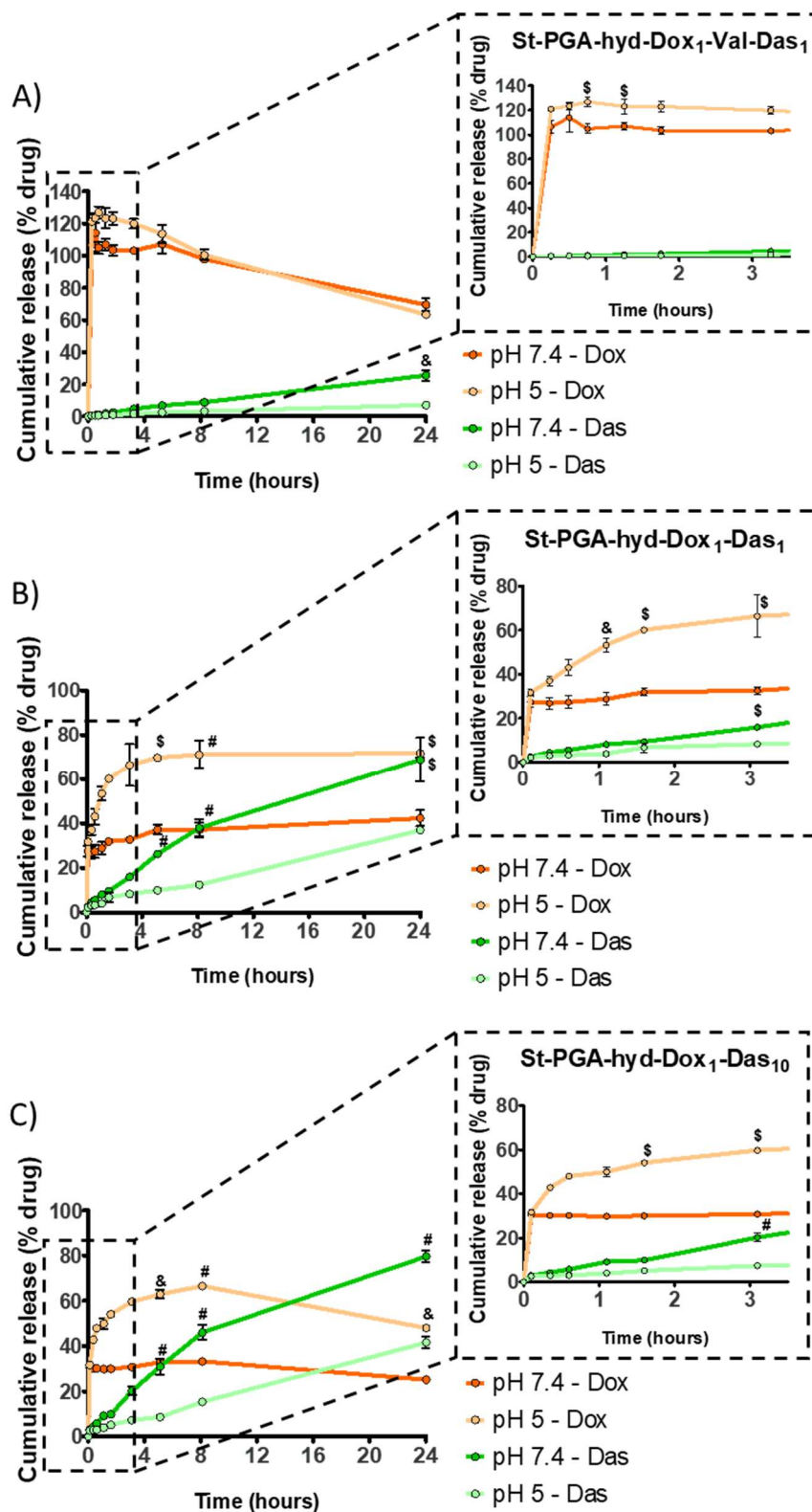
Figure 2.26. pH-dependent drug release from (**A**) St-PGA-hyd-Dox$_1$-Val-Das$_1$, (**B**) St-PGA-hyd-Dox$_1$-Das$_1$, and (**C**) St-PGA-hyd-Dox$_1$-Das$_{10}$. Data represented as the percentage of free drug normalized to total drug loading (mean ± SEM, n=3 for St-PGA-hyd-Dox$_1$-Val-Das$_1$, n=2 for St-PGA-hyd-Dox$_1$-Das$_1$ and St-PGA-hyd-Dox$_1$-Das$_{10}$). Statistical analysis performed by one-way ANOVA and Tukey's test for multiple comparisons. $^{\&}p<0.05$, $^{\$}p<0.01$, $^{\#}p<0.001$, pH 5.0 vs. pH 7.4.

209

St-PGA-hyd-Dox$_1$-Das$_1$ (**Figure 2.26B**) and St-PGA-hyd-Dox$_1$-Das$_{10}$ (**Figure 2.26C**) also exhibited similar Das release with no statistically significant differences found at any time point. Both conjugates displayed higher Das release at pH 7.4 than 5.0 from 3 h ($p<0.01$ at 3 and 24 h and $p<0.0001$ at 5 and 8 h for St-PGA-hyd-Dox$_1$-Das$_1$, $p<0.0001$ from 3 to 24 h for St-PGA-hyd-Dox$_1$-Das$_{10}$, **Figure 2.26B** and **C**).

St-PGA-hyd-Dox$_1$-Das$_1$ and St-PGA-hyd-Dox$_1$-Das$_{10}$ exhibited increased Das release at early time points compared to St-PGA-Das at pH 5.0 ($p<0.001$ vs. St-PGA-hyd-Dox$_1$-Das$_1$ and St-PGA-hyd-Dox$_1$-Das$_{10}$ at 15 and 30 min, $p<0.05$ vs. St-PGA-hyd-Dox$_1$-Das$_1$ at 1 h and St-PGA-hyd-Dox$_1$-Das$_{10}$ at 1.5 and 3 h) and 7.4 ($p<0.001$ vs. St-PGA-hyd-Dox$_1$-Das$_1$ and St-PGA-hyd-Dox$_1$-Das$_{10}$ at 15 and 30 min, $p<0.01$ vs. St-PGA-hyd-Dox$_1$-Das$_1$ at 1.5 and 3h, and St-PGA-hyd-Dox$_1$-Das$_{10}$ at 1.5 h); however, this did not translate into a significantly higher release at later time points.

Compared to St-PGA-hyd-Dox$_1$-Val-Das$_1$, St-PGA-hyd-Dox$_1$-Das$_1$ and St-PGA-hyd-Dox$_1$-Das$_{10}$ exhibited significantly increased Das release starting from very early time points at pH 7.4 (e.g., $p<0.05$ after 15 min vs. St-PGA-hyd-Dox$_1$-Das$_1$ and St-PGA-hyd-Dox$_1$-Das$_{10}$) but later at pH 5.0 ($p<0.05$ after 1.5 h vs. St-PGA-hyd-Dox$_1$-Das$_1$, $p<0.05$ after 3 h vs. St-PGA-hyd-Dox$_1$-Das$_{10}$). In this case, the difference at later time points increased, especially at pH 7.4, with 69% Das release at 24h for St-PGA-hyd-Dox$_1$-Das$_1$ ($p<0.001$ vs. St-PGA-hyd-Dox$_1$-Val-Das$_1$) and 80% for St-PGA-hyd-Dox$_1$-Das$_1$ over the same time ($p<0.001$ vs. St-PGA-hyd-Dox$_1$-Val-Das$_1$).

Overall, the results of the combination conjugates drug release study highlighted two different drug release profiles according to the use of the Val spacer or direct ester conjugation for Das. The conjugate with Val, St-PGA-hyd-Dox$_1$-Val-Das$_1$, exhibited a complete release of Dox at early time points with an extremely low release of Das; meanwhile, the conjugates with direct ester Das conjugation, St-PGA-hyd-Dox$_1$-Das$_1$ and St-PGA-hyd-Dox$_1$-Das$_{10}$, exhibited slower and lower Dox release with higher but gradual Das release.

While the use of the Val spacer can explain the low Das release observed for St-PGA-hyd-Dox$_1$-Val-Das$_1$, the burst Dox release suggests a different conformation in solution with enhanced exposure of the hydrazone-Dox moieties in St-PGA-hyd-Dox$_1$-Val-Das$_1$ compared to St-PGA-hyd-Dox$_1$-Das$_1$ and St-PGA-hyd-Dox$_1$-Das$_{10}$. The physico-chemical characterization of the conjugates also supports this hypothesis. Taken together, these data suggest a solution conformation for St-PGA-hyd-Dox$_1$-Val-Das$_1$ that shields Das from the media but exposes Dox on the surface of the conjugate.

The burst Dox release of St-PGA-hyd-Dox$_1$-Val-Das$_1$ implies that Dox will become released before the conjugate enters the cell, which, together with the low Das release, explains the low cytotoxic activity of St-PGA-hyd-Dox$_1$-Val-Das$_1$ compared to St-PGA-hyd-Dox$_1$-Das$_1$ (**Figure 2.20C** and **D**, **Table 2.1**), which possesses the same drug ratio but controlled Dox release and higher Das release.

The Dox release profile of St-PGA-hyd-Dox$_1$-Das$_{10}$ and St-PGA-hyd-Dox$_1$-Das$_1$ suggest lower Dox release in healthy tissues (pH 7.4) than in tumor tissues (pH 5.0) after conjugate administration, thereby meeting one of the requirements of our design; however, our results differ from previously reported data for linear PGA, where lower loadings of hydrazone-Dox correlated with higher release rates and enhanced *in vitro* cytotoxic activity (34). In our St-PGA-based conjugates, we encountered a similar Dox release profile for different drug loadings, suggesting that the star-shaped architecture exhibits lower sensitivity to drug loading than the linear counterpart.

Considering the different Dox loadings of St-PGA-hyd-Dox$_1$-Das$_1$ and St-PGA-hyd-Dox$_1$-Das$_{10}$, we next compared the total mass of released drugs and the released drug ratio. St-PGA-hyd-Dox$_1$-Das$_1$ exhibits delayed Das release compared to Dox, releasing more Dox than Das during the first hour at pH 7.4 and the first 8 h at pH 5.0 (**Figure 2.27A**). While we observed an excess of Dox at early time points for St-PGA-hyd-Dox$_1$-Das$_1$ (e.g., 1:0.1

ratio after 15 min at pH 5.0 – p=0.0035 vs. 1:1 – and 1:0.3 ratio after 15 min at pH 7.4 – p=0.0192 vs. 1:1) (**Figure 2.27A**), St-PGA-hyd-Dox$_1$-Das$_{10}$ exhibited a drug release ratio of 1:1 from very early time points (e.g., 1:0.6 after 15 min at pH 5.0, p=0.0544 vs. 1:1), which increased gradually up to a ratio 1:8 at pH 5.0 (p=0.0323 vs. 1:1) and 1:30 at pH 7.4 after 24 h (p=0.0124 vs. 1:1) (**Figure 2.27B**). Nevertheless, St-PGA-hyd-Dox$_1$-Das$_{10}$ exhibited higher cytotoxic activity *in vitro* than St-PGA-hyd-Dox$_1$-Das$_1$, thus disagreeing with previous reports that underscored the need for delayed Das administration for drug synergism (41).

Considering the high release of Das at pH 7.4, St-PGA-hyd-Dox$_1$-Das$_1$ and St-PGA-hyd-Dox$_1$-Das$_{10}$ will release Das while in circulation, thereby reducing Das bioavailability in tumor tissues. We hypothesize that low Dox loading in St-PGA-hyd-Dox$_1$-Das$_{10}$ will ensure the maintenance of a high Dox:Das ratio after tumor cell internalization to enhance anti-tumor activity.
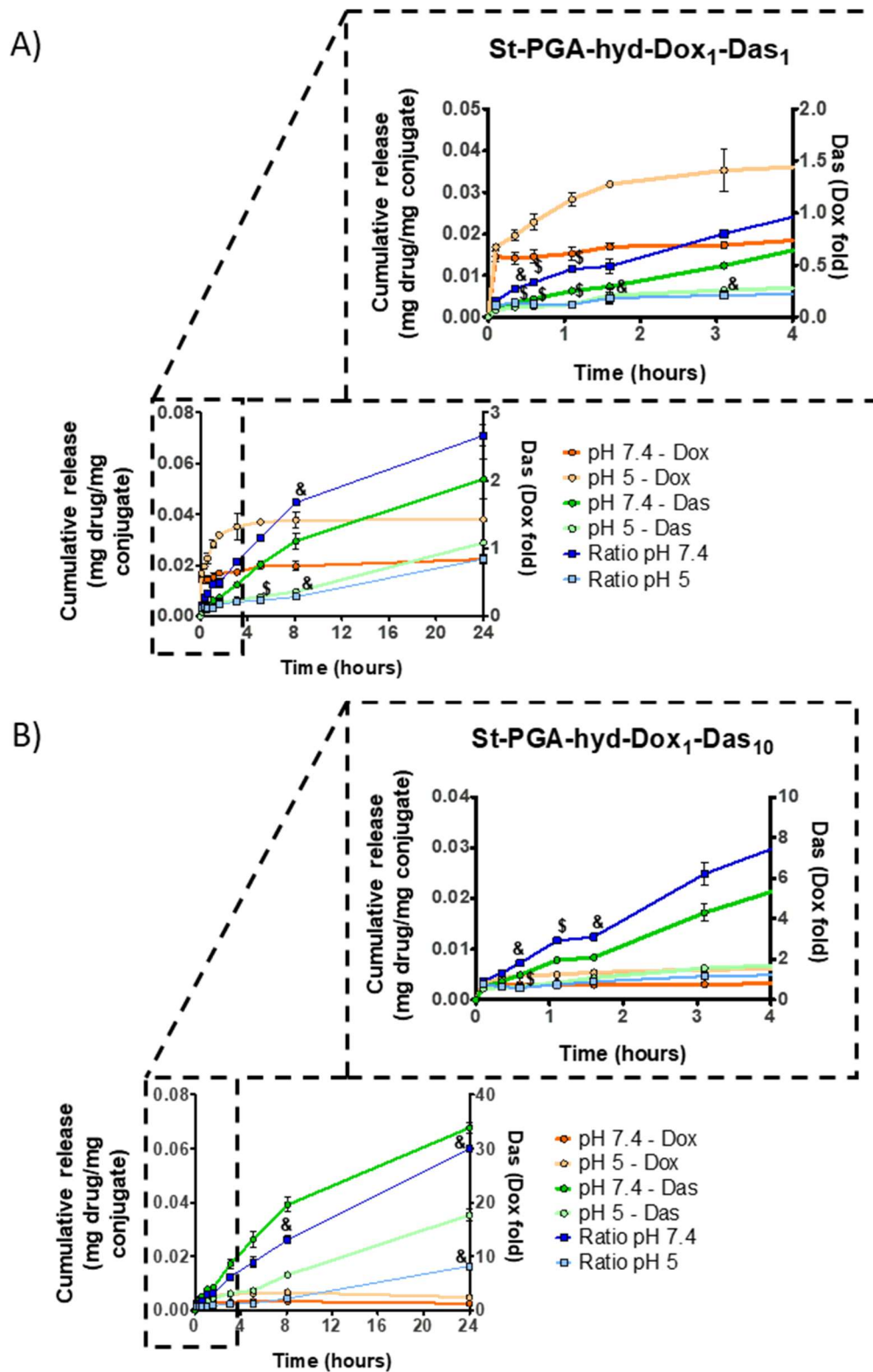
Figure 2.27. Comparison of (**A**) St-PGA-hyd-Dox$_1$-Das$_1$ and (**B**) St-PGA-hyd-Dox$_1$-Das$_{10}$ pH-dependent drug release. Data expressed in milligrams of drug per milligram of conjugate and molar ratio of Dox:Das (mean ± SEM, n=2). Statistical analysis performed by unpaired, two-way Student's t-test. $^\&p<0.05$, $^\$p<0.01$, $^\#p<0.001$, ratio in Dox fold vs. 1.

2.2.4.3. Cathepsin B-mediated Drug Release

To evaluate drug release after cell internalization of St-PGA-hyd-Dox$_1$-Das$_1$ and St-PGA-hyd-Dox$_1$-Das$_{10}$, we aimed to study release kinetics in the presence of the protease cathepsin B in an acidic environment (pH 5); however, incubation in the cathepsin B release buffer provoked conjugate precipitation at early time points. Therefore, we only examined protease-dependent drug release over 5 h.

Comparing the cathepsin B mediated drug release of St-PGA-hyd-Dox$_1$-Das$_1$ and St-PGA-hyd-Dox$_1$-Das$_{10}$ with the drug release in PBS pH 5.0 (same pH as the cathepsin B buffer), we observed a similar profile with no significant differences (**Figure 2.28A** for St-PGA-hyd-Dox$_1$-Das$_1$, **Figure 2.28B** for St-PGA-hyd-Dox$_1$-Das$_{10}$). We observed a slight increase of Dox release at early time points for both conjugates, but this failed to reach statistical significance for St-PGA-hyd-Dox$_1$-Das$_1$. Therefore, our data suggest that cathepsin B failed to induce Dox and Das release in our St-PGA-based combination conjugates; however, we note the preliminary nature of this study, and we require additional data points to confirm our results.

A)

St-PGA-hyd-Dox$_1$-Das$_1$

Cumulative release (% drug)

- Cathepsin B - Dox
- Cathepsin B - Das
- pH 5 - Dox
- pH 5 - Das

Time (hours)

B)

St-PGA-hyd-Dox$_1$-Das$_{10}$

Cumulative release (% drug)

- Cathepsin B - Dox
- Cathepsin B - Das
- pH 5 - Dox
- pH 5 - Das

Time (hours)
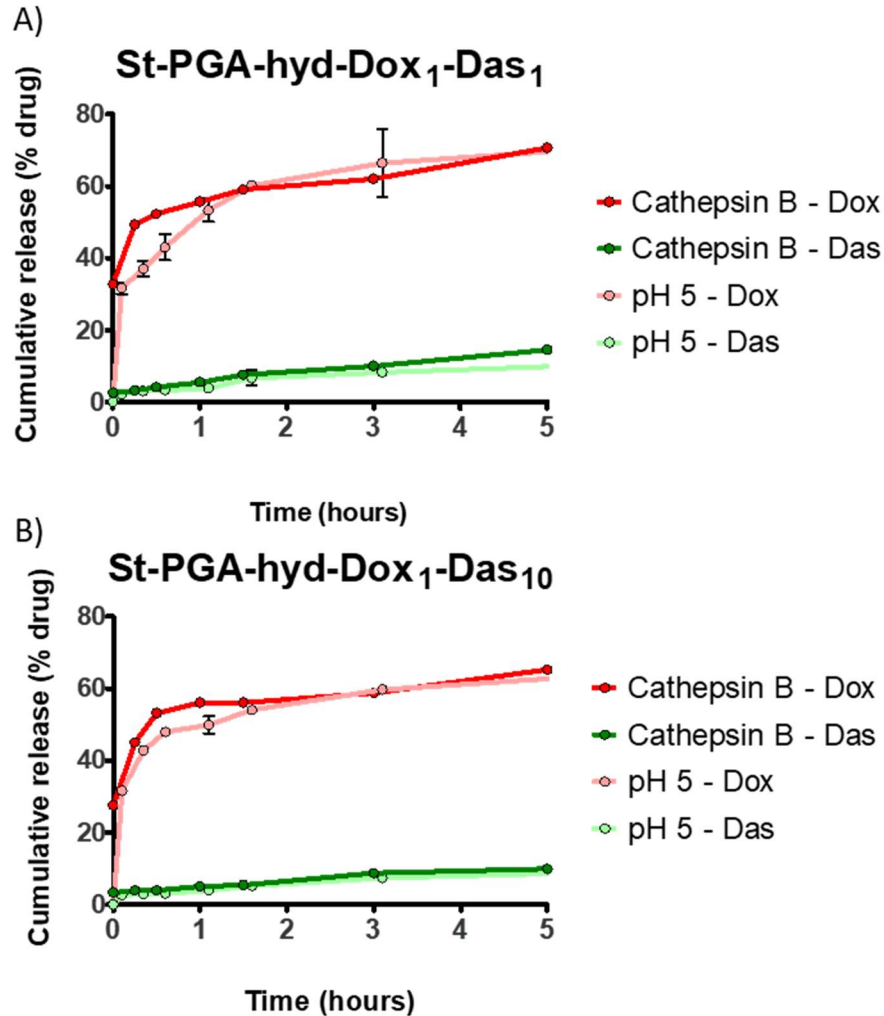
Figure 2.28. Cathepsin B mediated drug release profiles of (**A**) St-PGA-hyd-Dox$_1$-Das$_1$ and (**B**) St-PGA-hyd-Dox$_1$-Das$_{10}$. Data represented as the percentage of released drug normalized to the total drug loading (mean ± SEM, n=2 for St-PGA-hyd-Dox$_1$-Das$_1$, and n=1 for St-PGA-hyd-Dox$_1$-Das$_{10}$). Release profile in PBS pH 5.0 displayed for comparison. Statistical comparison between cathepsin B and pH 5.0 release performed by two-tailed unpaired t-test only for St-PGA-hyd-Dox$_1$-Das$_1$.

2.2.5. *In vivo* Evaluation of Anti-tumor and Anti-metastatic Activity

We next evaluated the anti-tumor and anti-metastatic activity of the combination conjugates and their single-drug counterparts in a spontaneously metastatic TNBC mouse model. In this model, the injection of MDA-MB-231-Luc cells in the second left mammary fat pad of immunodeficient NOD/SCID (non-obese diabetic/severe combined

immunodeficient) female mice gives rise to the orthotopic (i.e., located in the normal anatomical position) primary tumor (95). This mouse strain lacks mature B and T cells, which hampers adaptive immune responses, and displays a reduced innate immunity, with the absence of C5 complement and the reduced presence of natural killer cells and macrophages (107). This immunological profile allows for the growth of xenograft tumors (i.e., of a different species from the host); furthermore, our laboratory has previously optimized and characterized this specific mouse model (95). Our previous study highlighted spontaneous metastasis in axillary lymph nodes and lungs, with the first signs of lung metastasis appearing at day twenty-one after tumor induction and the first signs of axillary lymph node invasion at day fourteen.

Passive tumor accumulation via the EPR effect represents one of the main advantages of nanomedicines as a cancer treatment. Thus, maximal treatment efficacy requires the administration of said nanomedicine when EPR supports maximal accumulation. The "power" of the EPR effect associated with a tumor can be estimated by the intravenous administration of an Evans blue-albumin macromolecular complex and then quantifying dye accumulation in the tumor 1 h after injection. Previous studies with this TNBC model identified fourteen days after tumor induction (when the size of the primary tumor is approximatively 0.1 cm^3) as the time of maximal EPR effect (95). On day fourteen after induction, we examined tumor volume to confirm tumor size (**Figure 2.29A** and **B**) and began the intravenous treatment administration (see **Table 2.7** and **Table 2.8**) at day fifteen. We administered treatments through the tail vein twice a week for three weeks (six doses) (**Figure 2.29A**).
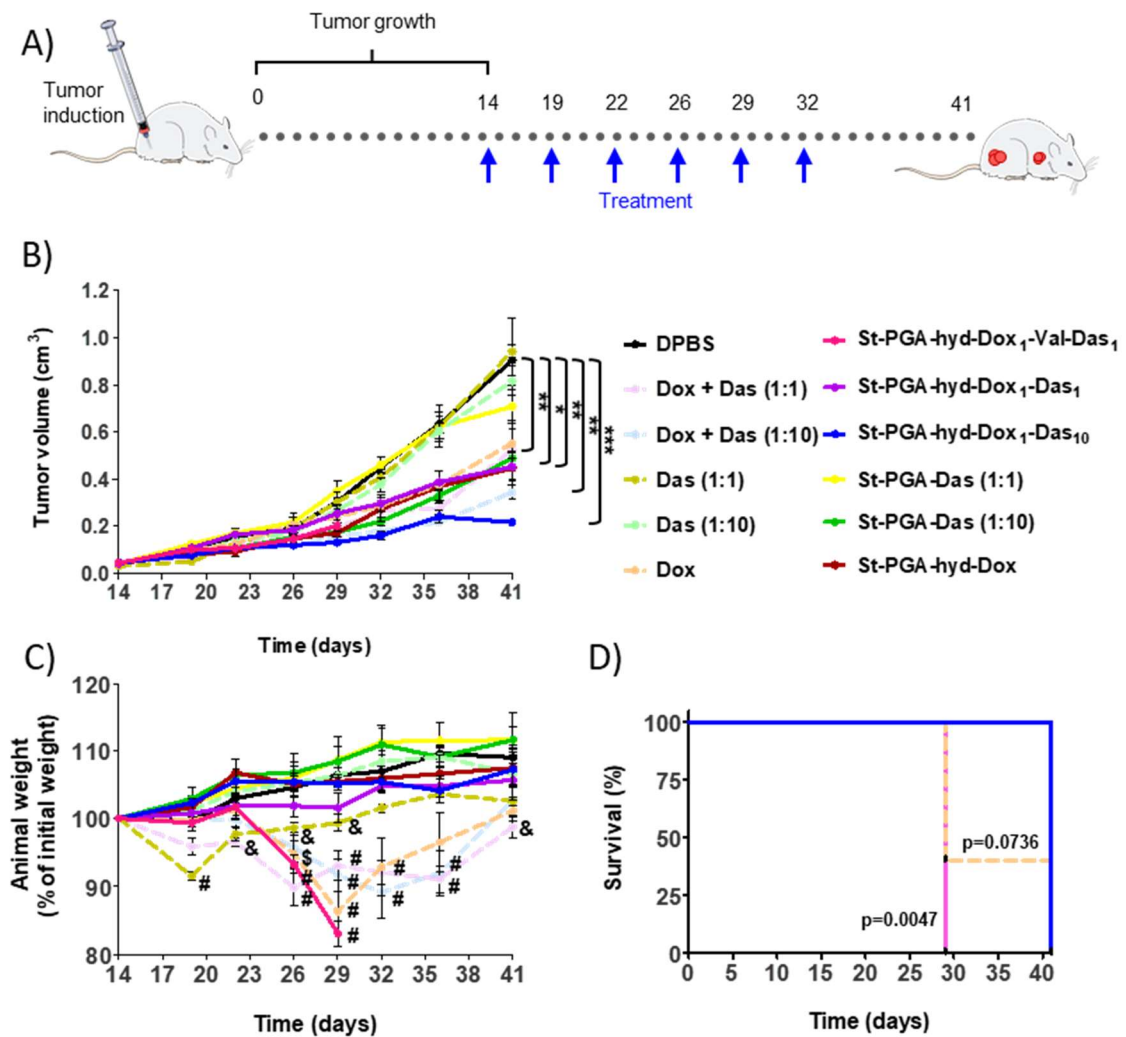
Figure 2.29. *In vivo* anti-tumor activity and safety evaluation. (**A**) Experiment timeline. Tumor induction established as "day 0". Administration of single-drug and combination conjugates, DPBS, and free drugs started on day fourteen. A total of six doses were administered for all the groups except for St-PGA-hyd-Dox_1-Val-Das_1. On day forty-one, animals were euthanized and examined for metastatic spread to the lungs by IVIS®. (**B**) Evolution of tumor volume (mean ± SEM, n≥4 for all groups). Statistical analysis performed by one-way ANOVA and Tukey's test for multiple comparisons. *$p<0.05$, **$p<0.01$, ***$p<0.001$. (**C**) Evolution of animal weight. Data represented as the percentage of animal weight relative to the initial (day fourteen) weight (mean ± SEM, n≥4 for all groups, except Dox, n=2 after day twenty-nine). Statistical analysis performed using one-way ANOVA and Dunnett's test for comparisons with the DPBS control. Comparison of Dox treatment after day twenty-nine was avoided due to the survival reduction. $^{\&}p<0.05$, $^{\$}p<0.01$, $^{\#}p<0.001$ vs. DPBS. (**D**) Kaplan-Meyer survival curve by treatment. Statistical analysis performed using a Log-rank test.

Table 2.7. Treatment block 1:1: treatment groups corresponding to the combination conjugates with 1:1 Dox:Das ratio, St-PGA-hyd-Dox$_1$-Val-Das$_1$, and St-PGA-hyd-Dox$_1$-Das$_1$.

Treatment group	Dox dose (mg/Kg)	Das dose (mg/Kg)	Conjugate dose (mg/Kg)	Total doses
DPBS	-	-	-	6
St-PGA-hyd-Dox$_1$-Val-Das$_1$	1.2	1.5	15.1	4
St-PGA-hyd-Dox$_1$-Das$_1$	1.2	1.7	22.3	6
St-PGA-Das (1:1)	-	1.7	17.6	6
Dox + Das (1:1)	1.2	1.7	-	6
Das (1:1)	-	1.7	-	6
St-PGA-hyd-Dox	1.2	-	12.6	6
Dox	1.2	-	-	6*

*This group showed limited survival; thus, only 40% of the treatment group received six doses.

Table 2.8. Treatment block 1:10: treatment groups corresponding to the combination conjugate with 1:10 Dox:Das ratio, St-PGA-hyd-Dox$_1$-Das$_{10}$.

Treatment group	Dox dose (mg/Kg)	Das dose (mg/Kg)	Conjugate dose (mg/Kg)	Total doses
DPBS	-	-	-	6
St-PGA-hyd-Dox$_1$-Das$_{10}$	1.2	10.0	120.0	6
St-PGA-Das (1:10)	-	10.0	101.0	6
Dox + Das (1:10)	1.2	10.0	-	6
Das (1:10)	-	10.0	-	6
St-PGA-hyd-Dox	1.2	-	12.6	6
Dox	1.2	-	-	6*

*This group showed limited survival; thus, only 40% of the treatment group received six doses.

Previous work performed in our laboratory demonstrated that administration of 1.5 mg of free Dox/Kg alone and in combination with free Das in a 1:1 ratio prompted significant toxicity, leading to significant weight loss that required the eventual euthanasia of animals for ethical reasons

(41). To increase survival in the control group while maintaining treatment efficacy, we administered 1.2 mg Dox/Kg (20% dose reduction) and the equivalent dose for the conjugates considering their drug loading. We adjusted the free Das dose to match the different drug ratios in the combination conjugates. We also employed two treatment groups for St-PGA-Das, one for each ratio (1.7 mg Das/Kg and 10.0 mg Das/Kg).

Considering the two ratios employed for combination conjugate synthesis, we divided treatments into two treatment blocks – 1:1 and 1:10. Treatment block 1:1 includes the St-PGA-hyd-Dox_1-Val-Das_1 and St-PGA-hyd-Dox_1-Das_1 combination conjugates administered at 1.2 mg/Kg of Dox (~1.7 mg/Kg of Das), the administration of St-PGA-Das and free Das at 1.7 mg/Kg of Das (St-PGA-Das (1:1) and Das (1:1), respectively), the administration of St-PGA-hyd-Dox and free Dox at 1.2 mg/Kg of Dox, and the DPBS control group (**Table 2.7**). Treatment block 1:10 includes the St-PGA-hyd-Dox_1-Das_{10} combination conjugate administered at 1.2 mg/Kg of Dox (~10.0 mg/Kg of Das), the administration of St-PGA-Das and free Das at 10.0 mg/Kg of Das (St-PGA-Das (1:10) and Das (1:10), respectively), the administration of St-PGA-hyd-Dox and free Dox at 1.2 mg/Kg of Dox, and the DPBS control group (**Table 2.8**).

We measured tumor volume twice a week to evaluate the anti-tumor activity of all treatments; additionally, we monitored animal weight as an indicator of animal wellbeing. On day forty-one, when the tumor of DPBS-treated animals achieved a volume of ~1.0 cm^3 (humane endpoint) (**Figure 2.29B**), we euthanized animals, harvested their main organs, and evaluated metastatic progression in the lungs *ex vivo* by detecting the bioluminescence emitted by MDA-MB-231-Luc cells.

Figure 2.29B-D depicts the results of the *in vivo* evaluation of the anti-tumor activity of all evaluated treatments. We failed to fully assess the anti-tumor and anti-metastatic potential of St-PGA-hyd-Dox_1-Val-Das_1, as administration provoked dramatic animal weight loss starting after the third

dose (**Figure 2.29C**, p<0.001 at day twenty-six and twenty-nine). By day twenty-nine (after the fourth dose), animals treated with St-PGA-hyd-Dox_1-Val-Das_1 experienced ~15% reduction in body weight, which prompted their euthanasia, reducing significantly animal survival (p=0.0047, **Figure 2.29D**). We observed a similar profile for free Dox treatment (**Figure 2.29C**, p<0.01 at day twenty-six, p<0.001 at day twenty-nine), which also reduced animal survival to 40% but lacked statistical significance (p=0.0763, **Figure 2.29D**). These results agree with data reported for free Dox treatment in the same *in vivo* model, where the toxicity of free Dox administered at 1.5 mg/Kg (with and without co-treatment with free Das) prompted euthanasia of animals after the second dose (41). As explained above, we reduced the Dox dose in this experiment, seeking to increase the survival of Dox, Dox + Das (1:1), and Dox + Das (1:10) free drug control groups. As a result, the combination of free Dox and Das in both ratios provoked significant reductions in animal weight but allowed the completion of the dosing scheme for all animals in these groups, and free Dox administered at 1.2 mg/Kg improved the survival compared to 1.5 mg/Kg (40% versus 0%, respectively (41)); however, due to the weight loss observed in the free Dox group and the associated reduction of survival (**Figure 2.29C** and **D**), we excluded the free Dox group from any statistical analyses. Meanwhile, neither single-drug nor combination conjugates provoked significant animal weight loss (**Figure 2.29C**) or reduced animal survival (**Figure 2.29D**), providing evidence for their safety.

Considering the similar body weight reduction profile observed for St-PGA-hyd-Dox_1-Val-Das_1 and free Dox, we hypothesize that the toxicity of St-PGA-hyd-Dox_1-Val-Das_1 results, at least in part, from rapid Dox release at pH 7.4 (see *2.2.4.pH and Cathepsin B-mediated Drug Release*). This finding suggests that drug release from the conjugate in circulation causes systemic toxicity; however, other factors, including interactions with blood proteins, could play a role in conjugate toxicity (which we will study in detail below - see *2.2.6.Characterization of Serum Protein Interaction by AF4*).

The evaluation of the tumor volume at the experimental endpoint demonstrated that the administration of St-PGA-hyd-Dox significantly reduced tumor growth compared to DPBS ($p<0.05$, **Figure 2.29**B) while avoiding weight loss (**Figure 2.29**C) and survival reduction associated with free Dox administration (**Figure 2.29**D). From these data, we conclude that Dox conjugation to St-PGA effectively improves safety while maintaining biological activity.

The administration of free Das failed to slow tumor growth (**Figure 2.29B**); however, St-PGA-Das treatment inhibited tumor growth when administered at 10 mg Das/Kg, although this failed to reach statistical significance. Therefore, Das conjugation to St-PGA failed to provide a significant advantage over free Das in terms of primary tumor growth inhibition.

St-PGA-hyd-Dox$_1$-Das$_1$ and St-PGA-hyd-Dox$_1$-Das$_{10}$ significantly reduced tumor growth compared to DPBS, with St-PGA-hyd-Dox$_1$-Das$_{10}$ exhibiting the most significant reduction ($p<0.001$ for St-PGA-hyd-Dox$_1$-Das$_{10}$, $p<0.01$ for St-PGA-hyd-Dox$_1$-Das$_1$, **Figure 2.29B**). The administration of free Dox in combination with free Das also prompted a significant reduction in tumor growth compared to DPBS for both ratios employed ($p<0.05$ for Dox + Das (1:1), $p<0.01$ for Dox + Das (1:10), **Figure 2.29B**). While St-PGA-hyd-Dox$_1$-Das$_1$ treatment prompted a similar reduction in primary tumor growth to Dox + Das (1:1) and St-PGA-hyd-Dox, St-PGA-hyd-Dox$_1$-Das$_{10}$ provided for a reduction in tumor size to a value below that of the combination of the free drugs at an equivalent ratio (Dox + Das (1:10)) (**Figure 2.29B**); however, we failed to find a statistically significant difference in this comparison.

We also evaluated primary tumor weight at the experimental endpoint by normalizing values to body weight; overall, these data agreed well with the tumor volume data (**Figure 2.30A**). Das (1:1), Das (1:10), and St-PGA-Das (1:1) displayed similar tumor weight to DPBS (**Figure 2.30A**),

suggesting a lack of anti-tumor efficacy. Treatment with St-PGA-hyd-Dox_1-Das_1, St-PGA-Das (1:10), and St-PGA-hyd-Dox led to similar reductions in tumor weight but failed to show statistically significant differences compared to DPBS (**Figure 2.30A**). Dox + Das (1:1) and Dox + Das (1:10) significantly reduced tumor weight compared to DPBS ($p<0.001$ for Dox + Das (1:1), $p<0.01$ for Dox + Das (1:1), **Figure 2.30A**), proving the anti-tumor activity of the drug combination. Furthermore, Dox + Das (1:10) significantly reduced tumor weight compared to free Das alone administered at the same dose (Das (1:10), $p<0.05$, **Figure 2.30A**), underscoring the advantage of the combination therapy over single drug administration. Animals treated with St-PGA-hyd-Dox_1-Das_{10} possessed the lowest tumor weight, significantly below the value obtained for DPBS ($p<0.001$) and Das (1:10) ($p<0.001$, **Figure 2.30A**), providing proof of the robust anti-tumor activity of St-PGA-hyd-Dox_1-Das_{10}.

We additionally evaluated the relative weight of main organs (spleen, liver, heart, and kidneys) to confirm treatment safety. Comparisons between all treatment groups failed to reveal any significant alterations in the weight of the liver (**Figure 2.30B**), heart (**Figure 2.30C**), or kidneys (**Figure 2.30D**).
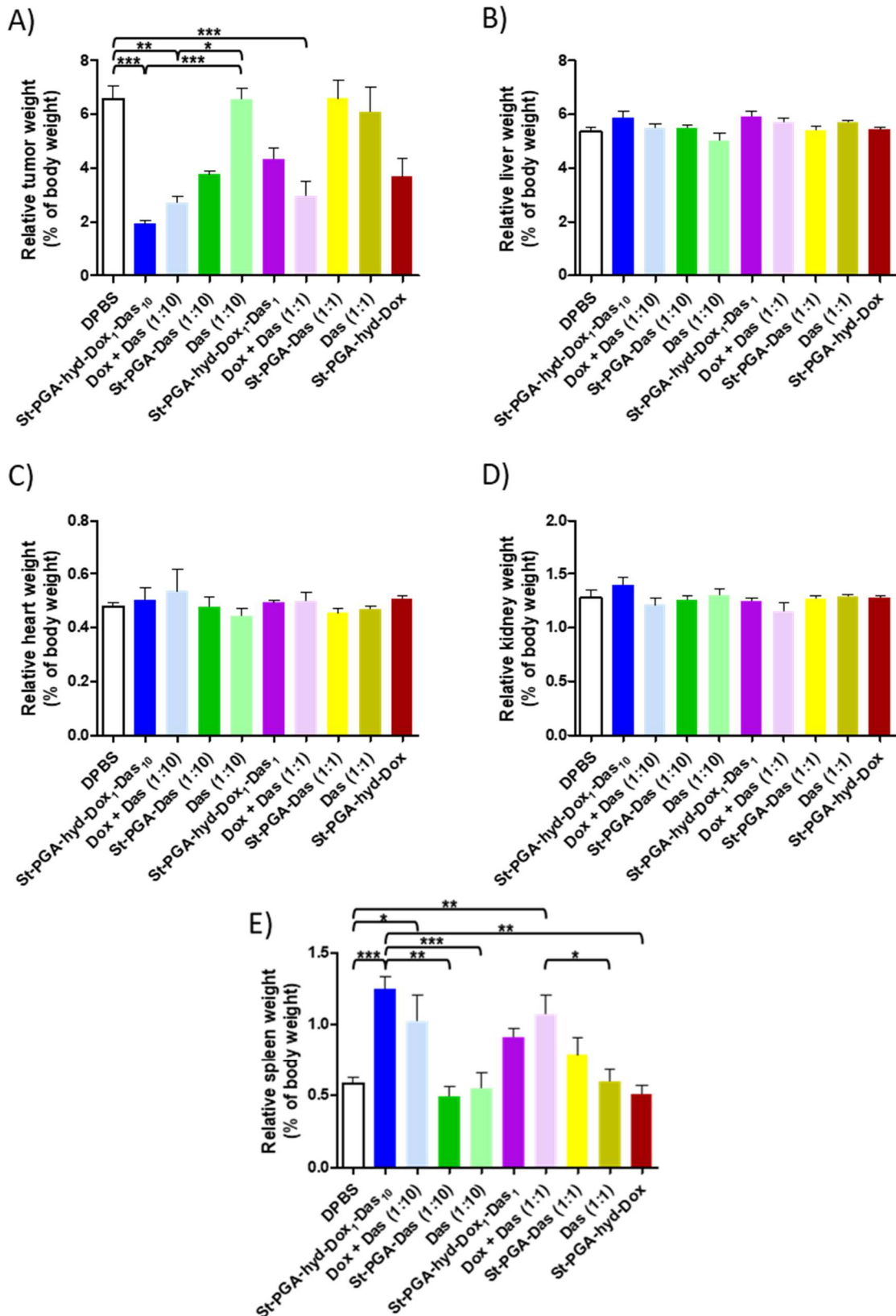
Figure 2.30. Relative weight of the (**A**) tumor, (**B**) liver, (**C**) heart, (**D**) kidney, and (**E**) spleen at the experimental endpoint. Data expressed as the percent organ weight normalized to overall body weight (mean ± SEM, n≥4). Statistical analysis performed using one-way ANOVA and Tukey's test for multiple comparisons. *p<0.05, **p<0.01, ***p<0.001.

Importantly, we did detect differences in spleen weight in certain treatment groups. Treatment with the combination of free Dox and Das (both ratios) provoked a significant increase in spleen weight compared to the DPBS control ($p<0.01$ for Dox + Das (1:1), $p<0.05$ for Dox + Das (1:10), **Figure 2.30E**). Dox + Das (1:1) also induced a significantly higher spleen weight than Das (1:1) ($p<0.05$), while treatment with Das as a free drug or single-drug conjugate (both ratios) failed to significantly alter spleen weight (**Figure 2.30E**). These data suggest the critical role of Dox in mediating alterations to spleen weight. Of note, we could not assess the effect of free Dox due to overt toxicity; however, we did discover that St-PGA-hyd-Dox treatment failed to induce an increase in spleen weight (**Figure 2.30E**). This result agreed with studies of linear PGA conjugates (41), where free Das, PGA-Val-Das, PGA-hyd-Dox, and PGA-hyd-Dox-Val-Das failed to significantly increase the weight of the spleen, kidney, or liver. However, treatment with St-PGA-hyd-Dox_1-Das_{10} prompted an increase in spleen weight compared to DPBS ($p<0.001$), displaying a similar value to Dox + Das (1:10) (**Figure 2.30E**), and thereby suggesting splenomegaly as a consequence of the administration of drug combination. Splenomegaly has been associated with disease progression in patients and breast cancer animal models (108–111); however, the characterization of this MDA-BM-231-Luc TNBC *in vivo* model failed to exhibit signs of splenomegaly in response to disease progression in the absence of treatments (95). Therefore, we attribute the increase in the spleen mass to the effect of the combined administration of Dox and Das.

We evaluated the anti-metastatic activity of treatments by *ex vivo* bioluminescence detection of MDA-MB-231-Luc cells within the lungs (**Figure 2.31A**). Due to the reduced survival of treated animals, we excluded St-PGA-hyd-Dox_1-Val-Das_1 and free Dox from the anti-metastatic activity analysis. The combination of free Dox and Das prompted a significant inhibition of lung metastasis (both ratios $p<0.05$ vs. DPBS). While the St-PGA-hyd-Dox_1-Das_{10} and St-PGA-hyd-Dox_1-Das_1 combination conjugates

also reduced lung metastasis, this failed to reach statistical significance compared to the DPBS control (**Figure 2.31A**). Interestingly, the administration of Das at 10 mg/Kg induced a significant increase in lung metastasis compared to the remaining treatments except for St-PGA-Das (1:1) (**Figure 2.31A**); thus, St-PGA-Das (1:10) treatment failed to induce a similar response (p<0.01 versus Das (1:10), **Figure 2.31A**), suggesting that polypeptide conjugation significantly enhanced the safety of free Das.
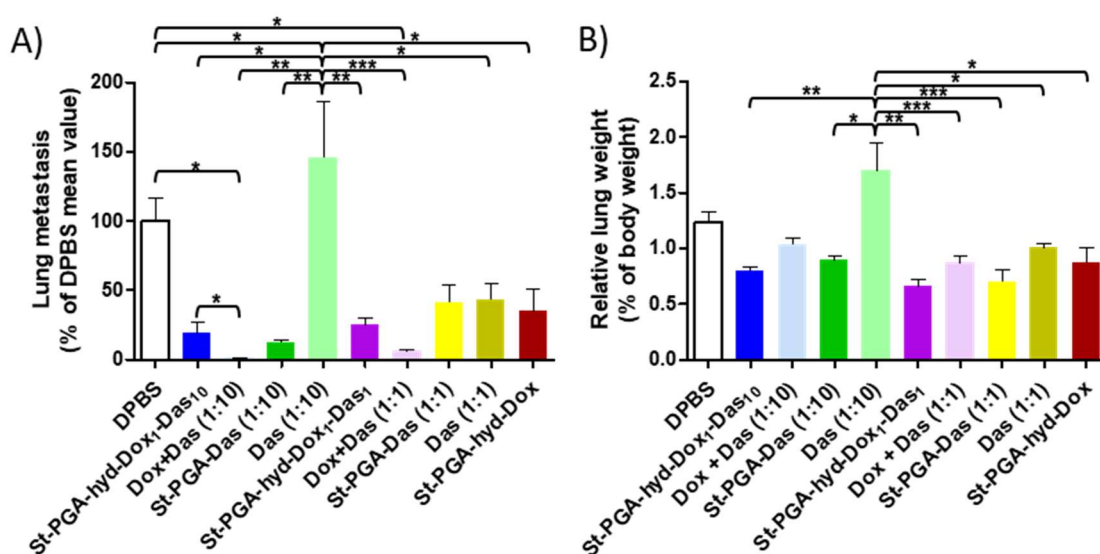
Figure 2.31. (**A**) Evaluation of lung metastasis after treatment. Data obtained by bioluminescence detection (photons/sec) by IVIS® and normalized to the DPBS mean value (mean ± SEM, n ≥ 4). (**B**) Relative lungs weight at the experimental endpoint. Data expressed as the percent organ weight normalized to overall body weight (mean ± SEM, n≥4). Statistical analysis performed using one-way ANOVA and Tukey's test for multiple comparisons. *p<0.05, **p<0.01, ***p<0.001.

The evaluation of the relative weight of lungs at the experimental endpoint confirmed the findings of the *ex vivo* bioluminescence detection (**Figure 2.31B**). While no treatment significantly increased lung weight compared to DPBS control, Das (1:10) increased lung weight compared to St-PGA-hyd-Dox$_1$-Das$_{10}$ (p<0.01), St-PGA-Das (1:10) (p<0.05), St-PGA-hyd-Dox$_1$-Das$_1$ (p<0.01), Dox + Das (1:1) (p<0.001), St-PGA-Das (1:1) (p<0.001), Das (1:1) (p<0.05), and St-PGA-hyd-Dox (p<0.05) (**Figure**

2.31B), suggesting that the administration of 10 mg/Kg Das induced lung metastasis but that Das conjugation to St-PGA reverted this effect.

In summary, we provide proof of the safety of all St-PGA-based conjugates (except for St-PGA-hyd-Dox$_1$-Val-Das$_1$) for intravenous administration and demonstrate that St-PGA-hyd-Dox$_1$-Das$_{10}$ possessed the most significant anti-tumor activity (**Table 2.9**). Furthermore, both St-PGA-hyd-Dox$_1$-Das$_{10}$ and St-PGA-hyd-Dox$_1$-Das$_1$ exhibited anti-metastatic potential. Considering the significant reduction in tumor volume and weight and the encouraging anti-metastatic activity encountered, we selected St-PGA-hyd-Dox$_1$-Das$_{10}$ as the optimal combination conjugate and the lead candidate to develop the brain-targeted version to treat brain metastasis (see *Chapter 4*).

Table 2.9 summarizes main results of the characterization and biological evaluation of single-drug and combination conjugates.

Table 2.9. Summary of the primary characterization and biological evaluation results of St-PGA-based single-drug and combination conjugates.

	% mol HYD[A]	% wt Dox[B]	% wt Das[B]	Ratio Dox:Das	Release	IC50 Dox (ng/mL)	IC50 Das (ng/mL)	Anti-tumor activity[C]	Anti-metastatic activity[D]
St-PGA-Das	-	-	9.9	-	pH 7.4 > 5.0	-	30.7	55%*	12%*
St-PGA-Val-Das	-	-	10.8	-	pH 7.4 > 5.0	-	102	n.d.	n.d.
St-PGA-hyd-Dox	6.0	9.4	-	-	pH 5.0 > 7.4	18.6	-	51%	35%
St-PGA-hyd-Dox$_1$-Val-Das$_1$	3.6	7.8	9.7	1:1.2	High and rapid for Dox, low for Das	4.15	5.16	40%	n.d.
St-PGA-hyd-Dox$_1$-Das$_1$	5.6	5.3	7.8	1:1.6	Dox pH 5.0 > 7.4, Das pH 7.4 > 5.0, pH 5.0 = cat. B	1.39	2.04	51%	25%
St-PGA-hyd-Dox$_1$-Das$_{10}$	5.6	1.0	8.5	1:9	Dox pH 5.0 > 7.4, Das pH 7.4 > 5.0, pH 5.0 = cat. B	0.205	1.75	25%	19%

(**A**) Total loading of hydrazide (HYD) obtained by ^{1}H-NMR (D$_2$O). (**B**) Drug loading in weight percent (% wt) determined by UV-VIS spectroscopy. (**C**) Percentage tumor volume normalized to DPBS control group at experimental endpoint (**D**) Percentage of bioluminescence normalized to DPBS control. *Data from St-PGA-Das (1:10).

2.2.6. Characterization of Serum Protein Interaction by AF4

We primarily attributed the high toxicity of St-PGA-hyd-Dox_1-Val-Das_1 *in vivo* to the burst release of Dox at pH 7.4 from the conjugate; however, St-PGA-hyd-Dox_1-Val-Das_1 exhibited higher toxicity compared to free Dox alone and Dox + Das (1:1). Therefore, we examined other potential sources of toxicity.

As described in *Chapter 1*, a conjugate interacts with blood constituents following intravenous administration, leading to the adsorption of circulating proteins and the formation of the so-called "protein corona" (112–114). This protein corona affects the biological performance of the conjugate, altering its interaction with cells, biodistribution, circulation time, and toxicity (114). Thus, we analyzed the protein corona of St-PGA-hyd-Dox_1-Val-Das_1 in comparison with St-PGA-hyd-Dox_1-Das_{10}, which provided optimal anti-tumoral activity and safety *in vivo* (see *2.2.5.In vivo Evaluation of Anti-tumor and Anti-metastatic Activity*) in the hope of understanding the high toxicity of St-PGA-hyd-Dox1-Val-Das1.

Traditionally, the study of the protein corona has relied on isolating the nanoparticle-corona complex after incubation with blood plasma or serum and then quantifying and identifying adhered proteins. Notably, the biological medium employed must be carefully considered regarding the research objective, especially the animal species and associated disease/condition. For instance, human plasma represents an adequate incubation media for human-targeted intravenously-administered conjugates. Plasma is obtained by centrifugation of a blood sample with an anticoagulant; therefore, the coagulation factors remain in the supernatant (plasma) as well as the anticoagulant. To avoid the interference of the anticoagulant in protein-nanoparticle interaction, blood serum is usually used as an alternative. Serum is obtained by centrifugation after clot formation (no use of anticoagulants) and, therefore, lacks coagulation factors, making the study of their participation in protein corona impossible (114).

The proteins adsorbed to the nanoparticle form two layers, known as the "hard" and "soft" coronae. The hard corona comprises an inner layer of proteins tightly bound to the nanoparticle, while the soft corona comprises an outer layer formed by weakly bound proteins that rapidly exchange. Some models propose that only proteins of the hard corona interact directly with the carrier and that the soft protein corona associates with the hard corona via weak protein-protein interactions (113,115). The isolation of nanoparticle-corona complexes generally employs separation techniques that rely on the different sizes of the nanoparticle-corona complex compared to free proteins (114); however, our conjugates display sizes comparable to that of the main plasma/serum proteins (e.g., albumin monomer, ~6 nm diameter), making their separation from serum proteins unfeasible via size-dependent separation techniques. Thus, we adopted a qualitative approach based on the separation of serum proteins by asymmetric flow field-flow fractionation (AF4) and online monitoring of conjugate elution, which takes advantage of the fluorescent properties of the drugs involved.

In an AF4 system, the separation of the particles occurs in a ribbon-like channel of trapezoidal geometry composed of a spacer placed between a porous and a non-porous plate (**Figure 2.32A**) (116). The porous plate is covered by an ultrafiltration membrane whose material and molecular weight cut-off (MWCO) should be carefully considered to allow eluent passage and retain the particles of interest with minimal adsorption (116,117). AF4 as a characterization technique has seen a recent increase in use due to several advantages over related, more traditional approaches (117). Encouragingly, multiple studies have explored AF4 as a means to isolate nanoparticle-corona complexes (118–120). Compared to centrifugation, the most conventional method for nanoparticle-corona complex isolation, AF4 represents a gentler technique, allowing the detection of the loosely bound proteins forming the soft protein corona. AF4 also requires only a small sample volume (< 100 µL) (114). Compared to SEC, the lack of stationary phase reduces the shear forces that can lead to sample degradation and the

loss of loosely attached proteins (114,116). Additionally, AF4 has a broader operational range, allowing the separation of particles distributed throughout two orders of magnitude in a single run (117). However, AF4 is highly sensitive to sample mass overloading, which can provoke peak broadening, tailing, and/or altered retention times (117,121).
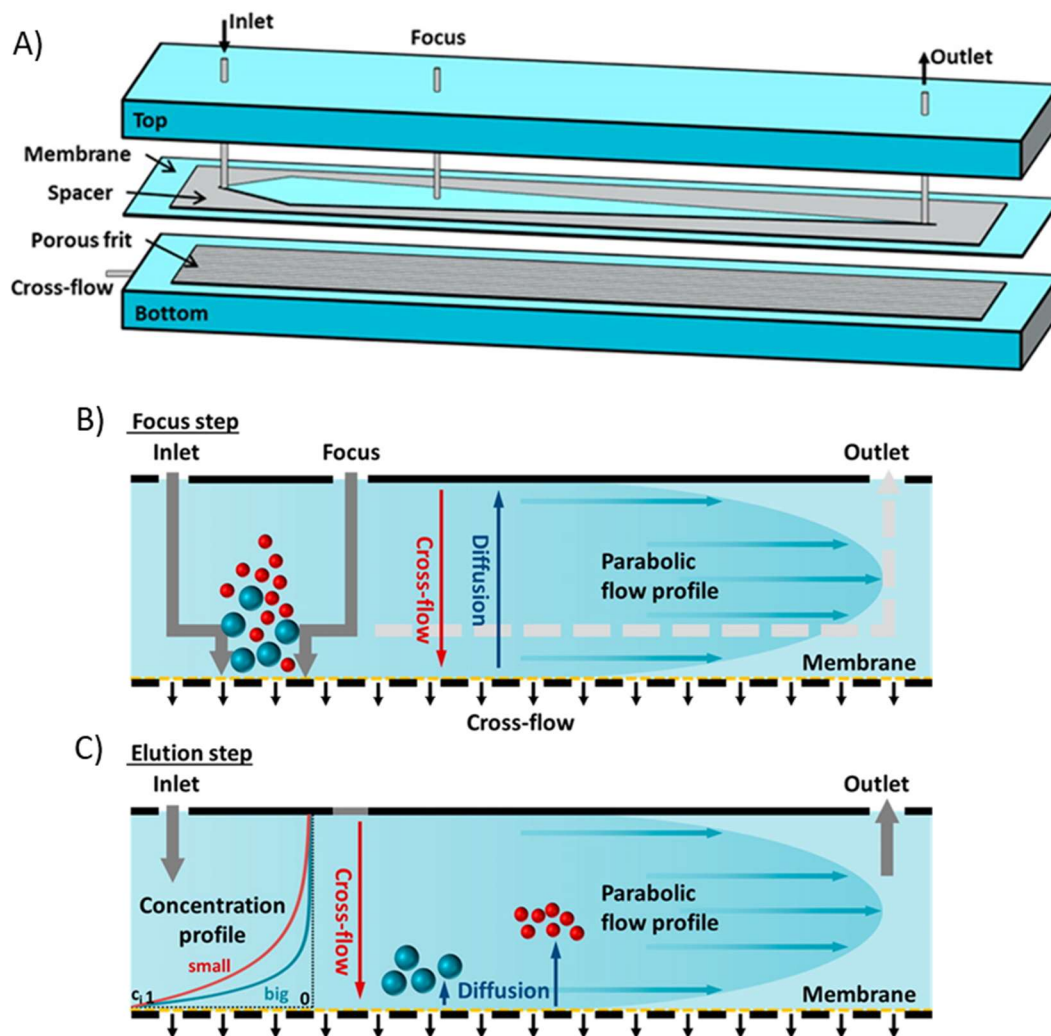
Figure 2.32. Asymmetric flow field-flow fractionation (AF4). (**A**) Schematic representation of an AF4 channel. (**B**) Focusing step. After injection of the sample into the channel, the focus flow keeps the solutes in the channel head to form a "focus zone," where the solutes remain until they reach a steady-state, distributing along the radius of the channel depending on their diffusion coefficient. (**C**) Elution step. Particles move along the channel towards the outlet while being pushed to the membrane by the crossflow, allowing for separation according to size (diffusion coefficient). Modified from Wagner et al. 2014 (116).

Three flows take part in separation by AF4 - the inlet, focus, and cross flows - and the development of an AF4 method involves optimizing each flow (116). The inlet flow creates the laminar flow that moves the particles towards the channel outlet. This laminar flow displays a parabolic speed distribution, where the speed remains low near the channel walls but increases to a maximum at the center (117). Flowing opposite the inlet flow, the focus flow allows for sample equilibration before elution (116). Pumping the solvent out of the porous plate generates the crossflow, pushing the solute towards the membrane. In reaction, the solute diffuses in the opposite direction with a size-dependent velocity, leading to the separation of solutes of different sizes across the laminar flow layers (117). Molecules with a higher diffusion coefficient (smaller) remain closer to the channel center where the flow speed is higher, thus eluting before molecules with a lower diffusion coefficient (larger) (116,121). The resulting flow leaving the channel to the detectors defines the detector flow.

An AF4 method consists of three main steps - focus, elution, and rinse steps (116). During the focusing step (**Figure 2.32B**), the sample is injected into the channel, and the focus flow keeps the sample in the head of the channel to form a "focus zone" (116). In this zone, the solutes need to reach a steady state where, due to the crossflow and the diffusion flow, they distribute across the channel radius depending on their size (117). Then, the inhibition of the focus flow and the maintenance of the crossflow during the elution step (**Figure 2.32C**) allows the solutes to move along the channel towards the outlet. The focusing step should be long enough for the solutes to achieve the steady-state condition for optimal separation. A short focusing time that does not permit the sample to reach a steady-state leads to peak broadening and inadequate fractionation. Alternatively, longer focusing times contribute to particle-particle interactions and particle-membrane interaction, leading to aggregation and/or sample loss (116,117). Finally, the absence of an applied field during the rinsing step (only inlet flow) allows for the elution of any particle or aggregate remaining in the channel.

The approach we propose herein has been employed for the study of the interaction of small drugs (121), antibodies (122), and polymeric micelles (123) with blood plasma or serum. For example, Leeman et al. (122) studied the interaction of a fluorescently-labeled antibody with rat plasma by AF4 and online fluorescence detection. The antibody alone eluted at 6.75 min, with the main peak showing a tail corresponding to the formation of dimers. In the presence of plasma, this peak (recorded by fluorescence) shifted to 6.90 min, suggesting an increment in the size of the antibody. The peak also displayed a more pronounced shoulder because of an increment in dimer formation. Overall, these results indicated the interaction of the antibody with plasma proteins (122).

As small drugs become filtered off the channel when their size is below the MWCO of the membrane, their presence in the eluting fractions reveals interaction with the larger proteins that cannot pass through the membrane. For example, Madörin et al. (121) studied the interaction of N-benzoyl-staurosporine (570.7 Da) with plasma proteins by quantifying drug concentration in the fractions collected after protein separation via AF4. The authors quantified the amount of drug in each collected fraction by offline detection of the fluorescence emitted by N-benzoyl-staurosporine (λ_{exc} = 295 nm, λ_{em} = 378 nm); however, the authors needed to increase the amount of sample injected in the system to detect the drug, which resulted in peak broadening and displacement to longer elution times, which prompted a loss in resolution. The presence of N-benzoyl-staurosporine in the fractions corresponding to the peak of albumin confirmed drug-protein interaction and proved the suitability of AF4 to study the interaction of small drugs with plasma proteins (121).

Considering these factors, we optimized a method for separating serum proteins by first choosing an appropriate membrane. To allow free drug elimination from the channel while maintaining serum proteins (≥70 kDa – albumin monomer) and the polymer (~26 kDa – St-PGA) inside, we chose

a 5 kDa MWCO membrane. As the study of conjugate-protein interaction requires minimal membrane interaction, we studied the recovery of St-PGA (with a similar size and zeta potential as St-PGA-hyd-Dox$_1$-Das$_{10}$ and St-PGA-hyd-Dox$_1$-Val-Das$_1$, **Table 2.4**) using a polyethersulfone (PES) membrane and a regenerated cellulose (RC) membrane using NaCl 0.9% w/v as mobile phase. We first injected the sample into the channel without any crossflow; thus, no forces pushed the sample towards the membrane. We then injected the sample, applying a focus flow of 1.8 mL/min and a crossflow of 1.5 mL/min to study the interaction of the sample with the membrane. Using the RI signal, we calculated the area of the peak obtained with both injections (**Supplementary Figure 2.8**). We obtained the percentage recovery by dividing the area obtained from the injection with crossflow to that obtained with direct injection. We obtained 96% and 83% recovery for the PES and RC membranes, respectively; thus, we selected the 5 kDa MWCO PES membrane for subsequent studies.

We next optimized the various flows for serum protein separation. As the use of serum instead of whole blood or plasma allows the study of protein-conjugate interactions without the interference of anticoagulant agents, we used mouse serum obtained by centrifuging blood to eliminate clots and blood cells. We used DPBS as an eluent for protein fractionation to preserve the structure and properties of the proteins and mimic the physiological ionic strength, adding 0.005% NaN$_3$ as an antimicrobial preservative. This media allowed an 85% recovery of St-PGA using the 5 kDa MWCO PES membrane (**Supplementary Figure 2.9**), a value suitable for our purpose. Based on the study by Madörin et al. (121), we selected an isocratic elution with 3 mL/min of crossflow for 50 min, after a focusing step of 4 min with a focus flow of 3.3 mL/min and a transition to the elution step of 1 min. We kept the detector flow constant at 0.5 mL/min. We diluted serum samples with one volume of DPBS to maintain the same conditions as incubation with the conjugate and reduce sample viscosity. Fractograms demonstrated adequate separation of the main protein components of blood

serum (**Figure 2.33**), with the first peak (~14 min) corresponding well with the elution of albumin monomers (~70 kDa, ~40 mg/mL in serum) (121,122) and the second peak (~20 min) corresponding well to the elution of immunoglobulin G monomers (~160 kDa, ~10 mg/mL in serum) (122). The third peak (~31 min) generally corresponds to the elution of α-2-macroglobulin (~720 kDa, ~3 mg/mL in serum) (121,122); however, these proteins can co-elute with a multitude of less abundant serum proteins of similar size or oligomers/aggregates of smaller proteins (122).
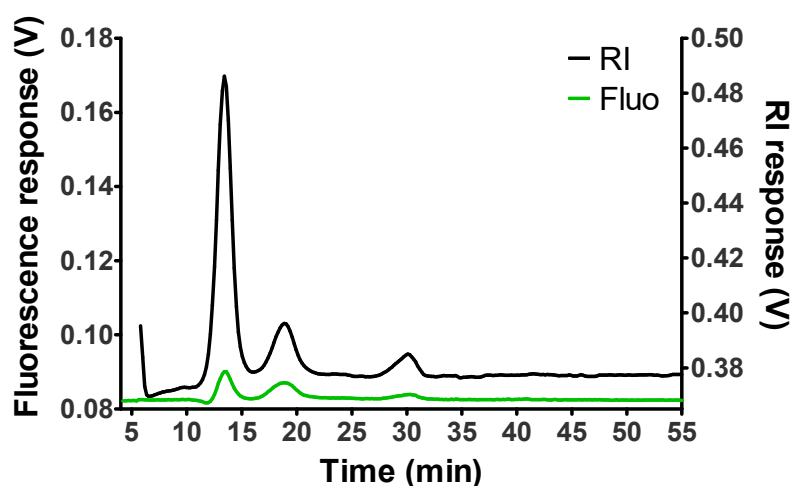

Figure 2.33. Representative AF4 fractogram of serum monitored by RI (black) and fluorescence detection (green) (λ_{exc} = 340 nm and λ_{em} = 374 nm). The peak at 14 min corresponds to the albumin monomer. The peak at 20 min corresponds to immunoglobulin G. The peak at 31 min corresponds to α-2-macroglobulin.

After confirming our ability to fractionate blood serum into its main components, we next incubated St-PGA-hyd-Dox$_1$-Val-Das$_1$ and St-PGA-hyd-Dox$_1$-Das$_{10}$ with mouse serum. We dissolved the conjugates at 6 mg/mL and mixed them with one volume of serum. After gently stirring, we left the samples at room temperature for 20 min before injection into the system. As a control, we injected serum (diluted with one volume of DPBS) and each conjugate (St-PGA-hyd-Dox$_1$-Val-Das$_1$ and St-PGA-hyd-Dox$_1$-Das$_{10}$) alone in DPBS (3 mg/mL). We monitored the elution of St-PGA-hyd-Dox$_1$-Das$_{10}$ and St-PGA-hyd-Dox$_1$-Val-Das$_1$ by fluorescence detection of Das (λ_{exc} = 340

nm and λ_{em} = 374 nm), as both conjugates displayed a similar Das loading (**Table 2.4**) and low Das release at early time points (see *2.2.4.pH and Cathepsin B-mediated Drug Release*, **Figure 2.26**). Additionally, we monitored the elution of serum (in DPBS) using the same setup for the fluorescence detector and observed minimal signal, discarding possible interference with conjugate detection (**Figure 2.33**). We injected conjugate-serum mixtures and controls at least three times for reproducibility.

We observed a clear difference in the elution profile of the selected combination conjugates with and without incubation with mouse serum. Both combination conjugates alone eluted as a broad peak immediately after the void peak with long tailing (**Figure 2.34A** and **B**), suggesting an interaction with the membrane due to the elevated crossflow applied for protein separation (117). After incubation with serum, the elution profile dramatically changed for both combination conjugates (**Figure 2.34A** and **B**). Overall, we discovered a similar elution profile for St-PGA-hyd-Dox$_1$-Das$_{10}$ (**Figure 2.34A**) and St-PGA-hyd-Dox$_1$-Val-Das$_1$ (**Figure 2.34B**) after incubation with serum - a small peak immediately after the void peak, corresponding to the fraction of conjugate that did not interact with serum proteins, and then three peaks that partially overlap with those of the main serum proteins. The first peak (~15 min) partially overlapped with the albumin monomer peak, the second broader peak (~24 min) partially overlapped with the immunoglobulin G monomer peak, and the third peak (~33 min) partially overlapped with the α-2-macroglobulin peak. Nevertheless, the third peak displayed a later elution compared to α-2-macroglobulin alone, suggesting the interaction of the conjugate with larger protein aggregates.
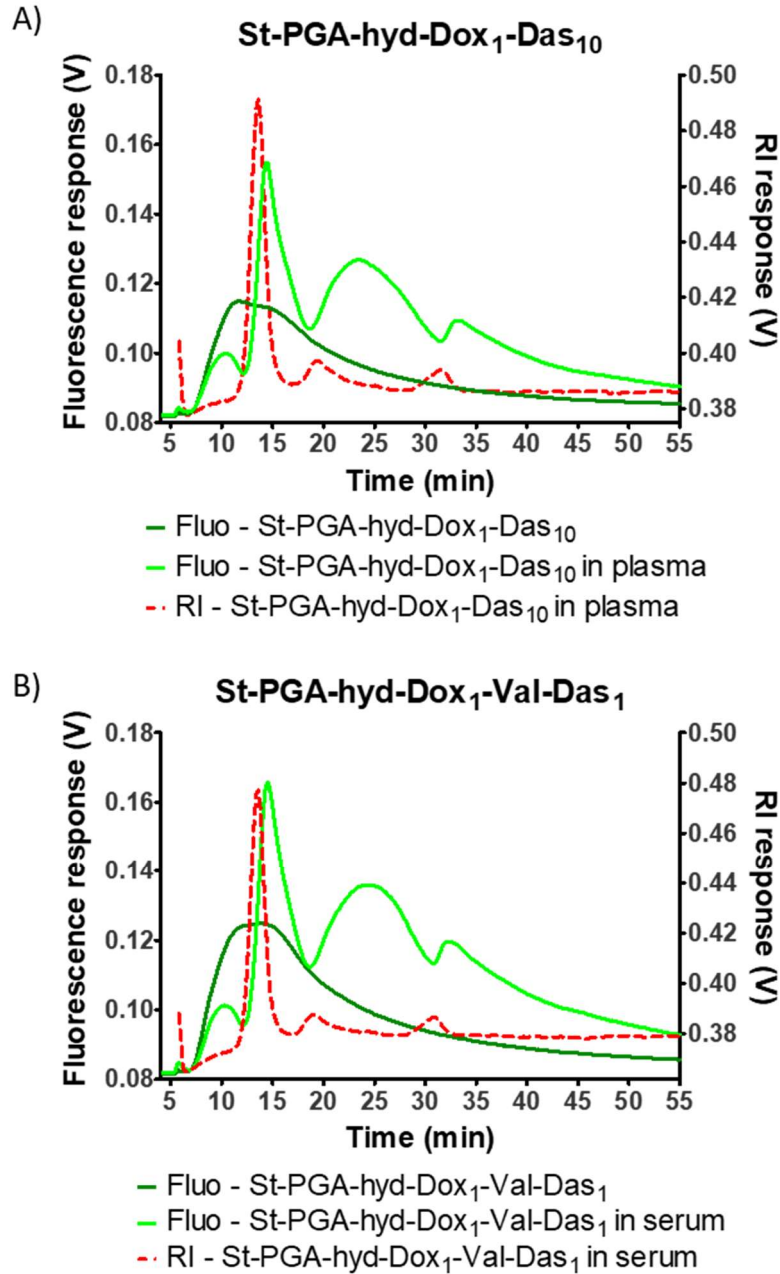
Figure 2.34. Study of conjugate-protein interaction in mouse blood serum. (**A**) AF4 fractograms corresponding to St-PGA-hyd-Dox$_1$-Das$_{10}$ (dark green) in DPBS monitored by fluorescence detection (λ_{exc} = 340 nm and λ_{em} = 374 nm), and the mixture of St-PGA-hyd-Dox$_1$-Das$_{10}$ with serum monitored by fluorescence (bright green) and RI (dotted red line). (**B**) AF4 fractograms corresponding to St-PGA-hyd-Dox$_1$-Val-Das$_1$ (dark green) in DPBS monitored by fluorescence detection (λ_{exc} = 340 nm and λ_{em} = 374 nm), and the mixture of St-PGA-hyd-Dox$_1$-Val-Das$_1$ with serum monitored by fluorescence (bright green) and RI (dotted red line).

236

We did encounter some differences between the two combination conjugates, finding a shift to longer elution times for the main protein peaks after the incubation of St-PGA-hyd-Dox$_1$-Val-Das$_1$ with serum, but not with St-PGA-hyd-Dox$_1$-Das$_{10}$ (**Figure 2.35** and **Table 2.10**); only the shift of the third peak, corresponding to the elution of α-2-macroglobulin, proved statistical significance (p=0.0244, **Table 2.10**).
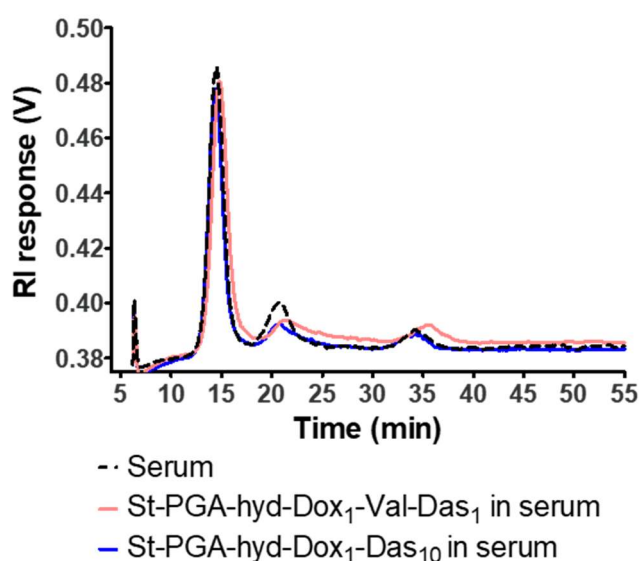

Figure 2.35. Study of conjugate-protein interaction in mouse blood serum – protein peak shift. Representative AF4 fractograms of blood serum (diluted with one volume of DPBS) (dotted black), St-PGA-hyd-Dox$_1$-Val-Das$_1$ in serum (pink), and St-PGA-hyd-Dox$_1$-Das$_{10}$ in serum (blue). All injections used the same conditions on the same day and were monitored by RI.

Table 2.10. Quantification of the shift of each serum protein peak after incubation with St-PGA-hyd-Dox_1-Val-Das_1 and St-PGA-hyd-Dox_1-Das_{10}.

		St-PGA-hyd-Dox_1-Val-Das_1	St-PGA-hyd-Dox_1-Das_{10}
Peak 1	**Shift**	0.25 ± 0.15	0.00 ± 0.11
	p value	0.1041	1.000
Peak 2	**Shift**	0.47 ± 0.23	0.00 ± 0.08
	p value	0.0732	1.000
Peak 3	**Shift**	1.07 ± 0.30	0.12 ± 0.30
	p value	0.0244	0.5430

Data obtained from three independent experiments (mean ± SD, n=3). Statistical analysis employed a two-tailed Student's t-test.

To confirm that our observations described the interaction of the conjugates with serum proteins and not with released Dox and Das, we mixed serum with one volume of a solution of Dox and Das at 0.1 mg/mL in DPBS. The elution profile of the serum with and without the free drugs failed to exhibit significant differences by RI and fluorescence (**Figure 2.36**), suggesting that Dox and Das do not interact with the proteins in these conditions and become filtered off due to the large MWCO of the membrane (5 kDa) and the applied crossflow.
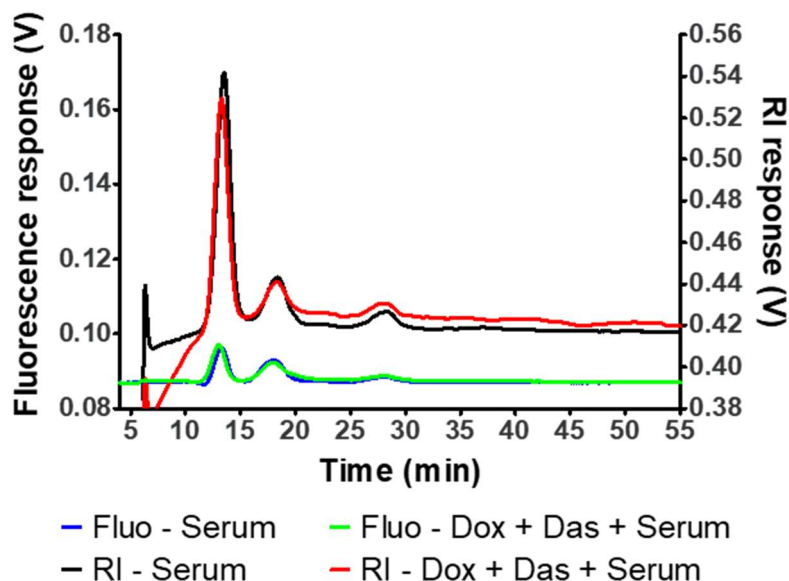
Figure 2.36. Free drug interaction with serum proteins. AF4 fractograms obtained by RI (black and red) and fluorescence detection (green and blue) (λ_{exc} = 340 nm and λ_{em} = 374 nm) for the separation of serum proteins with (green and red) and without (blue and black) previous incubation with Dox and Das.

Our results imply that both the change in the elution profile of the conjugates and the shift observed in the serum protein peaks after incubation with St-PGA-hyd-Dox$_1$-Val-Das$_1$ result from conjugate-protein interactions. The shift to longer elution times in AF4 responds to the formation of larger structures; even small shifts indicate aggregate formation (118,122,123). Leeman et al. (122) identified the interaction of a fluorescently labeled antibody with plasma proteins through a shift of 0.15 min in the elution peak of the antibody. Here, we observed shifts from 0.25 to 1 min in the main serum protein peaks (**Figure 2.35B**), revealing the formation of larger structures derived from conjugate-protein interactions with St-PGA-hyd-Dox$_1$-Val-Das$_1$. Given that St-PGA-hyd-Dox$_1$-Das$_{10}$ failed to display this shift in the serum elution profile, we hypothesize the formation of aggregates upon intravenous injection of St-PGA-hyd-Dox$_1$-Val-Das$_1$ could have contributed, together with the rapid Dox release, to the toxicity observed in animals. We believe that these findings support AF4 as a useful

239

tool for the rapid characterization of conjugate-protein interactions, providing useful insights into the *in vivo* behavior of the conjugate.

2.3. Conclusions

The effective therapeutic management of metastatic TNBC remains an unmet clinical need. As hormonal and HER2-targeted therapies do not provide clinical benefit due to the lack of expression of their therapeutic targets, chemotherapy remains the only possible systemic treatment for this subtype. Preclinical identification of new synergistic combinations of drugs has provided hope for these patients, including the cotreatment with the topoisomerase I/II Dox and the SRC-family inhibitor Das. Here, we report the synthesis, physico-chemical characterization, and biological evaluation of a novel family of polypeptide-based combination conjugates bearing Dox and Das to treat metastatic TNBC.

Previous work from our laboratory described the optimal ratio and dosage to maximize the synergy between Dox and Das (41). This study supported the development of an effective linear PGA combination conjugate with Dox and Das. Using a rational design approach, we aimed to further improve the efficacy of this treatment strategy by using novel PGA-based branched architectures with improved pharmacokinetic profiles.

As a result, we synthesized three St-PGA-based combination conjugates, exploring different linking chemistries and drug ratios. We performed an exhaustive physico-chemical characterization for each conjugate to allow iterative improvements. Overall, this approach supported the successful development of a St-PGA-based combination conjugate with enhanced anti-tumor and anti-metastatic activity in an orthotopic human metastatic TNBC mouse model.

In disagreement with linear PGA conjugates, we did not require a Val spacer between PGA and Das to achieve delayed drug release in the

combination conjugates, which underscores the influence of carrier architecture on release kinetics and provides additional advantages over linear PGA conjugates as the simplified associated synthetic protocol reduces time and cost. Moreover, the combination conjugate synthesized with the Val spacer, St-PGA-hyd-Dox$_1$-Val-Das$_1$, exhibited high toxicity *in vivo*. We studied the potential causes of said toxicity and detected significant conjugate-protein interactions in mouse serum. St-PGA-hyd-Dox$_1$-Val-Das$_1$ provoked the formation of large aggregates with the main proteins in serum, which could have contributed to the toxicity of the compound.

The St-PGA-based conjugates synthesized with direct ester Das conjugation (St-PGA-hyd-Dox$_1$-Das$_1$ and St-PGA-hyd-Dox$_1$-Das$_{10}$) displayed similar drug release profiles, with rapid Dox release and sustained Das release. Nevertheless, the high Dox:Das ratio of St-PGA-hyd-Dox$_1$-Das$_{10}$ favored the bioavailability of the drugs in the optimal ratio in the tumor, which reflected in the *in vitro* and *in vivo* anti-tumor activity of the conjugate, highlighting the importance of drug ratio in combination therapy.

The biological evaluation of combination conjugates in an orthotopic TNBC murine model revealed the robust anti-tumor capabilities of St-PGA-hyd-Dox$_1$-Das$_{10}$. This combination conjugate effectively reduced primary tumor size by approximately 75% compared to the control group with no signs of toxicity. St-PGA-hyd-Dox$_1$-Das$_{10}$ also safely reduced metastatic spread to the lungs, although to a lesser extent than the free drugs administered in combination at the same dose (which displayed significant toxicity). Thus, we conclude that St-PGA-hyd-Dox$_1$-Das$_{10}$ entails an improvement over free drug administration, thereby representing a step forward in the development of effective systemic treatments for metastatic TNBC.

2.4. Materials and Methods

2.4.1. Materials

All solvents were of analytical grade and obtained from Sharlab Chemicals (Sharlab S.L., Barcelona, Spain) except trifluoroacetic acid (TFA), which was obtained from TCI Deutschland GmbH (Eschborn, Germany), and tetrahydrofuran (THF), which was freshly distilled. Deuterated solvents were obtained from Deutero GmbH (Kastellaun, Germany). Unless otherwise indicated, all chemicals were reagent grade, obtained from Sigma-Aldrich (Merck KGaA, Darmstadt, Germany). 4-Dimethylaminopyridine (DMAP) was obtained from Fluka (Thermo Fisher GmbH, Kandel, Germany). Doxorubicin HCl was obtained from MedKoo Biosciences, Inc. (Morrisville NC, USA). Dasatinib was obtained from LC Laboratories Inc. (Woburn MA, USA). ɣ-Benzyl L-glutamate N-carboxyanhydride was purchased from PMC Isochem (Vert-Le-Petit, France). 4-(4,6-dimethoxy-1,3,5-triazin-2-yl)-4-methyl-morpholinium tetrafluoroborate (DMTMM BF$_4$) was synthesized as described in reference (124). Preparative SEC was performed using Sephadex LH-20 or Sephadex G25 medium from GE Healthcare (Global Life Sciences Solutions USA LLC, Marlborough, MA, USA). Ultrafiltration was performed in a Millipore (Merck KGaA, Darmstadt, Germany) ultrafiltration device fitted with a 3, 10, 30, or 50 kDa molecular weight cut-off (MWCO) regenerated cellulose membrane (Vivaspin^{TM}). HyClone Dulbecco's phosphate-buffered saline (DPBS) was obtained from Cytiva UK Ltd. (Buckinghamshire, UK).

2.4.2. Synthetic Protocols

2.4.2.1.   Synthesis of star-poly (glutamic acid) (St-PGA)

2.4.2.1.1.   Synthesis of 1,3,5-Tri-tert-butyl ((benzenetricarbonyltris (azanediyl)) tris(ethane-2,1-diyl)) tricarbamate

The ethyl-based initiator was synthesized as previously reported by our group (43). Briefly, in a two-neck round bottom flask fitted with a stir bar and an N_2 inlet and outlet, N-Boc-ethylenediamine (4.5 mmol, 1 equivalent) was dissolved in 40 mL of anhydrous (anh.) tetrahydrofuran (THF). N,N-diisopropylethylamine (DIEA) (15 mmol, 3.3 equivalents) was added and then, 1,2,3-benzenetricarbonyl chloride (15 mmol, 3.3 equivalents) dissolved in 10 mL of anh. THF was added dropwise. The reaction was left to proceed for 3 h under stirring at room temperature. After that, the solvent was completely removed under vacuum. The product was re-dissolved in chloroform and washed three times with MilliQ water and another three times with acid water. Finally, the organic phase was collected in a round bottom flask and removed under vacuum. Product identity was evaluated by ^{1}H-NMR.

Yield: 73%. ^{1}H-NMR: δ_H (300 MHz, DMSO) 8.75-8.56 (m, 3H), 8.43 (s,3H), 7.02-6.73 (m,3H), 3.43-3.27 (m, 6H), 3.25-3.01 (m, 6H), 1.36 (s, 27H).

2.4.2.1.2.   Synthesis   of   1,3,5-(benzenetricarbonyltris(azanediyl))-triethanammonium BF$_4$ Salt

1,3,5-Tri-tert-butyl ((benzenetricarbonyltris (azanediyl)) tris(ethane-2,1-diyl)) tricarbamate was dissolved in 50 mL of chloroform in a round bottom flask fitted with a stir bar. Once completely dissolved, tetrafluoroboric acid diethyl ether (HBF$_4$·Et$_2$O) was added. The formation of a white solid was observed upon HBF$_4$·Et$_2$O addition. The reaction was left for 30 min at room temperature. After that, the solvent was removed, yielding a white solid. The product was washed with hexane and dried under a high vacuum. Finally, the solid was resuspended in MilliQ water and freeze-dried. Identity and purity of the product was evaluated by ^{1}H-NMR and ^{19}F-NMR.

Yield: 71%. ^{1}H-NMR: δ_H (300 MHz, D_2O) 8.43 (s, 3H), 3.84-3.76 (t, 2H), 3.37-3.29 (t, 2H).

2.4.2.1.3.   Synthesis of Star-poly(γ-benzyl L-Glutamate) (St-PBLG)

The synthesis of St-PGA was done according to procedures previously published by our group (14, 15). Briefly, the initiator 1,3,5-(benzenetricarbonyltris(azanediyl))-triethanammonium BF_4 salt (1.5 mmol, 1 equivalent) was dissolved with 10mL of DMF anh. in a glass vial fitted with a stopper and an N_2 inlet and outlet. In a two-neck round bottom flask fitted with a stir bar and an N_2 inlet and outlet, γ-Benzyl L-glutamate N-carboxyanhydride (380 mmol, 250 equivalents) was dissolved in 390 mL of DMF anh. Once it was completely dissolved, the initiator was added. Finally, the N_2 inlet and outlet were replaced with a CO_2 outlet. The reaction was left at room temperature under stirring for seven days. After that, the product was precipitated in cold diethyl ether and filtered out. The degree of polymerization was obtained by ^{1}H-NMR by comparing the signal of the benzene tricarbonyl initiator (8.73 ppm) with the α-carbon proton in the polypeptide backbone (4.7 ppm).

Yield: 68%. ^{1}H-NMR: δ_H (300 MHz, D_2O) 8.73 (s, 1H), 7.37-7.20 (m, 5H), 5.32-5.00 (m, 2H), 4.84-4.62 (m, 1H), 2.84-1.87 (m, 4H).

2.4.2.1.4.   St-PBLG Deprotection

In a round bottom flask fitted with a stir bar St-PBLG (0.3 mol, 1 equivalent) was dissolved in 500 mL of TFA. Once completely dissolved, 80 mL of HBr 48% v/v in water were added (0.7 mol, 2.5 equivalents). The reaction was kept under stirring at room temperature overnight. Deprotection was monitored by ^{1}H-NMR. Once complete deprotection was achieved, the product was precipitated in cold diethyl ether, filtered out, and washed with

MilliQ water. Finally, freeze-drying yielded a white solid. Complete polymer deprotection was confirmed by ^{1}H-NMR.

Yield: 89%. ^{1}H-NMR: δ_H (300 MHz, D_2O) 8.29 (s, 1H), 4.40-4.22 (m, 1H), 2.39-1.66 (m, 4H).

2.4.2.2.   Synthesis of Valine-dasatinib Precursor

2.4.2.2.1.   Synthesis of Boc-valine-dasatinib

The derivative valine-dasatinib was synthesized as described elsewhere (41). Briefly, dasatinib (Das) (300 mg, 0.0146 mmol), Boc-valine-OH (33.2 mg, 1.05 eq.), 1-ethyl-3-(3-dimethylaminopropyl)carbodiimide (EDC) (35.3 mg, 1.2 equivalents of valine), and DMAP (cat.) were dissolved in DMF anh. inside a round-bottomed flask fitted with a stir bar and an N_2 inlet and outlet. The reaction was left to proceed for 6 h. Then, water was added to the reaction mixture until a precipitate was observed. Extraction with ethyl acetate was performed three times. All the organic fractions were merged and washed with diluted $NaHCO_3$ and water. Finally, the organic phase was dried with $MgSO_4$ and filtered off. A white fine powder was yielded after evaporation of the solvent.

The product was further purified by column chromatography using Silica gel 60 (Fluorochem Ltd., Derbyshire, UK) as stationary phase and a mixture of CH_2Cl_2, methanol, and $NH_4(OH)$ 100:7:1 (v/v/v) as mobile phase. Elution was monitored by TLC. Fractions containing the desired product were merged, and the solvent was evaporated. The identity of the product was evaluated by ^{1}H-NMR taking the signals of the isopropyl group of valine (1.06-0.85 ppm) as reference (6 protons).

Yield: 90%. ^{1}H-NMR: δ_H (300 MHz, DMFd) 9.89 (s, NH), 8.33 (s, NH), 7.46-7.36 (m, 1H), 7.36-7.21 (m, 2H), 6.22 (s, 1H), 4.47-4.15 (m, 2H), 4.14-

3.95 (m, 1H), 3.60 (m, 4H), 2.68 (m, 2H), 2.58 (m, 4H), 2.46 (s, 3H), 2.34 (s, 3H), 2.23-2.05 (m, 1H), 1.41 (s, 9H), 1.06-0.85 (m, 6H).

2.4.2.2.2.   Deprotection of Boc-valine-dasatinib

In a round-bottomed flask fitted with a stir bar, Boc-valine-dasatinib was suspended in a mixture of 1.2 mL of HCl 4M in dioxane and 5 mL of ethyl acetate. The deprotection was allowed to proceed for 90 min. Then, the reaction mixture was transferred to a 50 mL centrifuge tube where 5 mL of hexane was added. After gentle stirring, solid and liquid phases were separated by centrifugation. The pellet was washed with hexane and dried under vacuum. Then, the solid was suspended in water. The pH was adjusted to 7-8 with NaHCO$_3$. Then, the solid was yielded by centrifugation and washed with MilliQ water until the complete removal of salts. Finally, freeze-drying yielded a white solid. Complete removal of Boc protecting group was confirmed by ^{1}H-NMR.

Yield: 95%. ^{1}H-NMR: δ_H (300 MHz, DMFd) 9.95 (s, NH), 8.39 (s, NH), 7.45-7.36 (m, 1H), 7.35-7.22 (m, 2H), 6.26 (s, 1H), 4.54-4.15 (m, 2H), 2.60 (m, 4H), 2.46 (s, 3H), 2.34 (s, 3H), 1.11-0.93 (m, 6H).

2.4.2.3.   Conjugation of Dasatinib to Star-poly(glutamic acid) Through an Ester Bond (St-PGA-Das)

St-PGA (3.1 mmol, 1 equivalent) was dissolved in DMF anh. in a two-neck round bottom flask fitted with a stir bar and N$_2$ inlet and outlet. Once completely dissolved, DMAP (0.093 mmol, 0.030 equivalents) and EDC (0.47 mmol, 0.15 equivalents) was added to the reaction mixture and left stirring for 20 min. Then, Das (0.47 mmol, 0.15 equivalents) was added to the reaction, and the pH was adjusted to 8 with DIEA. The reaction was left to proceed under stirring at room temperature for 72 h. The product was

purified by size exclusion chromatography with a Sephadex LH-20 column using DMF as eluent. Elution was monitored by TLC, with methanol as the mobile phase. Fractions containing the product were collected in a round bottom flask, and 3 mL of sodium bicarbonate 0.1 M were added before evaporating the solvent under vacuum. To obtain the salt form of the polymer, MilliQ water was added. Size exclusion chromatography with a Sephadex G-25 column using MilliQ water as eluent was performed to eliminate the excess of salts. Elution was monitored by TLC (MeOH, R_f: 0.7). The fractions containing only the polymer-drug product were freeze-dried to yield a white solid. Identity of the product was evaluated by ^{1}H-NMR. Das loading was determined by UV-VIS spectroscopy (see *2.4.3.2.Drug Loading Determination by UV-VIS Spectroscopy*).

Yield: 75%. CE: 68%. ^{1}H-NMR: δ_H (300 MHz, D_2O) 8.71-7.09 (1H initiator, 5H Das), 6.24 (1H Das), 4.65-4.17 (1H αC PGA, 2H Das), 4.08-2.52 (10H Das), 2.52-1.65 (4H Glu PGA, 6H Das).

2.4.2.4.   Conjugation of Valine-dasatinib to Star-poly(glutamic acid) (St-PGA-Val-Das)

In a round-bottomed flask fitted with a stir bar and an N_2 inlet and outlet, St-PGA (3.1 mmol, 1 equivalent) was dissolved in DMF anh. Once completely dissolved, DMTMM BF_4 (0.28 mmol, 0.090 equivalents) was added, and the reaction was left to proceed under stirring for 30 min. After that, valine-dasatinib (0.19 mmol, 0.060 equivalents) was added to the reaction. pH was adjusted to 8 with DIEA, and the reaction was left under stirring at room temperature for 48 h. The product was purified by size exclusion chromatography with a Sephadex LH-20 column using DMF as eluent. Elution was monitored by TLC, with methanol as the mobile phase. The fractions containing the product were collected in a round bottom flask, and 3 mL of 0.1 M $NaHCO_3$ were added before the evaporation of the solvent in the vacuum pump. To obtain the salt form of the polymer, MilliQ water was

added. Size exclusion chromatography with a Sephadex G-25 column using MilliQ water as eluent was performed to eliminate the excess of salts. Elution was monitored by TLC, with methanol as the mobile phase. The fractions containing the polymer-drug conjugate were freeze-dried, yielding a white solid. Identity of the product was evaluated by ^{1}H-NMR. Das loading was determined by UV-VIS spectroscopy (see *2.4.3.2.Drug Loading Determination by UV-VIS Spectroscopy*).

Yield: 71%. CE: 62%. ^{1}H-NMR: δ_H (300 MHz, D$_2$O) 8.60-6.95 (1H initiator, 5H Das), 4.57-4.00 (1H αC PGA, 2H Das, 1H Val), 3.99-2.53 (10H Das), 2.52-1.75 (4H Glu PGA, 6H Das, 1H Val), 1.09-0.79 (6H Val).

2.4.2.5. Conjugation of Doxorubicin to Star-poly(glutamic acid) Through a Hydrazone Bond (St-PGA-hyd-Dox)

2.4.2.5.1. Conjugation of Tert-butyl Carbazate Moiety (St-PGA-TBC)

In a round bottom flask fitted with a stir bar and an N$_2$ inlet and outlet, St-PGA (3.1 mmol, 1 equivalent) was dissolved in DMF anh. Once completely dissolved, DMTMM BF$_4$ (0.28 mmol, 0.090 equivalents) was added, and the reaction was left to proceed under stirring for 30 min. After that, tert-butyl carbazate (0.19 mmol, 0.060 equivalents) was added to the reaction. pH was adjusted to 8 with DIEA, and the reaction was left stirring at room temperature for 48 h. The product was precipitated in cold diethyl ether and dried. The white solid product was washed three times with cold, acidic water and twice with cold MilliQ water and freeze-dried. TBC loading was obtained by ^{1}H-NMR by comparing Boc group signals (9 protons, 1.50 ppm) to the α-carbon proton signals of the St-PGA backbone (4.33 ppm).

Yield: 85%. CE: 100%. ^{1}H-NMR: δ_H (300 MHz, D$_2$O) 8.31 (1H initiator), 4.46-4.25 (1H αC PGA), 2.55-1.76 (4H Glu PGA), 1.48 (9H Boc).

2.4.2.5.2. Deprotection of Tert-butyl Carbazate (St-PGA-hydrazide)

In a round bottom flask fitted with a stir bar and a stopper, St-PGA-TBC (2.7 mmol, 1 equivalent) was dissolved in TFA, and it was left under stirring for 45 min. Then, the product was precipitated in cold diethyl ether and dried. Complete removal of Boc protecting group was confirmed by ^{1}H-NMR.

Yield: 100%. ^{1}H-NMR: δ_H (300 MHz, D$_2$O) 8.32 (1H initiator), 4.53-4.16 (1H αC PGA), 2.51-1.76 (4H Glu PGA).

2.4.2.5.3. Conjugation of Doxorubicin to St-PGA-hydrazide (St-PGA-hyd-Dox)

In a two-neck round bottom flask fitted with a stir bar and an N$_2$ inlet and outlet, St-PGA-hydrazide (2.8 mmol, 1 equivalent) was dissolved in DMSO anh. Once completely dissolved, doxorubicin (Dox) (0.24 mmol, 0.083 equivalents) was added to the reaction. Then, three drops of pure acetic acid were added to the reaction, and it was left to proceed protected from light, under stirring at room temperature for 48 h. After that, the solvent was evaporated under high vacuum. The product was dissolved in DMF and purified by size exclusion chromatography with a Sephadex LH-20 column using DMF as eluent. The fractions containing the red-colored product were collected in a round bottom flask, and 3 mL of sodium bicarbonate 0.1 M was added before evaporating the solvent in the vacuum pump. To obtain the salt form of the polymer, MilliQ water and sodium bicarbonate were added. Size exclusion chromatography with a Sephadex G-25 column using MilliQ water as eluent was performed to eliminate the excess of salts. The fractions containing the red-colored polymer-drug product were collected and freeze-dried. Product identity was evaluated by ^{1}H-NMR. Dox loading was determined by UV-VIS spectroscopy (see *2.4.3.2.Drug Loading Determination by UV-VIS Spectroscopy*).

Yield: 34%. CE: 58%. ^{1}H-NMR: δ_H (300 MHz, D$_2$O) 8.59-6.90 (1H initiator, 3H Dox), 4.55-3.97 (1H αC PGA, 2H Dox), 3.96-2.72 (6H Dox), 2.71-1.64 (4H Glu PGA, 2H Dox).

2.4.2.6. Synthesis of Star-poly(glutamic acid)-based Combination Conjugates with Doxorubicin and Dasatinib by Valine-ester Conjugation (St-PGA-hyd-Dox$_1$-Val-Das$_1$)

2.4.2.6.1. Conjugation of Tert-butyl Carbazate Moiety and Valine-dasatinib (St-PGA-TBC-Val-Das)

In a round bottom flask fitted with a stir bar and an N$_2$ inlet and outlet, St-PGA (3.1 mmol, 1 equivalent) was dissolved in DMF anh. Once completely dissolved, DMTMM BF$_4$ (0.56 mmol, 0.18 equivalents) was added, and the reaction was left to proceed under stirring for 30 min. After that, tert-butyl carbazate (0.19 mmol, 0.060 equivalents) and valine-dasatinib (0.19 mmol, 0.060 equivalents) were added to the reaction. pH was adjusted to 8 with DIEA, and the reaction was left to proceed under stirring at room temperature for 48 h. The product was precipitated in cold diethyl ether and freeze-dried. Then, the product was washed three times with cold, acidic water (pH 3) and two times with cold MilliQ water and freeze-dried. Product identity was evaluated by ^{1}H-NMR.

Yield: 89%. CE$_{TBC}$: 60%. CE$_{ValDas}$: 60%. ^{1}H-NMR: δ_H (300 MHz, D$_2$O) 8.30-6.90 (1H initiator, 5H Das), 4.40-4.22 (1H αC PGA, 2H Das, 1H Val), 4.21-2.40 (10H Das), 2.39-1.66 (4H Glu PGA, 6H Das, 1H Val), 1.48 (9H Boc), 1.09-0.75 (6H Val).

2.4.2.6.2. Deprotection of Tert-butyl Carbazate

In a round bottom flask fitted with a stir bar and a stopper, St-PGA-TBC-Val-Das (2.8 mmol, 1 equivalent) was dissolved in TFA, and it was left

under stirring for 45 min. Then, the product was precipitated and washed in cold diethyl ether and freeze-dried. Complete removal of Boc protecting group was confirmed by ^{1}H-NMR.

Yield: 92%. ^{1}H-NMR: δ_H (300 MHz, D_2O) 8.30-6.90 (1H initiator, 5H Das), 4.40-4.22 (1H αC PGA, 2H Das, 1H Val), 4.21-2.40 (10H Das), 2.39-1.66 (4H Glu PGA, 6H Das, 1H Val), 1.09-0.75 (6H Val).

2.4.2.6.3. Conjugation of Doxorubicin to St-PGA-hydrazide-Val-Das (St-PGA-hyd-Dox$_1$-Val-Das$_1$)

In a two-neck, round bottom flask fitted with a stir bar and an N_2 inlet and outlet, St-PGA-hydrazide-Val-Das (2.6 mmol, 1 equivalent) was dissolved in DMSO anh. Then, Dox (0.14 mmol, 0.054 equivalents) was added to the reaction. Then, three drops of pure acetic acid were added to the reaction, and it was left to proceed protected from light, under stirring at room temperature for 48 h. After that, the solvent was evaporated under high vacuum. The product was dissolved in DMF and purified by size exclusion chromatography with a Sephadex LH-20 column using DMF as eluent. The fractions containing the red-colored product were collected in a round bottom flask, and 3 mL of sodium bicarbonate 0.1 M were added before evaporating the solvent in the vacuum pump. To obtain the salt form of the polymer, MilliQ water and sodium bicarbonate were added. Size exclusion chromatography with a Sephadex G-25 column using MilliQ water as eluent was performed to eliminate the excess of salts. The fractions containing the red-colored polymer-drug product were collected and freeze-dried. Product identity was evaluated by ^{1}H-NMR. Drug loading was determined by UV-VIS spectroscopy (see *2.4.3.2.Drug Loading Determination by UV-VIS Spectroscopy*).

Yield: 71%. CE: 52%. ^{1}H-NMR: δ_H (300 MHz, D_2O) 8.44-6.90 (1H initiator, 5H Das, 3H Dox), 4.60-4.06 (1H αC PGA, 2H Das, 1H Val, 2H Dox),

4.05-2.64 (10H Das, 6H Dox), 2.63-1.50 (4H Glu PGA, 6H Das, 1H Val, 2H Dox), 1.09-0.70 (6H Val).

2.4.2.7. Synthesis of Star-poly(glutamic acid)-based Combination Conjugates with Doxorubicin and Dasatinib by Direct Ester Conjugation (St-PGA-hyd-Dox1-Das1 and St-PGA-hyd-Dox1-Das10)

2.4.2.7.1. Conjugation of Tert-butyl Carbazate Moiety (St-PGA-TBC)

The conjugation of TBC was performed as described earlier for St-PGA-hyd-Dox.

Yield: 55-95%. CE: 93%. ^{1}H-NMR: δ_H (300 MHz, D$_2$O) 8.31 (1H initiator), 4.46-4.25 (1H αC PGA), 2.55-1.76 (4H Glu PGA), 1.48 (9H Boc).

2.4.2.7.2. Conjugation of Dasatinib to St-PGA-TBC

In a round bottom flask fitted with a stir bar and an N$_2$ inlet and outlet, St-PGA-TBC (3.0 mmol, 1 equivalent) was dissolved in DMF anh. Once completely dissolved, DMAP (0.089 mmol, 0.030 equivalents) and EDC (0.44 mmol, 0.15 equivalents) were added to the reaction mixture, and it was left under stirring for 20 min. Then, Das (0.44 mmol, 0.15 equivalents) was added, and pH was adjusted to 8 with DIEA. The reaction was left to proceed at room temperature under stirring for 72 h. The product was precipitated and washed with cold diethyl ether, and dried. Then, the remaining EDC and DMAP were washed out with acidic water, and the polymer was freeze-dried. Product identity was evaluated by ^{1}H-NMR.

Yield: 95-99%. CE: 56-58%. ^{1}H-NMR: δ_H (300 MHz, D$_2$O) 8.81-6.80 (1H initiator, 5H Das), 4.50-4.10 (1H αC PGA, 2H Das), 4.09-2.46 (10H Das), 2.45-1.70 (4H Glu PGA, 6H Das), 1.48 (s, 9H).

2.4.2.7.3.   Deprotection of Tert-butyl Carbazate

In a round bottom flask fitted with a stir bar and a stopper, St-PGA-TBC-Das (2.8 mmol, 1 equivalent) was dissolved in TFA and left stirring for 45 min. Then, the product was precipitated and washed in cold diethyl ether and freeze-dried. Complete removal of Boc protecting group was confirmed by ^{1}H-NMR.

Yield: 62-96%. ^{1}H-NMR: δ_H (300 MHz, D$_2$O) 8.81-6.80 (1H initiator, 5H Das), 4.50-4.10 (1H αC PGA, 2H Das), 4.09-2.46 (10H Das), 2.45-1.70 (4H Glu PGA, 6H Das).

2.4.2.7.4.   Conjugation of Doxorubicin to St-PGA-hydrazide-Das

In a two-neck round bottom flask fitted with a stir bar and an N$_2$ inlet and outlet, St-PGA-hydrazide-Das (1.7 mmol, 1 equivalent) was dissolved in DMSO. Then, Dox (0.15 mmol, 0.084 equivalents) was added to the reaction. Then, three drops of pure acetic acid were added to the reaction, and it was left to proceed protected from light, under stirring at room temperature for 72 h. After that, the solvent was evaporated under high vacuum. The product was dissolved in DMF and purified by size exclusion chromatography with a Sephadex LH-20 column using DMF as eluent. The fractions containing the red-colored product were collected in a round bottom flask, and 3 mL of sodium bicarbonate 0.1 M was added before the evaporation of the solvent under high vacuum. To obtain the salt form of the polymer, MilliQ water was added. Size exclusion chromatography with a Sephadex G-25 column using MilliQ water as eluent was performed to eliminate the excess of salts. The fractions containing the red-colored polymer-drug product were freeze-dried. Product identity was evaluated by ^{1}H-NMR. Drug loading was determined by UV-VIS spectroscopy (see *2.4.3.2.Drug Loading Determination by UV-VIS Spectroscopy*).

St-PGA-hyd-Dox$_1$-Das$_1$. Yield: 50%. CE: 34%.^{1}H-NMR: δ_H (300 MHz, D$_2$O) 8.80-6.90 (1H initiator, 5H Das, 3H Dox), 4.60-4.01 (1H αC PGA, 2H Das, 2H Dox), 4.00-2.43 (10H Das, 6H Dox), 2.42-1.48 (4H Glu PGA, 6H Das, 2H Dox).

St-PGA-hyd-Dox$_1$-Das$_{10}$. Yield: 81%. CE: 60%. ^{1}H-NMR: δ_H (300 MHz, D$_2$O) 8.75-6.90 (1H initiator, 5H Das, 3H Dox), 4.60-4.05 (1H αC PGA, 2H Das, 2H Dox), 4.04-2.42 (10H Das, 6H Dox), 2.41-1.50 (4H Glu PGA, 6H Das, 2H Dox).

2.4.2.8. Synthesis of the Precursors with Free Hydrazides St-PGA-HYD and St-PGA-Das-HYD

2.4.2.8.1. St-PGA-HYD

The synthesis of St-PGA-TBC and the deprotection of the hydrazide moieties to yield St-PGA-HYD were performed as described in previous sections (see *2.4.2.5.Conjugation of Doxorubicin to Star-poly(glutamic acid) Through a Hydrazone Bond (St-PGA-hyd-Dox)*). To obtain the salt form of St-PGA-HYD, sodium bicarbonate with MilliQ water was added. Size exclusion chromatography with a Sephadex G-25 column using MilliQ water as eluent was performed to eliminate the excess of salts. The elution was monitored by TLC, and the fractions containing the product were freeze-dried to yield a white solid. The loading of hydrazide moieties was taken from the ^{1}H-NMR spectrum of the precursor St-PGA-TBC, comparing the signal of the Boc protecting group (1.50 ppm) with that of the α-carbon of PGA (4.33 ppm).

Yield: 89%. ^{1}H-NMR: δ_H (300 MHz, D$_2$O) 8.32 (1H initiator), 4.53-4.16 (1H αC PGA), 2.51-1.76 (4H Glu PGA).

2.4.2.8.2.   St-PGA-Das-HYD

The synthesis of St-PGA-TBC-Das and its deprotection to yield St-PGA-Das-HYD was performed as described in previous sections (see *2.4.2.7.Synthesis of Star-poly(glutamic acid)-based Combination Conjugates with Doxorubicin and Dasatinib by Direct Ester Conjugation (St-PGA-hyd-Dox1-Das1 and St-PGA-hyd-Dox1-Das10)*). After deprotection, St-PGA-Das-HYD was transformed to its salt form upon the addition of sodium bicarbonate and MilliQ water. Size exclusion chromatography with a Sephadex G-25 column using MilliQ water as eluent was performed to eliminate the excess of salts. The elution was monitored by TLC (MeOH, R_f: 0.7), and the fractions containing only the product without free drug were freeze-dried to yield a white solid. Complete removal of Boc protecting group was confirmed by ^{1}H-NMR. Das loading was determined by UV-VIS spectroscopy (see *2.4.3.2.Drug Loading Determination by UV-VIS Spectroscopy*).

Yield: 50%. CE: 82%. ^{1}H-NMR: δ_H (300 MHz, D_2O) 8.55-6.84 (1H initiator, 5H Das), 4.59-4.05 (1H αC PGA, 2H Das), 4.04-2.51 (10H Das), 2.50-1.48 (4H Glu PGA, 6H Das).

2.4.3. Characterization Techniques

2.4.3.1.   NMR Spectroscopy

^{1}H-NMR spectra were recorded on a 300 Ultrashield™ from Bruker (Billerica MA, USA) at 27 ºC and a frequency of 300 MHz and analyzed using the MestreNova 6.2 software (Mestrelab Research S.L., Santiago de Compostela, Spain).

2.4.3.2.   Drug Loading Determination by UV-VIS Spectroscopy

Drug loading was determined by UV-VIS spectroscopy. Calibration curves of the free drugs were prepared in DMSO:water (1:1 v/v) per triplicate. The absorbance spectrum of each sample was obtained with three accumulations. For Das, absorbance at 324 nm was plotted versus drug concentration to obtain the calibration curve. For Dox, two calibration curves were obtained, one at 480 nm and a second one at 324 nm. To determine the drug loading of the conjugates, the compounds were dissolved in the same solvent, and absorbance spectra were acquired using the same parameters. For single-drug conjugates, drug loading (in weight percent -% wt) was obtained by interpolating the absorbance value at 324 or 480 nm in the corresponding calibration curve. Dox loading was determined for combination conjugates by interpolating the absorbance value at 480 nm in the Dox calibration curve. Then, Dox concentration in the sample was used to determine the contribution of Dox in the total absorbance of the sample at 324 nm using the calibration curve of Dox at said wavelength. The obtained value was subtracted to the total absorbance of the sample at 324 nm, obtaining the absorbance of Das alone. This value was interpolated in the Das calibration curve to obtain Das loading. Loading in mol percent (% mol) was obtained by iterative calculation from the value in% wt.

UV-VIS absorbance spectra were obtained using the JASCO V-630 spectrophotometer (Jasco International Co., Ltd, Hachioji, Tokyo, Japan) at 25 °C with 1.0 cm matched quartz cells with a spectral bandwidth of 1 nm recording three accumulations.

2.4.3.3. Size Determination by Dynamic Light Scattering (DLS)

The size of the compounds was determined by DLS. The measurements were performed at 25 °C using a Malvern ZetasizerNanoZS instrument (Malvern Panalytical Ltd, Malvern, UK), equipped with a 532 nm laser at a fixed scattering angle of 173°, with acrylic cuvettes obtained from Sarstedt Inc. (Nümbrec, Germany). Solutions at 1, 0.5, and 0.1 mg/mL of

polymer were prepared in MilliQ water or DPBS, sonicated for 5 min, and left to stabilize overnight before the measurement.

2.4.3.4. Critical Aggregation Concentration (CAC) Determination by DLS

The CAC of St-PGA and St-PGA-based conjugates was determined by DLS. Samples of increasing polymer concentration (0.01 to 5 mg/mL) were prepared in MilliQ water and sonicated for 5 min. Samples were left to stabilize overnight. DLS measurements were done per duplicate with fixed parameters for all samples. Data were expressed as the mean count rate (MCR) versus the concentration (logarithmic scale). Data were separated into two linear fittings. CAC values were obtained graphically from the intersections of both fittings.

2.4.3.5. Zeta Potential Measurements

Zeta potential measurements were performed at 25 °C using a Malvern Zetasizer Nano ZS instrument (Malvern Panalytical Ltd, Malvern, UK), equipped with a 532 nm laser using Disposable folded capillary cells (DTS1070), provided by Malvern Instruments Ltd. (Worcestershire, UK). Polymer solutions (1 and 0.5 mg/mL) were prepared in KCl 1mM.

2.4.3.6. Circular Dichroism (CD)

CD Spectroscopy was performed with a J-1500 Circular Dichroism Spectropolarimeter (JASCO Corporation) using a Peltier thermostated cell holder (PTC-517, JASCO Corporation) with a recirculating cooler (CTU-100, JASCO Corporation) under nitrogen flow. Polymer solutions (0.5, 0.2, and 0.1 mg/mL) were prepared in MilliQ water and in DPBS. Measurements were

obtained in 0.1 cm matched quartz cells with a spectral bandwidth of 1 nm, recording three accumulations.

2.4.3.7. Size Exclusion Chromatography

Size exclusion chromatography (SEC) of the products was performed in a Postnova Analytics Modular SEC system (Postnova Analytics GmbH, Landsberg am Lech, Germany) equipped with a RI – Refractive Index Detector (PN3150 from Postnova Analytics GmbH), a UV-VIS detector (SPD-20A from Shimadzu Scientific Instruments, Kyoto, Japan), a fluorescence detector (RF-20A XS from Shimadzu Scientific Instruments, Kyoto, Japan), and a multi-angle light scattering (MALS) detector (PN3621 from Postnova Analytics GmbH). All the SEC studies were conducted using a TSK gel G3000PWXL column (5μm, 7.8 mm i.d. x 30 cm, Tosoh Corporation, Tokyo, Japan) with the same mobile phase (10 mM PB pH 7.4, 0.005% NaN_3) with a constant flow rate (0.5 mL/min). Samples were prepared with the mobile phase as a solvent at 2 mg/mL of compound. The volume of injection was 20 μL.

2.4.3.8. Drug Release Kinetics

2.4.3.8.1. pH-dependent Drug Release

The release kinetic of Dox and Das was studied in PBS buffer (10 mM phosphate buffer 150 mM NaCl) at pH 7.4, mimicking the bloodstream and healthy tissues, and at pH 5, mimicking the tumor and the lysosomal environment. The conjugates were dissolved at 2 mg/mL in each buffer and incubated at 37 ºC under stirring and covered from light. Starting from the complete dissolution of the conjugate, 100 μL aliquots were taken at fixed time points, and the free drug was extracted and analyzed as described below.

2.4.3.8.2. Liquid-liquid Extraction – PBS Buffers

The solvent and procedure for drug extraction were optimized for the simultaneous analysis of released Dox and Das in 10 mM PB 150 mM NaCl pH 7.4 and pH 5.0, and the percentage of recovery for each drug was determined. To this aim, solutions of St-PGA at 2 mg/mL with Dox and Das at 0.1 mg/mL in each buffer were prepared. Then, these solutions were diluted to 0.025 and 0.012 mg/mL of drug in the corresponding buffer. The six solutions were used as samples for the recovery study. Thus, 100 µL of each sample were placed in 2 mL Eppendorf tubes. The aliquots from pH 5.0 solutions were neutralized by adding 6 µL of 0.2 M NaOH. Then, 1 mL of chloroform:isopropanol 7:3 (v/v) was added to each tube. To extract the drugs, the samples were vortexed for 30 seconds, left for phase separation, and vortexed again for 30 seconds. Finally, the phases were separated by centrifugation (3200 g, 5 min). The aqueous phase was carefully removed with a pipette, and the organic phase was dried in a SpeedVac concentrator (SPD131DDA with an OFP400 vacuum pump and an RVT5105 refrigerated vapor trap, all from Thermo Fisher GmbH, Kandel, Germany). The dried samples were reconstituted with 300 µL of methanol (HPLC grade) and analyzed as described in *2.4.3.8.5.HPLC Method for Simultaneous Detection and Quantification of Dox and Das*.

2.4.3.8.3. Cathepsin B-mediated Drug Release

The release kinetics of Dox and Das in the presence of the peptidase cathepsin B was studied for selected conjugates. A buffer with 11.23 mM DTT and 4.5 mM disodium ethylenediaminetetraacetic acid (EDTA) in 40

mM sodium acetate was prepared and adjusted to pH 5 with NaOH/acetic acid to provide the enzyme with an adequate environment. For each conjugate, a 2 mL Eppendorf tube was prepared with 800 µL of said buffer and 100 µL of 20 mM sodium acetate. Then, 800 µL of a solution of the conjugate in MilliQ water at 4.5 mg/mL was added. Finally, 5U of cathepsin B in 20 mM sodium acetate were added in 100 µL, obtaining a final solution of 2 mg/mL of polymer, 5 mM DTT, 2 mM disodium EDTA, and 5U of cathepsin B in 20 mM sodium acetate. The samples were incubated at 37 ºC under stirring and covered from light. The addition of the enzyme marked the beginning of the experiment (time 0). Then, at fixed time points, 100 µL aliquots were taken, and the free drug was extracted and analyzed as described below.

2.4.3.8.4. Liquid-liquid Extraction – Cathepsin B Buffer

The procedure for drug extraction was optimized for the cathepsin B mediated drug release studies to analyze Dox and Das release simultaneously, and the percentage of recovery for each drug was determined. To this aim, a solution with 0.4 mg/mL of Dox and Das in 20 mM sodium acetate was prepared. St-PGA was dissolved at 4 mg/mL with this solution. Then, 600 µL of the solution with polymer and drugs was mixed with 600 µL of 10 mM DTT 4 mM disodium EDTA in 20 mM sodium acetate, obtaining a final solution with 2 mg/mL St-PGA, 0.2 mg/mL Dox, 0.2 mg/mL Das, 5 mM DTT, and 2 mM disodium EDTA in 20 mM sodium acetate at pH 5.0, which was used to evaluate drug recovery. 100 µL aliquots of the solution were placed in 2 mL Eppendorf tubes and neutralized by adding 6 µL of 0.2 M NaOH. Then, 0.5 mL of chloroform:isopropanol 7:3 (v/v) were added to each tube. To extract the drugs, the sample was vortexed for 30 seconds. Then, the phases were separated by centrifugation (3200 g, 5 min), the aqueous phase was transferred to a new tube, and the extraction process was repeated with 0.5 mL of fresh solvent. Finally, the organic

phases of both extractions were merged and dried in a SpeedVac concentrator. The dried samples were reconstituted with 300 µL of methanol (HPLC grade) and analyzed as described in *2.4.3.8.5.HPLC Method for Simultaneous Detection and Quantification of Dox and Das.*

2.4.3.8.5. HPLC Method for Simultaneous Detection and Quantification of Dox and Das

The samples were analyzed by reverse-phase high-performance liquid chromatography (RP-HPLC) using a Waters e2695 separation module equipped with a Waters 2998 photodiode array detector (PDA) and a Waters 2475 multi λ fluorescence detector. Chromatographic separation of the drugs was achieved using a LiChrospher 100 RP18 column (125 x 4.0 mm, 5 µm) and a mixture of acetonitrile and buffer in proportion 35:65 (v/v) as mobile phase at a flow rate of 0.75 mL/min. The buffer was 10 mM ammonium acetate with 0.15% TEA adjusted to pH 3.5 with acetic acid. The volume of injection was 20 µL. Dox was detected by fluorescence (λ_{exc} = 480 nm, λ_{em} = 565 nm), as well as Das (λ_{exc} = 340 nm, λ_{em} = 373 nm). Dox eluted at 3.0 min, while Das eluted at 4.8 min. Data acquisition was performed with Empower 2.0 software. Calibration curves were obtained using these chromatographic conditions. Samples containing both drugs at the same concentration in methanol (HPLC grade) were used for the calibration. The peaks for each drug were integrated, and the means obtained from three independent injections were adjusted to a linear equation in Microsoft Excel (Microsoft Corporation, Redmond, Washington, USA). Limit of detection (LOD) and limit of quantification (LOQ) for each drug and calibration curve were obtained using the following equations (106):

$$LOD = 3.3 \times \frac{SD}{m}$$

$$LOQ = 10 \times \frac{SD}{m}$$

Where SD is the standard deviation associated with the intercept, and m is the slope.

The peak area obtained for Dox and Das was interpolated in the calibration curves considering their limit of quantification to obtain the concentration of free drug in the sample. A correction factor was applied to the concentrations considering the mean drug recovery obtained for each drug in each buffer, i.e., 1.37 for Dox in pH 5.0 buffer, 1.28 for Dox in pH 7.4 buffer, 1.39 for Dox in cathepsin B release buffer, 1.14 for Das in pH 5.0 buffer, 1.20 for Das in pH 7.5 buffer, and 1.24 for Das in cathepsin B release buffer. The release percentage was calculated taking the drug loading of the conjugate as 100% of drug release.

The statistical analysis was performed by one-way ANOVA, followed by Tukey's test for comparisons between conjugates and release conditions in Prism software (GraphPad, La Jolla, California, USA). Comparisons between cathepsin B and pH 5.0 release were analyzed with an unpaired, two-tailed Student's t-test.

2.4.4. Biological Evaluation

2.4.4.1.   Cell Culture Conditions

The MDA-MB-231-Luc cell line was maintained in DMEM/F12 media supplemented with 10% inactivated fetal bovine serum (FBS) and 500 µg/mL of geneticin (Gibco, Waltham, MA) at 37 ºC and 5% CO_2. Media was replaced every 2-3 days. Cell passages were performed when the culture had reached 80% confluence.

2.4.4.2.   Mouse Strains

Immunodeficient non-obese diabetic NOD/SCID (NOD.CB17-*Prkdc^{scid}*/NCrHsd) and BALB/c (BALB/cOlaHsd) mice were purchased from

Envigo Laboratories Inc. (Spain) and maintained in a specific-pathogen-free facility, with controlled temperature and humidity, and using a 12-hour light-dark cycle. In all cases, food pellets and water were provided *ad-libitum* during the whole experiment.

2.4.4.3.   Ethical Considerations

Animal experiments were performed according to the European Communities Council Directive (86/609/ECC) guidelines and by the Spanish Royal Decree 1201/2005. All the experimental procedures were approved by the Institutional Animal Care and Use Committee (2015/VSC/PEA/00100) and accomplished by accredited and trained staff, meeting the animal care rules.

2.4.4.4.   Cell Viability Studies

MDA-MB-231-Luc cells were seeded in sterile 96-well microtitre plates at a density of 7500 cells per well. Plates were incubated for 24 h before treatment. Then, compounds (UV sterilized for 20 min) were dissolved in cell media to their solubility limit, and serial dilutions of that solution were added to the cells. After 72 h of incubation, 10 µL of MTS/PMS (20:1) were added to each well, and the cells were incubated for a further 3 h. The optical density of each well was measured at 490 nm using a CLARIOstar Plus plate reader (BMG Labtech GmbH, Ortenberg, Germany). The absorbance values were represented as the percentage of cell viability, taking as 100% the value of untreated control cells.

The data were fitted to a log(inhibitor) vs. response - variable slope non-linear model in Prism software (GraphPad, La Jolla, California, USA). IC50 values were determined by interpolation on the curve. The curves

obtained for different treatments were compared using the extra sum-of-squares F test.

2.4.4.5. *In vivo* Evaluation of Anti-tumor and Anti-metastatic Activity in MDA-MB-231-Luc Orthotopic Breast Tumor Animal Model

MDA-MB-231-Luc orthotopic breast tumors were induced via subdermal inoculation of 3×10^{6} MDA-MB-231-Luc cells suspended in 100 µl of Matrigel (20%) in the second left mammary fat pad of six-weeks-old NOD/SCID females under inhalatory anesthesia (3% isoflurane in 100% oxygen). Tumor growth was evaluated twice a week by using an electronic caliper to determine tumor volume. Considering a spheroidal tumor shape, tumor volume (V) was obtained using the following equation:

$$V = \frac{4}{3} \times \pi \times \left(\frac{h}{2} \times \frac{l}{2} \times \frac{w}{2} \right)$$

where h is tumor height, l is tumor length, and w is tumor width.

After fourteen days, when the tumor volume reached $0.1 \, cm^{3}$, treatments were injected through the tail vein twice per week. DPBS was injected as vehicle control. Tumor size and animal weight were monitored twice per week, and when the tumor of the vehicle control achieved the maximum size authorized ($1 \, cm^{3}$), animals were anesthetized and received a subdermal injection of 150 mg/kg D-luciferin 10 min before euthanasia with CO_2. Then, blood was collected by intracardiac puncture with heparinized syringes and the major organs, and the tumor were harvested. Lungs were analyzed ex vivo for bioluminescence using IVIS® technology. Images were acquired using automatic camera settings and bioluminescence data quantified with Living Image software (PerkinElmer, Japan) in terms of

photons per second. Data was relativized to the mean value of DPBS control.

The statistical analysis was performed by one-way ANOVA, followed by Tukey's test for comparisons between the experimental groups in Prism software (GraphPad, La Jolla, California, USA), except for body weight evaluation, where Dunnett's test was used after one-way ANOVA for comparisons with the DPBS group. The statistical analysis of the survival curves was performed by Log-rank test.

2.4.4.6. Study of the Interaction with Serum Proteins via AF4

2.4.4.6.1. Equipment

The AF4 analyses were performed on a Postnova Analytics GmbH (Landberg, Germany) AF2000 MultiFlow FFF system comprising a solvent organizer (PN7140), a solvent degasser (PN7520), two isocratic pumps for tip and focus flow (PN1130), a crossflow pump module (AF2000), an autosampler (PN5300), a channel oven (PN4020), and a separation channel fitted with a 350 µm spacer. The elution was monitored using a RI – Refractive Index Detector (PN3150 from Postnova Analytics GmbH), and a fluorescence detector (RF-20A XS from Shimadzu Scientific Instruments, Kyoto, Japan). The channel was fitted with regenerated cellulose (RC) or polyethersulfone (PES) Postnova AF2000 MF membranes of 5 kDa MWCO. The evaluation of the elugrams was performed using the AF2000 Control software, version 2.0.1.5 (Postnova Analytics GmbH).

2.4.4.6.2. Recovery Study

The recovery tests were conducted in 0.9% NaCl or DPBS with 0.005% NaN_3 injecting 100 µL of a solution 3 mg/mL of the St-PGA on its water-soluble sodium salt form dissolved in the correspondent eluent. Two

membranes were evaluated, a regenerated cellulose (RC) and a polyethersulfone (PES) membrane, with a 5 kDa MWCO. The RI peak area was recorded for different elution conditions for both membranes. The maximum theoretical area was obtained by conducting a Flow Injection Analysis (FIA), flushing the sample in the channel, at a detector flow rate of 0.5 mL/min and an injection flow of 0.5 mL/min, without any crossflow. To study the interaction of the sample with the membrane, the peak area obtained after a Focus FIA was calculated. The Focus FIA consisted of a 3 minute-long focusing step, applying a focus flow of 1.8 mL/min, a crossflow of 1.5 mL/min, an injection flow of 0.2 mL/min, a detector flow rate of 0.5 mL/min, and a transition time of 1 min after which the crossflow was reduced to 0 mL/min. The recovery was then calculated using the following equation:

$$Recovery\ (\%) = \frac{A_{Focus\ FIA}}{A_{FIA}} \times 100$$

where $A_{Focus\ FIA}$ is the peak area obtained in the Focus FIA injection and A_{FIA} is the peak area obtained in the FIA injection, both obtained using the RI signal.

2.4.4.6.3.   AF4 Method

Serum protein separation was obtained via isocratic elution using DPBS 0.005% NaN_3 as eluent. The detector flow rate and crossflow were maintained at 0.5 mL/min and 3.0 mL/min, respectively. The focusing step had a duration of 4 min, in which the focusing flow was 3.3 mL/min, and the injection flow was 0.2 mL/min. After a transition time of 1 min, the crossflow was maintained at 3.0 mL/min for 50 min. Then, the crossflow was linearly reduced to 0.1 mL/min in 5 min and maintained for 25 min to allow the elution of large aggregates. The protocol finalized with a 5-minute rinsing step without crossflow.

2.4.4.6.4. Sample Preparation

St-PGA-hyd-Dox$_1$-Das$_{10}$ and St-PGA-hyd-Dox$_1$-Val-Das$_1$ were dissolved in DPBS at 6 mg/mL and filtered through 0.22 μm nylon filters. The polymer was diluted 1/2 with DPBS before injection in the AF4 system for control experiments.

Blood serum was obtained from BALB/c mice. The animals were euthanized with CO_2, and the blood was collected by intracardiac puncture with non-heparinized syringes. Immediately after collection, the blood was centrifuged for 10 min at 3000 rpm at 4 ºC. The supernatant (blood serum) was kept on ice until aliquoted and frozen. The aliquots were kept frozen at -20 ºC until the experiment.

For each experiment, a serum aliquot was defrosted and mixed with either one volume of DPBS (control experiment) or one volume of St-PGA-hyd-Dox$_1$-Das$_{10}$ or St-PGA-hyd-Dox$_1$-Val-Das$_1$ stock solution. The mixture was gently stirred and placed in a 300 μL glass vial (Chromacol, Thermo Fisher GmbH, Kandel, Germany) fitted with a screw cap with a PTFE septum (VWR International LLC, Radnor, PA, USA). The sample was incubated for 20 min at room temperature before injection in the AF4 system. The injection volume was 5 μL.

A solution of bovine serum albumin (BSA) at 5 mg/mL in DPBS was injected each day before the experiments to evaluate the performance of the membrane. The AF4 method was the same as the samples, and the injection volume was 20 μL.

The statistical analysis was performed by an unpaired, two-tailed Student's t-test in Prism software (GraphPad, La Jolla, California, USA)

2.4.4.7. Statistical Analysis and Data Representation

Unless otherwise specified, statistical analysis and data representation was performed in Prism software (GraphPad, La Jolla, California, USA). The data were expressed as mean ± standard error of the mean (SEM) unless otherwise specified. Detailed information accompanies each relevant figure.

2.5. Bibliography

1. Sung H, Ferlay J, Siegel RL, Laversanne M, Soerjomataram I, Jemal A, et al. Global Cancer Statistics 2020: GLOBOCAN Estimates of Incidence and Mortality Worldwide for 36 Cancers in 185 Countries. CA Cancer J Clin. 2021 May 4;71(3):209–49.

2. Waks AG, Winer EP. Breast Cancer Treatment. JAMA. 2019 Jan 22;321(3):288.

3. Sharma P. Biology and Management of Patients With Triple-Negative Breast Cancer. Oncologist. 2016;21(9):1050–62.

4. Prat A, Pineda E, Adamo B, Galván P, Fernández A, Gaba L, et al. Clinical implications of the intrinsic molecular subtypes of breast cancer. The Breast. 2015 Nov 1;24:S26–35.

5. Januškevičienė I, Petrikaitė V. Heterogeneity of breast cancer: The importance of interaction between different tumor cell populations. Life Sci. 2019 Dec 15;239:117009.

6. Tsang JYS, Tse GM. Molecular Classification of Breast Cancer. Adv Anat Pathol. 2020 Jan;27(1):27–35.

7. Dai X, Li T, Bai Z, Yang Y, Liu X, Zhan J, et al. Breast cancer intrinsic subtype classification, clinical use and future trends. Am J Cancer Res. 2015;5(10):2929–43.

8. Jitariu AA, Cimpean AM, Ribatti D, Raica M. Triple negative breast cancer: the kiss of death. Oncotarget. 2017;8(28):46652–62.

9. Denkert C, Liedtke C, Tutt A, von Minckwitz G. Molecular alterations in triple-negative breast cancer-the road to new treatment strategies. Lancet. 2017;389(10087):2430–42.

10. Zheng R, Han S, Duan C, Chen K, You Z, Jia J, et al. Role of Taxane and Anthracycline Combination Regimens in the Management of Advanced Breast Cancer. Medicine (Baltimore). 2015 May;94(17):e803.

11. Saif MW, Katirtzoglou NA, Syrigos KN. Capecitabine: an overview of the side effects and their management. Anticancer Drugs. 2008 Jun;19(5):447–64.

12. Lebert JM, Lester R, Powell E, Seal M, McCarthy J. Advances in the Systemic Treatment of Triple-Negative Breast Cancer. Curr Oncol. 2018 Jun 1;25(11):142–50.

13. Gadi VK, Davidson NE. Practical Approach to Triple-Negative Breast Cancer. J Oncol Pr. 2017;13(5):293–300.

14. Bianchini G, Balko JM, Mayer IA, Sanders ME, Gianni L. Triple-negative breast cancer: challenges and opportunities of a heterogeneous disease. Nat Rev Clin

Oncol. 2016;13(11):674–90.

15. Cardoso F, Harbeck N, Fallowfield L, Kyriakides S, Senkus E. Locally recurrent or metastatic breast cancer: ESMO Clinical Practice Guidelines for diagnosis, treatment and follow-up. Ann Oncol. 2012 Oct;23(SUPPL. 7):vii11–9.

16. Alven S, Nqoro X, Buyana B, Aderibigbe BA. Polymer-Drug Conjugate, a Potential Therapeutic to Combat Breast and Lung Cancer. Pharmaceutics. 2020 Apr 29;12(5):406.

17. Thakor P, Bhavana V, Sharma R, Srivastava S, Singh SB, Mehra NK. Polymer–drug conjugates: recent advances and future perspectives. Drug Discov Today. 2020 Sep;25(9):1718–26.

18. Ringsdorf H. STRUCTURE AND PROPERTIES OF PHARMACOLOGICALLY ACTIVE POLYMERS. In: J Polym Sci Polym Symp. 1975. p. 135–53.

19. Duro-Castano A, Conejos-Sanchez I, Vicent MJ. Peptide-Based Polymer Therapeutics. Polymers (Basel). 2014;6(2):515–51.

20. Duncan R. Polymer therapeutics at a crossroads? Finding the path for improved translation in the twenty-first century. J Drug Target. 2017 Nov 26;25(9–10):759–80.

21. Fang J, Islam W, Maeda H. Exploiting the dynamics of the EPR effect and strategies to improve the therapeutic effects of nanomedicines by using EPR effect enhancers. Adv Drug Deliv Rev. 2020 Jan 1;157:142–60.

22. Prat A, Perou CM. Deconstructing the molecular portraits of breast cancer. Mol Oncol. 2011 Feb;5(1):5–23.

23. Markman JL, Rekechenetskiy A, Holler E, Ljubimova JY. Nanomedicine therapeutic approaches to overcome cancer drug resistance. Adv Drug Deliv Rev. 2013 Nov;65(13–14):1866–79.

24. Kobayashi H, Turkbey B, Watanabe R, Choyke PL. Cancer Drug Delivery: Considerations in the Rational Design of Nanosized Bioconjugates. Bioconjug Chem. 2014 Dec 17;25(12):2093–100.

25. Theek B, Rizzo LY, Ehling J, Kiessling F, Lammers T. The theranostic path to personalized nanomedicine. Clin Transl Imaging. 2014 Feb 19;2(1):67–76.

26. Vicent MJ, Greco F, Nicholson RI, Paul A, Griffiths PC, Duncan R. Polymer therapeutics designed for a combination therapy of hormone-dependent cancer. Angew Chemie - Int Ed. 2005 Jun 27;44(26):4061–6.

27. Rasines Mazo A, Allison-Logan S, Karimi F, Chan NJ-A, Qiu W, Duan W, et al. Ring opening polymerization of α-amino acids: advances in synthesis, architecture and applications of polypeptides and their hybrids. Chem Soc Rev. 2020;49(14):4737–834.

28. Melnyk T, Đorđević S, Conejos-Sánchez I, Vicent MJ. Therapeutic potential of polypeptide-based conjugates: Rational design and analytical tools that can boost clinical translation. Adv Drug Deliv Rev. 2020 May;160:136–69.

29. Barz M, Duro-Castano A, Vicent MJ. A versatile post-polymerization modification method for polyglutamic acid: synthesis of orthogonal reactive polyglutamates and their use in "click chemistry." Polym Chem. 2013 Apr 24;4(10):2989.

30. Córdoba-David G, Duro-Castano A, Castelo-Branco RC, González-Guerrero C, Cannata P, Sanz AB, et al. Effective Nephroprotection Against Acute Kidney Injury with a Star-Shaped Polyglutamate-Curcuminoid Conjugate. Sci Rep. 2020 Dec 1;10(1):1–15.

31. Conejos-Sánchez I, Cardoso I, Oteo-Vives M, Romero-Sanz E, Paul A, Sauri AR, et al. Polymer-doxycycline conjugates as fibril disrupters: An approach towards the treatment of a rare amyloidotic disease. J Control Release. 2015 Jan 28;198:80–90.

32. Cuesta CM, Ibañez F, Lopez-Hidalgo R, Ureña J, Duro-Castano A, Armiñán A, et al. A targeted polypeptide-based nanoconjugate as a nanotherapeutic for alcohol-induced neuroinflammation. Nanomedicine Nanotechnology, Biol Med. 2021 Jun 1;34:102376.

33. Dolz-Pérez I, Sallam MA, Masiá E, Morelló-Bolumar D, Pérez del Caz MD, Graff P, et al. Polypeptide-corticosteroid conjugates as a topical treatment approach to psoriasis. J Control Release. 2020 Feb;318:210–22.

34. Arroyo-Crespo JJ, Armiñán A, Charbonnier D, Balzano-Nogueira L, Huertas-López F, Martí C, et al. Tumor microenvironment-targeted poly-L-glutamic acid-based combination conjugate for enhanced triple negative breast cancer treatment. Biomaterials. 2018 Dec;186:8–21.

35. Duro-Castano A, Lim NH, Tranchant I, Amoura M, Beau F, Wieland H, et al. In Vivo Imaging of MMP-13 Activity Using a Specific Polymer-FRET Peptide Conjugate Detects Early Osteoarthritis and Inhibitor Efficacy. Adv Funct Mater. 2018 Sep 12;28(37):1802738.

36. Cheah HY, Gallon E, Dumoulin F, Hoe SZ, Japundžić-Žigon N, Glumac S, et al. Near-Infrared Activatable Phthalocyanine-Poly-L-Glutamic Acid Conjugate: Enhanced in Vivo Safety and Antitumor Efficacy toward an Effective Photodynamic Cancer Therapy. Mol Pharm. 2018 Jul 2;15(7):2594–605.

37. Arroyo-Crespo JJ, Deladriere C, Nebot VJ, Charbonnier D, Masiá E, Paul A, et al. Anticancer Activity Driven by Drug Linker Modification in a Polyglutamic Acid-Based Combination-Drug Conjugate. Adv Funct Mater. 2018 May 16;28(22):1800931.

38. Duro-Castano A, Nebot VJ, Niño-Pariente A, Armiñán A, Arroyo-Crespo JJ, Paul A, et al. Capturing "Extraordinary" Soft-Assembled Charge-Like Polypeptides as a Strategy for Nanocarrier Design. Adv Mater. 2017 Oct;29(39):1702888.

39. Niño-Pariente A, Armiñán A, Reinhard S, Scholz C, Wagner E, Vicent MJ. Design of Poly- <scp>l</scp> -Glutamate-Based Complexes for pDNA Delivery. Macromol Biosci. 2017 Oct 1;17(10):1700029.

40. Kiew LV, Cheah HY, Voon SH, Gallon E, Movellan J, Ng KH, et al. Near-infrared activatable phthalocyanine-poly-L-glutamic acid conjugate: increased cellular uptake and light–dark toxicity ratio toward an effective photodynamic cancer therapy. Nanomedicine Nanotechnology, Biol Med. 2017 May 1;13(4):1447–58.

41. Arroyo Crespo JJ. Polymer-based combination conjugates for the treatment of triple negative breast cancer : From rational design to preclinical evaluation. University of Valencia; 2018.

42. Conejos-Sánchez I, Duro-Castano A, Birke A, Barz M, Vicent MJ. A controlled and versatile NCA polymerization method for the synthesis of polypeptides. Polym Chem. 2013;4(11):3182.

43. Duro-Castano A, England RM, Razola D, Romero E, Oteo-Vives M, Morcillo MA, et al. Well-defined star-shaped polyglutamates with improved pharmacokinetic profiles as excellent candidates for biomedical applications. Mol Pharm. 2015 Oct 5;12(10):3639–49.

44. Pichot CS, Hartig SM, Xia L, Arvanitis C, Monisvais D, Lee FY, et al. Dasatinib synergizes with doxorubicin to block growth, migration, and invasion of breast

cancer cells. Br J Cancer. 2009 Jul 9;101(1):38–47.

45. Tacar O, Sriamornsak P, Dass CR. Doxorubicin: an update on anticancer molecular action, toxicity and novel drug delivery systems. J Pharm Pharmacol. 2012 Dec 26;65(2):157–70.

46. Araujo J, Logothetis C. Dasatinib: A potent SRC inhibitor in clinical development for the treatment of solid tumors. Cancer Treat Rev. 2010 Oct;36(6):492–500.

47. Song Z, Han Z, Lv S, Chen C, Chen L, Yin L, et al. Synthetic polypeptides: from polymer design to supramolecular assembly and biomedical application. Chem Soc Rev. 2017;46(21):6570–99.

48. Mandal BM. Ring-Opening Polymerization and Ring-Opening Metathesis Polymerization. In: Fundamentals of Polymerization. WORLD SCIENTIFIC; 2013. p. 323–71.

49. Duro-Castano A. Well-defined polyglutamates as carriers for the treatment of neurodegenerative diseases. University of Valencia; 2015.

50. Kelly SM, Jess TJ, Price NC. How to study proteins by circular dichroism. Biochim Biophys Acta - Proteins Proteomics. 2005 Aug;1751(2):119–39.

51. Mochida Y, Cabral H, Miura Y, Albertini F, Fukushima S, Osada K, et al. Bundled Assembly of Helical Nanostructures in Polymeric Micelles Loaded with Platinum Drugs Enhancing Therapeutic Efficiency against Pancreatic Tumor. ACS Nano. 2014 Jul 22;8(7):6724–38.

52. Aujard-Catot J, Nguyen M, Bijani C, Pratviel G, Bonduelle C. Cd 2+ coordination: an efficient structuring switch for polypeptide polymers. Polym Chem. 2018;9(30):4100–7.

53. Electrophoretic Light Scattering. In: Particle Characterization: Light Scattering Methods. Dordrecht: Kluwer Academic Publishers; p. 289–343.

54. Manning GS, Ray J. Counterion Condensation Revisited. J Biomol Struct Dyn. 1998 Oct;16(2):461–76.

55. Hsu H-P, Lee E. Counterion condensation of a polyelectrolyte. Electrochem commun. 2012 Feb;15(1):59–62.

56. Muthukumar M. Ordinary-extraordinary transition in dynamics of solutions of charged macromolecules. Proc Natl Acad Sci U S A. 2016;113(45):12627–32.

57. Koltzenburg S, Maskos M, Nuyken O. Functional Polymers. In: Polymer Chemistry. Berlin, Heidelberg: Springer Berlin Heidelberg; 2017. p. 493–513.

58. Babick F. Dynamic light scattering (DLS). In: Characterization of Nanoparticles. Elsevier; 2020. p. 137–72.

59. Wong PT, Choi SK. Mechanisms of Drug Release in Nanotherapeutic Delivery Systems. Chem Rev. 2015 May 13;115(9):3388–432.

60. Seidi F, Jenjob R, Crespy D. Designing Smart Polymer Conjugates for Controlled Release of Payloads. Chem Rev. 2018 Apr 11;118(7):3965–4036.

61. Shaffer SA, Baker-Lee C, Kennedy J, Lai MS, de Vries P, Buhler K, et al. In vitro and in vivo metabolism of paclitaxel poliglumex: identification of metabolites and active proteases. Cancer Chemother Pharmacol. 2007 Mar 19;59(4):537–48.

62. Singer JW, Baker B, de Vries P, Kumar A, Shaffer S, Vawter E, et al. Poly-(L)-Glutamic Acid-Paclitaxel (CT-2103) [XYOTAXTM], a Biodegradable Polymeric Drug Conjugate. In: Advances in experimental medicine and biology. Adv Exp Med Biol; 2004. p. 81–99.

63. Markovsky E, Baabur-Cohen H, Satchi-Fainaro R. Anticancer polymeric nanomedicine bearing synergistic drug combination is superior to a mixture of individually-conjugated drugs. J Control Release. 2014 Aug 10;187:145–57.

64. Tsakos M, Schaffert ES, Clement LL, Villadsen NL, Poulsen TB. Ester coupling reactions – an enduring challenge in the chemical synthesis of bioactive natural products. Nat Prod Rep. 2015;32(4):605–32.

65. Montalbetti CAGN, Falque V. Amide bond formation and peptide coupling. Tetrahedron. 2005 Nov;61(46):10827–52.

66. Sonawane SJ, Kalhapure RS, Govender T. Hydrazone linkages in pH responsive drug delivery systems. Eur J Pharm Sci. 2017 Mar;99:45–65.

67. Kölmel DK, Kool ET. Oximes and Hydrazones in Bioconjugation: Mechanism and Catalysis. Chem Rev. 2017 Aug 9;117(15):10358–76.

68. Vogus DR, Evans MA, Pusuluri A, Barajas A, Zhang M, Krishnan V, et al. A hyaluronic acid conjugate engineered to synergistically and sequentially deliver gemcitabine and doxorubicin to treat triple negative breast cancer. J Control Release. 2017 Dec 10;267:191–202.

69. Etrych T, Jelínková M, Íhová B, Ulbrich K. New HPMA copolymers containing doxorubicin bound via pH-sensitive linkage: Synthesis and preliminary in vitro and in vivo biological properties. J Control Release. 2001 May 18;73(1):89–102.

70. Etrych T, Šubr V, Laga R, Říhová B, Ulbrich K. Polymer conjugates of doxorubicin bound through an amide and hydrazone bond: Impact of the carrier structure onto synergistic action in the treatment of solid tumours. Eur J Pharm Sci. 2014 Jul 16;58(1):1–12.

71. Vasey PA, Kaye SB, Morrison R, Twelves C, Wilson P, Duncan R, et al. Phase I clinical and pharmacokinetic study of PK1 [N-(2-hydroxypropyl)methacrylamide copolymer doxorubicin]: first member of a new class of chemotherapeutic agents-drug-polymer conjugates. Cancer Research Campaign Phase I/II Committee. Clin Cancer Res. 1999 Jan;5(1):83–94.

72. Thomson AH, Vasey PA, Murray LS, Cassidy J, Fraier D, Frigerio E, et al. Population pharmacokinetics in phase I drug development: a phase I study of PK1 in patients with solid tumours. Br J Cancer. 1999 Sep 13;81(1):99–107.

73. Seymour. Phase II studies of polymer-doxorubicin (PK1, FCE28068) in the treatment of breast, lung and colorectal cancer. Int J Oncol. 2009 May 7;34(6):1629–36.

74. Seymour LW, Ferry DR, Anderson D, Hesslewood S, Julyan PJ, Poyner R, et al. Hepatic Drug Targeting: Phase I Evaluation of Polymer-Bound Doxorubicin. J Clin Oncol. 2002 Mar 15;20(6):1668–76.

75. Etrych T, Strohalm J, Chytil P, Černoch P, Starovoytova L, Pechar M, et al. Biodegradable star HPMA polymer conjugates of doxorubicin for passive tumor targeting. Eur J Pharm Sci. 2011 Apr 18;42(5):527–39.

76. Heinrich AK, Lucas H, Schindler L, Chytil P, Etrych T, Mäder K, et al. Improved tumor-specific drug accumulation by polymer therapeutics with pH-sensitive drug release overcomes chemotherapy resistance. Mol Cancer Ther. 2016 May 1;15(5):998–1007.

77. Kostka L, Kotrchová L, Šubr V, Libánská A, Ferreira CA, Malátová I, et al. HPMA-based star polymer biomaterials with tuneable structure and biodegradability tailored for advanced drug delivery to solid tumours. Biomaterials. 2020 Mar 1;235:119728.

78. Zagorodko O, Arroyo-Crespo JJ, Nebot VJ, Vicent MJ. Polypeptide-Based Conjugates as Therapeutics: Opportunities and Challenges. Macromol Biosci. 2017 Jan;17(1):1600316.

79. Sun J, Liu Y, Chen Y, Zhao W, Zhai Q, Rathod S, et al. Doxorubicin delivered by a redox-responsive dasatinib-containing polymeric prodrug carrier for combination therapy. J Control Release. 2017 Jul;258:43–55.

80. Zhang P, Li J, Ghazwani M, Zhao W, Huang Y, Zhang X, et al. Effective co-delivery of doxorubicin and dasatinib using a PEG-Fmoc nanocarrier for combination cancer chemotherapy. Biomaterials. 2015 Oct 1;67:104–14.

81. Morawiak M, Stolarska M, Cieślak M, Urbanczyk-Lipkowska Z. Interactions of rationally designed small peptide dendrons functionalized with valine or sinapic acid with α-helix and β-sheet structures of poly-l-lysine and poly-l-glutamic acid. Pept Sci. 2020 May 6;112(3).

82. Nagasawa M, Holtzer A. The Helix-Coil Transition in Solutions of Polyglutamic Acid. J Am Chem Soc. 1964 Feb 1;86(4):538–43.

83. Nitta K, Yoneyama M, Ohno N. Polymer concentration dependence of the helix to random coil transition of a charged polypeptide in aqueous salt solution. Biophys Chem. 1975 Oct;3(4):323–9.

84. Koltzenburg S, Maskos M, Nuyken O. Polymer Chemistry. Polymer Chemistry. Berlin, Heidelberg: Springer Berlin Heidelberg; 2017. 1–584 p.

85. WOODY RW. Circular Dichroism of Peptides. In: Conformation in Biology and Drug Design. Elsevier; 1985. p. 15–114.

86. Berova N, Ellestad GA, Harada N. Characterization by Circular Dichroism Spectroscopy. In: Comprehensive Natural Products II. Elsevier; 2010. p. 91–146.

87. Duro-Castano A, Sousa-Herves A, Armiñán A, Charbonnier D, Arroyo-Crespo JJ, Wedepohl S, et al. Polyglutamic acid-based crosslinked doxorubicin nanogels as an anti-metastatic treatment for triple negative breast cancer. J Control Release. 2021 Apr;332:10–20.

88. Gallois L, Fiallo M, Garnier-Suillerot A. Comparison of the interaction of doxorubicin, daunorubicin, idarubicin and idarubicinol with large unilamellar vesicles circular dichroism study. Biochim Biophys Acta - Biomembr. 1998 Mar 6;1370(1):31–40.

89. Kabakov AE, Gabai VL. Cell Death and Survival Assays. In: Chaperones. 2018. p. 107–27.

90. Berridge M V., Herst PM, Tan AS. Tetrazolium dyes as tools in cell biology: New insights into their cellular reduction. In: Biotechnology Annual Review. 2005. p. 127–52.

91. Stockert JC, Horobin RW, Colombo LL, Blázquez-Castro A. Tetrazolium salts and formazan products in Cell Biology: Viability assessment, fluorescence imaging, and labeling perspectives. Acta Histochem. 2018 Apr;120(3):159–67.

92. Riss TL, Moravec RA, Niles AL, Duellman S, Benink HA, Worzella TJ, et al. Cell Viability Assays. Assay Guidance Manual. Eli Lilly & Company and the National Center for Advancing Translational Sciences; 2004.

93. Sebaugh JL. Guidelines for accurate EC50/IC50 estimation. Pharm Stat. 2011 Mar;10(2):128–34.

94. Fallahi-Sichani M, Honarnejad S, Heiser LM, Gray JW, Sorger PK. Metrics other than potency reveal systematic variation in responses to cancer drugs. Nat Chem Biol. 2013 Nov 8;9(11).

95.   Arroyo-Crespo JJ, Armiñán A, Charbonnier D, Deladriere C, Palomino-Schätzlein M, Lamas-Domingo R, et al. Characterization of triple-negative breast cancer preclinical models provides functional evidence of metastatic progression. Int J Cancer. 2019 Oct 15;145(8):2267–81.

96.   Huang Z, Yu P, Tang J. Characterization of Triple-Negative Breast Cancer MDA-MB-231 Cell Spheroid Model. Onco Targets Ther. 2020 Jun;Volume 13:5395–405.

97.   Cailleau R, Young R, Olivé M, Reeves WJ. Breast Tumor Cell Lines From Pleural Effusions2. JNCI J Natl Cancer Inst. 1974 Sep 1;53(3):661–74.

98.   Priego N, Zhu L, Monteiro C, Mulders M, Wasilewski D, Bindeman W, et al. STAT3 labels a subpopulation of reactive astrocytes required for brain metastasis article. Nat Med. 2018 Jul 1;24(7):1024–35.

99.   Zhu L, Yebra N, Retana D, Miarka L, Hernández-Encinas E, Blanco-Aparicio C, et al. A drug-screening platform based on organotypic cultures identifies vulnerabilities to prevent local relapse and treat established brain metastasis. bioRxiv. 2020 Oct 19;2020.10.16.329243.

100.   Mousavi E, Tavakolfar S, Almasirad A, Kooshafar Z, Dehghani S, Afsharinasab A, et al. In vitro and in vivo assessments of two novel hydrazide compounds against breast cancer as well as mammary tumor cells. Cancer Chemother Pharmacol. 2017 Jun 27;79(6):1195–203.

101.   Lee S-H, Griffiths JR. How and Why Are Cancers Acidic? Carbonic Anhydrase IX and the Homeostatic Control of Tumour Extracellular pH. Cancers (Basel). 2020 Jun 18;12(6):1616.

102.   Peppicelli S, Bianchini F, Calorini L. Extracellular acidity, a "reappreciated" trait of tumor environment driving malignancy: perspectives in diagnosis and therapy. Cancer Metastasis Rev. 2014 Sep 2;33(2–3):823–32.

103.   Zhao Y, Ren W, Zhong T, Zhang S, Huang D, Guo Y, et al. Tumor-specific pH-responsive peptide-modified pH-sensitive liposomes containing doxorubicin for enhancing glioma targeting and anti-tumor activity. J Control Release. 2016 Jan;222:56–66.

104.   Selby LI, Cortez-Jugo CM, Such GK, Johnston APR. Nanoescapology: progress toward understanding the endosomal escape of polymeric nanoparticles. WIREs Nanomedicine and Nanobiotechnology. 2017 Sep 3;9(5).

105.   Aggarwal N, Sloane BF. Cathepsin B: Multiple roles in cancer. PROTEOMICS - Clin Appl. 2014 Jun;8(5–6):427–37.

106.   ICH. ICH Topic Q2 (R1) Validation of Analytical Procedures : Text and Methodology. International Conference on Harmonization. 2005.

107.   Boix-Montesinos P, Soriano-Teruel PM, Armiñán A, Orzáez M, Vicent MJ. The past, present, and future of breast cancer models for nanomedicine development. Adv Drug Deliv Rev. 2021 Jun 1;173:306–30.

108.   Jing W, Guo X, Wang G, Bi Y, Han L, Zhu Q, et al. Breast cancer cells promote CD169+ macrophage-associated immunosuppression through JAK2-mediated PD-L1 upregulation on macrophages. Int Immunopharmacol. 2020 Jan;78:106012.

109.   Castro F, Pinto ML, Pereira CL, Serre K, Barbosa MA, Vermaelen K, et al. Chitosan/γ-PGA nanoparticles-based immunotherapy as adjuvant to radiotherapy in breast cancer. Biomaterials. 2020 Oct;257:120218.

110.   P.S R, Alvi SB, Begum N, Veeresh B, Rengan AK. Self-Assembled Fluorosome–Polydopamine Complex for Efficient Tumor Targeting and Commingled Photodynamic/Photothermal Therapy of Triple-Negative Breast Cancer.

Biomacromolecules. 2021 Sep 13;22(9):3926–40.

111. Roberts JG, Wisbey M, Leach KG, Baum M. Spleen size in patients with breast cancer. Br J Cancer. 1975 Feb;31(2):262–262.

112. Atkinson S, Andreu Z, Vicent M. Polymer Therapeutics: Biomarkers and New Approaches for Personalized Cancer Treatment. J Pers Med. 2018 Jan 23;8(1):6.

113. Hadjidemetriou M, Kostarelos K. Evolution of the nanoparticle corona. Nat Nanotechnol. 2017 Apr 6;12(4):288–90.

114. Berrecoso G, Crecente-Campo J, Alonso MJ. Unveiling the pitfalls of the protein corona of polymeric drug nanocarriers. Drug Deliv Transl Res 2020 103. 2020 Mar 9;10(3):730–50.

115. Nguyen VH, Lee B-J. Protein corona: a new approach for nanomedicine design. Int J Nanomedicine. 2017 Apr;Volume 12:3137–51.

116. Wagner M, Holzschuh S, Traeger A, Fahr A, Schubert US. Asymmetric Flow Field-Flow Fractionation in the Field of Nanomedicine. Anal Chem. 2014 Jun 3;86(11):5201–10.

117. Quattrini F, Berrecoso G, Crecente-Campo J, Alonso MJ. Asymmetric flow field-flow fractionation as a multifunctional technique for the characterization of polymeric nanocarriers. Drug Deliv Transl Res. 2021 Apr;11(2):373–95.

118. Weber C, Simon J, Mailänder V, Morsbach S, Landfester K. Preservation of the soft protein corona in distinct flow allows identification of weakly bound proteins. Acta Biomater. 2018 Aug;76:217–24.

119. Alberg I, Kramer S, Schinnerer M, Hu Q, Seidl C, Leps C, et al. Polymeric Nanoparticles with Neglectable Protein Corona. Small. 2020 May 6;16(18):1907574.

120. Alberg I, Kramer S, Leps C, Tenzer S, Zentel R. Effect of Core-Crosslinking on Protein Corona Formation on Polymeric Micelles. Macromol Biosci. 2021 Apr 4;21(4):2000414.

121. Madörin M, van Hoogevest P, Hilfiker R, Langwost B, Kresbach GM, Ehrat M, et al. Analysis of drug/plasma protein interactions by means of asymmetrical flow field-flow fractionation. Pharm Res. 1997 Dec;14(12):1706–12.

122. Leeman M, Choi J, Hansson S, Storm MU, Nilsson L. Proteins and antibodies in serum, plasma, and whole blood—size characterization using asymmetrical flow field-flow fractionation (AF4). Anal Bioanal Chem. 2018 Aug 29;410(20):4867–73.

123. Liu Y, Fens MHAM, Capomaccio RB, Mehn D, Scrivano L, Kok RJ, et al. Correlation between in vitro stability and pharmacokinetics of poly(ε-caprolactone)-based micelles loaded with a photosensitizer. J Control Release. 2020 Dec 10;328:942–51.

124. Kaminski ZJ, Kolesinska B, Kolesinska J, Sabatino G, Chelli M, Rovero P, et al. N-triazinylammonium tetrafluoroborates. A new generation of efficient coupling reagents useful for peptide synthesis. J Am Chem Soc. 2005;127(48):16912–20.

CHAPTER 3. A BOTTOM-UP SELF-ASSEMBLY STRATEGY FOR THE GENERATION OF OPTIMIZED COMBINATION CONJUGATES FOR BREAST CANCER TREATMENT

3.1. Introduction and Background

In the previous chapter, we described the potential of St-PGA as a drug delivery system suitable for the conjugation of drug combinations with different linkers and drug loadings. This research yielded a polypeptide-based combination conjugate with anti-tumor and anti-metastatic activity; however, the self-assembly capacity of St-PGA in a non-salty aqueous solution provides an exciting opportunity to further improve the design of St-PGA-based combination conjugates.

Ionic interactions drive St-PGA self-assembly into large spherical structures in non-salty aqueous solutions in a concentration-dependent manner (200 nm diameter for the self-assembled structure vs. 10 nm for the unimer) (1–4). According to the counterion condensation theory, polymers with low charge densities lead to a uniform distribution of counterions in solution; in contrast, an increase in charge density over a threshold value (dependent on the counterion) prompts electrostatic attraction and counterion binding to the polyelectrolyte backbone (counterion condensation) (2). This phenomenon occurs with highly-charged polyelectrolytes, such as DNA, RNA, polysaccharides (3,4), or St-PGA (1).

Counterion adsorption to a polyelectrolyte chain leads to the formation of a strong transient dipole. The proximity of a pair of parallel or antiparallel dipoles provides for an attractive interaction, which acts as a transient crosslinking point. The simultaneous appearance of several dipole-dipole pairings can then prompt the formation of microgel-like aggregates (a concentration-dependent phenomenon). The polypeptide then switches from displaying an "ordinary" behavior in solution (the polymer appears as individual isolated molecules) to an "extraordinary" behavior (the polymer appears as aggregates stabilized by dipole-dipole pairings), with the critical aggregation concentration (CAC) acting as a transition point. For concentrations above the CAC, aggregate number and size (number of polypeptide chains in the aggregate) increase with polymer concentration.

The extraordinary behavior disappears upon an increase in the solution's salt content, which prompts aggregate disruption (1,4).

Studies have employed various strategies to evaluate the highly dynamic and reversible nature of such "assemblies". Förster resonance energy transfer (FRET) and stochastic optical reconstruction microscopy (STORM) experiments previously revealed that St-PGA unimers labeled with the fluorophores Cyanine (Cy)3 and Cy5 co-assembled with St-PGA in an aqueous solution into spherical structures that contain both fluorophores (1). Furthermore, the mixture of two uniform solutions of pre-assembled St-PGA-Cy3 and St-PGA-Cy5 assemblies prompted a rapid dynamic exchange of unimers (within 2 min) to yield structures containing both fluorophores (1).

Considering this dynamic behavior, we hypothesized that single-drug St-PGA conjugates co-assemble comparably to St-PGA-Cy5/3. Therefore, we could generate optimized combination conjugates by combining two single drug St-PGA conjugates at a desired ratio. Using this strategy, altering the amount of each conjugate in the reaction mixture would allow precise control over drug loading/ratio.

While ionic interactions drive St-PGA conjugate self-assembly, they do not provide stability in biological media (e.g., blood) (1); therefore, the self-assembled nanosystem would require covalent stabilization to support their use as a drug-delivery system. Our group previously reported a protocol for the stabilization of St-PGA assemblies using copper-catalyzed azide-alkyne cycloaddition (CuAAC) (1). Resultant stabilized St-PGA-based nanosystems (St-PGA-Click) displayed longer plasma half-lives compared to the St-PGA unimer (1) - a desirable feature for nanomedicines, as longer circulation times increase tumor accumulation via the enhanced permeability and retention (EPR) effect (5). Importantly, St-PGA-Click also accumulated in the lymph nodes (1), which may allow the treatment of lymph node invasion during the early stages of breast cancer development (see section *1.1.5.Breast Cancer Metastasis* in *Chapter 1*).

Unfortunately, CuAAC employs conditions (72 h incubations at 60 ºC) that promote linker hydrolysis and/or drug degradation (1). The study of drug release kinetics from single-drug St-PGA conjugates (depicted in *Chapter 2*) provided evidence for the cleavage of hydrazone and ester bonds under much milder conditions, with > 40% drug release observed after 24 h in phosphate buffer saline (PBS) pH 7.4 at 37 ºC. Thus, we cannot employ CuAAC to stabilize St-PGA-drug assemblies, and, therefore, we require an alternative crosslinking strategy that provides for rapid stabilization of self-assembled nanosystems under milder conditions.

St-PGA's versatility allows the introduction of stimuli-responsive linkers for the conjugation of active agents (as seen in *Chapter 2*); encouragingly, we can also take advantage of this approach to introduce elements that support crosslinking (intermolecular bonding) of St-PGA molecules. The introduction of stimuli-responsive linkers as reversible stabilizing elements would endow self-assembled nanosystems with an extra level of control and specificity.

The controlled disassembly of nanosystems has exploited various tumor-specific stimuli, including pH (6–9) or enzyme activity (10,11); however, we aimed to exploit the higher reductive potential of cancer cells in this study (12,13). The glutathione (GSH) concentration determines the medium's reductive potential - while this lies in the millimolar range (0.5-10 mM) in the cytosol, the extracellular concentration of GSH is generally 1000 times less (2-20 µM in plasma) (14). While displaying some variability, studies have highlighted an increase in GSH levels in cancer cells; for instance, studies have associated metastasis with increased GSH levels (12,15). Therefore, applying redox-responsive linkers (e.g., disulfide bonds) may support the reversible stabilization of self-assembled nanosystems. Disulfide bonds have been previously employed for the reversible stabilization of self-assembled nanosystems (16), nanogels (17,18), hydrogels (19–21), polymeric micelles (22,23), and polymer brushes (24),

yielding stable architectures in low reductive media that disassembled upon an increase in GSH levels.

We hypothesized that stabilizing self-assembled St-PGA-drug conjugate nanosystems using intermolecular disulfide bonds could yield drug delivery systems that remain stable in the bloodstream but readily disassemble following internalization within the target tumor cell. We hoped that a responsiveness to strongly reducing microenvironments combined with pH-labile linkers for drug conjugation would allow for the generation of a multi-stimuli-responsive nanosystem that specifically promotes drug release within the cell and reduces unwanted systemic exposure.

With this aim in mind, we designed a bottom-up strategy to synthesize combination conjugates by self- and co-assembly of single drug St-PGA-based conjugates and then stabilize self-assembled structure via disulfide bonds (**Scheme 3.1**). The first step requires the modification of St-PGA with pyridyl dithiol cysteamine (PD) to allow subsequent crosslinking via disulfide bonds. By separately conjugating doxorubicin (Dox) and dasatinib (Das) to different St-PGA-PD polypeptide chains, we aimed to synthesize combination conjugates with the desired drug ratios by simply mixing both St-PGA-PD-drug conjugates in water and crosslinking through the addition of a reducing agent (**Scheme 3.1**). The application of pH-labile linkers for drug conjugation provides pH-responsivity (see *Chapter 2*). Overall, this strategy permits fine control over drug loading and drug ratio (which supports the synthesis of personalized therapies) and controlled drug release (which supports safety by reducing off-target effects).
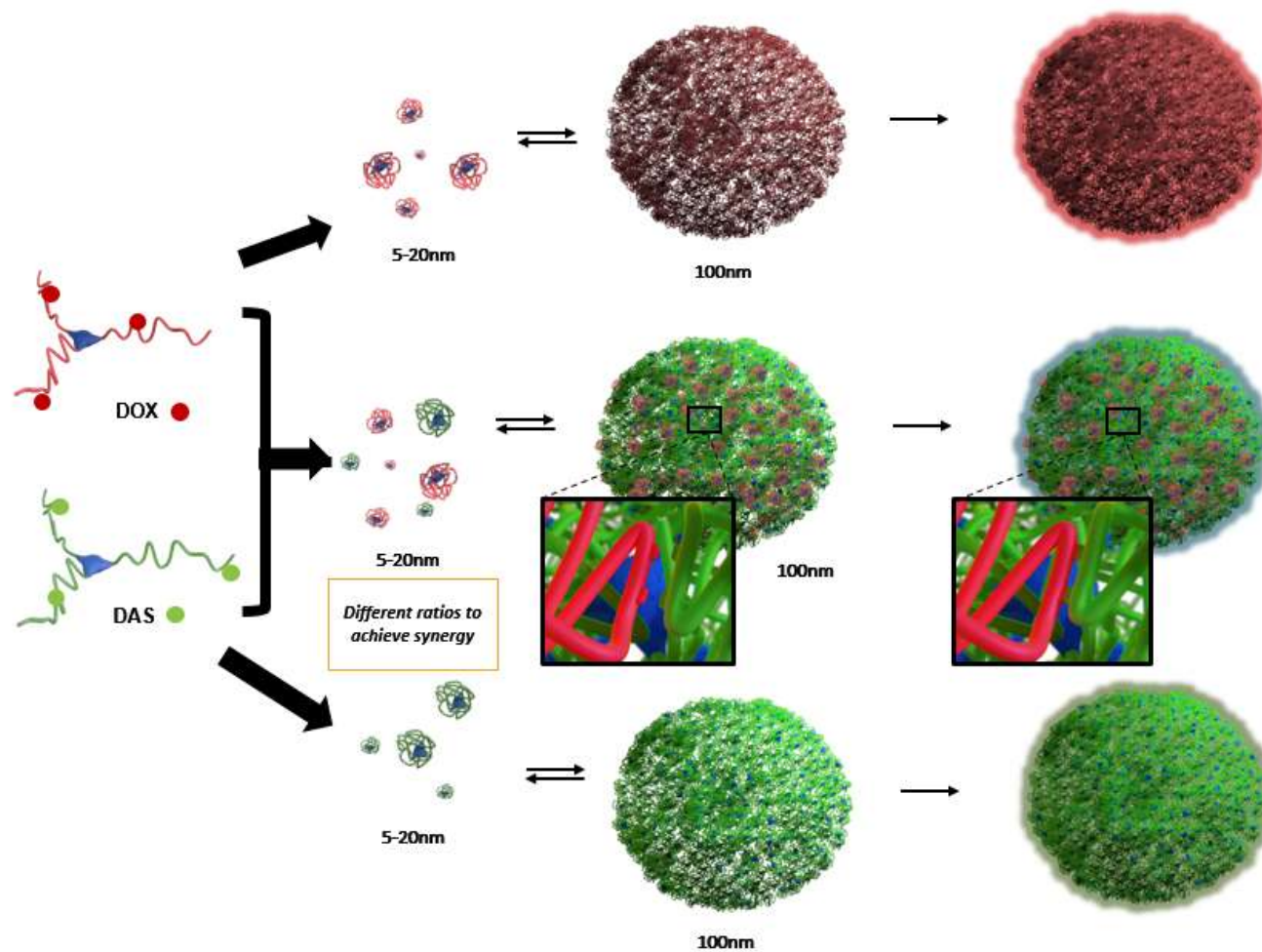
Scheme 3.1. The bottom-up strategy employed to synthesize combination conjugates via the self- and co-assembly of single drug St-PGA-based conjugates and stabilization via the incorporation of disulfide bonds.

3.2.   Results and Discussion

3.2.1.   Synthesis and Characterization of St-PGA-PD(5) y St-PGA-PD(10)

3.2.1.1.   Synthesis of St-PGA-PD(5) and St-PGA-PD(10)

We chose St-PGA modified with pyridyl dithiol cysteamine (PD) as a starting material to stabilize the assembled structures via disulfide bonds. As described in *Chapter 2*, we employed Dox and Das as the synergistic drug combination. We conjugated Dox via a pH-labile hydrazone bond and a non-stimuli-responsive amide bond linker for comparative purposes. We conjugated Das via a simple pH-labile ester bond as the valine spacer failed to provide significant advantages (see *Chapter 2*).

Stabilizing a nanosystem structure via disulfide bonds yields drug delivery systems that display stability in the weakly reducing (low GSH concentration) conditions of the blood but disassemble following cell uptake and exposure to the highly reducing intracellular environment (high GSH concentration). Thiol groups must be introduced in the polymer to allow stabilization, with several moieties allowing for this aim. We chose PD due to its multiple known advantages, including the high efficiency of the thiol-pyridyl disulfide exchange reaction since the pyridyl thione group is an excellent leaving group. This characteristic supports reactivity with almost any thiol-bearing compound and impedes thiol-disulfide exchange from the released group (**Scheme 3.2**) (25,26). Additionally, the reaction involves mild conditions suitable for crosslinking polymer-drug conjugates (25).
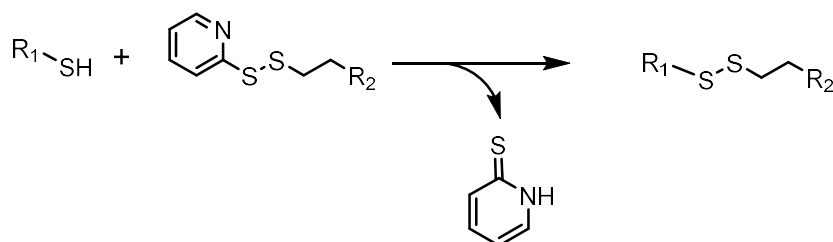
Scheme 3.2. General representation of the thiol-pyridyl disulfide exchange reaction.

We used St-PGA unimers as a starting material (171 glutamic acid units, 57 units per arm; synthesis and characterization described in *Chapter 2*). We conjugated PD to St-PGA through an amide bond by DMTMM chemistry in organic media (**Scheme 3.3**), aiming for 5 and 10% mol PD loadings (St-PGA-PD(5) and St-PGA-PD(10), respectively), as our previous unpublished studies revealed that higher loadings yielded products with very poor solubility in water or promoted gel formation. We obtained the salt forms of St-PGA-PD(5) and St-PGA-PD(10) for characterization purposes by adding sodium bicarbonate and subsequent desalting.
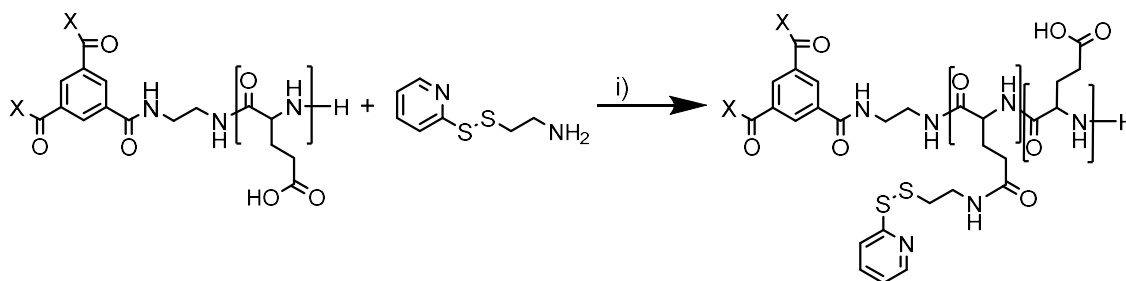
Scheme 3.3. Synthesis of St-PGA-PD(5) and St-PGA-PD(10). i) N,N'-dimethylformamide (DMF) anhydrous, 4-(4,6-dimethoxy-1,3,5-triazin-2-yl)-4-methylmorpholinium tetrafluoroborate salt (DMTMM BF$_4$), PD, N,N-diisopropylethylamine (DIEA), pH 8, 48 h.

We confirmed PD conjugation and determined the percentage of modification by ^{1}H-NMR by comparing the signals from the PD pyridyl group protons (two protons at 7.94-7.70 ppm and one proton at 7.38-7.18 ppm) to the PGA α-carbon proton (4.50-4.20 ppm). We obtained 5% mol of PD for St-PGA-PD(5) (**Figure 3.1A**) (100% conjugation efficacy – CE) and 8% mol for St-PGA-PD(10) (**Figure 3.1B**) (80% CE).
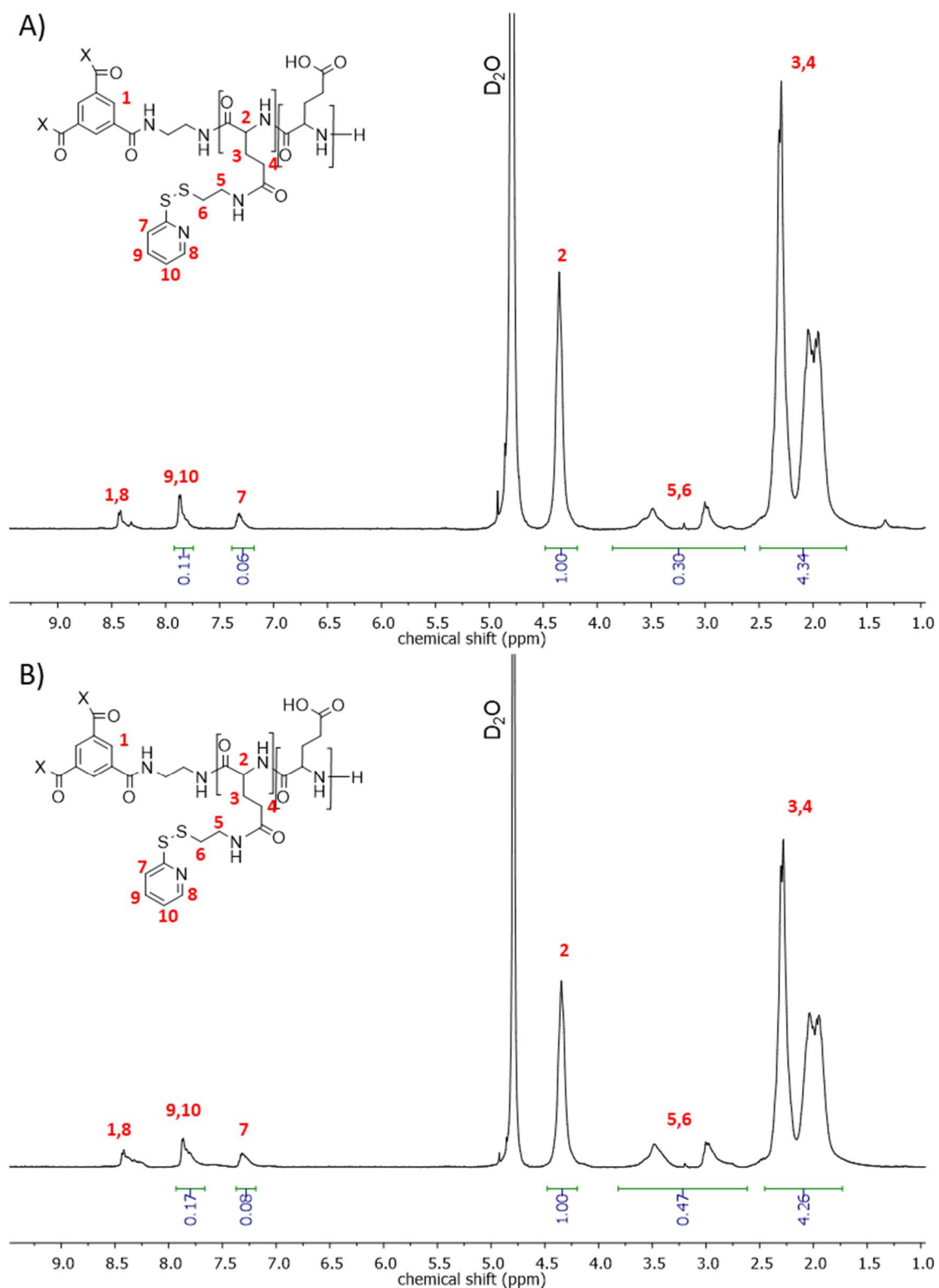
Figure 3.1. ^{1}H-NMR spectra (D$_2$O) of (**A**) St-PGA-PD(5) and (**B**) St-PGA-PD(10). The spectra confirm PD conjugation. Signals from the PD pyridyl group (7 – one proton, and 9+10 – two protons) and PGA α-carbon proton (2 – one proton) were used to calculate PD loading (% mol).

3.2.1.2. Physico-chemical characterization of St-PGA-PD(5) and St-PGA-PD(10)

Size exclusion chromatography (SEC) studies performed using 0.1 M NaNO₃, 0.005% NaN₃ as the mobile phase provided evidence for the single homogeneous molecular weight distribution of St-PGA-PD(5) and St-PGA-PD(10) as shown by the ultraviolet-visible (UV-VIS) absorbance ($\lambda = 250$ nm, **Figure 3.2A**) and refractive index (RI) detectors (**Figure 3.2B**), thereby suggesting a homogeneous distribution of PD content. We also identified the sodium counterion eluting at 17 min by RI (**Figure 3.2B**).
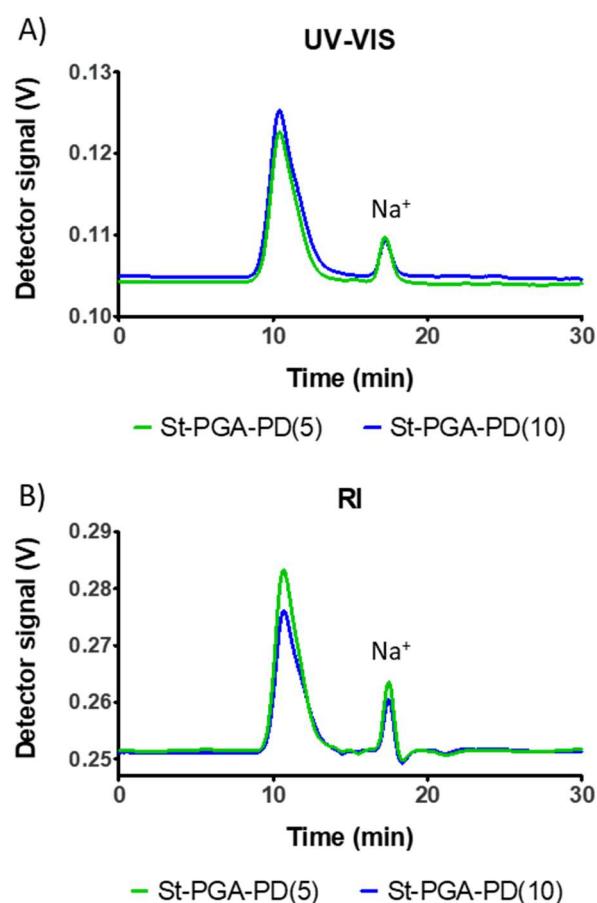
Figure 3.2. Representative SEC chromatograms of St-PGA-PD(5) (green) and St-PGA-PD(10) (blue). (**A**) UV-VIS absorbance detector at 250 nm. (**B**) RI detector. The peak at 17 min corresponds to the sodium counter-cation of PGA. Data obtained by injecting 30 µL of a 1 mg/mL polymer solution using NaNO₃ 0.1 M NaN₃ 0.005% as the mobile phase.

Circular dichroism (CD) analysis of St-PGA-PD(5) (**Figure 3.3A** and **B**) and St-PGA-PD(10) (**Figure 3.3C** and **D**) demonstrated a typical minimum at ~200 nm indicative of a random coil conformation in water and 10 mM phosphate buffer pH 7.4 (PB) at all concentrations evaluated. These findings indicate that 5 and 10% PD conjugation failed to significantly affect the secondary structure of the starting material as St-PGA exhibited a random coil profile in MilliQ water and DPBS (Dulbecco's phosphate-buffered saline) (see *Chapter 2*).
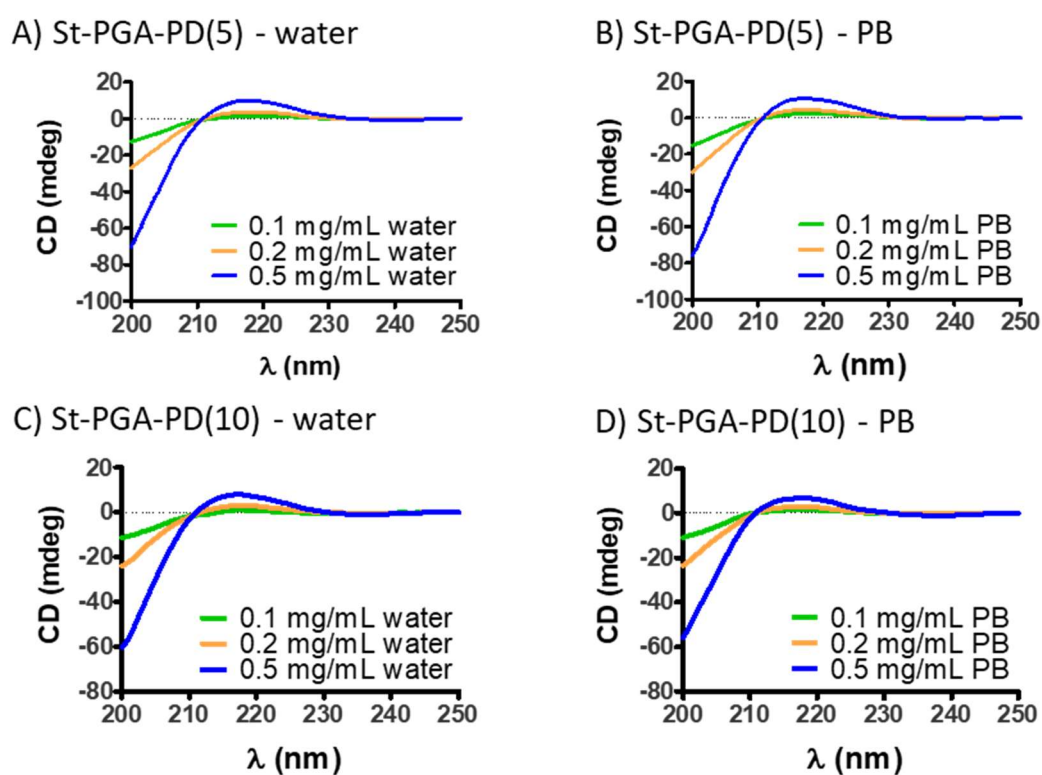
Figure 3.3. Secondary structure of (**A** and **B**) St-PGA-PD(5) in (**A**) MilliQ water and (**B**) PB 10 mM; and (**C** and **D**) St-PGA-PD(10) in (**C**) MilliQ water and (**D**) PB 10 mM. Data obtained by CD. Average results with three accumulated measurements displayed.

As expected for PGAs (27–29), St-PGA-PD(5) and St-PGA-PD(10) displayed negative zeta potential at all the concentrations evaluated (0.5 and 1 mg/mL) as determined by electrophoretic light scattering (ELS) (**Table 3.1**). As for the conjugates described in *Chapter 2*, zeta potential values did not significantly alter when increasing conjugate concentration, which

disagrees with previous results that demonstrated an increase in negative zeta potential with St-PGA concentration (i.e., upon formation of self-assembled structures) (1). Therefore, these data suggest a change in the assembly mechanism due to the incorporation of PD to St-PGA, which we will study in depth below.

Table 3.1. Summary of the characterization of St-PGA-PD(5) and St-PGA-PD(10).

	St-PGA-PD(5)	St-PGA-PD(10)
% mol PD[A]	5	8
Conjugation Efficacy (%)	100	80
Z-Pot$^{1mg/mL}$ (mV)	- 49 ± 2	- 49 ± 3
Z-Pot$^{0.5\ mg/mL}$ (mV)	-46 ± 2	-47 ± 3

(**A**) Obtained by ^{1}H-NMR. Z-pot: zeta potential. Z-Pot measured in in KCl 1 mM. Data expressed as mean ± SD of three measurements.

We assessed the size (hydrodynamic diameter) of St-PGA-PD(5) (**Figure 3.4**) and St-PGA-PD(10) (**Figure 3.5**) in MilliQ water and 10 mM PB at 0.5 and 1 mg/mL by dynamic light scattering (DLS). In water, St-PGA-PD(5) and St-PGA-PD(10) assembled into larger particles (> 80 nm) with St-PGA-PD(10) displaying larger sizes than St-PGA-PD(5). While size distribution by number for St-PGA-PD(5) remained similar at both concentrations (**Figure 3.4A**), St-PGA-PD(10) displayed a larger size at 0.5 mg/mL than at 1 mg/mL in water (**Figure 3.5A**). These findings run contrary to what was expected from the concentration-dependent self-assembly behavior of St-PGA in water, therefore suggesting the influence of PD in said behavior. Nevertheless, we found smaller sizes (by number) (~20 nm) when measuring St-PGA-PD(5) (**Figure 3.4B**) and St-PGA-PD(10) (**Figure 3.5B**) in 10 mM PB due to the media's ionic strength, which disrupts the self-assembly of St-PGA (1).
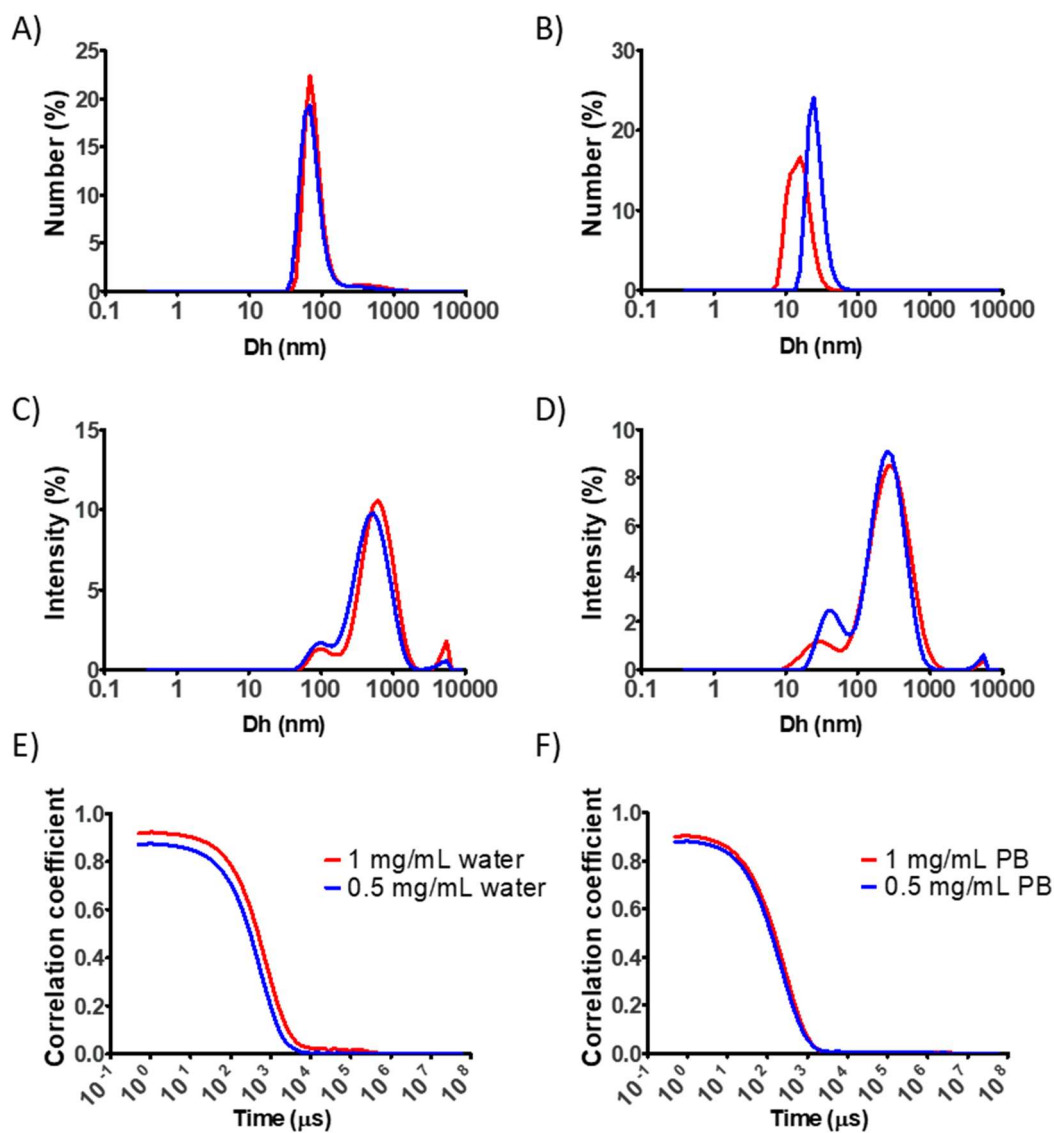
Figure 3.4. St-PGA-PD(5) size distribution obtained by DLS. The hydrodynamic diameter distribution by (**A** and **B**) number and (**C** and **D**) intensity and (**E** and **F**) the respective correlation functions are displayed. (**A**, **C**, and **E**) Samples prepared in MilliQ water. (**B**, **D**, and **F**) Samples prepared in 10 mM PB pH 7.4. Data obtained from the average result of at least three measurements.
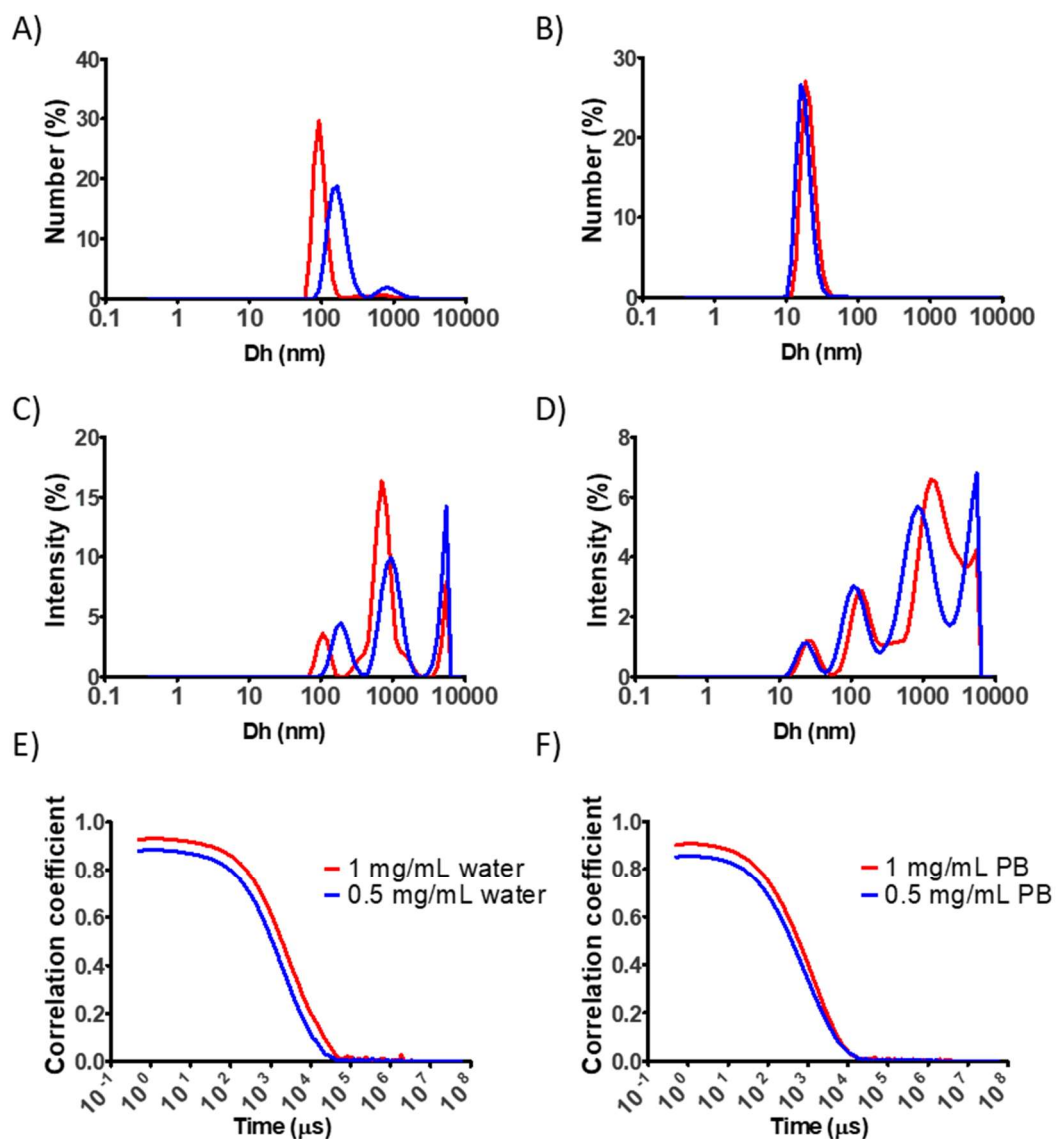
Figure 3.5. St-PGA-PD(10) size distribution obtained by DLS. The hydrodynamic diameter distribution by (**A** and **B**) number and (**C** and **D**) intensity and (**E** and **F**) the respective correlation functions are displayed. (**A**, **C**, and **E**) Samples prepared in MilliQ water. (**B**, **D**, and **F**) Samples prepared in 10 mM PB pH 7.4. Data obtained from the average result of at least three measurements.

Size measured by intensity revealed high heterogeneity for St-PGA-PD(10) in water, with up to three different populations (**Figure 3.5C**), while analysis of St-PGA-PD(5) produced two populations (**Figure 3.4C**). Interestingly, measurements of St-PGA-PD(5) and St-PGA-PD(10) by intensity (**Figure 3.4D** and **Figure 3.5D**) in 10 mM PB also depicted more than one population by size. These results suggest the coexistence of unimers (~20 nm) with a small number of large aggregates for St-PGA-PD(5) and St-PGA-PD(10) in both media and at all concentrations evaluated. The correlation functions reflected the overall quality of the measurements, with an intercept over 0.8 and below 1.0 and exponential decay (**Figure 3.4E** and **F**, and **Figure 3.5E** and **F**).

To further confirm the maintenance of St-PGA behavior after PD conjugation in aqueous solutions, we studied the evolution of the self-assembled structure's size in MilliQ water at different concentrations of polymer and salt (**Figure 3.6**). In agreement with the extraordinary behavior described for St-PGA in aqueous solution (4), the size of structures formed by St-PGA (**Figure 3.6A**) and St-PGA-PD(5) (**Figure 3.6B**) increased with polymer concentration in the absence of salt. St-PGA-PD(10) displayed similar behavior up to 5 mg/mL, where St-PGA-PD(10) possessed a mean hydrodynamic diameter of 145 nm (**Figure 3.6C**); however, St-PGA-PD(10) possessed a mean hydrodynamic diameter of 84 nm at 10 mg/mL (**Figure 3.6C**). The hydrophobic interactions introduced in St-PGA with PD may explain this finding. The hydrophobicity of PD provides hydrophilic polymers with the ability to form supramolecular amphiphilic nanosystems in aqueous media, allowing for the encapsulation of hydrophobic drugs (18). Therefore, we expect that the hydrophobic interactions of PD may prompt an alteration in the behavior of St-PGA in water.
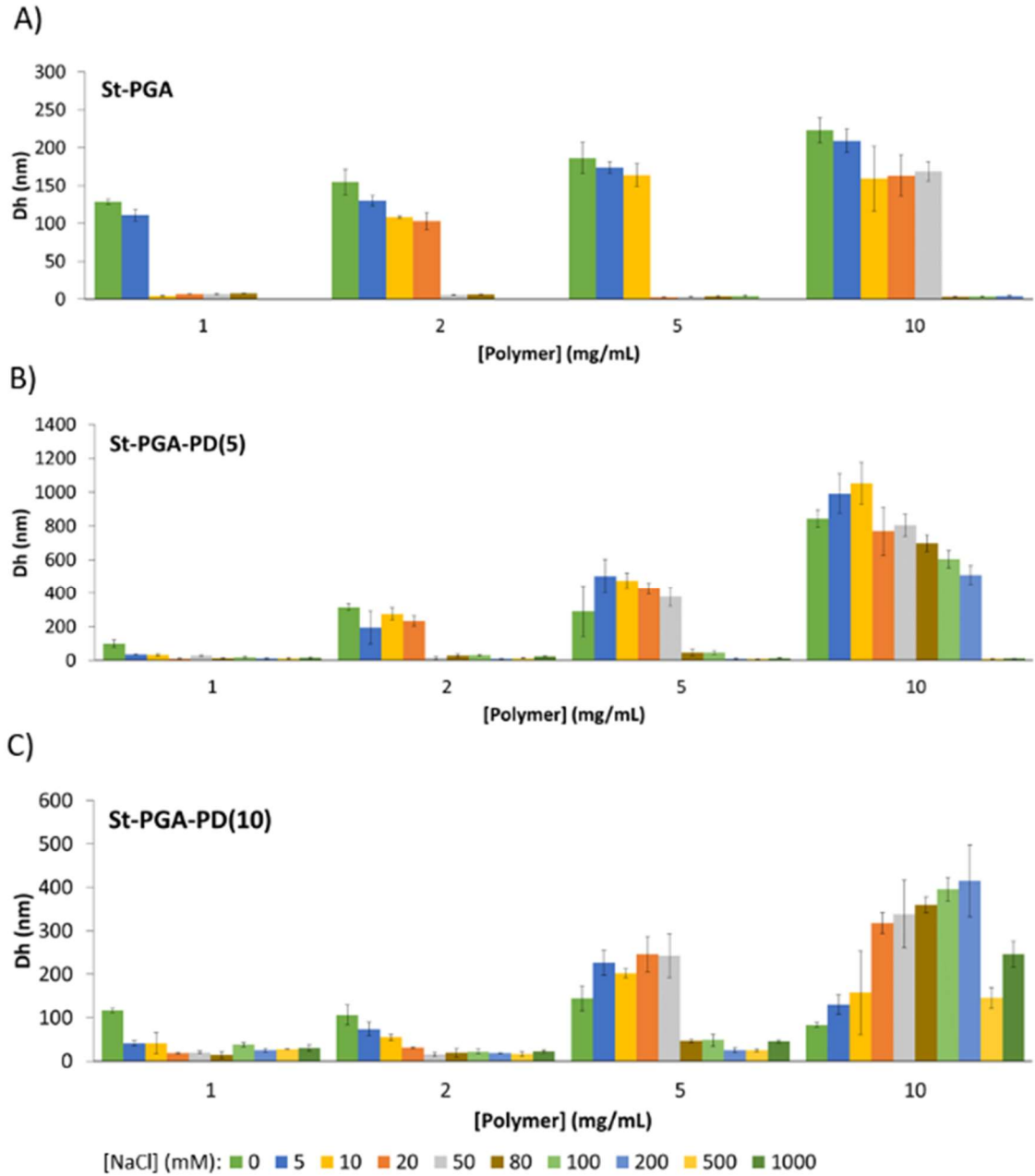
Figure 3.6. The evolution of assembled structure size for (**A**) St-PGA, (**B**) St-PGA-PD(5), and (**C**) St-PGA-PD(10) with increased ionic strength. Data obtained from at least three measurements by DLS and expressed as the mean hydrodynamic diameter by number ± SD.

For all polymers evaluated (St-PGA, St-PGA-PD(5), and St-PGA-PD(10)), solutions with a higher polymer concentration required higher amounts of NaCl to disrupt self-assembly (**Figure 3.6**); however, we failed to observe disassembly of St-PGA-PD(10) at 10 mg/mL (**Figure 3.6C**). Additionally, the size of St-PGA-PD(10) assemblies at 10 mg/mL appeared to increase with increasing ionic strength, suggesting a change in the supramolecular interactions that drive polymer aggregation at high concentrations.

Of note, this experiment demonstrates the disruption of a pre-assembled structure in water upon an increment of NaCl concentration after a minimum of 10 h of stabilization and not the size the nanosystem will display following the dissolution of St-PGA in a medium of a given NaCl concentration, where no pre-formed structures will be present and no interaction between molecules occurs before adding the salt.

The results of this exhaustive characterization suggest that St-PGA-PD(5) assembles into nanosystems displaying a concentration-dependent size in MilliQ water. Formed nanosystems disassemble after exposure to high ionic strength media, in agreement with the already reported behavior for St-PGA (1). The data obtained for St-PGA-PD(10) suggest that the hydrophobicity of PD interferes with the polymer's extraordinary behavior in an aqueous solution.

3.2.2. Synthesis and Characterization of St-PGA-PD-Doxorubicin Conjugates

3.2.2.1. Synthesis of St-PGA-PD(5)-Dox, St-PGA-PD(10)-Dox, and St-PGA-PD(5)-hyd-Dox

We chose two different linking moieties for the conjugation of Dox to St-PGA-PD(5) and St-PGA-PD(10) – an acid-sensitive hydrazone (hyd)

linker and a non-responsive amide linker (**Scheme 3.4**). We aimed for a 5% mol loading of Dox in all cases.
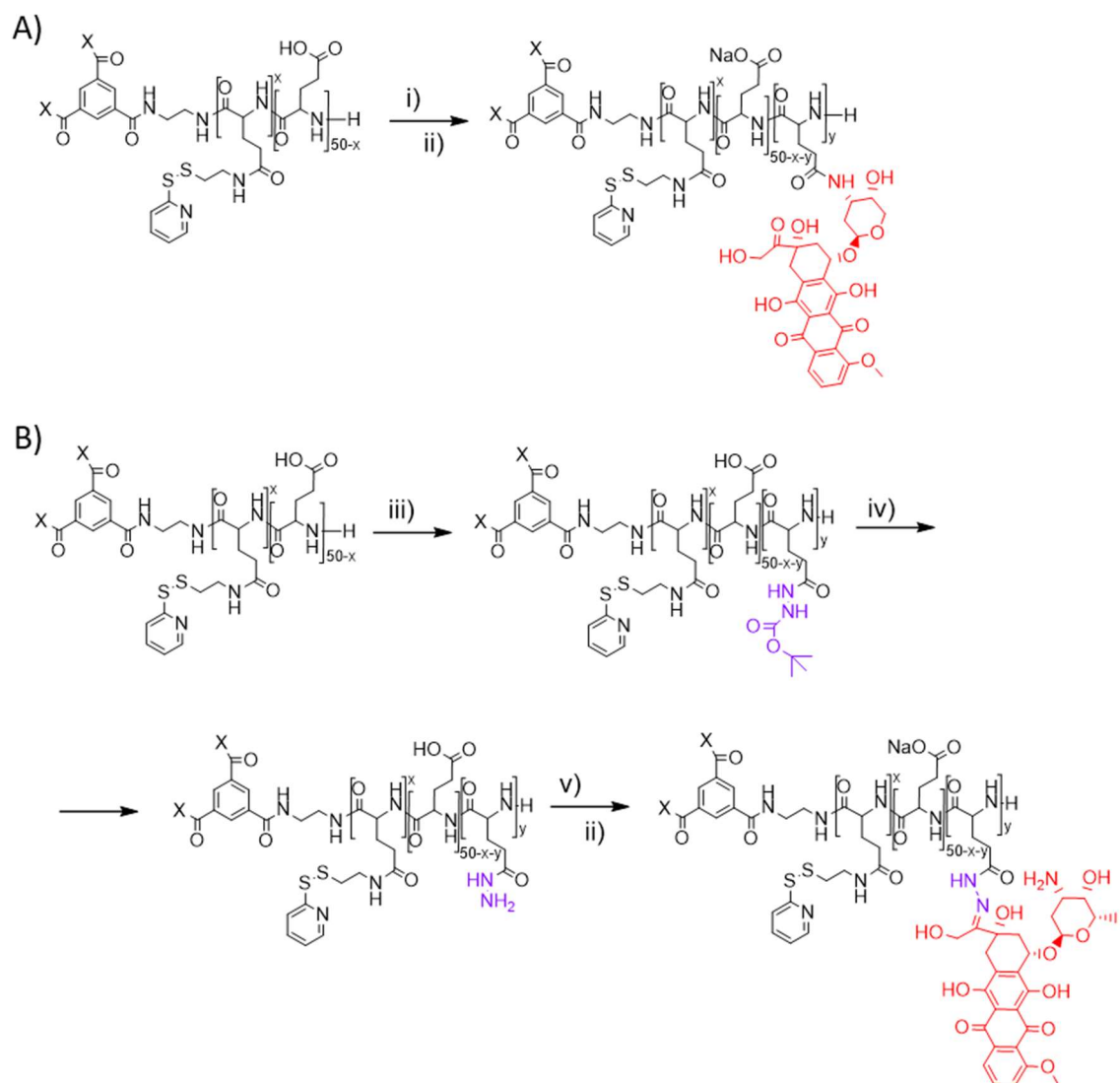
Scheme 3.4. (**A**) Synthesis of St-PGA-PD(5)-Dox and St-PGA-PD(10)-Dox. i) DMF anhydrous, DMTMM BF$_4$, Dox, DIEA, pH 8, 48 h. ii) sodium bicarbonate, MilliQ water. (**B**) Synthesis of St-PGA-PD(5)-hyd-Dox and St-PGA-PD(10)-hyd-Dox. iii) DMF anh., DMTMM BF$_4$, TBC, DIEA, pH 8, 48 h. iv) trifluoroacetic acid (TFA), 45 min. v) dimethylsulfoxide (DMSO) anh., Dox, acetic acid (catalytic). ii) sodium bicarbonate, MilliQ water.

Dox conjugation through a hydrazone linker requires the implementation of a three-step reaction, while amide bond conjugation employs a one-step reaction through DMTMM chemistry. While we successfully generated St-PGA-PD(5)-hyd-Dox, we failed in our attempts to conjugate tert-butyl carbazate (TBC) to St-PGA-PD(10) as the first step of hydrazone-mediated conjugation (TBC conjugation to St-PGA by DMTMM chemistry in organic media). We quantified TBC loading by ^{1}H-NMR by comparing Boc group signals (nine protons, 1.50 ppm) to the α-carbon proton signals of the St-PGA backbone (4.50-4.15 ppm) and obtained a value of 6% mol TBC for St-PGA-PD(5) (**Figure 3.7A**, 100% CE); however, we only achieved 1% mol of TBC in St-PGA-PD(10) (**Figure 3.7B**, 20% CE). We believe that this failure may derive from the low solubility of St-PGA-PD(10) in DMF and/or steric hindrance caused by the conjugated PD moiety.

We proceeded with St-PGA-PD(5)-TBC and deprotected TBC in TFA to expose the hydrazide moiety, obtaining St-PGA-PD(5)-HYD to allow Dox conjugation. After confirming the complete elimination of the Boc protecting group by ^{1}H-NMR (absence of Boc signal at 1.50 ppm, **Figure 3.8**), we conjugated Dox in DMSO with catalytic amounts of acetic acid to yield the final St-PGA-PD(5)-hyd-Dox conjugate.
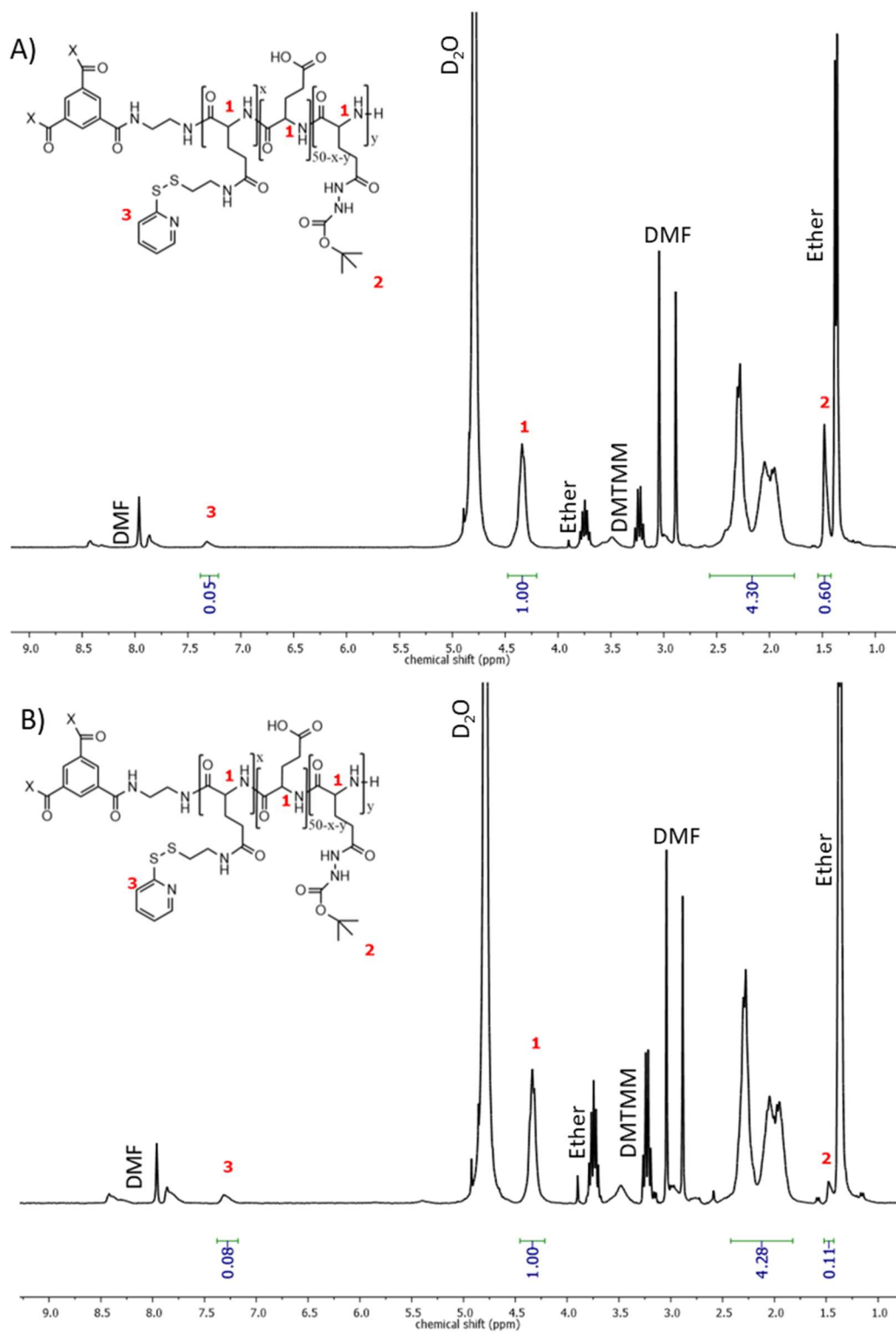
Figure 3.7. ^{1}H-NMR (D$_2$O) spectra of (**A**) St-PGA-PD(10)-TBC, and (**B**) St-PGA-PD(5)-TBC. The spectra confirm the conjugation of TBC (2 – nine protons) for St-PGA-PD(5)-TBC but not St-PGA-PD(10)-TBC.
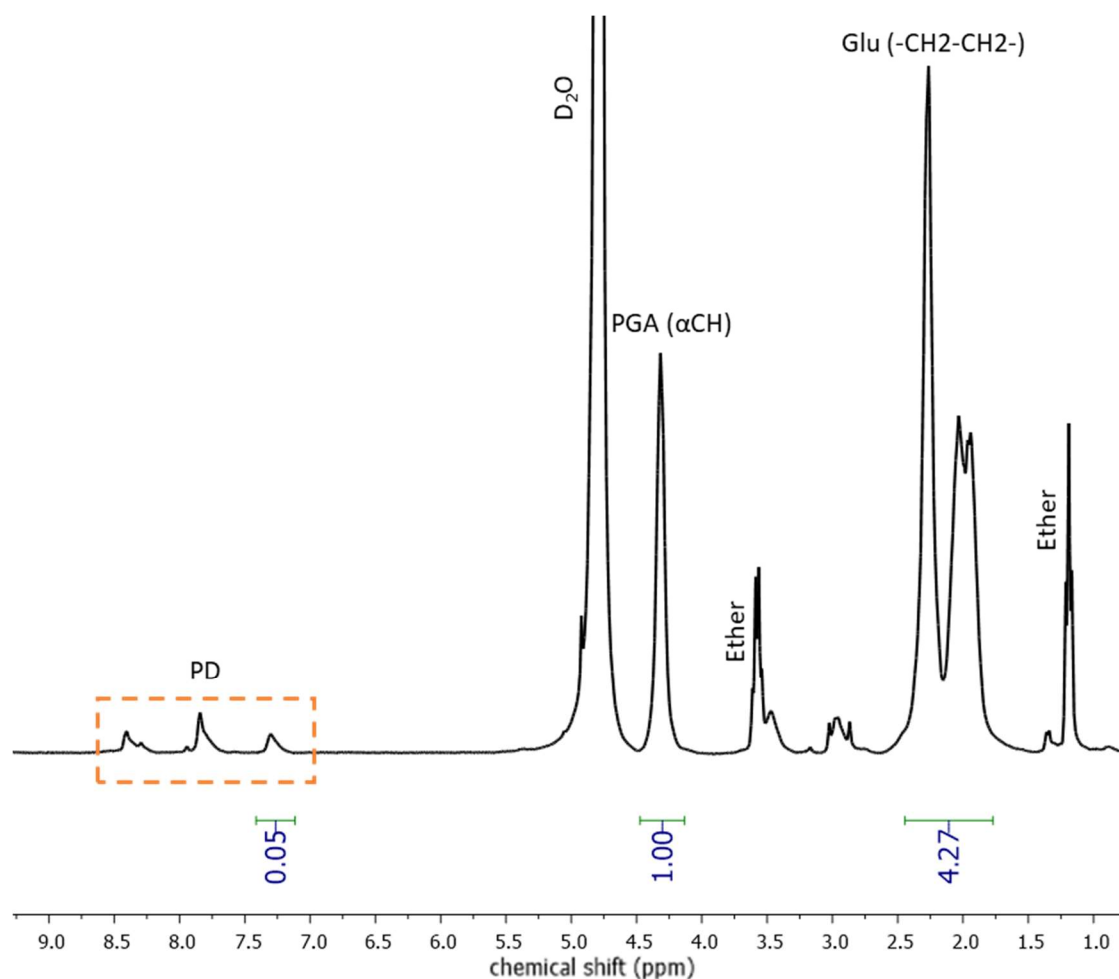
Figure 3.8. ^{1}H-NMR (D_2O) of St-PGA-PD(5)-HYD. The absence of the Boc signal at 1.5 ppm confirms complete deprotection of the hydrazide groups.

We also successfully generated St-PGA-PD(5)-Dox and St-PGA-PD(10)-Dox conjugates by direct conjugation through an amide bond. ^{1}H-NMR spectra confirmed the identity and purity of St-PGA-PD(5)-hyd-Dox, St-PGA-PD(5)-Dox, and St-PGA-PD(10)-Dox (**Figure 3.9A**). While we identified signals corresponding to Dox in the aromatic region (8.75-6.54 ppm) of the ^{1}H-NMR spectra, interference from PD-derived signals and a lack of peak definition impeded quantification of drug loading. Therefore, we confirmed Dox conjugation and drug loading by ultraviolet-visible (UV-VIS) spectroscopy (following the same protocol described in *Chapter 2*) (**Figure 3.9B**), obtaining high conjugation efficiencies for all three Dox conjugates. We determined 13.2% wt (4.35% mol, 87% CE) for St-PGA-PD(5)-Dox,

11.2% wt (3.74% mol, 75% CE) for St-PGA-PD(10)-Dox, and 13.7% wt (4.43% mol, 89% CE) for St-PGA-PD(5)-hyd-Dox.
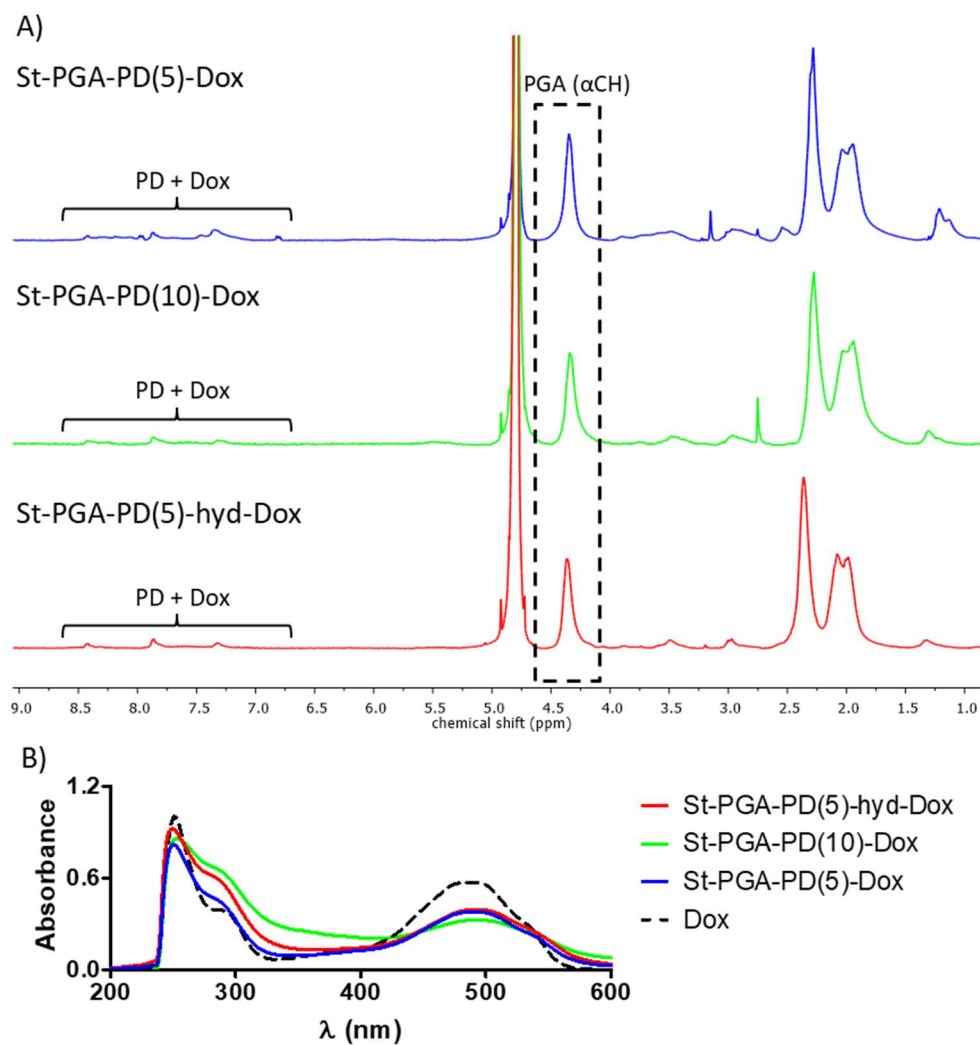
Figure 3.9. Identification of St-PGA-PD(5)-Dox, St-PGA-PD(5)-hyd-Dox, and St-PGA-PD(10)-Dox. (**A**) ^{1}H-NMR (D$_2$O) of St-PGA-PD(5)-Dox (blue), St-PGA-PD(10)-Dox (green), and St-PGA-PD(5)-hyd-Dox (red). Spectra confirm the conjugation of PD and Dox (broad signals in the aromatic region). (**B**) Absorbance spectra obtained for St-PGA-PD(5)-Dox (blue), St-PGA-PD(10)-Dox (green), and St-PGA-PD(5)-hyd-Dox (red) at 0.125 mg/mL and Dox at 0.025 mg/mL (black discontinuous line) in DMSO:water. The spectra show the peak of Dox absorbance at 480 nm in the conjugate samples.

3.2.2.2. Physico-chemical Characterization of St-PGA-PD(5)-Dox, St-PGA-PD(10)-Dox, and St-PGA-PD(5)-hyd-Dox

We next performed the exhaustive physico-chemical characterization of St-PGA-PD(5)-Dox, St-PGA-PD(10)-Dox, and St-PGA-PD(5)-hyd-Dox. SEC studies provided evidence for a single homogeneous molecular weight distribution by absorbance at 480 nm (maximum absorbance of Dox, (**Figure 3.10A**) and RI (**Figure 3.10B**), thereby suggesting a homogeneous distribution of Dox content. We also identified the sodium counterion eluting at 17 min by RI (**Figure 3.10B**).
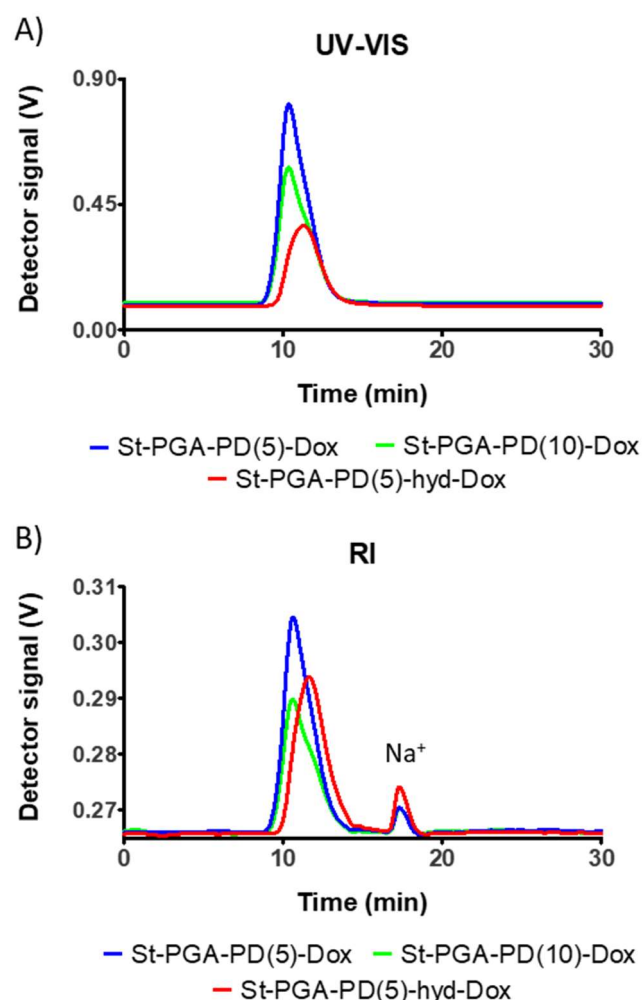
Figure 3.10. Representative SEC chromatograms of St-PGA-PD(5)-Dox (blue), St-PGA-PD(10)-Dox (green), and St-PGA-PD(5)-hyd-Dox (red). (**A**) UV-VIS absorbance detector at 480 nm. (**B**) RI detector. The peak at 17 min corresponds to the sodium counter-cation of PGA Data obtained by injecting 10 µL of a 5 mg/mL polymer solution using $NaNO_3$ 0.1 M NaN_3 0.005% as the mobile phase.

The evaluation of conjugate hydrodynamic diameter by DLS revealed larger sizes in MilliQ water than 10 mM PB in all cases (0.5 and 1 mg/mL) in the size distribution by number (**Figure 3.11A, D,** and **G**, and **Figure 3.12 A, D,** and **G**), in agreement with the data from the St-PGA-PD(5) and St-PGA-PD(10) precursors (see *3.2.1.2.Physico-chemical characterization of St-PGA-PD(5) and St-PGA-PD(10)*). Overall, the data suggest that 10 mM PB impedes the self-assembly of St-PGA-PD(5)-Dox and St-PGA-PD(10)-Dox as they displayed sizes consistent with the St-PGA unimer (20 - 9 nm, **Figure 3.12A** and **D**, and **Table 3.2**), thus agreeing with the behavior of their precursors (see *3.2.1.2.Physico-chemical characterization of St-PGA-PD(5) and St-PGA-PD(10)*). Nevertheless, we did not observe a comparable behavior for St-PGA-PD(5)-hyd-Dox, as the conjugate displayed sizes of 123 ± 29 nm at 1 mg/mL and 278 ± 108 nm at 0.5 mg/mL in 10 mM PB (**Figure 3.12G**, and **Table 3.2**). Thus, 10 mM PB does not impede the self-assembly of St-PGA-PD(5)-hyd-Dox.

Since we generated both St-PGA-PD(5)-derived compounds from the same precursor batch and they possess similar Dox loadings (4.35% mol for St-PGA-PD(5)-Dox and 4.43% mol for St-PGA-PD(5)-hyd-Dox), we attribute the different behavior in aqueous solutions to the use of alternate Dox linking chemistry. These data disagree with previously reported studies for linear PGA, where drug conjugation via an amide bond increased the conjugate's propensity to aggregate in PBS (which did not occur with more flexible linkers (e.g., glycine)) (27). In this study, the flexible linkers allowed the PGA backbone to dominantly influence solution structure; here, the effect of linker flexibility appears to induce an opposite effect, given that Dox conjugation via a hydrazone bond impedes the normal disassembly of St-PGA structures.
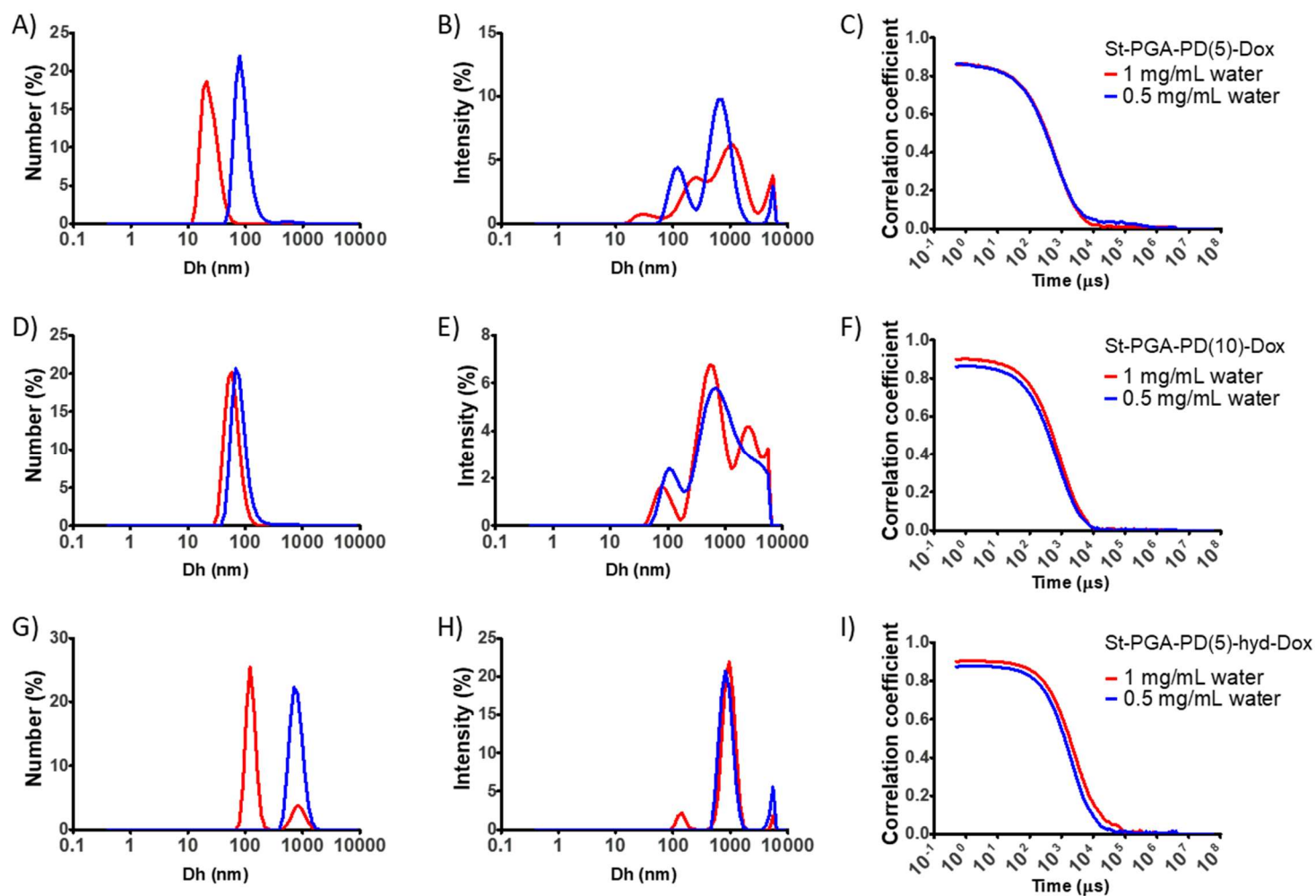
Figure 3.11. Size distribution of (**A-C**) St-PGA-PD(5)-Dox, (**D-F**) St-PGA-PD(10)-Dox, and (**G-I**) St-PGA-PD(5)-hyd-Dox obtained by DLS in MilliQ water. The hydrodynamic diameter distribution by number and intensity and the respective correlation functions are displayed. Data obtained from the average result of at least three measurements.
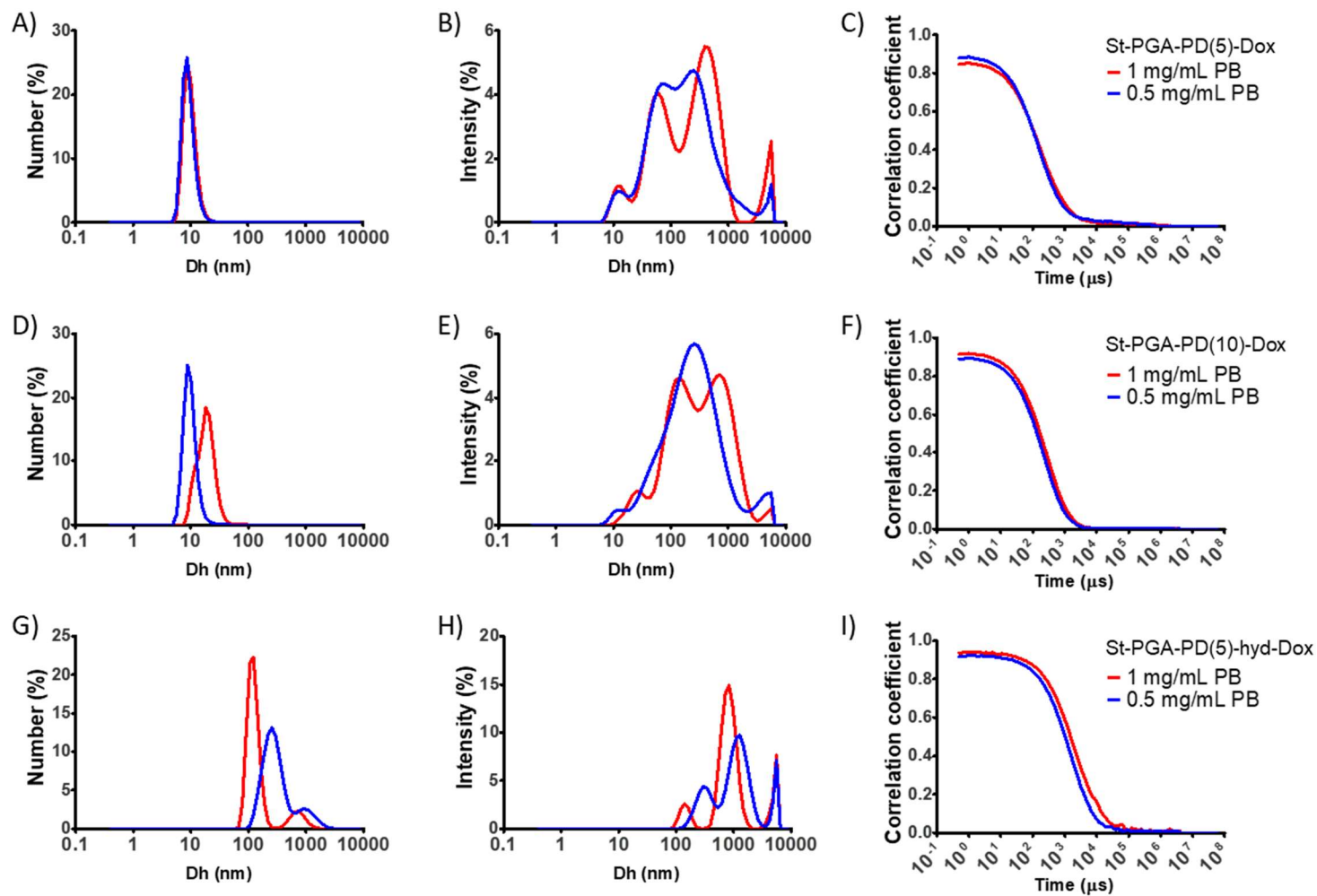
Figure 3.12. Size distribution of (**A-C**) St-PGA-PD(5)-Dox, (**D-F**) St-PGA-PD(10)-Dox, and (**G-I**) St-PGA-PD(5)-hyd-Dox obtained by DLS in 10mM PB. The hydrodynamic diameter distribution by number and intensity and the respective correlation functions are displayed. Data obtained from the average result of at least three measurements.

Table 3.2. Summary of synthesized St-PGA-PD-based Dox conjugates and their main physico-chemical characteristics.

	% wt[A]	% mol[B]	CE[C]	$Dh_{water}^{1\ mg/mL}$ (nm)	$Dh_{water}^{0.5\ mg/mL}$ (nm)	$Dh_{PB}^{1\ mg/mL}$ (nm)	$Dh_{PB}^{0.5\ mg/mL}$ (nm)	Z-Pot$^{1\ mg/mL}$ (mV)	Z-Pot$^{0.5\ mg/mL}$ (mV)
St-PGA-PD(5)-Dox(5)	13.2	4.35	87	25 ± 8	91 ± 30	10 ± 3	9 ± 3	-45 ± 3	-41 ± 5
St-PGA-PD(10)-Dox(5)	11.2	3.74	75	62 ± 19	92 ± 94	19 ± 7	10 ± 3	-51 ± 3	-45 ± 3
St-PGA-PD(5)-hyd-Dox(5)	13.7	4.43	89	127 ± 24	801 ± 209	123 ± 29	278 ± 108	-49 ± 1	-49 ± 1

(**A**) Obtained by UV-VIS spectroscopy. (**B**) Obtained by iterative calculation from the loading weight percent. (**C**) Conjugation efficacy. Dh = Hydrodynamic diameter. Z-Pot = zeta potential. Dh was obtained from the most abundant population in the size distribution by number in Figure 3.11 for water measurements and Figure 3.12 for PB measurements. Data displayed as mean ± SD. Z-Pot measured in in KCl 1 mM. Data expressed as mean ± SD of three measurements.

Furthermore, we expected to observe an increase in size with increasing conjugate concentration in water, as observed for St-PGA (**Figure 3.6A**); however, St-PGA-PD(5)-Dox, St-PGA-PD(10)-Dox, and St-PGA-PD(5)-hyd-Dox exhibited the opposite behavior (**Figure 3.11A, D,** and **G**). For instance, St-PGA-PD(5)-Dox displayed a hydrodynamic diameter of 25 ± 8 nm at 1 mg/ml and 91 ± 30 nm at 0.5 mg/ml in MilliQ water (**Figure 3.11G** and **Table 3.2**). This behavior possesses similarities to that observed for St-PGA-PD(10) in MilliQ water, which displayed larger aggregate sizes at 1, 2, and 5 mg/mL than 10 mg/mL (**Figure 3.6C**). Overall, these data suggest the robust influence of hydrophobic interactions in conjugate conformation in an aqueous solution.

Overall, St-PGA-PD(5)-hyd-Dox possessed a larger size than St-PGA-PD(5)-Dox and St-PGA-PD(10)-Dox in both media and at all concentrations (**Table 3.2**), suggesting that the drug linker affects conjugate size in aqueous solutions. We also observed a larger size for St-PGA-PD(5)-hyd-Dox in water than the single drug conjugate St-PGA-hyd-Dox (*Chapter 2*) with similar drug loading (~10 nm and 2.9% mol Dox for St-PGA-hyd-Dox vs. >100 nm and 4.4% mol Dox for St-PGA-PD(5)-hyd-Dox), suggesting the implication of PD hydrophobicity in conjugate size.

Finally, we observed a highly heterogeneous size distribution by intensity St-PGA-PD(5)-Dox, St-PGA-PD(10)-Dox, and St-PGA-PD(5)-hyd-Dox in all media, suggesting the presence of different sized aggregates in the samples (**Figure 3.11B**, **E**, and **H**, and **Figure 3.12B**, **E**, and **H**). Overall, the correlation functions corresponding to the size measurements possessed optimal intercepts (over 0.8 and below 1.0) and exponential decay (**Figure 3.11C**, and **F**, and **Figure 3.12C**, and **F**), indicating the quality of the measurements; however, St-PGA-PD(5)-hyd-Dox samples (**Figure 3.11I** and **Figure 3.12I**) possessed high noise levels at long delay times probably caused by the large size of the particles and/or sample.

To further understand the influence of PD, Dox, and the linking chemistry used for drug conjugation in conjugate conformation, we studied the secondary structure of St-PGA-PD(5)-Dox, St-PGA-PD(10)-Dox, and St-PGA-PD(5)-hyd-Dox by CD in MilliQ water and 10 mM PB at 0.1, 0.2, and 0.5 mg/mL. Analysis of St-PGA-PD(5)-Dox, St-PGA-PD(10)-Dox, and St-PGA-PD(5)-hyd-Dox demonstrated the presence of a negative band at ~200 nm typical of a random coil conformation in 10 mM PB (**Figure 3.13A** and **Supplementary Figure 3.1A**, **C**, and **E**) and MilliQ water (**Figure 3.13B** and **Supplementary Figure 3.1B**, **D**, and **F**) at all the concentrations evaluated in agreement with data regarding their precursors.
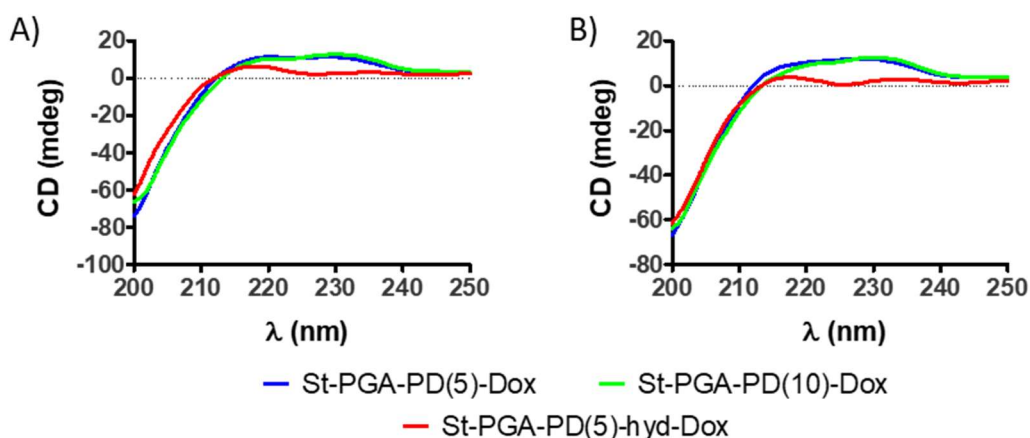
Figure 3.13. Secondary structure of St-PGA-PD(5)-Dox (blue), St-PGA-PD(10)-Dox (green), and St-PGA-PD(5)-hyd-Dox (red) in (**A**) 10 mM PB and (**B**) MilliQ water at 0.5 mg/mL. Data obtained by CD. Average results with three accumulated measurements displayed.

When studying the CD spectra of St-PGA-PD(5)-Dox, St-PGA-PD(10)-Dox, and St-PGA-PD(5)-hyd-Dox above 250 nm (where the peptide chromophores contribute negligibly) to allow the exploration of other chromophores present in the molecule (30), we identified some alterations compared to the parental St-PGA-PD(5) and St-PGA-PD(10) spectra in 10 mM PB (**Figure 3.14A**) and MilliQ water (**Figure 3.14B**). St-PGA-PD(5)-Dox, St-PGA-PD(10)-Dox, and St-PGA-PD(5)-hyd-Dox exhibited the typical

bands of the Dox chromophore with its set of π → π* and n → π* transitions (31); however, only the amide-dox conjugates (St-PGA-PD(5)-Dox and St-PGA-PD(10)-Dox) in 10 mM PB displayed the characteristic negative band at 540 nm of Dox in the associated state (**Figure 3.14A**) (31,32). These findings suggest the stacking of drug molecules (Dox dimerization). Therefore, the association between Dox molecules, forming a more compact structure, can contribute to the smaller size found for amide-Dox conjugates compared to St-PGA-PD(5)-hyd-Dox and to the size reduction with increasing conjugate concentration; however, this phenomenon cannot explain the self-assembly of St-PGA-PD(5)-hyd-Dox in 10 mM PB. Different Dox-Dox interactions possibly respond to the conjugation sites for hydrazone and amide bonds. The association constant of anthracycline dimer formation depends strongly on the substituents in C(4) and C(13) (31), with hydrazone conjugation directly affecting the latter. Meanwhile, amide bond conjugation occurs in the sugar moiety, far from the groups affecting drug dimerization.
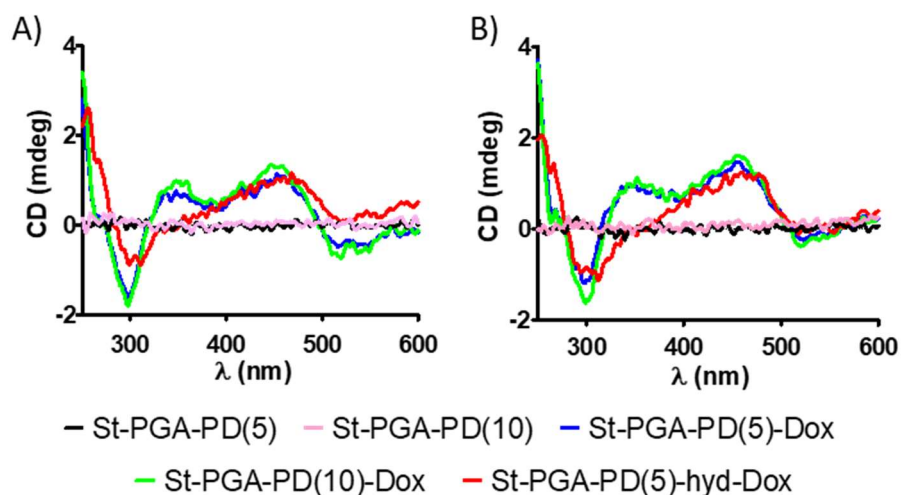
Figure 3.14. Characterization of Dox dimerization for St-PGA-PD(5)-Dox (blue), St-PGA-PD(10)-Dox (green), and St-PGA-PD(5)-hyd-Dox (red) at 0.5 mg/mL in (**A**) 10 mM PB and (**B**) MilliQ water. Data obtained by CD. Average results with three accumulated measurements displayed. Data for St-PGA-PD(5) (black) and St-PGA-PD(10) (pink) precursors displayed for comparison.

ELS measurement demonstrated negative zeta potentials ranging from -51 to -45 mV for all conjugates (similar to St-PGA-PDs, see **Table 3.1** and **Table 3.2**). As observed for the St-PGA-drug conjugates (*Chapter 2*), we observed similar zeta potential values for both polymer concentrations (1 and 0.5 mg/mL), contrary to previously reported data where St-PGA displayed increased negative zeta potential upon aggregation (1), suggesting a change in the self-assembly behavior.

In summary, we synthesized and characterized a family of St-PGA-based polymer-Dox conjugates bearing PD for reversible crosslinking of their assemblies. Our data suggest an important influence of PD and Dox hydrophobicity and drug linking chemistry in conjugate behavior in aqueous solution, which may undermine the interactions driving the dipole-dipole pairing-based aggregation of St-PGA. Regardless, conjugate size in water still implies the presence of aggregates, which supports the development of reversible crosslinked nanosystems.

3.2.3. Synthesis and Characterization of St-PGA-PD-Dasatinib Conjugates

3.2.3.1. Synthesis of St-PGA-PD(5)-Das and St-PGA-PD(10)-Das

We conjugated Das to St-PGA-PD(5) and St-PGA-PD(10) using a simple pH-labile ester bond (**Scheme 3.5**). As for Dox, we aimed for 5% mol Das loading to allow a comparison of both drugs' influence on the conjugate's physico-chemical parameters. We performed the reaction in DMF using carbodiimides as coupling agents and 4-dimethylaminopyridine (DMAP) as a catalyst (see *Chapter 2*).
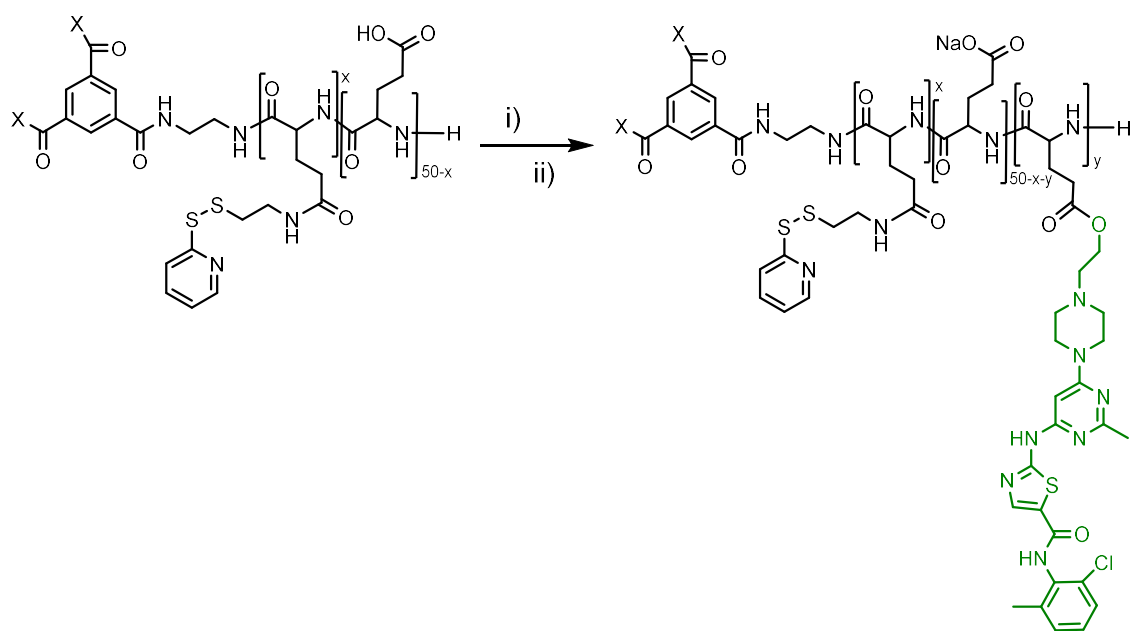
Scheme 3.5. Synthesis of St-PGA-PD(5)-Das and St-PGA-PD(10)-Das. i) DMF anhydrous, DMAP, 1-ethyl-3-(3-dimethylaminopropyl) carbodiimide (EDC), Das, DIEA, pH 8, 72 h. ii) sodium bicarbonate, MilliQ water.

^{1}H-NMR and absorbance spectra confirmed Das conjugation to St-PGA-PD(5) and St-PGA-PD(10), yielding St-PGA-PD(5)-Das and St-PGA-PD(10)-Das, respectively (**Figure 3.15**). Although we identified signals corresponding to Das in the aromatic region of the ^{1}H-NMR spectra (8.75-6.54 ppm), interference from PD-derived signals and the lack of peak definition impeded the quantification of drug loading (**Figure 3.15A**). We confirmed Das conjugation and quantified drug loading by UV-VIS spectroscopy, using a calibration curve in methanol (**Supplementary Figure 3.2**) and conjugate samples in water (**Figure 3.15B**). We determined a value of 9.79% wt (3.37% mol, 67% CE) for St-PGA-PD(5)-Das and 9.22% wt (3.19% mol, 64% CE) for St-PGA-PD(10)-Das.
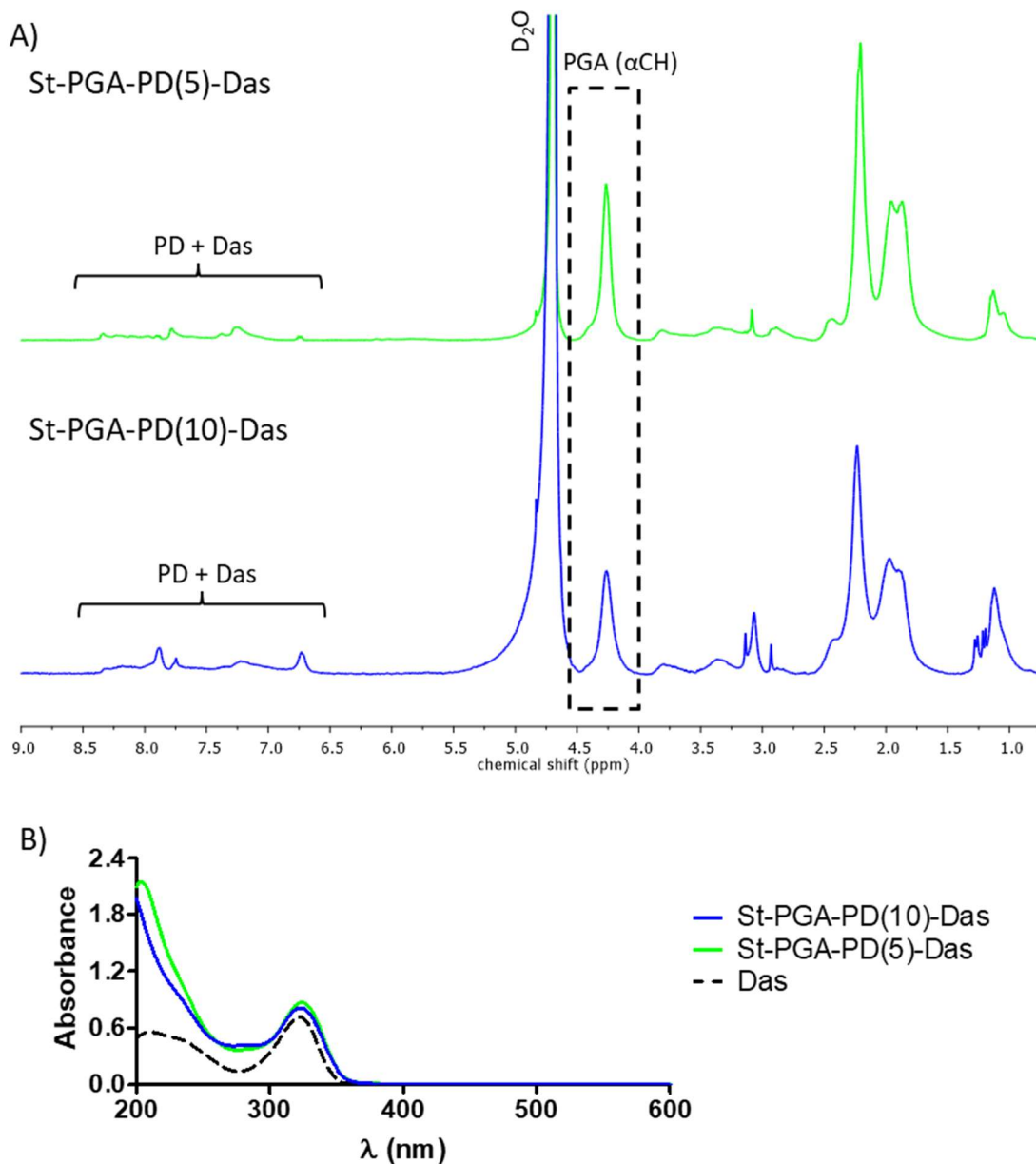
Figure 3.15. Identification of St-PGA-PD(5)-Das and St-PGA-PD(10)-Das. (**A**) ^{1}H-NMR (D$_2$O) spectra of St-PGA-PD(5)-Das (green) and St-PGA-PD(10)-Das (blue). The spectra confirm PD and Das conjugation (broad peaks in the aromatic region). (**B**) Absorbance spectra obtained for the conjugates at 0.125 mg/mL for St-PGA-PD(5)-Das (green) and 0.0625 mg/mL for St-PGA-PD(10)-Das (blue) in water, and 0.025 mg/mL for Das (black discontinuous line) in methanol.

3.2.3.2. Physico-chemical Characterization of St-PGA-PD(5)-Das and St-PGA-PD(10)-Das

As for the Dox conjugates, we performed an exhaustive physico-chemical characterization of St-PGA-PD(5)-Das and St-PGA-PD(10)-Das. SEC studies provided evidence of a single homogeneous molecular weight distribution by absorbance at 324 nm (Das maximum, **Figure 3.16A**) and RI (**Figure 3.16B**) for St-PGA-PD(5)-Das, thereby suggesting a homogeneous distribution of Das content. Of note, the single population observed for St-PGA-PD(10)-Das by absorbance (**Figure 3.16A**) and RI (**Figure 3.16B**) displayed a long tail, indicating high heterogeneity. For both conjugates, we also identified the sodium counterion eluting at 17 min by RI (**Figure 3.16B**).
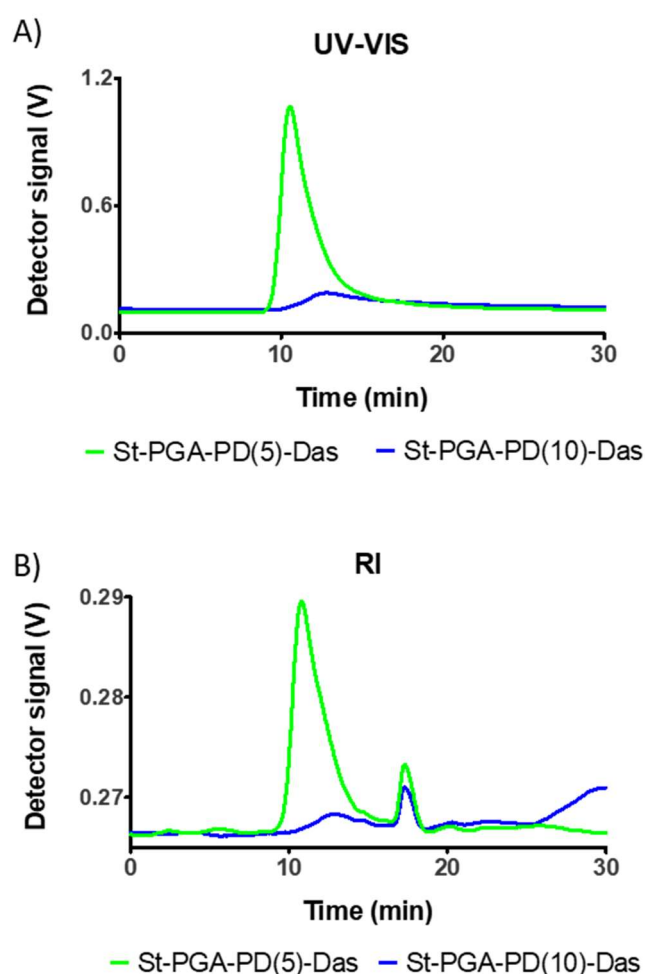
Figure 3.16. Representative SEC chromatogram of St-PGA-PD(5)-Das (green) and St-PGA-PD(10)-Das (blue). (**A**) UV-VIS absorbance detector at 324 nm. (**B**) RI detector. The

peak at 17 min corresponds to the sodium counter-cation of PGA. Data obtained by injecting 10 µL of a 5 mg/mL polymer solution using $NaNO_3$ 0.1 M NaN_3 0.005% as the mobile phase.

St-PGA-PD(5)-Das and St-PGA-PD(10)-Das exhibited larger hydrodynamic diameters in MilliQ water (**Figure 3.17A** and **D,** and **Table 3.3**) than in 10 mM PB (**Figure 3.18A** and **D**, and **Table 3.3**) as determined by DLS size distribution by number. These conjugates also displayed similar sizes to the single drug conjugate St-PGA-Das (*Chapter 2*) in water; however, size distribution by number displayed higher homogeneity for the PD-loaded compounds, highlighting the influence of PD on conjugate characteristics.

Despite possessing a similar level of Das loading, St-PGA-PD(10)-Das exhibited a smaller hydrodynamic diameter by number than St-PGA-PD(5)-Das in water at 1 mg/ml (62 ± 16 nm vs. 110 ± 40 nm, respectively) and 0.5 mg/ml (39 ± 9 nm vs. 79 ± 31 nm, respectively) (**Figure 3.17A** and **D** and **Table 3.3**). This behavior may be explained by the influence of PD hydrophobicity. In 10 mM PB, we observed the opposite behavior - St-PGA-PD(10)-Das exhibited a larger hydrodynamic diameter compared to St-PGA-PD(5)-Das at 1 mg/ml (33 ± 12 nm vs. 14 ± 4 nm, respectively) and 0.5 mg/ml (34 ± 15 nm vs. 14 ± 5 nm, respectively) (**Figure 3.18A** and **D**, and **Table 3.3**). Overall, these data suggest that St-PGA-PD(10)-Das behaves differently to St-PGA-PD(5)-Das in aqueous solution due to the higher loading of PD and the consequent increment of hydrophobic interactions in the conjugate.

Table 3.3. Summary of synthesized St-PGA-PD-based Das conjugates and their main physico-chemical characteristics

	% wt[A]	% mol[B]	CE[C]	$Dh_{water}^{1\ mg/mL}$ (nm)	$Dh_{water}^{0.5\ mg/mL}$ (nm)	$Dh_{PB}^{1\ mg/mL}$ (nm)	$Dh_{PB}^{0.5\ mg/mL}$ (nm)	Z-Pot$^{1\ mg/mL}$ (mV)	Z-Pot$^{0.5\ mg/mL}$ (mV)
St-PGA-PD(5)-Das(5)	9.79	3.37	67	110 ± 40	79 ± 31	14 ± 4	14 ± 5	-47 ± 1	-45 ± 3
St-PGA-PD(10)-Das(5)	9.22	3.19	64	62 ± 16	39 ± 9	33 ± 12	34 ± 15	-47 ± 1	-45 ± 0

(**A**) Obtained by UV-VIS spectroscopy. (**B**) Obtained by iterative calculation from the loading weight percent. (**C**) Conjugation efficacy. Dh = Hydrodynamic diameter. Z-Pot = zeta potential. Dh was obtained from the most abundant population in the size distribution by number in Figure 3.17 for water measurements and Figure 3.18 for PB measurements. Data displayed as mean ± SD. Z-Pot measured in in KCl 1 mM. Data expressed as mean ± SD of three measurements.
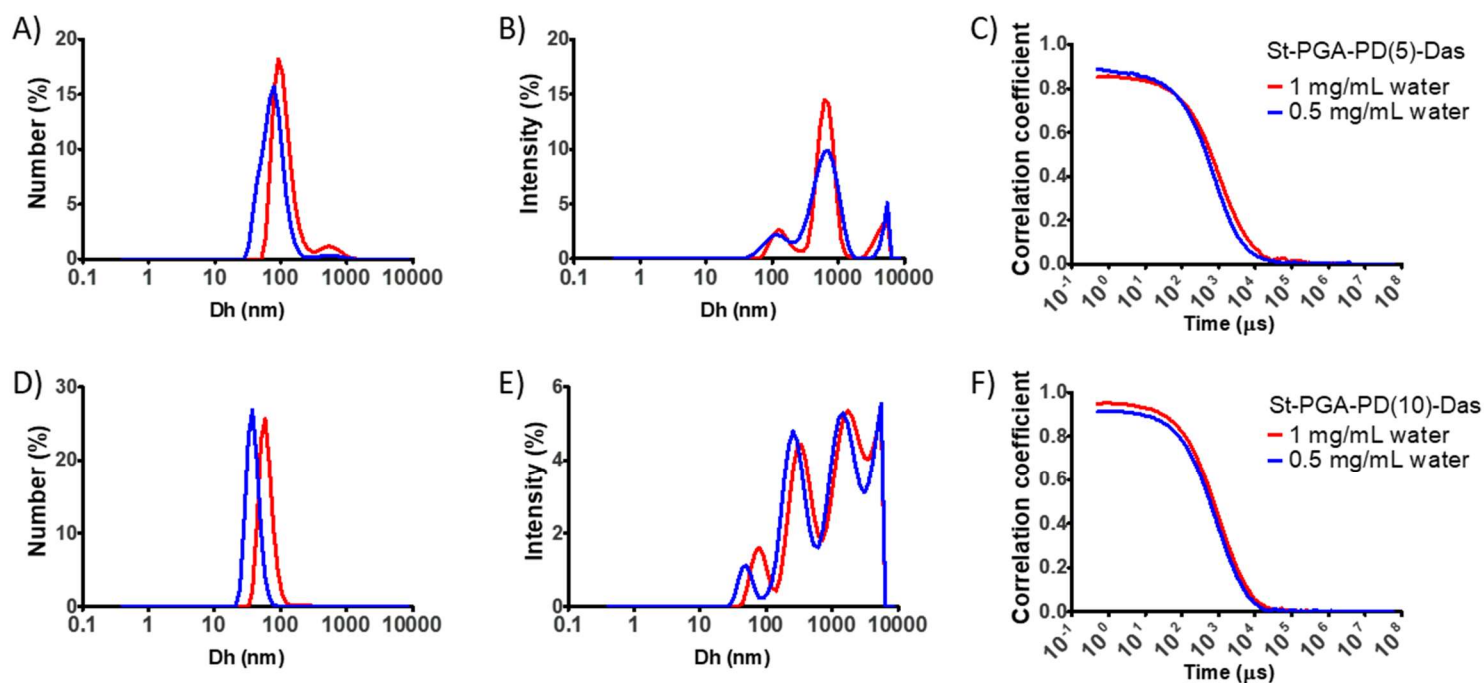
Figure 3.17. Size distribution of (**A-C**) St-PGA-PD(5)-Das and (**D-F**) St-PGA-PD(10)-Das obtained by DLS in MilliQ water. The hydrodynamic diameter distribution by number and intensity and the respective correlation functions are displayed. Data obtained from the average result of at least three measurements.
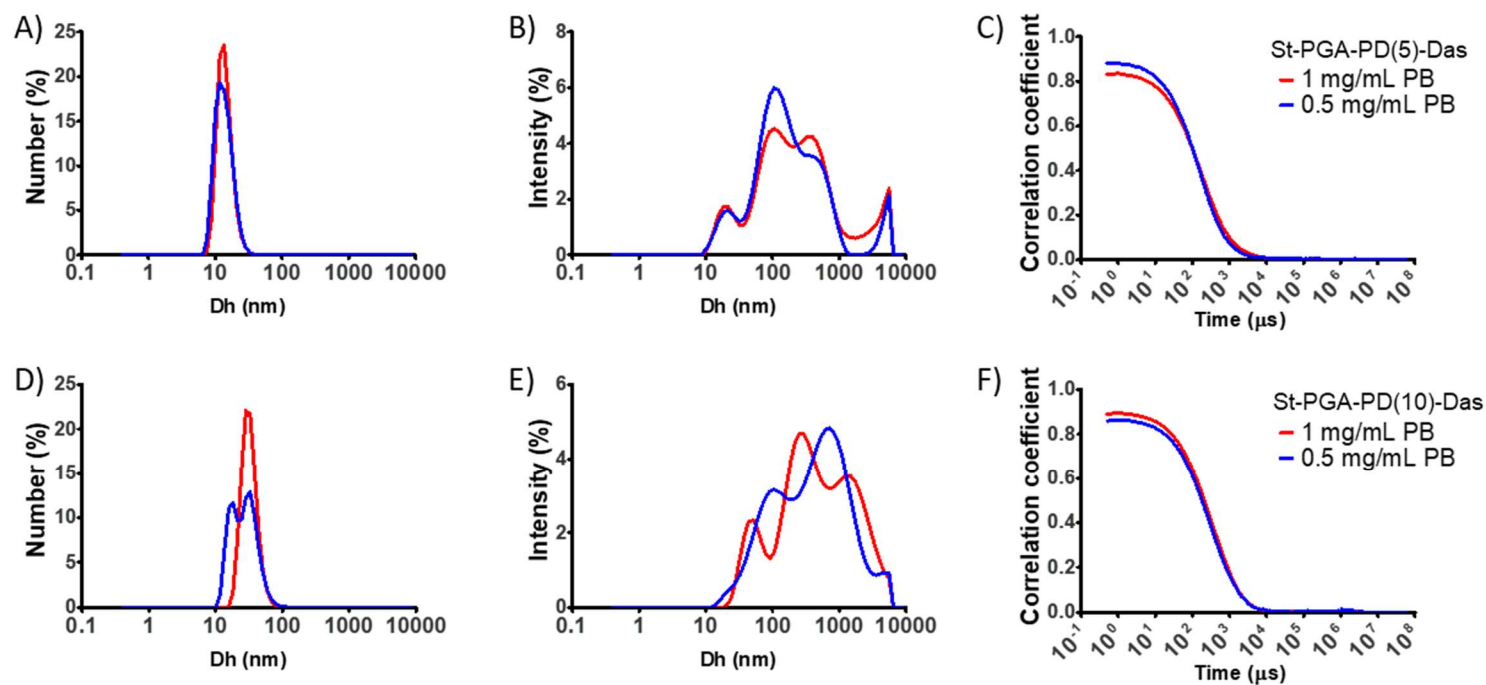
Figure 3.18. Size distribution of (**A**-**C**) St-PGA-PD(5)-Das and (**D**-**F**) St-PGA-PD(10)-Das obtained by DLS in 10 mM PB. The hydrodynamic diameter distribution by number and intensity and the respective correlation functions are displayed. Data obtained from the average result of at least three measurements.

We discovered heterogeneous size distributions by intensity in all media and concentrations evaluated for St-PGA-PD(5)-Das and St-PGA-PD(10)-Das (**Figure 3.17B** and **E** in water, and **Figure 3.18B** and **E** in 10 mM PB), suggesting the aggregation of a small proportion of St-PGA-PD(5)-Das and St-PGA-PD(10)-Das molecules. Overall, the correlation functions associated with these conjugates possessed optimal intercepts (over 0.8 and below 1.0) and exponential decay (**Figure 3.17C** and **F** in water, and **Figure 3.18C** and **F** in 10 mM PB), confirming the quality of the measurements.

CD spectra analysis in 10 mM PB demonstrated that St-PGA-PD(5)-Das and St-PGA-PD(10)-Das assumed a random coil conformation, displaying the typical minima at 200 nm at all the concentrations evaluated (**Figure 3.19A**, and **Supplementary Figure 3.3A** and **C**). St-PGA-PD(5)-Das also displayed a random coil conformation in water (**Figure 3.19B**, and **Supplementary Figure 3.3B**); however, St-PGA-PD(10)-Das displayed the typical double minima at 208 and 222 nm of the α-helix conformation (33) in water at all concentrations analyzed (**Figure 3.19B** and **Supplementary Figure 3.3D**).
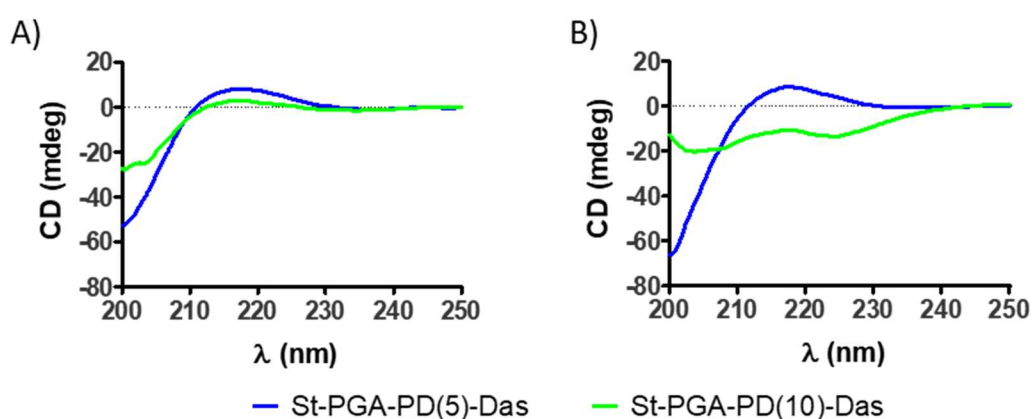
Figure 3.19. Secondary structure of St-PGA-PD(5)-Das (blue), and St-PGA-PD(10)-Das (green) in (**A**) 10 mM PB and (**B**) MilliQ water at 0.5 mg/mL. Data obtained by CD. Average results with three accumulated measurements displayed.

CD spectra analysis over 250 nm failed to provide evidence of any significant difference to the spectra of St-PGA-PD(5) and St-PGA-PD(10) in 10 mM PB (**Figure 3.20A**) and MilliQ water (**Figure 3.20B**); therefore, we believe that the conformation change does not rely on Das-Das interactions but on an increment in conjugate hydrophobicity, which also explains the different behavior of St-PGA-PD(10)-Das in aqueous solution in terms of size (by DLS).
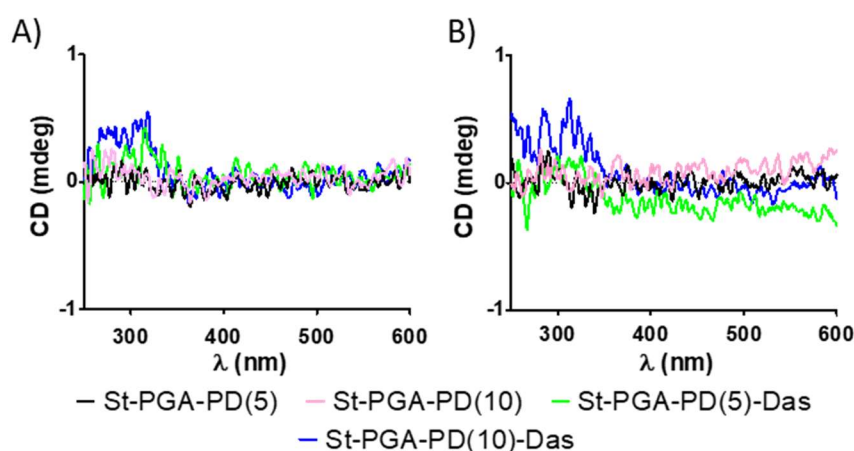

Figure 3.20. Characterization of Das dimerization in St-PGA-PD(5)-Das (green) and St-PGA-PD(10)-Das (blue) at 0.5 mg/mL in (**A**) 10 mM PB and (**B**) MilliQ water. Data obtained by CD. Average results with three accumulated measurements displayed. Data for St-PGA-PD(5) (black) and St-PGA-PD(10) (pink) precursors displayed for comparison.

ELS determined that St-PGA-PD(5)-Das and St-PGA-PD(10)-Das displayed a negative zeta potential, with a similar value at all concentrations evaluated (0.5 and 1 mg/mL), ranging from -45 to -47 mV (**Table 3.3**). As already observed for the St-PGA-based conjugates synthesized (this chapter and *Chapter 2*), these results do not agree with previously reported data where St-PGA displayed increased negative zeta potential upon aggregation (1), suggesting a change in the self-assembly behavior.

In summary, we successfully synthesized and fully characterized a family of St-PGA-based polymer-Das conjugates bearing PD for reversible crosslinking following self-assembly. The physico-chemical characterization of this family provided evidence for the influence of PD hydrophobicity in conjugate behavior in aqueous solutions; however, according to the size by DLS, this alteration does not seem to hamper the formation of aggregates in water, thereby supporting the development of reversible crosslinked nanosystems.

3.2.4. DTT-mediated Crosslinking

3.2.4.1. Reaction Kinetics

PD has been extensively used to introduce thiol functionalities into polymers for a wide variety of purposes, including drug (23,34), peptide (35,36), and protein (37) conjugation, stabilization of polymeric micelles (22,23), and hydrogel formation (19,20). Redox-responsive crosslinking via polymer functionalization with PD approaches fall into two categories. The first relies on the cleavage of a fraction (or all) of the polymeric PD groups of the polymer and their subsequent reaction with remaining PD groups to form the disulfide bonds that stabilize the structure. The second approach involves the addition of dithiol-containing molecules that react with the polymeric PD groups to form disulfide bonds via a thiol exchange reaction to interconnect polymer molecules (25).

The research group of S. Thayumanavan has widely contributed to the development of redox-responsive nanogels following the first approach (17,18). They synthesized poly(ethylene glycol) methacrylate (PEGMA) and pyridyl disulfide ethyl methacrylate (PDEM) random co-polymers that form spherical assemblies in water driven by the hydrophobicity of PD moieties (17,18). Assembly size relied on the ratio of PEGMA and PDEM monomers and the polymer's molecular weight, obtaining larger sizes with higher

molecular weight and higher PD percentage (18). Additional changes in polymer concentration further modulated size (17). The addition of dithiothreitol (DTT) to the reaction solution allowed PD cleavage and thiol group exposure to trigger the thiol-exchange reaction and yield crosslinked nanogels that maintained original assembly size with short reaction times (~12 h) (17,18). The authors modulated the percentage of cleaved PD groups (and, thus, the degree of crosslinking) by adding specific amounts of DTT. The remaining PD groups allowed for the maintenance of the nanogel's hydrophobic core, which permitted the loading of hydrophobic molecules such as Nile red (as a model) or Dox (18).

These studies also reported the evaluation of Nile red release at low (10 µM pH 7.4, mimicking the bloodstream) and high GSH concentrations (10 mM pH 7.4 and 5.0, mimicking the cytosol and lysosomes). Low GSH concentrations induced negligible dye release even after 72 h of incubation; however, higher concentrations prompted a significant increase in dye release, with more rapid release observed for nanogels with a lower degree of crosslinking. As expected, pH did not significantly affect the dye release kinetics. When loaded with Dox, nanogels possessed cytotoxic activity in MCF7 breast cancer cells; however, this failed to improve efficacy above that observed for the free drug (18).

We followed the first described approach to stabilize self-assembled St-PGA-PD structures in water via disulfide bonds, using DTT as the reductive agent to break the disulfide bonds between the pyridyl thione group and the polypeptide and prompt the formation of intermolecular disulfide bonds (**Scheme 3.6**). Given the conjugation of Dox and Das to St-PGA-PD through pH-labile linkers, we required a rapid stabilization reaction for the self-assembled structures and mild conditions to avoid drug release during the process. To prove the suitability of this stabilization reaction, we first studied DTT-mediated crosslinking kinetics for St-PGA-PD(5) and St-PGA-PD(10).
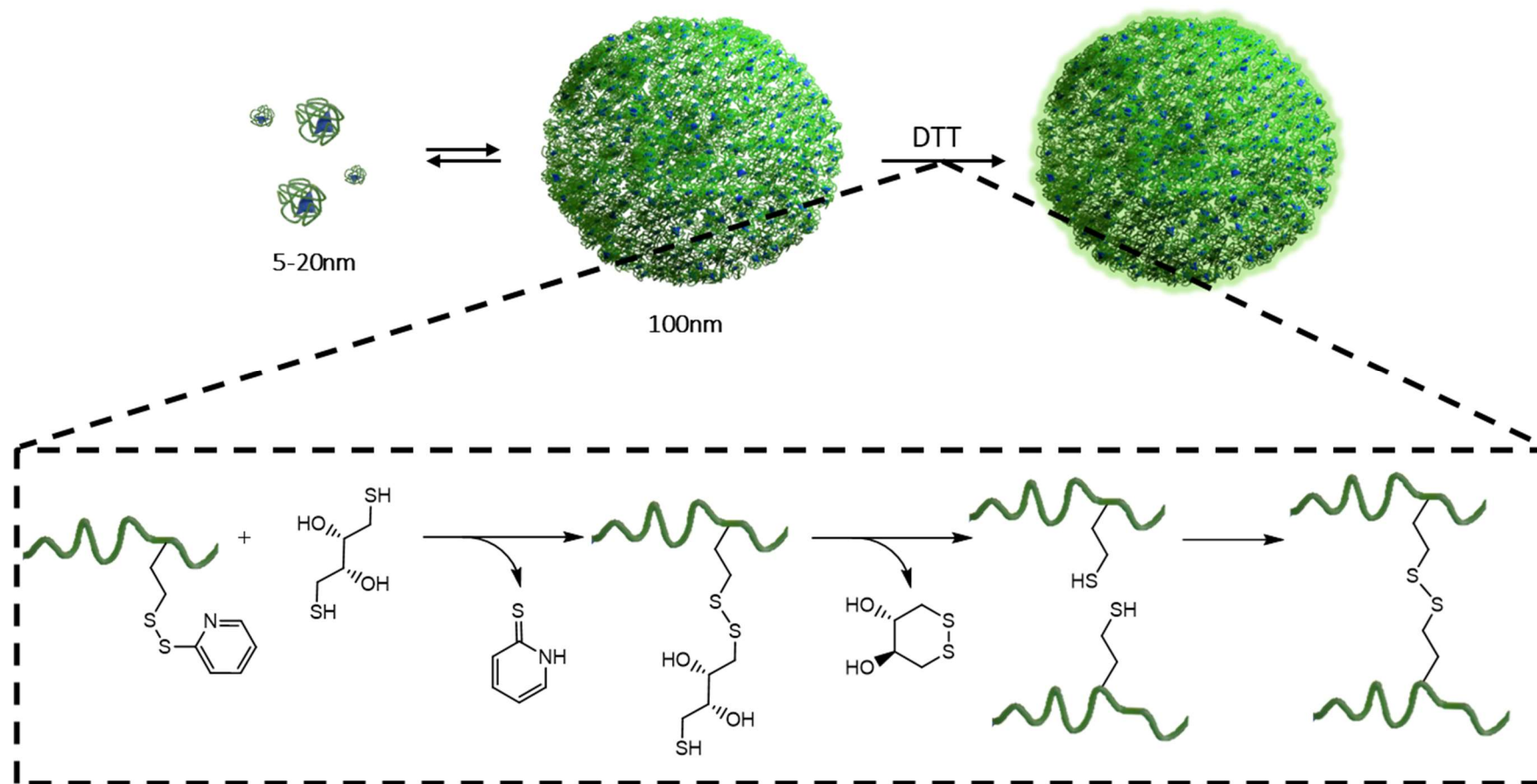
Scheme 3.6. DTT-mediated crosslinking reaction. DTT displaces the pyridyl thione in the polymer, allowing intermolecular disulfide bonds that stabilize the self-assembled structure.

We performed crosslinking reactions in water at a St-PGA-PD(5) or St-PGA-PD(10) concentration of 2 mg/mL (as used previously for CuAAC-mediated stabilization (1)). We measured the size of St-PGA-PD(5) and St-PGA-PD(10) in solution by DLS before adding DTT to evaluate self-assembly (**Figure 3.21A-C** and **Figure 3.22A-C**). Encouragingly, both conjugates appeared to assemble well at this concentration. For St-PGA-PD(5), we identified two peaks, one at ~90 nm - the main population by number (88%) - and a second peak at ~570 nm - corresponding to less abundant (12% by number) aggregates (**Figure 3.21A**). Size distribution by intensity also provided evidence of two populations - one at ~100 nm (37%) and a second population at ~770 nm corresponding to larger aggregates (94%) (**Figure 3.21B**). The measurement provided an optimal correlation function, with an intercept between 0.8 and 1.0 and exponential decay, confirming the quality of the results (**Figure 3.21C**). Overall, these data suggest the presence of St-PGA-PD(5) assemblies of 90-100 nm and a small number of larger aggregates.

For St-PGA-PD(10), we also identified two peaks - a prominent peak (98%) at ~84 nm by number and an exiguous population (2% by number) of ~660 nm corresponding to larger aggregates (**Figure 3.22A**). By intensity, we detected one population at ~100 nm (9%) and a second population at ~730 nm (57%) corresponding to larger aggregates (**Figure 3.22B**). We also identified a third peak at the micron-scale (**Figure 3.22B**), possibly a consequence of aggregate precipitation, which could explain the high noise level observed in the correlation function at longer delay times (**Figure 3.22C**). Overall, these data suggest the presence of St-PGA-PD(10) assemblies of 80-100 nm and a small number of aggregates, similar to St-PGA-PD(5).
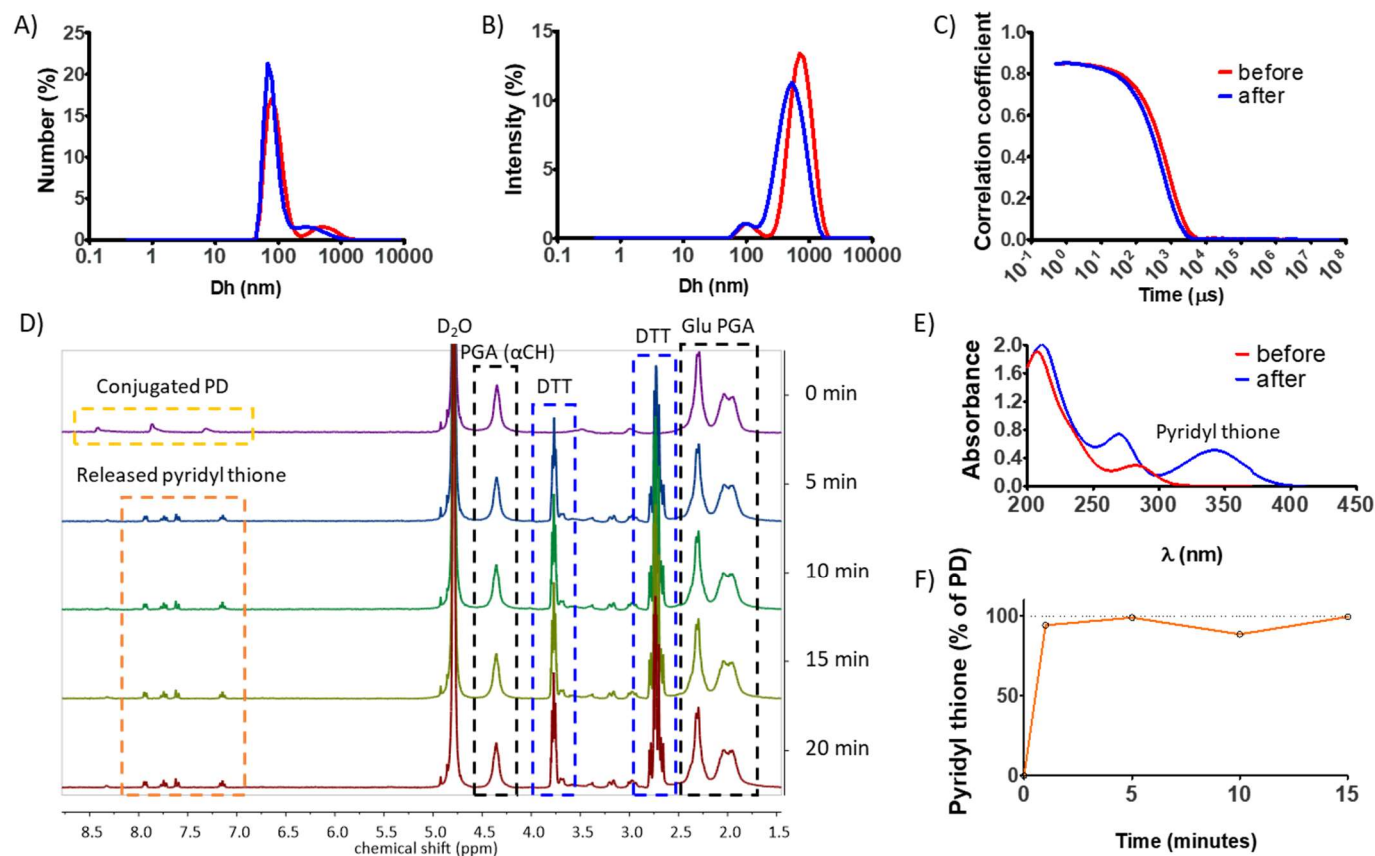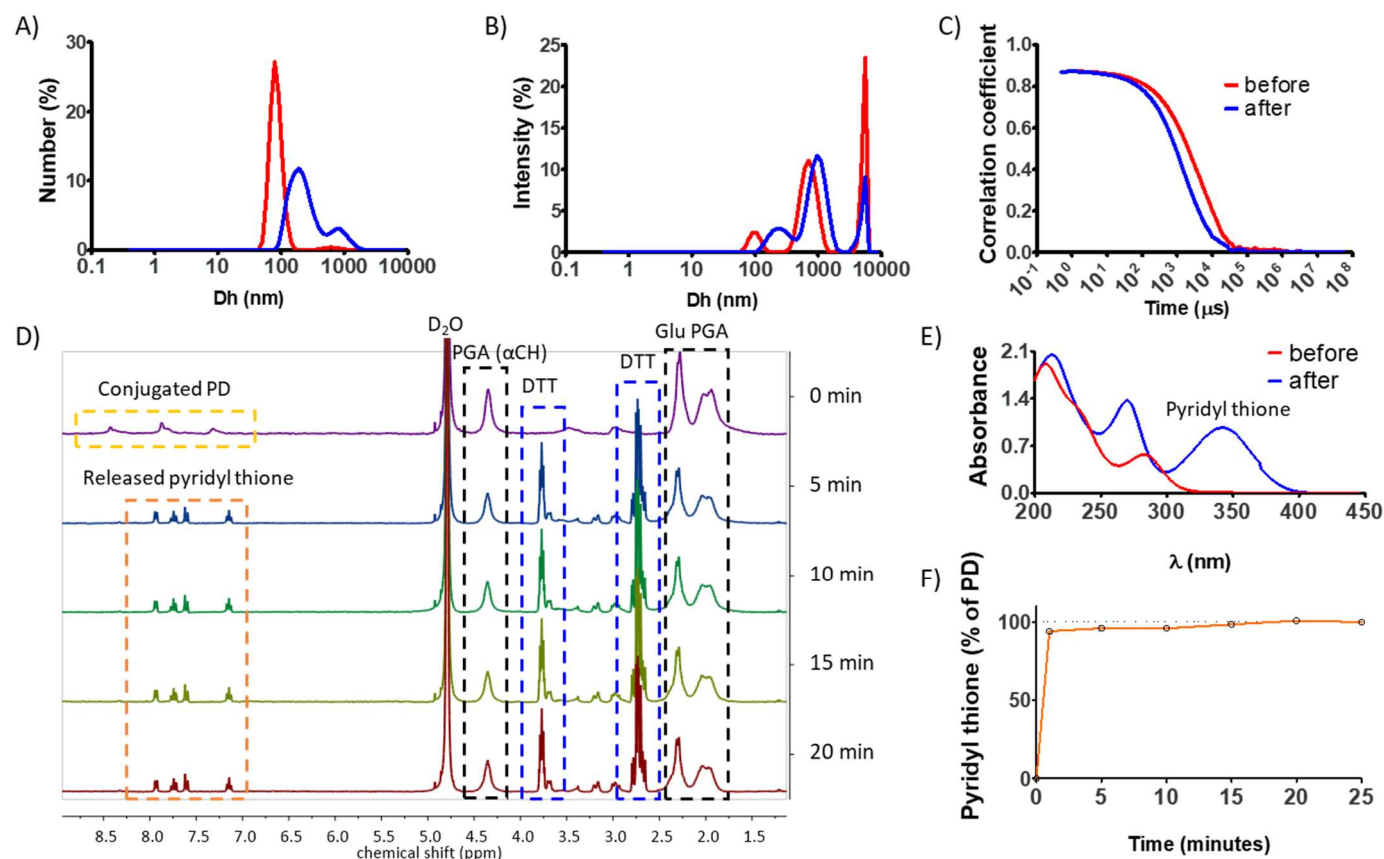
Figure 3.21. DTT-mediated reaction kinetics for St-PGA-PD(5) conjugate. (**A-C**) Size distribution of St-PGA-PD(5) obtained by DLS. The hydrodynamic diameter distribution by (**A**) number and (**B**) intensity and (**C**) the respective correlation functions are displayed. Data obtained before the addition of DTT (red) and after complete pyridyl thione release (blue) from the average result of three measurements. (**D**) Pyridyl thione release monitored by ^{1}H NMR (D_2O). (**E** and **F**) Pyridyl thione release monitored by UV-VIS spectroscopy. (**E**) Absorbance spectra before (red) and 15 min after (blue) the addition of DTT. (**F**) Evolution of pyridyl thione release. Data expressed as a percentage of released pyridyl thione versus reaction time. Dotted line marks the maximal PD release (100%).

Figure 3.22. DTT-mediated reaction kinetics for St-PGA-PD(10) conjugate. (**A-C**) Size distribution of St-PGA-PD(10) obtained by DLS. The hydrodynamic diameter distribution by (**A**) number and (**B**) intensity and (**C**) the respective correlation functions are displayed. Data obtained before the addition of DTT (red) and after complete pyridyl thione release (blue) from the average result of three measurements. (**D**) Pyridyl thione release monitored by ¹H NMR (D₂O). (**E** and **F**) Pyridyl thione release monitored by UV-VIS spectroscopy. (**E**) Absorbance spectra before (red) and 15 min after (blue) the addition of DTT. (**F**) Evolution of pyridyl thione release. Data expressed as a percentage of released pyridyl thione versus reaction time. Dotted line marks the maximal PD release (100%).

Since St-PGA-PD(5) and St-PGA-PD(10) assembled well in the reaction mixture, we added DTT and monitored the reaction via ^{1}H-NMR and UV-VIS spectroscopy. When conjugated to St-PGA, PD appears as broad peaks at 8.41, 7.88, and 7.33 ppm in the ^{1}H-NMR spectra; when released, pyridyl thione appears as sharp peaks between 7.00 and 8.10 ppm (**Figure 3.21D** and **Figure 3.22D**). We observed the complete disappearance of conjugated PD and the appearance of free pyridyl thione 5 min after the addition of DTT in the reaction with St-PGA-PD(5) (**Figure 3.21D**) and St-PGA-PD(10) (**Figure 3.22D**). By UV-VIS spectroscopy, free pyridyl thione possesses an absorbance peak at 343 nm that we monitored to determine reaction kinetics (18,22,38) (**Figure 3.21E** and **Figure 3.22E**). We determined the percentage of released pyridyl thione using its extinction coefficient at 343 nm (8.08×10^3 M^{-1} cm^{-1} (18)) and the PD molar concentration in the reaction. The results revealed the rapid cleavage of disulfide bonds, exposing the thiol groups of St-PGA-PD. 99% and 96% of pyridyl thione groups became released from St-PGA-PD(5) (**Figure 3.21F**) and St-PGA-PD(10) (**Figure 3.22F**), respectively, after 5 min.

After reaction completion, we assessed the hydrodynamic diameter of St-PGA-PD(5) and St-PGA-PD(10) self-assembled structures by DLS (**Figure 3.21A-C** and **Figure 3.22A-C**). While St-PGA-PD(5) displayed a similar size before and after DTT addition (**Figure 3.21A** and **B**), we observed an increase in size for St-PGA-PD(10) after DTT addition (**Figure 3.22A** and **B**); the main population by number (83%) exhibited a size of ~220 nm, and the minor population (18%) exhibited a size of ~870 nm. These data agree with the previous observation that St-PGA displays larger sizes (155 nm at 2 mg/mL) than St-PGA-PD(10) (106 nm at 2 mg/mL) in water (**Figure 3.6**) and reinforces the hypothesis that PD hydrophobicity interferes with the interaction between St-PGA molecules - the hydrophobic interactions introduced in St-PGA-PD(10) due to PD conjugation cease after pyridyl thione displacement and, therefore, the conjugate's behavior in water resembles to St-PGA's. The correlation functions of the measurements after

DTT addition possessed acceptable quality, with intercepts between 0.8 and 1.0 and exponential decay (**Figure 3.21C** and **Figure 3.22C**).

In summary, the DTT-mediated crosslinking protocol employed allows for pyridyl thione release, thereby rapidly exposing the thiol groups present in St-PGA-PD(5) and St-PGA-PD(10) in a manner that maintains assembly and has minimal influence on size. While most protocols reported in the literature employ a crosslinking reaction lasting several hours (17,18,22,23) and/or employing harsh conditions (e.g., 50 ºC (22)), our protocol provides the almost complete cleavage of the PD moiety in 5 min under mild conditions. These results suggest that DTT-mediated crosslinking represents a suitable approach for the aims of this study.

3.2.4.2. Synthesis and Characterization of Combination Conjugates

We next performed a series of crosslinking reactions with St-PGA-PD(5)-Das and St-PGA-PD(5)-Dox or St-PGA-PD(5)-hyd-Dox as starting materials, aiming to obtain combination conjugates through assembly stabilization.

We chose the St-PGA-PD(5) family to achieve proof-of-concept as we had both linkers (hydrazone and amide) available for Dox for St-PGA-PD(5)-derived compounds but not for St-PGA-PD(10). We synthesized a set of combination conjugates and their single-drug counterparts using the conditions optimized in the previous section for St-PGA-PD(5) crosslinking.

We synthesized two combination conjugates by mixing St-PGA-PD(5)-Dox or St-PGA-PD(5)-hyd-Dox with St-PGA-PD(5)-Das in water to obtain "St-PGA-Das-Dox-CL" and "St-PGA-Das-hyd-Dox-CL," respectively.

We aimed for a 1:1 drug ratio and calculated the amount of each precursor in drug equivalents. For St-PGA-Das-Dox-CL, we mixed 20.3 mg of St-PGA-PD(5)-Das (0.004 mmol of Das) with 16.8 mg of St-PGA-PD(5)-

Dox (0.004 mmol of Dox). For St-PGA-Das-hyd-Dox-CL, we mixed 12.7 mg of St-PGA-PD(5)-Das (0.003 mmol of Das) with 10.1 mg of St-PGA-PD(5)-hyd-Dox (0.003 mmol of Dox).

We synthesized the single drug counterparts ("St-PGA-Das-CL," "St-PGA-Dox-CL," and "St-PGA-hyd-Dox-CL") by dissolving the desired amount of each polypeptide-drug conjugate (St-PGA-PD(5)-Das, St-PGA-PD(5)-Dox, and St-PGA-PD(5)-hyd-Dox, respectively) in water. We also synthesized a crosslinked nanosystem ("St-PGA-CL") without drugs using St-PGA-PD(5).

We performed all crosslinking reactions at 2 mg/mL conjugate in MilliQ water. We measured the hydrodynamic diameter of all reaction mixtures by DLS before adding DTT to assess self- and co-assembly and after DTT addition, purification, and lyophilization to compare with the final size (**Figure 3.23**). As observed during precursor characterization, we identified two populations in the size distribution by number in most samples (St-PGA-PD(5), St-PGA-PD(5)-Das, St-PGA-PD(5)-Dox, and St-PGA-PD(5)-Das + St-PGA-PD(5)-Dox). By number, the most abundant population exhibited the smallest hydrodynamic diameter (~100 nm) (**Figure 3.23A**, **D**, **G**, and **M**); by intensity, the larger structures (~1000 nm) represented the predominant population (**Figure 3.23B**, **E**, **H**, and **N**). These data suggest the presence of a small number of large aggregates in the samples. The samples including St-PGA-PD(5)-hyd-Dox (St-PGA-PD(5)-hyd-Dox and St-PGA-PD(5)-Das + St-PGA-PD(5)-hyd-Dox) showed sizes of ~800 nm by number (**Figure 3.23J** and **P**) and intensity (**Figure 3.23K** and **Q**). Considering the predominant population by number, all reaction mixtures possessed sizes consistent with the presence of self- and co-assembled structures; however, we failed to observe homogeneous sizes from the different reaction mixtures (**Figure 3.23A**, **D**, **G**, **J**, **M**, and **P**). St-PGA-Das-Dox-CL presented the smallest size (89 ± 29 nm by number, **Figure 3.23M** and **Table 3.4**), while St-PGA-Das-hyd-Dox-CL presented the largest size (872 ± 370 nm by number, **Figure**

3.23P and **Table 3.4**). Overall, the measurements displayed acceptable quality as inferred from the correlation functions, which possessed optimal intercepts (over 0.8 and below 1.0) and exponential decay (**Figure 3.23C**, **F**, **L**, **O,** and **R**). Only St-PGA-PD(5)-Dox measurement possessed a low intercept (slightly below 0.8) and high noise level at long delay times (**Figure 3.23I**), which can be caused by the large particle size.

After confirming the presence of assembled structures in the reaction mixtures, we continued with DTT addition for crosslinking and subsequent purification by Vivaspin[TM] (30 kDa MWCO), which we monitored using UV-VIS spectroscopy until we failed to detect a signal from DTT or pyridyl thione in the ultrafiltration waste. Using a membrane cutoff of 30 kDa for Vivaspin[TM] assures the elimination of possible free unimers, pyridyl thione, and DTT while retaining the desired crosslinked structures. ^{1}H-NMR analysis of final compounds confirmed their purity, as we failed to identify any signals compatible with the presence of conjugated PD (8.50-7.15 ppm), released pyridyl thione (8.03-7.00 ppm), or DTT (multiplets at 3.77 and 2.73 ppm) (**Figure 3.24**). Additionally, we identified signals in the aromatic region (8.90-6.80 ppm) compatible with the presence of Dox and Das; however, these peaks lacked the definition required for the quantification of drug loading by ^{1}H-NMR.
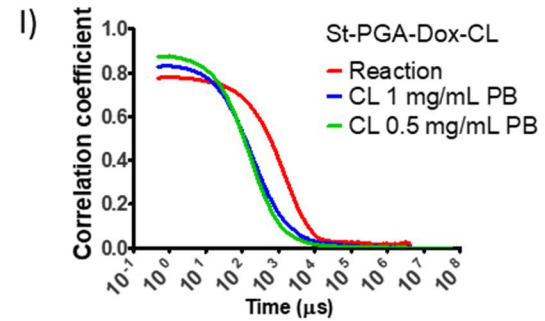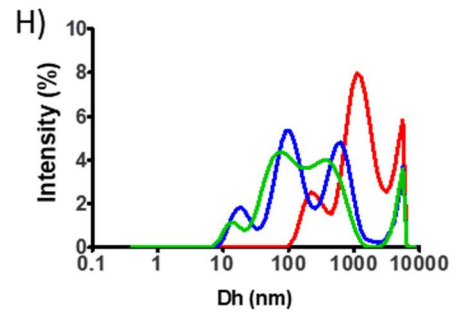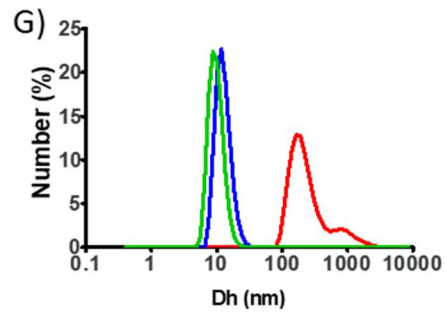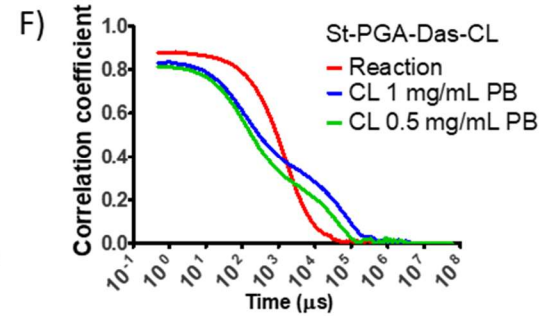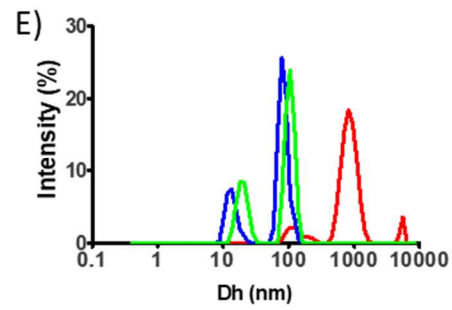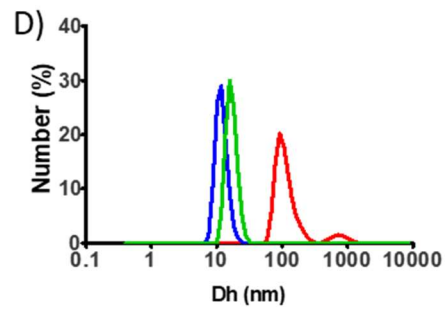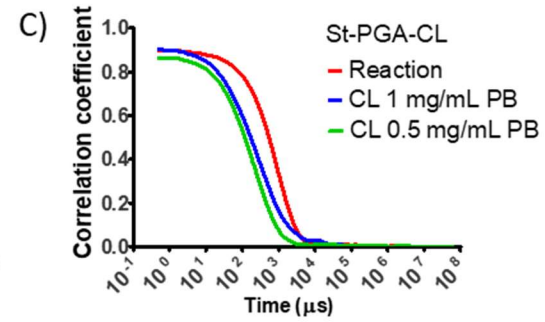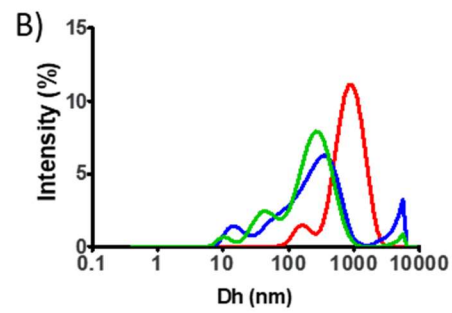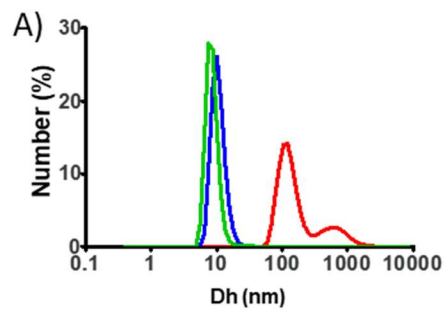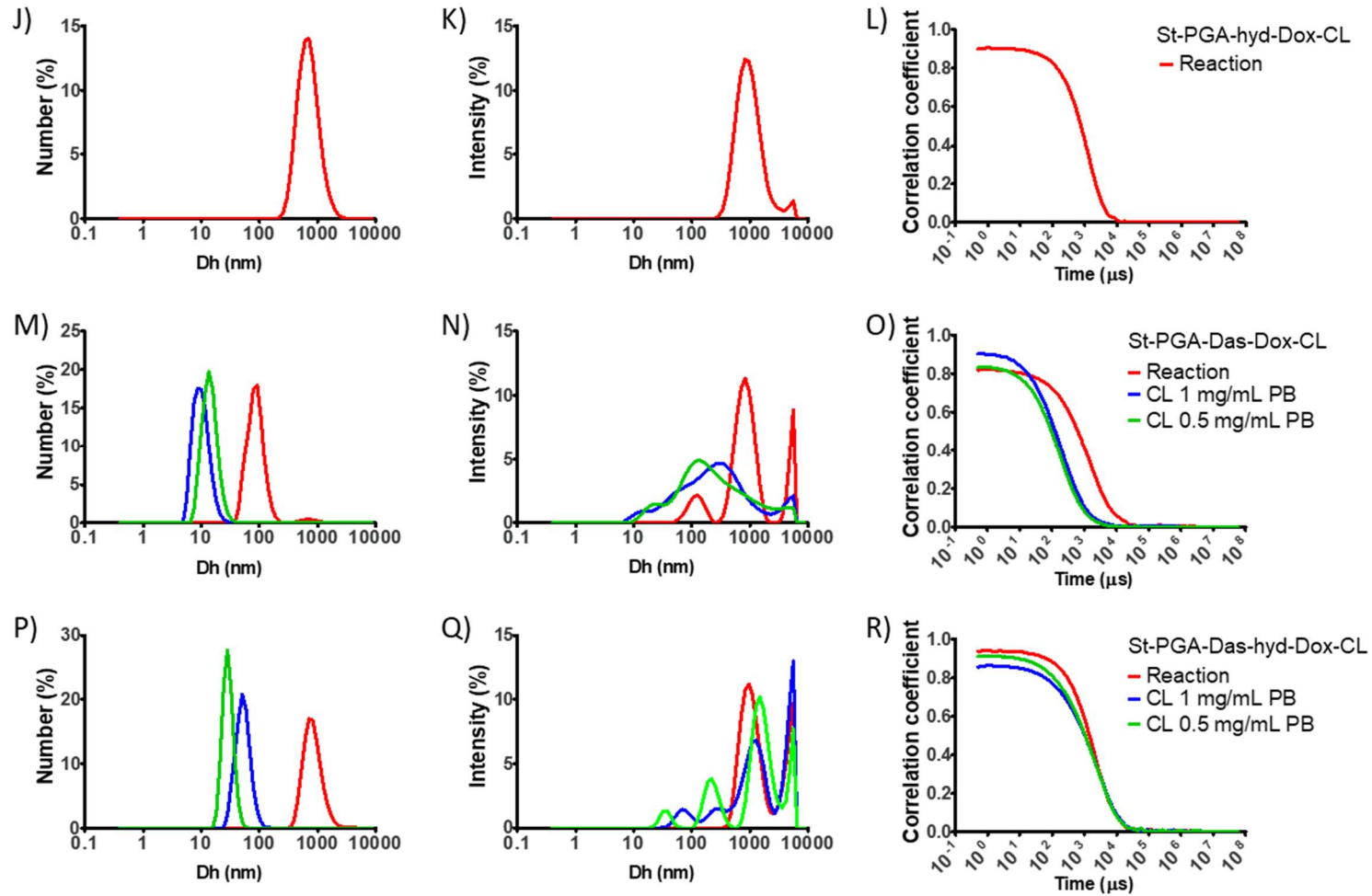
Figure 3.23. DTT-mediated crosslinking reaction size study of (**A-C**) St-PGA-CL, (**D-F**) St-PGA-Das-CL, (**G-I**) St-PGA-Dox-CL, (**J-L**) St-PGA-hyd-Dox-CL, (**M-O**) St-PGA-Das-Dox-CL, and (**P-R**) St-PGA-Das-hyd-Dox-CL. Data obtained by DLS for a sample of the reaction mixture before DTT addition (red) and the final nanosystems at 1 (blue) and 0.5 (green) mg/mL in 10 mM PB. The hydrodynamic diameter distribution by number and intensity and the respective correlation functions are displayed. Data obtained from the average result of at least three measurements.

Table 3.4. Summary of DTT-mediated crosslinked compounds characterization.

	Precursors	% wt Dox[A]	% wt Das[A]	% mol Dox[B]	% mol Das[B]	Ratio Dox:Das[C]	Dh before reaction[D] (nm)	Dh CL[E] (nm)	Dh CL[F] (nm)
St-PGA-CL	St-PGA-PD(5)	-	-	-	-	-	129 ± 47	11 ± 3	9 ± 2
St-PGA-Das-CL	St-PGA-PD(5)-Das	-	9.48	-	3.25	-	111 ± 38	12 ± 3	17 ± 3
St-PGA-Dox-CL	St-PGA-PD(5)-Dox	13.83	-	4.46	-	-	213 ± 94	13 ± 4	10 ± 3
St-PGA-hyd-Dox-CL	St-PGA-PD(5)-hyd-Dox	12.02	-	3.98	-	-	745 ± 337	n.d.	n.d.
St-PGA-Das-Dox-CL	St-PGA-PD(5)-Das and St-PGA-PD(5)-Dox	6.92	6.47	2.22	2.31	1:1.04	89 ± 29	10 ± 3	15 ± 5
St-PGA-Das-hyd-Dox-CL	St-PGA-PD(5)-Das and St-PGA-PD(5)-hyd-Dox	8.84	5.53	2.86	2.00	1:0.70	872 ± 370	54 ± 16	29 ± 6

(**A**) Obtained by UV-VIS spectroscopy. (**B**) Obtained by iterative calculation from the loading in weight percent. (**C**) Obtained using the loadings in mol percent. (**D**) Precursor assembly hydrodynamic diameter in the reaction mixture before DTT addition (2 mg/mL in MilliQ water). (**E** and **F**) Crosslinked nanosystem's hydrodynamic diameter in 10 mM PB at (**E**) 1 and (**F**) 0.5 mg/mL of polymer. Data obtained from the distributions presented in Figure 3.23 and expressed as mean ± SD.
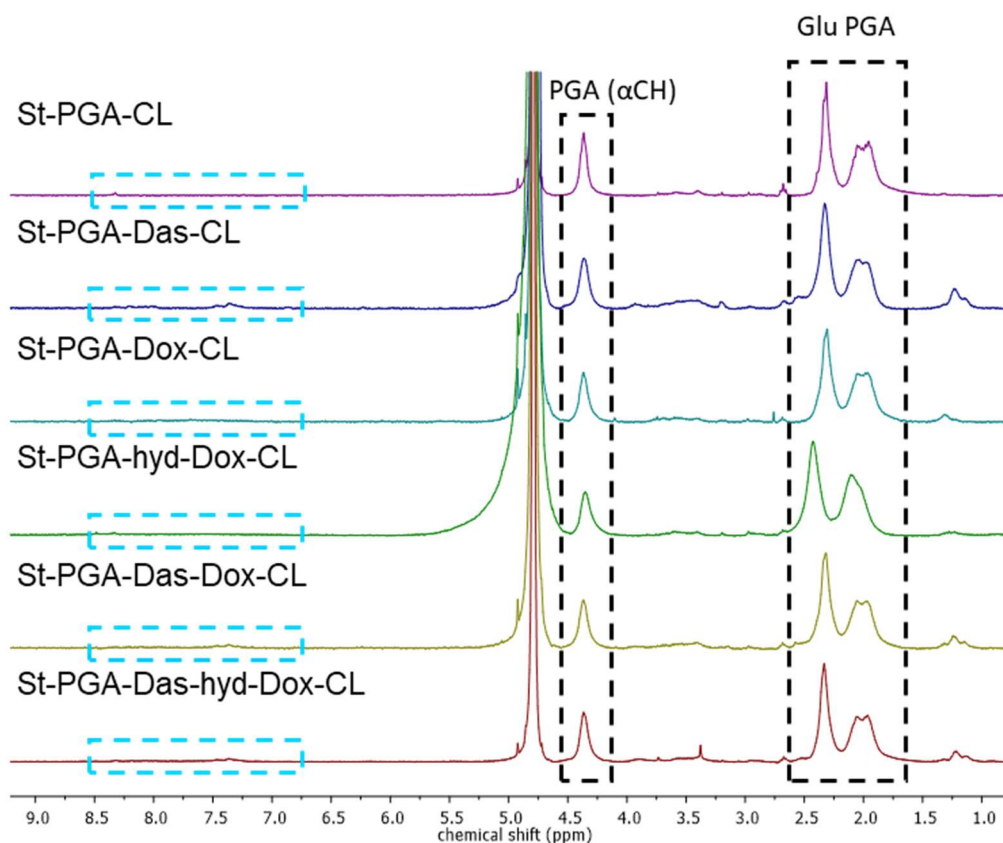
Figure 3.24. ^{1}H-NMR (D$_2$O) spectra of crosslinked compounds. The absence of aromatic signals (blue) of pyridyl thione confirms the removal of PD.

We next determined drug loading of single-drug and combination crosslinked nanosystems by UV-VIS spectroscopy (**Figure 3.25**). For the single-drug nanosystems, we obtained 3.25% mol for St-PGA-Das-CL, 4.46% mol for St-PGA-Dox-CL, and 3.98% mol for St-PGA-hyd-Dox-CL (**Table 3.4**), which agrees well with the values obtained for the precursors with PD (**Table 3.2** and **Table 3.3**). The slight decrease in conjugate loading with pH-labile linkers derives from drug release during the crosslinking reaction and purification in water. The absorbance spectra of St-PGA-Das-Dox-CL and St-PGA-Das-hyd-Dox-CL confirmed the presence of Das and Dox (**Figure 3.25**) at an approximate 1:1 ratio - 2.22% mol of Dox and 2.31% mol of Das for St-PGA-Das-Dox-CL, and 2.86% mol of Dox and 2.00% mol of Das for St-PGA-Das-hyd-Dox-CL (**Table 3.4**).
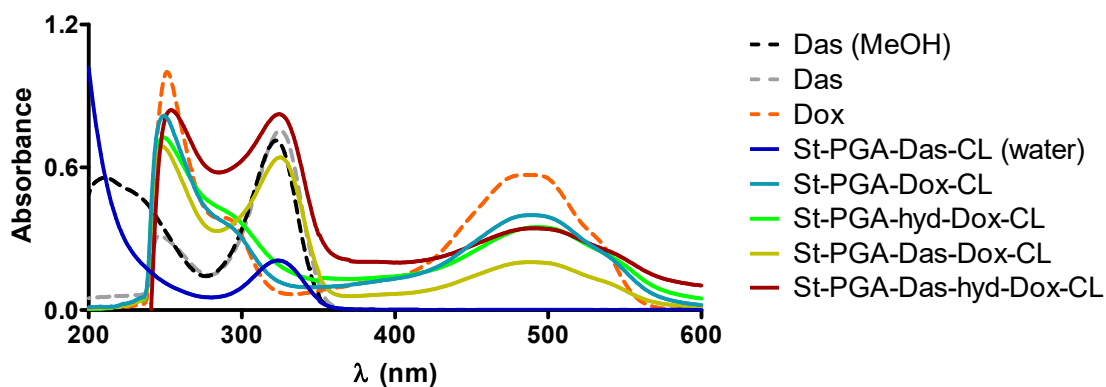
Figure 3.25. Absorbance spectra of crosslinked conjugates in DMSO:water (1:1 v/v) except St-PGA-Das-CL (prepared in MilliQ water). Spectra from Dox in DMSO:water (1:1 v/v) and Das in methanol (MeOH) and MilliQ water used as references.

Unfortunately, hydrodynamic diameter measurements of the final products in 10 mM PB failed to provide the expected results. DLS measurements provided sizes that agreed with the presence of unimers (< 20 nm, **Figure 3.23A**, **D**, **G**, and **M**, and **Table 3.4**) or small aggregates in the case of St-PGA-Das-hyd-Dox-CL (**Figure 3.23P**). Indeed, St-PGA-Das-hyd-Dox-CL displayed a hydrodynamic diameter of 54 ± 16 nm at 1 mg/mL in 10 mM PB, a size more than ten times smaller than the hydrodynamic diameter measured before the reaction - 872 ± 370 nm (**Table 3.4**). These results suggest that this first strategy failed to stabilize the self- and co-assembled combination conjugate structures.

Overall, the correlation functions associated with these measurements confirmed the acceptable quality of the measurements, with optimal intercepts (over 0.8 and below 1.0) and exponential decay (**Figure 3.23C**, **I**, **L**, **O**, and **R**) except St-PGA-Das-CL. While the measurement before DTT addition exhibited optimal quality, the measurements at 0.5 and 1 mg/mL of St-PGA-Das-CL crosslinked conjugate in 10 mM PB displayed a non-pure exponential decay and high noise level at long delay times (**Figure 3.23F**), suggesting a poor quality of the measurements probably due to the presence of two defined particle populations, which agrees with the size distribution by

intensity (**Figure 3.23E**). We failed to measure the size of St-PGA-hyd-Dox-CL in 10 mM PB due to low solubility.

We next performed Ellman's assay to detect free thiol groups in St-PGA-CL to evaluate the degree of crosslinking. We did not perform Ellman's assay for single or combination conjugates as the absorbance of Dox and Das interfere with the detection of free thiols at 412 nm. The results demonstrated that 37% of thiols present in St-PGA-CL remained unoxidized after crosslinking. Thus, the reaction allowed the release of pyridyl thione, exposing the thiol groups but failed to oxidize these groups completely, which may explain the lack of nanosystem stability.

In summary, the DTT-mediated crosslinking reaction successfully displaces pyridyl thione, exposing the free thiol groups introduced in the St-PGA polymer by PD conjugation; however, a percentage of these free thiols failed to oxidize and form disulfide bonds. The presence of free thiols hindered the stabilization of the self-assembled structure, as observed by comparisons of assembly size before and after crosslinking. These results suggest that stabilization requires a more considerable number of disulfide bonds to stabilize the structure or that St-PGA-PD(5) derivative assembly does not allow the adequate formation of intermolecular disulfide bonds but instead induces intramolecular disulfide bonds.

3.2.5. Study of Aggregation – CAC Determination by DLS

Inefficient self- and co-assembly may explain the disassembly in 10 mM PB and the high percentage of free thiol groups of crosslinked nanosystems. Thus, we aimed to confirm that St-PGA-PD(5)-based conjugates aggregate as expected by determining their critical aggregation concentration (CAC).

St-PGA-PD(5), St-PGA-PD(5)-Dox, St-PGA-PD(5)-hyd-Dox, and St-PGA-PD(5)-Das displayed similar behavior in water - they aggregated upon

increased conjugate concentration (**Figure 3.26**) and displayed CAC values below that determined for St-PGA (1.0 mg/mL, *Chapter 2*). For instance, St-PGA-PD(5) displayed a CAC value of 0.2 mg/mL (**Table 3.5**).
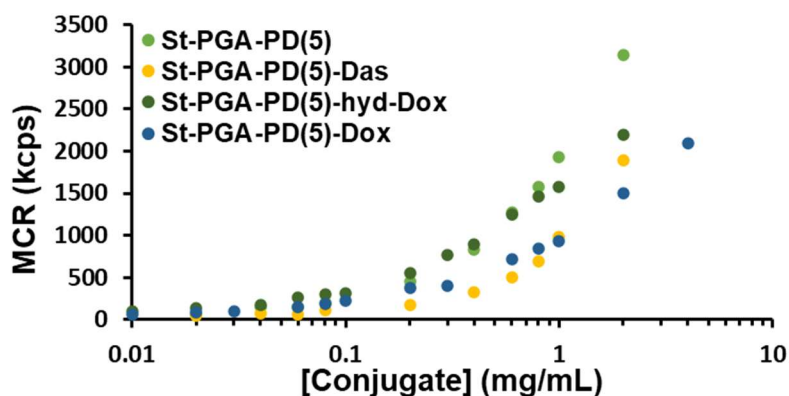

Figure 3.26. CAC determination graph of St-PGA-PD(5)-based conjugates. Data represented as average mean count rate (MCR) of two measurements vs. conjugate concentration (logarithmic scale). These data were employed for the graphical determination of CAC.

Table 3.5. St-PGA-PD(5)-based compounds CAC.

Conjugate	CAC (mg/mL)
St-PGA-PD(5)	0.2
St-PGA-PD(5)-Dox	0.4
St-PGA-PD(5)-hyd-Dox	0.1
St-PGA-PD(5)-Das	0.5

CAC calculated graphically from Figure 3.26.

When we compared the values obtained for these St-PGA-PD(5)-based conjugates with those obtained for St-PGA-drug conjugates (*Chapter 2*), we observed the influence of PD in conjugate aggregation. St-PGA-PD(5)-based compounds St-PGA-PD(5)-Das and St-PGA-PD(5)-hyd-Dox displayed lower CAC values compared to their St-PGA-drug counterparts (St-PGA-Das and St-PGA-hyd-Dox) - 0.5 mg/mL versus 0.8 mg/mL and 0.1 mg/mL versus 0.2 mg/mL, respectively.

St-PGA-PD(5)-Dox displayed a higher CAC value than its pH-labile counterpart - 0.4 mg/mL versus 0.1 mg/mL of St-PGA-PD(5)-hyd-Dox (**Table 3.5**), suggesting that the hydrazone linker may favor aggregation due to the greater exposure of Dox in the conjugate derived from the greater spacer length, or at least a different Dox intramolecular rearrangement. This result may explain the larger size exhibited by St-PGA-PD(5)-hyd-Dox in water and 10 mM PB compared to St-PGA-PD(5)-Dox (**Table 3.2**). This behavior does not agree with previous CD data (**Figure 3.12**), which demonstrates Dox dimerization only in the case of the direct amide conjugation (St-PGA-PD(5)-Dox). In the presence of hydrazone, significant Dox dimerization did not occur (absence of negative band at 540 nm, **Figure 3.12**). Therefore, these findings support the existence of a non-specific aggregation process occurring where drug-linker hydrophobic interactions play a role in impeding Dox dimerization. The effect of spacer length on pH-responsive Dox conjugates (hydrazone vs. N-ε-maleimidocaproic acid hydrazide - EMCH - linkers) has been previously reported in our group with linear PGA as a carrier (34). These findings demonstrate the importance of spacer design on conjugate solution conformation, which drives drug loading capabilities *and* drug release kinetics and, therefore, nanoconjugate safety and therapeutic output.

Despite the differences between conjugates, St-PGA-PD(5), St-PGA-PD(5)-Dox, St-PGA-PD(5)-hyd-Dox, and St-PGA-PD(5)-Das self-assembled at 2 mg/mL (above the CAC values, **Table 3.5**). Thus, a lack of self-assembly does not prompt the failed DTT-mediated crosslinking reaction in single-drug assemblies.

We aimed to confirm the co-assembly of St-PGA-PD(5) modified with Dox and Das, choosing a method based on the rapid exchange of unimers observed for St-PGA. The addition of another St-PGA conjugate to a pre-assembled nanosystem in water leads to the incorporation of the added conjugate to the previously formed structure (1). We can detect this

phenomenon by determining the CAC value of one St-PGA-based compound in the presence of a different St-PGA conjugate at a concentration below its CAC and comparing the value with that of the former species alone (39).

When we determined the CAC of St-PGA-PD(5)-Das in the presence of 0.1 mg/mL of St-PGA-PD(5)-Dox (below its CAC), we observed a shift in the graph to lower concentration values (**Figure 3.27**). This result suggests that the presence of St-PGA-PD(5)-Dox does not hamper conjugate assembly and that its presence enhances the process (39,40). When we performed the same experiment in the presence of St-PGA-PD(5)-hyd-Dox, the CAC shifted to higher values (**Figure 3.27**), meaning that the self-assembled structures start forming at higher St-PGA-PD(5)-Das concentrations on the presence of the second species. This result suggests that the presence of St-PGA-PD(5)-hyd-Dox interferes with the self-assembly of St-PGA-PD(5)-Das (4,41). Therefore, the co-assembly of St-PGA-PD(5)-drug molecules depends greatly on the drug and linker used for conjugation.
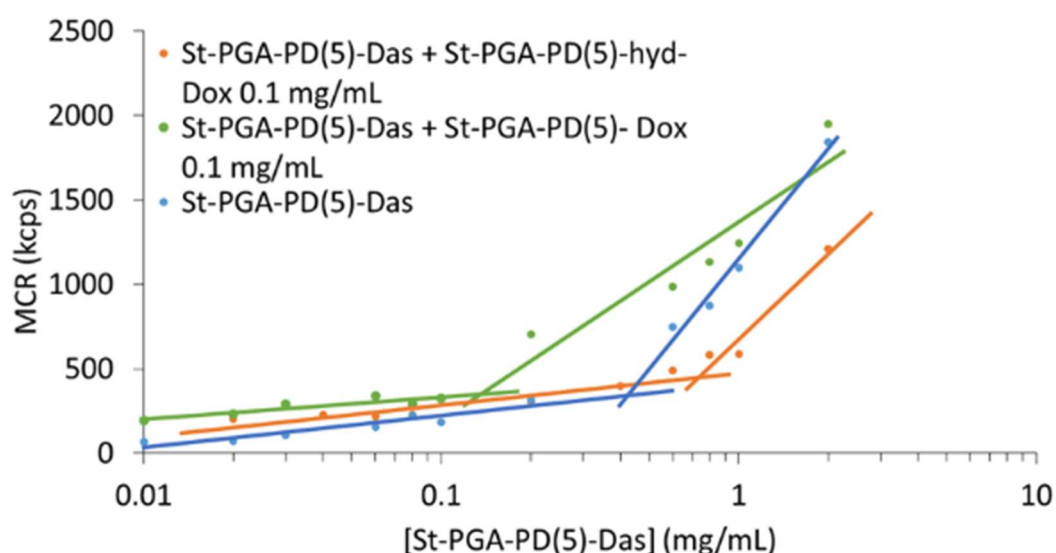

Figure 3.27. Characterization of co-assembly of St-PGA-PD(5)-Das with St-PGA-PD(5)-hyd-Dox and St-PGA-PD(5)-Dox by DLS. Average MCR obtained from two measurements plotted versus St-PGA-PD(5)-Das concentration.

Further studies will support a more in-depth understanding of the interaction between St-PGA-based conjugates and how the drugs and linkers define the co-assembly of these structures. Other spectroscopic techniques, such as diffusion-ordered spectroscopy (DOSY), have been used to study St-PGA co-assembly (1); however, we need to identify a specific ^{1}H-NMR signal in the spectra that unambiguously distinguishes one species from the other to evaluate co-assembly by DOSY. The conjugates synthesized in this work failed to provide a specific signal as the aromatic protons of Dox and Das appear in the same region of the spectrum, overlapping with PD's aromatic protons. Moreover, the peaks of the non-aromatic protons of Dox and Das overlap with PGA and/or PD signals (e.g., **Figure 3.9A** and **Figure 3.15A**), thereby impeding the use of DOSY to evaluate the co-assembly of our conjugates. Novel studies in our laboratory that lie outside the context of this work are currently exploring the use of different linkers and loadings to shed more light on the co-assembly behavior of St-PGA-based conjugates.

In summary, we proved the aggregation of St-PGA-PD(5)-based conjugates in water (**Figure 3.26**); however, the study of the co-assembly of St-PGA-PD(5)-Das with St-PGA-PD(5)-Dox and St-PGA-PD(5)-hyd-Dox suggested altered behaviors depending on the drug and linker used (**Figure 3.27**). These results disagree with previously reported data, where St-PGA molecules modified with different moieties efficiently co-assembled (39) and displayed a highly dynamic unimer exchange between pre-formed self-assembled structures (1). Regardless, the DTT-mediated crosslinking protocol (described in the previous section) failed to stabilize the structures formed by only one St-PGA-PD(5)-derived species, which efficiently self-assembled according to the CAC study. Therefore, the lack of stabilization after DTT reaction does not respond to a lack of aggregation. We believe the aggregation mechanism followed by St-PGA-PD(5)-based conjugates differs from the extraordinary behavior of St-PGA and may reduce thiol moiety

337

exposure, impeding the effective formation of intermolecular disulfide bonds between St-PGA and subsequent stabilization.

Therefore, we moved forward by exploring novel strategies to improve the exposure or access to thiol moieties.
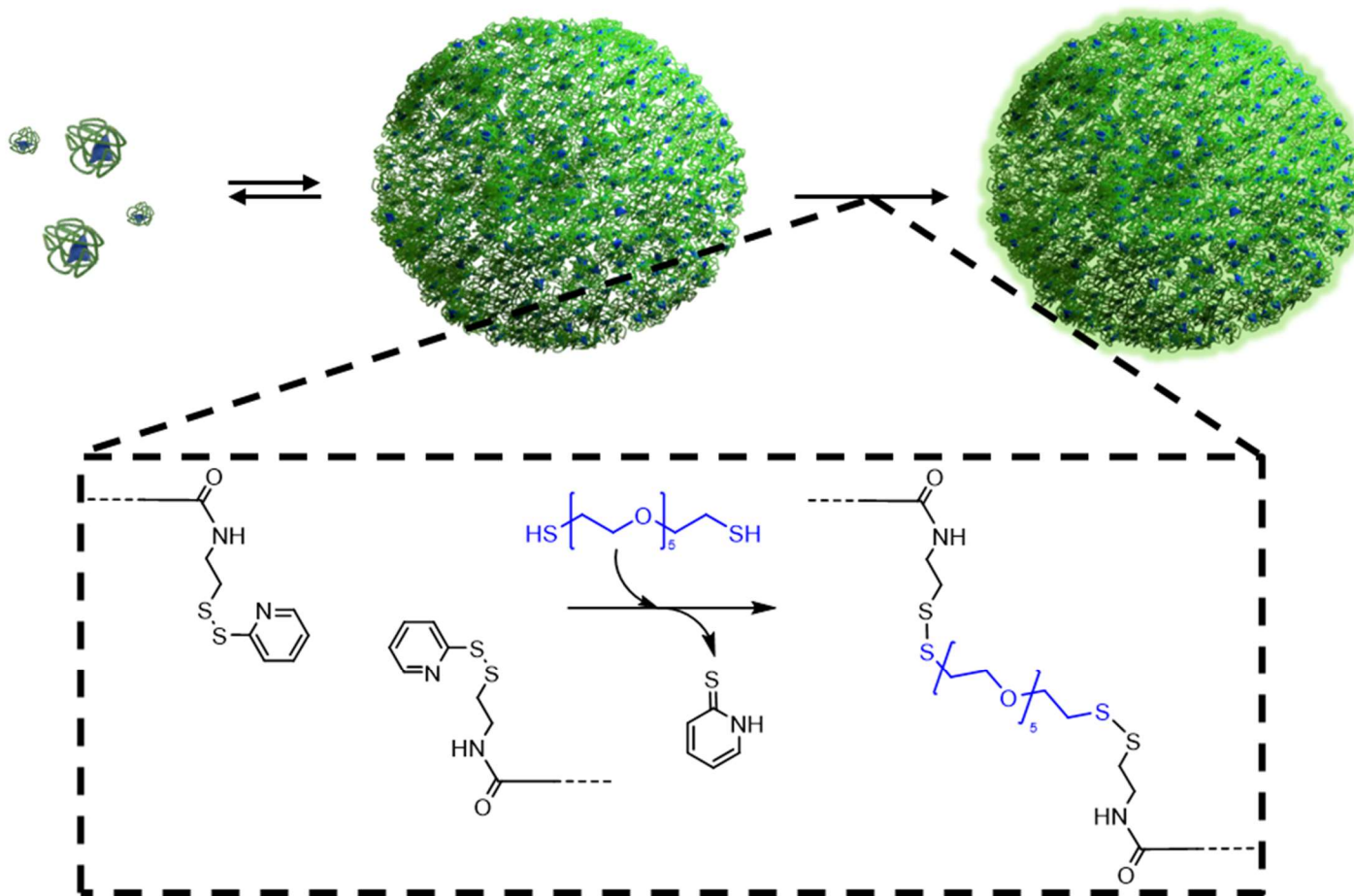
3.2.6.   PEG-mediated Crosslinking

Given that the DTT-mediated protocol for self- and co-assemblies stabilization by disulfide bonds failed to yield stable structures in 10 mM PB, the heterogeneous behavior of the conjugates regarding co-assembly, and the low solubility of St-PGA-hyd-Dox-CL in 10 mM PB, we considered using an alternative stabilization method. As described in previous sections, the PD moiety allows two different approaches for redox-responsive crosslinking of polymer assemblies. After exploring the first approach (as described in earlier sections), we switched focus to the second approach, which uses dithiol-containing molecules as bridges to form disulfide bonds via a thiol exchange reaction with the PD groups of different molecules (25).

Of note, several studies have employed this approach as an alternative to direct disulfide bond crosslinking when this strategy failed to stabilize nanostructures. Boehnke et al. (42) used a 1 kDa poly(ethylene glycol) (PEG)-dithiol molecule to form nanogels based on PDEM and methacrylate-functionalized trehalose (TrMA) random copolymers. The addition of the PEG crosslinker, even at low amounts (12.5% mol), yielded nanogels without the need for an additional reducing agent in aqueous media (PBS) in a short time frame (3 h). Following a similar approach, Fuoco et al. (43) obtained redox-responsive nanoparticles based on PD-modified poly-L-lactide polymers. They performed the reaction in organic media due to polymer insolubility in water, observing complete pyridyl thione release 30 min after adding PEG-dithiol (1 kDa). The PEG-containing nanoparticles

displayed solubility in aqueous media and stability in 10 µM GSH; however, the presence of 10 mM GSH prompted rapid disassembly and precipitation.

We followed this alternative approach using a short-length PEG-dithiol molecule as a spacer to facilitate access to the thiol moieties in St-PGA and, thus, prompt intermolecular crosslinking. We used a five-unit PEG chain with free thiol groups at both ends (SH-PEG$_5$-SH); we avoided using longer PEG chains to promote excretion after structure disassembly in the target cell. When added to the St-PGA-PD(5) solution in water, each free thiol group of the spacer displaces the pyridyl thione group of a different St-PGA-PD(5) molecule, crosslinking them and hence stabilizing the assembly (**Scheme 3.7**). In this case, we quenched the remaining free thiol groups with β-mercaptoethanol, aiming to reduce the percentage of free thiols in the final stabilized structure.

Scheme 3.7. PEG-mediated crosslinking reaction. Free thiol groups in SH-PEG$_5$-SH spacer induce the displacement of pyridyl thione, forming disulfide bonds. Structure crosslinking and stabilization occur when each thiol group of SH-PEG$_5$-SH forms a disulfide bond with a different St-PGA-PD(5) molecule.

We performed the reaction at 2 mg/mL of St-PGA-PD(5) to maintain the same conditions as used for the DTT-mediated and CuAAC crosslinking strategies (1). The study of reaction kinetics by UV-VIS spectroscopy revealed that the SH-PEG$_5$-SH-mediated crosslinking reaction took longer than the DTT-mediated procedure but less than CuAAC (1). While pyridyl thione release reached a plateau after 20 min (**Figure 3.28A**), this value remains adequate for the purpose of our study. Nevertheless, this procedure cleaved only 76% of the PD moieties in St-PGA-PD(5) after SH-PEG$_5$-SH addition. Quenching with β-mercaptoethanol did not increase this percentage (**Figure 3.28A** and **B**); therefore, St-PGA molecules with PD will remain in the mixture after the reaction has terminated. A 76% cleaved PD moieties is lower than reported for the DTT-mediated crosslinking procedure in the previous section and literature for direct disulfide nanogel stabilization (17,18,22). Together, these data further support the idea of a low exposure of the PD moieties due to St-PGA conformation in solution, which reduces the percentage of cleaved PD by SH-PEG$_5$-SH compared to other nanosystems and compared to the DTT-mediated reaction, as DTT can easily access the hidden PD moieties due to its small size.
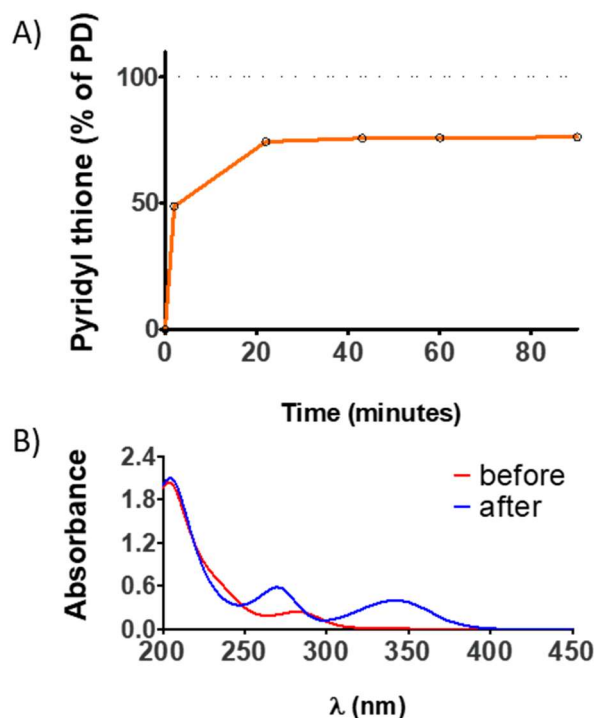
Figure 3.28. PEG-mediated crosslinking reaction kinetics for St-PGA-PD(5) conjugate. (**A** and **B**) Pyridyl thione release monitored by UV-VIS spectroscopy. (**A**) Evolution of pyridyl thione release. Data expressed as a percentage of released pyridyl thione versus reaction time. Dotted line marks the maximal PD release (100%). (**B**) Absorbance spectra before (red) and after reaction and β-mercaptoethanol addition (blue).

We evaluated aggregate size in the reaction mixture after each reaction step to define how the addition of each reagent affected particle size. Before adding any reagent, the nanosystem displayed a size of 476 ± 197 nm, considering the size distribution by number obtained by DLS (**Figure 3.29A**), even after filtration by a 0.22 µm filter, which demonstrates the nanosystem's dynamic behavior in aqueous solutions. By intensity, the nanosystem also exhibited a single population with a large size (604 ± 235 nm) (**Figure 3.29B**). We did not observe any variation in the hydrodynamic diameter after the addition of SH-PEG$_5$-SH (**Figure 3.29A** and **B**), which agrees with data reported for other systems (42). We also evaluated size after the addition of β-mercaptoethanol and during purification via dialysis (3.5-5 kDa MWCO) immediately before lyophilization (**Figure 3.29A** and **B**). While β-mercaptoethanol did not affect assembly size, we observed a slight reduction in the hydrodynamic diameter during dialysis (**Figure 3.29A** and

B), although this value remained compatible with the presence of St-PGA aggregates. The correlation functions associated with these measurements of the reaction mixture possessed optimal quality with exponential decay and intercepts between 0.8 and 1.0 (**Figure 3.29C**).
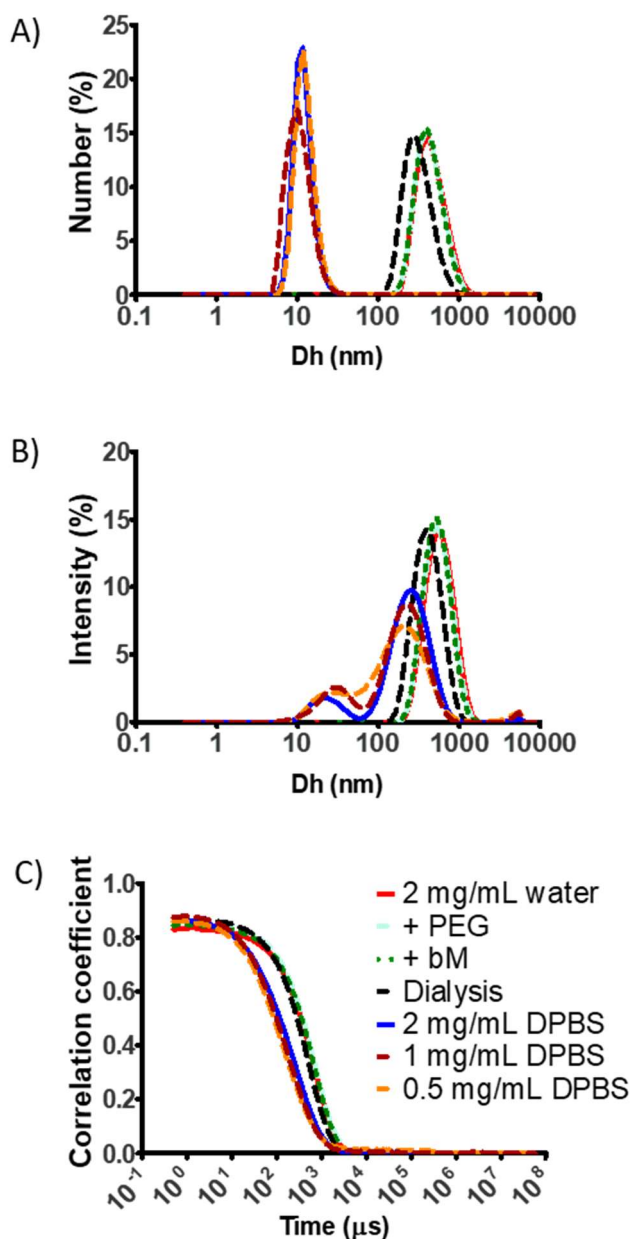

Figure 3.29. PEG-mediated crosslinking reaction size study for St-PGA-PD(5). Data obtained by DLS. The hydrodynamic diameter distribution by (**A**) number and (**B**) intensity and (**C**) the respective correlation functions are displayed. Data obtained from the average result of at least three measurements. PEG: SH-PEG$_5$-SH. bM: β-mercaptoethanol.

After lyophilization, we confirmed the removal of pyridyl thione (8.03-7.00 ppm) by ^{1}H-NMR (**Figure 3.30**). ^{1}H-NMR analysis failed to demonstrate any signals of conjugated PD (8.50-7.15 ppm). At 3.94-3.48 ppm, we identified peaks compatible with the presence of PEG in the nanosystem (twenty-four protons). Said signals allowed the estimation of PEG mol percentage in the final product by comparison with the peak corresponding to the α-carbon proton of PGA (4.56-4.11 ppm), obtaining 2.0% mol (**Figure 3.30**). Considering this estimation, we determined the presence of 8.5% free thiol groups in the final product by Ellman's assay. This percentage accounts for the number of free thiols in the structure (provided by SH-PEG$_5$-SH or St-PGA-PD(5)) that remain reduced (not forming a disulfide bond) despite β-mercaptoethanol quenching. This value represents an improvement compared to the DTT-mediated crosslinking protocol.
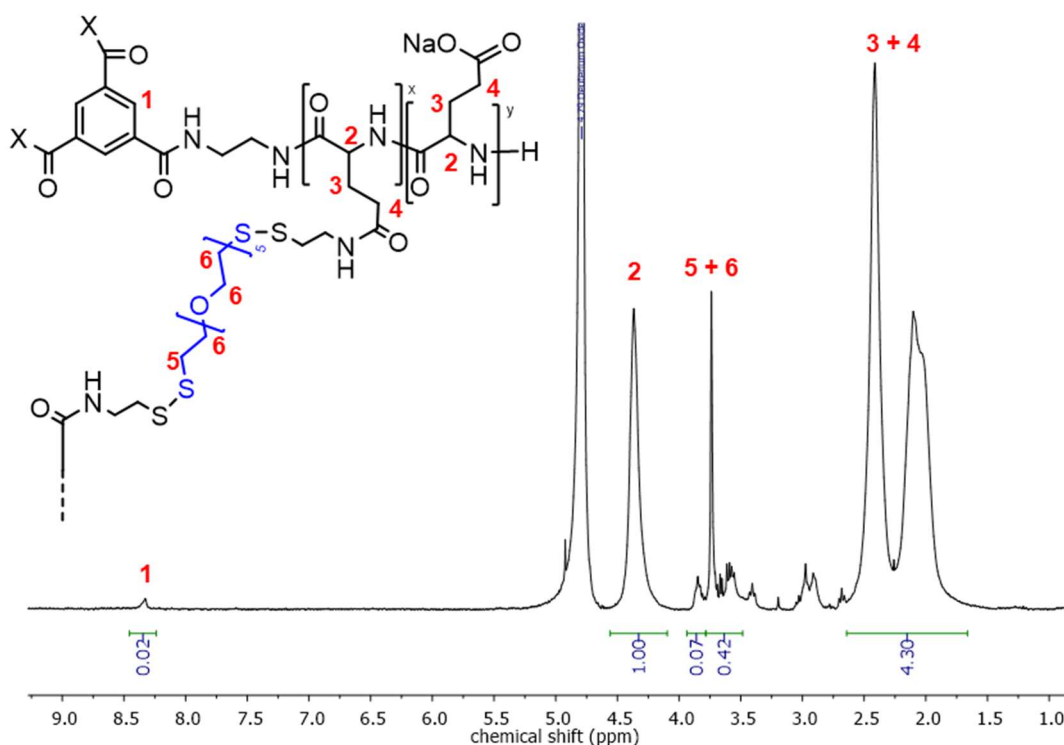

Figure 3.30. ^{1}H-NMR (D$_2$O) spectra of St-PGA-CL obtained via PEG-mediated crosslinking. The lack of PD-related signals in the aromatic region (8.5-7.0 ppm) confirms complete PD and pyridyl thione removal. The peaks at 4.0-3.5 ppm (5+6) confirm the presence of PEG in the final structure.

Unfortunately, the final compound size in DPBS failed to prove architectural stability in high ionic strength media, with single populations with sizes corresponding to the St-PGA unimer at different concentrations (2, 1, and 0.5 mg/mL), according to the DLS size distribution by number (**Figure 3.29A**). By intensity, the final compound displayed two populations, one with a size corresponding to the St-PGA unimer (~20%) and another one with a size compatible with the presence of aggregates (~80%) (**Figure 3.29B**). The correlation functions associated with these measurements possessed optimal quality, with exponential decay and intercepts between 0.8 and 1.0 (**Figure 3.29B**). Overall, these data suggest the presence of a small number of aggregates, which may be stabilized structures, in a sample otherwise formed by St-PGA unimers.

In summary, the addition of SH-PEG$_5$-SH prompts the displacement of pyridyl thione, incorporating itself into the architecture without altering structure size. The addition of β-mercaptoethanol for free thiol quenching does not alter structure size but fails to quench all the thiol groups present in the nanosystem. Nevertheless, the final compound displayed a lower free thiol percentage than the St-PGA-CL obtained by the DTT-mediated crosslinking protocol. Despite this reduction, SH-PEG$_5$-SH-mediated crosslinking failed to yield stable nanosystems in high ionic strength media, suggesting the need for a higher number of disulfide bonds to stabilize the structure or a better quenching procedure that impedes disulfide-thiol exchange reactions that destabilize the structure.

Additionally, we cannot rule out that the conjugate's aggregation behavior facilitates intramolecular disulfide bonding instead of intermolecular crosslinking. Studies have reported this phenomenon for other polymer-based drug delivery systems; a low polymer concentration in the reaction mixture led to the formation of intramolecular disulfide bonds, while an increase in the polymer concentration helped intermolecular bonding due to the increased proximity of polymer molecules, yielding stable nanosystems

(42,43). Thus, an increment in St-PGA-PD(5) concentration could lead to effective crosslinking; however, as described earlier (**Figure 3.6B**), increasing St-PGA-PD(5) concentration leads to the formation of larger structures (> 800 nm). The use of St-PGA-PD(10) could represent an alternative, as we observed a change in behavior in water at high polymer concentrations (**Figure 3.6C**). According to our study, we observed a size for St-PGA-PD(10) assemblies at 10 mg/mL of ~84 nm, which remains compatible with intravenous administration and optimal for our purpose; however, the application of this polymer for pH-responsive drug delivery requires the optimization of synthetic protocols for St-PGA-PD(10)-hyd-Dox and St-PGA-PD(10)-Das.

3.2.7. Stabilization by Inverse Nanoprecipitation

As the self-assembly-based crosslinking strategies failed to yield stable, viable nanosystems for further therapeutic development, we considered a different approach. The inverse nanoprecipitation method does not rely on the self- or co-assembly of polymer-drug molecules but polymer aggregation following the injection of a dilute polymer solution into a polymer non-solvent (44). Thus, this method allows the application of St-PGA-drug molecules regardless of their co-assembly status. Furthermore, due to the mild conditions involved, this method has supported the encapsulation of proteins (44) or siRNA (45) by co-precipitation and the crosslinking of polymer-drug conjugates bearing pH-labile linkers (46).

Following a similar strategy to the one we present here, the Calderón research group obtained polyglycerol (PG)-based nanogels bearing Dox and paclitaxel (PTX) conjugated through a pH-labile hydrazone linker (47). Vossen et al. modified PG molecules with thiol groups, which they then employed to conjugate drugs via EMCH to different PG molecules. The authors then used the remaining free thiol groups to stabilize the nanogels by reacting with acrylate groups introduced in another PG molecule used as

a macro crosslinker. The three polymers (PG-Dox-SH, PG-Ptx-SH, and PG-acrylate) were dissolved in water and precipitated in acetone to form nanogels. Water's fast diffusion into acetone increases polymer concentrations, thereby allowing the reaction between thiol and acrylate groups and the stabilization of the nanogel. Using this method, they effectively controlled drug ratio by altering the amount of PG-Dox-SH and PG-Ptx-SH in the reaction and final nanosystem size by changing the total polymer concentration in water and the water:acetone ratio. Due to conjugation via pH-responsive hydrazone bonds, the authors achieved controlled drug release in acidic (pH 4.0) environment, proving the potential of this nanosystem for the treatment of solid tumors (47).

We hypothesized that this method could also yield therapeutic St-PGA-based nanogels by co-precipitation of St-PGA-PD(5)-drug molecules. As a proof of concept, we pursued the crosslinking of St-PGA-PD(5). As in the previous section, we employed SH-PEG$_5$-SH as a spacer to facilitate crosslinking between molecules and improve the final compound's solubility. In this case, we dissolved St-PGA-PD(5) in MilliQ water to a concentration of 2 mg/mL, rapidly added SH-PEG$_5$-SH to the solution, and then immediately precipitated the mixture in cold acetone. We expected that rapid solvent diffusion (water) into the non-solvent (acetone) would increase St-PGA-PD(5) concentration, allowing the thiol exchange reaction between the free thiol groups of SH-PEG$_5$-SH and St-PGA-PD(5), stabilizing the structure. As described in the previous section, we added β-mercaptoethanol to quench the remaining free thiol groups.

After reaction and purification via dialysis (Float-A-Lyzer 1 kDa MWCO), we confirmed the complete removal of conjugated PD (8.50-7.15 ppm), free pyridyl thione (8.03-7.00 ppm), and the incorporation of PEG to the structure by ^{1}H-NMR (3.95-3.46 ppm) (**Figure 3.31**). Comparing PEG signals (twenty-four protons) and the α-carbon proton of PGA (4.47 - 4.00 ppm), we obtained 3.9% mol PEG in the final product. PEG-PEG

dimerization by disulfide bonds may explain this high percentage. Considering this percentage of PEG in the structure, Ellman's assay determined 1.9% of reduced (free) thiol groups in the final product. This value represents an improvement compared to the DTT-mediated and the SH-PEG$_5$-SH-mediated crosslinking protocols.
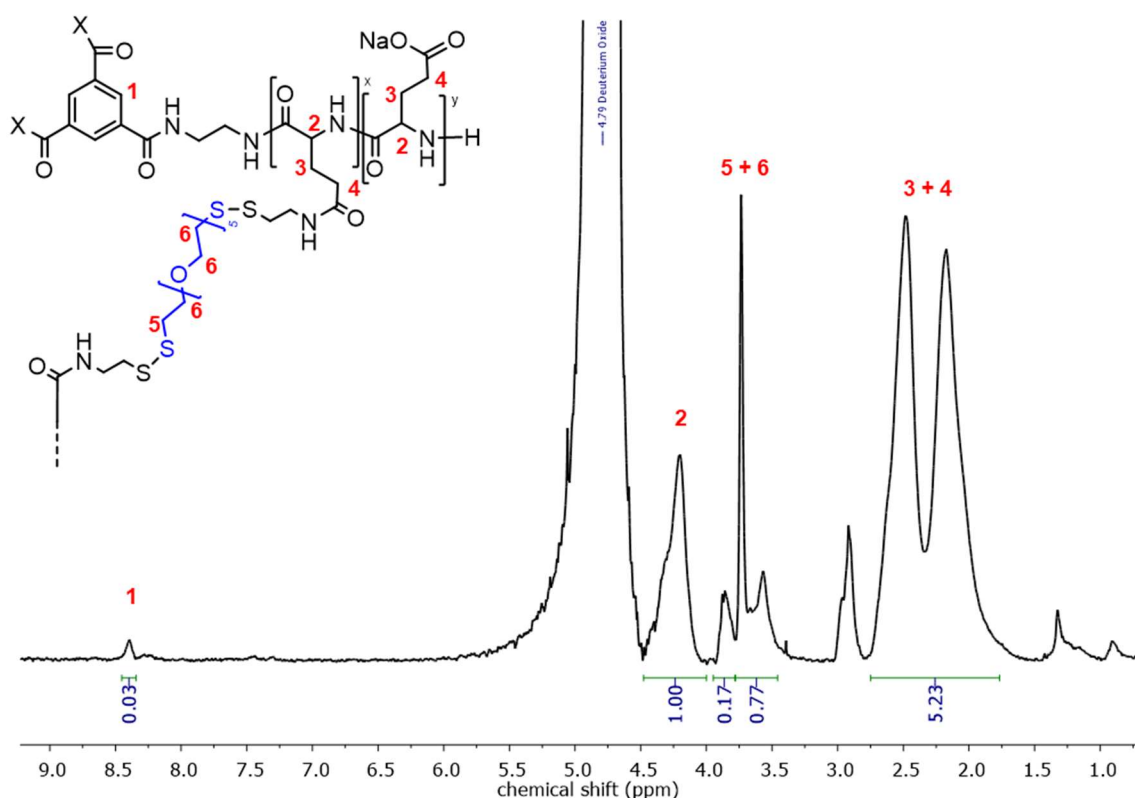

Figure 3.31. ^{1}H-NMR (PBS in D$_2$O) of St-PGA-CL obtained by inverse nanoprecipitation. The lack of PD-related signals in the aromatic region (8.5-7.0 ppm) confirms complete PD and pyridyl thione removal. The peaks at 4.0-3.5 ppm (5+6) confirm the presence of PEG in the final structure

Unfortunately, the evaluation of the final nanosystem size in high ionic strength conditions (e.g., DPBS) provided evidence that the nanosystem exhibited a hydrodynamic diameter similar to free St-PGA unimers (~14 nm) as determined by the number distribution obtained by DLS (**Figure 3.32A**). Similar to the results obtained for the protocols evaluated earlier, the size distribution by intensity provided evidence for a second large (~440 nm) population that suggests the presence of a low number of aggregates in the

sample (**Figure 3.32B**) that may represent stabilized structures. The correlation function associated with the measurement confirmed the quality of the results displaying an intercept over 0.8 and below 1.0 and exponential decay (**Figure 3.32C**).
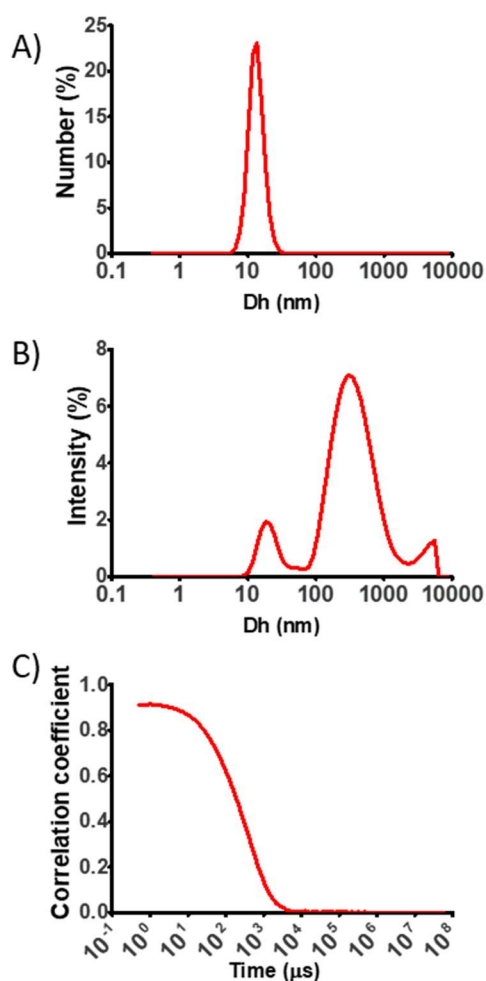

Figure 3.32. Size distribution of St-PGA-CL obtained by inverse nanoprecipitation obtained by DLS in DPBS at 2 mg/mL. The hydrodynamic diameter distribution by (**A**) number and (**B**) intensity and (**C**) the correlation function are displayed. Data obtained from the average result of at least three measurements

Overall, this protocol failed to form stable St-PGA-PD(5)-based nanogels. In this case, we discounted the idea that the lack of stabilization responds to a low polymer concentration in the reaction, as precipitation in acetone would increase the polymer concentration dramatically and, thus,

the proximity between St-PGA-PD(5) molecules. The lack of final structure stability may derive from the small percentage of free thiol groups, which could allow disulfide-thiol exchange reactions, destabilizing the final structure, or by an insufficient number of intermolecular bonds. The configuration of St-PGA-PD(5) in MilliQ water may impede the access of SH-PEG$_5$-SH to the PD moieties, hindering intermolecular bonding. We believe that further modifications in the protocol will enhance intermolecular bonding. Inverse nanoprecipitation trials with St-PGA-PD(10) are currently ongoing to increase the number of disulfide bonds present in the final structure.

Table 3.6 summarizes the three stabilization protocols explored in this work.

Table 3.6. Summary of evaluated crosslinking protocols.

Crosslinking method	Reducing agent	Crosslinker	Quenching	Time (min)	Efficiency (% of PD)	Free thiols (% of SH)	Dh^A (nm)
DTT-mediated	DTT	None	No	5	99*	37	11
SH-PEG$_5$-SH-mediated	None	SH-PEG$_5$-SH	β-mercaptoethanol	20	76	8.5	11
Inverse nanoprecipitation	None	SH-PEG$_5$-SH	β-mercaptoethanol	-	-	1.9	14

(**A**) Final product size in high ionic strength media (PB or DPBS) at 2 or 1 mg/mL. Data obtained from the distribution by number obtained by DLS. *Value obtained for St-PGA-PD(5) crosslinking reaction.

3.3. Conclusions

The use of stabilized self-assembled St-PGA nanosystems as macromolecular drug carriers provides numerous advantages. Specifically, their increased circulation time compared to the St-PGA unimer and its linear counterpart converts these nanosystems into potentially efficient drug delivery systems for the development of cancer therapeutic; however, the stabilization method employed for these structures employed a non-biodegradable linker (1,35,36). We aimed to develop an alternative stabilization method for said assemblies employing disulfide bonds. These reversible covalent bonds would provide the nanosystem with responsiveness to highly reducing conditions, such as that encountered in the tumor microenvironment.

Encouraged by the dynamic behavior of St-PGA self- and co-assemblies in aqueous solution, we designed a bottom-up strategy to synthesize combination conjugates by conjugating a pair of drugs (Dox and Das) to different St-PGA molecules and crosslinking the co-assembled structures. To this aim, we conjugated the crosslinking moiety PD and the drugs Dox or Das to the same St-PGA molecule, obtaining the building blocks for the synthesis of combination conjugates through the co-assembly of Dox and Das-bearing polymers.

The physico-chemical characterization of these conjugates demonstrated that St-PGA modification with hydrophobic moieties significantly influenced polymer behavior in aqueous media. We chose St-PGA-PD(5)-derived drug conjugates (St-PGA-PD(5)-Dox, St-PGA-PD(5)-hyd-Dox, and St-PGA-PD(5)-Das) to move forward as they maintained the secondary structure of the starting material under a wide range of conditions. We failed to generate the St-PGA-PD(10)-hyd-Dox conjugate, which would have allowed us to study the pH-labile hydrazone linker for PD(10) conjugates. The study of self- and co-assembly revealed that hydrophobic moieties alter the process with the extent depending on the moiety and the

352

linker used for conjugation. Nevertheless, conjugate size in water revealed the presence of aggregates. We believe that the hydrophobic interactions introduced by PD, Dox, and Das conjugation act with the glutamic acid ionic interactions in a complex fashion, altering the extraordinary behavior that drives St-PGA self- and co-assembly. New experiments performed following a quality-by-design approach may aid a fuller understanding of the effect of hydrophobic moieties and linkers in conjugate behavior in solution and allow us to control self- and co-assembly (48).

We explored various synthetic protocols to stabilize the assemblies formed by St-PGA-PD(5) (**Table 3.6**). In all cases, we observed the rapid and efficient release of the pyridyl thione group, leaving the thiol groups exposed to form disulfide bonds. The determination of free thiol groups in the final nanosystems demonstrated different efficacies in forming disulfide bonds. Given the lowest value of free thiol groups, the inverse nanoprecipitation protocol stands out among the other crosslinking protocols. Furthermore, this strategy does not rely on St-PGA-drug molecule co-assembly and thereby broadens the spectrum of usable drug-linker combinations and, thus, possible combination conjugates.

Unfortunately, none of the synthetic protocols examined herein yielded stable nanosystems under high ionic strength media, providing sizes in agreement with a complete structural disassembly in PB or DPBS. We hypothesize that this lack of stability derives from the presence of reduced (free) thiol groups in the final compound (which would trigger disulfide-thiol exchange reactions that destabilize the structure) or the poor exposure of the thiol groups of St-PGA-PD(5)-derived molecules (which would prompt the formation of intramolecular disulfide bonds instead of intermolecular bonds) or a low number of intermolecular disulfide bonds in the final product.

3.4. Materials and Methods

3.4.1. Materials

All solvents were of analytical grade and obtained from Scharlab Chemicals (Scharlab S.L., Barcelona, Spain), except trifluoroacetic acid (TFA), which was obtained from TCI Deutschland GmbH (Eschborn, Germany). Deuterated solvents were obtained from Deutero GmbH (Kastellaun, Germany). All chemicals were reagent grade, obtained from Sigma-Aldrich (Merck KGaA, Darmstadt, Germany), with the following exceptions: 4-Dimethylaminopyridine (DMAP) was obtained from Fluka (Thermo Fisher GmbH, Kandel, Germany) and N,N'-Diisopropylcarbodiimide (DIC) was obtained from Iris Biotech GmbH (Marktredwitz, Germany). 4-(4,6-dimethoxy-1,3,5-triazin-2-yl)-4-methyl-morpholinium tetrafluoroborate (DMTMM BF$_4$) was synthesized as described in reference (49). Pyridyl dithiol cysteamine (PD) was synthesized as described in reference (50). Doxorubicin HCl was obtained from MedKoo Biosciences, Inc. (Morrisville, NC, USA). Dasatinib was obtained from LC Laboratories Inc. (Woburn MA, USA). Ellman's reagent was obtained from Chem Cruz (Santa Cruz Biotechnology Inc., Heidelberg, Germany). Preparative SEC was performed using Sephadex LH-20 or Sephadex G25 medium from GE Healthcare (Global Life Sciences Solutions USA LLC, Marlborough, MA, USA). Ultrafiltration was performed in a Millipore (Merck KGaA, Darmstadt, Germany) ultrafiltration device fitted with a 3, 10, 30 or 50 kDa molecular weight cut off (MWCO) regenerated cellulose membrane (Vivaspin^{TM}). Float-A-Lyzer devices were obtained from Spectrum Laboratories Inc. (New Brunswick NJ, USA). HyClone Dulbecco's phosphate-buffered saline (DPBS) was obtained from Cytiva UK Ltd. (Buckinghamshire, UK).

3.4.2. Synthetic Protocols

3.4.2.1. Synthesis of Star-polyglutamic Acid

354

The 3-arm star-shaped polyglutamic acid used herein was synthesized as described in *Chapter 2*.

3.4.2.2. General Protocol for the Conjugation of Pyridyl Dithiol Cysteamine to Star-poly(glutamic acid) (St-PGA-PD(5/10))

In a round bottom flask fitted with a stir bar and an N_2 inlet and outlet, St-PGA (1 eq.) was dissolved in DMF anhydrous (anh.) to a concentration of 10 mg/mL. Once completely dissolved, pH was adjusted to 5 with DIEA. Then, DMTMM BF_4 was dissolved in DMF anh. and added to the reaction mixture. The reaction was left to proceed under stirring for 30 min. After that, pyridyl dithiol cysteamine (PD) was dissolved in DMF anh. and added to the reaction. Two percentages of modification were pursued, 5% mol and 10% mol, and the amounts of DMTMM BF_4 and PD were adjusted accordingly. For 5% and 10% mol, 0.075 eq. and 0.15 eq. of both compounds were added, respectively, and the pH was adjusted to 8 with DIEA. Then, the reaction was left to proceed at room temperature for 48 h. The product was precipitated in cold diethyl ether and dried. Then, the product was converted to its water-soluble salt form by adding the minimum amount of sodium bicarbonate in water. Once complete dissolution was achieved, the product was precipitated by dropwise addition of HCl 5 M. The white precipitated was recovered by centrifugation and washed two times with acid water (pH ~3) and one time with MilliQ water before lyophilization. PD loading was determined by ^{1}H-NMR by comparing the signals from the PD pyridyl group protons to the PGA α-carbon proton.

St-PGA-PD(5). Yield: 90%, CE: 100%. St-PGA-PD(10). Yield: 70%, CE 80%. ^{1}H-NMR: δ_H (300 MHz, D_2O) 8.53-8.20 (1H initiator, 1H PD), 7.94-7.70 (2H PD), 7.38-7.18 (1H PD), 4.50-4.20 (1H αC PGA), 4.00 – 2.55 (4H CH_2-CH_2 PD), 2.50-1.70 (4H Glu PGA).

3.4.2.3. Conjugation of Doxorubicin to St-PGA-PD(5/10) Through an Amide Bond (St-PGA-PD(5/10)-Dox)

In a two-neck round bottom flask fitted with a stir bar and an N_2 inlet and outlet, St-PGA-PD(5) (2.9 mmol, 1 eq.) or St-PGA-PD(10) (2.8 mmol, 1 eq.) was dissolved in DMF anh. DMTMM BF_4 (0.22 mmol for St-PGA-PD(5) or 0.21 mmol for St-PGA-PD(10), 0.075 eq.) was dissolved in DMF anh. and added to the St-PGA-PD solution. pH was adjusted to 5 by adding DIEA, and the reaction was left to proceed under stirring for 30 min. Then, Dox (0.21 mmol, 0.075 eq.) was dissolved in DMF anh. and added to the reaction. pH was adjusted to 8 with DIEA, and the reaction was left to proceed covered from the light, under stirring at room temperature, for 48 h. The product was precipitated in cold diethyl ether. Then, the dried product was purified by size exclusion chromatography with a Sephadex LH-20 column using DMF as eluent, followed by a second precipitation in cold diethyl ether. The product's salt form was obtained upon the addition of sodium bicarbonate and purification by Vivaspin™ (3 kDa MWCO). Finally, the red-colored product was freeze-dried. Dox loading was determined as described in *Chapter 2*.

St-PGA-PD(5)-Dox: yield: 85%, CE: 87%. St-PGA-PD(10)-Dox: yield: 65%, CE: 75%. ^{1}H-NMR: δ_H (300 MHz, D_2O) 8.75-6.54 (1H initiator, 4H pyridyl PD, 3H Dox), 4.50-4.10 (1H αC PGA, 2H Dox), 4.10-2.52 (4H CH_2-CH_2 PD, 6H Dox), 2.49-1.63 (4H Glu PGA, 2H Dox).

3.4.2.4. General Protocol for the Conjugation of Doxorubicin to St-PGA-PD(5/10) Through a Hydrazone Linker (St-PGA-PD(5)-hyd-Dox)

3.4.2.4.1. Conjugation of Tert-butyl Carbazate Moiety

The protocol for TBC conjugation was similar to that reported in *Chapter 2* with slight modifications. Briefly, in a round-bottom flask fitted with a stir bar and an N_2 inlet and outlet, St-PGA-PD(5) or St-PGA-PD(10) (1 eq.)

was dissolved in DMF anh. to a concentration of 10 mg/mL. Once completely dissolved, pH was adjusted to 5 with DIEA. Then, DMTMM BF$_4$ (0.075 eq.) was dissolved in DMF anh. and added to the reaction mixture. The reaction was left to proceed under stirring for 30 min. After that, tert-butyl carbazate (0.075 eq.) was dissolved in DMF anh. and added to the reaction. Then, pH was adjusted to 8 with DIEA, and the reaction was left under stirring at room temperature for 48 h. Finally, the product was precipitated in cold diethyl ether and dried. TBC loading was determined by ^{1}H-NMR by comparing Boc group signals to the PGA α-carbon proton.

St-PGA-PD(5)-TBC: yield: 95%, CE: 100%. St-PGA-PD(10)-TBC: yield: 95%, CE: 20%. ^{1}H-NMR: δ$_H$ (300 MHz, D$_2$O) 8.53-8.25 (1H initiator, 1H PD), 7.97-7.65 (2H PD), 7.40-7.15 (1H PD), 4.50-4.15 (1H αC PGA), 4.10-2.53 (4H CH$_2$-CH$_2$ PD), 2.50-1.70 (4H Glu PGA), 1.50 (9H Boc).

3.4.2.4.2. Deprotection of Tert-butyl Carbazate (St-PGA-PD(5)-hydrazine)

Deprotection of TBC to expose the hydrazine moiety was performed as described in *Chapter 2*.

St-PGA-PD(5)-hydrazine. Yield: 90%. ^{1}H-NMR: δ$_H$ (300 MHz, D$_2$O) 8.53-8.25 (1H initiator, 1H PD), 7.97-7.60 (2H PD), 7.50-7.10 (1H PD), 4.50-4.15 (1H αC PGA), 4.10-2.55 (4H CH$_2$-CH$_2$ PD), 2.54-1.60 (4H Glu PGA).

3.4.2.4.3. Conjugation of Doxorubicin to St-PGA-PD(5)-hydrazine (St-PGA-PD(5)-hyd-Dox)

The protocol for Dox conjugation to St-PGA-PD(5)-hydrazine was similar to that reported in *Chapter 2* with modifications. Briefly, in a two-neck round-bottom flask fitted with a stir bar and an N$_2$ inlet and outlet, St-PGA-PD-hydrazine (1 eq.) was dissolved in DMSO anh. Once completely

dissolved, Dox (0.075 eq.) was added to the reaction. Then, three drops of pure acetic acid were added, and the reaction was left to proceed protected from light, under stirring at room temperature for 72 h. After that, one volume of THF was added to the reaction mixture. Then the product was precipitated in cold diethyl ether. After that, the product was purified by size exclusion chromatography with a Sephadex LH-20 column using DMF as eluent, followed by a second precipitation in diethyl ether. The product's salt form was obtained upon the addition of sodium bicarbonate and purification by Vivaspin^{TM} (3 kDa MWCO). Finally, it was freeze-dried. Alternatively, DMSO was evaporated from the reaction mixture, and the product was dissolved in DMF to perform a preparative size exclusion chromatography with Sephadex LH-20 resin using DMF as eluent. Fractions containing the red-colored product were collected. Sodium bicarbonate 0.1 M was added to the collected fractions before DMF evaporation. Conversion to the salt form was achieved by water and sodium bicarbonate 1 M addition to the dried product and purification by preparative size exclusion chromatography using Sephadex G-25 medium resin and MilliQ water as eluent. Fractions containing the red-colored product were collected and freeze-dried. Dox loading was determined as described in *Chapter 2*.

St-PGA-PD(5)-hyd-Dox. Yield: 53%. CE: 89%. ^{1}H-NMR: δ_H (300 MHz, D$_2$O) 8.75-6.54 (1H initiator, 4H PD, 3H Dox), 4.55-4.05 (1H αC PGA, 2H Dox), 4.05-2.52 (4H CH$_2$-CH$_2$ PD, 6H Dox), 2.50-1.60 (4H Glu PGA, 2H Dox).

3.4.2.5.   General Protocol for the Conjugation of Dasatinib to St-PGA-PD(5/10) Through an Ester Bond (St-PGA-PD(5/10)-Das)

The protocol for Das conjugation was similar to that reported in *Chapter 2* with modifications. Briefly, St-PGA-PD(5) or St-PGA-PD(10) (1 eq.) was dissolved in DMF anh. in a two-neck round-bottom flask fitted with a stir bar and N$_2$ inlet and outlet. Once completely dissolved, DIC (0.15 eq.)

was added, and the reaction was left under stirring for 20 min. After that, DMAP (0.03 eq.) and Das (0.15 eq.) were dissolved in DMF anh. and added to the reaction. Finally, pH was adjusted to 8 with DIEA. The reaction was left to proceed under stirring at room temperature for 72 h. The product was precipitated in cold diethyl ether and purified by size exclusion chromatography with a Sephadex LH-20 column using DMF as eluent, followed by a second precipitation in cold diethyl ether. The product's salt form was obtained upon adding sodium bicarbonate in water and purification by Vivaspin™ (3kDa MWCO). Finally, the product was freeze-dried. Alternatively, the product was purified by size exclusion chromatography with Sephadex LH-20 resin using DMF as eluent. The elution was monitored by TLC, and the fractions containing the product were collected. Sodium bicarbonate 0.1 M was added to the collected fractions before DMF evaporation. Conversion to the salt form was achieved by water and sodium bicarbonate 1 M addition to the dried product and purification by size exclusion chromatography using Sephadex G-25 medium resin and MilliQ water as eluent. Fractions containing the product were collected and freeze-dried. Das loading was determined by UV-VIS spectroscopy using a calibration curve of the drug in methanol at 324 nm and conjugate samples in MilliQ water.

St-PGA-PD(5)-Das: yield: 85%, CE: 67%. St-PGA-PD(10)-Das: yield: 80%, CE: 64%. ^{1}H-NMR: δ_H (300 MHz, D$_2$O) 8.75-6.54 (1H initiator, 4H PD, 5H Das), 4.50-4.00 (1H αC PGA, 2H Das), 4.00-2.56 (4H CH$_2$-CH$_2$ PD, 10H Das), 2.55-1.50 (4H Glu PGA, 6H Das).

3.4.2.6. DTT-mediated Crosslinking Reaction

3.4.2.6.1. Study of Reaction Kinetics

The reaction kinetics was studied for reactions with St-PGA-PD(5) and St-PGA-PD(10). The release of pyridyl thione was monitored by UV-VIS spectroscopy and ^{1}H-NMR and used to determine reaction kinetics.

For UV-VIS spectroscopy, 2 mg of polymer were dissolved in 1 mL of MilliQ water. An absorbance spectrum from 190 to 400 nm was obtained for a 1/10 dilution of each polymer solution as time zero status (the absorbance at 343nm was considered as blank for pyridyl thione determination). Dithiothreitol (DTT) was added to the reaction as solid in the amount required to achieve a final concentration of 7.5 mM. Absorbance spectra of 1/10 dilutions of the reaction mixture were obtained at fixed time points after DTT addition. The spectra were obtained in a JASCO V-630 spectrophotometer at 25 °C with 1.0 cm matched quartz cells and with a spectral bandwidth of 1 nm. The accumulation of three spectra was recorded. Thus, absorbance at 343 nm was measured at each time point to determine reaction kinetics. The concentration of free pyridyl thione was obtained by the Lambert-Beer equation:

$$A = \varepsilon \times c \times l$$

where ε is the extinction coefficient of pyridyl thione at 343 nm (8.08 x 10^3 M^{-1} cm^{-1}), c is pyridyl thione concentration in the sample, and l is the optical path length in centimeters (1.0 cm). The percentage of cleaved PD was calculated considering the polymer PD loading (obtained by ^{1}H-NMR) and the polymer concentration in the reaction mixture.

For ^{1}H-NMR, 2 mg of polymer were dissolved in 1 mL of deuterated water (D_2O). A ^{1}H-NMR spectrum was obtained for each polymer in this condition as time zero. DTT was added as solid in the amount required to achieve a final concentration of 7.5 mM. Consecutive ^{1}H-NMR spectra were obtained. Changes in the PD signal were monitored in the spectra to

determine the release of pyridyl thione and, consequently, the reaction kinetics.

3.4.2.6.2. General Procedure for DTT-mediated Crosslinking Reaction

The St-PGA-PD-derived compound was dissolved in MilliQ water to a concentration of 2mg/mL inside a glass vial fitted with a stir bar. DTT was added as a solid in the amount required to achieve a final concentration of 7.5 mM. After the reaction was finished, the crosslinked product was purified by Vivaspin™ (30 kDa MWCO). The purification was monitored by UV-VIS spectra acquisition of water waste in each round of ultracentrifugation until no signal of DTT or pyridyl thione was observed. Then, the product was freeze-dried. PD removal was confirmed by ^{1}H-NMR. Free thiol quantification was performed as described in section *3.4.3.5.Free Thiol Determination by Ellman's Assay*. Dox and Das loading were determined as described in *Chapter 2*.

St-PGA-CL. Yield: 79%. ^{1}H-NMR: δ_H (300 MHz, D_2O) 8.32 (1H initiator), 4.56-4.11 (1H αC PGA), 4.11 – 2.57 (4H CH_2-CH_2 PD), 2.57-1.47 (4H Glu PGA).

St-PGA-Das-CL. Yield: 74%.^{1}H-NMR: δ_H (300 MHz, D_2O) 8.70-6.70 (1H initiator, 5H Das), 4.59-4.11 (1H αC PGA, 2H Das), 4.11-2.52 (4H CH_2-CH_2 PD, 10H Das), 2.52-1.60 (4H Glu PGA, 6H Das).

St-PGA-Dox-CL. Yield: 78%.^{1}H-NMR: δ_H (300 MHz, D_2O) 8.83-6.70 (1H initiator, 3H Dox), 4.52-4.15 (1H αC PGA, 2H Dox), 4.14-2.57 (4H CH_2-CH_2 PD, 6H Dox), 2.56-1.60 (4H Glu PGA, 2H Dox).

St-PGA-hyd-Dox-CL. Yield: 54%.^{1}H-NMR: δ_H (300 MHz, D_2O) 8.95-6.40 (1H initiator, 3H Dox), 4.49-4.09 (1H αC PGA, 2H Dox), 4.00-2.65 (4H CH_2-CH_2 PD, 6H Dox), 2.64-1.64 (4H Glu PGA, 2H Dox).

St-PGA-Das-Dox-CL. Yield: 72%. ^{1}H-NMR: δ_H (300 MHz, D$_2$O) 8.80-6.50 (1H initiator, 5H Das, 3H Dox), 4.55-4.13 (1H αC PGA, 2H Das, 2H Dox), 4.12-2.52 (4H CH$_2$-CH$_2$ PD, 10H Das, 6H Dox), 2.51-1.54 (4H Glu PGA, 6H Das, 2H Dox).

St-PGA-Das-hyd-Dox-CL. Yield: 49%. ^{1}H-NMR: δ_H (300 MHz, D$_2$O) 8.81-6.80 (1H initiator, 5H Das, 3H Dox), 4.61-4.08 (1H αC PGA, 2H Das, 2H Dox), 4.07-2.48 (4H CH$_2$-CH$_2$ PD, 10H Das, 6H Dox), 2.47-1.46 (4H Glu PGA, 6H Das, 2H Dox).

3.4.2.7. PEG-mediated Crosslinking Reaction

3.4.2.7.1. Reaction Protocol

In a glass vial fitted with a stir bar, St-PGA-PD(5) (0.15 mmol, 1 eq.) was dissolved in MilliQ water at 2 mg/mL and filtered through a 0.22 µm syringe filter. Then, SH-PEG$_5$-SH (0.006 mmol, 0.03 eq.) was added to the polymer solution, and the reaction was left to proceed for 120 min. Then, β-mercaptoethanol (0.007 mmol, 0.04 eq.) was added, and the reaction was left under stirring for 30 min to ensure the quenching of the remaining free thiols. The product was purified by dialysis (Float-A-Lyzer, 3.5 kDa MWCO) against water and freeze-dried. PD removal was confirmed by ^{1}H-NMR. PEG loading was determined by ^{1}H-NMR by comparing the peaks of PEG protons with the peak corresponding to PGA α-carbon proton. Free thiol quantification was performed as described in section *3.4.3.5.Free Thiol Determination by Ellman's Assay*.

Yield: 82%. ^{1}H-NMR: δ_H (300 MHz, D$_2$O) 8.32 (1H initiator), 4.56-4.11 (1H αC PGA), 4.00 – 2.60 (4H CH$_2$-CH$_2$ PD, 24H PEG), 2.63-1.67 (4H Glu PGA).

3.4.2.7.2. Study of Reaction Kinetics

At fixed time points, 80 µL aliquots were taken from the reaction mixture and diluted in 720 µL of MilliQ water (1/10 dilution). The absorbance spectrum of each diluted aliquot was obtained using JASCO V-630 spectrophotometer at 25 °C with 1.0 cm matched quartz cells and with a spectral bandwidth of 1 nm. The accumulation of three spectra from 190 nm to 600 nm was taken. The absorbance value at 343 nm was used to calculate the percentage of released pyridyl thione as described earlier (see *3.4.2.6.DTT-mediated Crosslinking Reaction*).

3.4.2.8. Stabilization by Inverse Nanoprecipitation

In a glass vial, St-PGA-PD(5) (0.13 mmol, 1.2 PD eq.) was dissolved to a concentration of 2 mg/mL in 10 mL of MilliQ water. SH-PEG$_5$-SH (0.005 mmol, 1 PD eq.) was mixed with 10 mL of MilliQ water in a separate glass vial. 10 mL of SH-PEG$_5$-SH in water were isolated using a 20 mL syringe. Immediately after, the 10 mL of polymer solution were taken with the same syringe, thus mixing both solutions. Then, the mixture was rapidly poured into 400 mL of cold acetone under vigorous stirring. The mixture was kept on ice and stirred for 15 min, then left at room temperature without stirring for 4 h. After that, β-mercaptoethanol (0.005 mmol, 1 PD eq.) was added to the mixture before acetone evaporation. The remaining aqueous phase was dialyzed against MilliQ water (Float-A-Lyzer 1 kDa MWCO). Finally, the product was freeze-dried. PD removal was confirmed by ^{1}H-NMR. PEG loading was determined by ^{1}H-NMR by comparing the peaks of PEG protons with the peak corresponding to PGA α-carbon proton. Free thiol quantification was performed as described in section *3.4.3.5.Free Thiol Determination by Ellman's Assay.*

Yield: 90%. ^{1}H-NMR: δ_H (300 MHz, D_2O) 8.39 (1H initiator), 4.47-4.00 (1H αC PGA), 4.00 – 2.77 (4H CH_2-CH_2 PD, 24H PEG), 2.77-1.50 (4H Glu PGA).

3.4.3. Characterization Techniques

NMR spectroscopy, UV-VIS spectroscopy, DLS size, and zeta potential measurements, and CAC determination were performed as described in *Chapter 2*.

3.4.3.1.   Circular Dichroism

CD Spectroscopy was performed with a J-815 CD Spectrometer (Jasco International Co., Ltd, Hachioji, Tokyo, Japan) using a Peltier thermostated cell holder (PTC-423, Jasco International Co., Ltd) with a recirculating cooler (JULABO F250, Jasco International Co., Ltd) and a 1.0 mm matched quartz cell. A nitrogen flow (~2.7 L·min^{-1}) was led through the spectrometer and controlled with a nitrogen flow monitor (Afriso Euro-Index). Polymer solutions (0.5 mg/mL, 0.2 mg/mL, and 0.1 mg/mL) were prepared in MilliQ water and in 10 mM PB pH 7.4.

3.4.3.2.   Size Exclusion Chromatography

Size exclusion chromatography (SEC) of products was performed in a Postnova Analytics Modular SEC system (Postnova Analytics GmbH, Landsberg am Lech, Germany) equipped with a RI – Refractive Index Detector (PN3150 from Postnova Analytics GmbH) and a UV-VIS detector (SPD-20A from Shimadzu Scientific Instruments, Kyoto, Japan). All the SEC studies were carried out using a TSK gel G3000PWXL column (5μm, 7.8 mm i.d. x 30 cm, Tosoh Corporation, Tokyo, Japan) with the same mobile

phase (0.1 M NaNO$_3$, 0.005% NaN$_3$) with a constant flow rate (0.7 mL/min). Samples were prepared with the mobile phase as a solvent.

3.4.3.3.   Size Determination by DLS - Evolution with Concentration and Ionic Strength

The evolution of self-assembly status with increasing amounts of salt (NaCl) was studied by DLS. Solutions of St-PGA, St-PGA-PD(5), or St-PGA-PD(10) in MilliQ water were prepared at 1, 2, 5, and 10 mg/mL. The solution's ionic strength was increased gradually by adding minimal volumes of NaCl 5 M. After each addition of NaCl, the samples were gently mixed and stabilized for at least 10 h. The size measurements were performed as described in *Chapter 2*.

3.4.3.4.   Co-assembly Studies by DLS

Co-assembly of different St-PGA-derived polymers was studied by DLS. A second species was added at a final concentration of 0.1 mg/mL (below its CAC value) to the samples of St-PGA compounds prepared for CAC determination. Samples were mixed and left to stabilize overnight before measuring the mean count rate. The mixture's CAC value was determined as described in *Chapter 2*.

3.4.3.5.   Free Thiol Determination by Ellman's Assay

The percentage of free thiol groups was determined by DTNB assay or Ellman's assay. A calibration curve was done with N-acetylcysteine. Serial dilutions were obtained from a stock solution at 0.4 mg/mL in MilliQ water. SH-PEG-SH was used as a positive control, and St-PGA-PD(5) or St-PGA was used as the negative control. Samples and controls were dissolved in MilliQ water, and 170 µL were pipetted in a 96-well plate per triplicate. Then,

20 μL of Tris 1M pH 8 were added to each well. Finally, 10 μL of DTNB stock solution (2 mM DTNB in 50 mM sodium acetate) was added to each well, and the plaque was left under stirring at room temperature for 5 min. Then, absorbance at 412 nm was measured in ClarioStar plus microplate reader (BMG Labtech).

The concentration of free thiols in the samples was obtained by interpolation in the calibration curve. The percentage of free thiols was obtained by dividing the concentration of free thiol groups in the sample between the total concentration of thiol moieties in the sample.

3.5. Bibliography

1. Duro-Castano A, Nebot VJ, Niño-Pariente A, Armiñán A, Arroyo-Crespo JJ, Paul A, et al. Capturing "Extraordinary" Soft-Assembled Charge-Like Polypeptides as a Strategy for Nanocarrier Design. Adv Mater. 2017 Oct;29(39):1702888.

2. Manning GS, Ray J. Counterion Condensation Revisited. J Biomol Struct Dyn. 1998 Oct;16(2):461–76.

3. Hsu H-P, Lee E. Counterion condensation of a polyelectrolyte. Electrochem commun. 2012 Feb;15(1):59–62.

4. Muthukumar M. Ordinary-extraordinary transition in dynamics of solutions of charged macromolecules. Proc Natl Acad Sci U S A. 2016;113(45):12627–32.

5. Fang J, Islam W, Maeda H. Exploiting the dynamics of the EPR effect and strategies to improve the therapeutic effects of nanomedicines by using EPR effect enhancers. Adv Drug Deliv Rev. 2020 Jan 1;157:142–60.

6. Chan Y, Wong T, Byrne F, Kavallaris M, Bulmus V. Acid-Labile Core Cross-Linked Micelles for pH-Triggered Release of Antitumor Drugs. Biomacromolecules. 2008 Jul;9(7):1826–36.

7. Lee SJ, Min KH, Lee HJ, Koo AN, Rim HP, Jeon BJ, et al. Ketal Cross-Linked Poly(ethylene glycol)-Poly(amino acid)s Copolymer Micelles for Efficient Intracellular Delivery of Doxorubicin. Biomacromolecules. 2011 Apr 11;12(4):1224–33.

8. Huynh VT, Binauld S, Souza PL de, Stenzel MH. Acid Degradable Cross-Linked Micelles for the Delivery of Cisplatin: A Comparison with Nondegradable Cross-Linker. Chem Mater. 2012 Aug 28;24(16):3197–211.

9.   Zhou Z, Li L, Yang Y, Xu X, Huang Y. Tumor targeting by pH-sensitive, biodegradable, cross-linked N-(2-hydroxypropyl) methacrylamide copolymer micelles. Biomaterials. 2014 Aug 1;35(24):6622–35.

10.   Wang Y, Qiao S-L, Wang H. Facile Synthesis of Peptide Cross-Linked Nanogels for Tumor Metastasis Inhibition. ACS Appl Nano Mater. 2018 Feb 23;1(2):785–92.

11.   Wang Y, Luo Y, Zhao Q, Wang Z, Xu Z, Jia X. An Enzyme-Responsive Nanogel Carrier Based on PAMAM Dendrimers for Drug Delivery. ACS Appl Mater Interfaces. 2016 Aug 10;8(31):19899–906.

12.   Bansal A, Simon MC. Glutathione metabolism in cancer progression and treatment resistance. J Cell Biol. 2018;217(7):2291–8.

13.   Lv H, Zhen C, Liu J, Yang P, Hu L, Shang P. Unraveling the Potential Role of Glutathione in Multiple Forms of Cell Death in Cancer Therapy. Oxid Med Cell Longev. 2019 Jun 10;2019:1–16.

14.   Wu G, Fang Y-Z, Yang S, Lupton JR, Turner ND. Glutathione Metabolism and Its Implications for Health. J Nutr. 2004;134(3):489–92.

15.   Estrela JM, Ortega A, Obrador E. Glutathione in Cancer Biology and Therapy. Crit Rev Clin Lab Sci. 2006 Jan 10;43(2):143–81.

16.   Wei JR, Sun J, Yang X, Ji SF, Wei YH, Li ZB. Self-crosslinking assemblies with tunable nanostructures from photoresponsive polypeptoid-based block copolymers. Polym Chem. 2020;11(2):337–43.

17.   Ryu J-H, Jiwpanich S, Chacko R, Bickerton S, Thayumanavan S. Surface-Functionalizable Polymer Nanogels with Facile Hydrophobic Guest Encapsulation Capabilities. J Am Chem Soc. 2010 Jun 23;132(24):8246–7.

18.   Ryu J-H, Chacko RT, Jiwpanich S, Bickerton S, Babu RP, Thayumanavan S. Self-Cross-Linked Polymer Nanogels: A Versatile Nanoscopic Drug Delivery Platform. J Am Chem Soc. 2010 Dec 8;132(48):17227–35.

19.   Choh S-Y, Cross D, Wang C. Facile Synthesis and Characterization of Disulfide-Cross-Linked Hyaluronic Acid Hydrogels for Protein Delivery and Cell Encapsulation. Biomacromolecules. 2011 Apr 11;12(4):1126–36.

20.   Zhang Y, Heher P, Hilborn J, Redl H, Ossipov DA. Hyaluronic acid-fibrin interpenetrating double network hydrogel prepared in situ by orthogonal disulfide cross-linking reaction for biomedical applications. Acta Biomater. 2016 Jul 1;38:23–32.

21.   Murphy RD, in het Panhuis M, Cryan S-A, Heise A. Disulphide crosslinked star block copolypeptide hydrogels: influence of block sequence order on hydrogel properties. Polym Chem. 2018;9(28):3908–16.

22.   Chen W, Meng F, Cheng R, Deng C, Feijen J, Zhong Z. Facile construction of dual-bioresponsive biodegradable micelles with superior extracellular stability and activated intracellular drug release. J Control Release. 2015 Jul 28;210:125–33.

23. Jia Z, Wong L, Davis TP, Bulmus V. One-Pot Conversion of RAFT-Generated Multifunctional Block Copolymers of HPMA to Doxorubicin Conjugated Acid- and Reductant-Sensitive Crosslinked Micelles. Biomacromolecules. 2008 Nov 10;9(11):3106–13.

24. Mocny P, Klok H-A. Reversibly Cross-Linking Polymer Brushes Using Interchain Disulfide Bonds. Macromolecules. 2020 Jan 28;53(2):731–40.

25. Altinbasak I, Arslan M, Sanyal R, Sanyal A. Pyridyl disulfide-based thiol–disulfide exchange reaction: shaping the design of redox-responsive polymeric materials. Polym Chem. 2020 Dec 22;11(48):7603–24.

26. Sui B, Cheng C, Xu P. Pyridyl Disulfide Functionalized Polymers as Nanotherapeutic Platforms. Adv Ther. 2019 Sep 24;2(9):1900062.

27. Arroyo-Crespo JJ, Deladriere C, Nebot VJ, Charbonnier D, Masiá E, Paul A, et al. Anticancer Activity Driven by Drug Linker Modification in a Polyglutamic Acid-Based Combination-Drug Conjugate. Adv Funct Mater. 2018 May 16;28(22):1800931.

28. Duro-Castano A, England RM, Razola D, Romero E, Oteo-Vives M, Morcillo MA, et al. Well-defined star-shaped polyglutamates with improved pharmacokinetic profiles as excellent candidates for biomedical applications. Mol Pharm. 2015 Oct 5;12(10):3639–49.

29. Dolz-Pérez I, Sallam MA, Masiá E, Morelló-Bolumar D, Pérez del Caz MD, Graff P, et al. Polypeptide-corticosteroid conjugates as a topical treatment approach to psoriasis. J Control Release. 2020 Feb;318:210–22.

30. WOODY RW. Circular Dichroism of Peptides. In: Conformation in Biology and Drug Design. Elsevier; 1985. p. 15–114.

31. Gallois L, Fiallo M, Garnier-Suillerot A. Comparison of the interaction of doxorubicin, daunorubicin, idarubicin and idarubicinol with large unilamellar vesicles circular dichroism study. Biochim Biophys Acta - Biomembr. 1998 Mar 6;1370(1):31–40.

32. Duro-Castano A, Sousa-Herves A, Armiñán A, Charbonnier D, Arroyo-Crespo JJ, Wedepohl S, et al. Polyglutamic acid-based crosslinked doxorubicin nanogels as an anti-metastatic treatment for triple negative breast cancer. J Control Release. 2021 Apr;332:10–20.

33. Mochida Y, Cabral H, Miura Y, Albertini F, Fukushima S, Osada K, et al. Bundled Assembly of Helical Nanostructures in Polymeric Micelles Loaded with Platinum Drugs Enhancing Therapeutic Efficiency against Pancreatic Tumor. ACS Nano. 2014 Jul 22;8(7):6724–38.

34. Arroyo-Crespo JJ, Armiñán A, Charbonnier D, Balzano-Nogueira L, Huertas-López F, Martí C, et al. Tumor microenvironment-targeted poly-L-glutamic acid-based combination conjugate for enhanced triple negative breast cancer treatment. Biomaterials. 2018 Dec;186:8–21.

35. Cuesta CM, Ibañez F, Lopez-Hidalgo R, Ureña J, Duro-Castano A, Armiñán A, et al. A targeted polypeptide-based nanoconjugate as a nanotherapeutic for alcohol-

induced neuroinflammation. Nanomedicine Nanotechnology, Biol Med. 2021 Jun 1;34:102376.

36. Duro-Castano A, Borrás C, Herranz-Pérez V, Blanco-Gandía MC, Conejos-Sánchez I, Armiñán A, et al. Targeting Alzheimer's disease with multimodal polypeptide-based nanoconjugates. Sci Adv. 2021 Mar 26;7(13):eabf9180.

37. Talelli M, Vicent MJ. Reduction Sensitive Poly(l-glutamic acid) (PGA)-Protein Conjugates Designed for Polymer Masked–Unmasked Protein Therapy. Biomacromolecules. 2014 Oct 8;15(11):4168–77.

38. Vanparijs N, Nuhn L, Paluck SJ, Kokkinopoulou M, Lieberwirth I, Maynard HD, et al. Core/shell protein-reactive nanogels via a combination of RAFT polymerization and vinyl sulfone postmodification. Nanomedicine. 2016 Oct;11(20):2631–45.

39. Duro-Castano A. Well-defined polyglutamates as carriers for the treatment of neurodegenerative diseases. University of Valencia; 2015.

40. Bahadur A, Cabana-Montenegro S, Aswal VK, Lage E V., Sandez-Macho I, Concheiro A, et al. NaCl-triggered self-assembly of hydrophilic poloxamine block copolymers. Int J Pharm. 2015 Oct;494(1):453–62.

41. Bernat V, Ringard-Lefebvre C, Le Bas G, Perly B, Djedaïni-Pilard F, Lesieur S. Inclusion Complex of n-Octyl β- <scp>d</scp> -Glucopyranoside and α-Cyclodextrin in Aqueous Solutions: Thermodynamic and Structural Characterization. Langmuir. 2008 Apr 1;24(7):3140–9.

42. Boehnke N, Kammeyer JK, Damoiseaux R, Maynard HD. Stabilization of Glucagon by Trehalose Glycopolymer Nanogels. Adv Funct Mater. 2018 Mar 17;28(10):1705475.

43. Fuoco T, Pappalardo D, Finne-Wistrand A. Redox-Responsive Disulfide Cross-Linked PLA–PEG Nanoparticles. Macromolecules. 2017 Sep 26;50(18):7052–61.

44. Steinhilber D, Witting M, Zhang X, Staegemann M, Paulus F, Friess W, et al. Surfactant free preparation of biodegradable dendritic polyglycerol nanogels by inverse nanoprecipitation for encapsulation and release of pharmaceutical biomacromolecules. J Control Release. 2013 Aug;169(3):289–95.

45. Dimde M, Neumann F, Reisbeck F, Ehrmann S, Cuellar-Camacho JL, Steinhilber D, et al. Defined pH-sensitive nanogels as gene delivery platform for siRNA mediated in vitro gene silencing. Biomater Sci. 2017;5(11):2328–36.

46. Zhang X, Achazi K, Steinhilber D, Kratz F, Dernedde J, Haag R. A facile approach for dual-responsive prodrug nanogels based on dendritic polyglycerols with minimal leaching. J Control Release. 2014 Jan 28;174(1):209–16.

47. Vossen L, Wedepohl S, Calderón M. A Facile, One-Pot, Surfactant-Free Nanoprecipitation Method for the Preparation of Nanogels from Polyglycerol–Drug Conjugates that Can Be Freely Assembled for Combination Therapy Applications. Polymers (Basel). 2018 Apr 3;10(4):398.

48. Đorđević S, Gonzalez MM, Conejos-Sánchez I, Carreira B, Pozzi S, Acúrcio RC, et al. Current hurdles to the translation of nanomedicines from bench to the clinic. Drug Deliv Transl Res. 2021 Jul 23;1–26.

49. Kaminski ZJ, Kolesinska B, Kolesinska J, Sabatino G, Chelli M, Rovero P, et al. N-triazinylammonium tetrafluoroborates. A new generation of efficient coupling reagents useful for peptide synthesis. J Am Chem Soc. 2005;127(48):16912–20.

50. Vlies AJ van der, O'Neil CP, Hasegawa U, Hammond N, Hubbell JA. Synthesis of Pyridyl Disulfide-Functionalized Nanoparticles for Conjugating Thiol-Containing Small Molecules, Peptides, and Proteins. Bioconjug Chem. 2010 Apr 21;21(4):653–62.

CHAPTER 4.   RATIONAL DESIGN OF BRAIN-TARGETED COMBINATION CONJUGATES FOR THE TREATMENT OF BREAST CANCER BRAIN METASTASIS

4.1. Introduction and Background

Breast cancer is the second most common cause of brain metastasis after lung cancer, with HER2+ and triple negative breast cancer (TNBC) displaying the highest incidence (1–3). Although the development of brain metastasis represents a late event in disease progress (4,5), 30-50% of patients with metastatic breast cancer develop brain metastasis (6), with incidence depending on the subtype and other risk factors such as the presence of metastasis in lungs or liver (7). The increasing incidence of breast cancer brain metastasis may derive from improvements in treatment strategies for primary disease, which has increased patients' life expectancy and, thus, the probability of developing brain metastasis (1,2,6). Brain metastases not only entail a poor prognosis (survival of TNBC patients who develop brain metastasis ranges from three to four months (1)) but also associate with neurological impairments and an associated reduction in quality of life (1–3).

The clinical management of breast cancer brain metastasis has traditionally relied on local approaches since the blood-brain barrier (BBB) hinders the penetration of 98% of small drugs and ~100% of biological agents from the blood to the brain (6,8,9). Additionally, during metastatic colonization in the brain, tumor cells co-opt brain capillaries and alter the BBB's structure, forming the so-called blood-tumor barrier (BTB) (3); however, this process is not uniform, provoking heterogeneous tumor perfusion (10). Thus, while the BTB may display greater permeability than the BBB, the underlying heterogeneity does not support the achievement of cytotoxic concentrations of systemically administered therapies in the brain (3,9).

Novel nanomedicine-based strategies to bypass the BBB have been developed to overcome this obstacle to the development of systemic therapies for brain disorders. The so-called "trojan horse" strategy represents the most studied approach for brain delivery of nanomedicines

373

(11,12). The trojan horse strategy employs the conjugation of ligands of specific BBB receptors to a nanocarrier to promote intact barrier crossing via receptor-mediated transcytosis (RMT) (13), an active transcellular pathway followed by hormones, growth factors, and lipoproteins, among other macromolecules (11). Differential expression of BBB receptors compared to other tissues and different pathological conditions make this strategy highly selective. Low-density lipoprotein receptor (LDLR)-related protein 1 (LRP-1) represent one of the most studied receptors for trojan horse strategies (11). Consequently, the LRP-1 ligand Angiopep-2 (ANG) peptide has shown promise as a component of drug delivery systems. ANG has been employed to deliver DNA plasmids (14), peptides (15), antibodies (16), and enzymes (17) to the brain. Angiochem Inc. (Montreal, Canada) has developed several ANG-drug conjugates to treat brain tumors (18,19); these include ANG1005, an ANG-paclitaxel conjugate, which demonstrated 161-fold greater uptake in the brain than free paclitaxel and a ten-fold increase in paclitaxel delivery to MDA-MB-231 brain metastasis in preclinical models (20). ANG1005 reached phase II clinical trials for metastatic breast cancer with brain metastases and has shown promise in reducing intracranial and extracranial disease progression (21), leading to a phase III clinical trial (NCT03613181).

ANG has also been used to transport polypeptide-based nanosystems across the BBB. For instance, our laboratory has recently developed a poly-L-glutamic acid (PGA)-based nanosystem to treat Alzheimer's disease by exploiting the self-assembly capacity of star-shaped PGA (St-PGA) and the efficacy of ANG as targeting moiety (22). Covalently captured St-PGA assemblies bearing ANG conjugated via a disulfide bond demonstrated increased brain accumulation compared to an untargeted counterpart with good diffusion in the brain parenchyma, accumulating 1.5% of the injected dose (ID) in the brain 1 h after intravenous administration. When loaded with bisdemethoxycurcumin by an ester linkage or with genistein, resultant conjugates significantly and safely ameliorated the classic symptoms of early-onset Alzheimer's disease, such as olfactory disfunction and loss of

recognition memory and hippocampal learning. Furthermore, ANG-tagged nanosystems remained attached to the brain vasculature, acting as a drug depot, which increased drug bioavailability in the brain (22).

In the context of this thesis, we previously developed an efficient St-PGA-based combination conjugate with doxorubicin (Dox) and dasatinib (Das) conjugated through pH-labile linkers at an optimal ratio, St-PGA-hyd-Dox_1-Das_{10}, which displayed robust antitumor and antimetastatic activity *in vivo* in an orthotopic MDA-MB-231-Luc TNBC mouse model (see *Chapter 2*). We next aimed to synthesize a brain-targeted version of St-PGA-hyd-Dox_1-Das_{10}, using ANG as targeting moiety. To do so, we optimized the protocols for ANG conjugation and employed the linking chemistry and drug ratio optimized in *Chapter 2* for Dox and Das to yield an ANG-conjugated St-PGA-hyd-Dox_1-Das_{10} combination conjugate. Finally, we obtained proof of anti-metastatic activity in an MDA-MB-231-derived brain metastasis mouse model.

4.2. Results And Discussion

4.2.1. Angiopep-2 Conjugation Protocol Optimization

4.2.1.1.   Maleimide-thiol Reaction Kinetics Study

Following the so-called " trojan horse " strategy, we aimed to achieve brain delivery via active targeting by conjugating a ligand for a specific BBB receptor to our St-PGA carrier. We chose ANG as targeting moiety - this peptide binds to LRP-1, which is expressed by brain endothelial cells (23,24) to mediate the transport of lipoproteins and other factors across the BBB by RMT (25). Of note, previous studies had demonstrated that the MDA-MB-231 TNBC cell line employed in this study also expresses LRP-1 (26). Thus, we hypothesized that ANG conjugation to St-PGA-hyd-Dox_1-Das_{10} (see *Chapter 2*) would further enhance the conjugate's anti-tumor and anti-metastatic activity *in vivo*.

We aimed to conjugate ANG via maleimide-thiol chemistry, a widely used strategy for ANG conjugation to various nanosystems (13,27–29). Peptide conjugation to St-PGA via non-biodegradable linkers such as maleimide-thiol assures that the nanosystem and peptide will remain attached during blood circulation and transcytosis. In RMT, transport across the endothelial cells starts with ligand binding to its receptor, which triggers receptor-ligand complex endocytosis with the surrounding fluid and cell membrane. The resulting vesicle travels across the cell to the abluminal side, where it fuses with the cell membrane to release its content in the extracellular media (12,30,31). Nanosystem-ANG bond stability remains a crucial concept since the strength of the interaction between ANG and LRP-1 decides the vesicular fate and, therefore, the nanosystem's capacity to cross the BBB and accumulate in the brain. Low avidity results in poor receptor binding on the luminal side, hindering transcytosis; however, high avidity allows for strong receptor binding but drives the vesicle towards the lysosomes for degradation instead of transcytosis. Intermediate avidity results in BBB crossing following a pathway independent of lysosomal sorting; this pathway also allows the detachment of ANG from LRP-1 to release the nanosystem at the abluminal side (13,30,31).

As previously described (22), we used ANG modified with an additional cysteinamide residue at the C-terminal end of the sequence (Ac-TFFYGGSRGKRNNFKTEEY-C-NH$_2$). We modified St-PGA with N-(2-aminoethyl)maleimide to permit ANG conjugation via maleimide-thiol chemistry. The maleimide-thiol reaction (**Scheme 4.1**) begins with the formation of the nucleophilic thiolate anion **1,** which attacks the π-bond of maleimide **2**, yielding the strongly basic enolate intermediate **3**. This intermediate deprotonates an additional thiol group perpetuating the catalytic cycle and forming the succinimidyl thioether **4** (32). Due to the selectivity of maleimide towards thiol groups (33), the use of maleimide-thiol chemistry instead of disulfide bonds allows the avoidance of undesirable intermolecular crosslinking between St-PGA molecules. This unwanted side-

reaction leads to reduced solubility (as depicted in *Chapter 3*) and could reduce ANG conjugation efficacy. Encouragingly, maleimides display high reactivity under mild conditions (e.g., pH 7.4 phosphate buffer saline [PBS] buffer at room temperature) (13,33,34), which allows for the conjugation of ANG to St-PGA-hyd-Dox$_1$-Das$_{10}$ without significant drug degradation.
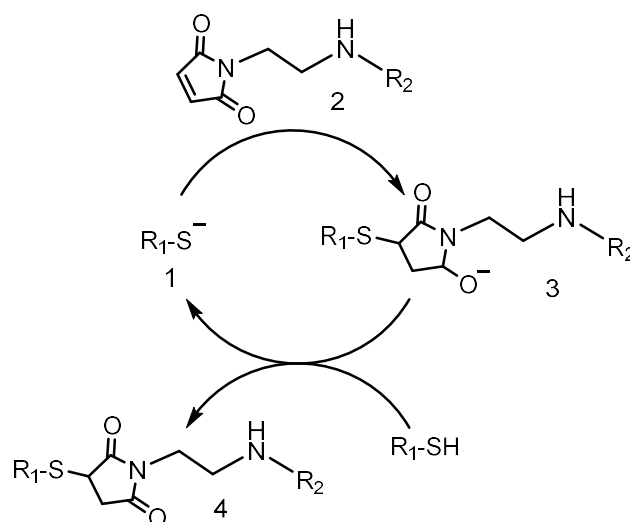

Scheme 4.1. Maleimide-thiol reaction. Adapted from Northrop et al. 2015 (32).

Our final aim is to synthesize an ANG-tagged St-PGA-based combination conjugate bearing the drug combination, drug ratio, and linkers of St-PGA-hyd-Dox$_1$-Das$_{10}$ (optimized in *Chapter 2*), i.e., Dox conjugated through a hydrazone bond and Das conjugated through an ester bond in a 1:10 ratio (Dox:Das). Considering the results of the pH-dependent drug release kinetics study performed for St-PGA-hyd-Dox$_1$-Das$_{10}$ (see *Chapter 2*), we needed to optimize the maleimide-thiol reaction. Efficiency, in this case, requires a reduction in reaction time to avoid drug release but support high ANG conjugation yield. For this reason, we made a detailed study of reaction kinetics.

We introduced 10 % mol maleimide groups in St-PGA (St-PGA-Malei) by N-(2-aminoethyl)maleimide conjugation via DMTMM (4-(4,6-dimethoxy-1,3,5-triazin-2-yl)-4-methylmorpholinium) chemistry in organic media

(**Scheme 4.2**), aiming to preserve maleimide group integrity (which degrades rapidly in basic [pH 8] aqueous media (34)). After purification, we obtained the salt form of the St-PGA-Malei conjugate by adding sodium bicarbonate with careful control over pH to preserve the maleimide groups. Conjugate desalting was impossible to perform by preparative size exclusion chromatography (SEC) due to the sample's high viscosity; therefore, we desalted the conjugate by dialysis at 4ºC (3 kDa MWCO). We quantified maleimide loading by ^{1}H-NMR comparing the signals of the 2,5-pyrrolidone of N-(2-aminoethyl)maleimide (7.05-5.80 ppm, two protons) with the α-carbon proton of the PGA backbone (4.33 ppm) (**Figure 4.1**), obtaining 10% mol of maleimide (high conjugation efficacy [100% CE]). In this step, material purity remains crucially important since DMTMM traces from the maleimide conjugation reaction can support the conjugation of ANG to St-PGA through lysine amino groups, forming an amide bond with the carboxylic acid of St-PGA. The ^{1}H-NMR spectra of St-PGA-Malei confirmed the absence of DMTMM, which appears as a multiplet at ~3.1 ppm.
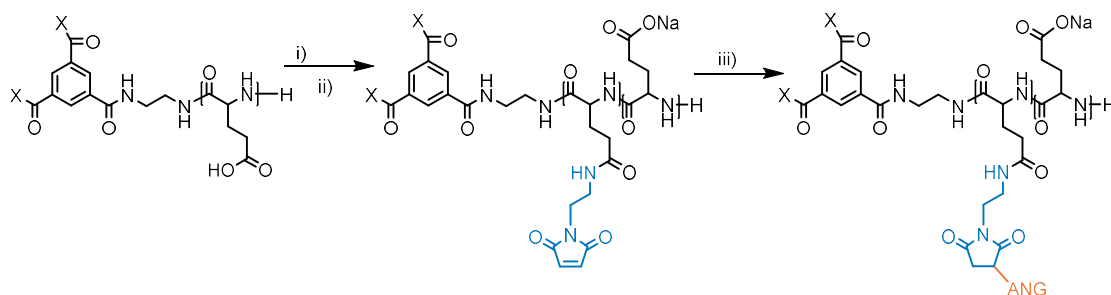
Scheme 4.2. Synthesis of St-PGA-ANG. i) N,N'-dimethylformamide (DMF) anhydrous, DMTMM BF$_4$, N-(2-aminoethyl)maleimide trifluoroacetate salt, N,N-diisopropylethylamine (DIEA), pH 8, 48 h. ii) Sodium bicarbonate, MilliQ water. iii) Degassed Dulbecco's phosphate-buffered saline (DPBS), Angiopep-2-SH, tris(2-carboxyethyl)phosphine (TCEP).
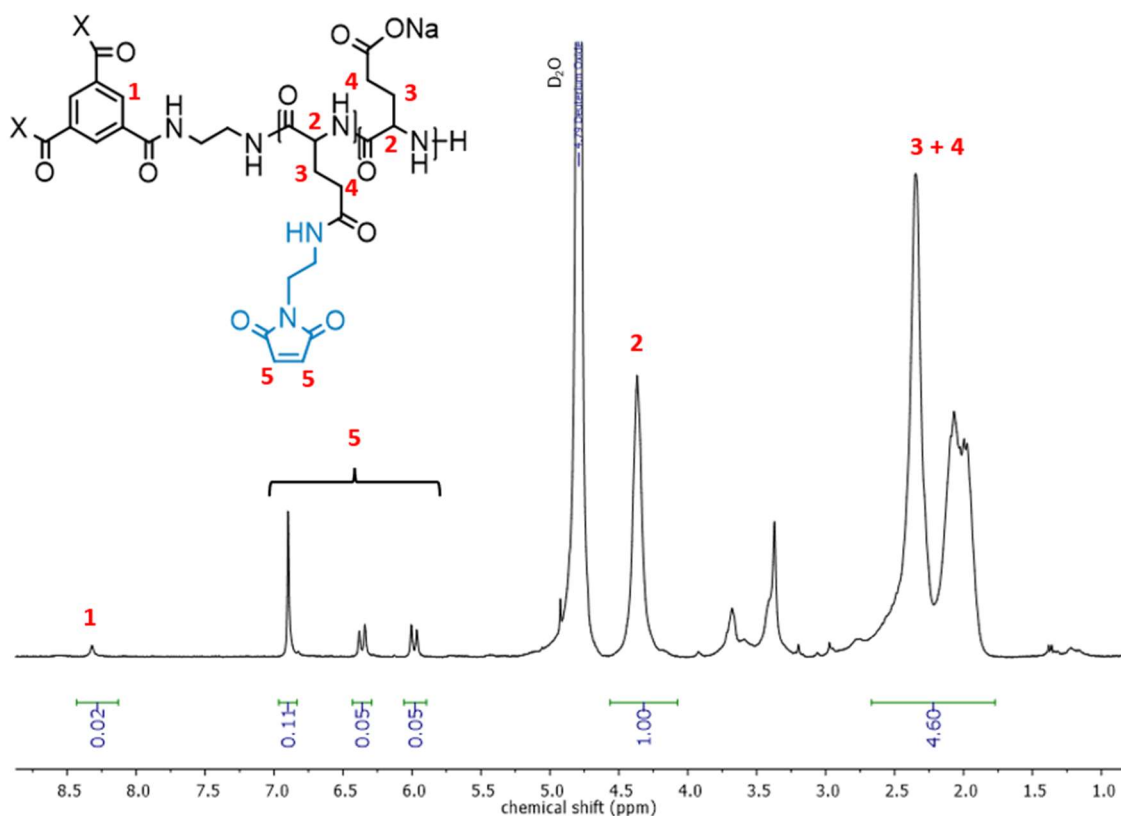
Figure 4.1. ¹H-NMR (D₂O) spectra of St-PGA-Malei confirm maleimide conjugation (5 - two protons) and product purity (absence of DMTMM signals at 3.1 ppm).

We performed ANG conjugation to St-PGA-Malei by maleimide-thiol chemistry in aqueous media (**Scheme 4.2**). Based on the protocol reported by Tian et al. (13), we carried out the reaction in previously degassed Dulbecco's PBS (DPBS – pH 7.2) in the presence of tris(2-carboxyethyl)phosphine (TCEP) to maintain ANG thiol groups in their reduced form and avoid peptide dimerization. Aiming for a 1.4% mol ANG loading (two molecules of ANG per 150-long St-PGA molecule), we added an excess of peptide in the reaction. We separately dissolved St-PGA-Malei, ANG, and TCEP in degassed DPBS and adjusted the pH of the TCEP solution to 7 with NaOH. Then, we added ANG and TCEP to the solution of St-PGA-Malei. We took a 100 µL reaction mixture aliquot as time 0 for reaction monitoring and then after 1, 3, 5, 17, and 25 h of reaction time.

We evaluated the reaction kinetics of ANG conjugation to St-PGA-Malei by SEC. Considering the high molecular weight (2300 Da) of ANG, we

hypothesized that ANG conjugation to St-PGA-Malei would cause a reduction in conjugate retention time by SEC. Thus, we monitored conjugate elution by multi-angle light scattering (MALS) and analyzed conjugate retention times. The conjugate peak increased over time, suggesting an increment in the light scattered by the conjugate and, thus, an increase in conjugate size due to ANG conjugation (**Figure 4.2A**). Importantly, when we plotted conjugate retention time versus reaction time, we observed a sharp reduction in retention time during the first 5 h of reaction (**Figure 4.2B**). After 5 h, the decrease in the retention time reached a plateau, suggesting that the conjugation of ANG to St-PGA-Malei occurs within the first 5 h of reaction time.
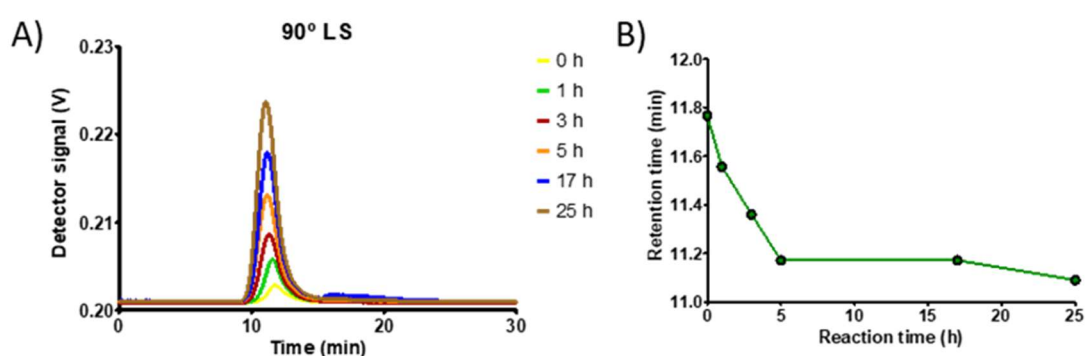
Figure 4.2. SEC study of maleimide-thiol reaction kinetics. (**A**) Reaction monitoring by MALS (90º light scattering – LS) demonstrates an increased height and a shift to shorter retention times for the St-PGA-Malei peak over time. (**B**) Evolution of St-PGA-Malei retention time monitored by MALS (90º LS).

We next purified St-PGA-ANG by dialysis (3.5 kDa MWCO). As we aimed to perform the reaction quickly to reduce the loss of conjugated drug during targeted combination conjugate synthesis, we purified a 1 mL aliquot from the reaction at 5 h to evaluate ANG conjugation and compare loading with St-PGA-ANG obtained after 25 h of reaction. We quantified ANG loading by ^{1}H-NMR comparing the signals of the phenylalanine and tyrosine residues of ANG in the aromatic region (7.55-6.70 ppm, twenty-three protons) (**Figure 4.3**) with the α-carbon proton of PGA (4.33 ppm) (**Figure 4.4**). We used this method as the first assessment of maleimide-thiol

reaction success; however, the maleimide moiety displays a singlet at 6.9 ppm, overlapping with the signals of phenylalanine and tyrosine of ANG. We assumed a negligible maleimide signal compared to ANG signals. Using this method, we found similar loadings for St-PGA-ANG purified after 5 h (2.4% mol, **Figure 4.4A**) and 25 h (2.3% mol, **Figure 4.4B**) of reaction time, agreeing with the SEC findings. The signals corresponding to the threonine residues of ANG (1.50-1.00 ppm, six protons, **Figure 4.3**) also confirmed these results (**Figure 4.4A** and **B**). Therefore, we set 5 h as the ANG conjugation reaction time.
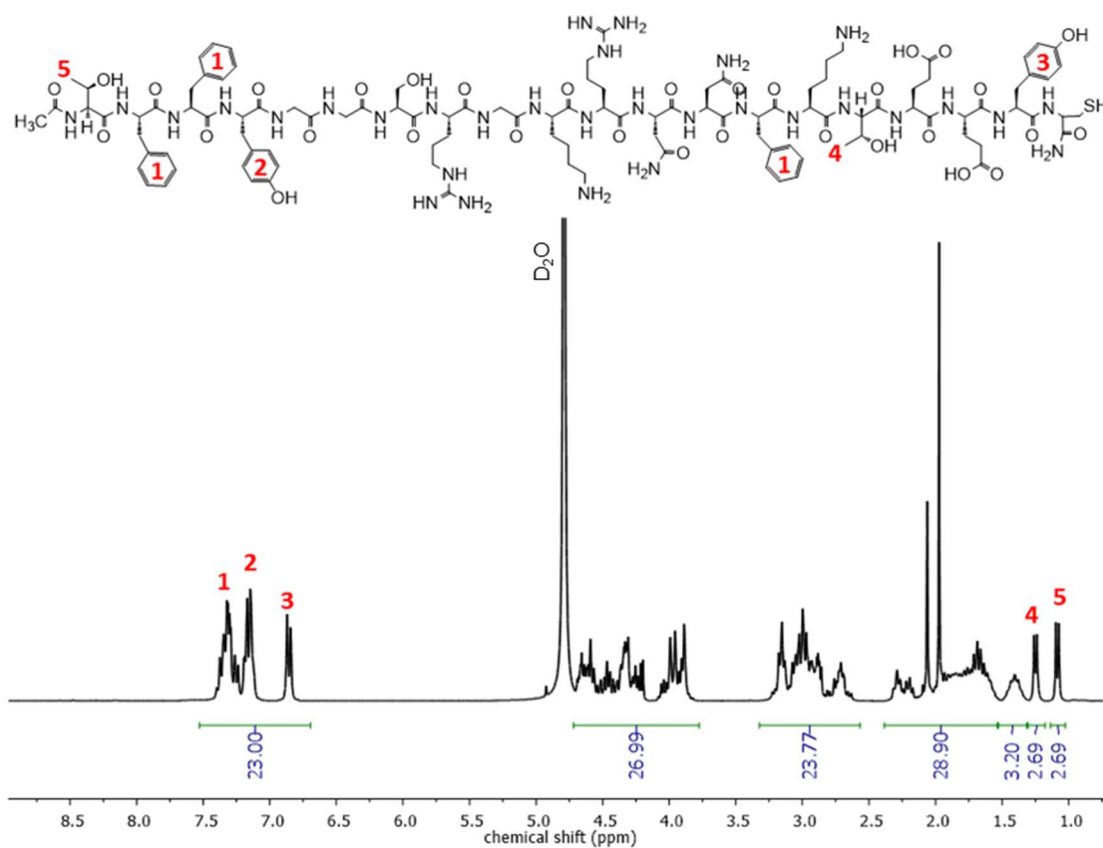
Figure 4.3. ^{1}H-NMR (D$_2$O) spectra of ANG with signals used for peptide loading quantification noted.
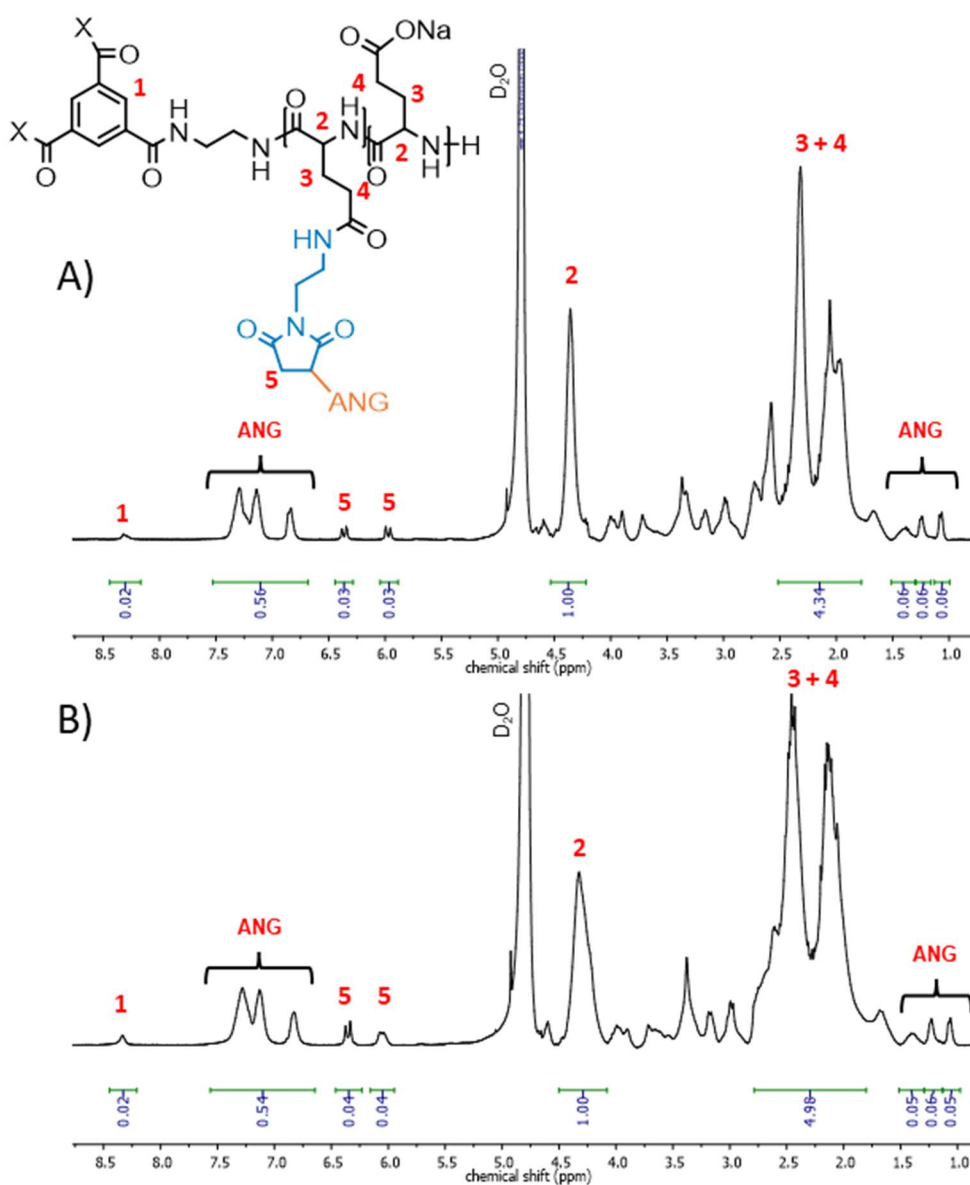
Figure 4.4. ^{1}H-NMR (D$_2$O) spectra of St-PGA-ANG taken from the reaction after (**A**) 5 and (**B**) 25 h shows similar ANG loading (as shown from a comparison between the signals of phenylalanine and tyrosine protons [ANG - twenty-three protons] and the α-carbon proton of PGA [2]).

St-PGA-ANG displays ~2.4% mol of ANG and 10% mol of maleimide moieties; therefore, a significant amount of maleimide groups remain unreacted. Even though the rapid hydrolysis rates and slow thiol exchange of N-(2-aminoethyl)maleimide deems it suitable for *in vivo* administration (33), we wanted to prevent any possible interaction of our conjugate with plasma proteins via maleimide-thiol chemistry by quenching the remaining unreacted maleimide groups. This group rapidly hydrolyzes to yield a stable

succinamic acid thioether in basic aqueous media (33,34); however, these conditions are not compatible with the implementation of pH labile linkers (35,36) or Dox (37). For this reason, we quenched the spare maleimide groups by maleimide-thiol reaction with N-acetyl cysteine (NAC) in the same conditions as ANG conjugation, i.e., degassed DPBS with TCEP to avoid the dimerization of NAC (using an excess of NAC). ^{1}H-NMR analysis of the final compound (St-PGA-ANG-NAC) demonstrates a similar ANG loading to St-PGA-ANG (~2.1%), as revealed by the comparison between the phenylalanine and tyrosine protons signals (7.55-6.70 ppm, twenty-three protons) of ANG and the α-carbon proton of PGA (4.33 ppm) (**Figure 4.5A**). These findings confirm maleimide-thiol bond stability in reductive environments or in the presence of other thiol groups.

4.2.1.2.   St-PGA-ANG-NAC Physico-chemical Characterization

Considering the high molecular weight of ANG, we assessed the peptide's influence on conjugate behavior in an aqueous solution, i.e., secondary structure, aggregation behavior, size, and zeta potential.

Circular dichroism (CD) spectra of St-PGA-ANG-NAC in MilliQ water and DPBS at 0.1, 0.2, and 0.5 mg/mL displayed the typical negative band at 200 nm for the random coil conformation (**Figure 4.5B** and **C**). These findings resemble the spectra for parental St-PGA (see *Chapter 2*), indicating that ANG conjugation failed to affect the secondary structure of St-PGA.
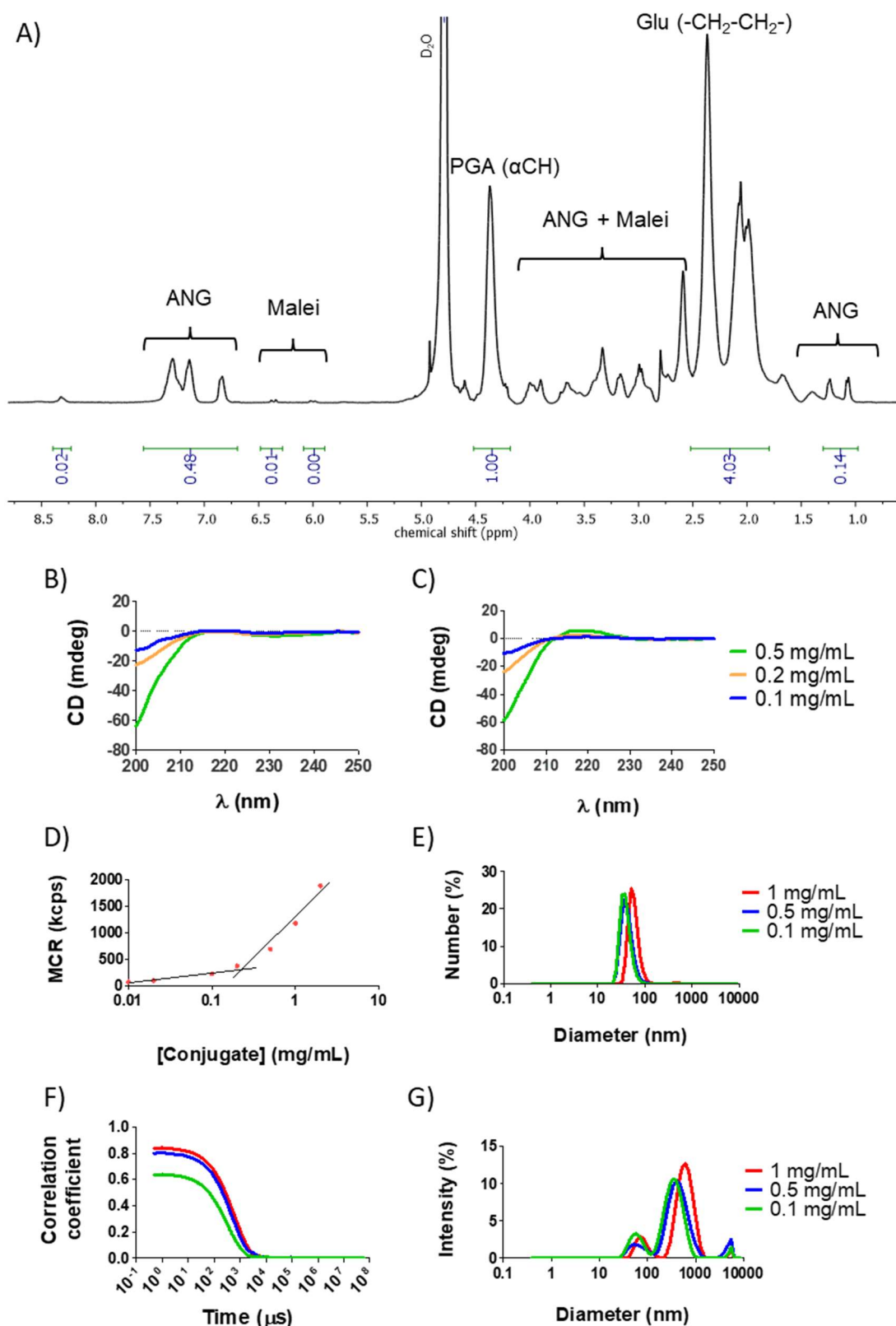
Figure 4.5. St-PGA-ANG-NAC characterization. (**A**) ^{1}H-NMR (D$_2$O) spectrum demonstrates the main signals for product identity evaluation and ANG loading determination. (**B** and **C**) Circular dichroism (CD) spectra in (**B**) water and (**C**) DPBS at 0.1, 0.2, and 0.5 mg/mL conjugate. (**D**) Graphical determination of the critical aggregation concentration (CAC) by dynamic light scattering (DLS). Data represented as average mean count rate (MCR) of two measurements vs. conjugate concentration (logarithmic

scale). (**E-G**) Size distribution by (**E**) number and (**G**) intensity, and (**F**) the respective correlation function. Data obtained by DLS at 0.1, 0.5, and 1 mg/mL in MilliQ water. Average result of at least three measurements displayed.

The study of St-PGA-ANG-NAC aggregation in MilliQ water revealed a lower critical aggregation concentration (CAC) value compared to the parental St-PGA (0.2 mg/mL versus 1 mg/mL, respectively), although the value observed remained in the range of the conjugates synthesized in previous chapters (**Figure 4.5D**). These findings suggested that ANG conjugation to St-PGA enhances aggregation similar to Dox or Das conjugation. When studying St-PGA-ANG-NAC size (hydrodynamic diameter) by dynamic light scattering (DLS) at concentrations below (0.1 mg/mL) and above the CAC value (0.5 and 1 mg/mL) in MilliQ water, we failed to observe the expected size increment associated with concentration-dependent St-PGA aggregation (**Figure 4.5E-G**). The size distribution by number of St-PGA-ANG-NAC provided evidence of a single population of ~46 nm (**Figure 4.5E**); however, unlike St-PGA (see *Chapter 2*), we identified two populations after analyzing size distribution by intensity; one population with a hydrodynamic diameter of ~ 70 nm and a second of ~ 500 nm (**Figure 4.5G**). These data suggest the co-exitance of a major population of St-PGA-ANG-NAC conjugates of ~46 nm with a residual population of larger aggregates. The correlation function associated with these measurements possessed acceptable quality with exponential decay; only the measurements at 0.1 mg/mL possessed a low intercept (~0.6, **Figure 4.5F**), suggesting high background noise interference in the measurement. The smaller sizes obtained for St-PGA-ANG-NAC according to the distribution by number than those obtained for St-PGA under the same conditions (see *Chapter 2*) suggest a more compact structure for St-PGA-ANG-NAC; however, larger aggregate size found in St-PGA-ANG-NAC samples compared to St-PGA (see *Chapter 2*) agreed with the enhanced aggregation observed in the CAC study.

The study of the zeta potential by electrophoretic light scattering (ELS) of St-PGA-ANG-NAC provided similar negative values at both concentrations (- 40.3 ± 1.1 mV at 0.5 mg/mL and - 40.2 ± 1.2 mV at 1 mg/mL), in agreement with the values observed for both parental St-PGA and St-PGA-based conjugates (see *Chapter 2* and *3*). Overall, these findings suggested that ANG conjugation failed to significantly affect the overall carrier charge.

In summary, we optimized a protocol for ANG conjugation that maintains the main structural and physical characteristics of the parent St-PGA (i.e., negative charge, random coil conformation, and aggregation in aqueous media). Furthermore, the reduced reaction time allows for peptide conjugation with St-PGA molecules bearing drugs conjugated through pH-labile bonds, making this protocol suitable for synthesizing a targeted combination conjugate with hydrazone-linked Dox and ester-linked Das.

4.2.2. Assessing Brain Targeting – *In vivo* Biodistribution

4.2.2.1.   Synthesis and Characterization of Cy5.5-labeled ANG-tagged St-PGA-based Conjugates

Due to the low permeability of the BBB/BTB, we hypothesized that an intravenously administered St-PGA-based conjugate would remain in the blood and not accumulate in the brain in the absence of a targeting moiety (i.e., ANG). Therefore, we studied the biodistribution of targeted and untargeted St-PGA-conjugates in healthy BALB/c mice using fluorescently labeled St-PGA-based nanosystems with ANG (St-PGA-Cy5.5-ANG-NAC – "targeted") and without ANG (St-PGA-Cy5.5-NAC - "untargeted").

Briefly, we modified St-PGA with 5% mol maleimide groups due to the high viscosity of St-PGA-Malei with 10% mol loading and a desire to preserve compound solubility and ease the conjugation of other moieties to the polymer. We labeled St-PGA with the fluorophore sulfo-cyanine5.5

(Cy5.5) to quantify conjugate accumulation in the principal organs by *ex vivo* fluorescence detection. We conjugated N-(2-aminoethyl)maleimide and Cy5.5 in a one-pot reaction by DMTMM chemistry in organic media (**Scheme 4.3**) to yield St-PGA-Cy5.5-Malei and obtained a water-soluble salt form of the conjugate by addition of sodium bicarbonate and subsequent desalting by preparative SEC, Vivaspin™, or dialysis (3-3.5 kDa MWCO).
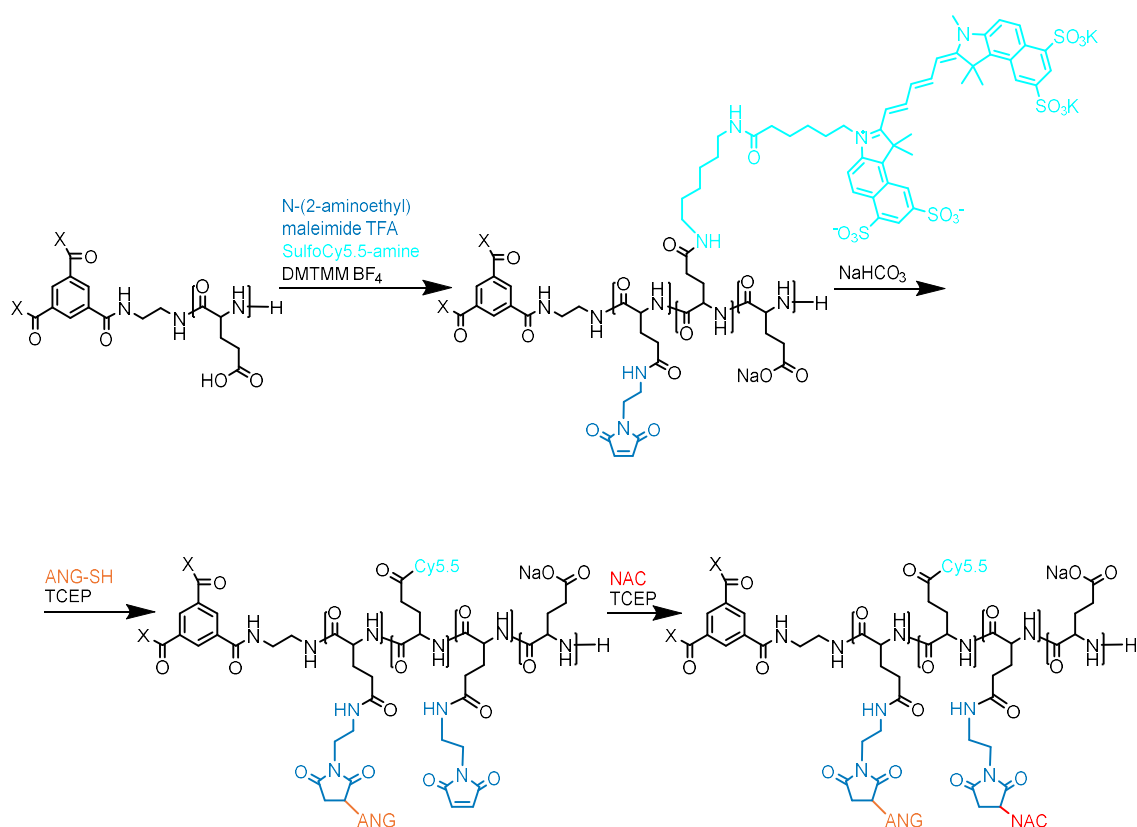
Scheme 4.3. Scheme of Cy5.5-labeled ANG-tagged St-PGA system synthesis for *in vivo* biodistribution study.

We evaluated the identity and purity of St-PGA-Cy5.5-Malei by ^{1}H-NMR and quantified the maleimide loading by comparing the signals of the 2,5-pyrrolidone of N-(2-aminoethyl)maleimide (7.05-5.80 ppm, two protons) with the α-carbon proton of the PGA backbone (4.33 ppm) (**Figure 4.6**). These evaluations provided a value of 4.0% mol (80% CE). We failed to identify any signal corresponding to DMTMM in the ^{1}H-NMR spectrum of St-PGA-Cy5.5-Malei (i.e., a multiplet at ~3.1 ppm), thereby confirming conjugate purity.
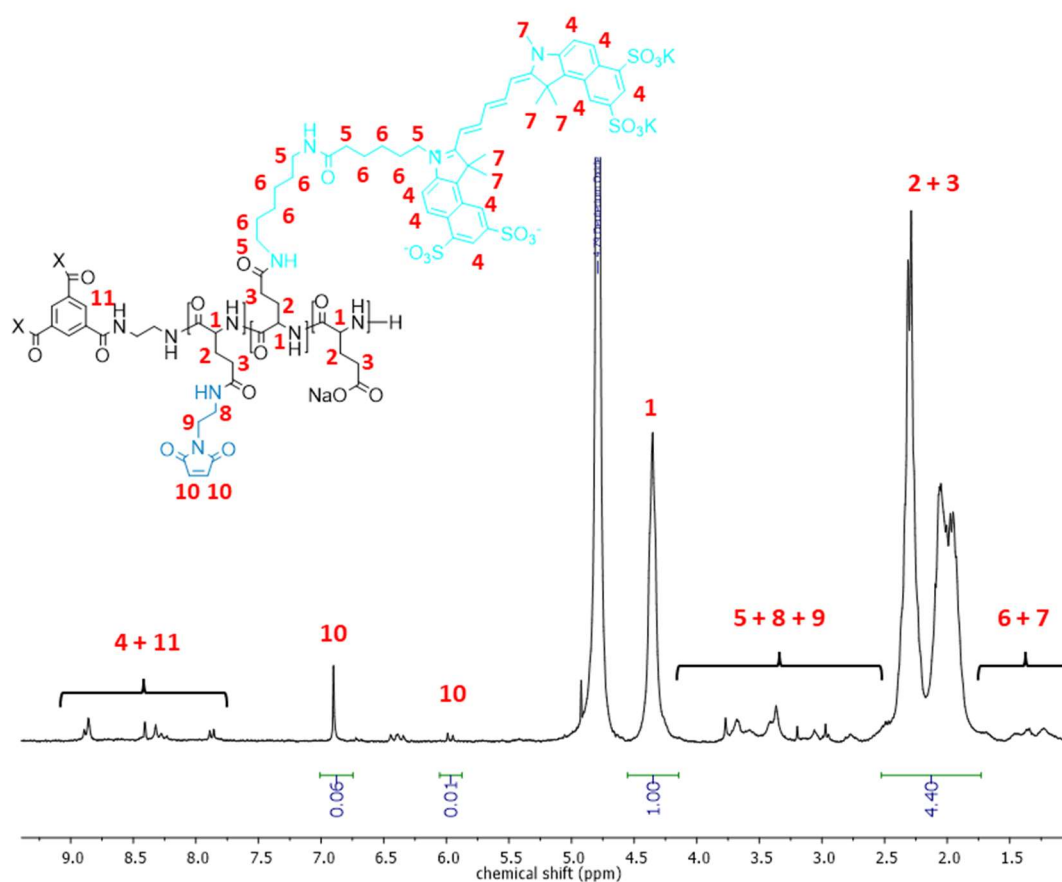
Figure 4.6. ^{1}H-NMR (D$_2$O) spectrum of St-PGA-Malei-Cy5.5. The spectrum depicts the signals used for maleimide loading determination (10) and fails to indicate residual DMTMM (multiplet at ~3.1 ppm).

We conjugated ANG to St-PGA-Cy5.5-Malei following the optimized protocol described in previous sections (see *4.2.1.1.Maleimide-thiol Reaction Kinetics* Study and **Scheme 4.3**) to obtain St-PGA-Cy5.5-ANG. Still aiming for 1.4 % mol ANG, we reduced the amount of ANG in the reaction compared to the reaction kinetics study as the maleimide-thiol reaction exhibited high CE. We confirmed the conjugation of ANG to St-PGA-Cy5.5-Malei by ^{1}H-NMR (twenty-three protons at 7.55-6.70 ppm, **Figure 4.7**) before quenching the spare maleimides with NAC.
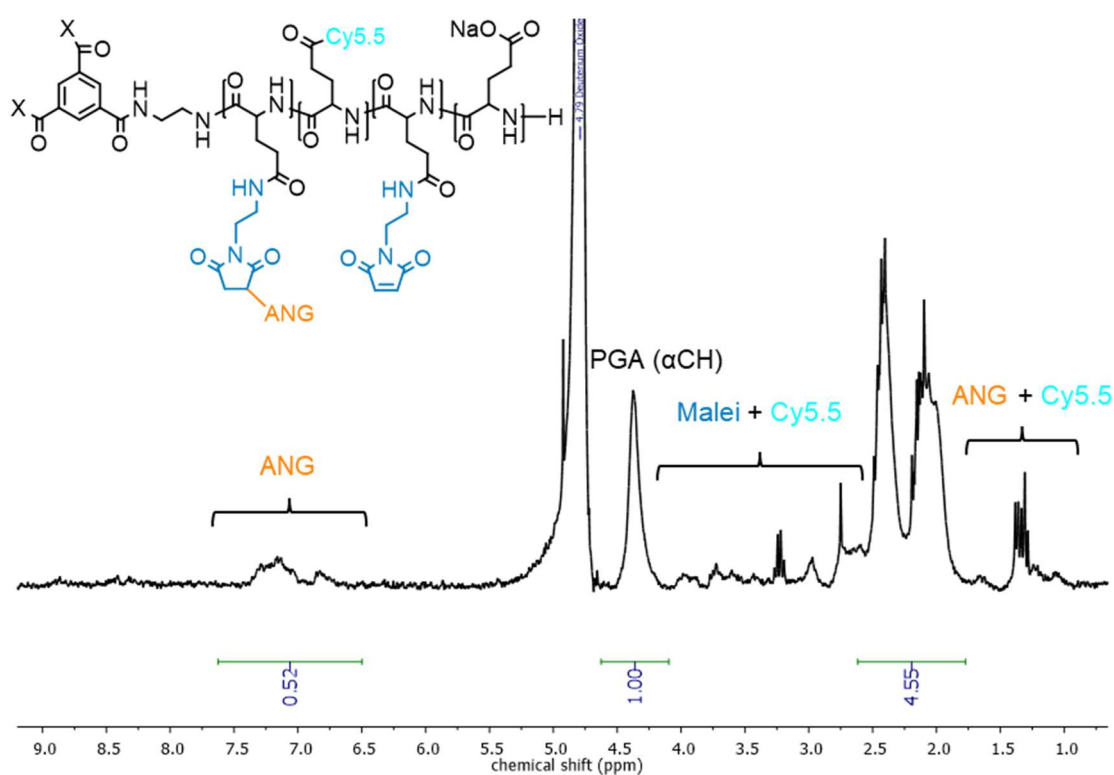
Figure 4.7. ^{1}H-NMR (D_2O) of St-PGA-Cy5.5-ANG confirming the presence of ANG, Cy5.5, and N-(2-aminoethyl)maleimide.

We performed NAC-mediated maleimide quenching as described in previous sections (see *4.2.1.1.Maleimide-thiol Reaction Kinetics* Study, **Scheme 4.3**) to yield the final compound, St-PGA-Cy5.5-ANG-NAC. We obtained the untargeted counterpart (St-PGA-Cy5.5-NAC) by simply quenching the maleimides in St-PGA-Cy5.5-Malei with NAC.

We quantified ANG loading in St-PGA-Cy5.5-ANG-NAC by ^{1}H-NMR by comparing the signals of the phenylalanine and tyrosine residues of ANG in the aromatic region (7.55-6.70 ppm, twenty-three protons) with the α-carbon proton of PGA (4.33 ppm). We obtained a value of 1.7% mol ANG (19.4% wt) (**Figure 4.8A**). As the signals of maleimide and Cy5.5 protons also appear in the aromatic region of the ^{1}H-NMR spectrum, we employed amino acid analysis to precisely quantify ANG loading. Using this method, we obtained a value of 1.4% mol ANG (16.2% wt, 100% CE). The higher loading obtained by ^{1}H-NMR than amino acid analysis may derive from maleimide signal interference in the ^{1}H-NMR spectrum.

The ^{1}H-NMR spectrum of St-PGA-Cy5.5-NAC displayed broad peaks corresponding to the presence of Cy5.5 (9.1-7.7 ppm, 4.0-2.5 ppm, and 1.5-1.0 ppm) and maleimide (4.0-2.5 ppm and 1.5-1.0 ppm); however, these peaks could not be used for loading determination due to the low definition and overlapping signals (**Figure 4.9A**).
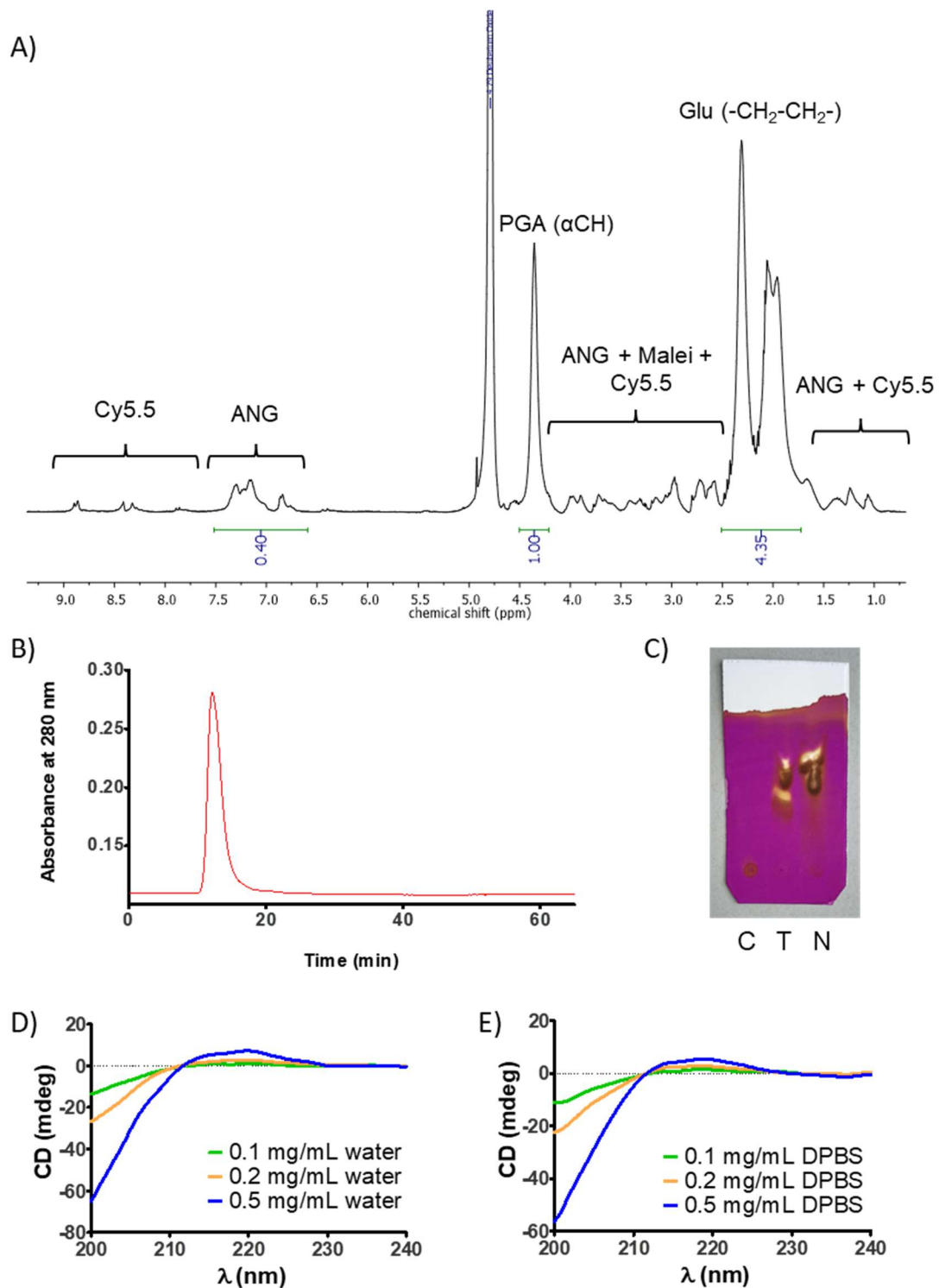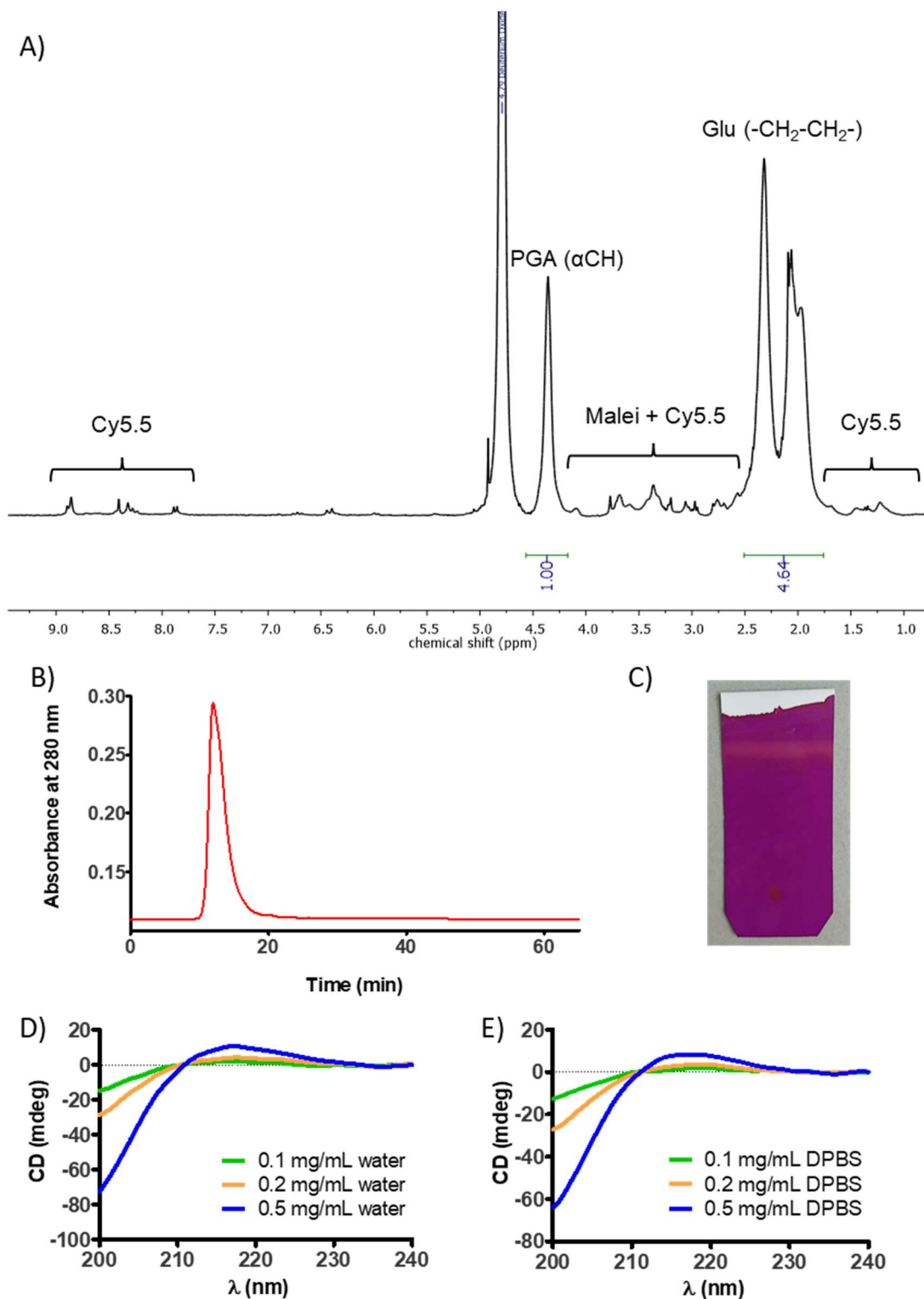
Figure 4.8. Physico-chemical characterization of St-PGA-Cy5.5-ANG-NAC. (**A**) ^{1}H-NMR (D$_2$O) spectrum demonstrates the main signals for product identity evaluation and ANG loading determination. (**B**) Representative SEC chromatogram monitored by absorbance at 280 nm. Chromatogram shows monomodal molecular weight distribution. (**C**) Thin-layer chromatography (TLC) of the conjugate (C), TCEP (T), and NAC (N), proving compound purity. TCEP and NAC spots revealed by permanganate staining. (**D**) CD spectra in water at 0.1 (green), 0.2 (orange), and 0.5 (blue) mg/mL. (**E**) CD spectra in DPBS at 0.1 (green), 0.2 (orange), and 0.5 (blue) mg/mL.

Figure 4.9. Physico-chemical characterization of St-PGA-Cy5.5-NAC. (**A**) ^{1}H-NMR (D$_2$O) spectrum demonstrates the main signals for product identity evaluation. (**B**) Representative SEC chromatogram monitored by absorbance at 280 nm. Chromatogram shows monomodal molecular weight distribution. (**C**) TLC of the conjugate after purification proves purity. TCEP and NAC spots revealed by permanganate staining. (**D**) CD spectra in water at 0.1 (green), 0.2 (orange), and 0.5 (blue) mg/mL. (**E**) CD spectra in DPBS at 0.1 (green), 0.2 (orange), and 0.5 (blue) mg/mL.

SEC chromatograms revealed the presence of single homogeneous molecular weight distribution for St-PGA-Cy5.5-ANG-NAC (**Figure 4.8B**) and St-PGA-Cy5.5-NAC (**Figure 4.9B**), revealing homogeneous moiety distribution throughout the conjugate population.

We further confirmed the purity of St-PGA-Cy5.5-ANG-NAC and St-PGA-Cy5.5-NAC by thin-layer chromatography (TLC) using MeOH as a mobile phase. We used standard permanganate staining to detect TCEP (R_f(TCEP): 0.5) and NAC (R_f(NAC): 0.7). Potassium permanganate reacts with strongly reducing groups, such as thiols, which appear as yellow dots upon heating. TLC failed to provide evidence of NAC or TCEP in St-PGA-Cy5.5-ANG-NAC (**Figure 4.8C**) and St-PGA-Cy5.5-NAC (**Figure 4.9C**), thereby confirming conjugate purity.

We quantified the Cy5.5 loading by fluorescence detection (λ_{exc} = 640 nm, λ_{em} = 700 nm), using a calibration curve of the fluorophore in DMSO:water (1:1 v/v), obtaining a value of 3.89% wt Cy5.5 for St-PGA-Cy5.5-ANG-NAC (0.7% mol, 88% CE) and 4.45% wt Cy5.5 for St-PGA-Cy5.5-NAC (0.7% mol, 88% CE).

We evaluated the secondary structure of St-PGA-Cy5.5-ANG-NAC and St-PGA-Cy5.5-NAC by CD in MilliQ water and DPBS at 0.1, 0.2, and 0.5 mg/mL. Both conjugates displayed the typical negative band at 200 nm of the random coil conformation in all media and concentrations evaluated (**Figure 4.8D** and **E**, and **Figure 4.9D** and **E**), as we observed for the parent St-PGA (see *Chapter 2*) and St-PGA-ANG-NAC. These findings suggest that the conjugation of the fluorophore and ANG failed to affect the carrier's secondary structure. We did not evaluate the size, CAC, or Zeta potential of St-PGA-Cy5.5-ANG-NAC and St-PGA-Cy5.5-NAC due to the interference of Cy5.5 fluorescence in detecting the scattered light from the sample.

4.2.2.2.   *In vivo* Biodistribution and Brain Accumulation

To study biodistribution and assess brain accumulation, we intravenously administered St-PGA-Cy5.5-ANG-NAC and St-PGA-Cy5.5-NAC to BALB/c mice through the tail vein and quantified the fluorescence from the main organs (including the brain). We injected St-PGA-Cy5.5-ANG-NAC and St-PGA-Cy5.5-NAC at equivalent doses of Cy5.5 (4.15 mg/Kg). After 4 h, we euthanized animals, collected the blood, and harvested the principal organs (lungs, liver, spleen, kidney, heart, and brain) for *ex vivo* Cy5.5 fluorescence detection by IVIS® technology with λ_{exc} = 640 nm and λ_{em} = 700 nm. We quantified the percentage of the injected dose (% ID) in each organ, interpolating the fluorescence value from each organ in a calibration curve of the conjugate (St-PGA-Cy5.5-ANG-NAC or St-PGA-Cy5.5-NAC) prepared in DPBS and measured in the same equipment with the same measurement parameters (**Supplementary Figure 4.1**). We employed the fluorescence value from mouse organs injected with DPBS (control group) as a blank. We selected 4 h as the experimental time frame since previously reported data obtained by our group provided evidence for maximal accumulation of St-PGA in the main organs at this time after intravenous injection (38,39).

St-PGA-Cy5.5-ANG-NAC exhibited a 1.4-fold accumulation in the brain compared to St-PGA-Cy5.5-NAC 4 h after intravenous administration of conjugates (0.7 % ID versus 0.5 % ID, p=0.0405) (**Figure 4.10A** and **B**, and **Table 4.1**). Thus, ANG conjugation significantly increased the accumulation of St-PGA conjugates in the brain, confirming the advantage of using ANG as targeting moiety for brain delivery. Nevertheless, we observed a value for St-PGA-Cy5.5-ANG-NAC lower than that reported for the Cy5.5-labelled St-PGA-based covalently-captured self-assembled nanosystem developed by our group, that presented with a value of ~1.5% ID in the brain 3 h after the intravenous administration of the ANG-tagged conjugate (22,39). The difference observed may derive from the longer

circulation time of the covalently-captured self-assembled conjugate than the St-PGA unimer-based conjugate (38), which increases the chances of conjugate binding to LRP-1 in the BBB and crossing from blood to brain.
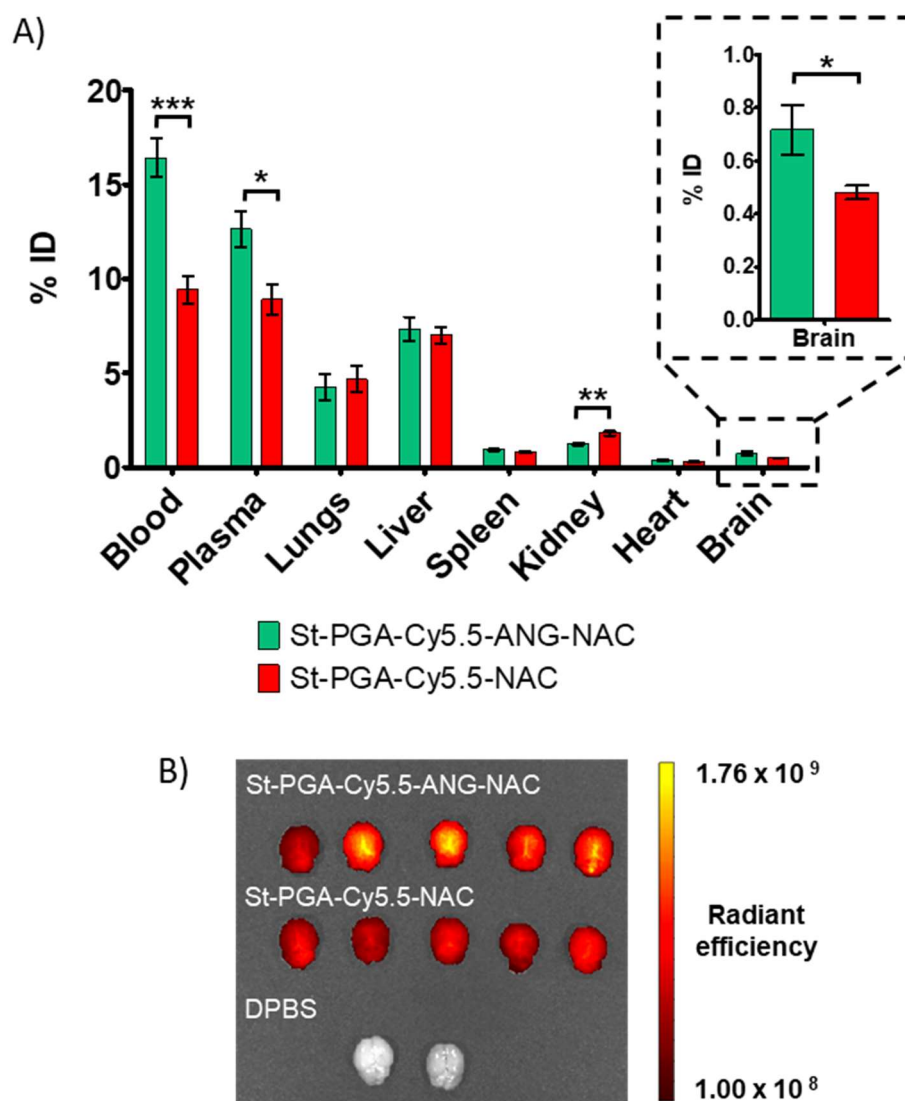

Figure 4.10. *In vivo* biodistribution of St-PGA-Cy5.5-ANG-NAC and St-PGA-Cy5.5-NAC. Results obtained 4 h after intravenous administration at 4.15 mg Cy5.5/Kg by *ex vivo* quantification of Cy5.5 fluorescence by IVIS® technology. (**A**) Accumulated dose in major organs, including the brain. Data expressed as a percentage of the injected polymer dose (%ID) (mean ± SEM, n=5). Statistical analysis performed by unpaired, two-way Student's t-test. *<0.05, **p<0.01, ***p<0.001. (**B**) Fluorescent images of brains used for quantification.

Table 4.1. Summary of the primary characterization of St-PGA-Cy5.5-ANG-NAC and St-PGA-Cy5.5-NAC.

	St-PGA-Cy5.5-ANG-NAC	St-PGA-Cy5.5-NAC
% wt Cy5.5[A]	3.9	4.5
% wt ANG[B]	16.2	-
% mol ANG[C]	1.4	-
CD[D]	Random coil	Random coil
% ID brain[E]	0.7 ± 0.1	0.5 ± 0.0

(**A**) Obtained by Cy5.5 fluorescence detection. (**B**) Obtained by amino acid analysis. (**C**) Obtained by iterative calculation from weight percent. (**D**) Secondary structure in water at all concentrations evaluated (**E**) Brain accumulation expressed as % injected dose (mean ± SEM, n=5).

Regarding the other organs analyzed in this experiment, St-PGA-Cy5.5-ANG-NAC and St-PGA-Cy5.5-NAC displayed similar biodistribution in the organs analyzed except in kidneys, where St-PGA-Cy5.5-NAC displayed a higher accumulation than St-PGA-Cy5.5-ANG-NAC at 4 h (1.8 %ID versus 1.2 %ID, p=0.0029) (**Figure 4.10A**). St-PGA-Cy5.5-ANG-NAC demonstrated a more significant presence in blood and plasma than St-PGA-Cy5.5-NAC at 4 h (16.4 %ID versus 9.4 %ID in blood - p=0.0006, 12.6 %ID versus 8.9 %ID in plasma - p=0.0182, **Figure 4.10A**). Together, these data suggest a longer circulation time and reduced renal excretion for St-PGA-Cy5.5-ANG-NAC. The similar accumulation of St-PGA-Cy5.5-ANG-NAC and St-PGA-Cy5.5-NAC in the liver and spleen (**Figure 4.10A**), tightly bound to the immune response and clearance by the reticuloendothelial system, suggest that ANG conjugation did not induce an immune response against the conjugate or conjugate clearance (13). Although we note the use of a short exposure time (4 h), we did not observe any signs of systemic toxicity in the animals, thereby suggesting the safety of St-PGA-Cy5.5-ANG-NAC and St-PGA-Cy5.5-NAC.

In summary, we optimized a protocol for ANG conjugation to St-PGA that allows for control over final ANG loading, yielding systems that can cross

the BBB and accumulate in the brain. The therapeutic efficiency of the drug combination (see *Chapter 2*), together with the enhanced permeation across the BBB provided by ANG, may yield an effective conjugate for treating breast cancer brain metastasis.

4.2.3. Synthesis and Characterization of a St-PGA-based Combination Conjugate for the Treatment of Brain Metastasis

4.2.3.1. Synthesis of St-PGA-hyd-Dox-Das-ANG-NAC

After optimizing the linking chemistry for ANG and evaluating ANG-tagged St-PGA-based conjugates for brain accumulation, we next combined the chemistry for ANG conjugation with the chemistry and ratio optimized for Dox and Das in *Chapter 2* to obtain a brain-targeted version of the St-PGA-hyd-Dox_1-Das_{10} conjugate as the last step for the synthesis of our St-PGA-based combination conjugate for the treatment of breast cancer brain metastasis.

Our strategy followed the protocol described in *Chapter 2* for the synthesis of St-PGA-hyd-Dox_1-Das_{10} but adding the conjugation of N-(2-aminoethyl)maleimide before tert-butyl carbazate (TBC) deprotection (**Scheme 4.4**). After loading the conjugate with Dox and Das and creating the water-soluble salt form, we conjugated ANG to the maleimide moieties and subsequently quenched unreacted maleimides with NAC following the protocols described earlier in this chapter to obtain St-PGA-hyd-Dox-Das-ANG-NAC. Finally, we obtained proof of therapeutic activity in a breast cancer brain metastasis mouse model.
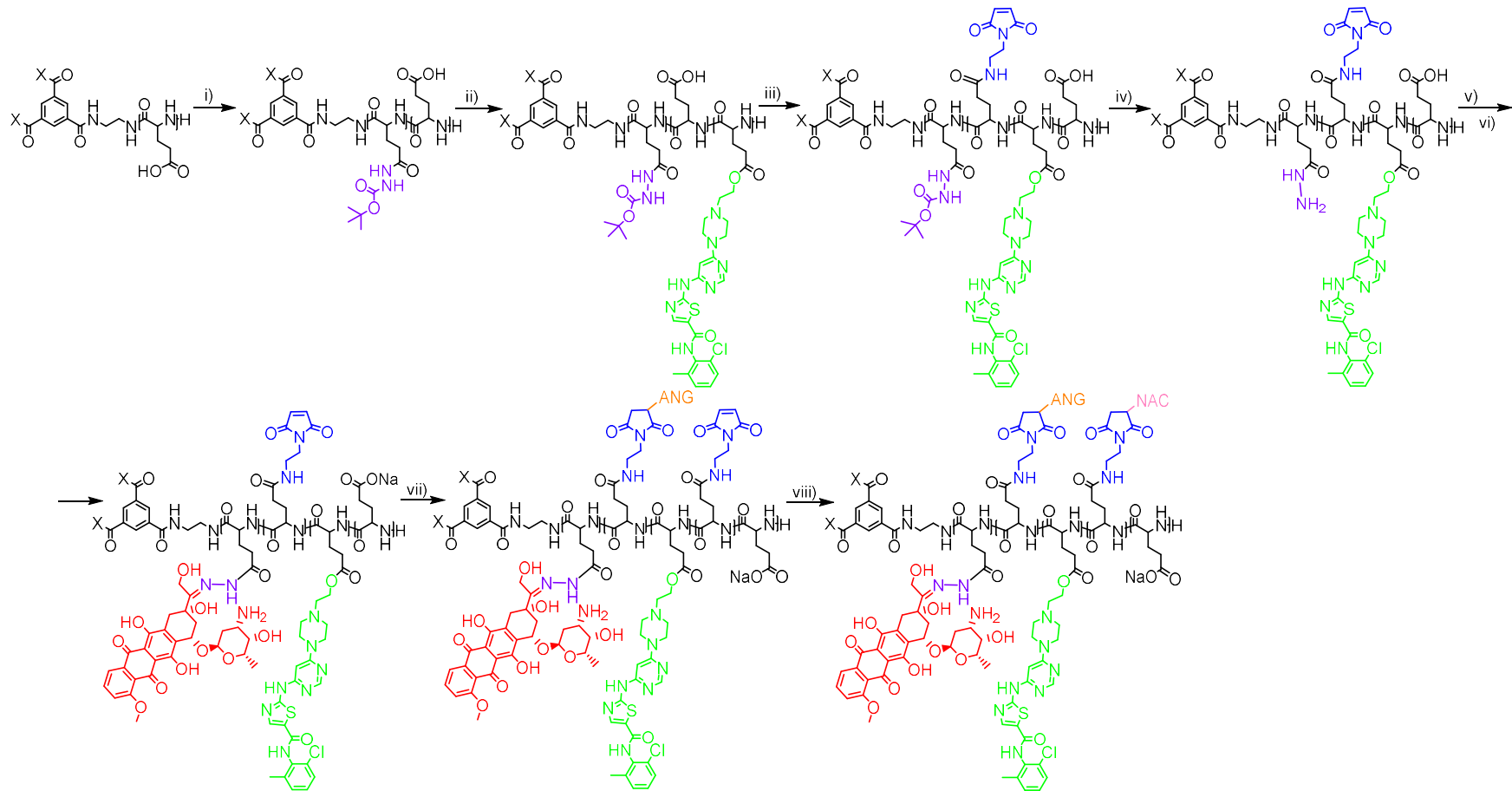
Scheme 4.4. Synthesis of St-PGA-hyd-Dox-Das-ANG-NAC. i) DMF anh., DMTMM BF$_4$, TBC, DIEA, pH 8, 48 h. ii) DMF anh., 4-dimethyl aminopyridine (DMAP), 1-Ethyl-3-(3-dimethylaminopropyl)carbodiimide (EDC), Das, DIEA, pH 8, 72 h. iii) DMF anh., DMTMM BF$_4$, N-(2-aminoethyl)maleimide trifluoroacetate salt, DIEA, pH 8, 48 h. iv) Trifluoroacetic acid (TFA), 40 min. v) Dimethylsulfoxide (DMSO) anhydrous, Dox, acetic acid (cat.), 72 h. vi) Sodium bicarbonate, MilliQ water. vii) Degassed DPBS pH 7.2, ANG, TCEP, 5 h. viii) Degassed DPBS pH 7.2, NAC, TCEP, 5 h.

The conjugation of TBC to St-PGA by DMTMM chemistry in organic media to obtain St-PGA-TBC represents the first synthetic step. We quantified TBC loading by ^{1}H-NMR by comparing the signals of the tert-butyloxycarbonyl (Boc) protecting group of TBC (1.50 ppm, nine protons) with the α-carbon proton of St-PGA backbone (4.33 ppm), obtaining 6% mol (100% CE) (**Figure 4.11**).
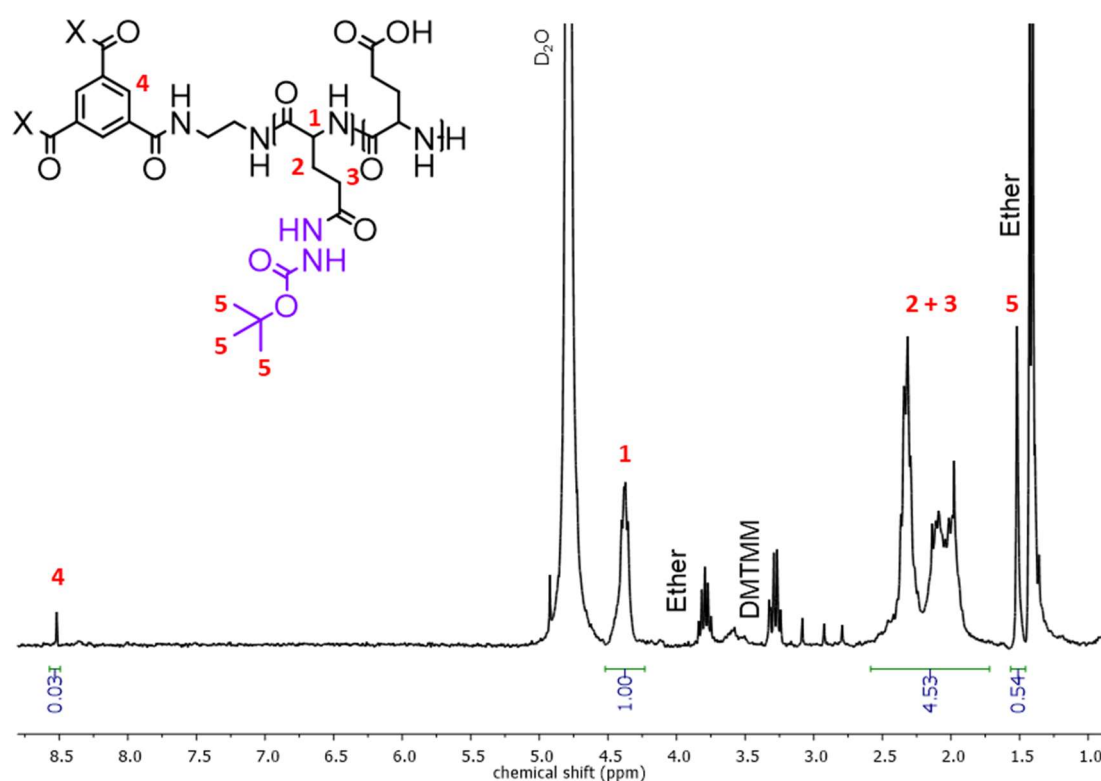
Figure 4.11. ^{1}H-NMR (D$_2$O) spectrum of St-PGA-TBC. The spectrum confirms TBC conjugation. Signals from the Boc protecting group (5 - nine protons) and PGA α-carbon proton (1) were used to calculate TBC loading (% mol).

We then conjugated Das to St-PGA-TBC through an ester bond by EDC/DMAP chemistry in organic media to obtain St-PGA-TBC-Das. We monitored the reaction by TLC (MeOH, R$_f$(Das): 0.7) to confirm the conjugation of Das before precipitating the compound in ether. After washes with acidic water and lyophilization, we evaluated the identity of St-PGA-TBC-Das by ^{1}H-NMR, finding broad peaks in the aromatic region of the

spectrum (8.9-6.3 ppm). We attribute these peaks to the conjugation of Das to the St-PGA backbone (five protons) (**Figure 4.12**).
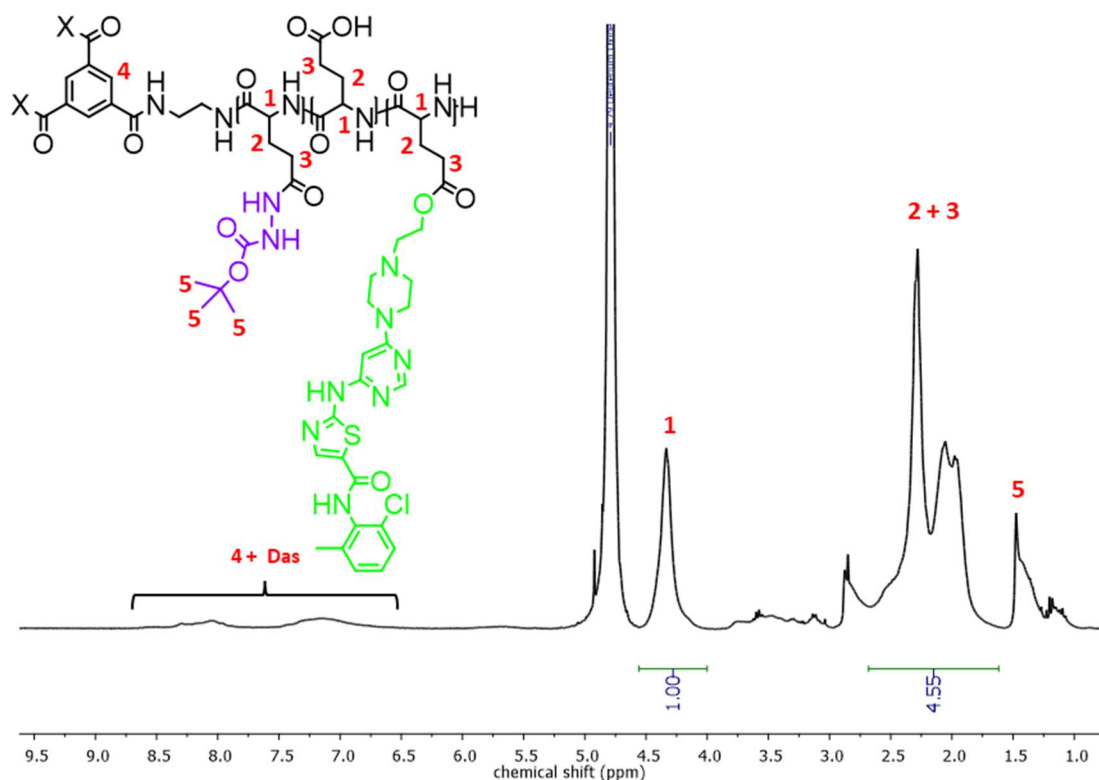

Figure 4.12. ^{1}H-NMR (D$_2$O) spectrum of St-PGA-TBC-Das confirms Das conjugation (Das - five protons).

We next conjugated the N-(2-aminoethyl)maleimide moiety to St-PGA-TBC-Das to yield St-PGA-TBC-Das-Malei. We performed the reaction as described in earlier sections, i.e., DMTMM chemistry in organic media to preserve maleimide moiety integrity. After purification, we assessed the identity and purity of St-PGA-TBC-Das-Malei by ^{1}H-NMR (**Figure 4.13**). The interference of Das signals in the ^{1}H-NMR spectrum of St-PGA-TBC-Das-Malei (8.7-6.5 ppm, five protons) hindered proper quantification of maleimide loading; however, we identified and integrated two signals from 2,5-pyrrolidone (6.35 ppm and 5.95 ppm, one proton each), providing a value of 3% mol of maleimide as the minimal loading obtained (**Figure 4.13**). We failed to identify signals of DMTMM protons in the ^{1}H-NMR spectrum (i.e., a

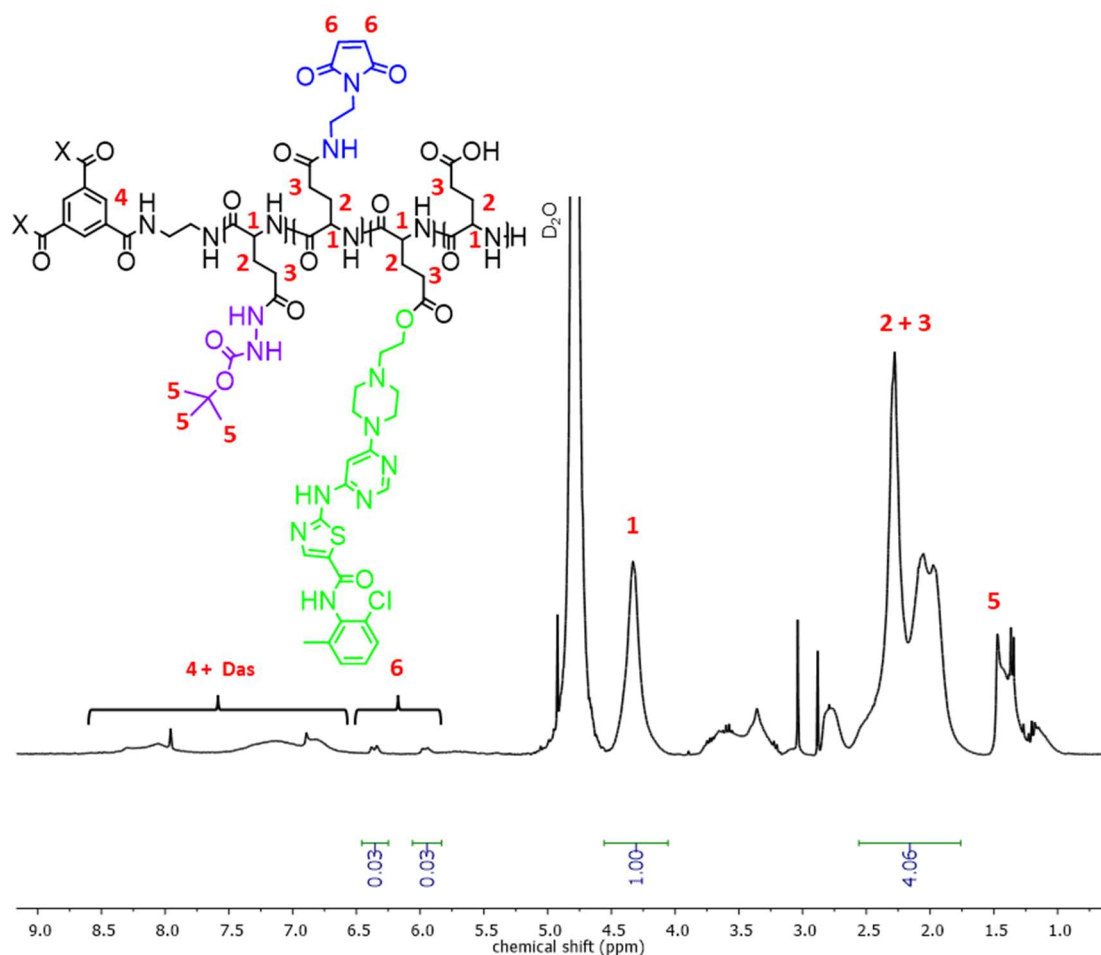multiplet at ~3.1 ppm), thereby confirming the purity of St-PGA-TBC-Das-Malei.

Figure 4.13. ^{1}H-NMR (D$_2$O) spectrum of St-PGA-TBC-Das-Malei. The spectrum confirms Das (Das - five protons) and N-(2-aminoethyl)maleimide (6 - two protons) conjugation.

After confirmation of maleimide conjugation, we deprotected TBC to expose the hydrazide moieties for Dox conjugation and obtain St-PGA-(HYD)-Das-Malei. We confirmed the complete removal of the Boc protecting group (1.50 ppm) by ^{1}H-NMR (**Figure 4.14**). In the ^{1}H-NMR spectra of St-PGA-(HYD)-Das-Malei, we also identified Das-derived (8.5-6.5 ppm, five protons) and maleimide-derived (6.5-6.2 and 6.1-5.8 ppm, one proton each) signals (**Figure 4.14**), thereby confirming product identity.
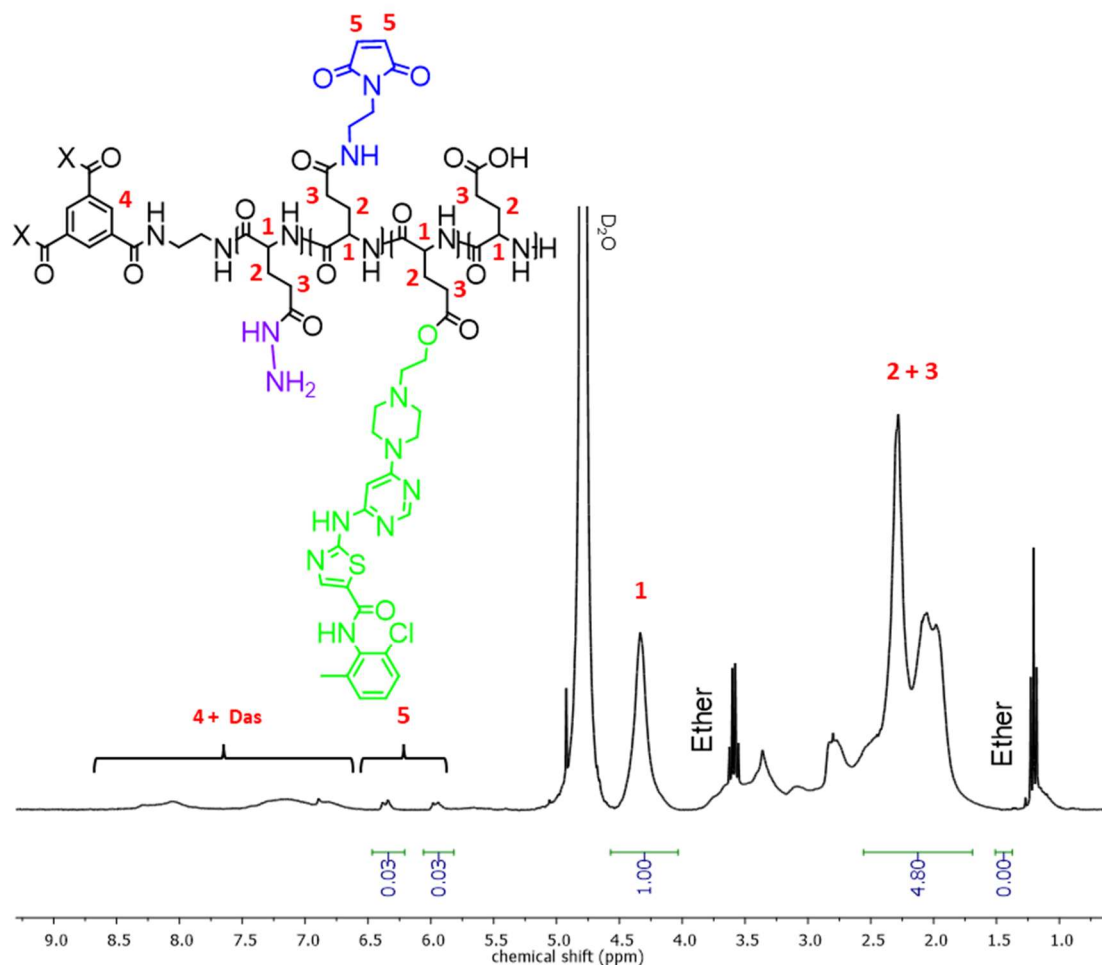
Figure 4.14. ^{1}H-NMR (D$_2$O) spectrum of St-PGA-(HYD)-Das-Malei. The absence of the Boc signal at 1.5 ppm confirms complete deprotection of the hydrazide groups.

We then performed the conjugation of Dox to St-PGA-(HYD)-Das-Malei in DMSO with catalytic amounts of acetic acid to obtain St-PGA-hyd-Dox-Das-Malei. To determine the equivalents of Dox required to obtain a final 1:10 drug ratio (Dox:Das) in St-PGA-hyd-Dox-Das-Malei, we quantified Das loading of St-PGA-(HYD)-Das-Malei by UV-VIS spectroscopy (following protocols described in previous chapters [see *Chapter 2*]), obtaining a value of 19.8% wt, ~6.8% mol Das. Considering this result, we aimed for 0.7% mol loading of Dox. After reaction completion (as determined by TLC [MeOH, R$_f$(DOX): 0.6]), we purified the conjugate from free Dox by preparative SEC in DMF using Sephadex LH-20 resin. We obtained the water-soluble salt form of the conjugate through the addition of sodium bicarbonate and desalting by preparative SEC using water as mobile phase with Sephadex

G25 resin. We evaluated the identity and purity of St-PGA-hyd-Dox-Das-Malei by ^{1}H-NMR and UV-VIS. In the ^{1}H-NMR spectrum of St-PGA-hyd-Dox-Das-Malei, we identified signals deriving from Dox and Das (8.7-6.7 ppm, eight protons), maleimide (6.5-5.8 ppm, one proton), and St-PGA (4.3 ppm for the proton in the α-carbon, 2.5-1.7 ppm for the four protons of glutamic acid residues) (**Figure 4.15A**). As a stop/go checkpoint for moving forward with ANG conjugation, we estimated the drug ratio in the conjugate by quantifying Dox and Das loading by UV-VIS spectroscopy (as described in *Chapter 2*) – this value serves as an estimative, as the maleimide and Das absorbance spectra overlap (**Figure 4.15B**). Encouragingly, we obtained 6.8% mol Das and 0.8% mol Dox (**Table 4.2**) - an approximate Dox:Das ratio of 1:9. As this value remained similar to the ratio in the St-PGA-hyd-Dox$_1$-Das$_{10}$ candidate, we continued with subsequent synthetic steps.
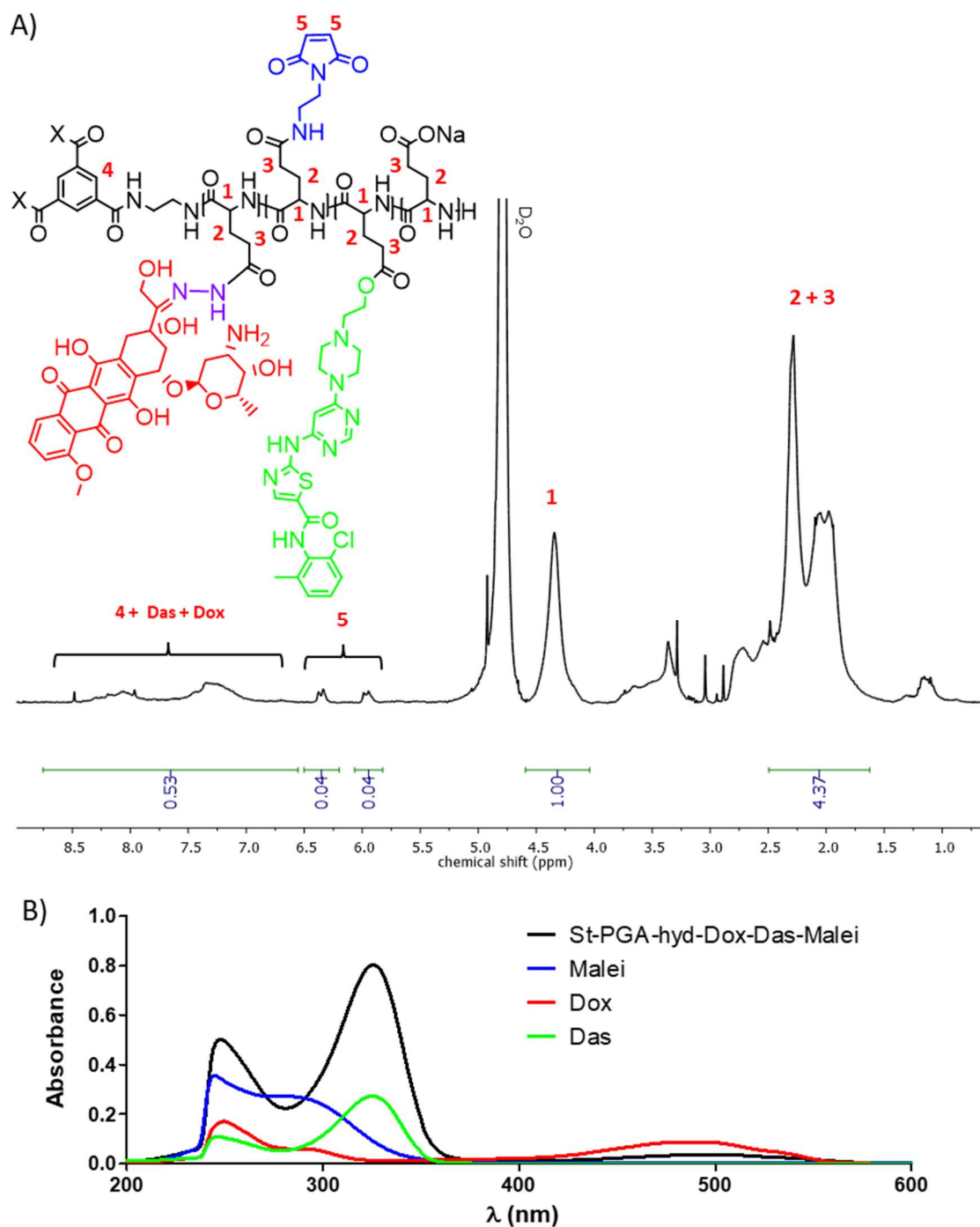
Figure 4.15. St-PGA-hyd-Dox-Das-Malei identity and purity. (**A**) ¹H-NMR (D₂O) spectrum of St-PGA-hyd-Dox-Das-Malei. Spectrum exhibits signals indicating the presence of Dox, Das, maleimide, and St-PGA in the conjugate. (**B**) Absorbance spectra of St-PGA-hyd-Dox-Das-Malei at 0.0625 mg/mL (black), N-(2-aminoethyl)maleimide TFA at 0.125 mg/mL (blue), Dox at 0.004 mg/mL (red), and Das at 0.004 mg/mL (green) in DMSO:water (1:1 v/v). The spectrum of St-PGA-hyd-Dox-Das-Malei shows the peaks of Dox (480 nm) and Das (324 nm) absorbance.

Table 4.2. Drug loading and ratio in the different precursors of St-PGA-hyd-Dox-Das-ANG-NAC.

Compound	% wt Dox[A]	% mol Dox[B]	% wt Das[A]	% mol Das[B]	Drug ratio (Dox:Das)
St-PGA-(HYD)-Das-Malei	-	-	19.8	6.8	-
St-PGA-hyd-Dox-Das-Malei	2.3	0.8	17.5	6.8	1:9
St-PGA-hyd-Dox-Das-ANG	n.d.	n.d.	n.d.	n.d.	n.d.
St-PGA-hyd-Dox-Das-ANG-NAC	2.0	0.8	10.6*	4.6	1:6

(**A**) Obtained by UV-VIS spectroscopy. (**B**) Obtained by iterative calculation from the loading in wight percent. *Obtained by ester hydrolysis, liquid-liquid extraction, and quantification by HPLC.

We conjugated ANG to the maleimide groups of St-PGA-hyd-Dox-Das-Malei to obtain St-PGA-hyd-Dox-Das-ANG. We performed this reaction in DPBS buffer at pH 7.2, as with the previous maleimide-thiol reactions described in this chapter. As described in *Chapter 2* for St-PGA-hyd-Dox$_1$-Das$_{10}$, 31% Das and 33% Dox loading became released after 5 h at pH 7.4 (37 ºC); of note, 5 h represents the reaction time for ANG conjugation to St-PGA-Malei derivatives. Thus, we modified the ANG conjugation protocol to reduce drug loss from St-PGA-hyd-Dox-Das-Malei due to ester and hydrazone hydrolysis during ANG conjugation. We dissolved St-PGA-hyd-Dox-Das-Malei in MilliQ water at 4 ºC (instead of degassed DPBS) and added 0.1 volumes of DPBS 10X (obtained by lyophilization of DPBS and reconstitution in MilliQ water) immediately before adding ANG and TCEP to the reaction mixture. We took a 100 µL aliquot at the reaction endpoint to assess the extent of drug loss by free drug extraction and quantification (as described in *Chapter 2*). This analysis revealed 15.4% Das and 8.3% Dox release during the reaction – a ~52% and ~76% reduction of Das and Dox release, respectively, compared to St-PGA-hyd-Dox$_1$-Das$_{10}$ in PBS pH 7.4 (37ºC). Therefore, we successfully reduced drug loss during the reaction.

After purification of St-PGA-hyd-Dox-Das-ANG by Vivaspin™ (3 kDa MWCO), we assessed compound identity and purity by ^{1}H-NMR (**Figure 4.16**). As Dox and Das signals appear in the same region of the ^{1}H-NMR

spectrum as those of the phenylalanine and tyrosine residues of ANG (8.7-6.7 ppm), we could not quantify ANG loading by ^{1}H-NMR. However, the increment in the integral value in the said region confirmed the conjugation of ANG to St-PGA-hyd-Dox-Das-Malei, allowing us to move forward with the maleimide quenching with NAC.
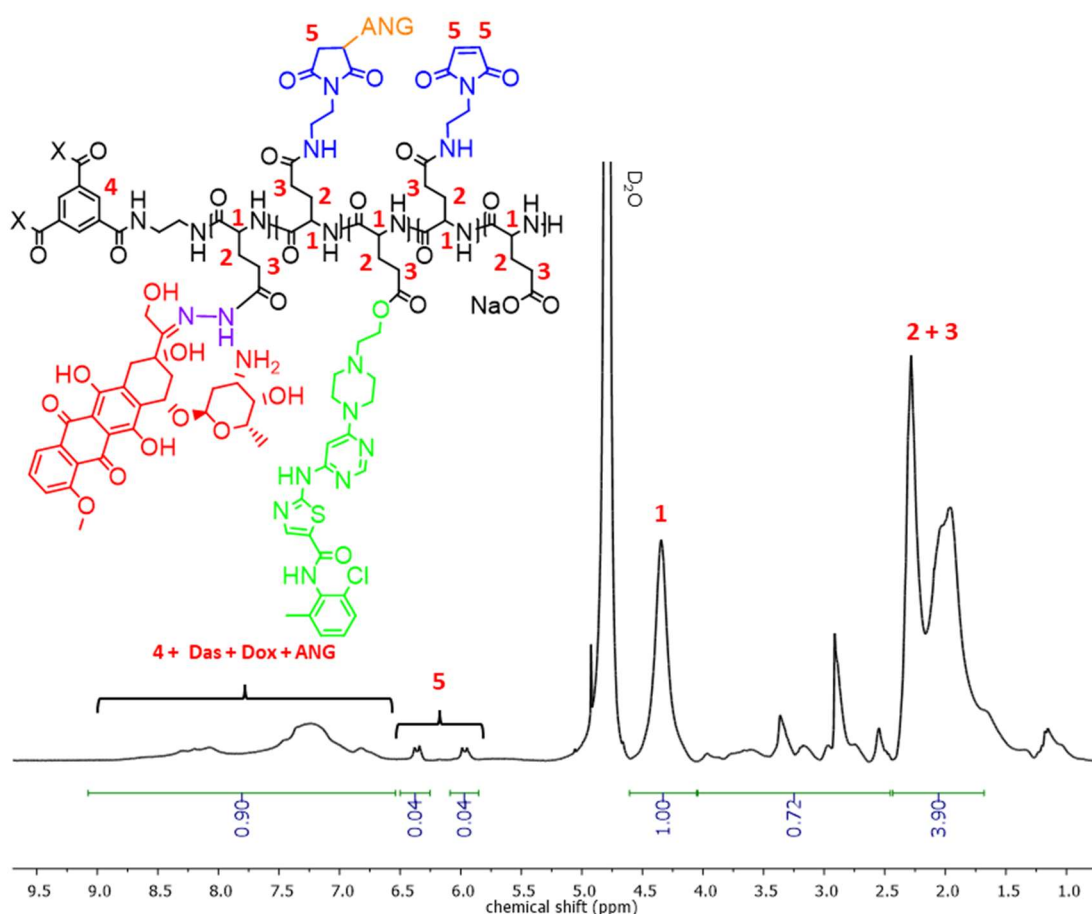

Figure 4.16. ^{1}H-NMR (D$_2$O) of St-PGA-hyd-Dox-Das-ANG. The increased integrated value in the aromatic region (8.7-6.7 ppm) suggests successful conjugation of ANG to St-PGA-hyd-Dox-Das-Malei; however, low peak definition and the overlapping Dox, Das, and maleimide signals impede the accurate assessment of ANG loading by ^{1}H-NMR.

Finally, following the same protocol above described, we quenched the unreacted maleimides of St-PGA-hyd-Dox-Das-ANG to obtain St-PGA-hyd-Dox-Das-ANG-NAC. We purified the conjugate by Vivaspin™ (3 kDa MWCO) and then by preparative SEC in water using Sephadex G25 resin. We monitored the elution by TLC (MeOH) to guarantee the absence of free Das (R_f(Das):0.7) and Dox (R_f(Dox): 0.6) in the collected fractions.

The ^{1}H-NMR spectrum of St-PGA-hyd-Dox-Das-ANG-NAC displayed signals compatible with the presence of Dox, Das, and ANG (**Figure 4.17A**). As with the St-PGA-hyd-Dox-Das-ANG precursor, we could not quantify ANG loading by ^{1}H-NMR due to interference from other signals (**Figure 4.17A**). Therefore, we quantified the final loading of ANG by amino acid analysis, obtaining a value of 13.9% wt, which corresponds to a 1.3% mol (93% CE, considering a maleimide loading of 4% mol), a similar value than for St-PGA-Cy5.5-ANG-NAC.
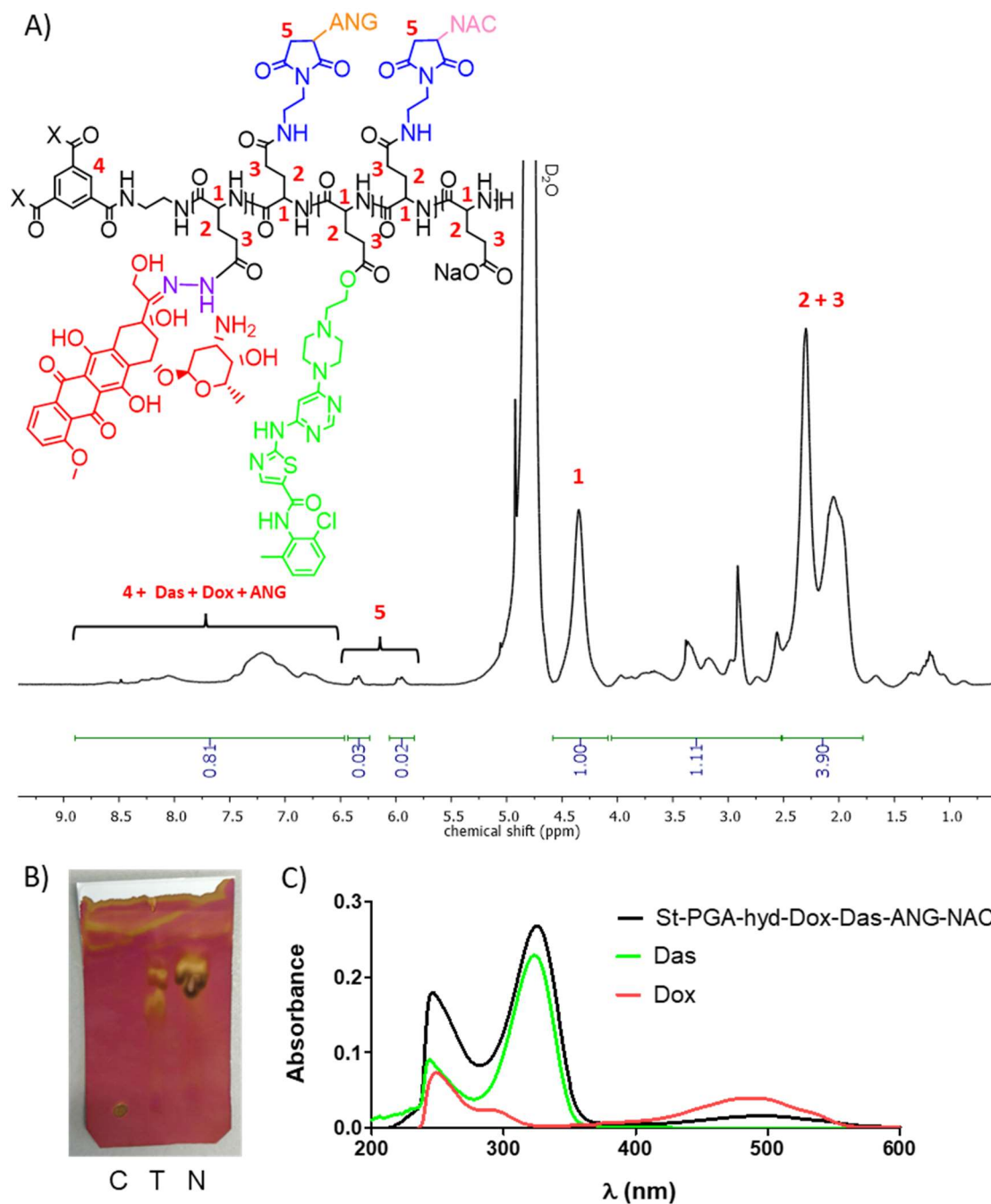
Figure 4.17. St-PGA-hyd-Dox-Das-ANG-NAC identity and purity. (**A**) ¹H-NMR (D₂O) spectrum demonstrates signals indicating the presence of Dox, Das, maleimide, ANG, and St-PGA in the conjugate. (**B**) TLC of St-PGA-hyd-Dox-Das-ANG-NAC (C), TCEP (T), and NAC (N). TCEP and NAC spots revealed by permanganate staining. (**C**) Absorbance spectra of St-PGA-hyd-Dox-Das-ANG-NAC at 0.003 mg/mL (black) and free drugs Das at 0.003 mg/mL (green) and Dox at 0.002 mg/mL (red) in DMSO:water (1:1 v/v). St-PGA-hyd-Dox-Das-ANG-NAC spectrum shows peaks of Dox (480 nm) and Das (324 nm) absorbance.

We confirmed the purity of St-PGA-hyd-Dox-Das-ANG-NAC by TLC using MeOH as mobile phase and standard permanganate staining to detect TCEP (R_f(TCEP): 0.5) and NAC (R_f(NAC): 0.7). TLC failed to provide evidence of NAC or TCEP in St-PGA-hyd-Dox-Das-ANG-NAC (**Figure 4.17B**), thereby confirming conjugate purity.

In the UV-VIS spectrum of St-PGA-hyd-Dox-Das-ANG-NAC, we identified the absorbance peaks of Dox (λ_{max} = 480 nm) and Das (λ_{max} = 324 nm) (**Figure 4.17C**). We used the St-PGA-hyd-Dox-Das-ANG-NAC spectrum to quantify Dox loading following the same protocol described in *Chapter 2* (i.e., interpolation in a calibration curve of Dox in DMSO:water [1:1 v/v]), obtaining a value of 2.0% wt Dox (~ 0.8% mol Dox). However, the peak absorbance of Das suffered from interference from the absorbance of the phenylalanine residues from ANG (λ_{max} = 280 nm) and maleimide (λ_{max} = 245 and 284 nm), leading to an imprecise quantification. Thus, we employed a different method for Das loading quantification – the acid hydrolysis of the ester bond attaching Das to the St-PGA backbone and free drug liquid-liquid extraction employing the same procedure depicted for the pH-dependent drug release study developed in *Chapter 2*. We submitted a sample of St-PGA-hyd-Dox$_1$-Val-Das$_1$ (synthesized in *Chapter 2*) with a known Das loading to the same procedure as a control and to apply a correction factor to the value obtained for St-PGA-hyd-Dox-Das-ANG-NAC to compensate for the loss of drug during liquid-liquid extraction. Following this protocol, we obtained a value of 10.6% wt Das (~4.6% mol) as total loading. Overall, we observed a Dox:Das ratio in the final conjugate of 1:6, which is lower than the ratio determined for St-PGA-hyd-Dox-Das-Malei precursor (1:9, **Table 4.2**) due to the drug release during ANG conjugation and product purification that, as described earlier, was higher for Das than Dox. Nevertheless, St-PGA-hyd-Dox-Das-ANG-NAC still exhibits a drug loading with an excess of Das compared to Dox.

4.2.3.2. Physico-chemical Characterization of St-PGA-hyd-Dox-Das-ANG-NAC

We performed exhaustive physico-chemical characterization of St-PGA-hyd-Dox-Das-ANG-NAC. By SEC, we monitored the elution by UV-VIS spectroscopy to detect Dox (λ_{max} = 480 nm) and by fluorescence detection (FLD) to detect Das (λ_{ex} = 340 nm and λ_{em} = 374 nm). By FLD, we detected a single peak with a slight shoulder, which was more evident by 480 nm absorbance (**Figure 4.18A**). We believe this elution profile responds to ANG loading. Considering the degree of polymerization of our starting material (St-PGA, 150 glutamic units), a level of 1.3% mol ANG suggests the existence of a mixed St-PGA-hyd-Dox-Das-ANG-NAC population; one bearing one ANG and another bearing two. Due to the peptide's molecular weight, this difference can result in slightly different retention times. Indeed, we observed this shift while optimizing the reaction time for ANG conjugation (**Figure 4.2**).

We assessed the CAC of St-PGA-hyd-Dox-Das-ANG-NAC by DLS, obtaining a value of ~0.2 mg/mL (**Figure 4.18B**). While this value remains lower than that obtained for St-PGA-hyd-Dox$_1$-Das$_{10}$, it remains within the range of St-PGA-based conjugates synthesized in *Chapters 2* and *3.*
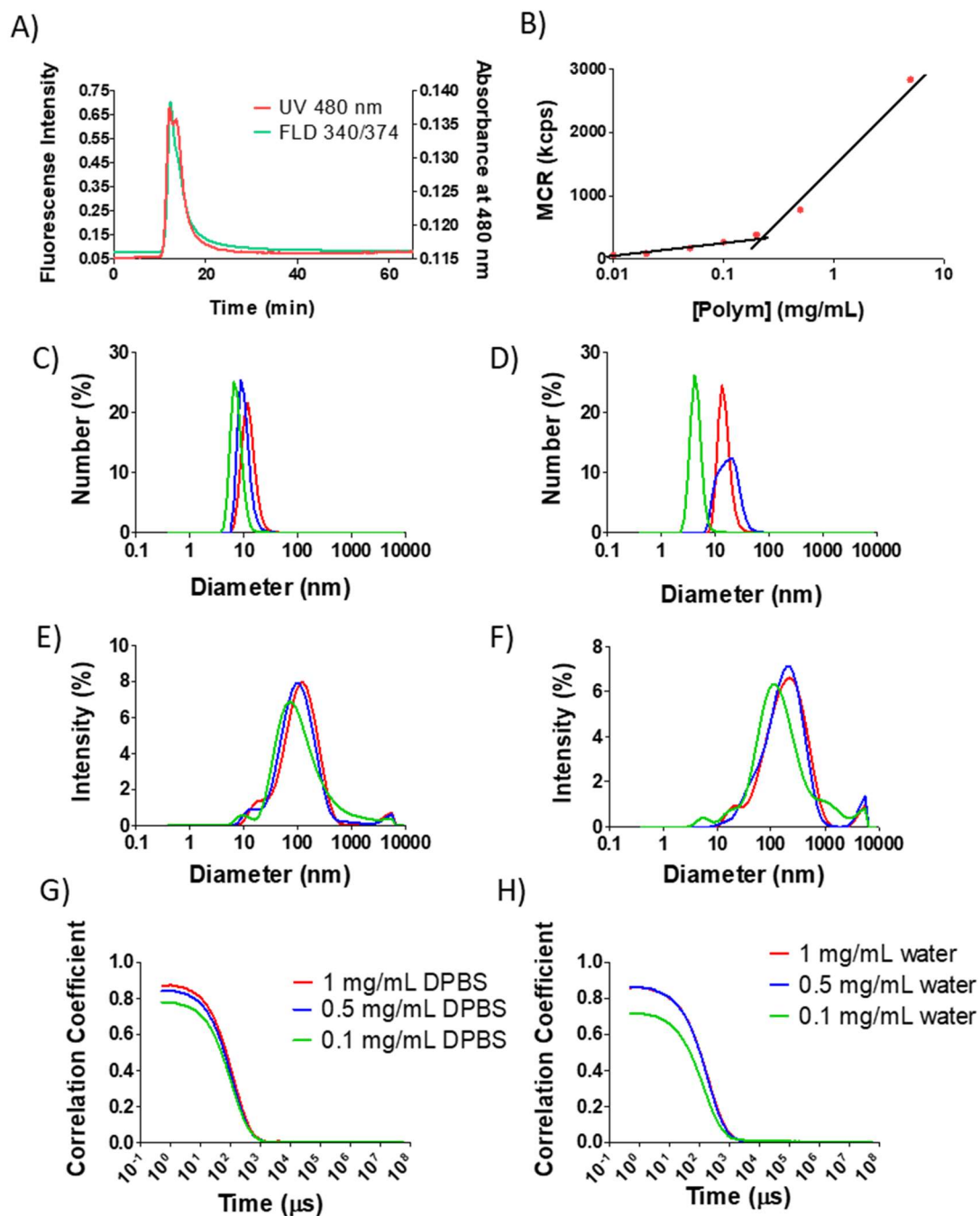
Figure 4.18. Size characterization of St-PGA-hyd-Dox-Das-ANG-NAC. (**A**) Representative SEC chromatogram monitoring the elution of Dox by absorbance at 480 nm, and Das by fluorescence detection with λex = 340 nm and λem = 374 nm. (**B**) Graphical determination of CAC by DLS. Data represented as average MCR of two measurements vs. conjugate concentration (logarithmic scale). (**C-H**) Size distribution in (**C**, **E,** and **G**) DPBS and (**D**, **F**, and **H**) MilliQ water at 1, 0.5, and 0.1 mg/mL. Data obtained by DLS. The hydrodynamic diameter distribution by (**C** and **D**) number and (**E** and **F**) intensity, and (**G** and **H**) the respective correlation functions are displayed. Data obtained from the average result of at least three measurements.

We evaluated the hydrodynamic diameter of St-PGA-hyd-Dox-Das-ANG-NAC by DLS at concentrations above (0.5 and 1 mg/mL) and below (0.1 mg/mL) the CAC value in DPBS (**Figure 4.18C, E,** and **G**) and MilliQ water (**Figure 4.18D, F,** and **H**). These measurements demonstrated the presence of small (~10 nm) particles by number (**Figure 4.18C** and **D**) but larger (~100 nm) particles by intensity (**Figure 4.18E** and **F**) in both media and at all concentrations evaluated. Overall, these findings suggested the presence of a reduced number of aggregates in the sample, with most conjugates remaining as unimers. All measurements possessed acceptable quality as revealed by the corresponding correlation functions, which displayed an intercept of ~0.8 and evident exponential decay (**Figure 4.18G** and **H**). Interestingly, St-PGA-hyd-Dox-Das-ANG-NAC measured in DPBS and St-PGA-hyd-Dox$_1$-Das$_{10}$, the untargeted counterpart, display similar sizes (i.e., 11.3 ± 5.1 nm, 0.5 mg/mL in DPBS for St-PGA-hyd-Dox$_1$-Das$_{10}$, see *Chapter 2*) despite the conjugation of the 2.3 kDa ANG peptide. St-PGA-hyd-Dox-Das-ANG-NAC and St-PGA-hyd-Dox$_1$-Das$_{10}$ also exhibited similar zeta potential (~-45 mV and ~-41 mV, respectively, at 0.5 and 1 mg/mL) (**Table 4.3** and *Chapter 2*, respectively). These findings suggest that St-PGA-hyd-Dox-Das-ANG-NAC will possess a similar circulation half-life *in vivo* than St-PGA-hyd-Dox$_1$-Das$_{10}$; however, the confirmation of this hypothesis requires future studies of the pharmacokinetic profile of both conjugates.

.

Table 4.3. Summary of primary characterization of ANG-tagged conjugates for *in vivo* proof-of-activity experiments.

	% wt Dox[A]	% wt Das[A]	Ratio Dox:Das[B]	ANG[C] (% wt)	ANG[D] (% mol)	Dh[E] (nm)	Dh[F] (nm)	CAC[G] (mg/mL)	Z-Pot[H] (mV)	Z-Pot[I] (mV)	CD[J]
St-PGA-hyd-Dox-Das-ANG-NAC	1.9	10.6	1:6	13.9	1.3	12.6 ± 4.1	10.2 ± 3.2	0.2	-45.4 ± 0.9	-44.9 ± 4.6	Random coil
St-PGA-ANG-NAC	-	-	-	20.1	1.9	7.9 ± 3.1	12.1 ± 5.4	0.3	-51.9 ± 0.9	-47.4 ± 1.1	Random coil

(**A**) Obtained by UV-VIS spectroscopy. (**B**) Drug ratio calculated considering the mol percentage obtained by iterative calculation from the weight percent. (**C**) Obtained by amino acid analysis. (**D**) Obtained by iterative calculation from the weight percent. (**E** and **F**) Hydrodynamic diameter (Dh) of the conjugate at (**E**) 1 mg/mL and (**F**) 0.5 mg/mL in DPBS. Data obtained from the distributions presented in Figure 4.21C and expressed as mean ± SD. (**G**) CAC value obtained graphically following a DLS method. (**H** and **I**) Zeta potential obtained by ELS at (**H**) 1 mg/mL and (**I**) 0.5 mg/mL in 1 mM KCl. Data expressed as mean ± SD of three measurements. (**J**) Secondary structure determined by CD spectroscopy.

We also evaluated the secondary structure of St-PGA-hyd-Dox-Das-ANG-NAC in DPBS and MilliQ water at a range of concentrations (0.1, 0.2, and 0.5 mg/mL). St-PGA-hyd-Dox-Das-ANG-NAC displayed the typical minima at 200 nm for the random coil conformation under all conditions evaluated (**Figure 4.19A** and **B**). When we analyzed the spectra at longer wavelengths, we found the same pattern observed for St-PGA-hyd-Dox$_1$-Val-Das$_1$ (see *Chapter 2*), a negative band at ~ 300 nm followed by a positive band at ~ 335 nm, i.e., a negative first Cotton effect at a longer wavelength and a positive second Cotton effect at a shorter wavelength centered at ~ 324 nm (the maximum of absorbance for Das) (**Figure 4.19C** and **D**). This observation suggests the stacking of Das molecules (40). We observed this phenomenon more noticeably in MilliQ water than DPBS, suggesting a possible influence of the carboxylic acid residues of PGA – the salt in DPBS neutralizes the negative charge, which does not occur in water (41). More ordered folding could explain the small size of St-PGA-hyd-Dox-Das-ANG-NAC despite the conjugation of a large moiety such as ANG. Regarding the possible stacking of Dox molecules, we failed to identify any evidence of Dox dimerization (**Figure 4.19C** and **D**), such as a negative band at 540 nm (42,43).
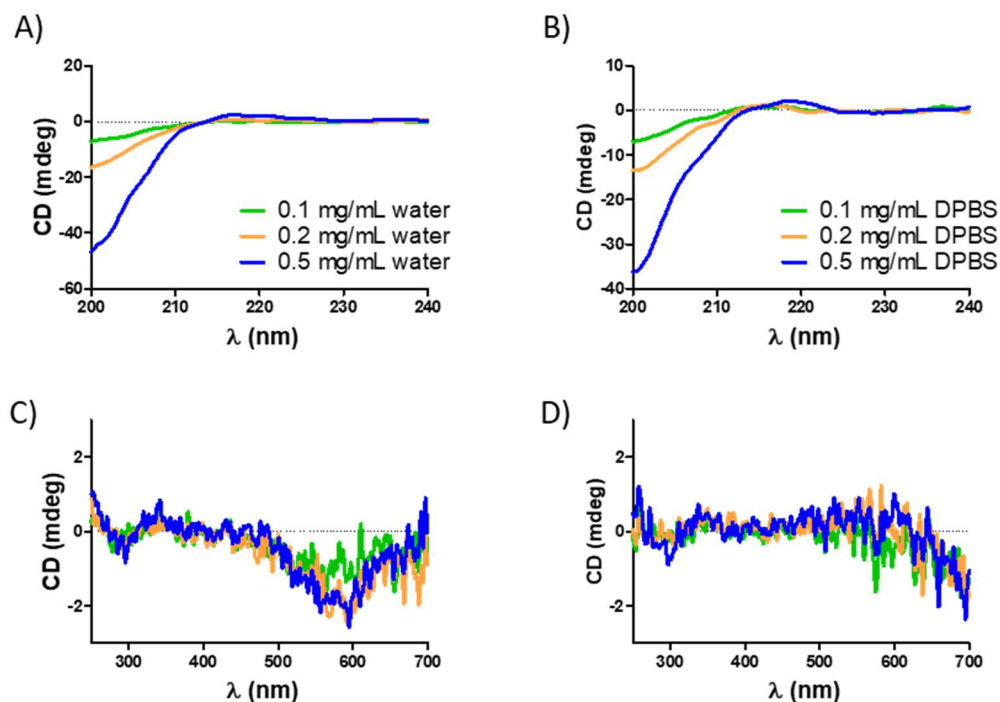
Figure 4.19. Secondary structure of St-PGA-hyd-Dox-Das-ANG-NAC. (**A-B**) CD spectra from 200 to 250 nm in (**A**) MilliQ water and (**B**) DPBS. (**C-D**) CD spectra from 250 to 700 nm in (**C**) MilliQ water and (**D**) DPBS. Average results with three accumulated measurements displayed.

Overall, we observed similar physico-chemical characteristics for St-PGA-hyd-Dox-Das-ANG-NAC and St-PGA-hyd-Dox_1-Das_{10} – similar sizes in DPBS, similar zeta potentials, and random coil conformation - suggesting that ANG conjugation fails to alter the main characteristics of St-PGA, as previously observed for St-PGA-ANG-NAC. St-PGA-hyd-Dox-Das-ANG-NAC and St-PGA-Cy5.5-ANG-NAC displayed random coil conformation and similar ANG loadings (1.3 vs. 1.4% mol). Therefore, we expect St-PGA-hyd-Dox-Das-ANG-NAC to accumulate in the brain in a comparable manner to St-PGA-Cy5.5-ANG-NAC. Studies of drug release profiles will shed more light on the similarities between St-PGA-hyd-Dox-Das-ANG-NAC and the untargeted St-PGA-hyd-Dox_1-Das_{10} counterpart (see *4.2.4.Drug Release Profile – Comparison with the St-PGA-hyd-Dox1-Das10 Untargeted Conjugate*), including potential anti-metastatic activity.

4.2.3.3. Synthesis and Physico-chemical Characterization of St-PGA-ANG-NAC as Vehicle Control for *In vivo* Proof of Activity Experiment

As a control for the *in vivo* experiment, we synthesized an ANG-tagged St-PGA conjugate without drugs (St-PGA-ANG-NAC) following the protocol described earlier (see *4.2.1.1.Maleimide-thiol Reaction Kinetics* Study). We used the St-PGA-Malei synthesized in earlier sections as a starting material (see **Figure 4.1** for ^{1}H-NMR spectrum confirming conjugate identity and purity). After ANG conjugation (St-PGA-ANG, **Supplementary Figure 4.2**) and NAC-mediated maleimide quenching, we obtained the final compound, St-PGA-ANG-NAC. The ^{1}H-NMR spectra of St-PGA-ANG-NAC confirmed conjugate purity and allowed the first assessment of ANG loading, obtaining 2.4% mol (**Figure 4.20**). We confirmed this value by amino acid analysis, obtaining a value of 20.1% wt, which corresponds to 1.9% mol ANG.
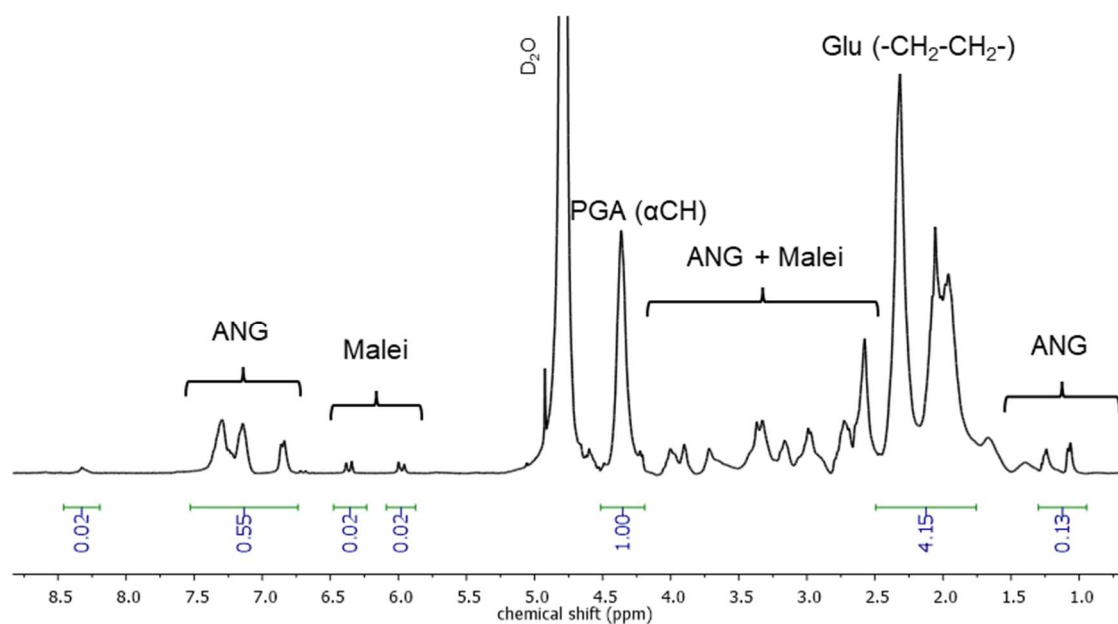

Figure 4.20. ^{1}H-NMR (D$_2$O) spectrum of St-PGA-ANG-NAC. The spectrum depicts the signals used for conjugate identification.

We exhaustively characterized St-PGA-ANG-NAC. We studied the secondary structure of St-PGA-ANG-NAC by CD in DPBS and MilliQ water at 0.1, 0.2, and 0.5 mg/mL. The CD spectra displayed the typical negative band at 200 nm corresponding to a random coil conformation (**Figure 4.21A**) at all conditions evaluated, as observed in the previous batch (see *4.2.1.2.St-PGA-ANG-NAC Physico-chemical Characterization*). The study of the zeta potential exhibited negative values similar to St-PGA-hyd-Dox-Das-ANG-NAC (**Table 4.3**).

We studied the aggregation of St-PGA-ANG-NAC in water by DLS, obtaining a CAC value of ~0.3 mg/mL (**Figure 4.21B** and **Table 4.3**), a value similar to that of the St-PGA-ANG-NAC conjugate obtained during reaction optimization (see *4.2.1.2.St-PGA-ANG-NAC Physico-chemical Characterization*) and St-PGA-hyd-Dox-Das-ANG-NAC.
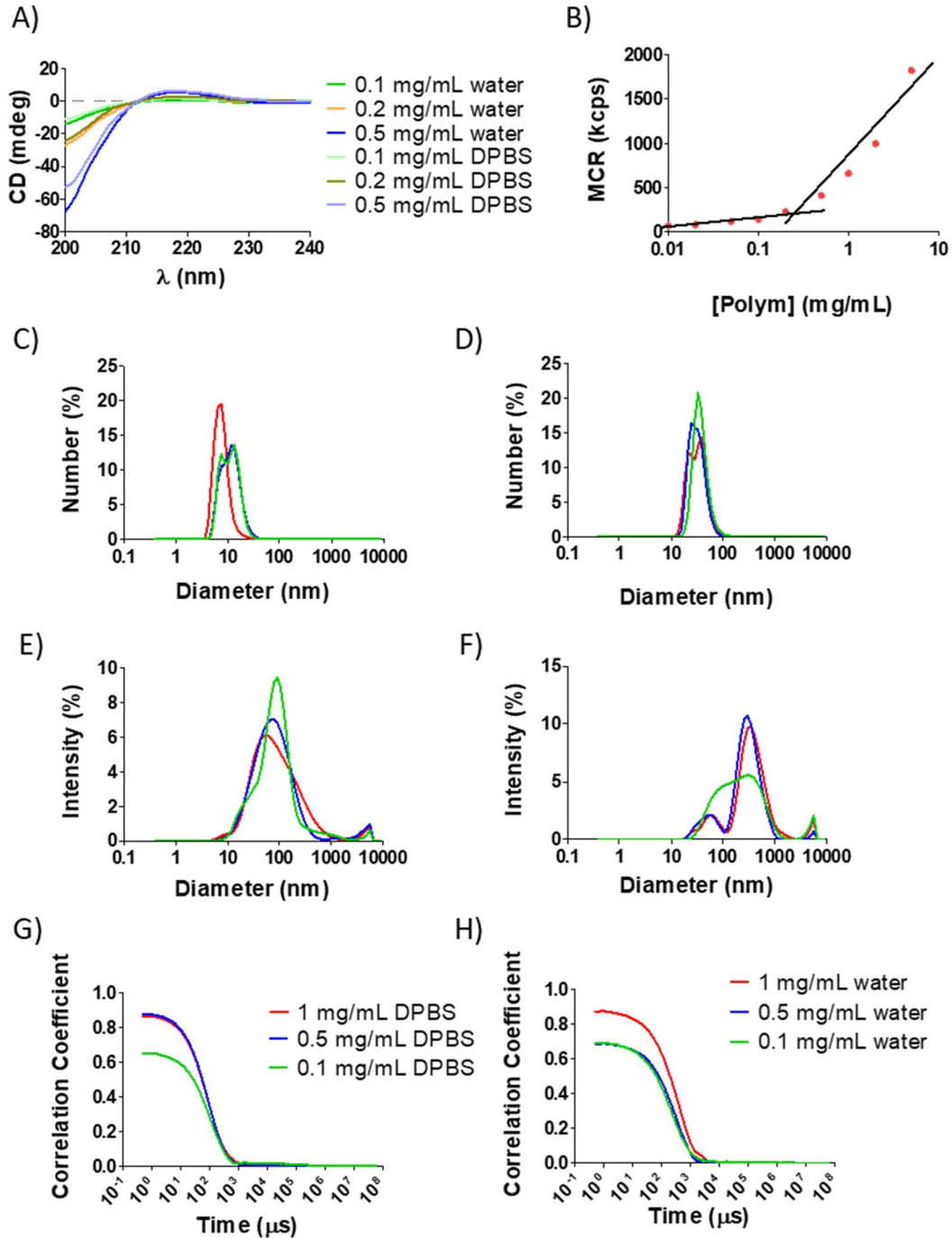
Figure 4.21. Characterization of St-PGA-ANG-NAC. (**A**) Secondary structure of St-PGA-ANG-NAC. CD spectra from 200 to 250 nm in MilliQ water and DPBS. Average results with three accumulated measurements displayed. (**B**) Graphical determination of CAC by DLS. Data represented as average MCR of two measurements vs. conjugate concentration (logarithmic scale). (**C-H**) Size distribution in (**C**, **E,** and **G**) DPBS and (**D**, **F**, and **H**) MilliQ water at 1, 0.5, and 0.1 mg/mL. Data obtained by DLS. The hydrodynamic diameter distribution by (**C** and **D**) number and (**E** and **F**) intensity, and (**G** and **H**) the respective correlation functions are displayed. Data obtained from the average result of at least three measurements.

We studied St-PGA-ANG-NAC size at concentrations below (0.1 mg/mL) and above (0.5 and 1 mg/mL) its CAC value in DPBS and MilliQ water (**Figure 4.21C-H**). We found a small hydrodynamic diameter for St-PGA-ANG-NAC in DPBS by number (~ 10 nm), which was similar at all concentrations evaluated (**Figure 4.21B**). This small size corresponds to the St-PGA unimer, thus displaying a comparable size to St-PGA-hyd-Dox-Das-ANG-NAC. By intensity, we identified one population with a broad size distribution centered at ~100 nm for St-PGA-ANG-NAC in DPBS (**Figure 4.21E**), suggesting the presence of a reduced number of aggregates in the sample as observed for St-PGA-hyd-Dox-Das-ANG-NAC. In water, we obtained results comparable to the St-PGA-ANG-NAC batch obtained during reaction optimization (see *4.2.1.2.St-PGA-ANG-NAC Physico-chemical Characterization*), i.e., we observed two populations in the size distribution by intensity (~60 nm and ~380 nm) and only one by number (~56 nm), suggesting the presence of a major population of ~56 nm diameter and a minor group of aggregates of ~380 nm diameter in the samples (**Figure 4.21F**). The associated correlation functions demonstrated an exponential decay implying the quality of the measurement; however, at low concentrations (0.1 mg/mL in DPBS and ≤0.5 mg/mL in MilliQ water), the intercept was low (<0.8), suggesting high background noise interference in the measurement at said concentrations (**Figure 4.21G** and **H**).

Overall, the data suggest that St-PGA-ANG-NAC displays similar behavior to St-PGA-hyd-Dox-Das-ANG-NAC in solution – a negative zeta potential, random coil conformation, similar CAC value, and comparable size in MilliQ water and DPBS. The similar physico-chemical characteristics of St-PGA-ANG-NAC and St-PGA-hyd-Dox-Das-ANG-NAC suggest that their post-administration behavior (e.g., circulation time) will be similar, thus defining St-PGA-ANG-NAC as an adequate control for our targeted combination conjugate. Furthermore, given the similarities observed for the two batches of St-PGA-ANG-NAC generated, these data also confirm the reproducibility of our ANG conjugation protocol.

4.2.4. Drug Release Profile – Comparison with the St-PGA-hyd-Dox$_1$-Das$_{10}$ Untargeted Conjugate

As described in *Chapter 2*, the biological activity of our combination conjugates depends on the drug ratio and drug release profile. For this reason, we studied pH and cathepsin B-mediated drug release kinetics for St-PGA-hyd-Dox-Das-ANG-NAC and compared the results with those obtained in *Chapter 2* for our lead candidate, St-PGA-hyd-Dox$_1$-Das$_{10}$.

The pH-mediated release profile obtained for St-PGA-hyd-Dox-Das-ANG-NAC (**Figure 4.22**) displayed similarities to St-PGA-hyd-Dox$_1$-Das$_{10}$ (see *Chapter 2*). The hydrazone linker displayed elevated sensitivity in aqueous media and underwent rapid hydrolysis, which supported elevated levels of Dox release immediately after dissolution (**Figure 4.22**). As hoped for, we observed significantly higher Dox release at pH 5.0 than at pH 7.4 at most time points ($p < 0.05$ at 15 min, 1.5 and 8 h; $p < 0.01$ at 30 min, 1, 3, and 5 h; **Figure 4.22**). We observed similar Das release at both pHs during the first hour of incubation, but then significantly higher Das release at pH 7.4 than pH 5.0 ($p < 0.05$ at 1.5, 3, and 8 h; $p < 0.01$ at 5 and 24 h; **Figure 4.22**).

A more detailed analysis of these results demonstrated that St-PGA-hyd-Dox$_1$-Das$_{10}$ displayed higher Dox and Das release at pH 5 compared to St-PGA-hyd-Dox-Das-ANG-NAC. For Das, St-PGA-hyd-Dox$_1$-Das$_{10}$ achieved 42% release after 24 h (see *Chapter 2*) versus 22% Das for St-PGA-hyd-Dox-Das-ANG-NAC ($p = 0.022$, **Figure 4.22**), while for Dox, St-PGA-hyd-Dox$_1$-Das$_{10}$ achieved 67% release after 8 h (see *Chapter 2*) versus 55% Dox for St-PGA-hyd-Dox-Das-ANG-NAC ($p = 0.003$, **Figure 4.22**). The reduced sensitivity of St-PGA-hyd-Dox-Das-ANG-NAC to an acidic environment may derive from the influence of ANG in the conjugate's solution conformation.
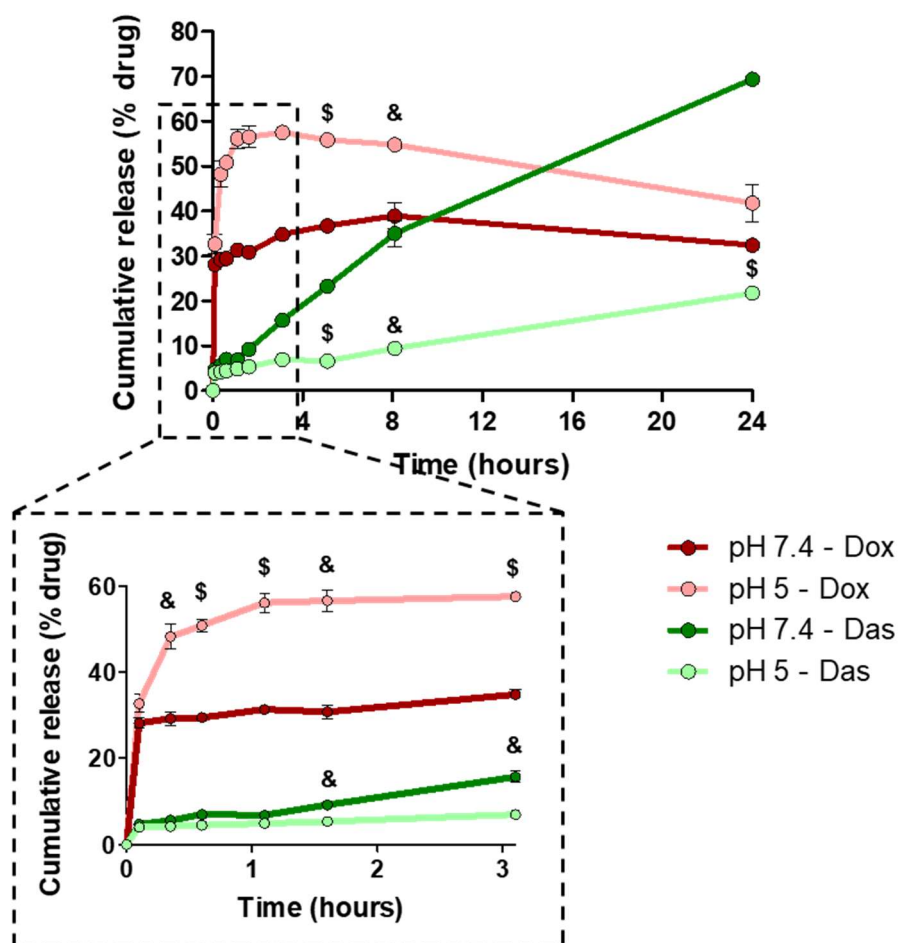
Figure 4.22. pH-dependent drug release of St-PGA-hyd-Dox-Das-ANG-NAC. Data represented as the percentage of free drug normalized to drug loading (mean ± SEM, n=2). Statistical analysis performed by unpaired, two-way Student's t-test. pH 5.0 vs. 7.4, [&]p<0.05, [$]p<0.01.

Importantly, we must also consider drug loadings to compare drug release from St-PGA-hyd-Dox-Das-ANG-NAC and St-PGA-hyd-Dox_1-Das_{10}. For this reason, we calculated the drug mass released per milligram of conjugate and observed that St-PGA-hyd-Dox-Das-ANG-NAC released a significantly higher mass of Dox than St-PGA-hyd-Dox_1-Das_{10} at both pHs (**Figure 4.23A**). Meanwhile, we observed a similar level of Das release from both conjugates, with a significant increase for St-PGA-hyd-Dox-Das-ANG-NAC at pH 7.4 only at very early time points (p<0.01 up to 30 min, **Figure 4.23B**). Overall, these results translate into significantly different available drug ratios over time (**Figure 4.23C**).

421

As described in *Chapter 2*, St-PGA-hyd-Dox$_1$-Das$_{10}$ supported a Dox:Das ratio of approximatively 1:1 from early time points (e.g., 1:0.8 after 1 hour at pH 5.0), increasing gradually up to a ratio of 1:8 after 24 h at pH 5.0, and 1:30 at pH 7.4. St-PGA-hyd-Dox-Das-ANG-NAC displayed a similar profile to St-PGA-hyd-Dox$_1$-Das$_{10}$ at pH 5, with no significant differences up to 1.5 h. After this point, St-PGA-hyd-Dox-Das-ANG-NAC displayed a significantly different Dox:Das ratio with lower Das excess than St-PGA-hyd-Dox$_1$-Das$_{10}$ ($p<0.01$ at 3 and 24 h, $p<0.05$ at 8 h, **Figure 4.23C**). At pH 7.4, we found a significant difference between St-PGA-hyd-Dox-Das-ANG-NAC and St-PGA-hyd-Dox$_1$-Das$_{10}$ starting at 30 min ($p<0.05$), with St-PGA-hyd-Dox-Das-ANG-NAC showing significantly less Das excess until the experimental endpoint ($p<0.001$ at 1 h, $p<0.05$ from 1.5 to 8h, $p<0.01$ at 24 h, **Figure 4.23C**).
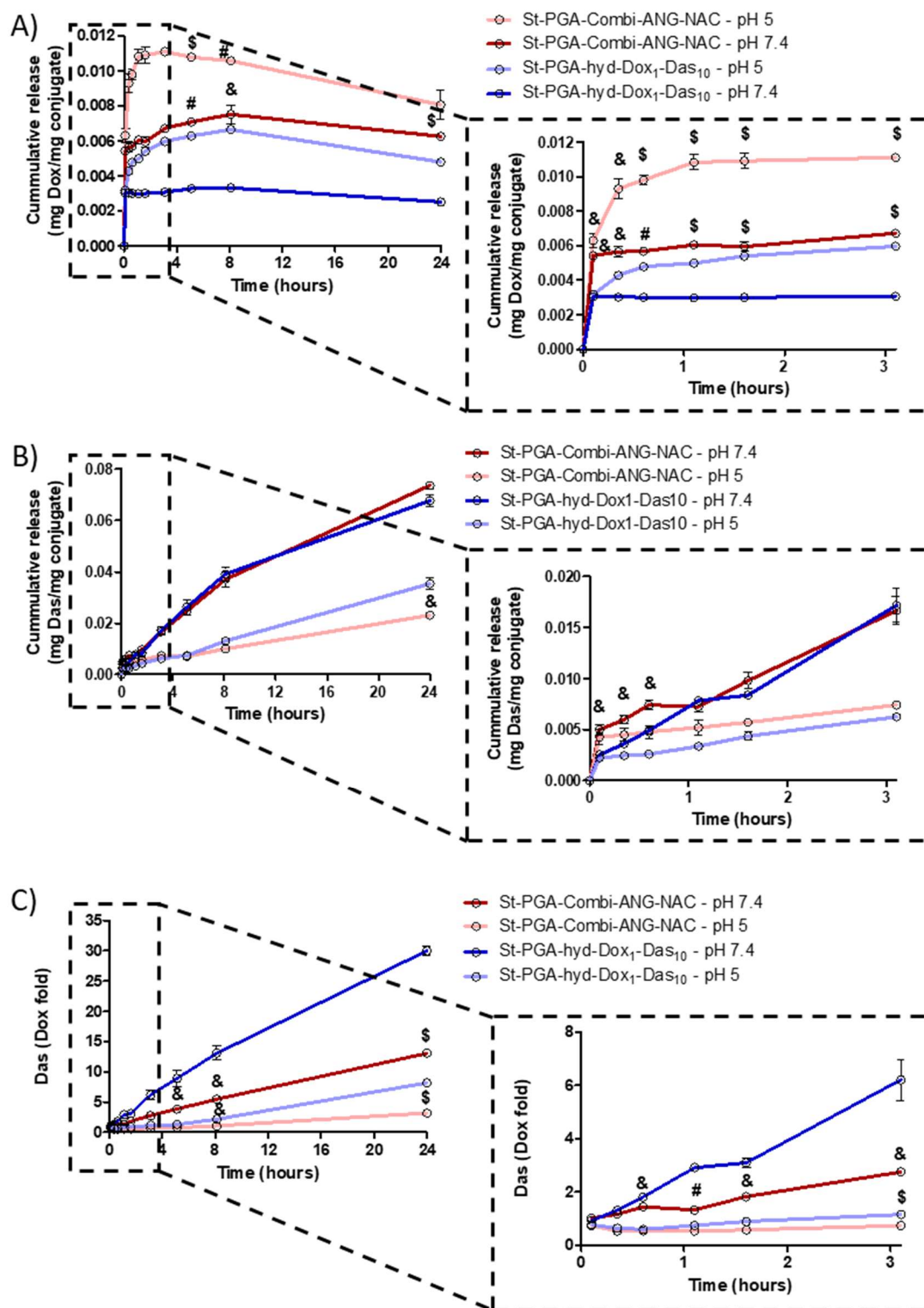
Figure 4.23. Comparison of pH-dependent drug release of St-PGA-hyd-Dox-Das-ANG-NAC and St-PGA-hyd-Dox$_1$-Das$_{10}$. (**A**) Data represented as mass of free Dox per milligram of conjugate (mean ± SEM, n=2). (**B**) Data represented as mass of free Das per milligram of conjugate (mean ± SEM, n=2). (**C**) Data represented as drug ratio (Das equivalents) (mean ± SEM, n=2). Statistical analysis performed by unpaired, two-way Student's t-test. St-PGA-hyd-Dox-Das-ANG-NAC vs. St-PGA-hyd-Dox$_1$-Das$_{10}$, $^{\&}p<0.05$, $^{\$}p<0.01$, $^{\#}p<0.001$.

To evaluate drug release after cell internalization, we studied drug release kinetics of St-PGA-hyd-Dox-Das-ANG-NAC in the presence of the protease cathepsin B in acidic media, thereby mimicking the lysosomal environment. In this media, St-PGA-hyd-Dox$_1$-Das$_{10}$ precipitated after 5 h; however, St-PGA-hyd-Dox-Das-ANG-NAC remained soluble for 72 h under the same conditions. This result suggests that ANG conjugation increases conjugate solubility through a conformational change, most probably due to the more efficient steric hindrance of hydrophobic drugs, a hypothesis supported by the reduced drug release (compared to St-PGA-hyd-Dox$_1$-Das$_{10}$) in pH 5 PBS. St-PGA-hyd-Dox-Das-ANG-NAC exhibited rapid Dox release, reaching 60% after 3 h before reaching a plateau (**Figure 4.24A**). On the contrary, we observed slow Das release that gradually increased to 55% after 72 h (**Figure 4.24A**). Compared with drug release at pH 5.0 (PBS buffer without cathepsin B), we discovered similar Dox release and higher Das release starting at 8 h (**Figure 4.24B**). Das release from St-PGA-hyd-Dox-Das-ANG-NAC displayed similarities to St-PGA-hyd-Dox$_1$-Das$_{10}$ cathepsin B-mediated drug release (only up to 5 h), while we found higher Dox release than for St-PGA-hyd-Dox-Das-ANG-NAC, thus reducing the ratio of Dox:Das release (**Figure 4.24C**). Nevertheless, we note the preliminary nature of this study, and we require additional data points to confirm our results.
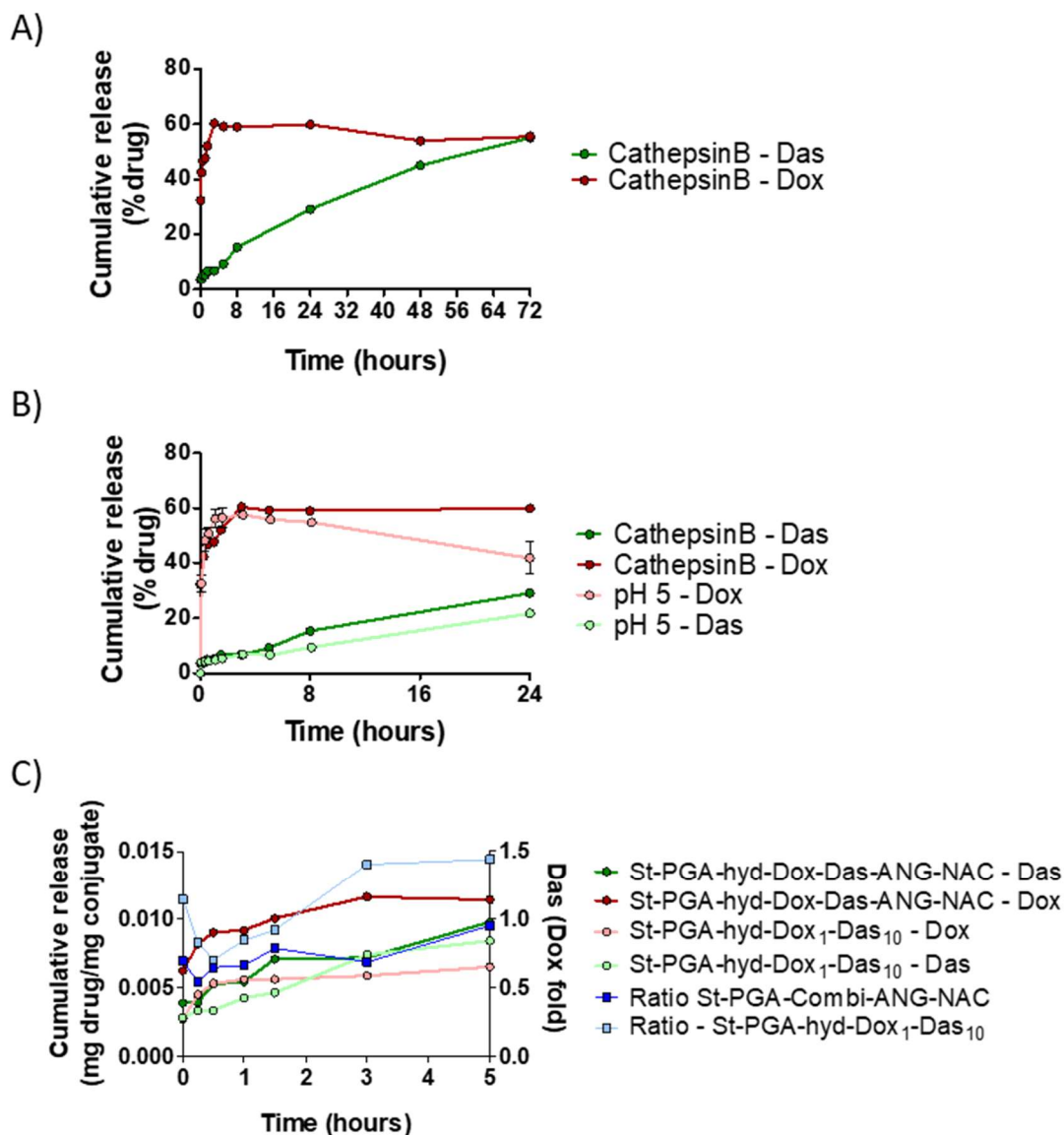
Figure 4.24. Cathepsin B mediated drug release profile of St-PGA-hyd-Dox-Das-ANG-NAC. (**A**) Cathepsin B mediated drug release profile represented as the percentage of released drug normalized to the total drug loading (n=1). (**B**) Comparison of drug release at pH 5.0 and in the presence of cathepsin B. Data represented as the percentage of released drug normalized to the total drug loading (n=1 for cathepsin B, n=2 for pH 5, mean ± SD). (**C**) Comparison of cathepsin B mediated drug release of St-PGA-hyd-Dox-Das-ANG-NAC and St-PGA-hyd-Dox_1-Das_{10}. Data represented as milligram of drug released per milligram of conjugate and Dox:Das ratio in Dox equivalents.

In summary, St-PGA-hyd-Dox-Das-ANG-NAC displays a similar release profile to St-PGA-hyd-Dox_1-Das_{10}, with rapid Dox release and higher at pH 5 than 7.4, and higher Das release at pH 7.4 than 5.0. Nevertheless, the different drug loading/ratio of St-PGA-hyd-Dox-Das-ANG-NAC supports

425

a lower ratio of released drugs in all media (i.e., less excess of Das in the media compared to St-PGA-hyd-Dox$_1$-Das$_{10}$). Despite the noted reduction in the released drug ratio, a higher loading of Das than Dox helps to maintain an excess of free Das in the media, which enhances the anti-tumor and anti-metastatic activity of the conjugate (see *Chapter 2*). Thus, we still expect satisfactory results *in vivo*, comparable to that of the untargeted St-PGA-hyd-Dox$_1$-Das$_{10}$ counterpart.

4.2.5. In vivo Proof-of-activity Against Breast Cancer Brain Metastasis

We evaluated the anti-metastatic activity of St-PGA-hyd-Dox-Das-ANG-NAC in a TNBC brain metastasis mouse model through a collaboration with the laboratory of Manuel Valiente at the *Centro Nacional de Investigaciones Oncológicas* (CNIO, Madrid, Spain). The model employs the intracardiac injection of MDA-MB-231-BrM3 (MDA231-BrM) cells in immunocompromised nude mice. MDA231-BrM cells were previously obtained by successive injection cycles into immunocompromised mice and the primary culture of tumor cells found in the brain (5). This cell line displays robust brain tropism, increased secondary tumor induction efficiency, and generates lesions in the cerebrum, cerebellum, brainstem, and leptomeninges. MDA231-BrM cells also constitutively express green fluorescent protein (GFP) and luciferase to allow the identification in tissue slides and monitoring by the *in vivo*/*ex vivo* detection of bioluminescence (5).

The injection of MDA231-BrM cells into the left ventricle induces secondary brain tumor formation (5,44,45); after 24 h, MDA231-BrM cells adhere to the blood vessel endothelium within the brain, from where they extravasate to give rise to the secondary tumor (5). After four to six weeks, brain metastases are fully developed and mice reach disease endpoint, displaying significant weight loss and neurological symptoms (46).

We injected the MDA231-BrM cells into the left ventricle of sixteen athymic female nude mice and started treatment with St-PGA-hyd-Dox-Das-ANG-NAC ("Combi," eight mice) or St-PGA-ANG-NAC ("Vehicle," eight mice) after seven days (**Figure 4.25A**). Considering that St-PGA-hyd-Dox$_1$-Das$_{10}$ displayed anti-tumor activity against primary and secondary tumors derived from the MDA-BM-231-Luc cell line without signs of systemic toxicity when administered at 1.2 mg Dox/Kg equivalents (see *Chapter 2*), we injected our targeted conjugate, St-PGA-hyd-Dox-Das-ANG-NAC, at an equivalent dose. We injected St-PGA-ANG-NAC at an equivalent polymer dose (53.5 mg/Kg) as control. We retro-orbitally injected the conjugates dissolved in DPBS twice a week for three weeks (six doses) and monitored the evolution of metastatic growth in the head and extracranial region of the animal by bioluminescence detection after luciferin administration (**Figure 4.25A**). We also monitored animal weight as an indicator of animal wellbeing/treatment safety. After administering six doses, we euthanized animals and harvested brains and lungs for *ex vivo* bioluminescence quantification. We also selected four brains per treatment group for histological analysis to detect and measure MDA-231-BrM metastatic lesions by immunofluorescence (**Figure 4.25A**).
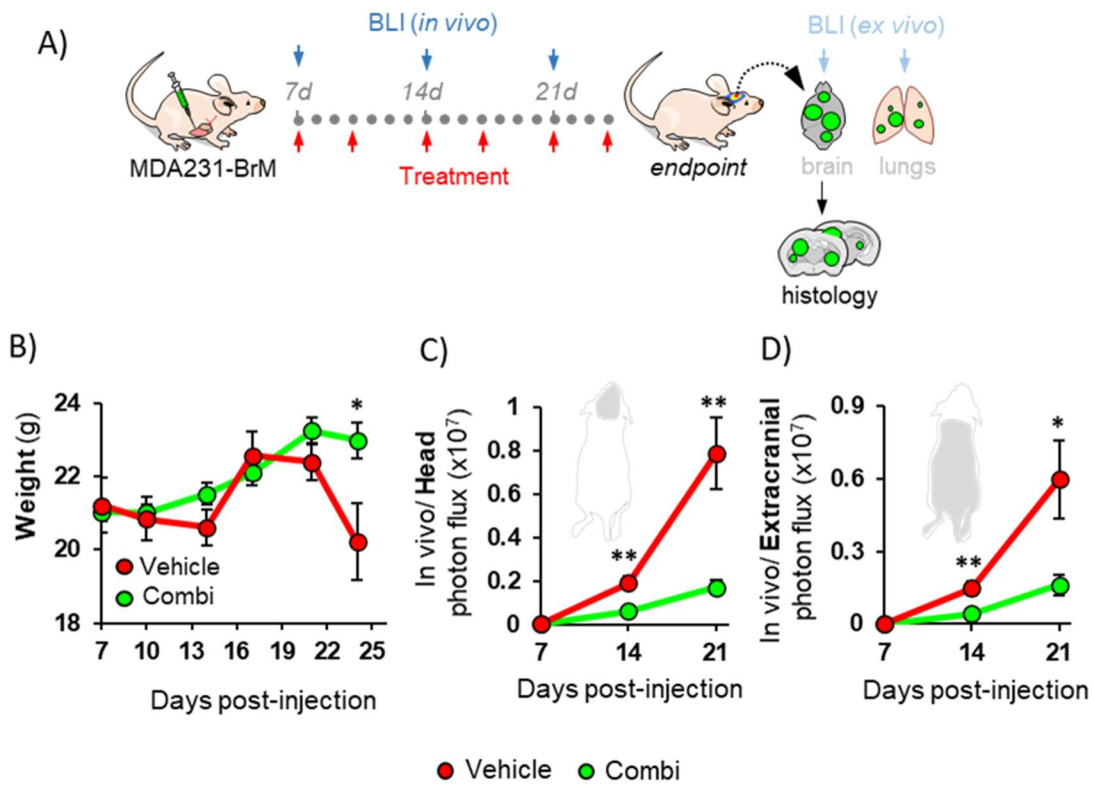
Figure 4.25. *In vivo* anti-metastatic activity of St-PGA-hyd-Dox-Das-ANG-NAC. (**A**) Experiment timeline. Cells were injected into the left ventricle at day 0, with retro-orbital conjugate administration beginning on day seven and compounds administered twice a week at a 1.2 mg/Kg dose in Dox equivalents. Metastasis progression was assessed every week by bioluminescence detection by IVIS® technology. On day twenty-four, animals were euthanized, and metastatic spread in the brain and lungs examined *ex vivo* by IVIS® technology. Brains were also harvested for histological analysis. (**B**) Animal weight evolution. Data represented as animal weight in grams versus time (mean ± SEM, n=8). (**C** and **D**) Metastasis progression assessed by bioluminescence detection (photon flux) *in vivo* in (**D**) head and (**E**) extracranial regions. Data expressed as photon flux versus time (mean ± SEM; n=8). Statistical analysis performed by unpaired, two-way Student's t-test. *p<0.05. **p<0.01.

While animals treated with St-PGA-hyd-Dox-Das-ANG-NAC (Combi) failed to display any weight loss or negative impacts on wellbeing, mice treated with St-PGA-ANG-NAC (Vehicle) experienced a dramatic disease progression-associated weight loss (>20%) from day twenty-one (**Figure 4.25B**, p=0.0255 versus St-PGA-hyd-Dox-Das-ANG-NAC) (46). Monitoring metastatic colonization by bioluminescence provided evidence that treatment with St-PGA-hyd-Dox-Das-ANG-NAC significantly reduced metastatic spread to the head (**Figure 4.25C**, p=0.0016 for day fourteen and p=0.0026 for day twenty-one) and extracranial region (**Figure 4.25D**, p=0.0081 for day fourteen and p=0.0200 for day twenty-one). In agreement with the latter, *ex vivo* bioluminescence detection at the endpoint (day twenty-five) demonstrated a significant reduction of metastatic spread in lungs (**Figure 4.26B** and **C**, p=0.0244 versus St-PGA-ANG-NAC). This result also agrees with the anti-metastatic activity of St-PGA-hyd-Dox$_1$-Das$_{10}$ in the metastatic TNBC mouse model employed in *Chapter 2*; however, St-PGA-hyd-Dox$_1$-Das$_{10}$ failed to reach a statistically significant difference versus DPBS. We believe the improved efficacy of St-PGA-hyd-Dox-Das-ANG-NAC in reducing extracranial disease spread relies, at least partially, on the expression of LRP-1 by MDA-MB-231 cells (which binds to ANG).
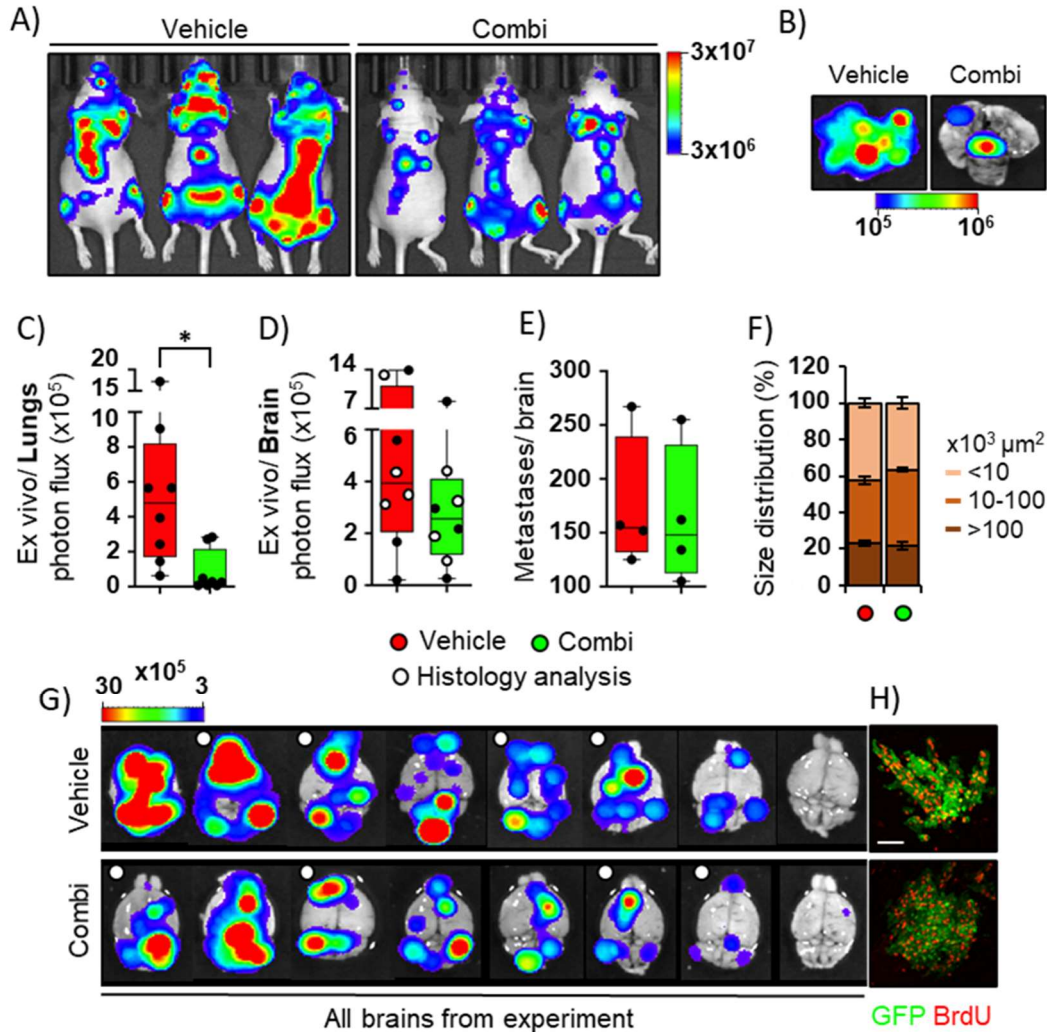
Figure 4.26. Evaluation of metastatic spread. (**A**) Representative IVIS® images of mice at day twenty-one. (**B**) Representative *ex vivo* IVIS® images of lungs. (**C** and **D**) *Ex vivo* evaluation of metastatic spread by bioluminescence detection in (**C**) lungs and (**D**) brain. Data expressed as photon flux (mean ± SEM, n=8). (**E** and **F**) Histological analysis of metastatic brain spread. Data expressed as (**E**) number of metastasis and (**F**) size of metastatic foci (mean ± SEM, n=4). (**G**) *Ex vivo* IVIS® images of brains. (**H**) Representative immunofluorescence image from metastatic lesions. BrdU: bromodeoxyuridine. Statistical analysis performed by unpaired, two-way Student's t-test. *p<0.05.

Bioluminescence detection in the brain *ex vivo* exhibited a reduction in the metastatic spread in the brain for St-PGA-hyd-Dox-Das-ANG-NAC treatment compared to St-PGA-ANG-NAC; however, we failed to find a statistically significant difference for this comparison (**Figure 4.26D** and **G**, p=0.2053). Histological analysis of selected brains (n=4) suggested a lack of efficacy of St-PGA-hyd-Dox-Das-ANG-NAC in reducing the number (**Figure 4.26E**) and size (**Figure 4.26F** and **H**) of the metastatic lesions

compared to St-PGA-ANG-NAC. Therefore, while significantly reducing metastatic lung colonization, we note the limited activity of St-PGA-hyd-Dox-Das-ANG-NAC in the brain.

Overall, these data demonstrate the anti-metastatic activity of St-PGA-hyd-Dox-Das-ANG-NAC (considering the reduction in lung metastasis) but suggest that we failed to reach a therapeutic drug concentration (or ratio) in the brain at this concentration and dose schedule. Therefore, we plan to perform further experiments using an increased conjugate dose, an approach supported by the lack of toxicity observed with the current concentrations. We selected the *in vivo* experiment dose after the proof-of-activity obtained in *Chapter 2* for St-PGA-hyd-Dox$_1$-Das$_{10}$ untargeted conjugate with 1.2 mg Dox/Kg. We used this low dose of Dox since our previous research provided evidence that higher doses of free Dox (1.5 mg Dox/Kg) resulted in systemic toxicity and, eventually, animal death (47). However, the brain metastasis model employed was developed using an athymic nude mouse strain which, according to literature, can support higher Dox doses than the non-obese diabetic/severe combined immunodeficient (NOD/SCID) strain used in *Chapter 2* (28,48). Thus, we plan to perform a new *in vivo* experiment to administer higher doses of Dox equivalents. First, we will determine the maximum tolerated dose in an athymic nude mouse strain to adjust the dose for the model with brain metastasis. We expect the dose increment to lead to a higher concentration of therapeutic agents in metastatic tissues, leading to a more significant reduction in the metastatic spread in both the lungs and brain.

If an increment in the injected dose fails to enhance the anti-metastatic activity of the conjugate, we could explore alterations to the conjugate design. For example, Guo et al. (28) included statins in their Dox-loaded ANG-tagged nanoparticles to increase the expression of LRP-1 receptor in both brain endothelial cells and brain metastatic tumor cells to increase brain uptake and Dox accumulation in the tumor. Alternatively, ANG could be

replaced for another peptide targeting a different receptor in the BBB, such as T7, which targets the transferrin receptor (12). This strategy has shown promising results in delivering a combination of gene therapy and Dox to glioblastoma tumors (49).

4.3. CONCLUSIONS

Brain metastasis represents the most lethal complication of breast cancer. With the BBB and BTB hampering the efficacy of systemically administered therapies, the clinical management of brain metastasis relies on local approaches, such as surgical resection or radiotherapy, which have limited efficacy and numerous side effects. The development of nanomedicinal strategies to bypass the BBB provides new hope for disease treatment. Here, we have synthesized, physicochemically characterized, and biologically evaluated a new St-PGA-based targeted combination conjugate bearing Dox and Das as drug combination and ANG for brain targeting to treat TNBC brain metastasis.

Our earlier work (see *Chapter 2*) described the synthesis of St-PGA-hyd-Dox_1-Das_{10}, a St-PGA-based combination conjugate bearing an optimized ratio of Dox and Das as a synergistic drug combination conjugated through pH-labile linkers (hydrazone for Dox and ester for Das). St-PGA-hyd-Dox_1-Das_{10} demonstrated elevated anti-tumor activity against primary tumor and lung metastasis in an orthotopic human TNBC mouse model. Following a rational design, we aimed to obtain a targeted version of St-PGA-hyd-Dox_1-Das_{10} to treat TNBC brain metastasis by incorporating ANG into the conjugate.

Towards this aim, we optimized a rapid and straightforward synthetic protocol for ANG conjugation to St-PGA via maleimide-thiol chemistry. The mild conditions (i.e., DPBS pH 7.2, room temperature) and short reaction times (5 h) allowed the use of this protocol for drug-bearing St-PGA

conjugates with reduced drug loading loss. Physico-chemical characterization provided evidence that ANG conjugation did not change the main polymer characteristics, maintaining negative charge, secondary structure, and aggregation capacity in water.

The biodistribution study performed with Cy5.5-labeled St-PGA conjugates in healthy mice proved the brain targeting capacity of ANG by demonstrating a more significant accumulation in the brain for St-PGA-Cy5.5-ANG-NAC than St-PGA-Cy5.5-NAC. Additionally, these conjugates displayed a similar accumulation in the liver and spleen, suggesting that ANG conjugation did not alter immune responses or conjugate clearance.

We believe that conjugate efficacy relies as much on brain targeting as the drug combination and linking chemistry employed. For this reason, although we observed limited accumulation in the brain in the biodistribution study, we expected encouraging outcomes from the *in vivo* proof-of-activity experiment.

Thanks to the orthogonal chemistries used for drug and ANG conjugation, we combined both synthetic protocols to yield an ANG-bearing St-PGA combination conjugate, i.e., St-PGA-hyd-Dox-Das-ANG-NAC. Compared to St-PGA-hyd-Dox$_1$-Das$_{10}$, St-PGA-hyd-Dox-Das-ANG-NAC displayed a higher Dox loading (1.9% wt for St-PGA-hyd-Dox-Das-ANG-NAC versus 1% wt for St-PGA-hyd-Dox$_1$-Das$_{10}$), which changed the final drug ratio of the conjugate (1:6 for St-PGA-hyd-Dox-Das-ANG-NAC versus 1:9 for St-PGA-hyd-Dox$_1$-Das$_{10}$). St-PGA-hyd-Dox-Das-ANG-NAC displayed similar physico-chemical characteristics to St-PGA-hyd-Dox$_1$-Das$_{10}$, with sizes of ~10 nm on its St-PGA unimer form, negative zeta potential, and random coil conformation. We also observed similar pH-dependent drug release profiles for St-PGA-hyd-Dox-Das-ANG-NAC and St-PGA-hyd-Dox$_1$-Das$_{10}$; however, the different drug loading significantly changed the released drug ratio. We observed this behavior in *Chapter 2* with St-PGA-hyd-Dox$_1$-Das$_{10}$ and St-PGA-hyd-Dox$_1$-Das$_1$, where we

described that drug release relied mainly on the linking chemistry used for drug conjugation, with drug loading having no influence on drug release but being determinant on drug bioavailability in target tissues.

The biological evaluation of St-PGA-hyd-Dox-Das-ANG-NAC on an MDA-MB-231-based brain metastasis mouse model provided promising results. Our compound displayed significant efficacy in reducing extracranial metastatic spread (especially in the lungs), which agrees with the anti-metastatic activity observed for the untargeted counterpart (see *Chapter 2*). We believe the expression of LRP-1 by MDA-MB-231 cells served to target these cells *in vivo*, increasing conjugate efficacy in reducing extracranial metastatic spread; however, we did not observe elevated anti-metastatic activity in the brain, suggesting that we failed to reach a therapeutic concentration (or ratio) of drugs in the target tissue. Nevertheless, we did observe an improvement in animal wellbeing with St-PGA-hyd-Dox-Das-ANG-NAC treatment compared to the St-PGA-ANG-NAC vehicle control. This result highlighted the safety of our compound and suggested partial activity against metastatic brain disease.

Therefore, we believe we can further improve the therapeutic outcome of our conjugate by increasing the administered dose. We used 1.2 mg Dox/Kg since higher doses of free Dox-induced toxicity in the orthotopic human TNBC model used in *Chapter 2* obtained in NOD/SCID mice. The brain metastasis model was developed using an athymic nude mouse strain, which affords higher Dox doses (28,48). Thus, we plan to perform *in vivo* experiments to administer higher doses of Dox equivalents. We expect incrementing the injected dose will lead to a higher concentration of drugs in metastatic tissue, significantly reducing secondary tumor spread/growth in both lungs and the brain.

4.4. MATERIALS AND METHODS

4.4.1. Materials

All solvents were of analytical grade and obtained from Sharlab Chemicals (Sharlab S.L., Barcelona, Spain) except trifluoroacetic acid (TFA), which was obtained from TCI Deutschland GmbH (Eschborn, Germany), and THF and that was freshly distilled. Water was type I (MilliQ) unless otherwise specified. Deuterated solvents were obtained from Deutero GmbH (Kastellaun, Germany). All chemicals were reagent grade, obtained from Sigma-Aldrich (Merck KGaA, Darmstadt, Germany) except 4-dimethyl aminopyridine (DMAP), which was obtained from Fluka (Thermo Fisher GmbH, Kandel, Germany). 4-(4,6-dimethoxy-1,3,5-triazin-2-yl)-4-methyl-morpholinium tetrafluoroborate (DMTMM BF_4) was synthesized as described in reference (50). Doxorubicin HCl was obtained from MedKoo Biosciences, Inc. (Morrisville, NC, USA). Dasatinib was obtained from LC Laboratories Inc. (Woburn MA, USA). Sulfo-cyanine5.5 amine was obtained from Lumiprobe GmbH (Hannover, Germany). St-PGA (108 glutamic acid units, ~14 KDa) was obtained from Polypeptide Therapeutic Solutions S.L. (Valencia, Spain) unless otherwise specified. Angiopep-2-SH (Ac-TFFYGGSRGKRNNFKTEEY-C-NH$_2$) was obtained from Selleck Chemicals LLC (Houston, TX, USA). Preparative SEC was performed using Sephadex LH-20 or Sephadex G25 medium from GE Healthcare (Global Life Sciences Solutions USA LLC, Marlborough, MA, USA). Ultrafiltration was performed in a Millipore (Merck KGaA, Darmstadt, Germany) ultrafiltration device fitted with a 3 kDa molecular weight cut-off (MWCO) regenerated cellulose membrane (Vivaspin^{TM}). Dialysis membranes were obtained from Spectrum Chemicals Mfg. Corp. (New Brunswick, NJ, USA). HyClone Dulbecco's phosphate-buffered saline (DPBS) was obtained from Cytiva UK Ltd. (Buckinghamshire, UK).

4.4.2. Synthetic Protocols

4.4.2.1. Modification of Star-poly(glutamic acid) with Maleimide Moieties (St-PGA-Malei)

N-(2-Aminoethyl)maleimide trifluoroacetate salt was conjugated to St-PGA by DMTMM chemistry in organic media, following protocols detailed earlier (see *Chapter 2*). Maleimide loading was obtained by ^{1}H-NMR comparing the signal of the two protons in the 2,5-pyrrolidone of N-(2-aminoethyl)maleimide with the α-carbon proton of PGA.

Yield: 73%. CE: 100%. ^{1}H-NMR: δ_H (300 MHz, D_2O) 8.32 (1H initiator), 7.04-6.73 and 6.47-5.85 (2H maleimide), 4.55-4.17 (1H αC PGA), 4.10-2.71 (4H CH_2CH_2 maleimide), 2.66-1.77 (4H, Glu).

4.4.2.2. Synthesis of Vehicle Control St-PGA-ANG-NAC and Maleimide-thiol Reaction Monitorization

4.4.2.2.1. Angiopep-2-SH Conjugation via Maleimide-thiol Chemistry – Reaction Monitorization

DPBS was degassed by sonication and N_2 (g) purging. St-PGA-Malei (0.50 mmol, 1 eq.) was dissolved in 7 mL of degassed DPBS in a one-neck round bottom flask fitted with a stir bar, a septum, and an N_2 (g) inlet and outlet. A stock solution of TCEP at 50 mg/mL in degassed DPBS was prepared, and the pH was adjusted to 7 with NaOH 5M, reaching a final concentration of 44 mg/mL. Anigiopep-2-SH (0.012 mmol, 0.024 eq.) was dissolved in 3 mL of degassed DPBS. Then, Angiopep-2-SH and the appropriate volume of TCEP stock (0.035 mmol, 0.070 eq.) were added to the polymer solution, and the reaction mixture was purged with N_2 (g). The reaction was left to proceed at room temperature. The reaction kinetics was monitored by SEC. At 1, 3, 5, 17, and 25 h, 100 μL aliquots were taken, diluted with 200 μL of DPBS, filtered through a nylon 0.45 μm filter, and injected into the chromatographic system (see *4.4.3.5.Size Exclusion Chromatography*). The elution was monitored by multi-angle light scattering

(MALS). The retention time (recorded by 90º light scattering) versus reaction time was plotted to study the evolution of ANG conjugation. At 5 h, 1 mL of the reaction mixture was isolated for purification by dialysis in a Float-A-Lyzer device (3 kDa MWCO) versus water at 4ºC. At 25 h, the remaining reaction mixture (~ 72 mg of polymer) was transferred to a dialysis bag (3.5 kDa MWCO) for purification in water at 4º C. A small precipitate was observed, which was eliminated by centrifugation at 3000 g for 5 min. After lyophilization, Angiopep-2 loading was assessed by ^{1}H-NMR by comparing the signals of the phenylalanine and tyrosine residues (23 protons) of the peptide with the α-carbon proton of PGA.

Yield: ~ 86%. CE: ~ 136%.^{1}H-NMR: δ_H (300 MHz, D_2O) 8.34 (1H initiator), 7.55-6.64 (23H Phe and Tyr Angiopep-2), 6.49-5.94 (2H maleimide), 4.51-4.08 (1H αC PGA), 4.09-2.79 (4H CH_2CH_2 maleimide, 24 H Angiopep-2), 2.77-1.78 (4H Glu), 1.52-0.87 (9H Angiopep-2).

4.4.2.2.2.   Maleimide Quenching with N-acetyl Cysteine

DPBS was degassed by sonication and N_2 (g) purging. St-PGA-ANG was dissolved to ~ 18 mg/mL with degassed DPBS in a one-neck round bottom flask fitted with a stir bar, a septum, and an N_2 (g) inlet and outlet. N-acetyl cysteine (10 times the maleimide amount in mmol) was dissolved in degassed DPBS at 50 mg/mL. Then, TCEP (10 times the maleimide amount in mmol) was dissolved with the solution of N-acetyl cysteine. The mixture's pH was adjusted to 7 with NaOH 5M before its addition to the reaction mixture. Then, the reaction mixture was purged with N_2 (g), and the reaction was left to proceed at room temperature for 5 h. Finally, the products were purified by dialysis (3.5 kDa MWCO) and Vivaspin™ (3kDa MWCO) with MilliQ water. After lyophilization, Angiopep-2 loading was obtained by ^{1}H-NMR comparing the signals of the phenylalanine and tyrosine residues (23 protons) of the peptide with the α-carbon proton of PGA and by amino acid analysis (see *4.4.3.4.Amino Acid* Analysis).

Yield: ~ 72%. ^{1}H-NMR: δ_H (300 MHz, D$_2$O) 8.31 (1H initiator), 7.55-6.67 (23H Phe and Tyr Angiopep-2), 6.49-5.88 (2H maleimide), 4.53-4.12 (1H αC PGA), 4.10-2.51 (4H CH$_2$CH$_2$ maleimide, 24 H Angiopep-2, 2H N-acetyl cysteine), 2.52-1.79 (4H Glu, 1 H N-acetyl cysteine), 1.53-0.90 (9H Angiopep-2).

4.4.2.3. General Procedure for the Synthesis of Fluorescently Labeled Angiopep-2-tagged Star-poly(glutamic acid)

4.4.2.3.1. One-pot Conjugation of N-(2-Aminoethyl)maleimide and Sulfo-cyanine5.5

In a round bottom flask fitted with a stir bar and an N$_2$ inlet and outlet, St-PGA (1.01 mmol, 1 eq.) was dissolved in DMF anh. Once completely dissolved, DMTMM BF$_4$ (0.117 mmol, 0.117 eq.) was added, and the reaction was left to proceed under stirring for 30 min. After that, sulfo-cyanine5.5 amine (0.012 mmol, 0.012 eq.) and N-(2-aminoethyl)maleimide trifluoroacetate salt (0.05 mmol, 0.05 eq.) was added to the reaction. pH was adjusted to 8 with DIEA, and the reaction was left under stirring at room temperature and covered from light for 48 h. Then, the product was precipitated and washed with cold diethyl ether and dried. The product was washed with acid water and then converted to its water-soluble salt form by the addition of sodium bicarbonate. The excess of salt was eliminated by Vivaspin^{TM} (3 kDa MWCO). Finally, the product was freeze-dried, yielding a blue-colored solid. Maleimide loading was obtained by ^{1}H-NMR comparing the signal of the 2,5-pyrrolidone of N-(2-Aminoethyl)maleimide (2 protons) with the α-carbon proton of PGA.

Yield: 84%. CE$_{Cy5.5}$: 88%. CE$_{Malei}$: 80%. ^{1}H-NMR: δ_H (300 MHz, D$_2$O) 9.10-7.58 (1H initiator, 8H sulfoCy5.5), 7.02-6.19 (1H maleimide), 4.52-3.99 (m, 1H αC PGA), 3.90-2.72 (4H CH$_2$CH$_2$ maleimide, 8 H sulfoCy5.5), 2.69-1.77 (4H, Glu), 1.77-0.94 (29H, sulfoCy5.5).

4.4.2.3.2. Conjugation of Angiopep-2 via Maleimide-thiol Chemistry

DPBS was degassed by sonication and N_2 (g) purging. St-PGA-Cy5.5-Malei (0.48 mmol, 1 eq.) was dissolved in the minimum volume of degassed DPBS needed in a two-neck round bottom flask fitted with a stir bar and septa. TCEP (0.025 mmol, 0.052 eq.) was dissolved in degassed DPBS at 50 mg/mL, and the pH was adjusted to 7 with NaOH 5M. Anigiopep-2-SH (0.008 mmol, 0.017 eq.) was dissolved in the minimum volume of degassed DPBS. Then, Angiopep-2-SH and TCEP were added to the polymer solution, and the reaction mixture was purged with N_2 (g). The reaction was left to proceed at room temperature and covered from light for 5 h. Then, the product was purified by dialysis (3.5 kDa MWCO) against MilliQ water and freeze-dried. Angiopep-2 loading was assessed by ^{1}H-NMR by comparing the signals of the phenylalanine and tyrosine residues of the peptide (23 protons) with the α-carbon proton of PGA.

Yield: 100%. CE_{ANG}: 100 %. ^{1}H-NMR: δ_H (300 MHz, D_2O) 9.10-7.75 (1H initiator, 8H sulfoCy5.5), 7.61-6.95 (19H Phe and Tyr Angiopep-2), 6.95-6.50 (1H maleimide, 4H Tyr Angiopep-2), 4.61-4.09 (1H αC PGA, 27H Angiopep-2), 4.08-2.62 (4H CH_2CH_2 maleimide, 8 H sulfoCy5.5, 24H Angiopep-2), 2.62-1.77 (4H Glu, 29H Angiopep-2), 1.77-0.94 (29H sulfoCy5.5, 9H Angiopep-2).

4.4.2.3.3. Maleimide Quenching with N-acetyl Cysteine

DPBS was degassed by sonication and N_2 (g) purging. Maleimide-bearing St-PGA was dissolved in the minimum volume of degassed DPBS needed in a two-neck round bottom flask fitted with a stir bar and septa. N-acetyl cysteine (10 times the maleimide amount in mmol) was dissolved in degassed DPBS at 100 mg/mL. Then, TCEP (10 times the maleimide amount in mmol) was dissolved with the solution of N-acetyl cysteine to a

concentration of 50 mg/mL. The mixture's pH was adjusted to 7 with NaOH 5M prior to its addition to the reaction mixture. Then, the reaction mixture was purged with N_2 (g) and was left to proceed at room temperature and covered from light for 5 h. Then, the product was purified by dialysis (3.5 kDa MWCO), Vivaspin™ (3kDa MWCO), and/or preparative SEC with MilliQ water and freeze-dried. Sulfo-Cy5.5 loading was determined by fluorescence spectroscopy as described in *4.4.3.2.Determination of Cy5.5 Loading by Fluorescence Spectroscopy*. Angiopep-2 loading was obtained by amino acid analysis (see *4.4.3.4.Amino Acid Analysis*).

St-PGA-Cy5.5-ANG-NAC. Yield: 85%. ^{1}H-NMR: δ_H (300 MHz, D_2O) 9.10-7.62 (1H initiator, 8H sulfoCy5.5), 7.61-6.55 (23H Phe and Tyr Angiopep-2), 4.53-4.10 (1H αC PGA, 27H Angiopep-2), 4.11-2.51 (4H CH_2CH_2 maleimide, 8 H sulfoCy5.5, 24H Angiopep-2, 2H N-acetyl cysteine), 2.52-1.53 (4H Glu, 29H Angiopep-2, 3H N-acetyl cysteine), 1.50-0.90 (29H sulfoCy5.5, 9H Angiopep-2).

St-PGA-Cy5.5-NAC. Yield: 78%. ^{1}H-NMR: δ_H (300 MHz, D_2O) 9.10-7.58 (1H initiator, 8H sulfoCy5.5), 6.91-5.82 (2H maleimide), 4.55-4.16 (m, 1H αC PGA), 4.16-2.52 (4H CH_2CH_2 maleimide, 8 H sulfoCy5.5, 2H N-acetyl cysteine), 2.51-1.57 (4H Glu, 3H N-acetyl cysteine), 1.54-0.87 (29H sulfoCy5.5).

4.4.2.4. Synthesis of Angiopep-2 Tagged Star-poly(glutamic acid) Based Combination Conjugate with Doxorubicin and Dasatinib (St-PGA-Combi-ANG-NAC)

4.4.2.4.1. Conjugation of Tert-butyl carbazate Moiety (St-PGA-TBC)

The conjugation of TBC to St-PGA was performed following the protocol described in *Chapter 2.*

Yield: 100%. CE: 100%. ^{1}H-NMR: δ_H (300 MHz, D$_2$O) 8.51 (m, 1H), 4.54-4.25 (m, 1H), 2.59-1.71 (m, 4H), 1.51 (s, 9H).

4.4.2.4.2. Conjugation of Dasatinib to St-PGA-TBC (St-PGA-TBC-Das)

The conjugation of Das via an ester bond to St-PGA-TBC was performed as described in *Chapter 2.*

Yield: 90%. CE: 94%.^{1}H-NMR: δ_H (300 MHz, D$_2$O) 8.92-6.28 (1H initiator, 5H Das), 4.56-4.00 (1H αC PGA, 2H Das), 3.93-2.69 (10H Das), 2.67-1.62 (4H Glu PGA, 6H Das), 1.47 (9H Boc).

4.4.2.4.3. Conjugation of N-(2-Aminoethyl)maleimide to St-PGA-TBC-Das (St-PGA-TBC-Das-Malei)

In a one-neck round bottom flask fitted with a stir bar and an N$_2$ inlet and outlet, St-PGA-TBC-Das (2.3 mmol, 1 eq.) was dissolved in DMF anh. Once completely dissolved, DMTMM BF$_4$ (0.17 mmol, 0.075 eq.) was added, and the reaction was left to proceed under stirring for 30 min. After that, N-(2-Aminoethyl)maleimide trifluoroacetate salt (0.17 mmol, 0.075 eq.) was added to the reaction, and pH was adjusted to 8 with DIEA. The reaction was left to proceed for 48 h. Then, the product was precipitated and washed with cold diethyl ether and dried. The final product was washed with acid water and freeze-dried. Maleimide loading was obtained by ^{1}H-NMR comparing the signal of the 2,5-pyrrolidone of N-(2-Aminoethyl)maleimide with the α-carbon proton of PGA.

Yield: 96%. CE: 60%.^{1}H-NMR: δ_H (300 MHz, D$_2$O) 8.69-6.48 (1H initiator, 5H Das, 1H maleimide), 6.46-6.24 and 6.06-5.83 (1H maleimide), 4.54-4.04 (1H αC PGA, 2H Das), 3.99-2.64 (10H Das, 4H CH$_2$CH$_2$ maleimide), 2.55-1.75 (4H Glu PGA, 6H Das), 1.47 (9H Boc).

4.4.2.4.4. Deprotection of Tert-butyl Carbazate (St-PGA-(HYD)-Das-Malei)

Boc deprotection was achieved following the protocol described in *Chapter 2.*

Yield: 89%. ^{1}H-NMR: δ_H (300 MHz, D_2O) 8.51-6.51 (1H initiator, 5H Das, 1H maleimide), 6.46-6.24 and 6.06-5.83 (1H maleimide), 4.54-4.04 (1H αC PGA, 2H Das), 3.99-2.65 (10H Das, 4H CH_2CH_2 maleimide), 2.58-1.69 (4H Glu PGA, 6H Das).

4.4.2.4.5. Conjugation of Doxorubicin to St-PGA-(HYD)-Das-Malei (St-PGA-hyd-Dox-Das-Malei)

In a two-neck round bottom flask fitted with a stir bar and an N_2 inlet and outlet, St-PGA-(HYD)-Das-Malei (1.6 mmol, 1 equivalent) was dissolved in DMSO. Then, Dox (0.017 mmol, 0.010 equivalents) was added to the reaction. Then, four drops of pure acetic acid were added to the reaction, and it was left to proceed protected from light. After 72 h, the reaction was monitored by TLC (MeOH, R_f: 0.6), and two drops of acetic acid were added. The reaction was left to proceed for another 24 h, and then the solvent was evaporated under a high vacuum. The product was dissolved in DMF and purified by size exclusion chromatography with a Sephadex LH-20 column using DMF as eluent. The fractions containing the red-colored product were collected in a round bottom flask. Before evaporating the solvent under a high vacuum, sodium bicarbonate 1 M was added to the product. To obtain the salt form of the polymer, MilliQ water and additional sodium bicarbonate 1 M was added. Size exclusion chromatography with a Sephadex G-25 column using MilliQ water as eluent was performed to eliminate the excess of salts. The fractions containing the red-colored product were freeze-dried.

Yield: 80%. CE: 104%. ^{1}H-NMR: δ_H (300 MHz, D_2O) 8.75-6.54 (1H initiator, 5H Das, 3H Dox, 1H maleimide), 6.50-6.21 and 6.07-5.83 (1H

maleimide), 4.60-4.04 (1H αC PGA, 2H Das, 2H Dox), 3.89-2.50 (10H Das, 4H CH_2CH_2 maleimide, 6H Dox), 2.49-1.63 (4H Glu PGA, 6H Das, 2H Dox).

4.4.2.4.6. Conjugation of Angiopep-2-SH by Maleimide-thiol Chemistry (St-PGA-hyd-Dox-Das-ANG)

DPBS and MilliQ water were degassed by sonication and N_2 (g) purging. In a two-neck round bottom flask fitted with a stir bar and septa, St-PGA-hyd-Dox-Das-Malei (1.12 mmol, 1 eq.) was dissolved with 21.2 mL of degassed MilliQ water and kept under stirring at 4ºC until the remaining reagents were added. TCEP (0.057 mmol, 0.051 eq.) was dissolved in degassed DPBS at 50 mg/mL, and the pH was adjusted to 7 with NaOH 5M. Anigiopep-2-SH (0.019 mmol, 0.017 eq.) was dissolved in the minimum volume of degassed DPBS needed. Then, 2.12 mL of 10X DPBS were added to the solution of St-PGA-hyd-Dox-Das-Malei, and a 100 µL aliquot was taken for analysis by SEC (see *4.4.3.5.Size Exclusion Chromatography*). After that, Angiopep-2-SH and TCEP were added to the reaction mixture. Finally, the reaction was purged with N_2 (g) and left to proceed at room temperature and covered from light. After 4 h 30 min of reaction, two 100 µL aliquots were taken for analysis by SEC (see *4.4.3.5.Size Exclusion Chromatography*) and free drug extraction and quantification by HPLC (as described in *Chapter 2*). After 5 h, the reaction was transferred to a 50 mL falcon tube and centrifuged (3000 rpm, 5 min) to yield a small pellet. The supernatant (the product) was purified by Vivaspin™ (3 kDa MWCO) with MilliQ water and freeze-dried.

Yield: 83%. CE: 93%. ^{1}H-NMR: δ_H (300 MHz, D_2O) 9.08-6.53 (1H initiator, 5H Das, 3H Dox, 1H maleimide, 23H Phe and Tyr Angiopep-2), 6.49-5.83 (2H maleimide), 4.59-4.05 (1H αC PGA, 2H Das, 2H Dox), 4.04-2.45 (10H Das, 4H CH_2CH_2 maleimide, 6H Dox, 24H Angiopep-2), 2.42-1.63 (4H Glu PGA, 6H Das, 2H Dox, 29H Angiopep-2), 1.29-0.70 (9H Angiopep-2).

4.4.2.4.7. Maleimide Quenching with N-acetyl cysteine (St-PGA-hyd-Dox-Das-ANG-NAC)

DPBS and MilliQ water were degassed by sonication and N_2 (g) purging. In a two-neck round bottom flask fitted with a stir bar and septa, St-PGA-hyd-Dox-Das-ANG (0.85 mmol, 1 eq.) was dissolved with 17.1 mL of degassed MilliQ water and kept under stirring at 4ºC until the remaining reagents were added. N-acetyl cysteine (0.34 mmol, 0.4 eq.) was dissolved in degassed DPBS at 100 mg/mL. Then, TCEP (0.34 mmol, 0.4 eq.) was dissolved with the solution of N-acetyl cysteine and degassed DPBS was added to have 50 mg/mL of TCEP. The mixture's pH was adjusted to 7 with NaOH 2 M prior to its addition to the reaction mixture. Then, the reaction was purged with N_2 (g) and was left to proceed under vigorous stirring at room temperature and covered from light for 5 h. After that, the reaction was transferred to a 50 mL falcon tube and centrifuged (3000 rpm, 5 min) to yield a small pellet. The supernatant (the product) was purified by Vivaspin^{TM} (3 kDa MWCO) with MilliQ water. The purification was monitored by TLC (MeOH) using permanganate staining. Once no signs of TCEP (R_f(TCEP): 0.5) or N-acetyl cysteine (R_f(NAC): 0.7), the product was lyophilized. Finally, the compound was dissolved in MilliQ water and purified by preparative SEC (Sephadex G25) using MilliQ water as a mobile phase. The elution was monitored by TLC (MeOH, R_f(Dox): 0.6, R_f(Das): 0.7). The red-colored compound fractions without signs of free drugs were merged and freeze-dried. Dox loading was determined as described in *Chapter 2*. Das loading was obtained by ester bond hydrolysis and liquid-liquid extraction of the released drug (see *4.4.3.3.Dasatinib Quantification*). Angiopep-2 loading was determined by amino acid analysis (see *4.4.3.4.Amino Acid Analysis*).

Yield: 80%. ^{1}H-NMR: δ_H (300 MHz, D_2O) ^{1}H-NMR: δ_H (300 MHz, D_2O) 8.88-6.45 (1H initiator, 5H Das, 3H Dox, 1H maleimide, 23H Phe and Tyr Angiopep-2), 6.44-5.82 (2H maleimide), 4.58-4.08 (1H αC PGA, 2H Das, 2H

Dox), 4.08-2.50 (10H Das, 4H CH_2CH_2 maleimide, 6H Dox, 24H Angiopep-2, 2H N-acetyl cysteine), 2.50-1.77 (4H Glu PGA, 6H Das, 2H Dox, 29H Angiopep-2, 3H N-acetyl cysteine), 1.54-0.70 (9H Angiopep-2).

4.4.3. Characterization Techniques

DLS (including CAC determination and Zeta potential), CD, and UV-VIS (for drug loading quantification) equipment were employed as described in *Chapter 2*. Drug release kinetics (pH and cathepsin B dependent) were also studied as described in *Chapter 2*.

4.4.3.1.   NMR Spectroscopy

^{1}H-NMR spectra were recorded on an Avance III 500 MHz Bruker spectrometer or a 300 Ultrashield^{TM} from Bruker (Billerica MA, USA) at 27 °C and a frequency of 300 MHz and analyzed using the MestreNova 6.2 software (Mestrelab Research S.L., Santiago de Compostela, Spain).

4.4.3.2.   Determination of Cy5.5 Loading by Fluorescence Spectroscopy

Fluorophore loading of sulfo-cyanine5.5-labeled compounds (St-PGA-Cy5.5-ANG-NAC and St-PGA-Cy5.5-NAC) were determined using a CLARIOstar Plus plate reader (BMG Labtech GmbH, Ortenberg, Germany). Calibration curves of the free fluorophores were prepared in DMSO:water (1:1 v/v) and pipetted in a black opaque 96 well plaque (OptiPlate-96 black from Perkin Elmer Inc., Waltham, MA, USA). Fluorescence was measured using λ_{ex}= 640 nm and λ_{em}= 700 nm. To determine the fluorophore loading of the conjugates, they were dissolved in the same solvent and pipetted in the same plaque using the same volume (100 µL). The fluorescence intensity in the corresponding $\lambda_{ex}/\lambda_{em}$ was recorded and interpolated in the

calibration curve. Loading in mol percent (% mol) was obtained by iterative calculation from the value in % wt.

4.4.3.3. Dasatinib Quantification

Dasatinib loading of St-PGA-hyd-Dox-Das-ANG-NAC was determined by ester hydrolysis followed by liquid-liquid extraction and analyzed by reverse-phase high-performance liquid chromatography (RP-HPLC). A solution of 4 mg/mL of the conjugate in MilliQ water was prepared, and 100 µL were placed in a 15 mL falcon tube with 100 µL of HCl 2 M. The mixture was incubated for 1 hour at 80 º C covered from light. After the solution was cooled down, 100 µL of NaOH 2 M were added to neutralize pH. The mixture was vortexed until it turned homogeneous. Then, 4 mL of chloroform: isopropanol (7:3 v/v) were added, and the free drug was extracted. The sample was vortexed for 30 seconds twice. Then, the phases were separated by centrifugation (3200 g, 5 min). The aqueous phase was discarded, and two aliquots (600 µL and 300 µL) of the organic phase were transferred to 2 mL Eppendorf tubes to evaporate the solvent in a SpeedVac concentrator. Then, the sample was redissolved in 300 µL of methanol HPLC grade and injected into the HPLC system for quantification using the same setup and calibration curves depicted in *Chapter 2*. As a reference, St-PGA-hyd-Dox$_1$-Val-Das$_1$ (whose synthesis and characterization are described in *Chapter 2*) was submitted to the same protocol of linker hydrolysis, drug extraction, and quantification. Considering the Das loading of the said conjugate, a correction factor was applied to the weight percent obtained for St-PGA-hyd-Dox-Das-ANG-NAC. Loading in mol percent (% mol) was obtained by iterative calculation from the value in % wt.

4.4.3.4. Amino Acid Analysis

The determination of ANG loading was performed via amino acid analysis by Unitat de Tècniques Separatives i Síntesi de Pèptids of the University of Barcelona.

Briefly, the conjugates were dissolved in HPLC water. Aliquots of sample, α-aminobutyric acid solution (2.5 mM), and 6 M HCl (1.0 % w/v phenol) were mixed and homogenized. Then, 12 M HCl was added up to a 6 M HCl (0.2 % w/v phenol) final concentration. Hydrolysis was performed at 110ºC for 24 h. Samples were evaporated, resuspended in HPLC water (500 µL), and filtered (0.45 µm). Before derivatization, these solutions were further diluted (100 µL/200 µL). The samples were derivatized with 6-aminoquinolyl-N-hydroxysuccinimidyl carbamate according to the Waters AccQ-Tag method. The derivatized samples were analyzed using a Waters 600 HPLC gradient system equipped with a Waters 2487 UV detector (λ = 254 nm). The data were acquired and analyzed using the Empower 2 software.

4.4.3.5.   Size Exclusion Chromatography

Size exclusion chromatography (SEC) of the products was performed in a Postnova Analytics Modular SEC system (Postnova Analytics GmbH, Landsberg am Lech, Germany) equipped with a RI – Refractive Index Detector (PN3150 from Postnova Analytics GmbH), a UV-VIS detector (SPD-20A from Shimadzu Scientific Instruments, Kyoto, Japan) and a fluorescence detector (RF-20A XS from Shimadzu Scientific Instruments, Kyoto, Japan). All SEC studies were carried out using a TSK gel G3000PWXL column (5µm, 7.8 mm i.d. x 30 cm, Tosoh Corporation, Tokyo, Japan) with the same mobile phase (DPBS) with a constant flow rate (0.6 mL/min). The aliquots taken from the reaction mixtures were diluted one-third in DPBS, filtered through 0.45 µm nylon filters, and 40 µL were injected into the system. The remaining samples were prepared in DPBS and filtered through 0.45 µm nylon filters. St-PGA-Cy5.5-NAC, St-PGA-Cy5.5-ANG-

NAC, and St-PGA-hyd-Dox-Das-ANG-NAC were dissolved at 2 mg/mL, and 15 µL were injected into the system.

4.4.4. Biological Evaluation

4.4.4.1.　　Ethical Considerations

Animal experiments were performed in accordance with the European Communities Council Directive (86/609/ECC) guidelines and by the Spanish Royal Decree 1201/2005.

4.4.4.2.　　Biodistribution

The experimental procedure was approved by the CIPF Institutional Animal Care and Use Committee and accomplished by accredited and trained staff, meeting the animal care rules. The animals were maintained in a specific-pathogen-free facility, with controlled temperature and humidity, using a 12-hour light-dark cycle. Food pellets and water were provided ad-libitum during the whole experiment.

The biodistribution study used 6-week-old female BALB/c mice (Envigo Laboratories Inc., Spain, EU). The labeled polymers St-PGA-Cy5.5-ANG-NAC and St-PGA-Cy5.5-NAC were injected through the tail vein at a dose of 4.15 mg Cy5.5 equivalent/Kg (n=5 for each conjugate). DPBS was injected as a control (n=2). After 4 h, mice were euthanized, and blood was collected using heparinized syringes. Major organs (lungs, liver, spleen, kidney, heart, and brain) were harvested after flushing with 20 mL of DPBS. Organs were immediately weighed and subjected to *ex vivo* fluorescence detection by IVIS® technology (Perkin Elmer Inc., Waltham, MA, USA) with λ_{ex} = 640 nm and λ_{em} = 700 nm. Calibration curves of the conjugates in DPBS were performed per duplicate in a black opaque 96 well plaque (OptiPlate-96 black from Perkin Elmer Inc., Waltham, MA, USA) and measured by

IVIS® technology using the same protocol to allow conjugate quantification. The fluorescence emitted by each organ was measured in total radiant efficiency and interpolated in the corresponding calibration curve. Organs of DPBS controls were used as blank. Considering the amount of polymer injected, the percentage of injected dose (%ID) in each organ was calculated and divided by the organ's weight in grams (%ID/g). Blood was also measured by IVIS® technology and then centrifuged (10 min, 4000 rpm) to yield the plasma (i.e., the supernatant) for fluorescence quantification. The %ID and %ID/mL of blood or plasma were calculated considering a volume of blood/plasma equivalent to 7% of animal weight (51).

The calibration curves were fitted to a linear equation, and fluorescence values were interpolated into said calibration curve using Microsoft Excel software.

4.4.4.3.   *In vivo* Proof of Anti-metastatic Activity in a Breast Cancer Brain Metastasis Mouse Model

The experiment was performed at Centro Nacional de Investigaciones Oncológicas (CNIO, Madrid, Spain). The experimental procedure was approved by the CNIO (IACUC.001-2020), Instituto de Salud Carlos III (CBA05_2020), and Comunidad de Madrid Institutional Animal Care and Use Committee (PROEX130.7/20), and accomplished by accredited and trained staff, meeting the animal care rules. The animals were maintained in a specific-pathogen-free facility, with controlled temperature and humidity, and using a 12-hour light-dark cycle. Food pellets and water were provided ad-libitum during the whole experiment.

Female athymic nu/nu (Harlan) mice of 4-10 weeks of age were used. The MDA-MB-231-BrM3 cell line used to establish brain tumors has been previously described (5,45). The brain tumors were generated by injecting 100 µL PBS into the left ventricle containing 100000 MDA-MB-231-BrM3

cells. After seven days, treatments were injected retro-orbitally twice per week for three weeks (six doses). Metastatic progression was analyzed *in vivo* once a week and *ex vivo* at the experimental endpoint by bioluminescence detection. Anesthetized mice (isoflurane) were injected retro-orbitally with D-luciferin (150 mg/kg; Syd Labs) and imaged with IVIS technology (Perkin Elmer, Japan). Bioluminescence analyses were performed using Living Image software, version 4.5. Four hours before sacrifice, animals were injected intraperitoneally with bromodeoxyuridine (BrdU, 40mg/kg, B9285, Sigma-Aldrich). The animals were euthanized, and brains and lungs were imaged by IVIS technology.

4.4.4.4. Histological Analysis

Tissue for immunofluorescence was obtained after overnight fixation with 4% paraformaldehyde at 4°C. Slicing the brain was carried out using a sliding microtome (Thermo Fisher Scientific). 80 µm slices were blocked in 10% normal goat serum (NGS), 2% bovine serum albumin (BSA), and 0.25% Triton X-100 in PBS for 2 h at room temperature. Primary antibodies were incubated overnight at 4°C in the blocking solution and for 30 min at room temperature the following day. After extensive washing in PBS-Triton 0.25%, the secondary antibody was added to the blocking solution and incubated for 2h, followed by extensive washing with PBS-Triton 0.25%. For staining against BrdU, mouse brain slices were treated with HCl 2N 30 min at 37ºC, followed by 0.1M borate buffer (pH 8.5) incubation for 10 min at room temperature. After extensive washing in tris-buffered saline (TBS), slices were blocked in 3% NGS in TBS-Triton 0.25% for 1 h at room temperature, and the primary antibody was incubated for 72h at 4ºC. After extensive washing with TBS-Triton 0.25%, the secondary antibody was incubated in blocking solution for 2 h at room temperature, followed by extensive washing with TBS. Primary antibodies: GFP (1:1,000; GFP-1020, Aves Labs), BrdU

(1:500; ab6326, Abcam). Secondary antibodies: Alexa-Fluor anti-chicken 488 and anti-rat 555 (dilution 1:300; Invitrogen).

Immunofluorescence images were acquired with a Leica SP5 upright confocal microscope x10, x20 objectives and analyzed with ImageJ software. Whole slides were acquired with a slide scanner (AxioScan Z1, Zeiss).

4.4.4.5.   Statistical Analysis

Statistical analysis was performed in Prism 5 software (GraphPad, La Jolla, California, USA). Data were expressed as mean ± standard error of the mean (SEM) unless specified. Comparisons between two experimental groups were analyzed with an unpaired, two-tailed Student's t-test.

4.5.   Bibliography

1.   Leone JP, Leone BA. Breast cancer brain metastases: the last frontier. Exp Hematol Oncol. 2015/11/24. 2015 Dec 24;4(1):33.

2.   Witzel I, Oliveira-Ferrer L, Pantel K, Müller V, Wikman H. Breast cancer brain metastases: biology and new clinical perspectives. Breast Cancer Res. 2016 Dec 19;18(1):8.

3.   Achrol AS, Rennert RC, Anders C, Soffietti R, Ahluwalia MS, Nayak L, et al. Brain metastases. Nat Rev Dis Prim. 2019 Dec 17;5(1):5.

4.   Chen W, Hoffmann AD, Liu H, Liu X. Organotropism: new insights into molecular mechanisms of breast cancer metastasis. npj Precis Oncol. 2018 Dec 16;2(1):4.

5.   Bos PD, Zhang XHF, Nadal C, Shu W, Gomis RR, Nguyen DX, et al. Genes that mediate breast cancer metastasis to the brain. Nature. 2009 Jun 6;459(7249):1005–9.

6.   Witzel I, Oliveira-Ferrer L, Müller V. Brain Metastasis in Breast Cancer Patients— Need for Improvement. Cancers (Basel). 2020 Oct 30;12(11):3190.

7.   Kim Y-J, Kim J-S, Kim IA. Molecular subtype predicts incidence and prognosis of brain metastasis from breast cancer in SEER database. J Cancer Res Clin Oncol. 2018 Sep 3;144(9):1803–16.

8.   Cerna T, Stiborova M, Adam V, Kizek R, Eckschlager T. Nanocarrier drugs in the treatment of brain tumors. J Cancer Metastasis Treat. 2016;2(10):407–16.

9.   Mills MN, Figura NB, Arrington JA, Yu H-HM, Etame AB, Vogelbaum MA, et al. Management of brain metastases in breast cancer: a review of current practices and emerging treatments. Breast Cancer Res Treat. 2020 Apr 6;180(2):279–300.

10.   Er EE, Boire A. Molecular Mechanisms in Brain Metastasis. In: Central Nervous System Metastases. Cham: Springer International Publishing; 2020. p. 31–41.

11.   Rodriguez-Otormin F, Duro-Castano A, Conejos-Sánchez I, Vicent MJ. Envisioning the future of polymer therapeutics for brain disorders. WIREs Nanomedicine and Nanobiotechnology. 2019 Jan 14;11(1).

12.   Duro-Castano A, Moreira Leite D, Forth J, Deng Y, Matias D, Noble Jesus C, et al. Designing peptide nanoparticles for efficient brain delivery. Adv Drug Deliv Rev. 2020 May;160:52–77.

13.   Tian X, Nyberg S, Sharp PS, Madsen J, Daneshpour N, Armes SP, et al. LRP-1-mediated intracellular antibody delivery to the Central Nervous System. Sci Rep. 2015 Dec 20;5(1):11990.

14.   Ke W, Shao K, Huang R, Han L, Liu Y, Li J, et al. Gene delivery targeted to the brain using an Angiopep-conjugated polyethyleneglycol-modified polyamidoamine dendrimer. Biomaterials. 2009 Dec;30(36):6976–85.

15.   Demeule M, Beaudet N, Régina A, Besserer-Offroy É, Murza A, Tétreault P, et al. Conjugation of a brain-penetrant peptide with neurotensin provides antinociceptive properties. J Clin Invest. 2014 Mar 3;124(3):1199–213.

16.   Lachowicz J, Demeule M, Regina A, Boivin D, Larocque A, Tripathy S, et al. Brain-penetrant lysosomal enzymes constructed by fusion with Angiopep-2, a unique LRP-1 binding peptide. Mol Genet Metab. 2013 Feb 1;108(2):S57.

17.   Regina A, Demeule M, Tripathy S, Lord-Dufour S, Currie JC, Iddir M, et al. ANG4043, a novel brain-penetrant peptide-mAb conjugate, is efficacious against HER2-positive intracranial tumors in mice. Mol Cancer Ther. 2015 Jan 1;14(1):129–40.

18.   Ché C, Yang G, Thiot C, Lacoste MC, Currie JC, Demeule M, et al. New angiopep-modified doxorubicin (ANG1007) and etoposide (ANG1009) chemotherapeutics with increased brain penetration. J Med Chem. 2010 Apr 8;53(7):2814–24.

19.   Régina A, Demeule M, Ché C, Lavallée I, Poirier J, Gabathuler R, et al. Antitumour activity of ANG1005, a conjugate between paclitaxel and the new brain delivery vector Angiopep-2. Br J Pharmacol. 2008 Sep;155(2):185–97.

20.   Thomas FC, Taskar K, Rudraraju V, Goda S, Thorsheim HR, Gaasch JA, et al. Uptake of ANG1005, A Novel Paclitaxel Derivative, Through the Blood-Brain Barrier into Brain and Experimental Brain Metastases of Breast Cancer. Pharm Res. 2009 Nov 23;26(11):2486–94.

21.   Kumthekar P, Tang S-C, Brenner AJ, Kesari S, Piccioni DE, Anders C, et al. ANG1005, a Brain-Penetrating Peptide–Drug Conjugate, Shows Activity in Patients with Breast Cancer with Leptomeningeal Carcinomatosis and Recurrent Brain Metastases. Clin Cancer Res. 2020 Jun 15;26(12):2789–99.

22.   Duro-Castano A, Borrás C, Herranz-Pérez V, Blanco-Gandía MC, Conejos-Sánchez I, Armiñán A, et al. Targeting Alzheimer's disease with multimodal polypeptide-based nanoconjugates. Sci Adv. 2021 Mar 26;7(13):eabf9180.

23.   Daneman R, Zhou L, Agalliu D, Cahoy JD, Kaushal A, Barres BA. The Mouse Blood-Brain Barrier Transcriptome: A New Resource for Understanding the

Development and Function of Brain Endothelial Cells. Ikezu T, editor. PLoS One. 2010 Oct 29;5(10):e13741.

24. Uchida Y, Ohtsuki S, Katsukura Y, Ikeda C, Suzuki T, Kamiie J, et al. Quantitative targeted absolute proteomics of human blood-brain barrier transporters and receptors. J Neurochem. 2011 Apr;117(2):333–45.

25. Candela P, Saint-Pol J, Kuntz M, Boucau M-C, Lamartiniere Y, Gosselet F, et al. In vitro discrimination of the role of LRP1 at the BBB cellular level: Focus on brain capillary endothelial cells and brain pericytes. Brain Res. 2015 Jan 12;1594:15–26.

26. Dong H, Zou M, Bhatia A, Jayaprakash P, Hofman F, Ying Q, et al. Breast Cancer MDA-MB-231 Cells Use Secreted Heat Shock Protein-90alpha (Hsp90α) to Survive a Hostile Hypoxic Environment. Sci Rep. 2016 Feb 5;6(1):20605.

27. Gao S, Tian H, Xing Z, Zhang D, Guo Y, Guo Z, et al. A non-viral suicide gene delivery system traversing the blood brain barrier for non-invasive glioma targeting treatment. J Control Release. 2016 Dec 10;243:357–69.

28. Guo Q, Zhu Q, Miao T, Tao J, Ju X, Sun Z, et al. LRP1-upregulated nanoparticles for efficiently conquering the blood-brain barrier and targetedly suppressing multifocal and infiltrative brain metastases. J Control Release. 2019 Jun 10;303:117–29.

29. Wang L, Hao Y, Li H, Zhao Y, Meng D, Li D, et al. Co-delivery of doxorubicin and siRNA for glioma therapy by a brain targeting system: angiopep-2-modified poly(lactic-co-glycolic acid) nanoparticles. J Drug Target. 2015 Oct 21;23(9):832–46.

30. Fullstone G, Nyberg S, Tian X, Battaglia G. From the Blood to the Central Nervous System. In: International Review of Neurobiology. 2016. p. 41–72.

31. Tian X, Leite DM, Scarpa E, Nyberg S, Fullstone G, Forth J, et al. On the shuttling across the blood-brain barrier via tubule formation: Mechanism and cargo avidity bias. Sci Adv. 2020 Nov 27;6(48):eabc4397.

32. Northrop BH, Frayne SH, Choudhary U. Thiol-maleimide "click" chemistry: Evaluating the influence of solvent, initiator, and thiol on the reaction mechanism, kinetics, and selectivity. Polym Chem. 2015 May 14;6(18):3415–30.

33. Fontaine SD, Reid R, Robinson L, Ashley GW, Santi D V. Long-term stabilization of maleimide-thiol conjugates. Bioconjug Chem. 2015 Jan 21;26(1):145–52.

34. Christie RJ, Fleming R, Bezabeh B, Woods R, Mao S, Harper J, et al. Stabilization of cysteine-linked antibody drug conjugates with N-aryl maleimides. J Control Release. 2015 Dec;220:660–70.

35. Wong PT, Choi SK. Mechanisms of Drug Release in Nanotherapeutic Delivery Systems. Chem Rev. 2015 May 13;115(9):3388–432.

36. Seidi F, Jenjob R, Crespy D. Designing Smart Polymer Conjugates for Controlled Release of Payloads. Chem Rev. 2018 Apr 11;118(7):3965–4036.

37. Beijnen JH, van der Houwen OAGJ, Underberg WJM. Aspects of the degradation kinetics of doxorubicin in aqueous solution. Int J Pharm. 1986 Oct 1;32(2–3):123–31.

38. Duro-Castano A, Nebot VJ, Niño-Pariente A, Armiñán A, Arroyo-Crespo JJ, Paul A, et al. Capturing "Extraordinary" Soft-Assembled Charge-Like Polypeptides as a Strategy for Nanocarrier Design. Adv Mater. 2017 Oct;29(39):1702888.

39. Duro-Castano A. Well-defined polyglutamates as carriers for the treatment of neurodegenerative diseases. University of Valencia; 2015.

40. Berova N, Ellestad GA, Harada N. Characterization by Circular Dichroism Spectroscopy. In: Comprehensive Natural Products II. Elsevier; 2010. p. 91–146.

41. Koltzenburg S, Maskos M, Nuyken O. Functional Polymers. In: Polymer Chemistry. Berlin, Heidelberg: Springer Berlin Heidelberg; 2017. p. 493–513.

42. Duro-Castano A, Sousa-Herves A, Armiñán A, Charbonnier D, Arroyo-Crespo JJ, Wedepohl S, et al. Polyglutamic acid-based crosslinked doxorubicin nanogels as an anti-metastatic treatment for triple negative breast cancer. J Control Release. 2021 Apr;332:10–20.

43. Gallois L, Fiallo M, Garnier-Suillerot A. Comparison of the interaction of doxorubicin, daunorubicin, idarubicin and idarubicinol with large unilamellar vesicles circular dichroism study. Biochim Biophys Acta - Biomembr. 1998 Mar 6;1370(1):31–40.

44. Zhu L, Yebra N, Retana D, Miarka L, Hernández-Encinas E, Blanco-Aparicio C, et al. A drug-screening platform based on organotypic cultures identifies vulnerabilities to prevent local relapse and treat established brain metastasis. bioRxiv. 2020 Oct 19;2020.10.16.329243.

45. Priego N, Zhu L, Monteiro C, Mulders M, Wasilewski D, Bindeman W, et al. STAT3 labels a subpopulation of reactive astrocytes required for brain metastasis article. Nat Med. 2018 Jul 1;24(7):1024–35.

46. Masmudi-Martín M, Zhu L, Sanchez-Navarro M, Priego N, Casanova-Acebes M, Ruiz-Rodado V, et al. Brain metastasis models: What should we aim to achieve better treatments? Adv Drug Deliv Rev. 2021 Feb 1;169:79–99.

47. Arroyo Crespo JJ. Polymer-based combination conjugates for the treatment of triple negative breast cancer : From rational design to preclinical evaluation. University of Valencia; 2018.

48. Khan NU, Ni J, Ju X, Miao T, Chen H, Han L. Escape from abluminal LRP1-mediated clearance for boosted nanoparticle brain delivery and brain metastasis treatment. Acta Pharm Sin B. 2021 May 1;11(5):1341–54.

49. Liu S, Guo Y, Huang R, Li J, Huang S, Kuang Y, et al. Gene and doxorubicin co-delivery system for targeting therapy of glioma. Biomaterials. 2012 Jun 1;33(19):4907–16.

50. Kaminski ZJ, Kolesinska B, Kolesinska J, Sabatino G, Chelli M, Rovero P, et al. N-triazinylammonium tetrafluoroborates. A new generation of efficient coupling reagents useful for peptide synthesis. J Am Chem Soc. 2005;127(48):16912–20.

51. Parasuraman S, Raveendran R, Kesavan R. Blood sample collection in small laboratory animals. J Pharmacol Pharmacother. 2010 Jul;1(2):87–93.

GENERAL DISCUSSION

Breast cancer represents the most frequently diagnosed cancer worldwide (1) and the second most common cause of brain metastasis (after lung cancer (2–4)). Accounting for approximately 15% of all breast tumors (5,6), triple negative breast cancer (TNBC) is the most aggressive breast cancer molecular subtype. Overall, TNBC suffers from the worst prognosis (7) and an earlier and higher rate of recurrence and distant metastasis (6,8), with lungs and brain the most common metastatic sites (9). At the molecular level, the lack of expression of estrogen receptor (ER), progesterone receptor (PR), and human epidermal growth factor receptor 2 (HER2) characterize TNBC (7,10,11). For this reason, TNBC patients have not benefited from advances in endocrine and HER2-targeted therapies that have significantly increased survival rates in other subtypes (8,12,13). Treatments for metastatic TNBC are currently considered palliative rather than therapeutic and usually comprise the sequential administration of chemotherapeutics (often in combination) until the patient displays maximal response or maximal tolerance (14–16). Thus, the clinical management of metastatic TNBC remains a critical unmet clinical need.

Although the development of brain metastasis represents a late event in disease progress (17,18), 30-50% of metastatic breast cancer patients develop brain metastasis (19). Brain metastases entail not only a poor prognosis (survival of TNBC patients who develop brain metastasis ranges from three to four months (2)) but also neurological impairments and a consequent reduction in patient quality of life (2–4). The clinical management of breast cancer brain metastasis has traditionally relied on local approaches since the blood-brain barrier (BBB) and blood-tumor barrier (BTB) hinder the accumulation of systemically administered therapies at cytotoxic concentrations in the brain (4,19–21). Therefore, developing new effective systemic therapies for brain metastasis treatment represents a significant challenge.

In this context, we pursued the development of targeted polymer-drug conjugates to treat brain metastasis, focusing on TNBC. Polymer-drug conjugates minimally comprise a water-soluble polymeric carrier with a therapeutic agent attached through a cleavable linker; however, they can optionally carry an active targeting moiety. The nanoscale size of conjugates combined with the rational design of the covalent drug linkage offers unique advantages, such as (i) an increment in the water solubility of the drug (22,23), (ii) passive targeting in solid tumors due to the enhanced permeability and retention (EPR) effect (24), (iii) the ability to cross biological barriers and overcome chemoresistance (25,26), (iv) improved pharmacokinetics due to the controlled release of the drugs achieved by rational selection of a stimuli-responsive linker and polymer (22,27), and (v) the capacity to accommodate several therapeutic agents, probes, and/or targeting moieties, allowing for combination therapy, theranostics, and active targeting, respectively (28,29).

Using polypeptides as the polymeric carrier provides additional advantages, including their inherent biocompatibility and biodegradability mediated by the amide bonds forming the polypeptide backbone (30). A range of varied studies has provided evidence for the versatility of poly-L-glutamic acid (PGA) regarding conjugation of a wide variety of moieties (31–42), which represents a crucial aspect of combination therapy design. PGA supports the conjugation of drug combinations with different chemical characteristics, the control of drug ratio, and the use of myriad orthogonal linkers that support the controlled release of therapeutic agents (36,39,43,44). Furthermore, the development of controlled polymerization techniques has fostered the synthesis of PGA-based nanosystems with different topologies at a large scale (45–47). Our laboratory developed a three-armed star-shaped PGAs (St-PGA) with increased cell uptake, prolonged half-lives, and more significant organ accumulation in mice compared to linear PGAs with a similar molecular weight (46). Overall, together with the inherent biodegradability, safety, and versatility of PGA, the

advantages of the star-shaped architecture make St-PGA an excellent nanocarrier for the development of advanced therapeutics for cancer treatment. Additionally, St-PGA displays self-assembly behavior in non-salty aqueous solutions; St-PGA forms large spherical structures driven by ionic interactions in a concentration-dependent fashion; however, these same structures subsequently disassemble in response to increased ionic strength. Covalent capture of self-assembled structures yielded large (~200 nm diameter) stable spheric structures (St-PGA-Click) that further increased cellular uptake and circulation time when compared to the St-PGA unimer (40); thereby enhancing the potential of St-PGA-Click as drug delivery system. Indeed, St-PGA-Click has been used for the development of advanced therapeutics for acute kidney injury (32), alcohol-induced neuroinflammation (34), and Alzheimer's disease (48).

In this thesis, we aimed to develop a St-PGA-based combination conjugate with optimized drug ratios and pH-responsive linkers to treat metastatic TNBC (*Chapter 2*). We also pursued the development of a bottom-up strategy for the synthesis of larger crosslinked St-PGA self-assembly-based combination conjugates employing reversible stimuli-responsive bonds for assembly stabilization (*Chapter 3*). Finally, we aimed to develop the brain-targeted version of the candidate with the best anti-tumor and anti-metastatic activity from the combination conjugates obtained by both strategies (*Chapter 4*).

1.   Rational Design of St-PGA Combination Conjugates: Drug Ratio and Linking Chemistry Optimization

Delivering combinations of drugs that target different signaling pathways or various aspects of the same pathway remains a potentially exciting approach for cancer treatment, considering the myriad genetic mutations and dysregulated pathways associated with cancer development. Indeed, treatment of metastatic TNBC often relies on administering drug

combinations (14–16). Integrating the conjugation of drug combinations with the rational design of polymer-drug linkers allows the fine-tuning of drug release kinetics to enhance drug combination synergism (49). Our research group has extensive experience in this realm (36,39,43); for instance, our laboratory developed a family of PGA-based combination conjugates with doxorubicin (Dox) and aminoglutethimide (AGM) using different drug linkers and loadings for AGM, which provoked alterations to conjugate conformation and yielded different drug release profiles and, consequently, different biological outputs (39). In this study, the small flexible glycine (G) residue used as a linker for AGM conjugation induced drug synergism in mouse 4T1 TNBC cells regardless of AGM loading. The conjugate with low AGM loading displayed optimal anti-tumor activity in an orthotopic spontaneously metastatic 4T1 TNBC model; furthermore, this combination conjugate performed significantly better than a combined treatment of the PGA-Dox *and* PGA-G-AGM single-agent conjugates, underscoring the importance of having both drugs in the same polymeric carrier to assure co-delivery (39).

A follow-up study evaluated Dox linkers (pH-responsive versus protease labile) and loadings while maintaining a constant AGM loading (36). The pH-labile linkers employed in this second study included a simple hydrazine moiety and a longer, flexible, and hydrophobic N-ε-maleimidocaproic acid hydrazide (EMCH) moiety. Conjugates with low Dox loading displayed stability at pH 7.4 but released the drug at pH 5.0; however, conjugates with high Dox loading failed to release the drug at either pH, which translated into poor cytotoxic activity in 4T1 cells. Furthermore, conjugates with low loading exhibited optimal performance with regard to tumor growth inhibition and metastatic spread reduction *in vivo*; however, treatment with the combination conjugate with low loading and the longer EMCH spacer prompted reduced overall survival and hepatotoxicity compared to the remaining combination conjugates and free Dox (36). This study highlighted the importance of drug loading and linking chemistry in

defining drug release and, thus, the therapeutic outcome associated with conjugate treatment.

Continuing with the rational design of combination conjugates for TNBC treatment, a recent study performed by our laboratory explored different linking chemistries for a new drug (dasatinib – Das) but maintained the linking chemistry optimized for Dox (direct hydrazone bond) (43). As part of conjugate development, we discovered that the delayed administration of Das (compared to Dox) combined with an excess of Das (1:5 Dox:Das ratio) provided for enhanced drug synergism. Thus, we optimized the Das linking chemistry to support delayed release by employing both a direct ester bond as a linking moiety and a selection of spacers (between PGA and ester-Das bond). Das conjugation using a valine (Val) spacer reduced Das release from linear PGA conjugates at pH 5.0 and 7.4, which allowed for the delayed release of Das (compared to Dox) from the combination conjugate in acidic media in the presence of cathepsin B. As a result, the linear PGA combination conjugate (PGA-hyd-Dox-Val-Das) demonstrated robust *in vitro* anti-tumor activity and effectively reduced primary tumor growth and lung metastasis in an orthotopic *in vivo* mouse model of metastatic TNBC (43).

Encouraged by these studies, we synthesized St-PGA-based combination conjugates with Dox and Das using pH-labile linking moieties to support the controlled release of the drugs under acidic conditions (the tumor microenvironment (50) and lysosomes (51,52)) and explored the conjugation of different drug ratios to increase the anti-tumor activity of combination conjugates further (*Chapter 2*). Considering the increased cell uptake, prolonged half-lives, and more significant organ accumulation of St-PGA compared to linear PGA (40,46), we hypothesized that using St-PGA as a carrier would further improve the anti-tumor and anti-metastatic activity of the linear PGA conjugates.

1.1. St-PGA Conjugation Enhances Drug(s) Aqueous Solubility While Maintaining its Main Physico-chemical Properties

We synthesized three St-PGA-based combination conjugates with Dox and Das (*Chapter 2*). We conjugated Dox to St-PGA using a direct hydrazone linker. For Das, we explored two alternatives: (i) direct conjugation through an ester bond (obtaining St-PGA-hyd-Dox_1-Das_1 and St-PGA-hyd-Dox_1-Das_{10}) and (ii) the use of a Val spacer between the St-PGA backbone and the ester bond (obtaining St-PGA-hyd-Dox_1-Val-Das_1). We also synthesized single polymer-drug conjugates for comparative purposes (St-PGA-hyd-Dox, St-PGA-Das, and St-PGA-Val-Das).

Polymer-drug conjugates with sizes above the renal filtration threshold (6-8 nm) exhibit prolonged circulation times (39,53), permitting more amenable dosing schedules and passive accumulation in solid tumors by the EPR effect (24,27,54,55). While St-PGA has proven long circulation times (>15-fold increase compared to a linear PGA counterpart, 0.59 h vs. 12.05 h) (46), drug conjugation can dramatically change conjugate size and, therefore, the pharmacokinetic profile. For this reason, we studied the size of the single-drug and combination conjugates; however, the aggregation behavior of St-PGA in non-salty aqueous media (40) makes the proper determination of conjugate size a challenging task. We screened a series of media and concentrations to determine optimal conditions for unimer size measurement. As a result, we employed the size distribution by number by dynamic light scattering (DLS) of samples at 0.5 mg/mL conjugate in Dulbecco's phosphate-buffered saline (DPBS) to determine the hydrodynamic diameter of the unimers. Under these conditions, all conjugates displayed hydrodynamic diameters similar to the "parental" St-PGA unimer, ranging from 3 to 18 nm. We failed to observe significant differences between conjugate sizes that correlated with drug loading or linking chemistry.

St-PGA typically displays a negative zeta potential, which increases (becomes more negative) upon aggregation (40). Our St-PGA-based conjugates displayed negative zeta potentials, which supports increased circulation times (24), but failed to display an increase in value with aggregation, suggesting a modification in the aggregation behavior of the parent St-PGA. Of note, all conjugates aggregated as expected, displaying critical aggregation concentration (CAC) values in agreement with previous reports (40). St-PGA also exhibited a random coil conformation in the water-soluble salt form (40,45,46,56,57). Accordingly, when we evaluated the secondary structure of our St-PGA-based conjugates in MilliQ water and DPBS by circular dichroism (CD), we observed a random coil conformation profile in each case, except for St-PGA-hyd-Dox. This conjugate showed a more rigid, less soluble α-helix conformation in MilliQ water but not in DPBS; however, this conformational change did not rely on Dox-Dox interactions (as revealed by the CD spectra), suggesting a complex mechanism for the coil-to-helix transition.

Therefore, St-PGA supported the conjugation of Dox and Das with different ratios and linking chemistries without inducing significant alterations to critical physico-chemical characteristics (i.e., size, aggregation behavior, zeta potential, and secondary structure).

1.2. Dasatinib Linking Chemistry Drives the pH-dependent Drug Release Kinetics Profile of St-PGA-based Combination Conjugates

Previous studies performed by our laboratory demonstrated that a delayed administration of Das compared to Dox with an excess of Das (1:5 Dox:Das ratio) enhanced drug synergism in the *in vitro* TNBC model cell line MDA-MB-231-Luc (43). Therefore, we evaluated the drug release profile of our family of St-PGA single-drug and combination conjugates in relevant media, i.e., PBS at pH 7.4 (physiological pH) and pH 5.0 (tumor

microenvironment/lysosomal pH), and pH 5.0 acetate buffer in the presence of cathepsin B (lysosomes) (*Chapter 2*).

Overall, the pH-mediated drug release study for our family of conjugates demonstrated higher Das release at pH 7.4 than 5.0, in good agreement with other reports of ester-mediated drug conjugation (35,43). The use of the Val spacer reduced Das release at pH 7.4 and 5.0, as also observed for linear PGA conjugates (43). Overall, the conjugates displayed higher Dox release at pH 5.0 than 7.4, which agrees well with related reports (36,43,58,59).

The study of pH-mediated drug release from St-PGA-based combination conjugates revealed two different drug release profiles according to the use of the Val spacer or direct ester conjugation for Das. St-PGA-hyd-Dox_1-Val-Das_1 exhibited a burst release of Dox with an extremely low release of Das; meanwhile, St-PGA-hyd-Dox_1-Das_1 and St-PGA-hyd-Dox_1-Das_{10} exhibited rapid but lower Dox release with higher but gradual Das release. While the use of the Val spacer explains the low Das release observed for St-PGA-hyd-Dox_1-Val-Das_1, the burst Dox release suggests a different conformation in solution with enhanced exposure of the hydrazone-Dox moieties in St-PGA-hyd-Dox_1-Val-Das_1 compared to St-PGA-hyd-Dox_1-Das_1 and St-PGA-hyd-Dox_1-Das_{10}. The physico-chemical characterization of conjugates supported this hypothesis. The analysis of conjugate secondary structure by CD suggested Das-Das interactions in the conjugates bearing the Val linker (St-PGA-Val-Das and St-PGA-hyd-Dox_1-Val-Das_1). According to the study of the CAC by DLS, these conjugates also exhibited enhanced aggregation in water. Taken together, these data suggest a solution conformation for St-PGA-hyd-Dox_1-Val-Das_1 that shields Das from the media but exposes Dox on the surface of the conjugate, facilitating linker hydrazone cleavage and Dox release. However, specific conformational studies should be performed to prove this hypothesis.

Besides linking chemistry, drug loading has also been identified as a crucial parameter for drug release kinetics. The study of the linear PGA combination conjugate with AGM and Dox comparing the EMCH linker and direct hydrazone bond discovered that, independently of the linker, lower Dox loading correlated with higher release rates (36); however, our conjugates failed to follow the same tendency, with St-PGA-hyd-Dox$_1$-Das$_1$ and St-PGA-hyd-Dox$_1$-Das$_{10}$ displaying similar drug release profiles. This result suggests that St-PGA conformation exhibits lower sensitivity to drug loading than the linear counterpart. Given the similar drug release profile, the drug loading/drug ratio determines drug bioavailability for these conjugates. Therefore, we compared drug release from St-PGA-hyd-Dox$_1$-Das$_1$ and St-PGA-hyd-Dox$_1$-Das$_{10}$ as a drug ratio (Dox equivalents) and discovered that St-PGA-hyd-Dox$_1$-Das$_1$ displayed the desired delayed Das release at pH 5.0 and 7.4. St-PGA-hyd-Dox$_1$-Das$_{10}$ exhibited simultaneous Dox and Das release at early time points at both pH values, but the low Dox loading supported an increment of the Dox:Das ratio (Das excess) over time.

Incubation with cathepsin B usually increases drug release compared to the pH 5.0 buffer due to the ability of the enzyme to degrade PGA (35,36); however, our preliminary study of the cathepsin B-mediated drug release of St-PGA-hyd-Dox$_1$-Das$_1$ and St-PGA-hyd-Dox$_1$-Das$_{10}$ failed to provide evidence for any such increase .

Overall, our data demonstrate that in our St-PGA-based combination conjugates, Das linking chemistry critically defines the drug release kinetics, switching from a fast Dox release with sustained Das release to a burst Dox release with low Das release. Meanwhile, drug loading has a negligible effect on the drug release profile but defines the released drug ratio in the media.

1.3. Drug Loading/ratio and Drug Release Profile Define the Cytotoxic Activity of St-PGA-based Combination Conjugates

To evaluate how the different drug release profiles affected the anti-tumor activity of our family of St-PGA-based single-drug and combination conjugates, we evaluated the cytotoxic activity of all family members in MDA-MB-231-Luc cells, a well-established *in vitro* TNBC model (60,61) (*Chapter 2*). All family members of single-drug and combination conjugates exhibited robust cytotoxic activity. In agreement with the low Das release prompted by the Val-mediated conjugation, St-PGA-Das possessed greater cytotoxic activity than St-PGA-Val-Das, which also agrees with data reported for linear PGA conjugates (43). Also in good agreement with this result, St-PGA-hyd-Dox_1-Val-Das_1 displayed lower cytotoxic activity compared to St-PGA-hyd-Dox_1-Das_1 and St-PGA-hyd-Dox_1-Das_{10}. We could not compare these results with linear PGA conjugates as we lacked the St-PGA-hyd-Dox_1-Das_1/St-PGA-hyd-Dox_1-Das_{10} linear counterparts (43). Importantly, we discovered that St-PGA-hyd-Dox exhibited greater cytotoxic activity than free Dox, an improvement that linear PGA counterpart failed to provide (43). We hypothesize that this enhanced cytotoxic activity relies on the increased cell uptake of St-PGA-based conjugates, which was reported in the SHSY5Y neuroblastoma cell line (40,46); however, we require additional cell uptake studies in MDA-MB-231-Luc to confirm this hypothesis.

Despite exhibiting the desired Das release delay, St-PGA-hyd-Dox_1-Das_1 displayed lower cytotoxic activity than St-PGA-hyd-Dox_1-Das_{10}. We attribute this result to the excess of Das over Dox in St-PGA-hyd-Dox_1-Das_{10}, which allows the release of a drug ratio with an excess of Das in the media which reportedly enhanced drug combination synergy (43).

Therefore, our results suggest that conjugate drug release profile and drug loading/ratio have equal importance when defining the final cytotoxic activity.

1.4. *In vivo* Results Highlight St-PGA-hyd-Dox_1-Das_{10} as the Lead Candidate

We subsequently evaluated the anti-tumor and anti-metastatic activity of the selected St-PGA-based combination conjugates and single-drug counterparts in a spontaneously metastatic TNBC *in vivo* model obtained by injecting MDA-MB-231-Luc cells in the second left mammary fat pad of NOD/SCID (non-obese diabetic/severe combined immunodeficient) female mice (*Chapter 2*). We evaluated the anti-tumor activity of the treatments by monitoring tumor volume twice a week and tumor weight at the experimental endpoint. Additionally, we evaluated the anti-metastatic activity of conjugates by detecting MDA-MB-231-Luc cells via bioluminescence and measuring lung weight at the experimental endpoint. We evaluated treatment safety by monitoring animal body weight twice a week and relative organ weight (liver, heart, kidney, and spleen) at the experimental endpoint.

In agreement with previous reports (43), treatment with Dox alone prompted animal weight loss and reduced survival rates. The administration of the drug combination (Dox and Das) also prompted animal weight reduction but maintained animal survival. Overall, the St-PGA single-drug and combination conjugates evaluated failed to provoke animal weight loss or reduce animal survival, except for St-PGA-hyd-Dox_1-Val-Das_1. The administration of St-PGA-hyd-Dox_1-Val-Das_1 caused significant animal weight loss, which led to reduced animal survival rates. The burst release of Dox at physiological pH observed for this conjugate offers a likely explanation for the high systemic toxicity; however, we also explored additional sources for the systemic toxicity observed (described below).

Overall, organ weight analysis confirmed the safety of the remaining conjugates but provided evidence for increased spleen weight after administering Dox and Das in combination as free drugs (at 1:1 and 1:10 Dox:Das ratio) and for St-PGA-hyd-Dox_1-Das_{10}. Splenomegaly has been associated with disease progression in patients and breast cancer animal models (62–65); however, the MDA-BM-231-Luc TNBC *in vivo* mouse model failed to exhibit signs of splenomegaly in response to disease progression in

the absence of treatments (60). Dox and Das treatment at a 1:1 ratio also induced a significantly higher spleen weight than Das treatment alone (same dose); meanwhile, St-PGA-hyd-Dox$_1$-Das$_{10}$ displayed a similar increase in spleen weight than the combination of Dox and Das at the same dose. Therefore, we attributed the increase in the spleen mass to the effect of the combined administration of Dox and Das. Of note, the *in vivo* study of the linear PGA counterparts failed to evaluate spleen weight for the combination of Dox and Das as free agents due to low animal survival rates; however, PGA-hyd-Dox-Val-Das failed to increase spleen weight compared to the DPBS control (43).

The analysis of primary tumor volume underscored the advantages of polymer-drug conjugation. The Dox single conjugate (St-PGA-hyd-Dox) significantly reduced tumor growth while avoiding Dox systemic toxicity. St-PGA-hyd-Dox$_1$-Das$_1$ and St-PGA-hyd-Dox$_1$-Das$_{10}$ combination conjugates displayed significant primary tumor reduction compared to DPBS but failed to improve the activity of the free drugs combined; importantly, both combination conjugates avoided the animal weight loss provoked by the administration of free Dox and Das. St-PGA-hyd-Dox$_1$-Das$_{10}$ exhibited the lowest tumor volume at the experimental endpoint (the most significant reduction compared to DPBS control). Only Das single conjugates (St-PGA-Das) failed to significantly inhibit primary tumor growth, with similar activity to the free drug. The analysis of tumor weight at the experimental endpoint ratified these results.

The analysis of metastatic spread in the lungs by bioluminescence revealed the robust anti-tumor activity of Dox in combination with Das at 1:10 Dox:Das ratio. While the St-PGA-based single-drug and combination conjugates displayed moderate anti-metastatic activity, Das administered at a high dose prompted a significant increment in lung metastasis. In agreement with this data, we observed a significantly higher lung weight with high dose Das compared to the remaining treatments (except Dox + Das at

468

1:10 ratio). Several studies have previously described how chemotherapy can promote metastasis through various mechanisms (66–68); however, to the best of our knowledge, studies have failed to describe a similar effect in response to Das treatment. Interestingly, the conjugation of Das to St-PGA counteracted the increase in metastatic spread observed for high doses of Das, and St-PGA-Das administered at the same dose displayed moderate anti-metastatic activity. Co-administration with Dox (1:10 ratio) also prevented the increment in metastasis caused by high dose Das and prompted the highest anti-metastatic activity among the treatments. These data underscore both the advantages of drug conjugation and combination therapy.

Overall, the *in vivo* evaluation of our family of St-PGA-based single-drug and combination conjugates identified St-PGA-hyd-Dox_1-Das_{10} as the optimal conjugate, with treatment associated with the lowest tumor volume at the experimental endpoint (the most significant reduction compared to DPBS control), moderate anti-metastatic activity in lungs, and the avoidance of toxicity caused by free drug treatment.

1.5. Conjugate Interaction with Serum Proteins Could be a Tool for Predicting Systemic Toxicity *In vivo*

We primarily attributed St-PGA-hyd-Dox_1-Val-Das_1 systemic toxicity to the burst Dox release at pH 7.4 from the conjugate; however, St-PGA-hyd-Dox_1-Val-Das_1 exhibited higher toxicity than free Dox administered as a single agent in combination with Das (1:1 ratio, as in St-PGA-hyd-Dox_1-Val-Das_1). Therefore, we sought to examine other potential sources of toxicity.

The interaction of polymer-drug conjugates with blood leads to the adsorption of circulating proteins and the formation of the so-called "protein corona" (69,70), which affects the biological performance of the conjugate by altering its interaction with cells, biodistribution, circulation time, and

toxicity (71). Therefore, we hypothesized that the interaction of the conjugate with serum proteins could be an additional source of systemic toxicity.

With this aim in mind, we developed a novel approach for the qualitative study of protein corona in polymer-drug conjugates via asymmetric flow field-flow fractionation (AF4) (*Chapter 2*). Traditionally, the study of the protein corona has relied on isolating the nanoparticle-corona complex via size-dependent separation techniques and then quantifying and identifying adhered proteins (71); however, our conjugates display sizes comparable to that of the main plasma/serum proteins (e.g., albumin monomer, ~6 nm diameter), making their separation from serum proteins unfeasible by said techniques. Our approach is based on the separation of serum proteins by AF4 and the study of the elution profile of the conjugate after incubation with serum, taking advantage of the fluorescent properties of Dox and Das. This AF4 method can be employed to characterize protein-conjugate interactions in polymer-drug conjugates of sizes comparable to our St-PGA-based conjugates. The simplicity, reduced sample handling, and minimal sample requirements associated with this protocol suggest the utility of this approach to evaluate the influence of the protein corona associated with polymer-drug conjugates (potentially at high-throughput). Of note, the reliance on the fluorescent properties of the conjugated moieties and the low interference of serum/plasma protein autofluorescence represents a significant limitation to this technique. In the case of sensitive linkers employed for drug conjugation, a control with the free drug must be included in the screening to discard the interactions of released drugs with proteins. Furthermore, this method is qualitative; to allow for precise protein quantification and identification, modifications to the method can be applied, such as using a thicker channel to increase the amount of sample injected and supply enough material for complementary analyses.

We successfully optimized an AF4 method for serum protein fractionation and demonstrated a non-significant contribution of serum

protein fluorescence in detecting the conjugates. Employing this method, we discovered that St-PGA-hyd-Dox$_1$-Val-Das$_1$ and St-PGA-hyd-Dox$_1$-Das$_{10}$ interacted with serum proteins, but only St-PGA-hyd-Dox$_1$-Val-Das$_1$ prompted the formation of large aggregates, which could explain the high toxicity of the conjugate *in vivo*. We explored conjugate interaction with serum proteins over a brief time frame (20 min); however, we anticipate that further studies of protein corona formation at longer incubation times could shed more light on the toxicity of St-PGA-hyd-Dox$_1$-Val-Das$_1$.

2. Exploiting Self-assembly to Increase Treatment Efficacy

Previous work by our laboratory (40) revealed that St-PGA displays self-assembly behavior in non-salty aqueous solutions driven by ionic interactions. Overall, St-PGA forms large spherical structures in a concentration-dependent fashion (200 nm diameter for the self-assembled structure vs. 10 nm for the unimer). This study also described the dynamic behavior of St-PGA assemblies, providing evidence for the co-assembly of St-PGA conjugates with different attached moieties and rapid unimer exchange between assemblies; however, high ionic strength and polymer dilution disrupted these assemblies. For this reason, we developed a protocol based on copper-catalyzed azide-alkyne cycloaddition (CuAAC) to covalently capture these assemblies and allow their use as drug delivery systems. Resultant stabilized St-PGA-based self-assembled structures (St-PGA-Click) exhibited increased cellular uptake and circulation time when compared to St-PGA unimers and linear counterparts (40), which converts these nanosystems into potentially efficient drug delivery systems for the development of advanced cancer therapeutics. St-PGA-Click maintained a lack of toxicity, cathepsin B-mediated degradation, and renal excretion profiles (40,46) despite the increase in complexity. These encouraging results prompted the use of St-PGA-Click as a drug delivery system, which provided some promising results (32,34,48).

Considering this previously published research, we hypothesized that the co-assembly of single-drug St-PGA conjugates could generate combination conjugates with increased circulation time and cellular uptake (as St-PGA-Click), further enhancing the anti-tumor and anti-metastatic activity of our combination conjugate and facilitating transport across the BBB; however, CuAAC employs conditions (72 h incubations at 60 ºC) that promote linker hydrolysis and/or drug degradation (40). Thus, we explored alternate protocols that would stabilize St-PGA-drug assemblies under milder conditions (*Chapter 3*). Furthermore, CuAAC results in non-bioresponsive assembly stabilization; therefore, we used this opportunity to optimize a stimuli-responsive crosslinking strategy to promote intracellular drug release and reduce unwanted systemic drug exposure (*Chapter 3*).

Tumor cells provide a myriad of specific stimuli that can be exploited for drug conjugation/nanosystem stabilization. We exploited the low pH of the tumor microenvironment and lysosomal pathway for drug release in *Chapter 2*; in *Chapter 4*, we needed to employ orthogonal chemistries for drug conjugation (using the drug linking chemistries optimized in *Chapter 2*) and structure stabilization.

Cancer cells generally display higher reductive potential than cells from healthy tissues (72,73). The glutathione/glutathione disulfide ratio (GSH/GSSG) is responsible for redox status - cytosolic GSH occurs at a concentration in the millimolar range (0.5-10 mM) while the extracellular concentration of GSH is generally 1000 times less (2-20 µM in plasma) (74). Cancer cells generally display a higher level of GSH, although the exact level depends on factors such as tumor type and stage (72,73,75); we pursued the development of a redox-responsive crosslinking strategy with this situation in mind.

Therefore, the second goal of this thesis involved the development of a bottom-up strategy to synthesize combination conjugates by co-assembly

of single-drug St-PGA-based conjugates and the subsequent stabilization of assembled structures via stimuli-responsive linkers.

2.1. Hydrophobic Moieties Alter St-PGA Behavior in Aqueous Solutions

Disulfide bonds have been previously employed for the redox-responsive stabilization of self-assembled nanosystems (76), nanogels (77,78), hydrogels (79–81), polymeric micelles (82,83), and polymer brushes (84), yielding stable architectures in low reductive media that disassembled upon an increase in GSH levels. We hypothesized disulfide-mediated St-PGA assembly stabilization would yield comparable results.

Using an amide bond, we introduced thiol moieties to St-PGA by pyridyl dithiol cysteamine (PD) conjugation (*Chapter 3*). The use of PD provides multiple advantages, including the high efficiency of the thiol-pyridyl disulfide exchange reaction as the pyridyl thione group represents an excellent leaving group, which also supports reactivity with almost any thiol-bearing compound and impedes thiol-disulfide exchange from the released group (85,86). Additionally, thiol-pyridyl disulfide exchange involves mild conditions suitable for crosslinking St-PGA-drug conjugates (85).

We conjugated PD to St-PGA, aiming for 5 and 10% mol PD loadings (St-PGA-PD(5) and St-PGA-PD(10), respectively). We then conjugated Dox and Das to St-PGA-PD(5) and St-PGA-PD(10) via the pH-responsive hydrazone (for Dox) and ester (for Das) bonds (*Chapter 3*). We discarded the use of the Val spacer given the lack of advantage over simple ester Das conjugation in St-PGA unimers (*Chapter 2*). We also conjugated Dox through an amide bond, a non-responsive linker, for comparison. Of note, we failed to obtain a St-PGA-PD(10)-based hydrazone-Dox conjugate as the low solubility of the precursor in organic media and/or steric hindrance caused by the PD moiety impeded the conjugation of tert-butyl carbazate (the first step of hydrazone-mediated conjugation).

The introduction of hydrophobic moieties into the PGA backbone can induce changes in conjugate conformation in aqueous media. Linear PGA conjugates with AGM and Dox with different AGM loadings and linkers displayed different overall hydrophobicity depending on linker nature (Gly versus Gly-Gly) and AGM loading (39). Overall, conjugates with higher hydrophobicity displayed a propensity to aggregate and exhibited coil-to-helix transitions. PD, Das, and Dox hydrophobicity have been exploited to create polymeric micelles or hydrogels with hydrophobic pockets and drug encapsulation capacity using hydrophilic polymeric carriers (77,78,87,88). Therefore, we pursued the exhaustive physico-chemical characterization of the St-PGA-based conjugates to study the effect of PD, Dox, and Das conjugation in conjugate size, secondary structure, and self- and co-assembly behavior (*Chapter 3*).

We studied St-PGA, St-PGA-PD(5), and St-PGA-PD(10) size at increasing concentrations in MilliQ water and at increasing salt concentrations and discovered that St-PGA-PD(10) behavior deviated from the concentration-dependent size increment observed for St-PGA. Additionally, St-PGA-PD(10) assemblies at a high conjugate concentration (10 mg/mL) failed to disassemble upon an increase in ionic strength (as opposed to St-PGA-PD(5) and St-PGA assemblies, which readily disassembled).

To evaluate the influence of drug conjugation in conjugate behavior in aqueous media, we studied the size and secondary structure of St-PGA-PD(5)-drug and St-PGA-PD(10)-drug conjugates in MilliQ water and high ionic strength media (i.e., 10 mM phosphate buffer [PB]). The use of amide and hydrazone bonds for Dox conjugation to St-PGA-PD conjugates provided evidence of the influence of drug linkers - while the conjugates containing amide-Dox disassembled in high ionic strength media (10 mM PB), Dox conjugation via the flexible hydrazone bond impeded the normal disassembly of St-PGA structures. Nevertheless, only the amide-Dox

conjugate exhibited Dox-Dox dimerization in 10 mM PB as determined by CD, which suggests that the aggregation behavior of these St-PGA-based Dox conjugates relies on a complex mechanism independent from Dox stacking. Furthermore, St-PGA-PD(5)-Dox, St-PGA-PD(10)-Dox, and St-PGA-PD(5)-hyd-Dox displayed a reduction in size with an increasing conjugate concentration in water – the opposite behavior expected from St-PGA-based conjugates (40). Meanwhile, St-PGA-PD(5)-Das and St-PGA-PD(10)-Das displayed the expected increase in size with conjugate concentration; however, St-PGA-PD(10)-Das size in water was significantly smaller than St-PGA-PD(5)-Das, suggesting a more compact structure.

While the hydrophobic interactions introduced in St-PGA by PD and Dox conjugation failed to alter the typical secondary structure of St-PGA, Das conjugation to St-PGA-PD(10) prompted the transition from random coil to α-helix conformation in MilliQ water following a mechanism independent of Das-Das interactions (as the CD spectra failed to show evidence of Das-Das interaction), in agreement with the data reported for linear PGA conjugates (39). This study with linear PGA conjugates also analyzed how drug loading and linking chemistry influenced the conjugate size, compactness, and structural organization in solution by small-angle neutron scattering (SANS), a scattering technique that measures neutron diffraction and has been employed for the study of PGA-based nanosystems conformation in solution (39,40). Therefore, we believe the use of SANS to study St-PGA solution structure and moiety interactions in St-PGA-PD-drug conjugates will shed more light on the influence of hydrophobic moieties in conjugate structure and aggregation behavior in aqueous media.

A requirement for assembly stabilization is adequate conjugate self- or co-assembly. The co-assembly of St-PGA derivatives has been studied for various moieties (including large fluorophores) by myriad techniques providing robust evidence for adequate co-assembly (40); nevertheless, this

thesis describes the first study of the self- and co-assembly of St-PGA-drug conjugates.

To study self- and co-assembly, we determined the CAC of St-PGA-PD(5) and the derived drug conjugates alone and mixtures of St-PGA-PD(5)-Das with St-PGA-PD(5)-Dox or St-PGA-PD(5)-hyd-Dox. While all the conjugates self-assembled as expected in MilliQ water, St-PGA-PD(5)-Das effectively co-assembled with St-PGA-PD(5)-Dox but not with St-PGA-PD(5)-hyd-Dox. Therefore, both conjugated drugs and linking moieties profoundly influence the co-assembly of St-PGA conjugates; however, we lack a proper understanding of the mechanism.

Considering this data with the results from previous sections, we hypothesize that PD, Das, and/or Dox conjugation to St-PGA increases the overall hydrophobicity of the system and alters the forces driving self- and co-assembly, with the linking moiety employed significantly influencing final conjugate conformation. Future experiments with model hydrophobic molecules (e.g., Nile red) may confirm this hypothesis (40,78). If our hypothesis is correct, the self- and co-assembly of these St-PGA-based conjugates could be studied with the pyrene fluorescence assay (35). These techniques would permit a systematic study of the hydrophobic interactions in conjugates with different moieties and loadings and eventually identify a "hydrophobic threshold," i.e., maximal loading of a specific hydrophobic moiety that supports normal self-assembly by ionic interactions.

2.2. Altered Behavior in Solution Impedes Structure Stabilization by Disulfide Bonds

We pursued the disulfide-mediated stabilization of St-PGA-PD(5)-based conjugates using three different approaches – direct disulfide bond formation between St-PGA molecules, incorporation of a short poly(ethylene glycol)-based crosslinker, and inverse nanoprecipitation (*Chapter 3*).

Unfortunately, the synthetic protocols examined failed to yield stable nanosystems in high ionic strength media; however, data deriving from the physico-chemical characterization of the final products revealed valuable information regarding the cause of the instability. Our data suggest that the lack of stabilization does not derive from a lack of conjugate aggregation or low conjugate concentration in the reaction. Therefore, we believe that the lack of stability derives from the presence of reduced (free) thiol groups in the final compound (which trigger disulfide-thiol exchange reactions that destabilize the structure), poor exposure of the thiol groups of St-PGA-PD(5)-derived molecules (which prompt the formation of intramolecular disulfide bonds instead of intermolecular stabilizing bonds), or a reduced number of intermolecular disulfide bonds in the final product. A more profound analysis of conjugate structure and aggregation in aqueous media may help to explain the lack of efficacy of the disulfide cross-linking protocols explored in this thesis.

The inverse nanoprecipitation protocol yielded optimal results in terms of free thiol groups in the final product but failed to promote the formation of stable assemblies in high ionic strength media. This protocol does not rely on the self- or co-assembly of polymer-drug molecules but polymer aggregation following the injection of a dilute polymer solution into a polymer non-solvent (89), which broadens the spectrum of usable drug-linker combinations and, thus, possible combination conjugates. Therefore, our laboratory is exploring St-PGA-PD(10) to synthesize stable large (~200 nm) assemblies by inverse nanoprecipitation to increase the number of stabilizing disulfide bonds in the final product. The use of St-PGA-PD(10) for the synthesis of combination conjugates by self- and co-assembly of single drug St-PGA-based conjugates entails the optimization of new synthetic protocols for drug conjugation, as St-PGA-PD(10) exhibits low solubility and steric hindrance due to PD conjugation.

3. Targeting the Brain by Active Transport Across the BBB

As our attempts to obtain a redox-responsive stabilization method for St-PGA-based assemblies failed to provide stable architectures in high ionic strength media (which would increase circulation time and cell uptake), we developed the brain-targeted version of the optimal candidate synthesized in *Chapter 2* (St-PGA-hyd-Dox_1-Das_{10}).

We aimed to provide the conjugate with the ability to cross the BBB and accumulate in the brain using active targeting employing the so-called "trojan horse" strategy, which involves the conjugation of ligands of specific BBB receptors to the conjugate to promote intact barrier crossing via receptor-mediated transcytosis (90). We employed the peptide Angiopep-2 (ANG), a ligand of the low-density lipoprotein receptor-related protein 1 (LRP-1, expressed by brain endothelial cells) (91), as a targeting moiety. As a component of drug delivery systems, ANG has been employed to deliver DNA plasmids (92,93), antibodies (90), and small drugs (34) to the brain. Our work was encouraged by results obtained from a previous study reported by our laboratory that employed an ANG-conjugated St-PGA-Click nanosystem to deliver small drugs to the brain to treat Alzheimer's disease (48). ANG-conjugated St-PGA-Click supported increased brain accumulation compared to a non-targeted counterpart and displayed excellent diffusion throughout the brain parenchyma. Overall, the authors observed the accumulation of 1.5% of the injected dose in the brain 3 h after intravenous administration in healthy mice. Additionally, confocal microscopy revealed that ANG-conjugated St-PGA-Click remained attached to the brain vasculature, acting as a drug "depot" (48). This study proved the utility of ANG-conjugated St-PGA-based structures as drug delivery systems to treat brain diseases; however, this study employed reversible disulfide bonds for ANG conjugation to St-PGA-Click (48).

Nanosystem-ANG bond stability remains a crucial concept since the strength of the interaction between ANG and LRP-1 decides cell trafficking

and, therefore, the nanosystem's capacity to cross the BBB and accumulate in the brain (90,94,95). Peptide conjugation to St-PGA via non-biodegradable linkers ensures that the peptide remains attached to the nanosystem during blood circulation and transcytosis; therefore, we aimed to conjugate ANG to St-PGA through a maleimide-thiol bond, a non-biodegradable linker widely used for ANG conjugation to various nanosystems (90,93,96,97). The associated chemistry generally employs mild conditions (i.e., phosphate buffers at physiological pH and room temperature (90,93,96)), thereby avoiding drug degradation.

Our final aim was the synthesis of an ANG-tagged St-PGA-based combination conjugate bearing the drug combination, drug ratio, and linkers of St-PGA-hyd-Dox$_1$-Das$_{10}$ (optimized in *Chapter 2*).

3.1. St-PGA Maintains its Physico-chemical Characteristics After Angiopep-2 Conjugation

We aimed to conjugate ANG to a St-PGA combination conjugate with Dox and Das attached via pH-labile linkers; therefore, we required mild conditions and reduced reaction times to avoid drug release and/or degradation. Maleimide-thiol reactions are usually carried out in phosphate buffers at physiological pH with tris(2-carboxyethyl)phosphine (TCEP) to avoid peptide dimerization and at room temperature for times ranging from 1 to 17 h (90,93,96); however, the study of the drug release kinetics in *Chapter 2* demonstrated significant Dox and Das release under similar conditions. Therefore, we studied maleimide-thiol ANG conjugation reaction kinetics by size exclusion chromatography (SEC) to optimize reaction time and reduce associated drug release (*Chapter 4*). We discovered that conjugation of ANG to maleimide-conjugated St-PGA occurred during the first 5 h of reaction. We also quantified ANG loading after 5 and 24 h of reaction via ^{1}H-NMR and found similar values, thereby confirming the SEC findings. With the aim to support the fine control over the final conjugate and

avoid any interaction of our conjugate with plasma proteins via maleimide-thiol reaction, we quenched the maleimide groups that failed to react with ANG. Maleimide quenching reactions often employ harsh conditions that lead to drug release (98,99); therefore, we chose to quench spare maleimide groups by reaction with a thiol-containing molecule such as N-acetyl cysteine (NAC), employing the conditions optimized for ANG conjugation (degassed DPBS, TCEP, 5 h at room temperature). The application of this protocol for ANG conjugation and maleimide quenching yielded comparable results (in terms of conjugation efficacy) for St-PGA and St-PGA conjugates with fluorophores (St-PGA-Cy5.5) and drugs (this will be discussed below), proving the versatility and reproducibility of the protocol.

ANG is a 2.3 kDa peptide including the aromatic amino acids phenylalanine and tyrosine, and our targeted conjugates included between two and three ANG molecules (~20% wt). Therefore, we exhaustively physico-chemicaly characterized conjugates to evaluate the influence of peptide conjugation on St-PGA. We discovered that ANG conjugation to the St-PGA and St-PGA-Cy5.5 unimers failed to significantly alter the main physico-chemical characteristics of the carrier, i.e., secondary structure in aqueous solutions, concentration-dependent aggregation in water, size in high ionic strength media corresponding to the St-PGA unimer, and negative charge.

In summary, we developed an efficient and reproducible protocol for ANG conjugation to St-PGA conjugates in aqueous media using maleimide-thiol chemistry and demonstrated that ANG conjugation to the St-PGA-unimer fails to alter the main physico-chemical characteristics of the carrier significantly.

3.2. Angiopep-2 Conjugation Enhances St-PGA Accumulation in the Brain in Healthy Mice

The ability of ANG to enhance the brain accumulation of nanosystems has been widely confirmed (91). For instance, Khan et al. (100) exhibited a 1.9-fold accumulation in healthy mice brain upon ANG conjugation to poly(lactic-co-glycolic acid)-poly(ε-carbobenzoxy-l-lysine) nanoparticles. Meanwhile, Ke et al. (92) increased the accumulation of their polyamidoamine dendrimers in healthy mice brain from 3.06-fold to 8.42-fold (than an untargeted counterpart) by modulating ANG loading.

To verify the influence of ANG in the brain accumulation of St-PGA unimer, we studied the biodistribution of an ANG-conjugated fluorescently labeled St-PGA conjugate (St-PGA-Cy5.5-ANG-NAC) and an untargeted counterpart (St-PGA-Cy5.5-NAC) and quantified conjugate accumulation in primary organs, including the brain (*Chapter 4*). Our data demonstrated the capacity of the ANG-bearing conjugate to cross the BBB and accumulate in the brain - St-PGA-Cy5.5-ANG-NAC exhibited a 1.4-fold accumulation in the brain (0.7 % of the injected dose) compared to the untargeted St-PGA-Cy5.5-NAC 4 h after intravenous administration. While this value represents an increment in accumulation compared to related ANG-tagged nanosystems (92,100,101), accumulation remained at values below that observed for St-PGA-Click-ANG (48), perhaps as a consequence of the increased circulation time of the latter (40). Importantly, St-PGA-Cy5.5-ANG-NAC and St-PGA-Cy5.5-NAC failed to exhibit toxicity (healthy mice) or differential accumulation in immune-related organs (i.e., liver and spleen); however, our data suggested an increment in circulation time and a reduction in the renal excretion of the ANG-decorated conjugate. Nevertheless, we note that the study of conjugate biodistribution used a short exposure time (4 h), which impedes the evaluation of pharmacokinetics and long-term toxicity. Furthermore, the method employed for conjugate quantification in the brain (i.e., *ex vivo* fluorescence detection by IVIS® technology) impedes the differentiation of the conjugate that has permeated and diffused in the brain parenchyma from the conjugate that remained attached to the brain vasculature. Alternate protocols allow the separation of

the brain parenchyma from the vasculature to precisely quantify the levels of brain-permeated conjugate (94), providing further insight into the efficiency of the targeted St-PGA conjugate in crossing the BBB and diffusing within brain tissue. Nevertheless, our laboratory reported the ability of St-PGA-Click-ANG to remain attached to the brain vasculature, which allowed its use as a drug "depot" and enhanced the therapeutic activity of the conjugate (48). Confocal microscopy analyses of brain tissue from the biodistribution study are ongoing to evaluate whether the ANG-conjugated St-PGA unimer acts comparably to St-PGA-Click-ANG.

In summary, ANG conjugation significantly increases the brain accumulation of St-PGA when compared to an untargeted counterpart, encouraging the use of this strategy to deliver our combination conjugate to brain metastases.

3.3. Attachment of Angiopep-2 to the Combination Conjugate Keeps Unaltered its Physico-chemical Characteristics

The use of orthogonal linking chemistries allowed us to combine both synthetic protocols (St-PGA-hyd-Dox_1-Das_{10} synthesis from *Chapter 2* and St-PGA-ANG-NAC from *Chapter 4*) to obtain our targeted St-PGA-based combination conjugate, St-PGA-hyd-Dox-Das-ANG-NAC.

During the synthesis of the targeted combination conjugate, we confirmed the precise control of drug ratios provided by the synthetic protocols developed in *Chapter 2*, obtaining a maleimide-bearing precursor with the same drug ratio as the untargeted St-PGA-hyd-Dox_1-Das_{10} conjugate (*Chapter 4*). Our protocol allowed for ANG conjugation to said precursor with minimal drug loading loss (a consequence of drug release in the reaction media and subsequent purification), obtaining St-PGA-hyd-Dox-Das-ANG-NAC targeted combination conjugate with a Dox:Das ratio of 1:6 (*Chapter 4*).

Compared to the untargeted St-PGA-hyd-Dox$_1$-Das$_{10}$ combination conjugate (*Chapter 2*), St-PGA-hyd-Dox-Das-ANG-NAC displayed similar physico-chemical characteristics in terms of size (unimer), aggregation behavior in water, secondary structure, and zeta potential (*Chapter 4*). St-PGA-hyd-Dox-Das-ANG-NAC and St-PGA-hyd-Dox$_1$-Das$_{10}$ also exhibited similar pH-dependent drug release profiles, with higher Dox release at pH 5.0 than 7.4 and higher Das release at pH 7.4 than 5.0. Although we observed lower Dox and Das release at pH 5.0 by St-PGA-hyd-Dox-Das-ANG-NAC than St-PGA-hyd-Dox$_1$-Das$_{10}$, the targeted conjugated supports the release of Dox and Das at a ratio with an excess of Das, which we found beneficial for drug combination synergism (*Chapter 2*).

Therefore, we optimized a protocol for maleimide-thiol conjugation of ANG to St-PGA-drug combination conjugates that allowed peptide conjugation with minimal drug loading loss. We verified that the final targeted conjugate maintained the main physico-chemical characteristics of the untargeted combination conjugate. Potentially, our ANG conjugation protocol can be used to conjugate thiol-modified peptides to maleimide-modified polymer-drug conjugates that employ pH-labile linkers for drug conjugation.

3.4. St-PGA-hyd-Dox-Das-ANG-NAC Effectively Reduces Extracranial Metastatic Progression with Limited but Promising Anti-metastatic Activity in the Brain

In collaboration with the group of Dr. Manuel Valiente at the CNIO (Madrid, Spain), we evaluated the anti-metastatic activity of St-PGA-hyd-Dox-Das-ANG-NAC in the brain in a mouse model of TNBC brain metastasis obtained by the injection of MDA-MB-231-BrM3 cells (brain metastatic derivative from MDA-MB-231 cell line) into the left ventricle of female athymic nude mice (18,102,103) (*Chapter 4*). Of note, this mouse model also develops lung metastasis, to which our untargeted St-PGA-hyd-Dox$_1$-Das$_{10}$

conjugate displayed anti-metastatic activity (in the *in vivo* model employed in *Chapter 2*). We also monitored animal weight as an indicator of animal wellbeing/treatment safety.

The *in vivo* study demonstrated the robust anti-metastatic activity of St-PGA-hyd-Dox-Das-ANG-NAC, which significantly reduced metastatic spread throughout the body – overall, we observed a robust reduction of lung metastasis and a lower non-significant reduction in brain metastasis. Notably, St-PGA-hyd-Dox-Das-ANG-NAC possessed an excellent safety profile, and treatment avoided disease progression-associated animal weight loss. We believe these results derive from both the efficacy of the drug combination and the ability of ANG to target LRP-1 receptor-expressing MDA-MB-231 cells (104). Further studies of the biodistribution of targeted and untargeted conjugates in the *in vivo* TNBC brain metastasis model could reveal additional findings in this regard. If our hypothesis is correct, St-PGA-Cy5.5-ANG-NAC will display higher accumulation in brains and lungs harboring MDA-MB-231-BrM3-derived metastasis, specifically in metastatic tissue. Khan et al. (100) compared the brain accumulation of ANG-tagged poly(lactic-co-glycolic acid)-poly(ε-carbobenzoxy-l-lysine) nanoparticles in healthy brains and brains harboring MDA-MB-231-HER2 brain metastasis; the accumulation of targeted nanoparticles increased from 1.9-fold (compared to the untargeted counterpart) in healthy brains to 2.4-fold in brains harboring brain metastasis.

Overall, our data demonstrate that our treatment strategy effectively reduced metastatic spread without causing systemic toxicity; however, this approach must be further optimized to deliver an adequate therapeutic drug(s) concentration in the brain. We note that the drug/conjugate dose employed in this *in vivo* experiment may be suboptimal for brain metastasis treatment. We chose the dose after the *in vivo* experiment performed in *Chapter 2* in the orthotopic MBA-MB-231-Luc TNBC mouse model (1.2 mg/Kg Dox). We used this low dose of Dox since our previous research

provided evidence that higher doses of free Dox (1.5 mg/Kg) resulted in systemic toxicity and, eventually, animal death (43); however, the mouse model of brain metastasis was developed using an athymic nude mouse strain, which can support higher Dox doses than the non-obese diabetic/severe combined immunodeficient (NOD/SCID) strain used in *Chapter 2* (96,100). Considering this data and encouraged by St-PGA-hyd-Dox-Das-ANG-NAC's anti-metastatic activity in the lungs and excellent safety profile, we plan to perform new experiments using an increased conjugate/Dox dose to increase drug bioavailability in brain metastases. These studies will include the determination of the maximum tolerated dose in healthy athymic nude mice to select the dose for the new anti-metastatic activity experiment. We expect the dose increment to lead to a higher concentration of therapeutic agents in metastatic tissues, leading to a more significant reduction in metastatic spread to the lungs and brain.

We note the relevance of the efficient reduction of lung metastasis in the translational scenario. Brain metastasis and extracranial tumors (primary and secondary) are often concomitant, and the presence of uncontrolled extracranial disease reduces the therapeutic options for brain metastasis patients (105). Therefore, developing a treatment that can simultaneously address brain metastasis and extracranial tumors provides hope for these patients and could potentially change the clinical scenario for brain metastasis treatment.

We also note that we administered St-PGA-hyd-Dox-Das-ANG-NAC at the initial stages of metastatic disease, i.e., seven days after intracardiac injection of MDA-MB-BrM3 cells; however, brain metastasis diagnosis in the clinical scenario usually comes after the patient suffers from disease progression-related side effects (e.g., seizures) at later stages. Brain metastasis screening via imaging techniques has failed to prove clinical benefit (106), probably due to the lack of available treatments for early-stage disease. We believe the development of efficient treatments for early-stage

brain metastasis and the implementation of brain metastasis screening for early diagnosis will significantly benefit brain metastasis patients.

Importantly, this thesis represents the first described use of a Dox and Das combination for the treatment of brain metastases. Examples of treatment with Dox (96,101,107) or Das (108) can be found in the literature, but their use as a combination therapy had remained unassessed until now. We believe the results reported in this thesis support using a Dox and Das combination therapy to treat breast cancer brain metastasis.

In summary, we believe that this thesis provides evidence to support the use of St-PGA unimer as a polymeric carrier to develop polypeptide-based combination conjugates to treat solid tumors and paves the way for the development of rationally-designed treatments for brain metastasis.

References

1.   Sung H, Ferlay J, Siegel RL, Laversanne M, Soerjomataram I, Jemal A, et al. Global Cancer Statistics 2020: GLOBOCAN Estimates of Incidence and Mortality Worldwide for 36 Cancers in 185 Countries. CA Cancer J Clin. 2021 May 4;71(3):209–49.

2.   Leone JP, Leone BA. Breast cancer brain metastases: the last frontier. Exp Hematol Oncol. 2015/11/24. 2015 Dec 24;4(1):33.

3.   Witzel I, Oliveira-Ferrer L, Pantel K, Müller V, Wikman H. Breast cancer brain metastases: biology and new clinical perspectives. Breast Cancer Res. 2016 Dec 19;18(1):8.

4.   Achrol AS, Rennert RC, Anders C, Soffietti R, Ahluwalia MS, Nayak L, et al. Brain metastases. Nat Rev Dis Prim. 2019 Dec 17;5(1):5.

5.   Waks AG, Winer EP. Breast Cancer Treatment. JAMA. 2019 Jan 22;321(3):288.

6.   Sharma P. Biology and Management of Patients With Triple-Negative Breast Cancer. Oncologist. 2016;21(9):1050–62.

7.   Prat A, Pineda E, Adamo B, Galván P, Fernández A, Gaba L, et al. Clinical implications of the intrinsic molecular subtypes of breast cancer. The Breast. 2015 Nov 1;24:S26–35.

8.   Januškevičienė I, Petrikaitė V. Heterogeneity of breast cancer: The importance of interaction between different tumor cell populations. Life Sci. 2019 Dec 15;239:117009.

9.   Lebert JM, Lester R, Powell E, Seal M, McCarthy J. Advances in the Systemic Treatment of Triple-Negative Breast Cancer. Curr Oncol. 2018 Jun 1;25(11):142–50.

10. Tsang JYS, Tse GM. Molecular Classification of Breast Cancer. Adv Anat Pathol. 2020 Jan;27(1):27–35.

11. Dai X, Li T, Bai Z, Yang Y, Liu X, Zhan J, et al. Breast cancer intrinsic subtype classification, clinical use and future trends. Am J Cancer Res. 2015;5(10):2929–43.

12. Jitariu AA, Cimpean AM, Ribatti D, Raica M. Triple negative breast cancer: the kiss of death. Oncotarget. 2017;8(28):46652–62.

13. Denkert C, Liedtke C, Tutt A, von Minckwitz G. Molecular alterations in triple-negative breast cancer-the road to new treatment strategies. Lancet. 2017;389(10087):2430–42.

14. Gadi VK, Davidson NE. Practical Approach to Triple-Negative Breast Cancer. J Oncol Pr. 2017;13(5):293–300.

15. Bianchini G, Balko JM, Mayer IA, Sanders ME, Gianni L. Triple-negative breast cancer: challenges and opportunities of a heterogeneous disease. Nat Rev Clin Oncol. 2016;13(11):674–90.

16. Cardoso F, Harbeck N, Fallowfield L, Kyriakides S, Senkus E. Locally recurrent or metastatic breast cancer: ESMO Clinical Practice Guidelines for diagnosis, treatment and follow-up. Ann Oncol. 2012 Oct;23(SUPPL. 7):vii11–9.

17. Chen W, Hoffmann AD, Liu H, Liu X. Organotropism: new insights into molecular mechanisms of breast cancer metastasis. npj Precis Oncol. 2018 Dec 16;2(1):4.

18.	Bos PD, Zhang XHF, Nadal C, Shu W, Gomis RR, Nguyen DX, et al. Genes that mediate breast cancer metastasis to the brain. Nature. 2009 Jun 6;459(7249):1005–9.

19.	Witzel I, Oliveira-Ferrer L, Müller V. Brain Metastasis in Breast Cancer Patients—Need for Improvement. Cancers (Basel). 2020 Oct 30;12(11):3190.

20.	Cerna T, Stiborova M, Adam V, Kizek R, Eckschlager T. Nanocarrier drugs in the treatment of brain tumors. J Cancer Metastasis Treat. 2016;2(10):407–16.

21.	Mills MN, Figura NB, Arrington JA, Yu H-HM, Etame AB, Vogelbaum MA, et al. Management of brain metastases in breast cancer: a review of current practices and emerging treatments. Breast Cancer Res Treat. 2020 Apr 6;180(2):279–300.

22.	Duro-Castano A, Conejos-Sanchez I, Vicent MJ. Peptide-Based Polymer Therapeutics. Polymers (Basel). 2014;6(2):515–51.

23.	Duncan R. Polymer therapeutics at a crossroads? Finding the path for improved translation in the twenty-first century. J Drug Target. 2017 Nov 26;25(9–10):759–80.

24.	Fang J, Islam W, Maeda H. Exploiting the dynamics of the EPR effect and strategies to improve the therapeutic effects of nanomedicines by using EPR effect enhancers. Adv Drug Deliv Rev. 2020 Jan 1;157:142–60.

25.	Prat A, Perou CM. Deconstructing the molecular portraits of breast cancer. Mol Oncol. 2011 Feb;5(1):5–23.

26.	Markman JL, Rekechenetskiy A, Holler E, Ljubimova JY. Nanomedicine therapeutic approaches to overcome cancer drug resistance. Adv Drug Deliv Rev. 2013 Nov;65(13–14):1866–79.

27.	Kobayashi H, Turkbey B, Watanabe R, Choyke PL. Cancer Drug Delivery: Considerations in the Rational Design of Nanosized Bioconjugates. Bioconjug Chem. 2014 Dec 17;25(12):2093–100.

28.	Theek B, Rizzo LY, Ehling J, Kiessling F, Lammers T. The theranostic path to personalized nanomedicine. Clin Transl Imaging. 2014 Feb 19;2(1):67–76.

29.	Vicent MJ, Greco F, Nicholson RI, Paul A, Griffiths PC, Duncan R. Polymer therapeutics designed for a combination therapy of hormone-dependent cancer. Angew Chemie - Int Ed. 2005 Jun 27;44(26):4061–6.

30.	Rasines Mazo A, Allison-Logan S, Karimi F, Chan NJ-A, Qiu W, Duan W, et al. Ring opening polymerization of α-amino acids: advances in synthesis, architecture and applications of polypeptides and their hybrids. Chem Soc Rev. 2020;49(14):4737–834.

31.	Barz M, Duro-Castano A, Vicent MJ. A versatile post-polymerization modification method for polyglutamic acid: synthesis of orthogonal reactive polyglutamates and their use in "click chemistry." Polym Chem. 2013 Apr 24;4(10):2989.

32.	Córdoba-David G, Duro-Castano A, Castelo-Branco RC, González-Guerrero C, Cannata P, Sanz AB, et al. Effective Nephroprotection Against Acute Kidney Injury with a Star-Shaped Polyglutamate-Curcuminoid Conjugate. Sci Rep. 2020 Dec 1;10(1):1–15.

33.	Conejos-Sánchez I, Cardoso I, Oteo-Vives M, Romero-Sanz E, Paul A, Sauri AR, et al. Polymer-doxycycline conjugates as fibril disrupters: An approach towards the treatment of a rare amyloidotic disease. J Control Release. 2015 Jan 28;198:80–90.

34. Cuesta CM, Ibañez F, Lopez-Hidalgo R, Ureña J, Duro-Castano A, Armiñán A, et al. A targeted polypeptide-based nanoconjugate as a nanotherapeutic for alcohol-induced neuroinflammation. Nanomedicine Nanotechnology, Biol Med. 2021 Jun 1;34:102376.

35. Dolz-Pérez I, Sallam MA, Masiá E, Morelló-Bolumar D, Pérez del Caz MD, Graff P, et al. Polypeptide-corticosteroid conjugates as a topical treatment approach to psoriasis. J Control Release. 2020 Feb;318:210–22.

36. Arroyo-Crespo JJ, Armiñán A, Charbonnier D, Balzano-Nogueira L, Huertas-López F, Martí C, et al. Tumor microenvironment-targeted poly-L-glutamic acid-based combination conjugate for enhanced triple negative breast cancer treatment. Biomaterials. 2018 Dec;186:8–21.

37. Duro-Castano A, Lim NH, Tranchant I, Amoura M, Beau F, Wieland H, et al. In Vivo Imaging of MMP-13 Activity Using a Specific Polymer-FRET Peptide Conjugate Detects Early Osteoarthritis and Inhibitor Efficacy. Adv Funct Mater. 2018 Sep 12;28(37):1802738.

38. Cheah HY, Gallon E, Dumoulin F, Hoe SZ, Japundžić-Žigon N, Glumac S, et al. Near-Infrared Activatable Phthalocyanine-Poly-L-Glutamic Acid Conjugate: Enhanced in Vivo Safety and Antitumor Efficacy toward an Effective Photodynamic Cancer Therapy. Mol Pharm. 2018 Jul 2;15(7):2594–605.

39. Arroyo-Crespo JJ, Deladriere C, Nebot VJ, Charbonnier D, Masiá E, Paul A, et al. Anticancer Activity Driven by Drug Linker Modification in a Polyglutamic Acid-Based Combination-Drug Conjugate. Adv Funct Mater. 2018 May 16;28(22):1800931.

40. Duro-Castano A, Nebot VJ, Niño-Pariente A, Armiñán A, Arroyo-Crespo JJ, Paul A, et al. Capturing "Extraordinary" Soft-Assembled Charge-Like Polypeptides as a Strategy for Nanocarrier Design. Adv Mater. 2017 Oct;29(39):1702888.

41. Niño-Pariente A, Armiñán A, Reinhard S, Scholz C, Wagner E, Vicent MJ. Design of Poly- <scp>l</scp> -Glutamate-Based Complexes for pDNA Delivery. Macromol Biosci. 2017 Oct 1;17(10):1700029.

42. Kiew LV, Cheah HY, Voon SH, Gallon E, Movellan J, Ng KH, et al. Near-infrared activatable phthalocyanine-poly-L-glutamic acid conjugate: increased cellular uptake and light–dark toxicity ratio toward an effective photodynamic cancer therapy. Nanomedicine Nanotechnology, Biol Med. 2017 May 1;13(4):1447–58.

43. Arroyo Crespo JJ. Polymer-based combination conjugates for the treatment of triple negative breast cancer : From rational design to preclinical evaluation. University of Valencia; 2018.

44. Markovsky E, Baabur-Cohen H, Satchi-Fainaro R. Anticancer polymeric nanomedicine bearing synergistic drug combination is superior to a mixture of individually-conjugated drugs. J Control Release. 2014 Aug 10;187:145–57.

45. Conejos-Sánchez I, Duro-Castano A, Birke A, Barz M, Vicent MJ. A controlled and versatile NCA polymerization method for the synthesis of polypeptides. Polym Chem. 2013;4(11):3182.

46. Duro-Castano A, England RM, Razola D, Romero E, Oteo-Vives M, Morcillo MA, et al. Well-defined star-shaped polyglutamates with improved pharmacokinetic profiles as excellent candidates for biomedical applications. Mol Pharm. 2015 Oct 5;12(10):3639–49.

47. Zagorodko O, Nebot VJ, Vicent MJ. The generation of stabilized supramolecular nanorods from star-shaped polyglutamates. Polym Chem. 2020 Feb 11;11(6):1220–9.

48. Duro-Castano A, Borrás C, Herranz-Pérez V, Blanco-Gandía MC, Conejos-Sánchez I, Armiñán A, et al. Targeting Alzheimer's disease with multimodal polypeptide-based nanoconjugates. Sci Adv. 2021 Mar 26;7(13):eabf9180.

49. Greco F, Vicent MJ. Combination therapy: Opportunities and challenges for polymer–drug conjugates as anticancer nanomedicines. Adv Drug Deliv Rev. 2009 Nov;61(13):1203–13.

50. Lee S-H, Griffiths JR. How and Why Are Cancers Acidic? Carbonic Anhydrase IX and the Homeostatic Control of Tumour Extracellular pH. Cancers (Basel). 2020 Jun 18;12(6):1616.

51. Patel S, Kim J, Herrera M, Mukherjee A, Kabanov A V., Sahay G. Brief update on endocytosis of nanomedicines. Adv Drug Deliv Rev. 2019 Apr;144:90–111.

52. Selby LI, Cortez-Jugo CM, Such GK, Johnston APR. Nanoescapology: progress toward understanding the endosomal escape of polymeric nanoparticles. WIREs Nanomedicine and Nanobiotechnology. 2017 Sep 3;9(5).

53. Vasey PA, Kaye SB, Morrison R, Twelves C, Wilson P, Duncan R, et al. Phase I clinical and pharmacokinetic study of PK1 [N-(2-hydroxypropyl)methacrylamide copolymer doxorubicin]: first member of a new class of chemotherapeutic agents-drug-polymer conjugates. Cancer Research Campaign Phase I/II Committee. Clin Cancer Res. 1999 Jan;5(1):83–94.

54. Matsumura Y, Maeda H. A new concept for macromolecular therapeutics in cancer chemotherapy: mechanism of tumoritropic accumulation of proteins and the antitumor agent smancs. Cancer Res. 1986 Dec;46(12 Pt 1):6387–92.

55. Nichols JW, Bae YH. EPR: Evidence and fallacy. J Control Release. 2014 Sep;190:451–64.

56. Mochida Y, Cabral H, Miura Y, Albertini F, Fukushima S, Osada K, et al. Bundled Assembly of Helical Nanostructures in Polymeric Micelles Loaded with Platinum Drugs Enhancing Therapeutic Efficiency against Pancreatic Tumor. ACS Nano. 2014 Jul 22;8(7):6724–38.

57. Aujard-Catot J, Nguyen M, Bijani C, Pratviel G, Bonduelle C. Cd 2+ coordination: an efficient structuring switch for polypeptide polymers. Polym Chem. 2018;9(30):4100–7.

58. Kostka L, Kotrchová L, Šubr V, Libánská A, Ferreira CA, Malátová I, et al. HPMA-based star polymer biomaterials with tuneable structure and biodegradability tailored for advanced drug delivery to solid tumours. Biomaterials. 2020 Mar 1;235:119728.

59. Etrych T, Šubr V, Laga R, Říhová B, Ulbrich K. Polymer conjugates of doxorubicin bound through an amide and hydrazone bond: Impact of the carrier structure onto synergistic action in the treatment of solid tumours. Eur J Pharm Sci. 2014 Jul 16;58(1):1–12.

60. Arroyo-Crespo JJ, Armiñán A, Charbonnier D, Deladriere C, Palomino-Schätzlein M, Lamas-Domingo R, et al. Characterization of triple-negative breast cancer preclinical models provides functional evidence of metastatic progression. Int J Cancer. 2019 Oct 15;145(8):2267–81.

61. Huang Z, Yu P, Tang J. Characterization of Triple-Negative Breast Cancer MDA-MB-231 Cell Spheroid Model. Onco Targets Ther. 2020 Jun;Volume 13:5395–405.

62. Jing W, Guo X, Wang G, Bi Y, Han L, Zhu Q, et al. Breast cancer cells promote CD169+ macrophage-associated immunosuppression through JAK2-mediated PD-L1 upregulation on macrophages. Int Immunopharmacol. 2020 Jan;78:106012.

63. Castro F, Pinto ML, Pereira CL, Serre K, Barbosa MA, Vermaelen K, et al. Chitosan/γ-PGA nanoparticles-based immunotherapy as adjuvant to radiotherapy in breast cancer. Biomaterials. 2020 Oct;257:120218.

64. P.S R, Alvi SB, Begum N, Veeresh B, Rengan AK. Self-Assembled Fluorosome–Polydopamine Complex for Efficient Tumor Targeting and Commingled Photodynamic/Photothermal Therapy of Triple-Negative Breast Cancer. Biomacromolecules. 2021 Sep 13;22(9):3926–40.

65. Roberts JG, Wisbey M, Leach KG, Baum M. Spleen size in patients with breast cancer. Br J Cancer. 1975 Feb;31(2):262–262.

66. D'Alterio C, Scala S, Sozzi G, Roz L, Bertolini G. Paradoxical effects of chemotherapy on tumor relapse and metastasis promotion. Semin Cancer Biol. 2020 Feb 1;60:351–61.

67. Ortiz-Otero N, Marshall JR, Lash B, King MR. Chemotherapy-induced release of circulating-tumor cells into the bloodstream in collective migration units with cancer-associated fibroblasts in metastatic cancer patients. BMC Cancer. 2020 Sep 11;20(1):1–13.

68. Karagiannis GS, Condeelis JS, Oktay MH. Chemotherapy-induced metastasis: Mechanisms and translational opportunities. Clin Exp Metastasis. 2018 Apr 1;35(4):269.

69. Atkinson S, Andreu Z, Vicent M. Polymer Therapeutics: Biomarkers and New Approaches for Personalized Cancer Treatment. J Pers Med. 2018 Jan 23;8(1):6.

70. Hadjidemetriou M, Kostarelos K. Evolution of the nanoparticle corona. Nat Nanotechnol. 2017 Apr 6;12(4):288–90.

71. Berrecoso G, Crecente-Campo J, Alonso MJ. Unveiling the pitfalls of the protein corona of polymeric drug nanocarriers. Drug Deliv Transl Res 2020 103. 2020 Mar 9;10(3):730–50.

72. Bansal A, Simon MC. Glutathione metabolism in cancer progression and treatment resistance. J Cell Biol. 2018;217(7):2291–8.

73. Lv H, Zhen C, Liu J, Yang P, Hu L, Shang P. Unraveling the Potential Role of Glutathione in Multiple Forms of Cell Death in Cancer Therapy. Oxid Med Cell Longev. 2019 Jun 10;2019:1–16.

74. Wu G, Fang Y-Z, Yang S, Lupton JR, Turner ND. Glutathione Metabolism and Its Implications for Health. J Nutr. 2004;134(3):489–92.

75. Estrela JM, Ortega A, Obrador E. Glutathione in Cancer Biology and Therapy. Crit Rev Clin Lab Sci. 2006 Jan 10;43(2):143–81.

76. Wei JR, Sun J, Yang X, Ji SF, Wei YH, Li ZB. Self-crosslinking assemblies with tunable nanostructures from photoresponsive polypeptoid-based block copolymers. Polym Chem. 2020;11(2):337–43.

77. Ryu J-H, Jiwpanich S, Chacko R, Bickerton S, Thayumanavan S. Surface-Functionalizable Polymer Nanogels with Facile Hydrophobic Guest Encapsulation Capabilities. J Am Chem Soc. 2010 Jun 23;132(24):8246–7.

78. Ryu J-H, Chacko RT, Jiwpanich S, Bickerton S, Babu RP, Thayumanavan S. Self-Cross-Linked Polymer Nanogels: A Versatile Nanoscopic Drug Delivery Platform. J Am Chem Soc. 2010 Dec 8;132(48):17227–35.

79. Choh S-Y, Cross D, Wang C. Facile Synthesis and Characterization of Disulfide-Cross-Linked Hyaluronic Acid Hydrogels for Protein Delivery and Cell Encapsulation. Biomacromolecules. 2011 Apr 11;12(4):1126–36.

80. Zhang Y, Heher P, Hilborn J, Redl H, Ossipov DA. Hyaluronic acid-fibrin interpenetrating double network hydrogel prepared in situ by orthogonal disulfide cross-linking reaction for biomedical applications. Acta Biomater. 2016 Jul 1;38:23–32.

81. Murphy RD, in het Panhuis M, Cryan S-A, Heise A. Disulphide crosslinked star block copolypeptide hydrogels: influence of block sequence order on hydrogel properties. Polym Chem. 2018;9(28):3908–16.

82. Chen W, Meng F, Cheng R, Deng C, Feijen J, Zhong Z. Facile construction of dual-bioresponsive biodegradable micelles with superior extracellular stability and activated intracellular drug release. J Control Release. 2015 Jul 28;210:125–33.

83. Jia Z, Wong L, Davis TP, Bulmus V. One-Pot Conversion of RAFT-Generated Multifunctional Block Copolymers of HPMA to Doxorubicin Conjugated Acid- and Reductant-Sensitive Crosslinked Micelles. Biomacromolecules. 2008 Nov 10;9(11):3106–13.

84. Mocny P, Klok H-A. Reversibly Cross-Linking Polymer Brushes Using Interchain Disulfide Bonds. Macromolecules. 2020 Jan 28;53(2):731–40.

85. Altinbasak I, Arslan M, Sanyal R, Sanyal A. Pyridyl disulfide-based thiol–disulfide exchange reaction: shaping the design of redox-responsive polymeric materials. Polym Chem. 2020 Dec 22;11(48):7603–24.

86. Sui B, Cheng C, Xu P. Pyridyl Disulfide Functionalized Polymers as Nanotherapeutic Platforms. Adv Ther. 2019 Sep 24;2(9):1900062.

87. Sun J, Liu Y, Chen Y, Zhao W, Zhai Q, Rathod S, et al. Doxorubicin delivered by a redox-responsive dasatinib-containing polymeric prodrug carrier for combination therapy. J Control Release. 2017 Jul;258:43–55.

88. Yoo HS, Park TG. Folate receptor targeted biodegradable polymeric doxorubicin micelles. J Control Release. 2004 Apr 28;96(2):273–83.

89. Steinhilber D, Witting M, Zhang X, Staegemann M, Paulus F, Friess W, et al. Surfactant free preparation of biodegradable dendritic polyglycerol nanogels by inverse nanoprecipitation for encapsulation and release of pharmaceutical biomacromolecules. J Control Release. 2013 Aug;169(3):289–95.

90. Tian X, Nyberg S, Sharp PS, Madsen J, Daneshpour N, Armes SP, et al. LRP-1-mediated intracellular antibody delivery to the Central Nervous System. Sci Rep. 2015 Dec 20;5(1):11990.

91. Rodriguez-Otormin F, Duro-Castano A, Conejos-Sánchez I, Vicent MJ. Envisioning the future of polymer therapeutics for brain disorders. WIREs Nanomedicine and Nanobiotechnology. 2019 Jan 14;11(1).

92. Ke W, Shao K, Huang R, Han L, Liu Y, Li J, et al. Gene delivery targeted to the brain using an Angiopep-conjugated polyethyleneglycol-modified polyamidoamine dendrimer. Biomaterials. 2009 Dec;30(36):6976–85.

93. Gao S, Tian H, Xing Z, Zhang D, Guo Y, Guo Z, et al. A non-viral suicide gene delivery system traversing the blood brain barrier for non-invasive glioma targeting treatment. J Control Release. 2016 Dec 10;243:357–69.

94. Tian X, Leite DM, Scarpa E, Nyberg S, Fullstone G, Forth J, et al. On the shuttling across the blood-brain barrier via tubule formation: Mechanism and cargo avidity bias. Sci Adv. 2020 Nov 27;6(48):eabc4397.

95.   Fullstone G, Nyberg S, Tian X, Battaglia G. From the Blood to the Central Nervous System. In: International Review of Neurobiology. 2016. p. 41–72.

96.   Guo Q, Zhu Q, Miao T, Tao J, Ju X, Sun Z, et al. LRP1-upregulated nanoparticles for efficiently conquering the blood-brain barrier and targetedly suppressing multifocal and infiltrative brain metastases. J Control Release. 2019 Jun 10;303:117–29.

97.   Wang L, Hao Y, Li H, Zhao Y, Meng D, Li D, et al. Co-delivery of doxorubicin and siRNA for glioma therapy by a brain targeting system: angiopep-2-modified poly(lactic-co-glycolic acid) nanoparticles. J Drug Target. 2015 Oct 21;23(9):832–46.

98.   Christie RJ, Fleming R, Bezabeh B, Woods R, Mao S, Harper J, et al. Stabilization of cysteine-linked antibody drug conjugates with N-aryl maleimides. J Control Release. 2015 Dec;220:660–70.

99.   Fontaine SD, Reid R, Robinson L, Ashley GW, Santi D V. Long-term stabilization of maleimide-thiol conjugates. Bioconjug Chem. 2015 Jan 21;26(1):145–52.

100.   Khan NU, Ni J, Ju X, Miao T, Chen H, Han L. Escape from abluminal LRP1-mediated clearance for boosted nanoparticle brain delivery and brain metastasis treatment. Acta Pharm Sin B. 2021 May 1;11(5):1341–54.

101.   Ché C, Yang G, Thiot C, Lacoste MC, Currie JC, Demeule M, et al. New angiopep-modified doxorubicin (ANG1007) and etoposide (ANG1009) chemotherapeutics with increased brain penetration. J Med Chem. 2010 Apr 8;53(7):2814–24.

102.   Zhu L, Yebra N, Retana D, Miarka L, Hernández-Encinas E, Blanco-Aparicio C, et al. A drug-screening platform based on organotypic cultures identifies vulnerabilities to prevent local relapse and treat established brain metastasis. bioRxiv. 2020 Oct 19;2020.10.16.329243.

103.   Priego N, Zhu L, Monteiro C, Mulders M, Wasilewski D, Bindeman W, et al. STAT3 labels a subpopulation of reactive astrocytes required for brain metastasis article. Nat Med. 2018 Jul 1;24(7):1024–35.

104.   Dong H, Zou M, Bhatia A, Jayaprakash P, Hofman F, Ying Q, et al. Breast Cancer MDA-MB-231 Cells Use Secreted Heat Shock Protein-90alpha (Hsp90α) to Survive a Hostile Hypoxic Environment. Sci Rep. 2016 Feb 5;6(1):20605.

105.   Soffietti R, Abacioglu U, Baumert B, Combs SE, Kinhult S, Kros JM, et al. Diagnosis and treatment of brain metastases from solid tumors: guidelines from the European Association of Neuro-Oncology (EANO). Neuro Oncol. 2017 Feb 1;19(2):162–74.

106.   Bailleux C, Eberst L, Bachelot T. Treatment strategies for breast cancer brain metastases. Br J Cancer. 2021 Jan 5;124(1):142–55.

107.   Li J, Cai P, Shalviri A, Henderson JT, He C, Foltz WD, et al. A multifunctional polymeric nanotheranostic system delivers doxorubicin and imaging agents across the blood-brain barrier targeting brain metastases of breast cancer. ACS Nano. 2014 Oct 28;8(10):9925–40.

108.   Zhao H, Jin G, Cui K, Ren D, Liu T, Chen P, et al. Novel Modeling of Cancer Cell Signaling Pathways Enables Systematic Drug Repositioning for Distinct Breast Cancer Metastases. Cancer Res. 2013 Oct 15;73(20):6149–63.

FINAL CONCLUSIONS

The work carried out during the development of this thesis provides evidence for the successful development of rationally-designed polypeptide-based therapeutics for brain metastases and associated solid primary tumor treatment.

Herein, we highlight the main conclusions resulting from this work:

1. Star-shaped poly-L-glutamic acid (St-PGA) represents a versatile polypeptidic carrier for the conjugation of doxorubicin (Dox) and dasatinib (Das) at different ratios using varying linking chemistries without inducing significant alterations to critical physico-chemical characteristics (i.e., size, aggregation behavior, zeta potential, and secondary structure). These features allowed the synthesis of a family of combination conjugates with Dox and Das conjugated via pH-labile linkers to support the controlled release of the drugs under acidic conditions (the tumor microenvironment and lysosomes).

2. Das linking chemistry significantly influences Das and Dox release profile from combination conjugates in pH 7.4 and 5.0 buffers, switching from rapid Dox release/sustained Das release to burst Dox release/low Das release. Meanwhile, drug loading exhibited an insignificant effect on the drug release profile but, instead, defined the released drug ratio, which eventually determined the biological output of the conjugates.

3. St-PGA-based single-drug and combination conjugates displayed robust cytotoxic activities in human MDA-MB-231-Luc TNBC cells defined by the drug release profile and the drug loading/ratio in the case of combination conjugates. A combination of drug release and loading that allows for excess Das release over Dox supports the enhanced cytotoxic activity of conjugates.

4. The safety profiles of our family of St-PGA-based conjugates suggested their suitability for intravenous administration except for St-PGA-hyd-Dox_1-Val-Das_1, which caused significant animal weight loss and reduced

survival rates in a spontaneously metastatic MDA-MB-231-Luc TNBC mouse model. St-PGA-hyd-Dox$_1$-Das$_{10}$ displayed optimal anti-tumor activity; however, no combination conjugates significantly improved the anti-tumor or anti-metastatic activity of the free drugs administered in combination at the same dose. Overall, the advantage of St-PGA-based combination conjugates relies on the improved safety profile.

5. Asymmetric flow field-flow fractionation (AF4) supported the development of a novel and simple method for the qualitative study of the polypeptide-drug conjugate-associated protein corona. AF4 can characterize protein-conjugate interactions in polypeptide-drug conjugates of sizes comparable to main plasma/serum proteins (~6 nm diameter). This approach supplied additional data explaining the high toxicity of St-PGA-hyd-Dox$_1$-Val-Das$_1$ observed *in vivo*.

6. The self- and co-assembly of St-PGA molecules in water provided a basis for the development of a bottom-up strategy to synthesize redox-responsive combination conjugates by co-assembly of single-drug conjugates employing pyridyl dithiol cysteamine (PD) to introduce thiol groups in St-PGA. The physico-chemical characterization of St-PGA building blocks for this strategy demonstrated that the conjugation of hydrophobic moieties significantly influenced St-PGA behavior in aqueous media. The conjugation of hydrophobic moieties altered the self- and co-assembly behavior of St-PGA in water, with the extent change depending on the moiety and the linking moiety used for conjugation. We currently lack a complete understanding of how hydrophobic interactions interact with glutamic acid ionic interactions, which alters the extraordinary behavior that drives St-PGA self- and co-assembly.

7. Unfortunately, the synthetic protocols examined to stabilize St-PGA-PD-based assemblies by redox-responsive disulfide bonds failed to yield stable nanosystems in high ionic strength media. The lack of stabilization

498

does not respond to a lack of conjugate aggregation or a low conjugate concentration in the reaction. Therefore, we hypothesize that the lack of stability derives from the presence of reduced (free) thiol groups in the final compound (triggering disulfide-thiol exchange reactions that destabilize the structure), the poor exposure of thiol groups of St-PGA-PD(5)-derived molecules (prompting the formation of intramolecular disulfide bonds instead of intermolecular stabilizing bonds), or a low number of intermolecular disulfide bonds in the final product.

8. The use of maleimide-thiol chemistry supported the development of an efficient and reproducible protocol for Angiopep-2 conjugation to St-PGA conjugates in aqueous media with mild conditions. Our protocol limited drug loss due to pH-labile linker cleavage during the reaction, thereby suggesting the applicability of this strategy for the conjugation of a variety of thiol-modified peptides to maleimide-modified polymer-drug conjugates. Angiopep-2 conjugation to St-PGA conjugates failed to significantly alter the main physico-chemical characteristics of the carrier (i.e., secondary structure in aqueous solutions, concentration-dependent aggregation in water, size in high ionic strength media corresponding to the St-PGA unimer, negative charge, and overall drug release profile).

9. The St-PGA-Angiopep-2 combination conjugate effectively reduced extracranial metastatic spread and the disease progression-associated loss in animal weight; however, even given encouraging signs of conjugate activity against brain metastasis, therapeutic output in this regard remains insufficient. These preliminary results suggest that a sub-optimal dose caused the lack of significant activity within the brain. As our combination conjugate demonstrated an adequate safety profile, planned further experiments with higher conjugated drug doses to increase drug bioavailability in the brain may support improved therapeutic outcomes.

ANNEX I. SUPPLEMENTARY INFORMATION

CHAPTER 2.
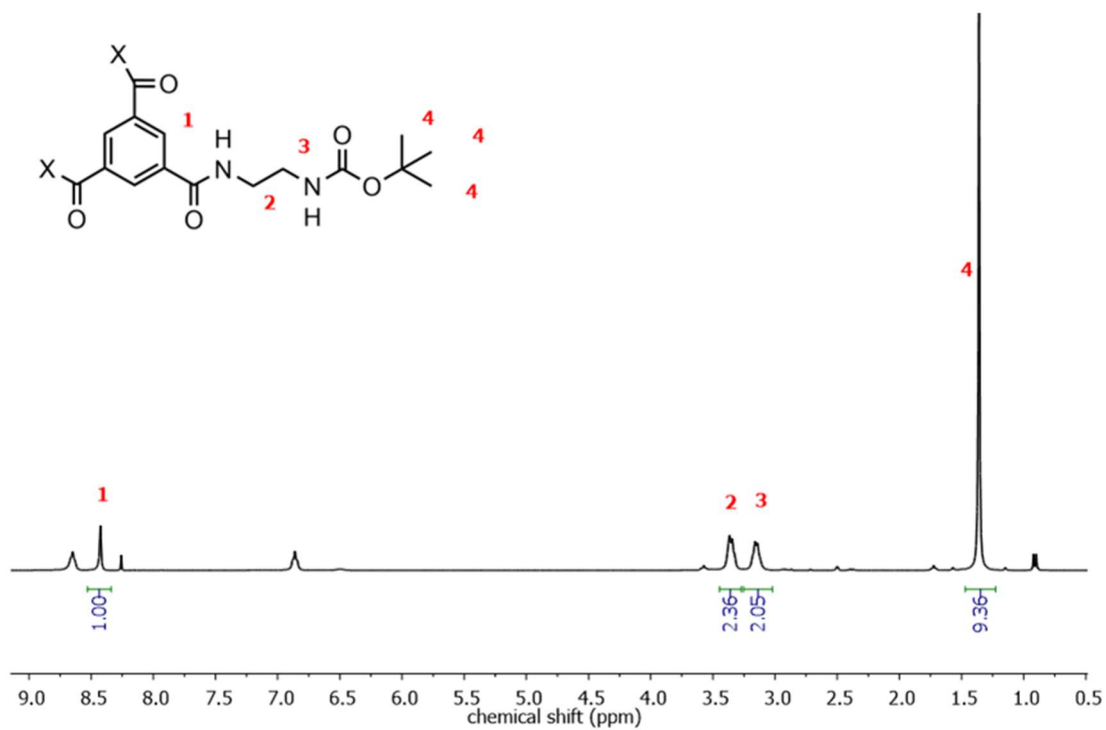
Supplementary Figure 2.1. ^{1}H-NMR spectrum (DMSO-d6) of 1,3,5-tri-tert-butyl ((benzenetricarbonyltris (azanediyl)) tris(ethane-2,1-diyl)) tricarbamate.
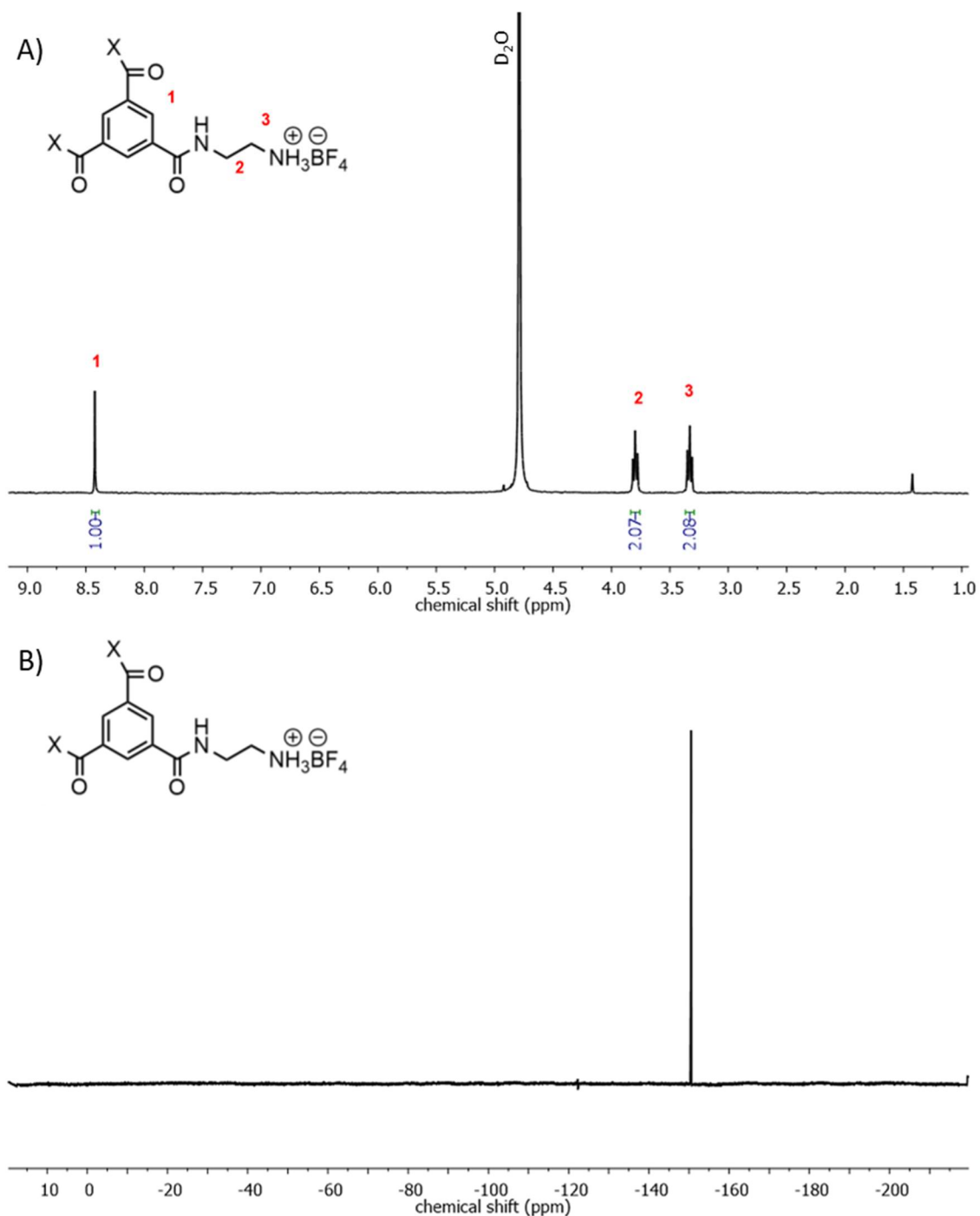
Supplementary Figure 2.2. Identity and purity of 1,3,5-(benzenetricarbonyltris(azanediyl))-triethanammonium BF₄ salt initiator. (**A**) ¹H-NMR (D₂O) spectrum confirms the complete elimination of the Boc protecting group and the purity of the three-armed initiator. (**B**) ¹⁹F-NMR (D₂O) spectrum confirms the obtention of the BF₄ salt form of the initiator.
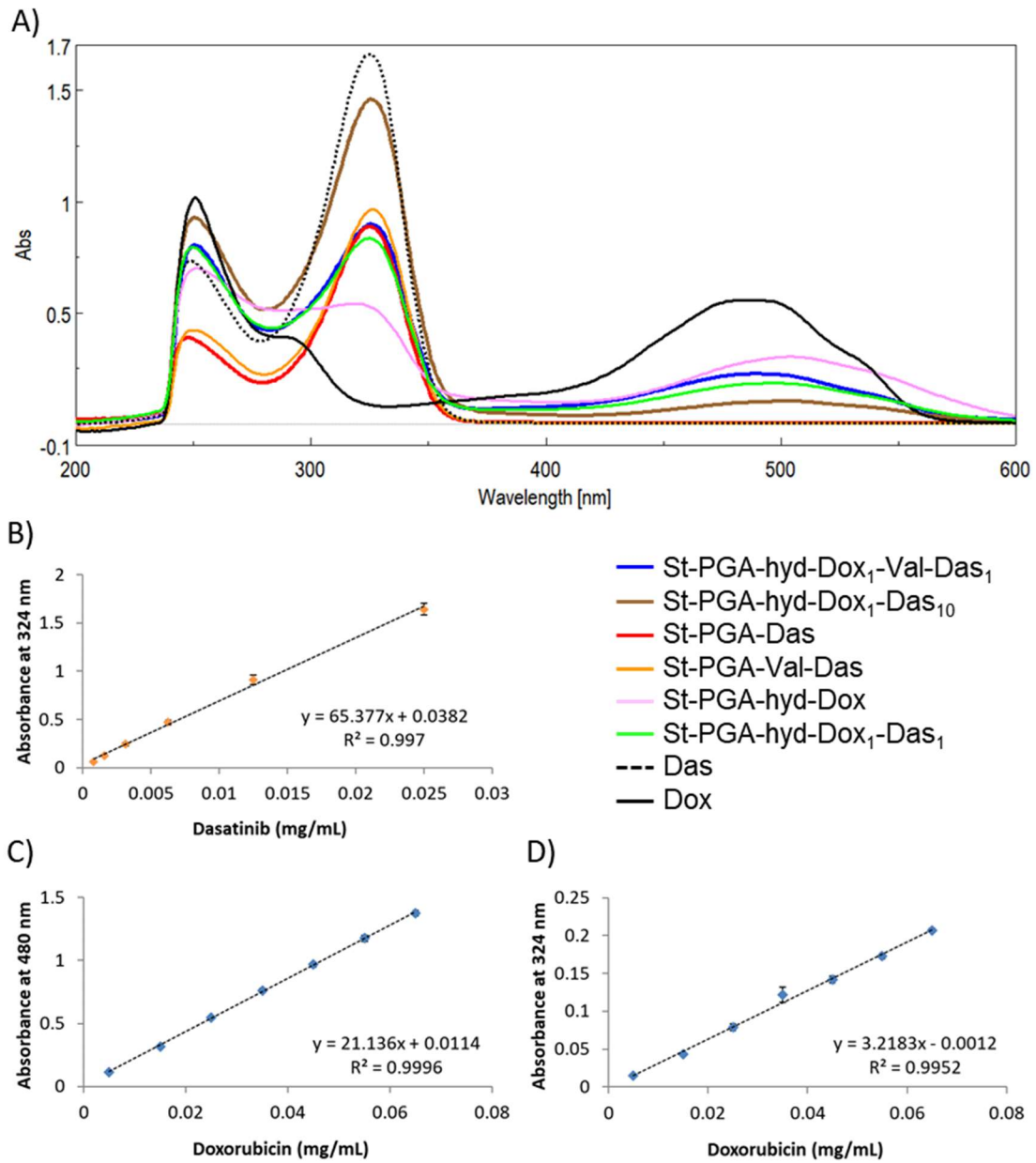
Supplementary Figure 2.3. Drug loading determination by UV-VIS spectroscopy. (**A**) Absorbance spectra of St-PGA-drug conjugates and free drugs in DMSO:water (1:1 v/v). (**B**) Calibration curve of Das in DMSO:water at 324 nm. (**C**) Calibration curve of Dox in DMSO:water (1:1 v/v) at 480 nm. (**D**) Calibration curve of Dox in DMSO:water (1:1 v/v) at 324 nm.
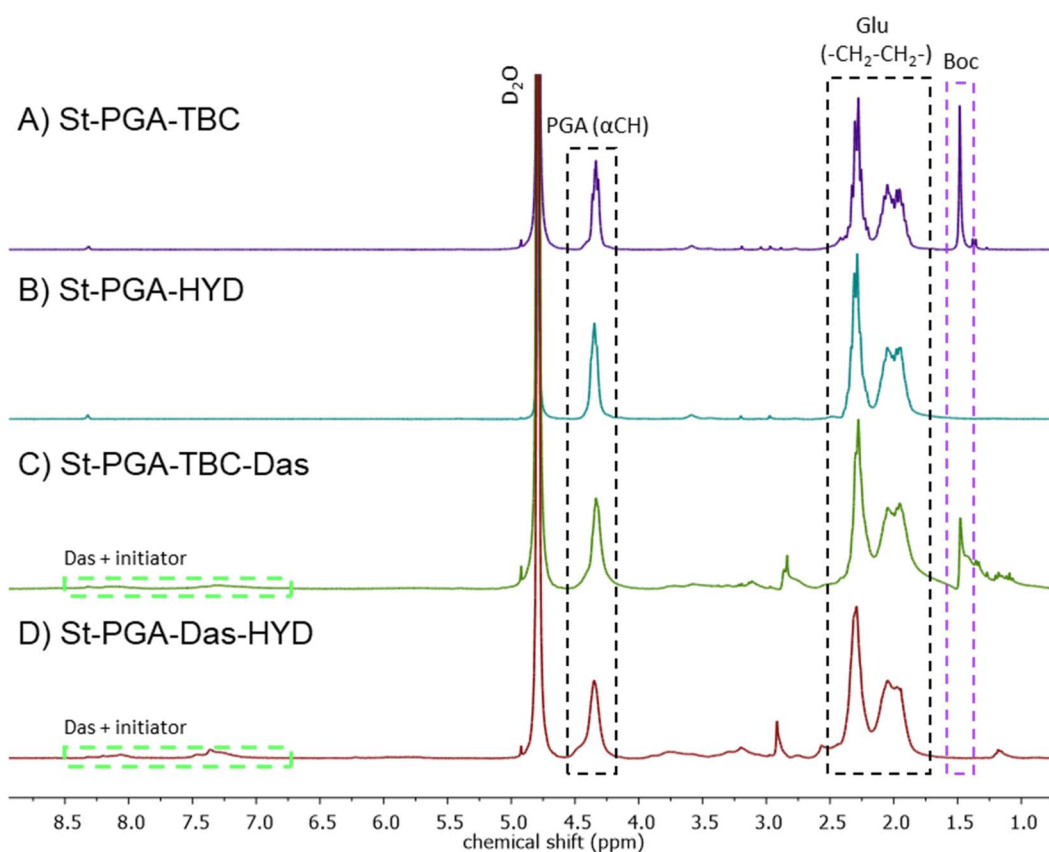
Supplementary Figure 2.4. ^{1}H-NMR spectra of St-PGA-HYD, St-PGA-Das-HYD, and their precursors. St-PGA-TBC was the precursor of St-PGA-HYD, St-PGA-TBC-Das, and St-PGA-Das-HYD. St-PGA-TBC-Das was the precursor of St-PGA-Das-HYD. (**A**) ^{1}H-NMR (D$_2$O) spectrum of St-PGA-TBC confirms TBC's conjugation (Boc – nine protons). (**B**) ^{1}H-NMR (D$_2$O) spectrum of St-PGA-HYD confirms the complete removal of the Boc protecting group. (**C**) ^{1}H-NMR (D$_2$O) spectrum of St-PGA-TBC-Das confirms Das conjugation (Das, five protons). (**D**) ^{1}H-NMR (D$_2$O) spectrum of St-PGA-Das-HYD confirms the complete removal of Boc protecting group while keeping Das (Das – five protons).
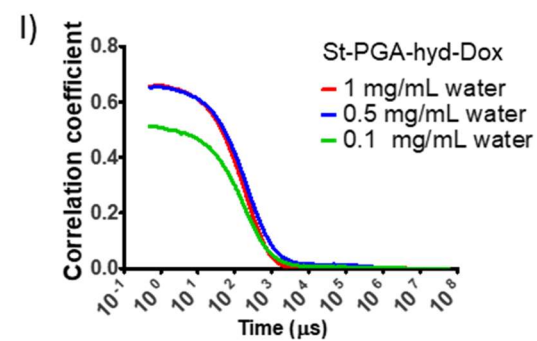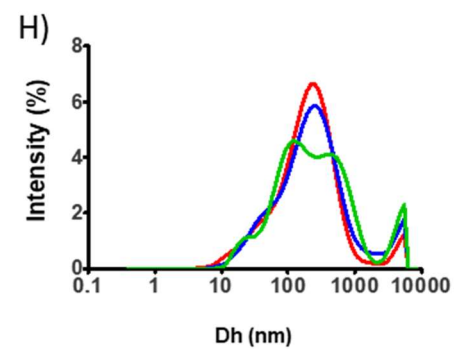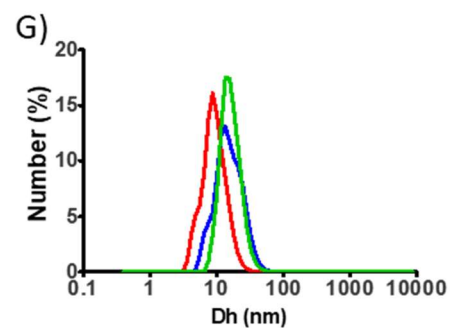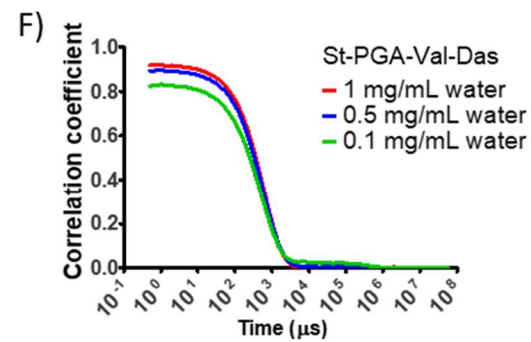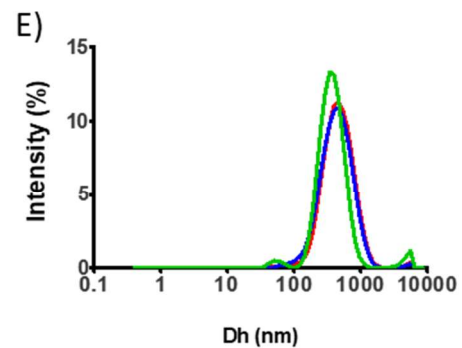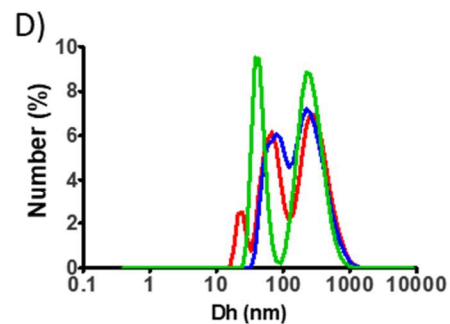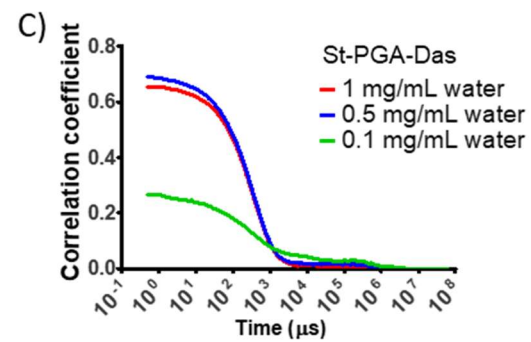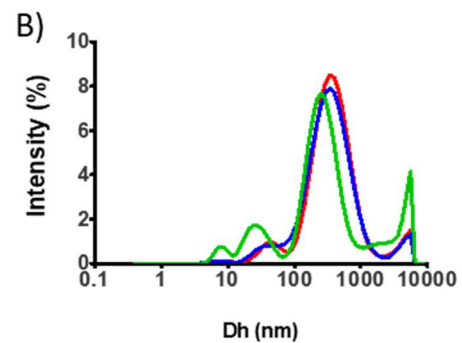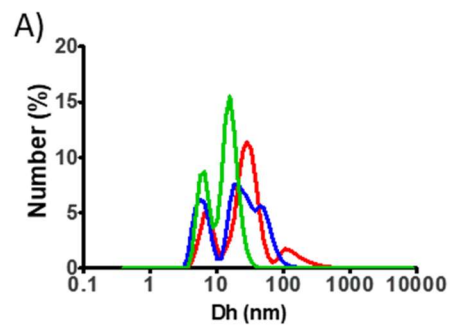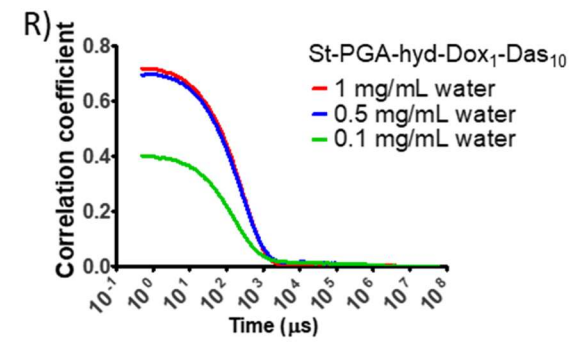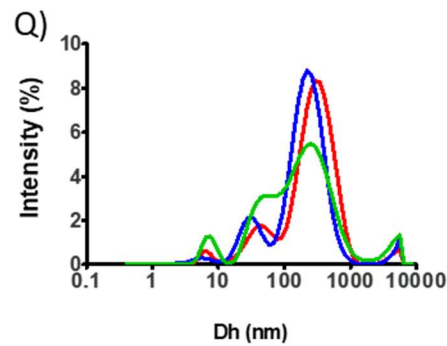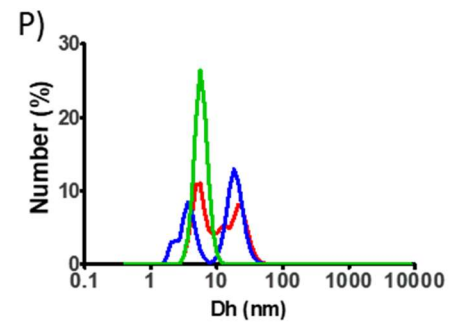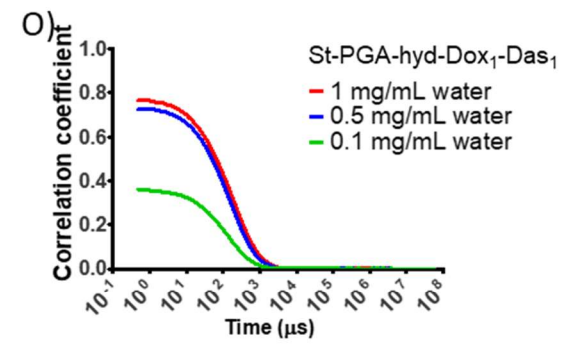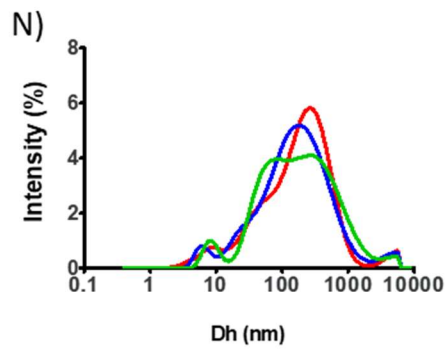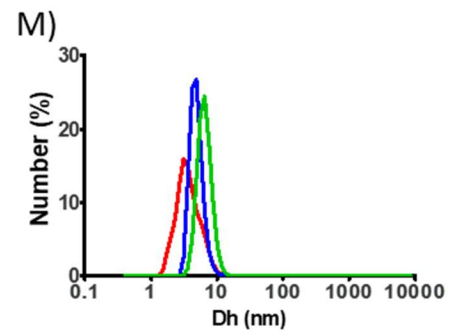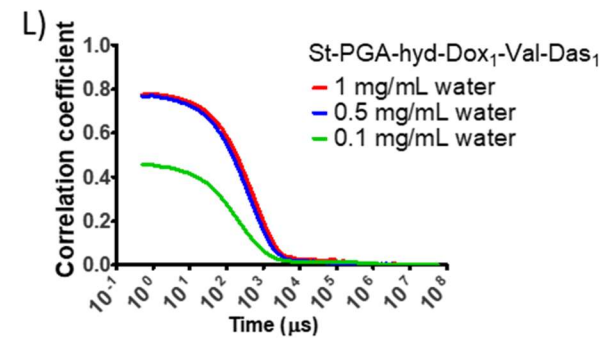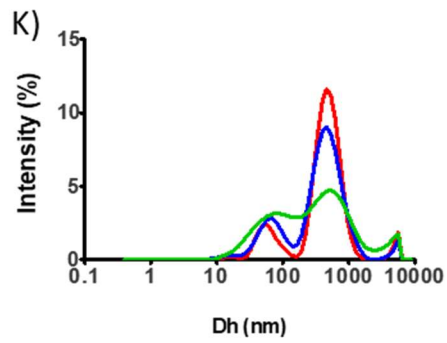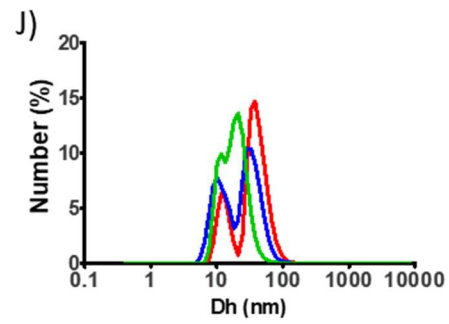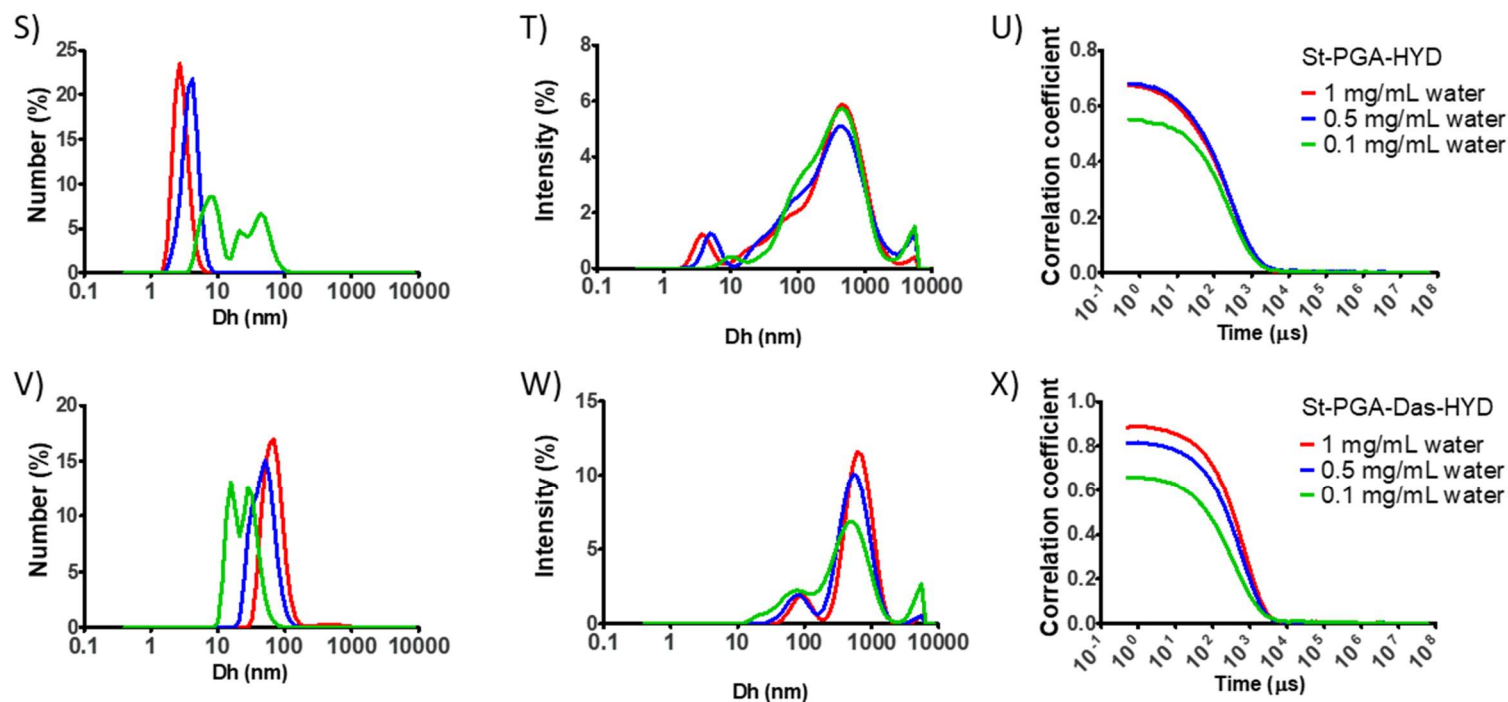
Supplementary Figure 2.5. DLS size distribution of (**A-C**) St-PGA-Das, (**D-F**) St-PGA-Val-Das, (**G-I**) St-PGA-hyd-Dox, (**J-L**) St-PGA-hyd-Dox$_1$-Val-Das$_1$, (**M-O**) St-PGA-hyd-Dox$_1$-Das$_1$, (**P-R**) St-PGA-hyd-Dox$_1$-Das$_{10}$, (**S-U**) St-PGA-HYD, and (**V-X**) St-PGA-Das-HYD in MilliQ water represented as hydrodynamic diameter by number and intensity. The respective correlation functions are displayed. Data obtained from the average result of at least four measurements.
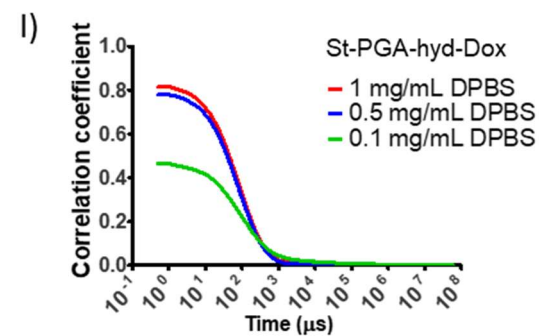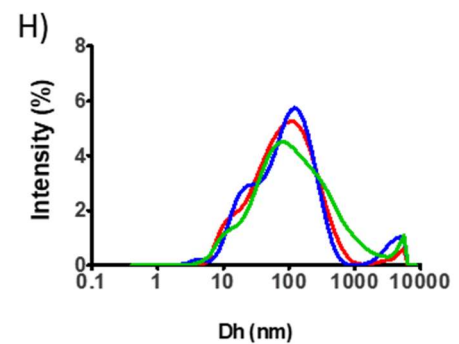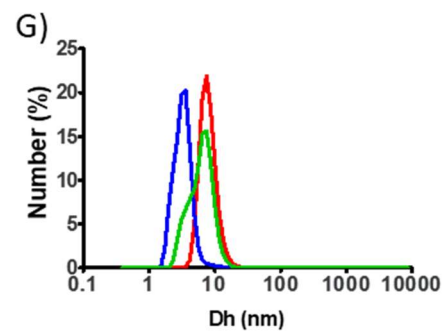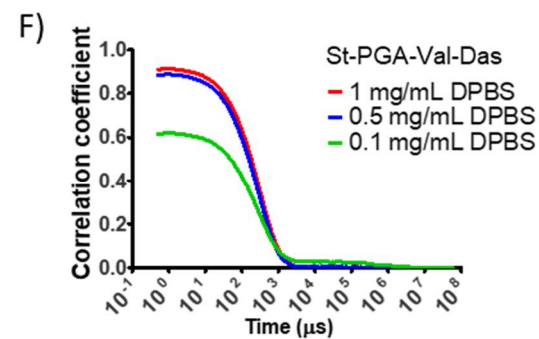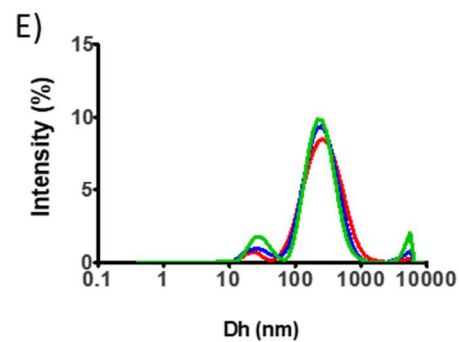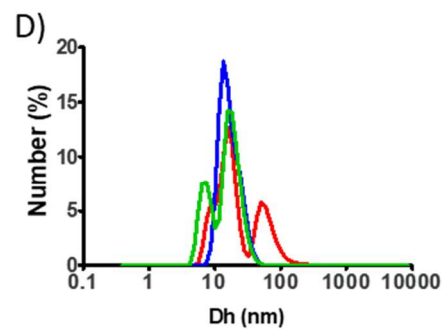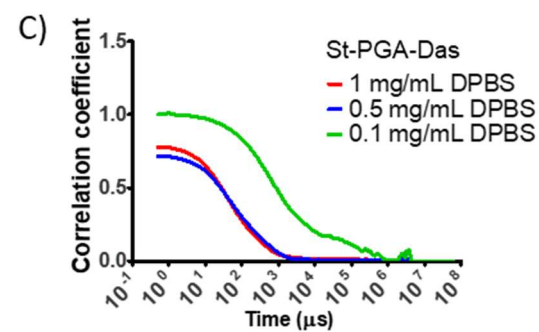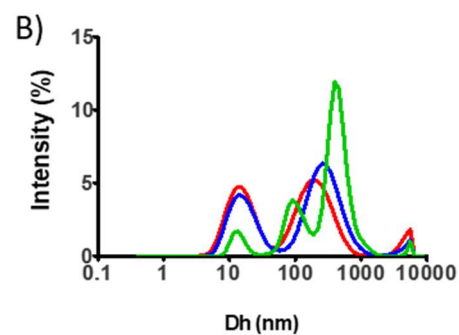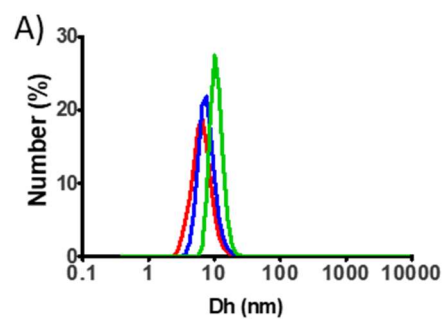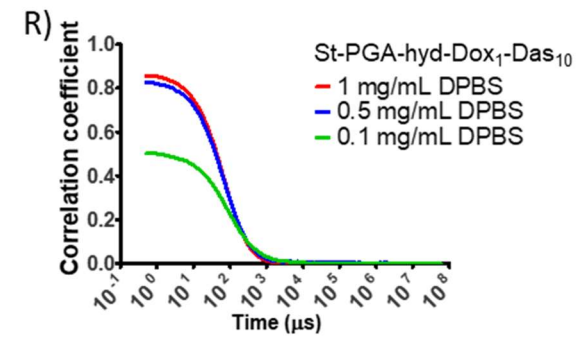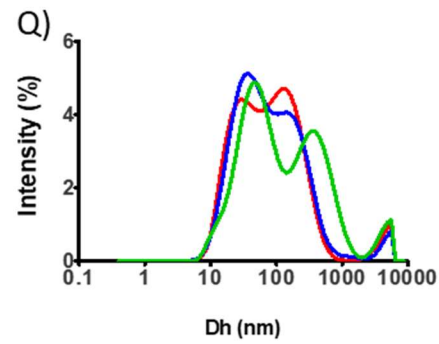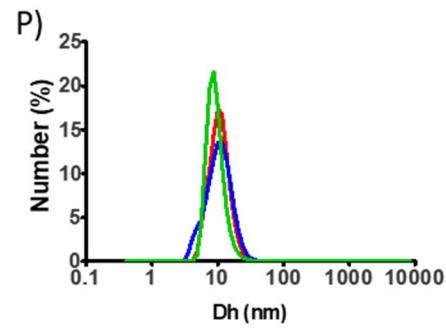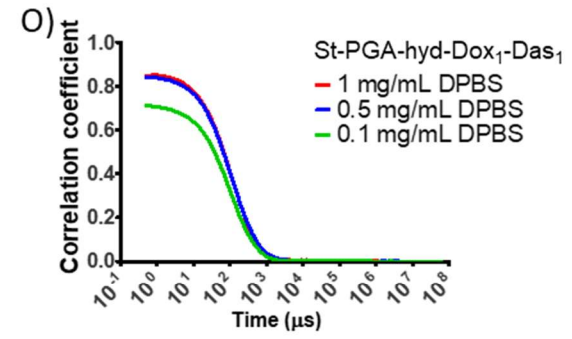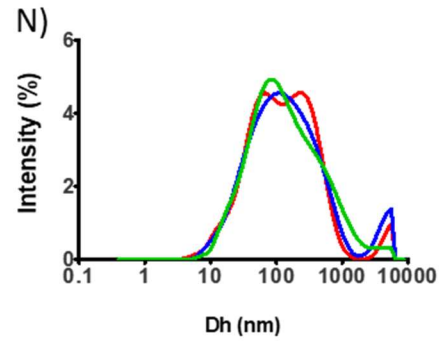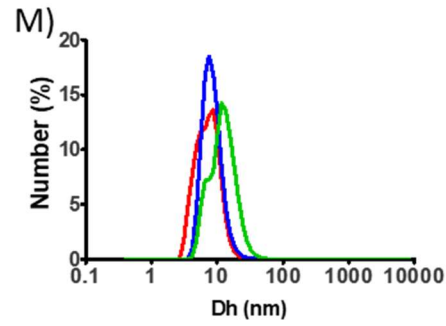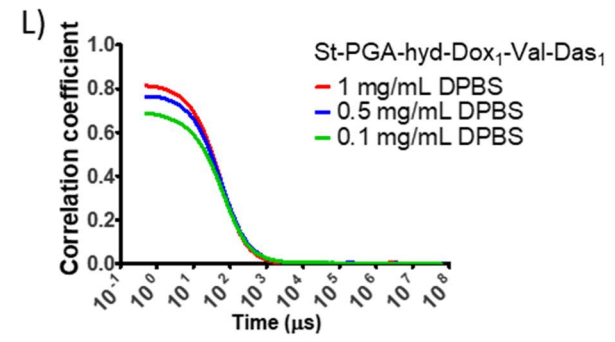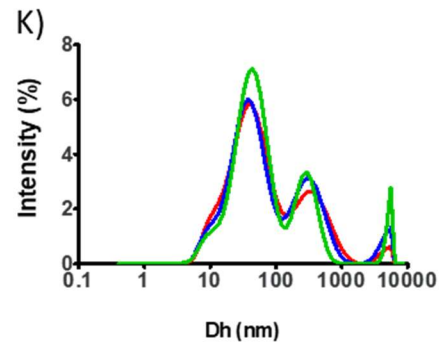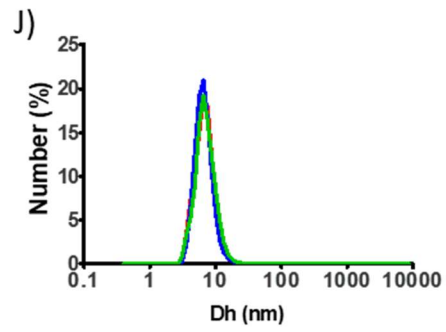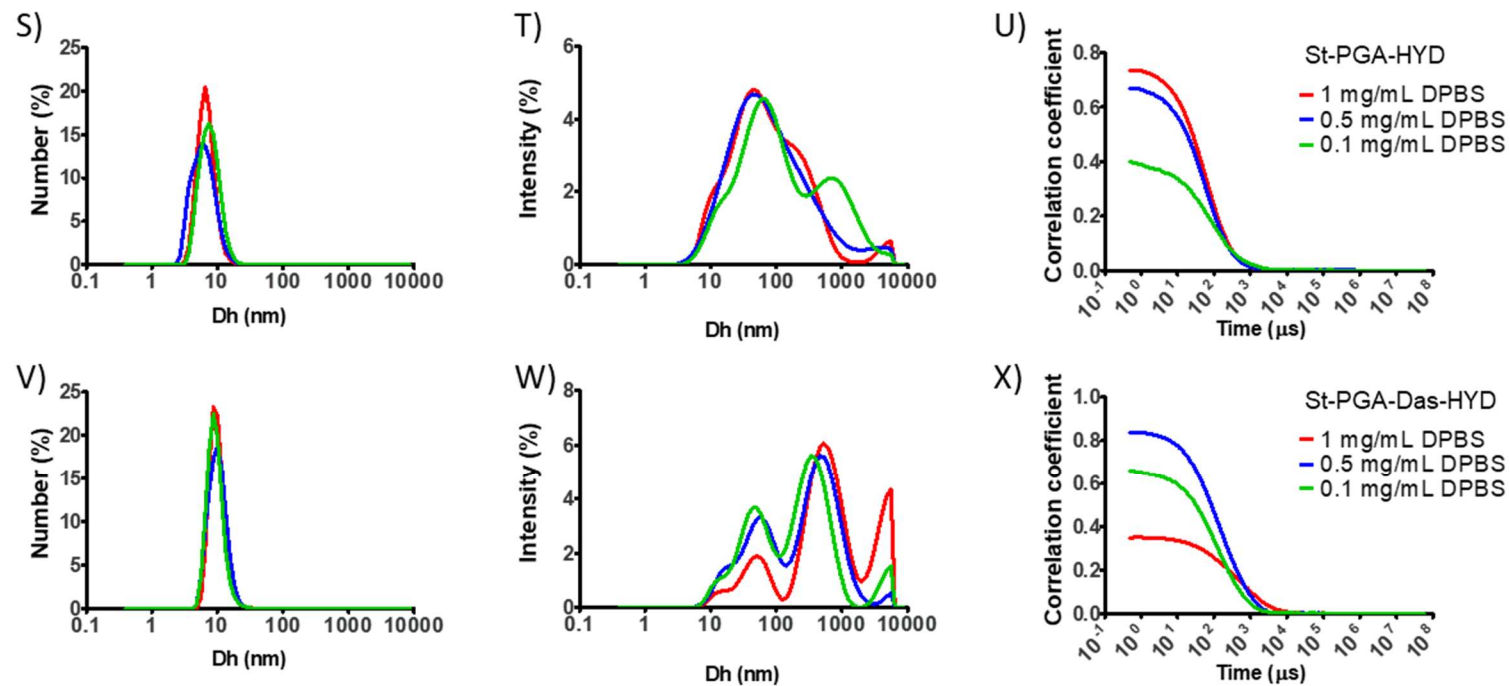
Supplementary Figure 2.6. DLS size distribution of (**A-C**) St-PGA-Das, (**D-F**) St-PGA-Val-Das, (**G-I**) St-PGA-hyd-Dox, (**J-L**) St-PGA-hyd-Dox$_1$-Val-Das$_1$, (**M-O**) St-PGA-hyd-Dox$_1$-Das$_1$, (**P-R**) St-PGA-hyd-Dox$_1$-Das$_{10}$, (**S-U**) St-PGA-HYD, and (**V-X**) St-PGA-Das-HYD in DPBS obtained represented as hydrodynamic diameter by number and intensity. Respective correlation functions are displayed. Data from the average result of at least four measurements.
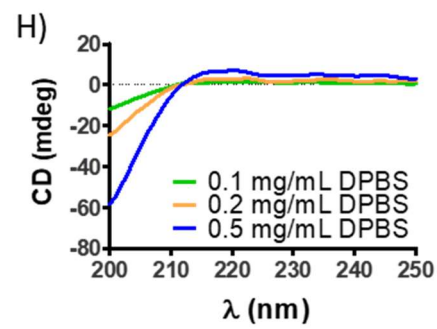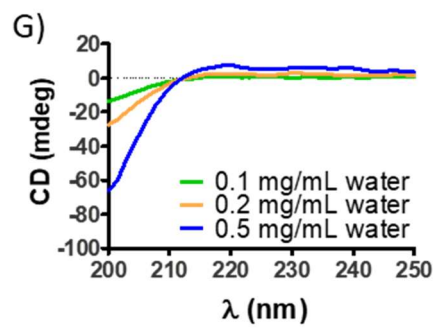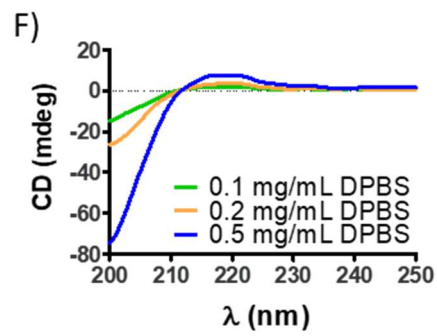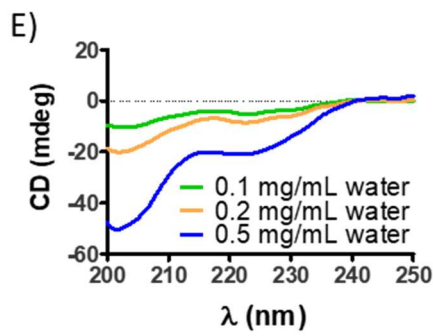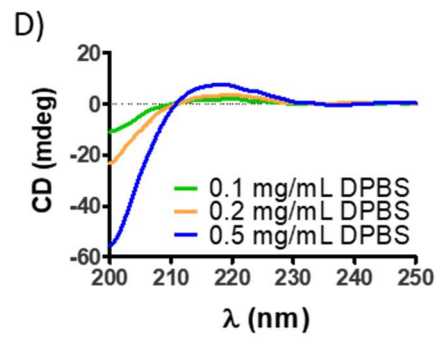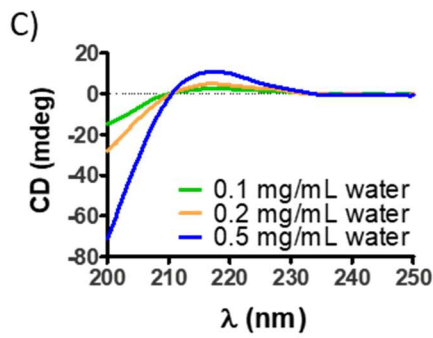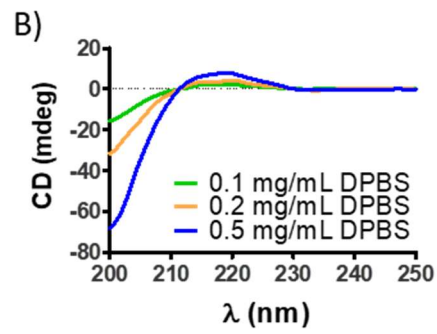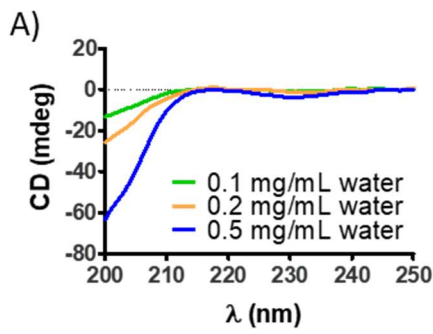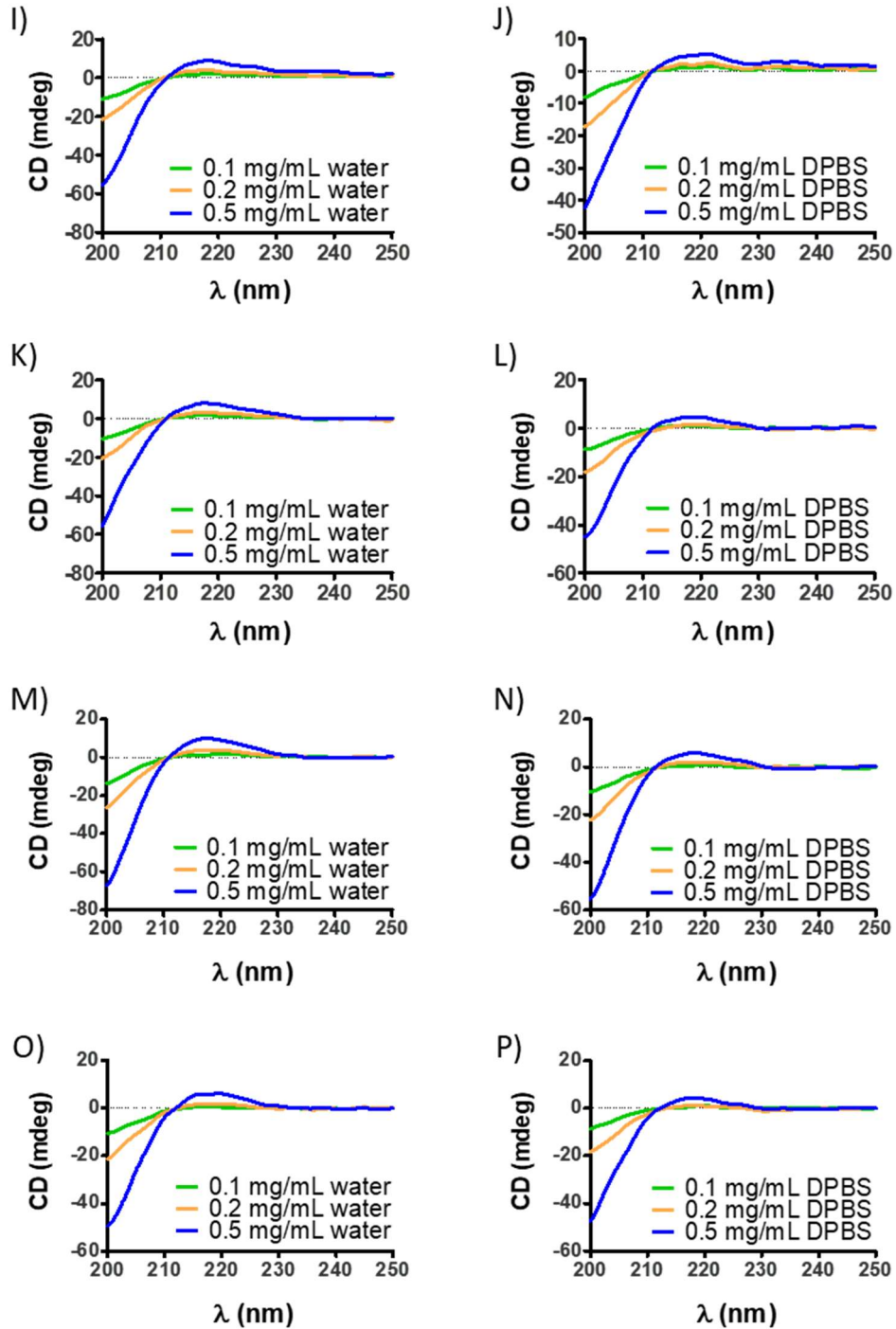
Supplementary Figure 2.7. CD spectra of (**A-B**) St-PGA-Das, (**C-D**) St-PGA-Val-Das, (**E-F**) St-PGA-hyd-Dox, (**G-H**) St-PGA-hyd-Dox_1-Val-Das_1, (**I-J**) St-PGA-hyd-Dox_1-Das_1, (**K-L**) St-PGA-hyd-Dox_1-Das_{10}, (**M-N**) St-PGA-HYD, and (**O-P**) St-PGA-Das-HYD in DPBS and MilliQ water at 0.1, 0.2, and 0.5 mg/mL. The results with three accumulated measurements are displayed.
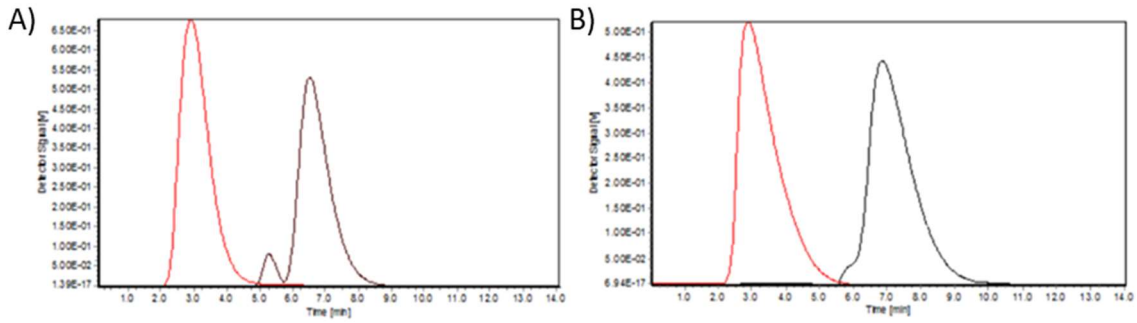
Supplementary Figure 2.8. AF4 recovery study of St-PGA in NaCl 0.9 w/v for (**A**) RC membrane and (**B**) PES membrane. The elution of St-PGA was monitored by RI. The graph shows the elugram of the FIA in red and the Focus FIA in black.
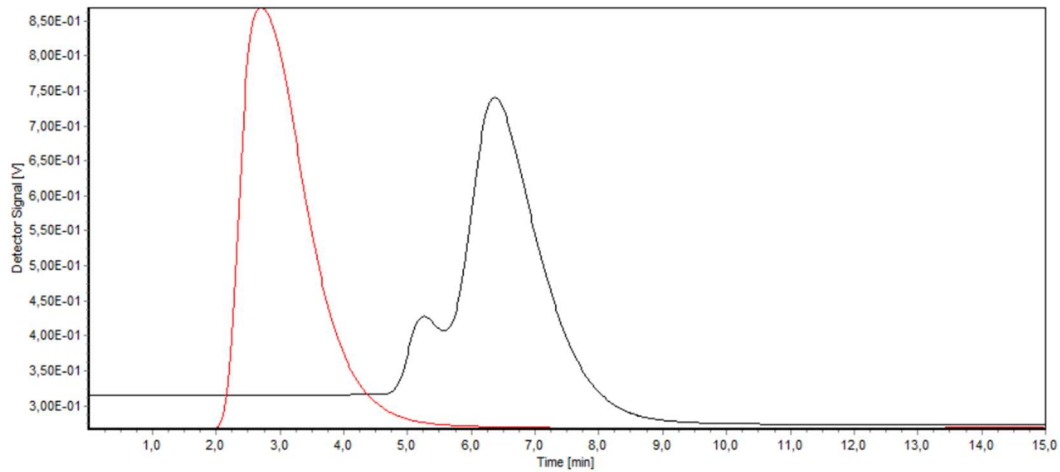
Supplementary Figure 2.9. AF4 recovery study of St-PGA in DPBS for the PES membrane. The elution of St-PGA was monitored by RI. The graph shows the elugram of the FIA in red and the Focus FIA in black.
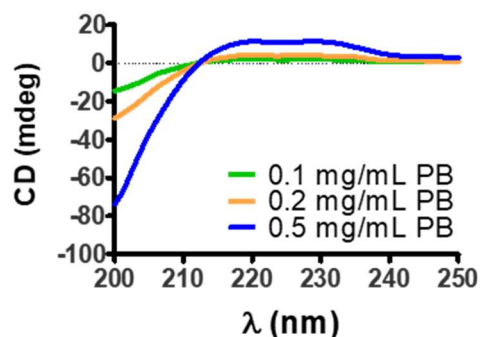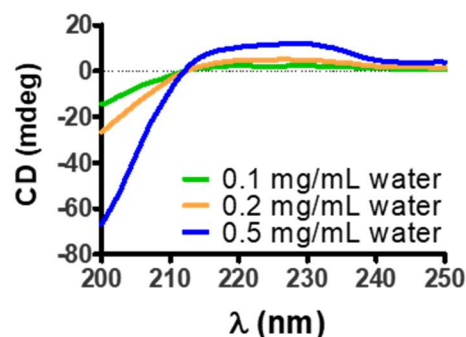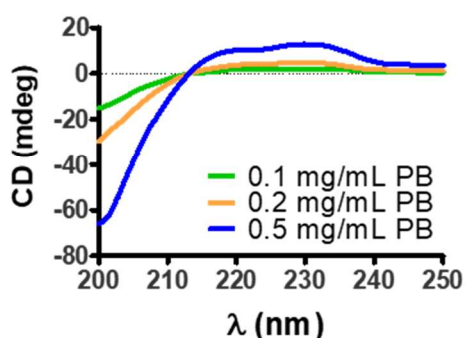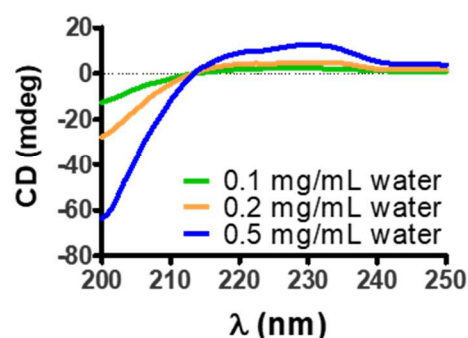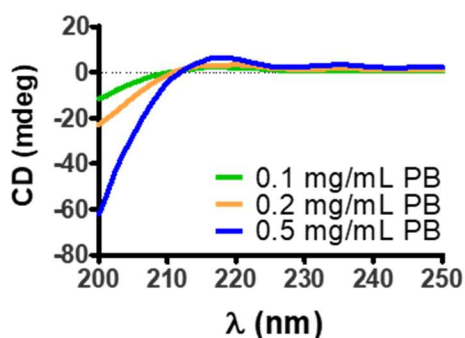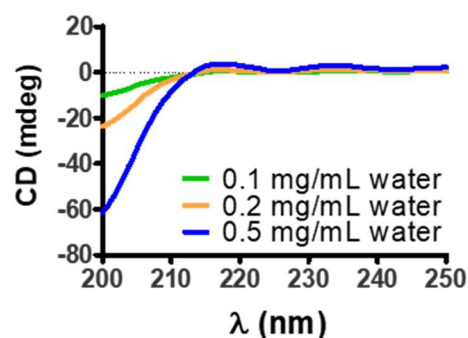
Supplementary Figure 3.1. CD spectra of Dox conjugates at 0.1 (green), 0.2 (orange), and 0.5 (blue) mg/mL conjugate. (**A** and **B**) St-PGA-PD(5)-Dox(5) in (**A**) 10 mM PB and (**B**) MilliQ water. (**C** and **D**) St-PGA-PD(10)-Dox(5) in (**C**) 10 mM PB and (**D**) MilliQ water. (**E** and **F**) St-PGA-PD(5)-hyd-Dox(5) in (**E**) 10 mM PB and (**F**) MilliQ water. Average results with three accumulated measurements displayed.

$y = 75.591x - 0.0263$
$R^2 = 0.9991$
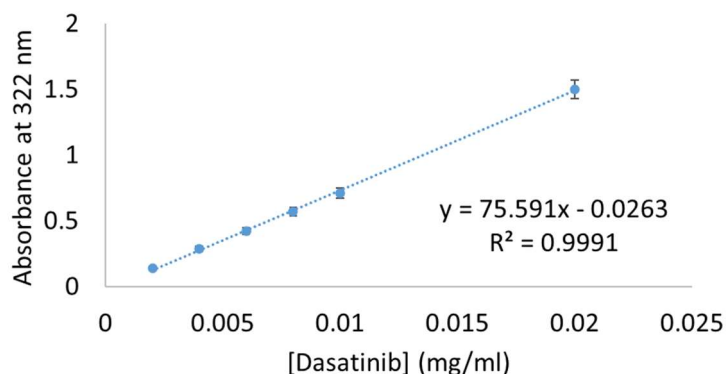
Supplementary Figure 3.2. UV-VIS absorbance Das calibration curve performed in methanol. Data expressed as average absorbance at 322 nm ± SD versus Das concentration obtained from three samples per concentration.
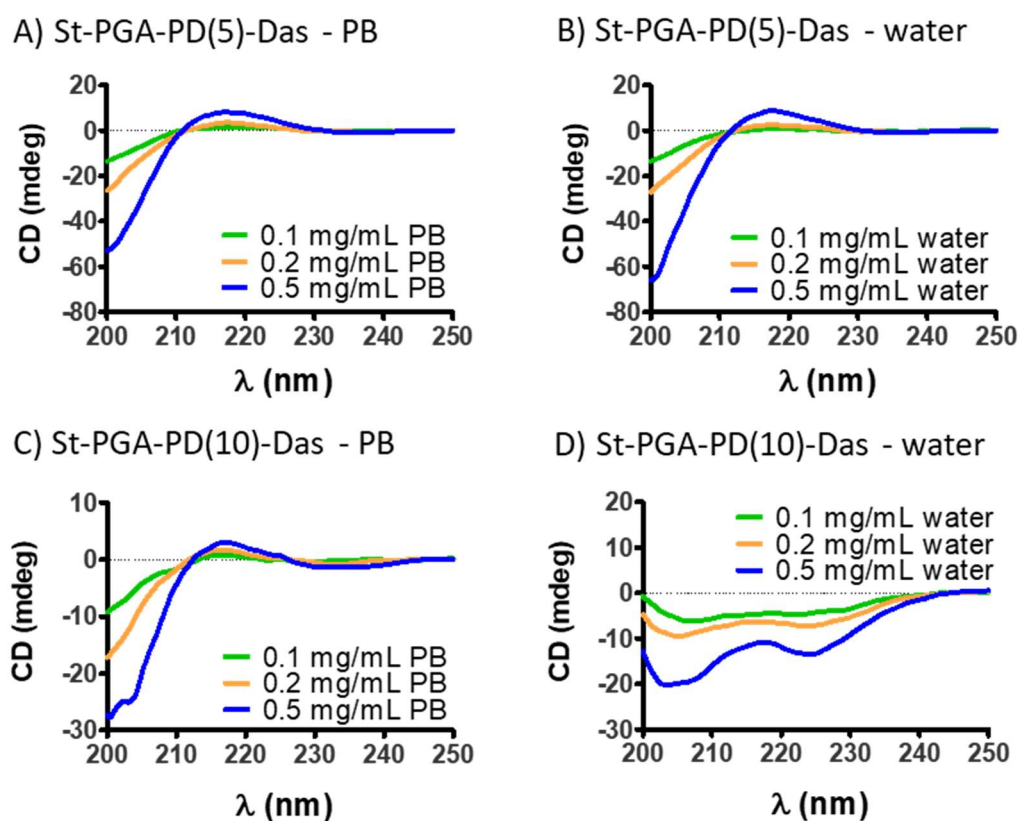
Supplementary Figure 3.3. CD spectra of Das conjugates at 0.1 (green), 0.2 (orange), and 0.5 (blue) mg/mL of polymer. (**A** and **B**) St-PGA-PD(5)-Das(5) in (**A**) MilliQ water and (**B**) PB 10 mM. (**C** and **D**) St-PGA-PD(10)-Das(5) in (**C**) MilliQ water and (**D**) PB 10 mM. Average results with three accumulated measurements displayed.

CHAPTER 4.
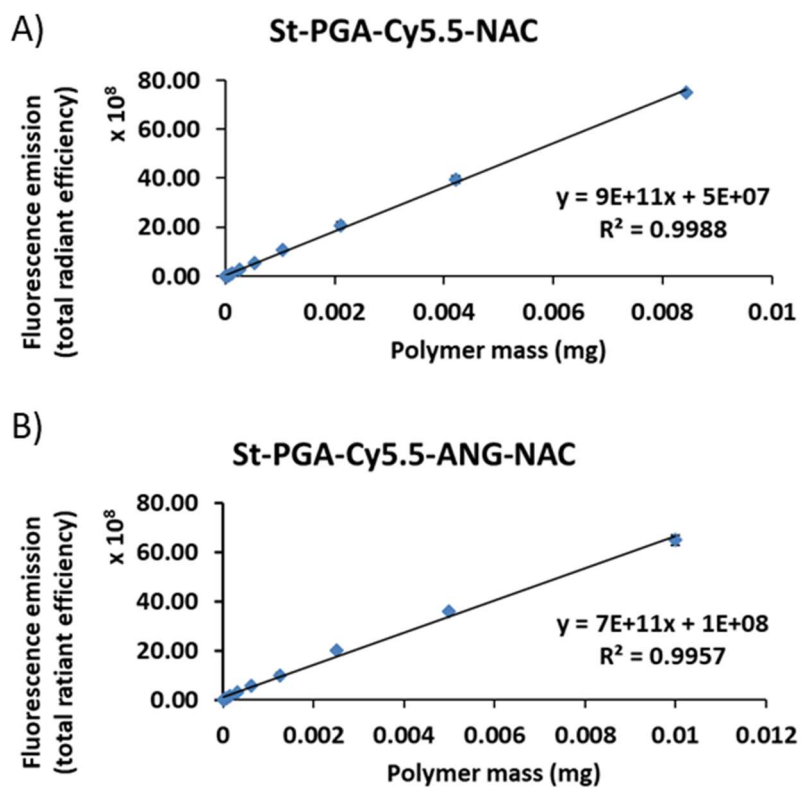
Supplementary Figure 4.1. Calibration curves for conjugate quantification *ex vivo*. (A) St-PGA-Cy5.5-NAC. (B) St-PGA-Cy5.5-ANG-NAC. Data represented as total radiant efficiency versus polymer mass (n=2, mean ± SD).
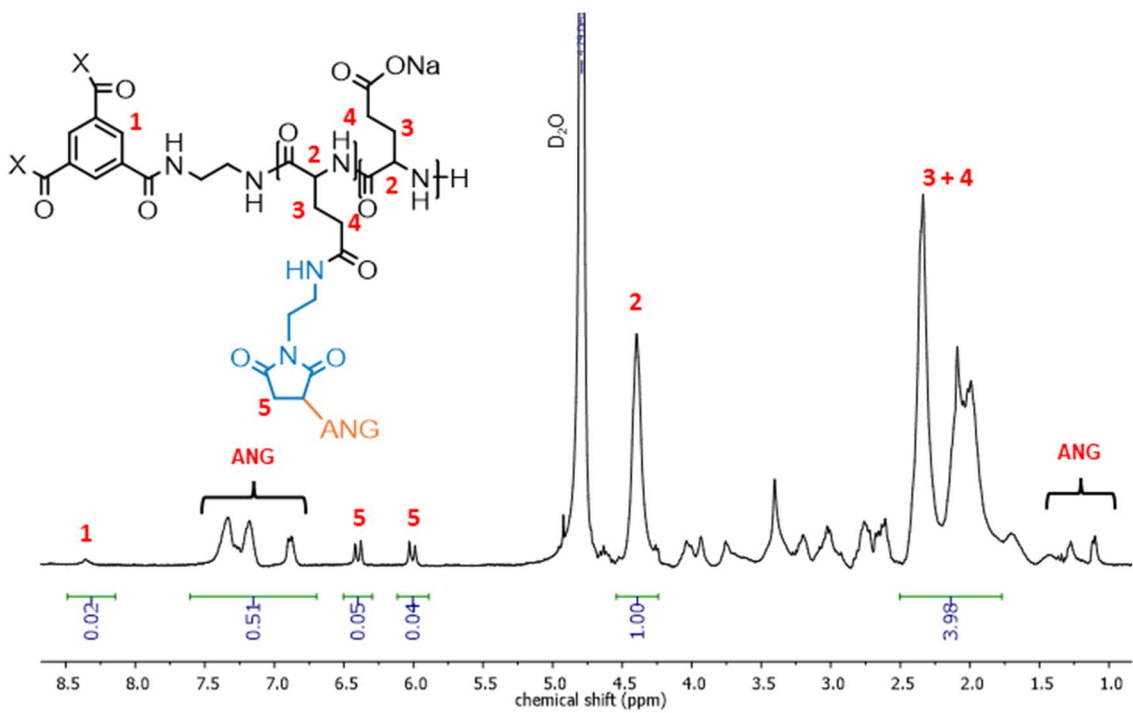
Supplementary Figure 4.2. ¹H-NMR spectrum of St-PGA-ANG shows signals of phenylalanine and tyrosine protons of the ANG peptide (labeled as ANG at 7.55 – 6.70 ppm).

ANNEX II. THESIS PROJECT, OBJECTIVES, MAIN METHODOLOGY, RESULTS, AND CONCLUSIONS IN SPANISH

1. Introducción y Marco Temático de la Tesis

El cáncer de mama es el cáncer más frecuentemente diagnosticado en todo el mundo (1) y la segunda causa más común de metástasis cerebrales (después del cáncer de pulmón (2–4)). Representando aproximadamente el 15% de todos los tumores de mama (5,6), el cáncer de mama triple negativo (CMTN) es el subtipo más agresivo. En general, el CMTN tiene el peor pronóstico (7) y la tasa más alta de recurrencia temprana y metástasis (6,8), siendo los pulmones y el cerebro los sitios metastásicos más comunes (9). A nivel molecular, el CMTN carece de la expresión del receptor de estrógeno, el receptor de progesterona y el receptor del factor de crecimiento epidérmico humano 2 (HER2) (7,10,11). Por esta razón, los pacientes con CMTN no se han beneficiado de los avances en terapias endocrinas y dirigidas a HER2 que han aumentado significativamente las tasas de supervivencia en otros subtipos (8,12,13). Los tratamientos para el CMTN metastásico actualmente son consierados paliativos en lugar de terapéuticos y generalmente comprenden la administración secuencial de agentes quimioterapéuticos (a menudo en combinación) hasta que el paciente alcanza la respuesta máxima o mientras muestra tolerancia al tratamiento (14–16). Por lo tanto, el tratamiento del CMTN metastásico sigue representando un desafío.

Aunque el desarrollo de metástasis cerebrales es un evento tardío en el progreso de la enfermedad (17,18), ente el 30 y el 50% de los pacientes con cáncer de mama metastásico desarrollan metástasis cerebrales (19). Las metástasis cerebrales conllevan un mal pronóstico (la supervivencia de los pacientes con CMTN que desarrollan metástasis cerebrales es de entre tres y cuatro meses (2)) y deterioros neurológicos con la consiguiente reducción de la calidad de vida del paciente (2–4). El manejo clínico de las metástasis cerebrales de cáncer de mama se basa en tratamientos locales, ya que la barrera hematoencefálica (BHE) y la barrera hemato-tumoral (BHT) dificultan el acceso de las terapias administradas sistémicamente al

cerebro (4,19–21). Por lo tanto, el desarrollo de nuevas terapias sistémicas efectivas para el tratamiento de metástasis cerebrales representa un desafío importante.

En este contexto, hemos desarrollado conjugados polímero-fármaco para tratar las metástasis cerebrales, centrándonos en el CMTN. Los conjugados polímero-fármaco comprenden mínimamente un polímero (vehículo) soluble en agua unido a un agente terapéutico a través de un enlace covalente (normalmente sensible a estímulos); también pueden llevar una molécula directora. El tamaño nanométrico de los conjugados de combinación junto con el diseño racional del enlace covalente del fármaco ofrece ventajas únicas, como (i) un incremento en la solubilidad en agua del fármaco (22,23), (ii) acumulación pasiva debido al efecto de la permeabilidad y retención aumentadas (EPR) en tumores sólidos (24), (iii) la capacidad de cruzar barreras biológicas y contrarrestar mecanismos de quimiorresistencia (25), (iv) perfil farmacocinético mejorado debido a la liberación controlada de los fármacos lograda mediante la selección racional de un enlace sensible a estímulos entre fármaco y polímero (22,26), y (v) la capacidad de incorporar varios agentes terapéuticos, agentes reporteros y/o moléculas directoras, lo que permite desarrollar terapias de combinación, agentes teranósticos y/o proveer de direccionamiento activo, respectivamente (27,28).

El uso de polipéptidos como vehículo proporciona ventajas adicionales, incluida su biocompatibilidad y biodegradabilidad inherentes gracias a los enlaces amida que forman el esqueleto polipeptídico (29). Gran cantidad de estudios han proporcionado evidencia de la versatilidad del ácido poliglutámico (PGA) en referencia a la conjugación de una amplia variedad de moléculas (30–41), lo que representa un aspecto crucial del diseño de terapias de combinación. El PGA admite la conjugación de combinaciones de fármacos con diferentes características químicas, el control de la proporción de dichos fármacos y el uso de diferentes enlaces

con química ortogonal que respaldan la liberación controlada de los agentes terapéuticos (35,38,42,43). El desarrollo de técnicas de polimerización controlada ha fomentado la síntesis de nanosistemas basados en PGA con diferentes topologías y a gran escala (44–46). Nuestro laboratorio ha desarrollado un PGA en forma de estrella de tres brazos (St-PGA) con internalización celular aumentada, vidas medias en circulación prolongadas y una acumulación más significativa en órganos en ratones en comparación a PGA lineales de peso molecular similar (45). En general, junto con la biodegradabilidad, la seguridad y la versatilidad inherentes del PGA, las ventajas de la arquitectura en forma de estrella hacen que el St-PGA represente un excelente vehículo para el desarrollo de terapias avanzadas para el tratamiento del cáncer.

Por otro lado, el St-PGA muestra un comportamiento de autoensamblaje en medio acuoso: impulsado por interacciones iónicas, el St-PGA forma grandes estructuras esféricas al aumentar la concentración de polipéptido en agua. Estas mismas estructuras se desensamblan en respuesta a un aumento de la fuerza iónica de la solución. La estabilización de estas estructuras autoensambladas mediante enlace covalentes genera estructuras esféricas estables de ~200 nm de diámetro (St-PGA-Click) que presentan una internalización celular y tiempo de circulación aún mayores (39); mejorando así el potencial de St-PGA como sistema de administración de fármacos.

En esta tesis, nuestro objetivo fue desarrollar una nueva terapia de combinación basada en la conjugación de combinaciones sinérgicas de fármacos a St-PGA, con proporciones optimizadas y enlaces sensibles al pH, para tratar el CMTN metastásico (Capítulo 2). También perseguimos el desarrollo de una estrategia para la síntesis de conjugados de combinación basados en autoensamblaje de conjugados St-PGA-fármaco rempleando enlaces reversibles sensibles a estímulos para la estabilización del ensamblaje (Capítulo 3). Nuestro objetivo final fue desarrollar la versión

dirigida al cerebro del candidato con mejor actividad antitumoral y antimetastásica, elegido entre los conjugados obtenidos mediante ambas estrategias (Capítulo 4).

2. Objetivos de la Investigación

El principal objetivo de esta tesis es el diseño y desarrollo de un conjugado de combinación dirigido a cerebro basado en ácido poliglutámico para el tratamiento de las metástasis cerebrales de cáncer de mama. Ciclos de diseño reiterativos empleando modelos *in vitro* e *in vivo* bien establecidos y técnicas de caracterización físico-química de última generación permitieron optimizar las proporciones de los fármacos y la química de conjugación de los fármacos y el péptido director.

Siguiendo un enfoque de diseño racional, dividimos este objetivo principal en los siguientes subobjetivos:

i. El diseño, la síntesis y la caracterización fisicoquímica exhaustiva de conjugados de combinación de ácido poliglutámico en forma de estrella y la evaluación de su actividad antitumoral y antimetastásica en modelos *in vitro* e *in vivo* de cáncer de mama triple negativo relevantes (Capítulo 2).

ii. El desarrollo de una estrategia ascendente (en inglés, "bottom-up") para la síntesis de conjugados de combinación basados en ácido poliglutámico en forma de estrella mediante la explotación de su autoensamblaje/agregación en agua y el uso de enlaces reversibles que responden a estímulos para la estabilización de los nanosistemas resultantes (Capítulo 3).

iii. El desarrollo de la versión dirigida a cerebro del candidato principal (seleccionado del Capítulo 2 o 3), incluyendo su caracterización fisicoquímica completa, estudio de la biodistribución *in vivo* para evaluar la acumulación en cerebro

y la evaluación de su actividad farmacológica en un modelo *in vivo* relevante de metástasis cerebral de cáncer de mama (Capítulo 4).

3. Resultados y Discusión

3.1. CAPÍTULO 2: Conjugados de combinación basados en poliglutamatos en forma de estrella para el tratamiento del cáncer de mama triple negativo metastásico

La identificación preclínica de nuevas combinaciones sinérgicas de fármacos ha brindado esperanza a los pacientes de CMTN que no se han podido beneficiar del avance en terapias endocrinas y dirigidas a HER2. Dentro de estas combinaciones sinérgicas se incluye el tratamiento con doxorrubicina (Dox), inhibidor de la topoisomerasa I/II, y dasatinib (Das), inhibidor de la familia de quinasas SRC (47). En este capítulo, reportamos la síntesis, caracterización fisicoquímica y evaluación biológica de una nueva familia de conjugados de combinación basados en polipéptidos que contienen Dox y Das para tratar el CMTN metastásico.

Trabajo realizado previamente en nuestro laboratorio describió la proporción y secuencia de administración óptimas de Dox y Das para maximizar su sinergia (42). Este estudio propició el desarrollo de un conjugado de combinación basado en PGA lineal con Dox y Das unidos mediante enlaces sensibles a pH que demostró eficacia contra tumor primario y metástasis de CMTN. Utilizando un enfoque de diseño racional, en esta tesis buscamos mejorar aún más la eficacia de esta estrategia de tratamiento mediante el uso de nuevas arquitecturas ramificadas basadas en PGA con perfil farmacocinético mejorado.

Como resultado, sintetizamos tres conjugados combinados basados en St-PGA (St-PGA-hyd-Dox1-Das10, St-PGA-hyd-Dox1-Das1 y St-PGA-hyd-Dox1-Val-Das1), explorando diferentes enlaces y proporciones de fármacos, y sus respectivos conjugados de fármaco único (St-PGA-Das, St-

PGA-Val-Das y St-PGA-hyd-Dox). Realizamos una caracterización fisicoquímica exhaustiva de cada conjugado para permitir ciclos reiterativos de diseño. En general, este enfoque permitió el desarrollo de un conjugado de combinación basado en St-PGA con actividad antitumoral y antimetastásica en un modelo ortotópico de células MDA-MB-231-Luc de CMTN metastásico en ratones.

Al contrario que los conjugados de PGA lineal, el St-PGA no requirió el uso de un espaciador de valina entre PGA y Das para lograr la liberación retardada del fármaco en los conjugados de combinación, lo que sugiere la influencia de la arquitectura del transportador en la cinética de liberación del fármaco. Además, el conjugado de combinación sintetizado con el espaciador de valina, St-PGA-hyd-Dox1-Val-Das1, exhibió una alta toxicidad in vivo. Estudiamos las causas potenciales de dicha toxicidad y detectamos interacciones entre el conjugado y proteínas del suero de ratón. St-PGA-hyd-Dox1-Val-Das1 formó agregados con las principales proteínas en suero, lo que podría haber contribuido a la toxicidad del compuesto.

Los conjugados basados en St-PGA sintetizados con conjugación directa de Das mediante enlace éster (St-PGA-hyd-Dox1-Das1 y St-PGA-hyd-Dox1-Das10) mostraron perfiles de liberación de fármacos similares, con liberación rápida de Dox y liberación sostenida de Das. Sin embargo, el ratio Dox:Das de St-PGA-hyd-Dox1-Das10 (con exceso de Das) favoreció la liberación de los fármacos a un ratio óptimo, lo que se reflejó en la actividad antitumoral in vitro e in vivo del conjugado, lo cual destaca la importancia de la proporción de fármacos en el desarrollo de terapias de combinación.

La evaluación biológica de los conjugados de combinación en un modelo murino ortotópico de CMTN demostró la actividad antitumoral de St-PGA-hyd-Dox1-Das10. Este conjugado de combinación redujo efectivamente el tamaño del tumor primario en aproximadamente un 75 % en comparación con el grupo de control sin mostrar signos de toxicidad

significativa. St-PGA-hyd-Dox1-Das10 también redujo de forma segura la propagación metastásica en pulmones, aunque en menor medida que los fármacos libres administrados en combinación a la misma dosis (que mostraron una toxicidad significativa). Por tanto, concluimos que St-PGA-hyd-Dox1-Das10 supone una mejora respecto a la administración libre de fármacos, lo que supone un paso adelante en el desarrollo de tratamientos sistémicos eficaces para el CMTN metastásico.

3.2. CAPÍTULO 3: Desarrollo de una estrategia para la síntesis de conjugados de combinación para el tratamiento del cáncer de mama mediante el ensamblaje de conjugados de fármaco único

El uso de nanosistemas de St-PGA autoensamblados y estabilizados como vehículo de fármacos ofrece numerosas ventajas. Específicamente, su mayor tiempo de circulación en comparación con el unímero de St-PGA y el PGA lineal convierte estos nanosistemas en potencialmente eficientes para el desarrollo de terapias contra el cáncer; sin embargo, en la actualidad el método de estabilización empleado para estas estructuras emplea un enlace no biodegradable (33,39,48). Nuestro objetivo en este capítulo fue desarrollar un método de estabilización alternativo para las estructuras autoensambladas de St-PGA empleando enlaces disulfuro. Estos enlaces covalentes reversibles proporcionarían al nanosistema capacidad de desensamblarse en respuesta a condiciones altamente reductoras, como las que se encuentran en el microambiente tumoral.

Alentados por el comportamiento dinámico de los autoensamblajes y co-ensamblajes de St-PGA en solución acuosa (39), diseñamos una estrategia para sintetizar conjugados de combinación conjugando un par de fármacos (Dox y Das) a diferentes moléculas de St-PGA y entrecruzando el estructuras co-ensambladas formadas por ambos unímeros. Con este fin, conjugamos piridil ditiol cisteamina (PD) a un 5 % mol y 10 % mol de carga (St-PGA-PD(5) y St-PGA-PD(10), respectivamente) y los fármacos Dox o

Das a la misma molécula de St-PGA (5% mol), obteniendo los bloques para la síntesis de conjugados de combinación mediante el co-ensamblaje de polímeros portadores de Dox y Das.

La caracterización fisicoquímica de estos conjugados demostró que la modificación de St-PGA con residuos hidrofóbicos (como Dox, Das y PD) influyó significativamente en el comportamiento del polímero en medios acuosos. Elegimos los conjugados derivados de St-PGA-PD(5) (St-PGA-PD(5)-Dox, St-PGA-PD(5)-hyd-Dox y St-PGA-PD(5)-Das) para evaluar el proceso de estabilización, ya que mantuvieron la estructura secundaria del material de partida en una amplia gama de condiciones. Además, no logramos generar el conjugado St-PGA-PD(10)-hyd-Dox, lo que nos habría permitido estudiar el enlace hidrazona sensible a pH para los conjugados de St-PGA-PD(10). El estudio del autoensamblaje y el co-ensamblaje de estas moléculas reveló que los residuos hidrófobos alteran el proceso con el residuo y el enlace utilizado para su conjugación determinando el grado de alteración. Sin embargo, el estudio del tamaño de los conjugados en agua reveló la presencia de agregados. Creemos que las interacciones hidrofóbicas introducidas mediante la conjugación de PD, Dox y Das actúan junto a las interacciones iónicas del ácido glutámico de una manera compleja, alterando el comportamiento que impulsa el autoensamblaje y co-ensamblaje del St-PGA. Nuevos experimentos, planteados siguiendo un enfoque de "calidad por diseño" (QbD del inglés *quality by design*), pueden ayudar a aumentar nuestra comprensión sobre efecto de los residuos hidrofóbicos y sus enlaces en el comportamiento del conjugado en solución y permitirnos controlar mejor el autoensamblaje y el co-ensamblaje (49).

Exploramos el uso de varios protocolos sintéticos para estabilizar los ensamblajes formados por St-PGA-PD(5). En todos los casos, observamos una liberación rápida y eficiente del grupo piridil tiona, dejando los grupos tiol expuestos para formar enlaces disulfuro. La determinación de grupos tiol libres en los nanosistemas finales (tras reacción y purificación) reveló

diferencias en la formación de enlaces disulfuro según el protocolo utilizado. Presentando el valor más bajo de grupos tiol libres, el protocolo de nanoprecipitación inversa destaca sobre los otros protocolos de estabilización. Además, este protocolo no se basa en el co-ensamblaje de las moléculas de St-PGA-fármaco y, por tanto, permite ampliar el espectro de combinaciones de fármaco-enlace utilizables.

Desafortunadamente, ninguno de los protocolos examinados en este capítulo generó nanosistemas estables en medios con alta fuerza iónica, proporcionando tamaños en concordancia con un desmontaje estructural completo. Nuestra hipótesis es que esta falta de estabilidad se deriva de la presencia de grupos tiol reducidos (libres) en el compuesto final (lo que desencadenaría reacciones de intercambio disulfuro-tiol que desestabilizarían la estructura) o a la escasa exposición de los grupos tiol de St-PGA-PD(5) y sus derivados (que provocarían la formación de enlaces disulfuro intramoleculares en lugar de enlaces intermoleculares) o un bajo número de enlaces disulfuro intermoleculares en el producto final.

Actualmente, se está estudiando en el laboratorio el uso del protocolo de nanoprecipitación inversa para la estabilización de autoensamblajes de St-PGA-PD(10). Si esta estrategia genera nanosistemas estables, los protocolos de síntesis de St-PGA-PD(10)-fármaco deberían revisarse para poder generar el conjugado de Dox con hidrazona (St-PGA-PD(10)-hyd-Dox), un enlace que ha demostrado mayor eficacia que el amida (35,38).

3.3. CAPÍTULO 4: Diseño racional de conjugados de combinación dirigidos a cerebro para el tratamiento de metástasis cerebrales de cáncer de mama

Las metástasis cerebrales representan la complicación más letal del cáncer de mama. Con la BHE y la BHT obstaculizando la acumulación en cerebro de las terapias administradas sistémicamente, el tratamiento de las

metástasis cerebrales se basa en enfoques locales, como la resección quirúrgica o la radioterapia, que tienen una eficacia limitada y numerosos efectos secundarios (50). El desarrollo de estrategias basadas en nanotecnología para eludir la BHE ofrece una nueva esperanza para el tratamiento de enfermedades del sistema nervioso central. En este capítulo, hemos sintetizado, caracterizado fisicoquímicamente y evaluado biológicamente un nuevo conjugado de combinación dirigido a cerebro basado en St-PGA con el objetivo de tratar las metástasis cerebrales de CMTN. Para ello, hemos conjugado Dox, Das y el péptido Angiopep-2 (ANG), ligando de la proteína LRP-1 (del inglés *low density lipoprotein receptor-related protein 1*) sobreexpresado por las células endoteliales de la BHE, para obtener direccionamiento a cerebro.

El trabajo realizado anteriormente (ver Capítulo 2) resultó en la síntesis de St-PGA-hyd-Dox1-Das10, un conjugado de combinación basado en St-PGA con una proporción optimizada de Dox y Das conjugados a través de enlaces sensibles a pH (hidrazona para Dox y éster para Das). St-PGA-hyd-Dox1-Das10 demostró tener actividad antitumoral elevada contra el tumor primario y la metástasis pulmonar en un modelo ortotópico de CMTN humano en ratón. Siguiendo un diseño racional, nuestro objetivo fue obtener una versión de St-PGA-hyd-Dox1-Das10 dirigida a cerebro para tratar las metástasis cerebrales de CMTN mediante la incorporación de ANG en el conjugado.

Con este objetivo en mente, optimizamos un protocolo sintético rápido y sencillo para la conjugación de ANG a St-PGA a través de un enlace maleimida-tiol no reversible. Las condiciones de reacción (DPBS pH 7,2, temperatura ambiente) y tiempos de reacción cortos (5 h) permitieron el uso de este protocolo para la conjugación de ANG a moléculas de St-PGA que contienen fármaco con una pérdida de carga de fármaco reducida. La caracterización fisicoquímica de los conjugados con ANG proporcionó evidencia de que la incorporación de ANG no cambió las características

530

principales de St-PGA, manteniendo su carga negativa, estructura secundaria y capacidad de agregación en agua.

El estudio de biodistribución realizado con conjugados de St-PGA marcados con fluoróforos (Cy5.5) en ratones sanos demostró la capacidad de ANG de dirigir nuestros conjugados a cerebro, con St-PGA-Cy5.5-ANG-NAC aumentando 1.4 veces la acumulación de conjugado en el cerebro en comparación a St-PGA-Cy5.5-NAC (el conjugado sin ANG).

Creemos que la eficacia del conjugado de combinación dirigido recae tanto en la acumulación en cerebro como en la eficacia de la combinación de fármacos y los enlaces empleados.

Gracias a las químicas ortogonales utilizadas para la conjugación de los fármacos y ANG, combinamos ambos protocolos sintéticos para producir un conjugado de combinación de St-PGA con ANG, es decir, St-PGA-hyd-Dox-Das-ANG-NAC. En comparación con St-PGA-hyd-Dox1-Das10, St-PGA-hyd-Dox-Das-ANG-NAC mostró una mayor carga de Dox (1,9 % en peso para St-PGA-hyd-Dox-Das-ANG-NAC versus 1 % en peso para St-PGA-hyd-Dox1-Das10), lo que cambió la relación de fármaco final del conjugado (1:6 para St-PGA-hyd-Dox-Das-ANG-NAC frente a 1:9 para St-PGA- hidr-Dox1-Das10). St-PGA-hyd-Dox-Das-ANG-NAC mostró características fisicoquímicas similares a St-PGA-hyd-Dox1-Das10, con tamaños de ~ 10 nm como unímero, potencial zeta negativo y estructura secundaria *random coil*. También observamos perfiles similares de liberación de fármacos para St-PGA-hyd-Dox-Das-ANG-NAC y St-PGA-hyd-Dox1-Das10; sin embargo, las diferentes cargas de fármaco cambiaron significativamente las ratios de fármaco liberado. Observamos este comportamiento en el Capítulo 2 con St-PGA-hyd-Dox1-Das10 y St-PGA-hyd-Dox1-Das1, donde describimos que la liberación del fármaco dependía principalmente de la química de enlace utilizada para la conjugación del fármaco, sin que la carga del fármaco tuviera influencia en la liberación del

fármaco, pero siendo determinante en la biodisponibilidad del fármaco en los tejidos diana.

La evaluación biológica de St-PGA-hyd-Dox-Das-ANG-NAC en un modelo de ratón de metástasis cerebral basado en MDA-MB-231 reportó resultados prometedores. Nuestro compuesto mostró una eficacia significativa en la reducción de las metástasis extracraneales (especialmente en los pulmones), lo que concuerda con la actividad antimetastásica observada para su equivalente no dirigido (ver Capítulo 2). Creemos que la expresión de LRP-1 por las células MDA-MB-231 sirvió para dirigir St-PGA-hyd-Dox-Das-ANG-NAC a las células tumorales, aumentando la eficacia del conjugado para reducir la propagación metastásica extracraneal; sin embargo, no observamos actividad antimetastásica elevada en el cerebro, lo que sugiere que no logramos alcanzar una concentración (o proporción) de fármacos óptima en las metástasis cerebrales. Sin embargo, observamos una mejora en el bienestar animal con el tratamiento con St-PGA-hyd-Dox-Das-ANG-NAC en comparación al control del vehículo sin fármacos St-PGA-ANG-NAC. En resumen, este estudio confirmó la seguridad de nuestro conjugado y demostró su actividad antimetastásica, aunque reducida, en metástasis cerebrales.

Por lo tanto, creemos que podemos mejorar aún más el resultado terapéutico de nuestro conjugado aumentando la dosis administrada. En este estudio, utilizamos 1,2 mg de Dox/Kg ya que dosis más altas de Dox libre en el modelo ortotópico de CMTN utilizado en el Capítulo 2 provocaron alta toxicidad sistémica y una reducción significativa de la supervivencia. No obstante, éste modelo se obtuvo en ratones NOD/SCID mientras que el modelo de metástasis cerebral se desarrolló en una cepa de ratón atímico (*athymic nude*), que soporta dosis más altas de Dox (51,52). Por tanto, planeamos realizar nuevos experimentos in vivo para administrar dosis más altas de Dox/conjugado. Esperamos que el aumento de la dosis inyectada

conduzca a una mayor concentración de fármacos en el tejido metastásico, lo que reducirá significativamente el crecimiento del tumor secundario tanto en los pulmones como en el cerebro.

4. Conclusiones

1. El ácido poliglutámico en forma de estrella (St-PGA) como portador polipeptídico versátil admitió la conjugación de Dox y Das en diferentes proporciones y enlaces sin inducir alteraciones significativas en las principales características fisicoquímicas del polipéptido (tamaño, agregación, potencial zeta y estructura secundaria). Esto permitió la síntesis de una familia de conjugados de combinación con Dox y Das conjugados a través de enlaces sensibles a pH para respaldar la liberación controlada de los fármacos en condiciones ácidas (el microambiente tumoral y lisosomal).

2. El estudio de la cinética de liberación de los fármacos en medios relevantes reveló la influencia de la química de conjugación de Das en el perfil de liberación de los fármacos, pasando de una liberación rápida de Dox con liberación sostenida de Das a una liberación súbita de Dox con baja liberación de Das. Mientras tanto, la carga de fármaco tuvo poco efecto sobre el perfil de liberación de los fármacos, pero definió la proporción de fármaco liberado en los medios, lo que finalmente determinó la actividad biológica de los conjugados.

3. Los conjugados de fármaco único y de combinación basados en St-PGA demostraron una actividad citotóxica robusta en células humanas MDA-MB-231-Luc de CMTN definida por el perfil de liberación de los fármacos y la carga/proporción de fármacos en el caso de los conjugados de combinación. Una combinación de liberación y carga del fármaco que permita un exceso de Das

sobre Dox en el medio respalda la actividad citotóxica del conjugado.

4. La familia de conjugados basados en St-PGA demostró su seguridad para la administración intravenosa excepto St-PGA-hyd-Dox1-Val-Das1, que causó una pérdida de peso significativa en los animales y redujo las tasas de supervivencia en un modelo de CMTN espontáneamente metastásico basado en MDA-MB-231-Luc. St-PGA-hyd-Dox1-Das10 mostró una actividad antitumoral óptima; sin embargo, ninguno de los conjugados de combinación mejoró significativamente la actividad antitumoral o antimetastásica de los fármacos libres administrados en combinación a la misma dosis. En general, la ventaja de los conjugados basados en St-PGA se basa en su perfil de seguridad (toxicidad) mejorado.

5. El fraccionamiento mediante flujo asimétrico (AF4 del inglés *asymmetrical flow field-flow fractionation*) permitió el desarrollo de un método novedoso y simple para el estudio cualitativo de la corona de proteínas en conjugados polipéptido-fármaco. Este método puede usarse para caracterizar las interacciones proteína-conjugado en conjugados polipéptido-fármaco de tamaño comparable al de las principales proteínas de plasma/suero (~6 nm de diámetro). Este enfoque proporcionó datos adicionales que explican la alta toxicidad de St-PGA-hyd-Dox1-Val-Das1 observada in vivo.

6. El autoensamblaje y co-ensamblaje del St-PGA en agua proporcionó la base para el desarrollo de una estrategia para sintetizar conjugados de combinación sensibles a medios reductores mediante el co-ensamblaje de conjugados de un solo fármaco empleando piridil ditiol cisteamina (PD) para introducir grupos tiol en St-PGA. La caracterización fisicoquímica de los componentes básicos de St-PGA para esta estrategia demostró

que la conjugación de residuos hidrofóbicos influyó significativamente en el comportamiento del St-PGA en medios acuosos. La conjugación de residuos hidrofóbicos alteró el comportamiento de autoensamblaje y co-ensamblaje de St-PGA en agua, un cambio cuya extensión depende del residuo y el enlace utilizado para la conjugación. Actualmente no entendemos completamente cómo las interacciones hidrofóbicas interactúan con las interacciones iónicas del ácido glutámico alterando el comportamiento extraordinario que impulsa el autoensamblaje y el co-ensamblaje de St-PGA.

7. Desafortunadamente, ninguno de los protocolos sintéticos examinados para la estabilización de los ensamblajes basados en St-PGA-PD mediante enlaces disulfuro generó nanosistemas estables en medios de alta fuerza iónica. La falta de estabilización no responde a una falta de agregación del conjugado o a una baja concentración de conjugado en la reacción. Por lo tanto, planteamos la hipótesis de que la falta de estabilidad deriva de la presencia de grupos tiol reducidos (libres) en el compuesto final (desencadenando reacciones de intercambio disulfuro-tiol que desestabilizan la estructura), de la escasa exposición de los grupos tiol en St-PGA-PD(5) y sus derivados (impulsando la formación de enlaces disulfuro intramoleculares en lugar de enlaces estabilizadores intermoleculares), o un bajo número de enlaces disulfuro intermoleculares en el producto final.

8. El uso de la química maleimida-tiol permitió el desarrollo de un protocolo eficiente y reproducible para la conjugación de Angiopep-2 a conjugados basados en St-PGA en medio acuoso. Nuestro protocolo limitó la pérdida de carga de fármacos debido a la hidrólisis de los enlaces sensibles a pH durante la reacción, lo que sugiere posible aplicación para conjugar una variedad de péptidos modificados con grupos tiol a conjugados polímero-

fármaco modificados con maleimida. La conjugación de Angiopep-2 a conjugados de combinación basados en St-PGA no alteró significativamente las principales características fisicoquímicas del vehículo, es decir, estructura secundaria en soluciones acuosas, agregación en agua dependiente de la concentración, tamaño en soluciones de alta fuerza iónica, carga negativa y perfil de liberación del fármacos.

9. El conjugado de combinación de St-PGA-Angiopep-2 redujo de manera efectiva las metástasis extracraneales y la pérdida de peso de los animales asociada con la progresión de la enfermedad; sin embargo, aunque la actividad de nuestro conjugado de combinación contra las metástasis cerebrales fue alentadora, el rendimiento terapéutico en este sentido sigue siendo insuficiente. Estos resultados preliminares sugieren que una dosis subóptima de conjugado/fármacos provocó la falta de efecto dentro del cerebro. Como nuestro conjugado demostró un perfil de seguridad adecuado, hemos planificado más experimentos con dosis más altas de conjugado para aumentar la biodisponibilidad del fármaco en las metástasis cerebrales y mejorar el resultado terapéutico.

5. Materiales y Métodos

5.1. Materiales

Todos los disolventes eran de grado analítico y se obtuvieron de Sharlab Chemicals (Sharlab S.L., Barcelona, España), excepto el ácido trifluoroacético (TFA), que se obtuvo de TCI Deutschland GmbH (Eschborn, Alemania), y el tetrahidrofurano (THF), que fue recién destilado. Los disolventes deuterados se obtuvieron de Deutero GmbH (Kastellaun, Alemania). Todos los productos químicos eran de grado reactivo, obtenidos de Sigma-Aldrich (Merck KGaA, Darmstadt, Alemania) a menos que se indique lo contrario. Todos los productos químicos eran de grado reactivo,

obtenidos de Sigma-Aldrich (Merck KGaA, Darmstadt, Alemania) a menos que se indique lo contrario. La 4-dimetilaminopiridina (DMAP) se obtuvo de Fluka (Thermo Fisher GmbH, Kandel, Alemania). Doxorrubicina HCl se obtuvo de MedKoo Biosciences, Inc. (Morrisville NC, EE. UU.). Dasatinib se obtuvo de LC Laboratories Inc. (Woburn MA, EE. UU.). El monómero de ácido glutámico se adquirió en PMC Isochem (Vert-Le-Petit, Francia). El tetrafluoroborato de 4-(4,6-dimetoxi-1,3,5-triazin-2-il)-4-metil-morfolinio (DMTMM BF4) se sintetizó siguiendo protocolos descritos en literatura. Los fluoróforos se obtubieron de Lumiprobe GmbH (Hannover, Alemania). El St-PGA fue sintetizado siguiendo los protocolos descritos a continuación o se obtuvo de Polypeptide Therapeutic Solutions S.L. (Valencia, España). Angiopep-2-SH (Ac-TFFYGGSRGKRNNFKTEEY-C-NH2) se obtuvo de Selleck Chemicals LLC (Houston, TX, EE. UU.). La SEC preparativa se realizó utilizando Sephadex LH-20 o Sephadex G25 de GE Healthcare (Global Life Sciences Solutions USA LLC, Marlborough, MA, EE. UU.). La ultrafiltración se realizó en un dispositivo de ultrafiltración Millipore (Merck KGaA, Darmstadt, Alemania) equipado con una membrana de celulosa regenerada de corte de peso molecular de 3, 10, 30 o 50 kDa (Vivaspin™). Las membranas de diálisis se obtuvieron de Spectrum Chemicals Mfg. Corp. (New Brunswick, NJ, USA). La solución salina tamponada con fosfato HyClone (DPBS) se obtuvo de Cytiva UK Ltd. (Buckinghamshire, Reino Unido).

5.2. Métodos más relevantes

5.2.1. Conjugación mediante enlace amida

En un matraz de fondo redondo equipado con un agitador y una entrada y salida de N_2, se disolvió el St-PGA (1 equivalente) en DMF anhidro. Una vez completamente disuelto, se añadió DMTMM BF4 (la cantidad correspondiente para el porcentaje de modificación deseado, p. ej., 0.15 eq. para 10% mol) y se dejó que la reacción prosiguiera en agitación durante 30 minutos. Después de eso, se añadió la correspondiente amina a

la reacción (la cantidad correspondiente para el porcentaje de modificación deseado, p. ej., 0.15 eq. para 10% mol). El pH se ajustó a 8 con DIEA y la reacción se dejó en agitación a temperatura ambiente durante 48 horas. Tras ello, se realizaron purificaciones estándar (p. ej., precipitación en éter dietílico o cromatografía de exclusión molecular) y el producto se secó mediante liofilizado. Si el producto es final, se obtuvo la forma sal mediante adición de bicarbonato de sodio y posterior eliminación de las sales mediante cromatografía de exclusión molecular, ultrafiltración o diálisis. Todos los productos se caracterizaron por ^{1}H-RMN.

5.2.2. Conjugación mediante enlace hidrazona

5.2.2.1. Síntesis del precursor St-PGA-TBC

La conjugación del carbazato de terc-butilo (TBC) se realizó siguiendo el protocolo de *Conjugación mediante enlace amida*.

5.2.2.2. Desprotección de las hidracidas

En un matraz de fondo redondo provisto de imán agitador y tapón, se disolvió el precursor St-PGA-TBC (1 equivalente) en ácido trifluoroacético y se dejó en agitación durante 45 min. Luego, el producto se precipitó en éter dietílico frío y se secó. La eliminación del grupo protector Boc se confirmó mediante ^{1}H-NMR.

5.2.2.3. Conjugación de doxorubicina mediante enlace hidrazona

En un matraz de fondo redondo de dos bocas equipado con un imán agitador y entrada y salida de N_2, se disolvió el precursor St-PGA-hidrazida (1 equivalente) en dimetilsulfóxido (DMSO) anhidro. Una vez completamente disuelto, se añadió doxorrubicina (Dox) (0,083 equivalentes) a la reacción. Luego, se añadieron tres gotas de ácido acético puro a la reacción y se dejó en agitación a temperatura ambiente durante 48 h. Después, el disolvente se evaporó en alto vacío. El producto se disolvió en DMF y se purificó por cromatografía de exclusión molecular con una

columna Sephadex LH-20 usando DMF como eluyente. Las fracciones que contenían el producto de color rojo se recolectaron en un matraz de fondo redondo al que se le añadieron 3 mL de bicarbonato de sodio 0.1 M antes de evaporar el disolvente en la bomba de vacío. Para obtener la forma de sal del polímero, se añadieron agua MilliQ y bicarbonato de sodio. Se realizó una cromatografía de exclusión por tamaño con una columna Sephadex G-25 utilizando agua MilliQ como eluyente para eliminar el exceso de sales. Las fracciones que contenían el producto de color rojo se recogieron y se secaron por liofilización. La identidad del producto se evaluó mediante ^{1}H-NMR. La carga de Dox se determinó mediante espectrofotometría UV-VIS.

5.2.3. Conjugación mediante enlace éster

El St-PGA (1 equivalente) se disolvió en DMF anh. en un matraz de fondo redondo de dos bocas equipado con un imán agitador y entrada y salida de N$_2$. Una vez completamente disuelto el St-PGA, DMAP (0.030 equivalentes) y EDC (0.15 equivalentes) se añadieron a la mezcla de reacción, que se dejó en agitación durante 20 min. Luego, se añadió Das (0.15 equivalentes) a la reacción y el pH se ajustó a 8 con DIEA. La reacción se dejó en agitación a temperatura ambiente durante 72 h. El producto se purificó por cromatografía de exclusión molecular con una columna Sephadex LH-20 usando DMF como eluyente. La elución se monitorizó mediante cromatografía de capa fina (TLC del inglés *thin layer chromatography*) usando metanol como fase móvil. Las fracciones que contenían el producto se recogieron en un matraz de fondo redondo y se añadieron 3 mL de bicarbonato de sodio 0,1 M antes de evaporar el disolvente en alto vacío. Para obtener la forma de sal del polímero, se añadió agua MilliQ. Se realizó una cromatografía de exclusión molecular con una columna Sephadex G-25 utilizando agua MilliQ como eluyente para eliminar el exceso de sales. La elución se monitorizó mediante TLC (MeOH, Rf: 0.7). Sólo las fracciones que contenían únicamente el conjugado

polímero-fármaco se liofilizaron. La identidad del producto se evaluó por ^{1}H-NMR. La carga de Das se determinó mediante espectrofotometría UV-VIS.

5.2.4. Reacción de estabilización mediante DTT

El compuesto derivado de St-PGA-PD se disolvió en agua MilliQ a una concentración de 2 mg/mL dentro de un vial de vidrio equipado con un agitador. Se añadió DTT en sólido en la cantidad necesaria para lograr una concentración final de 7,5 mM. Una vez finalizada la reacción, el producto se purificó mediante Vivaspin™ (30 kDa). La purificación se controló mediante la adquisición de espectros UV-VIS de los desechos de cada ronda de ultracentrifugación hasta que no se observó ninguna señal de DTT o piridil tiona. Finalmente, el producto se liofilizó. El producto se caracterizó mediante ^{1}H-RMN.

5.2.5. Reacción de estabilización usando PEG

En un vial de vidrio equipado con un agitador, se disolvió St-PGA-PD(5) (0.15 mmol, 1 eq.) en agua MilliQ a 2 mg/mL y se filtró a través de un filtro de jeringa de 0.22 µm. Luego, se añadió SH-PEG$_5$-SH (0.006 mmol, 0.03 eq.) a la solución de polímero y se dejó que la reacción prosiguiera durante 120 minutos. Luego, se añadió β-mercaptoetanol (0.007 mmol, 0.04 eq.) y la reacción se dejó en agitación durante 30 minutos para asegurar la extinción de los tioles libres restantes. El producto se purificó mediante diálisis (Float-A-Lyzer, 3,5 kDa) en agua y se liofilizó. El producto se caracterizó mediante ^{1}H-RMN.

5.2.6. Reacción de estabilización mediante nanoprecipitación inversa

En un vial de vidrio, se disolvió St-PGA-PD(5) (0.13 mmol, 1.2 PD eq.) a una concentración de 2 mg/mL en 10 mL de agua MilliQ. Se añadió el SH-PEG$_5$-SH (0,005 mmol, 1 PD eq.) a 10 mL de agua MilliQ en un vial de vidrio separado. Se aislaron los 10 mL de SH-PEG$_5$-SH en agua usando una jeringa de 20 mL. Inmediatamente después, se tomaron los 10 mL de solución de St-PGA-PD(5) con la misma jeringa, mezclando así ambas

soluciones. Luego, la mezcla se vertió rápidamente en 400 mL de acetona fría en agitación fuerte. La mezcla se mantuvo en hielo y en agitación durante 15 min, luego se dejó a temperatura ambiente sin agitar durante 4 h. Después de eso, se añadió β-mercaptoetanol (0.005 mmol, 1 PD eq.) a la mezcla antes de la evaporar la acetona. La fase acuosa restante se dializó en agua MilliQ (Float-A-Lyzer 1 kDa). Finalmente, el producto se liofilizó. El producto se caracterizó mediante ^{1}H-RMN.

5.2.7. Conjugación del péptido director Angiopep-2 mediante reacción maleimida-tiol

El DPBS se desgasificó mediante sonicación y purga con N$_2$. El precursor de St-PGA con maleimida (1 eq.) se disolvió en el mínimo volumen de DPBS desgasificado en un matraz de fondo redondo de dos bocas equipado con un imán agitador y tapones. El TCEP (0,052 eq.) se disolvió en DPBS desgasificado a 50 mg/mL y se ajustó el pH a 7 con NaOH 5M. El Anigiopep-2-SH (0,017 eq.) se disolvió en el volumen mínimo de DPBS desgasificado. Luego, se añadieron ambos reactivos a la solución de polímero y la mezcla de reacción resultante se purgó con N$_2$ (g). La reacción se dejó a temperatura ambiente durante 5 h. Luego, el producto se purificó por diálisis (MWCO de 3,5 kDa) frente a agua MilliQ y se secó mediante liofilización. La carga de Angiopep-2 se obtuvo mediante ^{1}H-NMR comparando las señales de los residuos de fenilalanina y tirosina del péptido (23 protones) con el protón del carbono α del St-PGA.

5.2.8. Extinción de los grupos maleimida libres con N-acetilcisteína

El DPBS se desgasificó mediante sonicación y purga con N$_2$. El precursor de St-PGA con maleimida (1 eq.) se disolvió en el mínimo volumen de DPBS desgasificado en un matraz de fondo redondo de dos bocas equipado con un imán agitador y tapones. La N-acetilcisteína (NAC, 10 veces los moles de maleimida en la reacción) se disolvió en DPBS desgasificado a 100 mg/mL. El TCEP (10 veces los moles de maleimida en la reacción) se disolvió a 50 mg/mL en la solución de NAC, se ajustó el pH

a 7 con NaOH 5M y se añadió a la mezcla de reacción. Luego, la mezcla de reacción se purgó con N_2 y se dejó a temperatura ambiente durante 5 h. Luego, el producto se purificó por diálisis (MWCO de 3,5 kDa), VivaspinTM (MWCO de 3 kDa) y/o SEC preparativa con agua MilliQ y se secó mediante liofilización. La carga final de Angiopep-2 se determinó mediante análisis de aminoácidos.

5.3. Técnicas de caracterización más relevantes

5.3.1. Resonancia magnética nuclear

Los espectros ^{1}H-NMR se registraron en un UltrashieldTM 300 de Bruker (Billerica MA, EE. UU.) a 27 ºC y con una frecuencia de 300 MHz y se analizaron con el software MestreNova 6.2 (Mestrelab Research S.L., Santiago de Compostela, España).

5.3.2. Cuantificación de la carga de fármaco mediante espectrofotometría ultravioleta-visible

La carga de fármaco se determinó mediante espectroscopia UV-VIS. Se prepararon curvas de calibrado de los fármacos libres en una mezcla de DMSO:agua (1:1 v/v) por triplicado. El espectro de absorción de cada muestra se obtuvo con tres acumulaciones. Para el Das, se representó gráficamente la medida de absorbancia a 324 nm frente a la concentración de fármaco para obtener la curva de calibrado. Para la Dox se obtuvieron dos curvas de calibrado, una a 480 nm y otra a 324 nm. Para determinar la carga de fármaco de los conjugados, los compuestos se disolvieron en el mismo disolvente y los espectros de absorción se adquirieron utilizando los mismos parámetros. Para los conjugados de un solo fármaco, la carga de fármaco (en porcentaje en peso – % peso) se obtuvo interpolando el valor de absorbancia a 324 o 480 nm en la curva de calibrado correspondiente. Para los conjugados de combinación, la carga de Dox se determinó interpolando el valor de absorbancia a 480 nm en la curva de calibrado de Dox. Luego, se utilizó la concentración de Dox en la muestra para

determinar la contribución de Dox en la absorbancia total a 324 nm utilizando la curva de calibrado de Dox a dicha longitud de onda. El valor obtenido se restó a la absorbancia total de la muestra a 324 nm, obteniendo la absorbancia del Das. Este valor se interpoló en la curva de calibrado de Das para obtener la carga. La carga en porcentaje molar (% mol) se obtuvo mediante cálculo iterativo a partir del valor en (% peso).

Los espectros de absorción UV-VIS se obtuvieron utilizando el espectrofotómetro JASCO V-630 (Jasco International Co., Ltd, Hachioji, Tokio, Japón) a 25 °C con celdas de cuarzo de 1,0 cm con un ancho de banda espectral de 1 nm y registrando tres acumulaciones.

5.3.3. Medida del tamaño mediante dispersión dinámica de luz

El tamaño de los compuestos se determinó mediante dispersión dinámica de luz (DLS del inglés *dynamic light scattering*). Las mediciones se realizaron a 25 °C utilizando un instrumento Malvern ZetasizerNanoZS (Malvern Panalytical Ltd, Malvern, Reino Unido), equipado con un láser de 532 nm con un ángulo de dispersión fijo de 173°, en cubetas acrílicas obtenidas de Sarstedt Inc. (Nümbrec, Alemania). Se prepararon soluciones a 1, 0.5 y 0.1 mg/mL de polímero en agua MilliQ o DPBS, se sonicaron durante 5 min y se dejaron estabilizar durante la noche antes de la medición.

5.3.4. Potencial zeta

Las mediciones de potencial zeta se realizaron a 25 °C con un instrumento Malvern Zetasizer Nano ZS (Malvern Panalytical Ltd, Malvern, Reino Unido), equipado con un láser de 532 nm usando celdas capilares desechables (DTS1070) de Malvern Instruments Ltd. (Worcestershire, Reino Unido). Se midieron soluciones de polímero a 1 y 0.5 mg/ml en KCl 1 mM.

5.3.5. Dicroísmo circular

Los espectros de dicroísmo circular se obtuvieron con un espectropolarímetro J-1500 (JASCO Corporation) usando un soporte de celda termostatizado Peltier (PTC-517, JASCO Corporation) bajo flujo de nitrógeno. Se prepararon soluciones de polímero (0.5, 0.2 y 0.1 mg/ml) en agua MilliQ y en DPBS. Las medidas se obtuvieron en celdas de cuarzo de 0.1 cm con un ancho de banda espectral de 1 nm y registrando tres acumulaciones.

5.3.6. Cromatografía de exclusión molecular analítica

El análisis por cromatografía de exclusión molecular (SEC del inglés *size exclusion chromatography*) de los productos se realizó en un sistema modular de Postnova Analytics (Postnova Analytics GmbH, Landsberg am Lech, Alemania) equipado con un detector de índice de refracción (PN3150 de Postnova Analytics GmbH), un detector UV-VIS (SPD-20A de Shimadzu Scientific Instruments, Kioto, Japón), un detector de fluorescencia (RF-20A XS de Shimadzu Scientific Instruments, Kioto, Japón) y un detector de dispersión de luz multiángulo (MALS del inglés *multi-angle light scattering*) (PN3621 de Postnova Analytics GmbH). Todos los análisis se realizaron utilizando una columna TSK gel G3000PWXL (5 µm, 7,8 mm x 30 cm, Tosoh Corporation, Tokio, Japón) con la misma fase móvil (10 mM tampón fosfato pH 7,4, 0,005 % NaN$_3$) con un flujo constante (0,5 mL/min). Las muestras se prepararon con la fase móvil como disolvente a 2 mg/mL de compuesto. El volumen de inyección fue de 20 µL.

5.3.7. Estudio del ensamblaje de derivados de St-PGA mediante dispersión dinámica de luz

La concentración crítica de agregación (CAC) de los conjugados basados en St-PGA y St-PGA se determinó mediante DLS. Se prepararon muestras de concentración creciente de polímero (0.01 a 5 mg/mL) en agua MilliQ y se sonicaron durante 5 min. Las muestras se dejaron estabilizar durante la noche. Las mediciones de DLS se realizaron por duplicado con parámetros fijos para todas las muestras. Los datos se expresaron como la

tasa de recuento media (en inglés, "mean count rate" – MCR) frente a la concentración de conjugado en escala logarítmica. Los datos se ajustaron a dos ecuaciones lineales. Los valores de CAC se obtuvieron gráficamente de las intersecciones de ambas líneas.

5.3.8. Estudio de co-ensamblaje mediante dispersión dinámica de luz

El co-ensamblaje de diferentes polímeros derivados de St-PGA se estudió mediante DLS. A las muestras de derivados de St-PGA preparadas para la determinación de CAC se le añadieron un segundo derivado de St-PGA a una concentración final de 0.1 mg/mL (por debajo de su valor de CAC). Las muestras se mezclaron y se dejaron estabilizar durante la noche antes de medir la tasa de recuento media. El valor CAC de la mezcla se determinó como se describe en el apartado anterior.

5.3.9. Cuantificación de tioles libres mediante el ensayo de Ellman

El porcentaje de grupos tiol libres se determinó mediante el ensayo DTNB o el ensayo de Ellman. Se realizó una curva de calibrado con N-acetilcisteína. Se obtuvieron diluciones en serie a partir de una solución madre a 0.4 mg/mL en agua MilliQ. Se utilizó SH-PEG$_5$-SH como control positivo y St-PGA-PD(5) o St-PGA como control negativo. Las muestras y los controles se disolvieron en agua MilliQ y se pipetearon 170 µL en una placa de 96 pocillos por triplicado. A continuación, se añadieron a cada pocillo 20 µL de Tris 1 M pH 8. Finalmente, se añadieron a cada pocillo 10 µL de solución madre de DTNB (DTNB 2 mM en acetato de sodio 50 mM) y la placa se dejó en agitación a temperatura ambiente durante 5 min. Luego, se midió la absorbancia a 412 nm en el lector de placas ClarioStar plus (BMG Labtech).

La concentración de tioles libres en las muestras se obtuvo por interpolación en la curva de calibrado. El porcentaje de tioles libres se obtuvo dividiendo la concentración de grupos tiol libres en la muestra entre la concentración total de grupos tiol en la muestra.

5.4. Evaluación biológica

5.4.1. Estudios de viabilidad celular

Las células MDA-MB-231-Luc se sembraron en placas de microtitulación estériles de 96 pocillos a una densidad de 7500 células por pocillo. Las placas se incubaron durante 24 h antes del tratamiento. Luego, los compuestos (esterilizados con luz ultravioleta durante 20 min) se disolvieron en medio de cultivo hasta su límite de solubilidad y se prepararon diluciones en serie de esa solución para administrar a las células. Después de 72 h de incubación, se agregaron 10 µL de MTS/PMS (20:1) a cada pocillo y las células se incubaron durante 3 h más. La absorbancia de cada pocillo se midió a 490 nm utilizando un lector de placas CLARIOstar Plus (BMG Labtech GmbH, Ortenberg, Alemania). Los valores de absorbancia se representaron como el porcentaje de viabilidad celular, tomando como 100% el valor de las células control sin tratar.

5.4.2. Evaluación de la actividad antitumoral y antimetastásica en un modelo *in vivo* de cáncer de mama triple negativo

Los tumores de mama ortotópicos se indujeron mediante la inyección subdérmica de 3 x 10 6 células MDA-MB-231-Luc suspendidas en 100 µl de Matrigel (20 %) en la segunda mama izquierda de hembras NOD/SCID de seis semanas de edad seis semanas bajo anestesia inhalatoria (3% de isoflurano en 100% de oxígeno). El crecimiento tumoral se evaluó dos veces por semana utilizando un calibre electrónico para determinar el volumen tumoral. Considerando una forma de tumor esferoidal, el volumen del tumor (V) se obtuvo mediante la siguiente ecuación:

$$V = \frac{4}{3} \times \pi \times \left(\frac{h}{2} \times \frac{l}{2} \times \frac{w}{2} \right)$$

donde h es la altura del tumor, l es la longitud del tumor y w es el ancho del tumor.

Después de catorce días, cuando el volumen del tumor alcanzó 0.1 cm^3, los tratamientos se inyectaron a través de la vena de la cola dos veces por semana. Se inyectó DPBS como control. El tamaño del tumor y el peso del animal fueron monitorizados dos veces por semana. Cuando el tumor del grupo tratado con DPBS alcanzó el tamaño máximo autorizado ($1cm^3$), los animales se anestesiaron y recibieron una inyección subdérmica de 150 mg/Kg de D-luciferina 10 min antes de la eutanasia con CO_2. Se recolectó la sangre mediante punción intracardiaca con jeringas heparinizadas y se extrajeron los órganos principales y el tumor. Los pulmones se analizaron *ex vivo* para cuantificar la bioluminiscencia emitida por las células tumorales utilizando la tecnología IVIS®. Las imágenes se adquirieron utilizando la configuración automática de la cámara y los datos de bioluminiscencia se cuantificaron con el software Living Image (PerkinElmer, Japón) en fotones por segundo. Los datos se relativizaron al valor medio del control DPBS.

5.4.3. Evaluación de la actividad antimetastásica de los compuestos dirigidos a cerebro en un modelo de metástasis cerebral de cáncer de mama triple negativo

Este modelo se generó en ratones nu/nu (Harlan) atímicos hembra de cuatro a diez semanas de edad. La línea celular MDA-MB-231-BrM3 utilizada para establecer tumores cerebrales se encuentra descrita en literatura (18,53). Los tumores cerebrales se generaron inyectando 100 000 células MDA-MB-231-BrM3 en 100 μl de PBS en el ventrículo izquierdo de los ratones. Después de siete días, los tratamientos se inyectaron retro-orbitalmente dos veces por semana durante tres semanas (seis dosis). El crecimiento metastásico se analizó *in vivo* una vez por semana y *ex vivo* en el punto final experimental mediante detección de bioluminiscencia. Para ello, los ratones se anestesiaron con (anestesia inhalatoria) y se les inyectó retro-orbitalmente D-luciferina (150 mg/kg; Syd Labs) y se tomaron imágenes mediante IVIS® (Perkin Elmer, Japón). Los datos de bioluminiscencia se analizaron en el software Living Image, versión 4.5.

Cuatro horas antes del sacrificio, a los animales se les inyectó por vía intraperitoneal bromodesoxiuridina (BrdU, 40 mg/kg, B9285, Sigma-Aldrich). Se sacrificó a los animales y se tomaron imágenes de los cerebros y los pulmones mediante IVIS®.

6. Bibliografía

1.   Sung H, Ferlay J, Siegel RL, Laversanne M, Soerjomataram I, Jemal A, et al. Global Cancer Statistics 2020: GLOBOCAN Estimates of Incidence and Mortality Worldwide for 36 Cancers in 185 Countries. CA Cancer J Clin. 2021 May 4;71(3):209–49.

2.   Leone JP, Leone BA. Breast cancer brain metastases: the last frontier. Exp Hematol Oncol. 2015/11/24. 2015 Dec 24;4(1):33.

3.   Witzel I, Oliveira-Ferrer L, Pantel K, Müller V, Wikman H. Breast cancer brain metastases: biology and new clinical perspectives. Breast Cancer Res. 2016 Dec 19;18(1):8.

4.   Achrol AS, Rennert RC, Anders C, Soffietti R, Ahluwalia MS, Nayak L, et al. Brain metastases. Nat Rev Dis Prim. 2019 Dec 17;5(1):5.

5.   Waks AG, Winer EP. Breast Cancer Treatment. JAMA. 2019 Jan 22;321(3):288.

6.   Sharma P. Biology and Management of Patients With Triple-Negative Breast Cancer. Oncologist. 2016;21(9):1050–62.

7.   Prat A, Pineda E, Adamo B, Galván P, Fernández A, Gaba L, et al. Clinical implications of the intrinsic molecular subtypes of breast cancer. The Breast. 2015 Nov 1;24:S26–35.

8.   Januškevičienė I, Petrikaitė V. Heterogeneity of breast cancer: The importance of interaction between different tumor cell populations. Life Sci. 2019 Dec 15;239:117009.

9.   Lebert JM, Lester R, Powell E, Seal M, McCarthy J. Advances in the Systemic Treatment of Triple-Negative Breast Cancer. Curr Oncol. 2018 Jun 1;25(11):142–50.

10.   Tsang JYS, Tse GM. Molecular Classification of Breast Cancer. Adv Anat Pathol. 2020 Jan;27(1):27–35.

11.   Dai X, Li T, Bai Z, Yang Y, Liu X, Zhan J, et al. Breast cancer intrinsic subtype classification, clinical use and future trends. Am J Cancer Res. 2015;5(10):2929–43.

12.   Jitariu AA, Cimpean AM, Ribatti D, Raica M. Triple negative breast cancer: the kiss of death. Oncotarget. 2017;8(28):46652–62.

13.   Denkert C, Liedtke C, Tutt A, von Minckwitz G. Molecular alterations in triple-negative breast cancer-the road to new treatment strategies. Lancet. 2017;389(10087):2430–42.

14.   Gadi VK, Davidson NE. Practical Approach to Triple-Negative Breast Cancer. J Oncol Pr. 2017;13(5):293–300.

15. Bianchini G, Balko JM, Mayer IA, Sanders ME, Gianni L. Triple-negative breast cancer: challenges and opportunities of a heterogeneous disease. Nat Rev Clin Oncol. 2016;13(11):674–90.

16. Cardoso F, Harbeck N, Fallowfield L, Kyriakides S, Senkus E. Locally recurrent or metastatic breast cancer: ESMO Clinical Practice Guidelines for diagnosis, treatment and follow-up. Ann Oncol. 2012 Oct;23(SUPPL. 7):vii11–9.

17. Chen W, Hoffmann AD, Liu H, Liu X. Organotropism: new insights into molecular mechanisms of breast cancer metastasis. npj Precis Oncol. 2018 Dec 16;2(1):4.

18. Bos PD, Zhang XHF, Nadal C, Shu W, Gomis RR, Nguyen DX, et al. Genes that mediate breast cancer metastasis to the brain. Nature. 2009 Jun 6;459(7249):1005–9.

19. Witzel I, Oliveira-Ferrer L, Müller V. Brain Metastasis in Breast Cancer Patients—Need for Improvement. Cancers (Basel). 2020 Oct 30;12(11):3190.

20. Cerna T, Stiborova M, Adam V, Kizek R, Eckschlager T. Nanocarrier drugs in the treatment of brain tumors. J Cancer Metastasis Treat. 2016;2(10):407–16.

21. Mills MN, Figura NB, Arrington JA, Yu H-HM, Etame AB, Vogelbaum MA, et al. Management of brain metastases in breast cancer: a review of current practices and emerging treatments. Breast Cancer Res Treat. 2020 Apr 6;180(2):279–300.

22. Duro-Castano A, Conejos-Sanchez I, Vicent MJ. Peptide-Based Polymer Therapeutics. Polymers (Basel). 2014;6(2):515–51.

23. Duncan R. Polymer therapeutics at a crossroads? Finding the path for improved translation in the twenty-first century. J Drug Target. 2017 Nov 26;25(9–10):759–80.

24. Fang J, Islam W, Maeda H. Exploiting the dynamics of the EPR effect and strategies to improve the therapeutic effects of nanomedicines by using EPR effect enhancers. Adv Drug Deliv Rev. 2020 Jan 1;157:142–60.

25. Markman JL, Rekechenetskiy A, Holler E, Ljubimova JY. Nanomedicine therapeutic approaches to overcome cancer drug resistance. Adv Drug Deliv Rev. 2013 Nov;65(13–14):1866–79.

26. Kobayashi H, Turkbey B, Watanabe R, Choyke PL. Cancer Drug Delivery: Considerations in the Rational Design of Nanosized Bioconjugates. Bioconjug Chem. 2014 Dec 17;25(12):2093–100.

27. Theek B, Rizzo LY, Ehling J, Kiessling F, Lammers T. The theranostic path to personalized nanomedicine. Clin Transl Imaging. 2014 Feb 19;2(1):67–76.

28. Vicent MJ, Greco F, Nicholson RI, Paul A, Griffiths PC, Duncan R. Polymer therapeutics designed for a combination therapy of hormone-dependent cancer. Angew Chemie - Int Ed. 2005 Jun 27;44(26):4061–6.

29. Rasines Mazo A, Allison-Logan S, Karimi F, Chan NJ-A, Qiu W, Duan W, et al. Ring opening polymerization of α-amino acids: advances in synthesis, architecture and applications of polypeptides and their hybrids. Chem Soc Rev. 2020;49(14):4737–834.

30. Barz M, Duro-Castano A, Vicent MJ. A versatile post-polymerization modification method for polyglutamic acid: synthesis of orthogonal reactive polyglutamates and their use in "click chemistry." Polym Chem. 2013 Apr 24;4(10):2989.

31. Córdoba-David G, Duro-Castano A, Castelo-Branco RC, González-Guerrero C, Cannata P, Sanz AB, et al. Effective Nephroprotection Against Acute Kidney Injury

with a Star-Shaped Polyglutamate-Curcuminoid Conjugate. Sci Rep. 2020 Dec 1;10(1):1–15.

32. Conejos-Sánchez I, Cardoso I, Oteo-Vives M, Romero-Sanz E, Paul A, Sauri AR, et al. Polymer-doxycycline conjugates as fibril disrupters: An approach towards the treatment of a rare amyloidotic disease. J Control Release. 2015 Jan 28;198:80–90.

33. Cuesta CM, Ibañez F, Lopez-Hidalgo R, Ureña J, Duro-Castano A, Armiñán A, et al. A targeted polypeptide-based nanoconjugate as a nanotherapeutic for alcohol-induced neuroinflammation. Nanomedicine Nanotechnology, Biol Med. 2021 Jun 1;34:102376.

34. Dolz-Pérez I, Sallam MA, Masiá E, Morelló-Bolumar D, Pérez del Caz MD, Graff P, et al. Polypeptide-corticosteroid conjugates as a topical treatment approach to psoriasis. J Control Release. 2020 Feb;318:210–22.

35. Arroyo-Crespo JJ, Armiñán A, Charbonnier D, Balzano-Nogueira L, Huertas-López F, Martí C, et al. Tumor microenvironment-targeted poly-L-glutamic acid-based combination conjugate for enhanced triple negative breast cancer treatment. Biomaterials. 2018 Dec;186:8–21.

36. Duro-Castano A, Lim NH, Tranchant I, Amoura M, Beau F, Wieland H, et al. In Vivo Imaging of MMP-13 Activity Using a Specific Polymer-FRET Peptide Conjugate Detects Early Osteoarthritis and Inhibitor Efficacy. Adv Funct Mater. 2018 Sep 12;28(37):1802738.

37. Cheah HY, Gallon E, Dumoulin F, Hoe SZ, Japundžić-Žigon N, Glumac S, et al. Near-Infrared Activatable Phthalocyanine-Poly-L-Glutamic Acid Conjugate: Enhanced in Vivo Safety and Antitumor Efficacy toward an Effective Photodynamic Cancer Therapy. Mol Pharm. 2018 Jul 2;15(7):2594–605.

38. Arroyo-Crespo JJ, Deladriere C, Nebot VJ, Charbonnier D, Masiá E, Paul A, et al. Anticancer Activity Driven by Drug Linker Modification in a Polyglutamic Acid-Based Combination-Drug Conjugate. Adv Funct Mater. 2018 May 16;28(22):1800931.

39. Duro-Castano A, Nebot VJ, Niño-Pariente A, Armiñán A, Arroyo-Crespo JJ, Paul A, et al. Capturing "Extraordinary" Soft-Assembled Charge-Like Polypeptides as a Strategy for Nanocarrier Design. Adv Mater. 2017 Oct;29(39):1702888.

40. Niño-Pariente A, Armiñán A, Reinhard S, Scholz C, Wagner E, Vicent MJ. Design of Poly- <scp>l</scp> -Glutamate-Based Complexes for pDNA Delivery. Macromol Biosci. 2017 Oct 1;17(10):1700029.

41. Kiew LV, Cheah HY, Voon SH, Gallon E, Movellan J, Ng KH, et al. Near-infrared activatable phthalocyanine-poly-L-glutamic acid conjugate: increased cellular uptake and light–dark toxicity ratio toward an effective photodynamic cancer therapy. Nanomedicine Nanotechnology, Biol Med. 2017 May 1;13(4):1447–58.

42. Arroyo Crespo JJ. Polymer-based combination conjugates for the treatment of triple negative breast cancer : From rational design to preclinical evaluation. University of Valencia; 2018.

43. Markovsky E, Baabur-Cohen H, Satchi-Fainaro R. Anticancer polymeric nanomedicine bearing synergistic drug combination is superior to a mixture of individually-conjugated drugs. J Control Release. 2014 Aug 10;187:145–57.

44. Conejos-Sánchez I, Duro-Castano A, Birke A, Barz M, Vicent MJ. A controlled and versatile NCA polymerization method for the synthesis of polypeptides. Polym Chem. 2013;4(11):3182.

45. Duro-Castano A, England RM, Razola D, Romero E, Oteo-Vives M, Morcillo MA, et al. Well-defined star-shaped polyglutamates with improved pharmacokinetic profiles as excellent candidates for biomedical applications. Mol Pharm. 2015 Oct 5;12(10):3639–49.

46. Zagorodko O, Nebot VJ, Vicent MJ. The generation of stabilized supramolecular nanorods from star-shaped polyglutamates. Polym Chem. 2020 Feb 11;11(6):1220–9.

47. Pichot CS, Hartig SM, Xia L, Arvanitis C, Monisvais D, Lee FY, et al. Dasatinib synergizes with doxorubicin to block growth, migration, and invasion of breast cancer cells. Br J Cancer. 2009 Jul 9;101(1):38–47.

48. Duro-Castano A, Borrás C, Herranz-Pérez V, Blanco-Gandía MC, Conejos-Sánchez I, Armiñán A, et al. Targeting Alzheimer's disease with multimodal polypeptide-based nanoconjugates. Sci Adv. 2021 Mar 26;7(13):eabf9180.

49. Đorđević S, Gonzalez MM, Conejos-Sánchez I, Carreira B, Pozzi S, Acúrcio RC, et al. Current hurdles to the translation of nanomedicines from bench to the clinic. Drug Deliv Transl Res. 2021 Jul 23;1–26.

50. Cardoso F, Paluch-Shimon S, Senkus E, Curigliano G, Aapro MS, André F, et al. 5th ESO-ESMO international consensus guidelines for advanced breast cancer (ABC 5). Ann Oncol. 2020 Dec;31(12):1623–49.

51. Guo Q, Zhu Q, Miao T, Tao J, Ju X, Sun Z, et al. LRP1-upregulated nanoparticles for efficiently conquering the blood-brain barrier and targetedly suppressing multifocal and infiltrative brain metastases. J Control Release. 2019 Jun 10;303:117–29.

52. Khan NU, Ni J, Ju X, Miao T, Chen H, Han L. Escape from abluminal LRP1-mediated clearance for boosted nanoparticle brain delivery and brain metastasis treatment. Acta Pharm Sin B. 2021 May 1;11(5):1341–54.

53. Priego N, Zhu L, Monteiro C, Mulders M, Wasilewski D, Bindeman W, et al. STAT3 labels a subpopulation of reactive astrocytes required for brain metastasis article. Nat Med. 2018 Jul 1;24(7):1024–35.